Copyright

by

Widianto

2003

General Behavior of a Steel Trapezoidal Box-Girder during Construction

by

Widianto, B.S.C.E

Thesis

Presented to the Faculty of the Graduate School of

The University of Texas at Austin

in Partial Fulfillment

of the Requirements

for the Degree of

Master of Science in Engineering

The University of Texas at Austin

December 2003

General Behavior of a Steel Trapezoidal Box-Girder during Construction

Approved by
Supervising Committee:

Joseph A. Yura, Supervisor

Eric B. Williamson

For my Mom and Dad

with all my love and respect

Acknowledgements

First, I would like to extend my sincere appreciation and gratitude to Professor Joseph A. Yura for his guidance of my entire study. His advice and enlightened mentoring were inspiring and made this research a wonderful learning experience. Dr. Yura, thank you for all that you have taught me, not only about research but also about life in general. Thank you also for granting me an opportunity to work under your supervision. I would also like to thank Dr. Eric B. Williamson for his advice, ideas, and comments.

I am especially indebted to Daniel Popp for all his ideas and comments for my writing. He patiently proofread my entire thesis. This thesis would not have been completed without his ideas and humor. Daniel, thank you for your countless hours of hard work and your friendship.

I acknowledge the Texas Department of Transportation for their funding of this research project.

I am grateful to my fellow graduate students before me, Cem Topkaya and Brian Chen. Thank you for being my mentors. I would like to thank Ms. Larayne Dallas and all of the library staff for their help in my literature review.

Finally, I would like to thank my parents for all their love, support, and encouragement. And I wish to thank my closest friend, Thadea, for her support. All of you made all of the hard work worthwhile.

December 2003

Abstract

General Behavior of a Steel Trapezoidal Box-Girder during Construction

Widianto, M.S.E.

The University of Texas at Austin, 2003

Supervisor: Joseph A. Yura

During its lifetime, a composite box girder bridge experiences both construction and serviceability stages. The construction stage is the most critical design stage for box girders, since during this period they have lower torsional rigidity compared to the composite section and are very susceptible to cross-section distortion due to torsional loading. Recent failures of box girders, ranging from buckling of bracing members to complete collapse, all happened during construction, indicating that the behavior of box girders during construction is not yet well understood.

Currently, design specifications do not provide designers with sufficient guidance regarding the behavior of box girders during construction. This thesis provides additional information about girder behavior during construction by presenting the results of parametric studies using a finite element computer program. Available hand methods are also presented. The required internal diaphragm spacing for limiting cross-section distortion and distortional normal stress is provided. The effect of using different top lateral bracing systems during monolithic and sequenced concrete pours on bracing forces, girder deformations, and normal stresses are presented. The sources of bracing forces, girder

deformations, and total normal stresses are explained. Based on the parametric studies, recommendations for the optimal top lateral bracing system and pouring sequence with regard to top lateral bracing forces, girder stresses and deformations are discussed.

Table of Contents

CHAPTER 1 INTRODUCTION 1

1.1 General……..... 1

1.2 Box Girder Versus I-Girder 2

1.3 Composite Box Girder during Construction Stage 4

1.3.1 Historical failure cases 5

1.3.2 Lack of guidance for designers..... 6

1.4 UTRAP Program Description 8

1.5 Review of Literature..... 8

1.6 Purpose and Scope.....11

1.7 Organization..…..14

CHAPTER 2 BASIC THEORY OF THIN-WALLED BEAMS.....16

2.1 Vertical bending.....16

2.1.1 Normal stress due to vertical bending.....17

2.1.2 Shear stresses due to vertical bending.....18

2.1.3 Shear lag effect.....20

2.2 Torsion……. 21

2.2.1 Pure torsion (Saint-Venant torsion) 22

2.2.2 Warping torsion 25

2.2.3 Total resistance to a torsional moment.....30

2.3 Distortion…….....31

CHAPTER 3 CROSS-SECTIONAL FORCES.....34

3.1 Straight Girders.....34

3.2 Curved Girders.....36

3.2.1 Exact solution.....37

3.2.2 Approximate solutions.....44

3.2.2.1 Shear force.....44

3.2.2.2 Midspan bending moment.....44

3.2.2.3 Support torque.....46

3.2.2.4 M/R Method.....48

3.2.3 Comparisons between approximate solution and exact solution.....49

3.3 Continuous Girder.....54

3.3.1 Shear force.....56

3.3.2 Bending moment.....56

3.3.3 Torsional moment.....61

3.4 Summary…… 65

CHAPTER 4 CROSS-SECTION PROPERTIES.....67

4.1 Flexural Properties.....67

4.2 Shear Center.....70

4.2.1 Force method.....71

4.2.2 Numerical method.....73

4.2.3 Comparison between force method and numerical method results.....73

4.2.4 Shear center location of thin-walled closed section.....74

4.3 Pure Torsional Constant.....75

4.4 Torsional Warping Function.....75

4.5 Warping Moment of Inertia.....84

4.6 Warping Shear Parameter and Central Second Moment of Area.....88

4.7 Sample Calculations of Cross-section Properties.....89

4.7.1 Centroidal axis and moment of inertia.....91

4.7.2 Shear center location....94
4.7.3 Pure torsional constant....98
4.7.4 Torsional warping function....99
4.7.5 Warping moment of inertia....99
4.7.6 Warping shear parameter and central second moment of area....102
4.7.7 Parameter *X*....103

CHAPTER 5 BEHAVIOR OF A STRAIGHT GIRDER....104

5.1 Vertical Deflection Prediction using Classical Beam Theory....104
5.1.1 Shear deformation....107

5.2 Behavior of an Open-section Straight Girder....113
5.2.1 Preventing Bending Distortion....117
5.2.2 Required strut spacing....120

5.3 Behavior of A Pseudo-closed Section Straight Girder....124
5.3.1 Localized normal stress in the X-type system....126
5.3.2 Localized normal stress in Alternating-Diagonal system....127
5.3.3 Localized normal stress in the Single-Diagonal system....130

5.4 Summary....131

CHAPTER 6 BEHAVIOR OF A CURVED GIRDER....133

6.1 Vertical Deflection and Rotation....133
6.1.1 Analytical....133
6.1.2 Verification....137
6.1.3 Parametric study....140

6.2 Lateral Displacement....146
6.2.1 Lateral displacement of the top flanges....149
6.2.2 Lateral displacements of the bottom flange....151
6.2.3 Lateral displacement of the support....152
6.2.3.1 Analytical prediction of support lateral displacement....154
6.2.3.2 Verification....157

6.3 Cross-section Distortion....158
6.3.1 Existing recommendations for internal diaphragm spacing and area....161
6.3.2 Effect of internal diaphragms on total rotation....165
6.3.2.1 Parametric studies....168
6.3.3 Effect of internal diaphragm on the diagonal lengths....173
6.3.3.1 Parametric studies....175
6.3.4 Effect of changing plate thickness and cross-section dimensions....178
6.3.5 Cross-section distortion in a continuous girder....183
6.4 Summary…… 186

CHAPTER 7 WARPING NORMAL STRESSES....188

7.1 Analytical Method....189
7.2 Verification… 193
7.2.1 Open section....193
7.2.2 Pseudo-closed section....196
7.3 Parametric Studies....200
7.4 Warping Normal Stress in a Continuous Girder....210
7.5 Summary…… 215

CHAPTER 8 DISTORTIONAL NORMAL STRESS....216

8.1 Source of Distortional Normal Stress....216
8.2 UTRAP Solution for Distortional Normal Stress....219
8.3 Effect of The Internal Diaphragm....222
8.4 Parametric Studies....223
8.5 Distortional Normal Stress in a Continuous Girder....230
8.6 Development of Design Recommendation....232
8.6.1 Analytical modeling....232
8.6.2 Design recommendation and comparison to the existing recommendation....241

8.7 Summary…… 243

CHAPTER 9 TOP LATERAL BRACING FORCE 245

9.1 Top Lateral Bracing Force from The Horizontal Component of The Applied Load ..246
9.1.1 X-type top lateral bracing system 246
9.1.2 Alternating-Diagonal top lateral bracing system 248
9.1.3 Single-Diagonal top lateral bracing system 248

9.2 Top lateral bracing force due to vertical bending 248
9.2.1 X-Type lateral bracing system 253
9.2.1.1 Modification of top flange areas 257
9.2.2 Alternating-Diagonal top lateral bracing system 258
9.2.3 Single-Diagonal top lateral bracing system 261
9.2.4 Verifications of top lateral bracing forces formulas 261

9.3 Top Lateral Bracing Forces due to Torsional Moment 266
9.3.1 X-type top lateral bracing system 270
9.3.2 Alternating-Diagonal top lateral bracing system 273
9.3.3 Single-Diagonal top lateral bracing system 275

9.4 Total Axial Forces in Top Lateral Bracing Members of a Simply-Supported Curved Trapezoidal Box Girder 277

9.5 Summary…… 281

CHAPTER 10 CONTINUOUS CURVED GIRDER BEHAVIOR UNDER A UNIFORM LOAD 283

10.1 Analysis I…… 285
10.1.1 Top lateral bracing forces 287
10.1.2 Sample calculations of the forces in top lateral bracing member… 291
10.1.2.1 X-type top lateral bracing system 291
10.1.2.2 Alternating-Diagonal top lateral bracing system 295
10.1.2.3 Single-Diagonal top lateral bracing system 299
10.1.3 Deformation 301
10.1.4 Total normal stresses 305

10.2 Analysis II…..306
10.2.1 Designing top lateral bracing members.....307
10.2.2 Top lateral bracing forces.....308
10.2.3 Deformation 310
10.2.4 Total normal stresses.....315
10.3 Analysis III….316
10.3.1 Top lateral bracing forces.....317
10.3.2 Deformation 319
10.3.3 Total normal stress.....320
10.4 Summary…… 322
CHAPTER 11 CONTINUOUS CURVED GIRDER BEHAVIOR DURING THE POURING SEQUENCE 323
11.1 Pouring Sequence A 324
11.1.1 Case A-1….....324
11.1.1.1 Diagonal forces 324
11.1.1.2 Strut forces 330
11.1.1.3 Deformation.....333
11.1.1.4 Total normal stress 337
11.2 Change in Top Diagonal Size.....339
11.3 Change in Pouring Sequence.....341
11.3.1 Diagonal forces.....345
11.3.2 Strut forces.. 347
11.3.3 Summary… 347
11.4 Summary…… 351
CHAPTER 12 CONCLUSIONS AND FUTURE RESEARCH 353
12.1 Conclusions….....353
12.1.1 Cross-sectional forces 353
12.1.2 Internal diaphragm spacing 354

12.1.3 Top lateral bracing system....354
12.1.3.1 Member forces....354
12.1.3.2 Girder deformations....355
12.1.3.3 Normal stresses....356
12.1.3.4 Recommendation....357
12.1.4 Pouring sequence....358
12.2 Future Research....358

APPENDIX A DETERMINATION OF LOCAL PLATE BENDING STRESS....360

APPENDIX B DERIVATION OF SUPPORT TORQUE AND MIDSPAN BENDING MOMENT....364

B.1 Support Torque....364
B.2 Midspan Bending Moment....367

APPENDIX C DETERMINATION OF TORSIONAL MOMENTS IN CONTINUOUS CURVED GIRDER USING THE M/R METHOD....369

APPENDIX D EQUIVALENT PLATE THICKNESS FORMULAS....375

APPENDIX E DETERMINING SHEAR CENTER LOCATION OF AN OPEN-SECTION TRAPEZOIDAL BOX GIRDER....378

E.1 Force Method....378
E.2 Numerical Method....386

APPENDIX F TABLE FOR AREA INTEGRATION OF TWO LINEAR FUNCTIONS....392

REFERENCES....393

VITA....398

List of Tables

Table 2-1 Pure and Warping Torsional Predominance 31
Table 3-1 Comparison of UTRAP results with exact and approximate method to estimate midspan bending moment....51
Table 3-2 Comparison of UTRAP results with exact and approximate method to estimate support torque....53
Table 3-3 Analysis cases to study the effect of the central angle on the cross-sectional forces....55
Table 3-4 Analysis cases to study the effect of the ratio of EI/GJ on the cross-sectional forces 56
Table 4-1 Tabular method for making the torsional warping function diagram 77
Table 4-2 Visual integration technique for $\int_A \hat{\omega}_A x dA$ 83
Table 4-3 Integration for $\int_A \left(w(s)_{open}\right)^2 dA$ 86
Table 4-4 Integration for $\int_A \left(w(s)_{pseudo-closed}\right)^2 dA$ 87
Table 6-1 Diagonal area of the 2-ft panel the X-type system and the corresponding equivalent plate thickness....142
Table 6-2 Diagonal area for each top lateral bracing system and the corresponding equivalent plate thickness 142
Table 6-3 Required ratio of span length to internal diaphragm spacing recommended by Yabuki and Arizumi (1989) 163
Table 6-4 Analysis cases to study internal diaphragm spacing....171
Table 6-5 Existing recommendations for the maximum internal diaphragm spacing 172
Table 7-1 Areas of diagonal members corresponding to equivalent plate thicknesses....206
Table 8-1 Lateral load component due to curvature 229
Table 9-1 Vertical bending properties for the X-type system....265
Table 9-2 Vertical bending properties for the Alternating-Diagonal system....266
Table 10-1 Member size and the corresponding equivalent plate thickness used in Analysis I....287
Table 10-2 Summary of the maximum diagonal forces 288
Table 10-3 Summary of the maximum strut forces....290
Table 10-4 Accuracy of analytical solution for diagonal forces- X-type system....294
Table 10-5 Accuracy of analytical solution for diagonal forces – Alternating-Diagonal system .298
Table 10-6 Accuracy of analytical solution for diagonal forces – Single-Diagonal system....300
Table 10-7 Maximum total normal stresses 306
Table 10-8 Maximum total normal stresses in Model 3 with support A pinned....306
Table 10-9 Properties of the top lateral system used in Analysis II....308
Table 10-10 Maximum rotation in Analysis I and Analysis II 311
Table 10-11 Maximum total normal stresses....321
Table 11-1 Member sizes used in Case A-2....339
Table 11-2 Summary of maximum results 350
Table D-1 Equivalent plate thickness for different types of top lateral bracing systems....376
Table E-1 Required input to determine shear center using numerical method 389
Table E-2 Numerical example to find shear center for Model 1....391
Table F-1 Table of area integration of two functions F1 and F2: $\int_A F_1 F_2 dA$ 392

List of Figures

Figure 1.1 Cross section of the composite steel box girder (US Steel, 1978)..... 1
Figure 1.2 Bracing systems in a box girder during construction 4
Figure 1.3 Failure of Milford Haven bridge in June 1970 (Flint, 2001)..... 5
Figure 1.4 Failure of bracing member during construction (Chen, 2002)..... 6
Figure 1.5 Cross-section dimensions of trapezoidal box girder models.....13
Figure 1.6 Types of top lateral bracing system.....14
Figure 1.7 Inverted K-frame internal diaphragm.....14
Figure 2.1 Normal stress distribution due to vertical bending.....18
Figure 2.2 Shear stress distribution due to vertical bending.....19
Figure 2.3 Variation of bending normal stress including shear lag effect 20
Figure 2.4 Condition of rectangular hollow cross-section that does not warp under torsion (Boresi et.al, 1978) 21
Figure 2.5 Shear stress distribution on open and closed sections due to pure torsional moment T_t24
Figure 2.6 Warping deformation 27
Figure 2.7 End bimoment and warping normal stress.....28
Figure 2.8 Saint-Venant torsional and distortional components due to curvature effect.....32
Figure 2.9 Distribution of distortional normal stress 33
Figure 2.10 Distortional deformation and local plate bending moment 33
Figure 3.1 Torsional force diagram of a straight girder under a concentrated torsional loading 35
Figure 3.2 Simply supported curved girder under a uniformly distributed load p 36
Figure 3.3 Comparison of shear force between UTRAP and closed-form solutions.....39
Figure 3.4 Comparison of bending moment between UTRAP and closed-form solutions.....40
Figure 3.5 Comparison of total torsional moment between UTRAP and closed-form solutions....40
Figure 3.6 Simply supported curved girder under the uniform load 41
Figure 3.7 Plan view of curved girder (Memberg 2002).....46
Figure 3.8 Approximating a curved girder with a straight girder from a torsional point of view ...47
Figure 3.9 Percentage of error of the midspan bending moment obtained from approximate method 50
Figure 3.10 Shear force diagram of three-span continuous girder 57
Figure 3.11 Bending moment diagram of a straight continuous girder.....57
Figure 3.12 Bending moment diagram with EI/GJ=3.96 59
Figure 3.13 Bending moment with EI/GJ=12.....59
Figure 3.14 Bending moment diagram with central angle of 61° 60
Figure 3.15 Bending moment diagram with central angle of 122° 60
Figure 3.16 Torsional moment diagram.....62
Figure 3.17 Torsional moment diagram with central angle of 61°.....63
Figure 3.18 Torsional moment diagram with central angle of 122°.....63
Figure 3.19 Approximate and real torsional moment diagram 64
Figure 4.1 Notations for a trapezoidal box girder.....68
Figure 4.2 Shear stress distribution and shear flow in an open-section trapezoidal girder.....72
Figure 4.3 Representation of an open-section vertical web girder.....77
Figure 4.4 Torsional warping function diagram of an open-section vertical web girder.....78
Figure 4.5 Torsional warping function diagram for an open-section trapezoidal box girder.....79
Figure 4.6 Simplified pseudo-closed section of trapezoidal box girder with.....80
Figure 4.7 ω_A diagram for a pseudo-closed section 81
Figure 4.8 $\omega^{\wedge}_A$ diagram and x diagram of pseudo-closed trapezoidal box girder 82
Figure 4.9 Torsional warping function of pseudo-closed section 84

Figure 4.10 Perpendicular distance from a shear center to each element....89
Figure 4.11 Top lateral bracing system configuration and dimensions Model 1....90
Figure 4.12 Sectorial area diagram for the open-section....96
Figure 4.13 Reduced sectorial area diagram and x diagram for the pseudo-closed section....97
Figure 4.14 Torsional warping function of the open-section....100
Figure 4.15 Torsional warping function of the pseudo-closed....101
Figure 5.1 Type of top lateral bracing system used in each analysis case....105
Figure 5.2 Predicted vertical deflections and UTRAP solutions....106
Figure 5.3 Shear force diagram....108
Figure 5.4 Cross-section dimensions of Model 4 girder....109
Figure 5.5 Analysis case for UTRAP and hand calculation....110
Figure 5.6 Dimension of I girder....110
Figure 5.7 Midspan deflection and percent discrepancies between the predicted midspan deflection and the UTRAP solution....112
Figure 5.8 Bending distortion of an open-section trapezoidal box girder....113
Figure 5.9 Horizontal load component due to sloping webs....114
Figure 5.10 Nodes locations where deflections can be extracted from the UTRAP output....114
Figure 5.11 Horizontal deflection of the open-section....115
Figure 5.12 Deformed position at the midspan of an open-section....116
Figure 5.13 Normal stress in the open-section of Model 1 straight girder....117
Figure 5.14 Using struts with 10-ft spacing to prevent bending distortion....118
Figure 5.15 Total normal stress in the top flanges of the open-section....119
Figure 5.16 Horizontal displacement of the top flange of the open-section....119
Figure 5.17 Deformed position 86 ft from the left support of the open-section....120
Figure 5.18 Total normal flange stress with a 30-ft strut spacing....121
Figure 5.19 Additional normal stress at the tip of the top flanges....123
Figure 5.20 Additional normal stress at the tip of the top flanges....124
Figure 5.21 UTRAP solutions for vertical deflections....125
Figure 5.22 Bending normal stress of the open and pseudo-closed sections....126
Figure 5.23 Total normal stress variation on the top flange - X-type system....127
Figure 5.24 Total normal stress variation on the top flange - Alternating-Diagonal....128
Figure 5.25 Horizontal displacement of the right top flange with X-type and Alternating-Diagonal systems....129
Figure 5.26 Horizontal displacement of the top flange - Single-Diagonal....130
Figure 5.27 Total normal stress variation on the top flange - Single-Diagonal....131
Figure 6.1 Simply supported curved girder under a uniform load p....134
Figure 6.2 Cross-section rotation....136
Figure 6.3 X-type top lateral bracing system....137
Figure 6.4 Vertical deflections of Model 1 curved girder....138
Figure 6.5 Rotations of a pseudo-closed section curved girder....139
Figure 6.6 Rotations of an open-section curved girder....139
Figure 6.7 Effects of equivalent plate thickness on maximum vertical deflection....141
Figure 6.8 Effects of equivalent plate thickness on maximum rotation....141
Figure 6.9 Vertical deflection with different top lateral bracing systems....143
Figure 6.10 Rotation with different top lateral bracing systems....144
Figure 6.11 Rotation with the equivalent plate thickness of 0.03 in and using 10-ft panel....146
Figure 6.12 Lateral displacements of the top and the bottom flanges from UTRAP....147
Figure 6.13 Corrected lateral displacements of the top and bottom flanges....148
Figure 6.14 Lateral displacements of the top flanges....149
Figure 6.15 Lateral displacements with the 2-ft panel and the 10-ft panel of the Single-Diagonal system....150

Figure 6.16 Lateral displacements of the bottom flange 151
Figure 6.17 UTRAP solutions for support lateral displacements..... 153
Figure 6.18 Lateral displacement of an end support of the "U.S 290-Bridge" 154
Figure 6.19 Plan view of an out-of-plane warping displacement of the bottom flange..... 155
Figure 6.20 Plan view of the lateral displacement of the bottom flange 157
Figure 6.21 Total deformation at the midspan..... 159
Figure 6.22 Deformation at midspan due to distortion..... 160
Figure 6.23 Existing recommendations for internal diaphragm spacing 164
Figure 6.24 Total rotations of the bottom and the top flanges 165
Figure 6.25 Effect of internal diaphragm spacing on total rotation..... 167
Figure 6.26 Distortional rotations..... 167
Figure 6.27 Maximum distortional rotation as a function of an internal diaphragm spacing 169
Figure 6.28 Ratio of the maximum distortional rotation to the maximum rigid body rotation 170
Figure 6.29 Effect of s/L on distortional rotation 170
Figure 6.30 Effect of central angle on the ratio of the distortional rotation to the rigid body rotation 173
Figure 6.31 Diagonal lengths of a trapezoidal box girder 174
Figure 6.32 Change in diagonal lengths due to distortion 174
Figure 6.33 Change in right diagonal length due to distortion 175
Figure 6.34 Effect of diaphragm spacing on change in diagonal length 176
Figure 6.35 Ratio of the maximum change in diagonal length change due to distortion to the midspan vertical deflection 177
Figure 6.36 Effect of central angle on the ratio of the maximum change in a diagonal length to the midspan vertical deflection 178
Figure 6.37 Effect of changing the web thickness on the maximum distortional rotation and the maximum change in diagonal length 180
Figure 6.38 Maximum distortional rotation and maximum change in a diagonal length due to distortion for Model 1 and Model 3..... 181
Figure 6.39 Effect of changing the cross-section dimensions 182
Figure 6.40 Rigid body and distortional rotation of a two-equal-span 180-ft continuous curved girder 183
Figure 6.41 Ratio of the distortional rotation to the rigid body rotation..... 184
Figure 6.42 Ratio of the maximum change in a diagonal length to the maximum vertical deflection 185
Figure 7.1 X-type top lateral bracing system..... 188
Figure 7.2 Model 1 torsional properties - open section..... 191
Figure 7.3 Model 1 torsional properties - pseudo-closed section 191
Figure 7.4 Bimoment distribution for a simply supported curved girder 192
Figure 7.5 Predicted warping normal stress distribution 192
Figure 7.6 Node locations from UTRAP..... 193
Figure 7.7 Total and bending normal stress variation - open section..... 194
Figure 7.8 Warping normal stress variation – Open section..... 195
Figure 7.9 Distribution of warping normal stresses at midspan – open section..... 196
Figure 7.10 Total and bending normal stress variations - pseudo-closed..... 197
Figure 7.11 Warping normal stress for the open and pseudo-closed sections 198
Figure 7.12 Warping normal stress variation - pseudo-closed section 198
Figure 7.13 Distribution of the warping normal stresses at midspan – pseudo-closed section 199
Figure 7.14 Warping normal stresses for different equivalent plate thicknesses 201
Figure 7.15 Midspan bimoment..... 203
Figure 7.16 Torsional warping function..... 203
Figure 7.17 Warping moment of inertia..... 204

Figure 7.18 Effect of different top lateral bracing systems – t_{eq}=0.05 in.....205
Figure 7.19 Effect of different top lateral bracing systems – t_{eq}=0.01 in.....205
Figure 7.20 Maximum warping normal stress as a function of the equivalent plate thickness.....207
Figure 7.21 Variation of the maximum warping normal stress as a function of the central angle 209
Figure 7.22 Ratio of midspan warping normal stress to midspan bending normal stress.....210
Figure 7.23 Bending normal stress - two-equal-span 180-ft continuous girder.....212
Figure 7.24 Warping normal stress - two-equal-span 180-ft continuous girder.....212
Figure 7.25 Bending stress - three-equal-span 180-ft continuous girder.....213
Figure 7.26 Warping stress - three-equal-span 180-ft continuous girder 214
Figure 8.1 Bending normal stresses in the flanges of a curved girder.....217
Figure 8.2 Imaginary horizontal loads due to curvature.....218
Figure 8.3 Distribution of distortional normal stress 218
Figure 8.4 Variation of total and bending normal stresses - No internal diaphragm.....220
Figure 8.5 Variations of warping and distortional normal stresses - No internal diaphragm.....221
Figure 8.6 Variation of total and bending normal stresses - one internal diaphragm.....222
Figure 8.7 Variations of warping and distortional normal stresses - one internal diaphragm.....224
Figure 8.8 Effect of internal diaphragm area on the distortional normal stress 225
Figure 8.9 Effect of t_{eq} on the midspan distortional normal stress 226
Figure 8.10 Effect of web thickness on the midspan distortional normal stress 226
Figure 8.11 Ratio of the midspan distortional normal stress to the midspan bending normal stress 227
Figure 8.12 Effect of central angle on the ratio of distortional normal stress to bending normal stress 228
Figure 8.13 Ratio of the distortional normal stress to the bending normal stress in Model 1 and Model 3.....230
Figure 8.14 Warping and distortional normal stress in a two-equal-span continuous girder.....231
Figure 8.15 Distortional normal stress and the ratio of distortional to bending normal stresses in a continuous and a simply-supported girder 233
Figure 8.16 Simplified model of top and bottom flanges between two internal diaphragms.....235
Figure 8.17 Distortional normal stresses on the top and bottom flanges.....237
Figure 8.18 Distortional normal stress at the junction of the top flange and the web 238
Figure 8.19 Distortional normal stresses at the tip of the top flange.....238
Figure 8.20 Distortional normal stress at the edge of the bottom flange.....239
Figure 8.21 Variation of distortional normal stresses that cannot be predicted analytically.....240
Figure 8.22 Proposed and existing recommendations for diaphragm spacing.....243
Figure 9.1 Elongation of both struts and diagonals.....247
Figure 9.2 SAP 2000 Model of top flanges and top lateral bracing system.....250
Figure 9.3 Loading conditions to simulate the effect of vertical bending in a straight girder 250
Figure 9.4 Deflected shapes of top lateral bracing system under loading shown in Figure 9.3 (Scale factor : 100).....252
Figure 9.5 Top lateral bracing forces due to vertical bending 254
Figure 9.6 Interactive forces Q between top lateral bracing members and top flanges in X-type system 255
Figure 9.7 Elongation of diagonal in a panel of X-type system.....256
Figure 9.8 Resistance to the bending moment.....257
Figure 9.9 Interactive forces Q between top lateral bracing members and top flanges in Alternating-Diagonal system.....259
Figure 9.10 Relative deflection between two consecutive panels in Alternating-Diagonal system 260
Figure 9.11 UTRAP analysis cases and top lateral bracing systems.....262

Figure 9.12 Top lateral bracing forces in a straight trapezoidal box girder....264
Figure 9.13Top lateral bracing forces in the X-type system....265
Figure 9.14 Torsional analysis of a pseudo-closed section using the Equivalent Plate Method ...267
Figure 9.15 Forces on top lateral bracing members due to uniform torsional moment....268
Figure 9.16 Orientations of diagonal type 1 and diagonal type 2 270
Figure 9.17 Top lateral bracing forces in X-type system due to uniform torsional moment 271
Figure 9.18 Unbalanced diagonal forces in two-adjacent panels of X-type system....272
Figure 9.19 Top lateral bracing forces in Single-Diagonal system due to torsional moment....273
Figure 9.20 Simplified model of two-adjacent panels in Alternating-Diagonal system under the y-component of unbalanced diagonal forces 274
Figure 9.21 Top lateral bracing forces in Single-Diagonal system due to uniform torsional moment 276
Figure 9.22 Torsional moment diagram....278
Figure 9.23 Top lateral bracing forces in a curved trapezoidal box girder....279
Figure 10.1 Cross-section dimension of Model 3 girder....284
Figure 10.2 Top lateral bracing systems used in the analyses 285
Figure 10.3 Bending moment diagram....286
Figure 10.4 Torsional moment diagram....286
Figure 10.5 Diagonal forces – Analysis I....289
Figure 10.6 Strut Forces – Analysis I 290
Figure 10.7 Properties of the X-type top lateral bracing system....292
Figure 10.8 Properties of the Alternating-Diagonal top lateral bracing system....295
Figure 10.9 Properties of the Single-Diagonal top lateral bracing system 299
Figure 10.10 Rotation – Analysis I....301
Figure 10.11 Deflections - Analysis I 303
Figure 10.12 Horizontal displacements with the exterior support pinned....304
Figure 10.13 Diagonal forces for Analysis I and II....309
Figure 10.14 Strut forces for Analysis I and II....310
Figure 10.15 Rotation - Analysis II 311
Figure 10.16 Deflections – Analysis II 313
Figure 10.17 Deformed position at the midspan (at 320 ft from support A) 314
Figure 10.18 Horizontal displacements with the exterior support pinned....315
Figure 10.19 Comparison of total normal stresses from Analysis I and II 316
Figure 10.20 Diagonal forces – Analysis III 318
Figure 10.21 Strut forces – Analysis III....319
Figure 10.22 Rotation – Analysis III 320
Figure 10.23 Horizontal displacements – Analysis III....321
Figure 11.1 Pouring sequence A....325
Figure 11.2 Total diagonal forces after each pour – effect of concrete stiffness 326
Figure 11.3 Total diagonal forces after each pour 326
Figure 11.4 Diagonal force envelopes – Alternating-Diagonal 328
Figure 11.5 Diagonal force envelopes – Single-Diagonal....329
Figure 11.6 Envelope of tensile and compressive strut forces....331
Figure 11.7 Strut force envelopes - Alternating-Diagonal 332
Figure 11.8 Strut force envelopes - Single-Diagonal....332
Figure 11.9 Rotations of the bottom flange along the length....334
Figure 11.10 Vertical deflections along the length 335
Figure 11.11 Horizontal displacement along the length....336
Figure 11.12 Maximum total normal stresses with Alternating-Diagonal system 337
Figure 11.13 Maximum total normal stresses with Single-Diagonal system....338
Figure 11.14 Rotation of the bottom flange along the length....340

Figure 11.15 Horizontal displacement along the length....342
Figure 11.16 Pouring sequence B....343
Figure 11.17 Pouring sequence C....344
Figure 11.18 Envelope of tensile and compressive diagonal forces – Sequence B....346
Figure 11.19 Envelope of tensile and compressive diagonal forces – Sequence C....346
Figure 11.20 Envelope of tensile and compressive strut forces – Sequence B....348
Figure 11.21 Envelope of tensile and compressive strut forces – Sequence C....348
Figure A.1 Distortional deformation and local plate bending moment....360
Figure A.2 Simplified model under a horizontal load....361
Figure B.1 Simply-supported curved girder under the uniform load....364
Figure C.1 Bending moment diagram....370
Figure C.2 M/R loadings on the left exterior and interior spans....371
Figure C.3 Decomposition of the M/R loading into parabolic and straight line components....372
Figure C.4 Torsional moments of the girder....373
Figure C.5 Torsional moments in the left exterior and interior spans....374
Figure D.1 Angle of shear in the panel of equivalent wall element and panel of bracing....375
Figure E.1 Notations for an open-section trapezoidal box girder....379
Figure E.2 Shear stress distribution and shear flow in an open trapezoidal cross-section....380
Figure E.3 Shear stress diagram along the sloping web....381
Figure E.4 Perpendicular distance from sloping web to the shear center....385
Figure E.5 Selected element's flow vector on open-section trapezoidal box girder....387
Figure E.6 Cross-section dimension of the open-section of Model 1....388

CHAPTER 1
Introduction

1.1 GENERAL

In general, there are two types of steel box girders: all-steel box girders and composite steel box girders. All-steel box girders utilize steel plates for the bottom flange and webs and use an orthotropic steel deck as the top flange. The composite box girder, shown in Figure 1.1, consists of a steel box girder topped by a cast–in-place concrete slab. The concrete deck acts compositely with the steel box girder by means of shear studs on the top flanges. Only the composite box girder is discussed in this thesis.

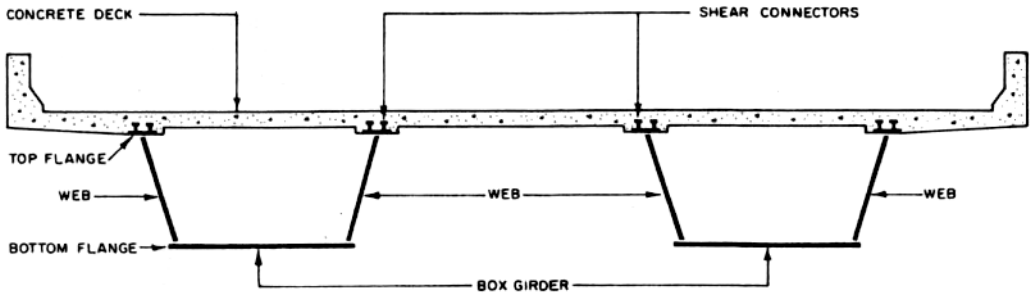

Figure 1.1 Cross section of the composite steel box girder (US Steel, 1978)

American steel box girder designs generally use a box girder with inclined webs as shown in Figure 1.1, instead of a rectangular box shape. For this reason, the girder is known as a trapezoidal box girder. Compared to the rectangular box shape, the trapezoidal shape uses less steel because the inclined webs allow a

narrower and more efficient bottom flange that permits reduction of steel in regions of low stress (Hall, 1997). In addition, the trapezoidal shape incorporates a much narrower and more compact flange (i.e. smaller width to thickness ratio) that requires less stiffening. From a fabrication standpoint, the trapezoidal shape is more practical than the rectangular box with regard to welding inside.

During its lifespan, a composite box girder experiences several stages. In the shop fabrication stage before top lateral bracings are attached, the steel box girder is an open section U-shape girder. The addition of a top lateral bracing system in the shop stabilizes the top flanges during transport and erection. The section is classified as a steel pseudo-closed box section during this stage. After the deck forms are attached and the concrete deck poured and cured, the section becomes a very stiff composite closed box section. This thesis is limited to the behavior of open and pseudo-closed section of steel box girder during construction.

1.2 BOX GIRDER VERSUS I-GIRDER

The behavior of I-girder systems is now relatively well understood, allowing them to be used more frequently. Even though the behavior of box girder systems is not yet fully understood, box girders have many advantages over I-girders, leading to their increasing popularity.

Some advantages of box girders over I-girders are as follows:

- Box girders have a superior torsional behavior to I-girders. The closed cross-sections of box girders have much higher torsional stiffness, which is often 100 to 1000 times larger than in the comparable I-girders. This feature makes box girders preferable for curved bridges.

- Box girder bridges require less maintenance because of their protected interior and smooth exterior. The smooth exterior reduces the potential corrosion problems in box girders, since corrosion in steel bridges typically occurs in regions where water and debris can collect.
- Box girder bridges have a low profile, which is beneficial in resisting wind-induced vibrations in long span bridges. In addition, the low profile of box girders is also beneficial for satisfying the minimum vertical clearance in metropolitan areas.
- Box girder bridges are usually lighter than comparable I-girder bridges because of their hollow structure.
- In dealing with the bending stress, using a wide, properly stiffened bottom flange with a reasonable thickness in box girder bridges is a better solution than using a very thick plate or a large number of plates in I-girder bridges.
- Under service loading, the multiple box girders exhibit better behavior than I-girders, as traffic loads are more efficiently distributed to girders in the lateral direction due to the large torsional stiffness of the individual boxes. (Helwig and Fan, 2000).

However, during transport, erection, and construction, the box girder consists of a pseudo-closed section with much lower torsional stiffness than that of the completed composite box system. This is a major problem during the early stages of curved bridge construction, when the girders are subjected to relatively large torques from loading of wet concrete during the deck pours. The following section discusses the construction stage of a trapezoidal box girder in more detail.

1.3 COMPOSITE BOX GIRDER DURING CONSTRUCTION STAGE

In a single box girder system, the most important bracing systems for improving its stability are top lateral bracing and internal diaphragm bracing systems. Top lateral bracing systems effectively close the cross section (i.e. make a pseudo-closed section) and enable the curved girders to resist large torsional moments from construction loads. In addition, they are also effective in increasing the buckling capacity of the top flanges (Chen, 1999). Internal diaphragm bracing systems prevent cross-section distortion and limit additional normal stress due to distortion. Figure 1.2 shows bracing systems in a box girder during construction.

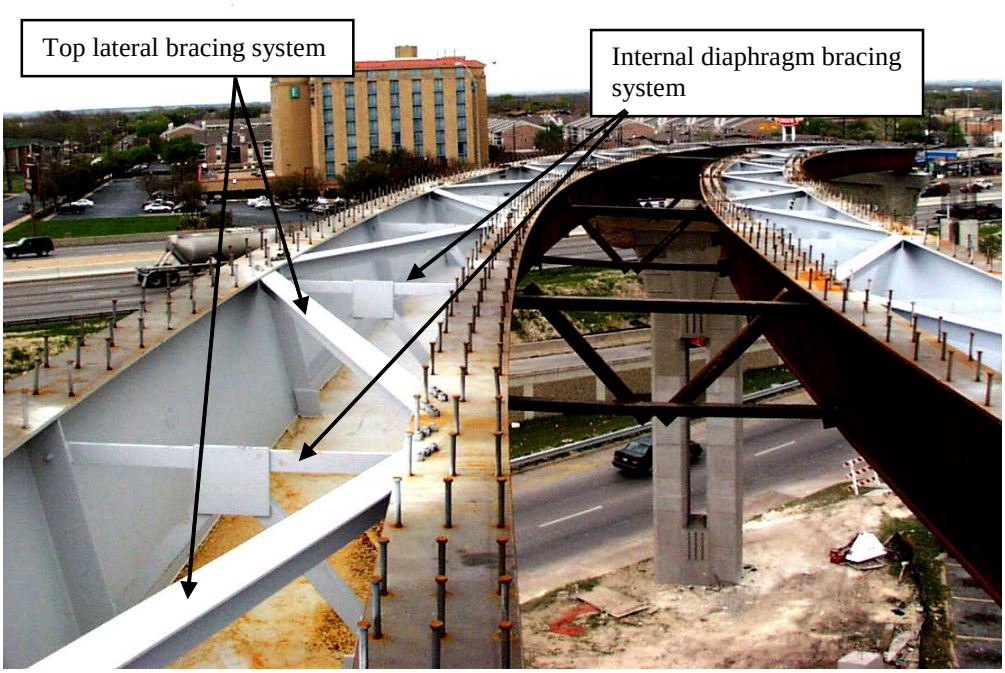

Figure 1.2 Bracing systems in a box girder during construction

In addition, stresses due to construction loading can reach up to 60-70 percent of the total design stress for a given cross-section (Topkaya et.al., 2002).

All of these facts indicate that a critical design stage for box girders occurs during construction.

1.3.1 Historical failure cases

That the construction stage is the most critical design stage for box girders has been highlighted by the failures of box girders, all of which happened during construction (Wolchuk and Mayrbaurl, 1980). In November 1969, the Fourth Danube Bridge, Vienna, was damaged during construction. In June 1970, a span of Milford Haven Bridge in Wales, shown in Figure 1.3, collapsed during the launching of a pre-assembled deck section due to unanticipated erection stresses.

Figure 1.3 Failure of Milford Haven bridge in June 1970 (Flint, 2001)

In October 1970, the West Gate Bridge in Melbourne suffered disastrous failures during erection. In November 1971, the bottom flange of the Koblenz Bridge in Germany buckled under temporary compression loadings. All of these

cases emphasize that the understanding of box girder behavior during construction is very important.

In addition to cases of overall failure, local failure of bracing members, such as the one shown in Figure 1.4, can also occur during construction. Certainly, the failure of bracing members will affect the overall stability of a girder and can lead to a catastrophic failure.

Figure 1.4 Failure of bracing member during construction (Chen, 2002)

1.3.2 Lack of guidance for designers

Even though the construction stage is a critical stage, design specifications do not commonly provide designers with sufficient guidance regarding the behavior of box girders during construction. Most of the time, design work only emphasizes the bridge performance under service condition, without carefully

considering the construction stage. Because of the lack of knowledge of girder behavior during construction, designers may possibly use a lateral bracing system that may not adequately stabilize the girder during construction, leading to large deformations and stresses. On the other hand, designers can use excessive bracing that results in the waste of material and labor, and imposes fatigue problems. From a concrete pouring perspective, using a less than optimum pouring sequence can result in very large bracing forces, deformations, and total normal stresses.

As an example, the American Association of State Highway and Transportation Officials (AASHTO) Guide Specifications 2003 provides very limited information on the internal diaphragm spacing and top lateral bracing requirements. Section 10.2.2.3 of the specification states that the spacing of internal bracing shall be such that the longitudinal warping stress does not exceed 10 percent of the longitudinal stress and shall not exceed 30 feet. Section 10.2.4 of the specification indicates that top flange bracing shall have adequate capacity to resist shear flow and forces induced by vertical and lateral bending in the non-composite section at the constructibility limit state. There is no guideline regarding the pouring sequence available in the specification.

Clearly, the current design guidelines do not provide sufficient information regarding the behavior of box girders during construction. Therefore, this thesis will examine girder behavior during construction by presenting the results of parametric studies.

1.4 UTRAP PROGRAM DESCRIPTION

The UTRAP program is used to conduct the parametric studies. Whenever hand calculations were made, UTRAP outputs are used as a basis of comparison.

UTRAP is a finite-element software package (Topkaya et.al., 2002), developed for the analysis of curved steel box girders under construction loads. The program consists of a Graphical User Interface, in which the input data is entered to the program, and an analysis module, which relies on the finite element method to compute the response of the three-dimensional bridge structure. UTRAP provides a more rigorous analysis of curved box girders than traditional grid analysis approaches. Since UTRAP analyzes a girder as a 3-D finite element model, it can determine stresses and deformations throughout the cross-section of a girder. In addition, all bracing members are modeled explicitly so that no simplifying assumptions are required for determining member forces.

Unlike currently available software, UTRAP has the capability to model the effects of semi-cured concrete. Therefore, the effect of pouring sequence on bracing forces, girder stresses, and deformations can be examined in a more realistic manner.

1.5 REVIEW OF LITERATURE

Steel trapezoidal box girders can be classified as thin-walled beams because the thickness of the elements is small compared to the height and width of the cross-section and the cross-section dimensions are small compared to the girder length. The first systematic study of the theory of thin-walled beams was conducted by Vlasov (1961). He explained the difference of behavior between

"thin-walled" and "thick-walled" beams under the same loading. In explaining torsional warping, Vlasov divided a torsional moment into pure and flexural components corresponding to the St. Venant and torsional warping shear stresses. Zbirohowski-Koscia (1967) tried to introduce the theory of open-section thin-walled beams to design offices. For that purpose, he described the physical meaning of the forces and properties introduced by Vlasov and kept the mathematical proofs to a minimum. Kollbrunner and Basler (1969) presented a thorough analysis of torsion in both single-span and continuous members with solid, thin-walled, open, or closed cross-sections. In addition, they developed the Equivalent Plate Method (EPM) for the torsional analysis of a pseudo-closed box girder.

Dabrowski (1968) was the first to derive the fundamental equations for deformable curved box girders subjected to non-uniform torsion. He presented sample calculations for determining cross-section properties of open, pseudo-closed, and closed sections. Tables that give the expressions for bending moment, total torque, St. Venant torque (primary torque), secondary torque, and bimoment of a curved girder with several common boundary and loading conditions are shown in Dabrowski's book. Wright, Abdel-Samad, and Robinson (1968) developed an analogy between the differential equation describing the response of a single-cell, straight trapezoidal box girder due to the distortional component of torsional loading and that of the beam on elastic foundation (BEF).

Oleinik and Heins (1974) developed design equations to predict the magnitude of induced distortional stresses due to dead and live loads for a single span curved box girder. Their empirical equations for determining the required internal diaphragm spacing were based on limiting the distortional normal stresses in the bottom flange. In addition, all cross-sections used in their parametric studies were rectangular box sections with the depth to width ratio smaller than

one. Heins (1978) examined the structural behavior of girders and provided design guidelines for economical box girder designs.

Branco and Green (1981, 1984, 1985) tested scaled models of straight, simply supported, open and pseudo-closed trapezoidal box girders under torsional loadings to study the effects of construction loadings and bracing configurations on the overall stability and deformation of box girders. They studied the effectiveness of transverse web stiffeners and internal diaphragms in preventing distortional stresses. Siddiqui (1985) tested one-quarter scaled models of closed-section rectangular and trapezoidal straight box girders under concentrated torsional loadings. The purpose of his studies was to confirm experimentally that deformation of the cross-section of a box girder induced warping and distortional stresses, and that inserting internal diaphragms can reduce these stresses.

Nakai and Yoo (1988) presented the formulation and solutions of the governing equations in curved box girders. They also discussed the design codes and specifications used in Japan, including the specifications for the internal diaphragms. Yabuki and Arizumi (1989) investigated the normal stress distribution and cross-sectional deformation in single-span curved box girders under symmetrical and eccentric uniform loads and under concentrated loads. They presented an internal diaphragm spacing provision based on parametric studies using the BEF analogy. All cross-sections used in their parametric studies were rectangular box sections without lattice walls.

Helwig and Fan (2000) developed design equations to evaluate the forces in the top lateral bracing and internal K-frames systems in pseudo-closed trapezoidal box girders during construction. Sennah and Kennedy (2001, 2002) summarized the most important references related to the development of current guide specifications for the design of straight and curved box girders in the form of single-cell, multiple spine, and multicell cross-sections.

1.6 PURPOSE AND SCOPE

The work presented herein was part of TxDOT research project No.0-4307 "Steel Trapezoidal Girders: State-of-the-Art". The research is intended to compile a state-of-the-art reference manual for the design of steel trapezoidal girders that will cover from the erection phase up to the hardening of the concrete deck. The purpose of this thesis is to present general behavior of a steel trapezoidal box girder during construction prior to the hardening of the concrete deck. Parametric studies were performed to examine the effects of different parameters on top lateral bracing forces, girder stresses and deformations. The UTRAP program was used to perform the studies. In order to aid understanding, available hand methods are presented to predict the top lateral bracing forces, bending and torsional stresses and deformations when possible.

Most of the previous research to determine the required internal diaphragm spacing focused on a completely closed rectangular box girder. All parametric studies reported herein focus on a trapezoidal steel box girder with a top lateral bracing system, which forms a. pseudo-closed section. Unlike the basis of many recommendations for internal diaphragm spacing, this thesis uses the ratio of distortional to bending normal stress in the top flange, distortional rotation, and the change in diagonal lengths as a basis for determining diaphragm spacing. It is believed that the distortional normal stress in the top flange is more important than that in the bottom flange since the maximum bending normal stress in a typical pseudo-closed trapezoidal girder occurs in the top flanges which are much smaller than the bottom flange.

Moreover, guidelines are provided for determining the best top lateral bracing system and pouring sequence with regard to bracing forces, deformations, and normal stresses. Even though much research has been conducted on the behavior of box girders during construction, there has been no comprehensive examination of the effect of different top lateral bracing systems on girder behavior during a monolithic or a sequenced pour. This thesis presents the effects of using different top lateral bracing systems during a monolithic and a sequenced pour on bracing forces, girder deformations, and normal stresses.

All parametric studies are performed using a single trapezoidal girder system with typical cross-section dimensions shown in Figure 1.5. The inclination of the web is not varied significantly and the width to depth ratio is about one. There are no web stiffeners or longitudinal stiffeners used in the modeling. The cross-section dimensions are constant along the length, whereas each plate thickness can be varied. All curved girders analyzed have constant radii of curvature and no superelevation. All supports are perpendicular to the girder; no skewed supports are used.

The weight of wet concrete is represented by applying a symmetrical uniform load on a girder. Since there is no eccentric loading, the only torsional loading discussed herein results from the curvature. Helwig and Fan indicated that the force distribution from torsional loading due to eccentric loading is different than that due to curvature. Most of the previous research used eccentric loading to create torsional loadings, whereas torsional loading resulting from the curvature is considered herein.

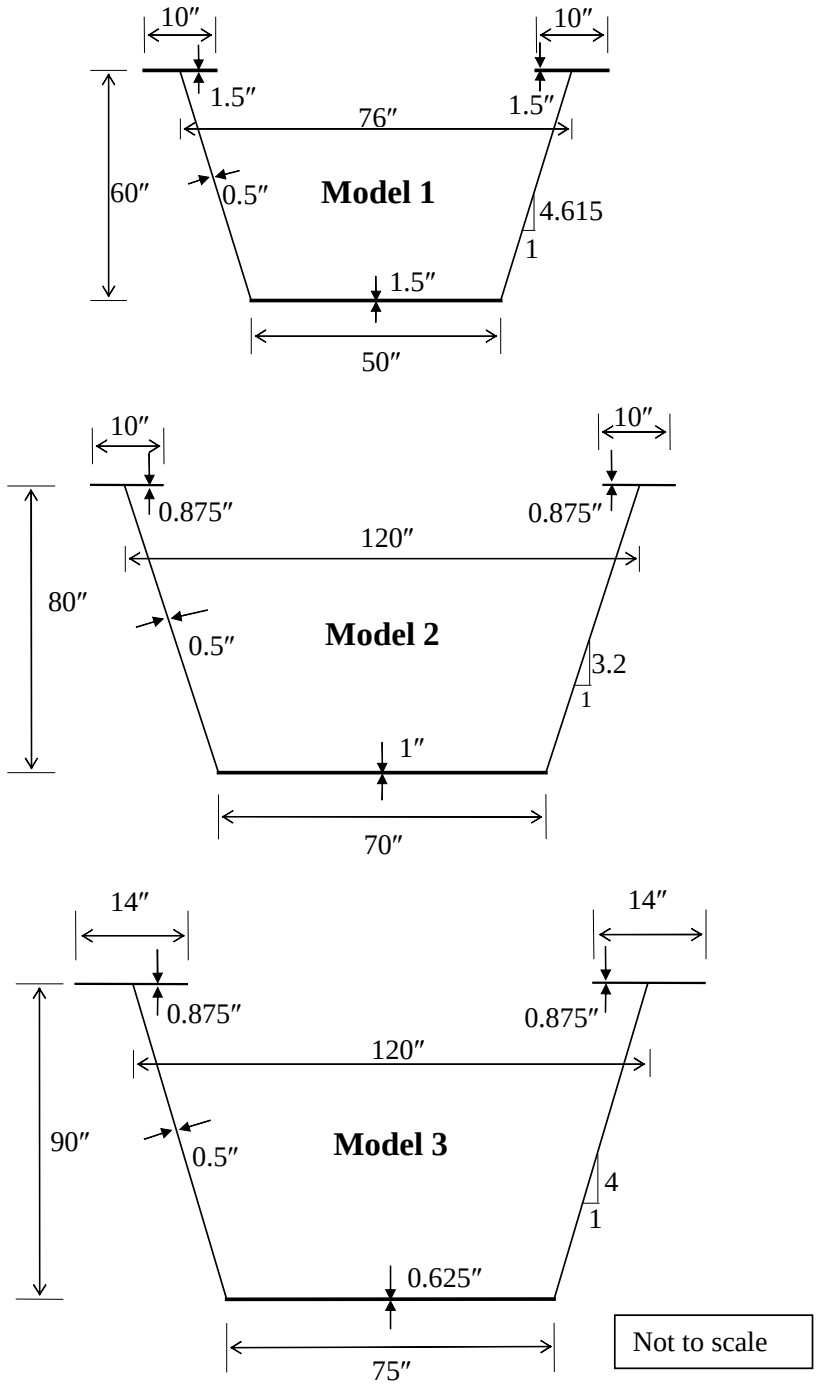

Figure 1.5 Cross-section dimensions of trapezoidal box girder models

Four different top lateral bracing systems, shown in Figure 1.6, were examined. There has been no research conducted to study the behavior of girders with the Single-Diagonal system. The only type of internal diaphragm used in this study is the inverted K-frame, shown in Figure 1.7. This system is common in modern box girders because it has a large space between the two diagonals that provides easy access for workers and inspectors.

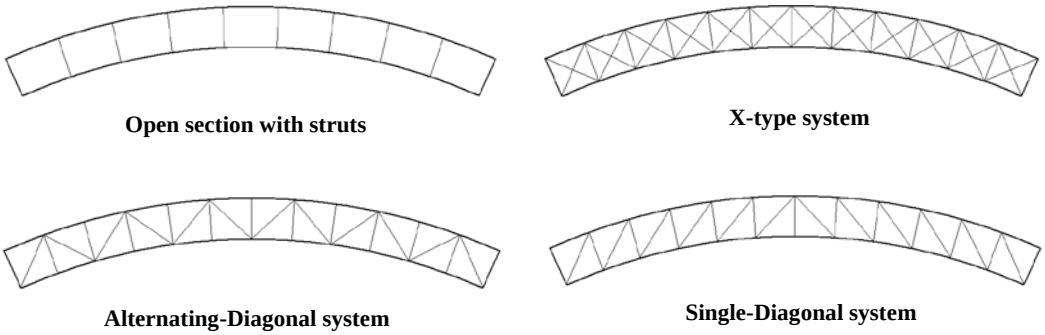

Figure 1.6 Types of top lateral bracing system

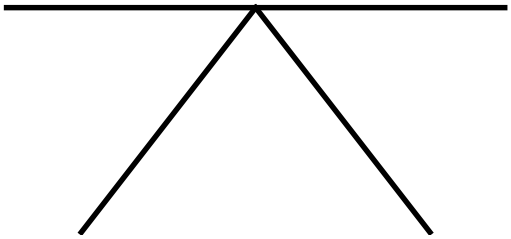

Figure 1.7 Inverted K-frame internal diaphragm

1.7 ORGANIZATION

Chapter two reviews the basic theory of thin-walled beams in bending and torsion. Chapter three discusses cross-sectional forces, including shear forces, support torque, and midspan bending moment, in a curved girder. Chapter four summarizes methods for calculating cross-section properties related to bending

and torsion of open and pseudo-closed sections. In chapter four, Dabwroski's methods for calculating the cross-section properties of general open and pseudo-closed sections are extended to a trapezoidal shape. The closed-form solutions for cross-section properties of open and pseudo-closed sections of a trapezoidal box girder are derived and sample calculations are shown.

Chapters five and six discuss the general behavior of straight and curved girders, respectively, focusing on deformations and total normal stresses. In a curved girder, there are additional normal stresses, the warping normal stress and the distortional normal stress. These types of normal stresses are discussed in chapters seven and eight, respectively.

Chapters nine through eleven discuss forces in top lateral bracing members. In chapter nine, analytical methods for estimating the forces developed in the top lateral bracing system in simply-supported straight and curved trapezoidal box girders are presented. This chapter illustrates how the configuration of top lateral bracing members affects the force distribution in the members. Chapter ten focuses on the top lateral bracing forces in a continuous curved girder under a symmetric uniformly distributed load (i.e. a monolithic pour). The effect of using different top lateral bracing systems on the behavior of a continuous curved girder, including comparisons of the deformations and the total normal stresses, is presented in that chapter. As an extension of chapter ten, chapter eleven discusses the top lateral bracing forces in a continuous curved girder during a sequenced pour. Comparisons between forces, girder deformations, and total normal stresses due to a monolithic pour and those due to a sequenced pour are presented in chapter eleven. Recommendations regarding the pouring sequence are presented.

Finally, chapter twelve summarizes the findings and recommendations and discusses future research needs for box girders.

CHAPTER 2
Basic Theory of Thin-Walled Beams

Steel trapezoidal box girders can be classified as thin-walled beams because the thickness of the elements are small compared to the height and width of the cross-section and the cross-section dimensions are small compared to the girder length. This chapter discusses the basic theory of thin-walled beam related to vertical bending, torsion, and distortion in general terms.

2.1 VERTICAL BENDING

Vertical bending occurs in a girder when it is subjected to transverse loads acting through the shear center, producing bending moment and shear force along the length of the girder. The general relationships between bending moment M and normal stresses σ, and between shear force V and shear stress τ are

$$M = \int_{area} y\sigma dA \tag{2.1}$$

$$V = \int_{area} \tau dA \tag{2.2}$$

where y is the distance of the fiber under consideration to the neutral axis and the integrations are evaluated over the cross-section area. Normal stresses and shearing stresses due to vertical bending are discussed in the following sections. The effect of vertical bending on a box girder can usually be analyzed using classical beam theory.

In general, the vertical bending behavior of a pseudo-closed section of a box girder is similar to that of an open section. The only difference is the fact that the bending moment of inertia of the pseudo-closed section is slightly higher due to the presence of a top lateral bracing system.

2.1.1 Normal stress due to vertical bending

Using the elastic behavior and plane sections remain plane (Navier hypothesis) assumptions, normal stresses due to vertical bending σ_B in a girder with a symmetric cross-section like a trapezoidal box girder can be calculated using

$$\sigma_B = \frac{My}{I_x} \tag{2.3}$$

where y is the distance from the neutral axis to the fiber under consideration along the y-axis and I_x is the moment of inertia about the x-axis.

Variation of the bending normal stress on the cross-section is shown in Figure 2.1. It can be seen from Figure 2.1 that the shear center is located on the axis of symmetry (y-axis). Methods to determine the shear center location will be discussed in chapter 4.

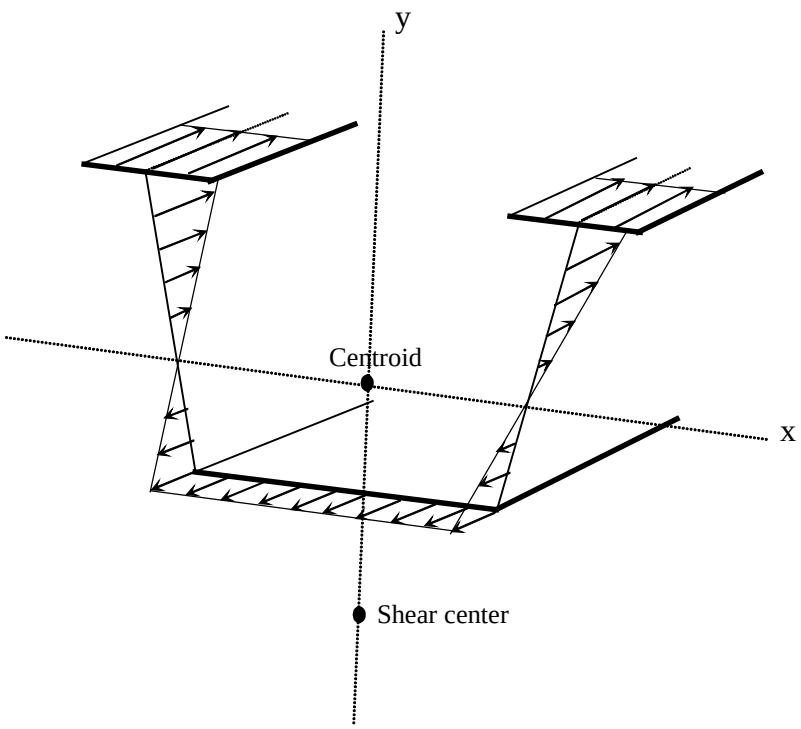

Figure 2.1 Normal stress distribution due to vertical bending

2.1.2 Shear stresses due to vertical bending

If the bending moment is not uniform along the length of a girder, shear stresses will be induced to satisfy equilibrium. For thin-walled cross-sections, the shear stress τ is assumed to be constant across the thickness of the wall. The magnitude of shear stress τ at any point in the cross-section at distance s from the free edge is

$$\tau = \frac{V_y Q_x}{I_x t} \tag{2.4}$$

where V_y is the shear force in the *y*-direction, Q_x is the first moment with respect to the bending neutral axis (x-axis in this case) of the cross-sectional area from *s=0 to s=s*, and *t* is the thickness at distance *s* from the free edge. The derivation

of this formula can be found in Gere and Timoshenko (1997). The direction of shear stresses τ is along the centerline of the cross-section, and for the thin-walled cross-section, τ is assumed to be constant across the thickness of the wall.

The shear flow q at any point in the cross-section, which is defined as the product of the shear stress and the thickness at that point, is

$$q = \tau t = \frac{V_y Q_x}{I_x} \tag{2.5}$$

The shear flow q is directly proportional to Q_x. The shear flow is zero at the top and bottom edges of the cross-section and maximum at the neutral axis. Shear flow on a cross-section is constant even though the thickness of the section wall varies and it flows in a continuous direction. At the neutral axis, shear flow q has the same direction as the shear force V.

Figure 2.2 shows the shear stress distribution on a trapezoidal box girder cross-section. The shear stress at points a and b, which are the free edges, are zero.

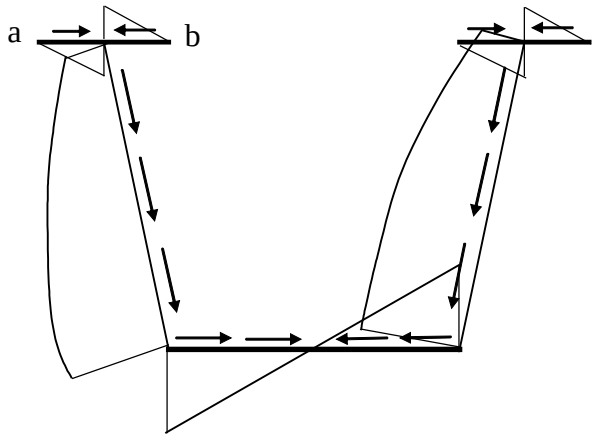

Figure 2.2 Shear stress distribution due to vertical bending

2.1.3 Shear lag effect

Branco and Green (1985) indicated that warping displacements are induced in the cross-section due to the bending shear stress distribution shown in Figure 2.2. This warping displacement can induce a shear lag effect, which is a phenomenon that reduces the bending capacity of a thin-walled beam because it causes the bending normal stress to become non uniform across the width (i.e. maximum at the junction point of flanges and web plate). The variation of bending normal stress on the cross-section, obtained by taking the shear lag effect into consideration, is shown schematically in Figure 2.3.

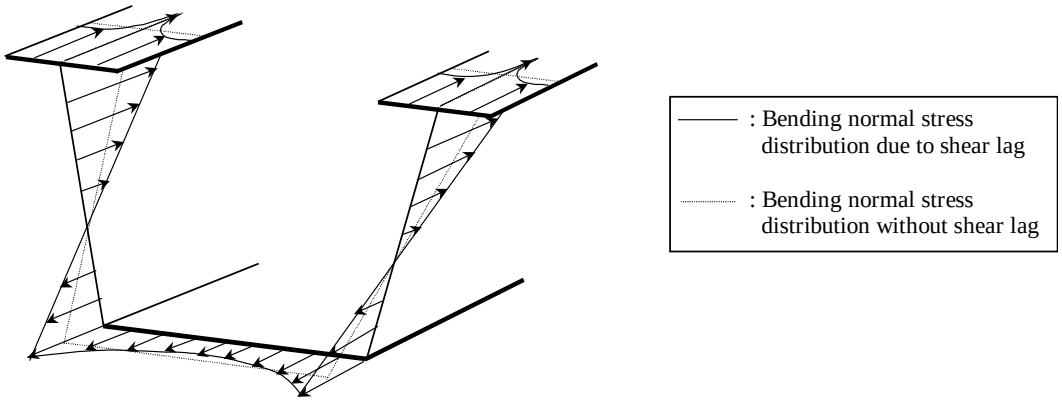

Figure 2.3 Variation of bending normal stress including shear lag effect

Branco and Green indicated that the shear lag effect is usually small in box girders, except at sections with large concentrated loads or in thin, wide flanges. Box girders having a large width to depth ratio are prone to shear lag, and that the effect of shear lag can be minimized by using a relatively "square" cross-section (i.e. width dimension is approximately the same as depth dimension) (Helwig and Fan, 2000).

Finite element programs such as UTRAP that represent the cross-section can capture the shear lag effect directly, whereas grid type analysis programs that represent the cross-section by a single point cannot.

2.2 TORSION

Twisting of the cross-section occurs in a girder when it is subjected to transverse loads that do not act through the shear center and/or the member is curved. For a non-circular cross-section, twisting of cross-section is accompanied by warping (i.e.plane section do not remain plane). However, Boresi et.al. (1978) indicated that rectangular hollow cross-sections with a constant wall thickness or with the conditions shown in Figure 2.4 do not warp under torsional loading.

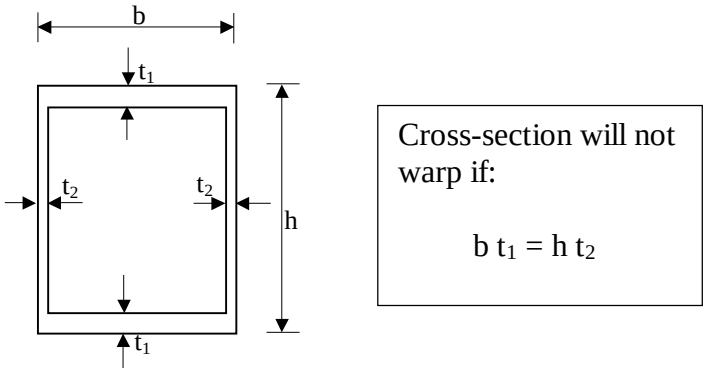

Figure 2.4 Condition of rectangular hollow cross-section that does not warp under torsion (Boresi et.al, 1978)

In general, the total torsional moment T resisted by the cross-section is the sum of pure torsion T_t (Saint-Venant torsion) and warping torsion T_w. In the following sections, these two contributions to torsional resistance will be explained.

2.2.1 Pure torsion (Saint-Venant torsion)

Generally, pure torsion occurs if a straight member is subjected only to torques at its ends (uniform torsion) and the warping (i.e. out-of-plane deformation of transverse sections do not remain plane) of the cross-section is not restrained. Thin-walled members subjected to pure torsion will only experience shear stresses (normal stress will not arise).

At any point along the length of members subjected to a torsional moment T_t, the cross-section will rotate through an angle θ. The relationship between torsional moment T_t and rotation angle θ is

$$T_t = GJ\frac{d\theta}{dz} \tag{2.6}$$

where G is the shear modulus of elasticity, J is the pure torsional constant of the cross-section, and $\frac{d\theta}{dz}$ is the rotation angle per unit length (first derivative of θ with respect to z measured along the length of member).

The pure torsional constant J is used to quantify the torsional stiffness of the element. The pure torsional constant for open sections, J_{open}, comprised of n narrow rectangular sections can be approximated by

$$J_{open} = \frac{1}{3}\sum_{i=1}^{n} b_i t_i^{\,3} \tag{2.7}$$

where b_i and t_i are the width and thickness of each section i, respectively. For closed sections, the pure torsional constant, J_{closed}, is

$$J_{closed} = \frac{4A_o^{\,2}}{\oint \frac{ds}{t_{(s)}}} \tag{2.8}$$

where A_o is the area enclosed by the centerline of the walls and $t_{(s)}$ is the wall thickness along the member arc length s. If the hollow cross section is made up of

n rectangular components, each of thickness t_i and width b_i, then the contour integral can be replaced with the following expression:

$$\oint \frac{ds}{t_{(s)}} = \sum_{i=1}^{n} \frac{b_i}{t_i} \tag{2.9}$$

Therefore the closed section pure torsional constant, J_{closed}, can be written as follows:

$$J_{closed} = \frac{4A_o^{\,2}}{\sum_{i=1}^{n} \frac{b_i}{t_i}} \tag{2.10}$$

Unlike the behavior due to vertical bending, the behavior of thin-walled open sections and the behavior of closed sections under pure torsion is not the same. In general, the pure torsional constant for a closed section is much higher than it is for an open-section, so under the same torsional loading, the rotation angle of a closed section will be much smaller than the rotation angle of an open section. For tosional loading, the shear stress distributions on thin-walled open and closed sections are different as shown in Figure 2.5(a) and (b).

Figure 2.5(a) shows that there is an anti-symmetrical linear distribution across the wall thickness of the shear stress on the open section. The shear stress at the center-line of the wall is zero and the shear stresses at the both edges of the wall are maximum. Because of the anti-symmetrical linear distribution of shear stress, the torsional moment T_{ti} for each narrow rectangular section i with thickness t_i and width b_i, can be expressed in Eq. 2.11 as follows:

$$T_{ti} = \frac{1}{3} b_i t_i^{\,2} \tau_{\max i} \tag{2.11}$$

where $\tau_{max,i}$ is the maximum shear stress at each narrow rectangular section i.

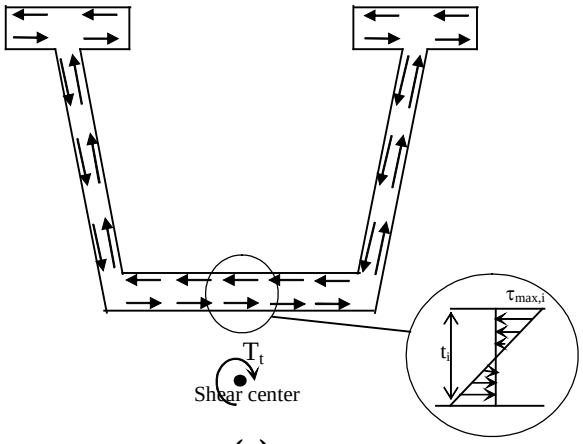

(a)

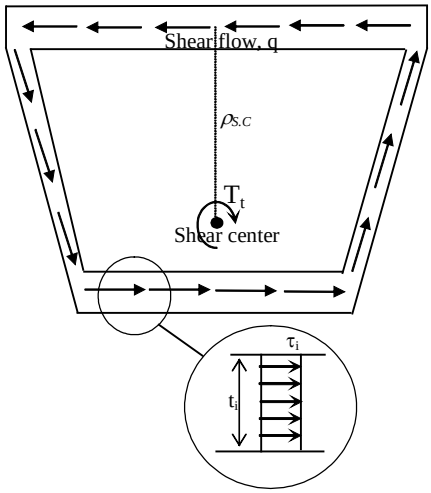

(b)

Figure 2.5 Shear stress distribution on open and closed sections due to pure torsional moment T_t

The total torsional moment T_t of the entire open-section consisting of n narrow rectangular elements is

$$T_t = \sum_{i=1}^{i=n} T_{ti} \qquad (2.12)$$

Figure 2.5(b) shows that the shear stress τ is uniformly distributed across the wall thickness of a thin-walled closed section. The shear flow (shear stress multiplied by thickness) in a thin-walled closed section is constant along the contour. Using equilibrium, the relation between shear flow q and torsional moment T_t can be expressed as

$$T_t = \oint r\, q\, ds \tag{2.13}$$

where r is the lever arm, measured from the shear center. Since the integral $\oint r\, ds$ is equal to twice the area enclosed by the shear flow, the torsional moment T_t can be expressed as follows:

$$T_t = 2\, A_o\, q \tag{2.14}$$

The shear flow q that develops along the contour of the box can be determined by using Eq. 2.15, also known as Bredt's equation.

$$q = \frac{T_t}{2\,\mathrm{A_o}} \tag{2.15}$$

Having determined the shear flow q using Eq. 2.15, the shear stress τ_i in each element i whose wall thickness is t_i can be calculated from

$$\tau_i = \frac{q}{t_i} \tag{2.16}$$

For most torsional applications, the pseudo-closed section can be treated as a closed section, rather than as an open-section (Kollbrunner and Basler, 1969).

2.2.2 Warping torsion

Twisting of a girder with a non-circular cross-section that does not satisfy the conditions shown in Figure 2.4 will be accompanied by warping. Figure

2.6(a), which is similar to the one shown in Zbirohowski-Koscia (1967), shows a view of the warped cross-section of a rectangular hollow girder. Both end surfaces of the girder do not remain plane but become warped. Because the girder shown in Figure 2.6(a) is free to warp, there will not be any warping normal stress induced. Figure 2.6(b) shows the same girder but with the warping displacement at the right end restrained. In this case, the flange bends and warping normal stresses will be induced. Warping normal stress will arise in a girder when any cross-section along the length is not free to warp when a torque is applied. In a simply supported girder, usually warping displacements are prevented at midspan due to symmetry.

In order to satisfy equilibrium, warping normal stress will induce warping shear stress. Warping normal stress will be additive with vertical bending normal stress, increasing or decreasing the vertical bending normal stress depending on the location on the cross-section. The warping shear stress will form a warping torsional moment, which combines with the pure torsional moment to resist the applied torsional loading.

In order to illustrate the state of warping normal stress, Figure 2.7 shows a curved thin-walled member with a completely free end cross-section subjected to a self-equilibrating set of forces applied at its end. The top width and girder depth are denoted by *a* and *d*, respectively. The set of self-equilibrating forces produces an end bimoment, which gives rise to normal stress, known as the warping normal stress. The general definition of a bimoment is a pair of equal but opposite bending moments acting in two parallel planes, which are the top and bottom flanges in this case. The numerical value of a bimoment is given by the product of the distance of these parallel planes, times the moment on one of them. For example, the numerical value of a bimoment shown in Figure 2.7 can be calculated as *F(a)(d)*.

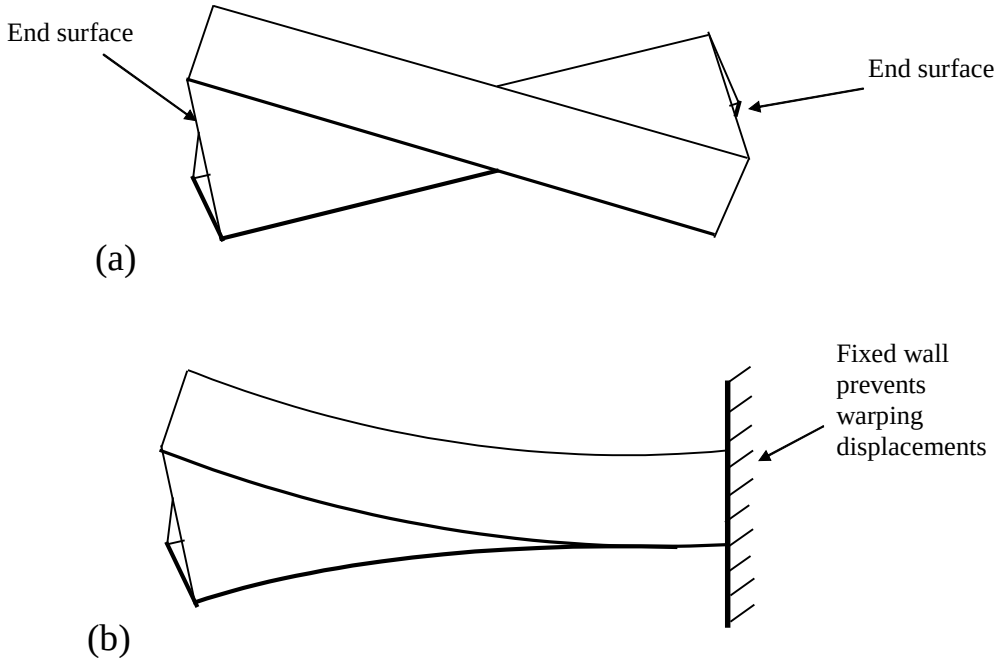

Figure 2.6 Warping deformation

Analytically, warping normal stress is

$$\sigma_W = \frac{B}{I_w} w(s) \qquad (2.17)$$

where B is the torsional warping moment or simply the bimoment, $w(s)$ is the torsional warping function, and I_w is the torsional warping constant. Dabrowski (1968) derived bimoment expressions for a curved girder with different boundary conditions and loading conditions.

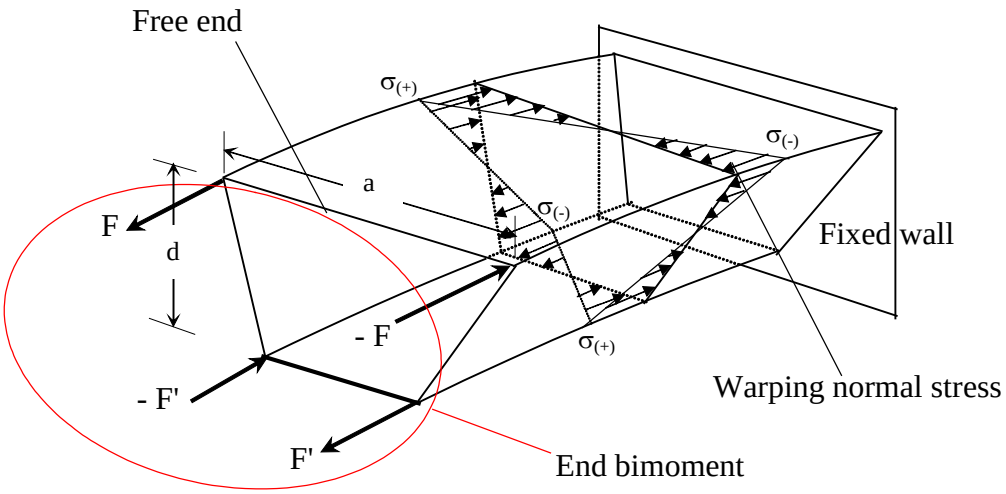

Figure 2.7 End bimoment and warping normal stress

For a simply supported curved girder under a symmetric uniformly-distributed load *w*, the bimoment is

$$B = \mu\left[\frac{wR\eta}{k^2}\left(1-\frac{\sinh(kz)+\sinh(kz')}{\sinh(kl)}\right)+\left(-wR^3\right)\eta\left(\frac{\sin\phi+\sin\phi'}{\sin\Phi}-1\right)\right] \qquad (2.18)$$

where:

μ = Warping shear parameter for closed and pseudo-closed sections

For an open section, μ=0

For a closed section, $\mu = 1-\frac{J_{closed}}{I_c}$

where: $I_c = \int_A r^2 dA$ (I_c: central second moment of area)

r : distance from contour tangent to the shear center

η = Dimensionless parameter $\eta = \frac{1}{1+(kR)^2}$

k = Decay coefficient for warping torsion $k = \sqrt{\frac{\mu GJ}{EI_w}}$

w = Uniformly distributed load (load per unit length).
Downward load is positive

R = Radius of curvature

l = Span length, measured along the curved centroidal axis

z = Ordinate of curved centroidal axis, measured from left support

z′= Ordinate of curved centroidal axis, measured from right support

ϕ = Angular ordinates, measured from left support

ϕ′= Angular ordinates, measured from right support

Φ = Central angle

The torsional warping function *w(s)* is the geometric function that is linearly proportional to warping axial displacement. The torsional warping functions for an open section $w(s)_{open}$ and for a closed section $w(s)_{closed}$ that is comprised of *n* narrow rectangular sections are expressed in Eqs. 2.19 and 2.20, respectively.

$$w(s)_{open} = \int_0^s r ds \tag{2.19}$$

$$w(s)_{closed} = w(s)_{open} - \frac{2A_o}{\sum_{i=1}^{n} \frac{b_i}{t_i}} \int_0^s \frac{ds}{t} \tag{2.20}$$

where *s* is the coordinate system along the contour of the beam, *r* is the perpendicular distance from the contour of each section to the shear center, A_o is the area enclosed by the shear flow, and b_i and t_i are the width and thickness of each section. Eqs. 2.19 and 2.20 assume that the origin *s=0* is located on the axis passing through the shear center and the section is traversed in clockwise

direction about the shear center. The right hand side of Eqs. 2.19 and 2.20 are called the sectorial area and the reduced sectorial area with respect to the shear center, respectively.

The torsional warping constant I_w that represents the geometric moment of inertia with respect to the warping function is

$$I_w = \int_A w(s)^2 \, dA \qquad \text{where } dA = t \, ds \tag{2.21}$$

The torsional warping constant is also called the warping moment of inertia. Warping normal stress will be accompanied by shear stresses in the plane of the cross section. These shear stresses will form a warping torsional moment T_w in addition to the pure torsional moment, which is given by

$$T_w = -EI_w \frac{d^3\theta}{dz^3} \tag{2.22}$$

where θ is the rotational angle, and z is the coordinate axis along the beam length.

2.2.3 Total resistance to a torsional moment

The torsional moment applied to a cross-section T will be resisted by pure torsional moment T_t (St. Venant torsion) and warping torsional moment T_w.

$$T = T_t + T_w \tag{2.23}$$

The pure torsional moment is always present in cross sections subjected to torque, whereas the warping torsional moment is only present when warping displacements of cross sections are restrained.

The relative proportion of each type of torsion present in a member depends on the length and cross-section dimensions. The parameter X, given in Eq. 2.24, is used to determine whether pure torsion or warping torsion dominates.

$$X = l\sqrt{\frac{GJ}{EI_w}} \tag{2.24}$$

where l is the length of member. The term inside the square root is the ratio of the pure torsional rigidity (GJ) to the warping torsional rigidity (EI_w). A larger parameter X indicates the dominance of pure torsion in the torsional resisting moment component. The torsional predominance of a member based on the value of parameter X is given in Table 2-1 (Chen, 1999).

Table 2-1 Pure and Warping Torsional Predominance

Torsional Predominance	X
Pure warping	< 0.3
Dominating Warping	0.3 – 2
Mixed	2 – 5
Dominating Saint-Venant	5 – 10
Pure Saint-Venant	> 10

Members dominated by one type of torsion can be analyzed approximately by neglecting the other type of torsion. In general, warping torsion is very small compared to the pure torsion in thin-walled closed-sections. For thin-walled open sections, pure torsion dominates in long members while warping torsion dominates in short ones (Chen, 1999).

2.3 DISTORTION

Box girder distortion is caused by torsional loads that are not distributed in proportion to the Saint-Venant shear flow on the cross-section of the girder (Helwig and Fan, 2000). Torsional loading on box girders can results from applied loads that do not act through the shear center (eccentric loading) and/or the girder geometry (curved member). Helwig and Fan indicated that the torsional loading due to eccentric gravity loading can be represented by a pair of vertical forces, whereas that due to the girder curvature is applied by a pair of horizontal

forces of *M/(hR)*, where h and R are the girder depth and the radius of curvature, respectively. The torsional loading due to the eccentric loading are generally very small and will not be considered in this research. Saint-Venant torsional and distortional components due to curvature effect are shown in Figure 2.8. The magnitude of the Saint-Venant torsional and distortional components are given in Helwig and Fan.

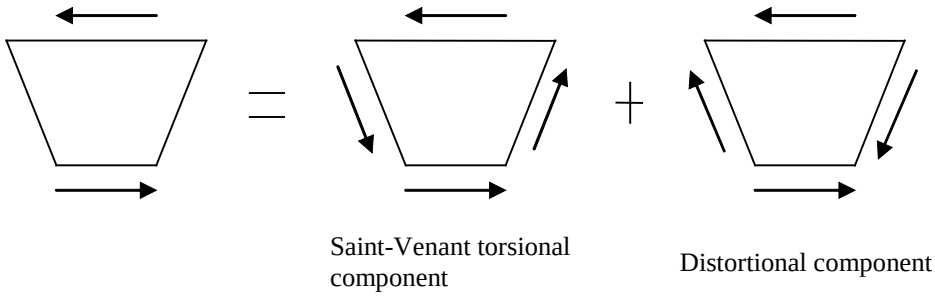

Figure 2.8 Saint-Venant torsional and distortional components due to curvature effect

In general, the cross-sections of thin-walled beams will distort from the original shape due to the distortional component. Helwig and Fan indicated that thin-walled beam distortion results in additional longitudinal normal stress, called distortional normal stress, and local plate bending moment. Figure 2.9 shows the distribution of distortional normal stress on the cross-section. More detailed discussions of the source of distortional normal stress are presented in chapter 11. shows the distortional deformation of a rectangular box girder under distortional load and the distribution of local plate bending moment on the cross-section produced by frame action of the box.

Nakai and Yoo (1988) derived a general equation for the local plate bending moment in a rectangular box section due to distortion. The expression is fairly complex since properties of top and bottom flanges are different. The distortion of a simpler model considering an open section (i.e. equivalent plate thickness taken as zero) is derived in Appendix A. It is shown in Appendix A that the local plate bending stress is so small that it can be ignored. Nakai and Yoo also concluded that the local plate bending stress is negligible. Therefore, it will not be discussed herein.

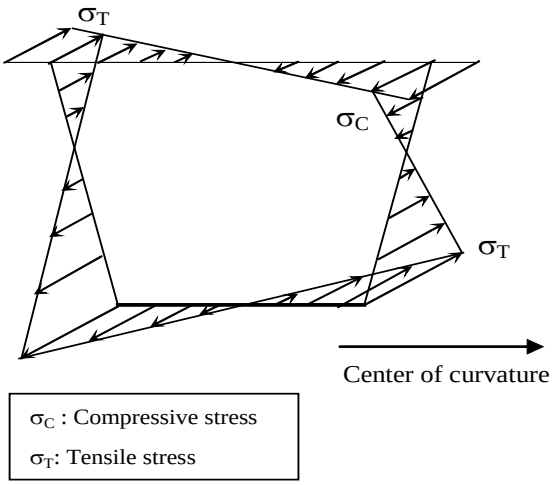

Figure 2.9 Distribution of distortional normal stress

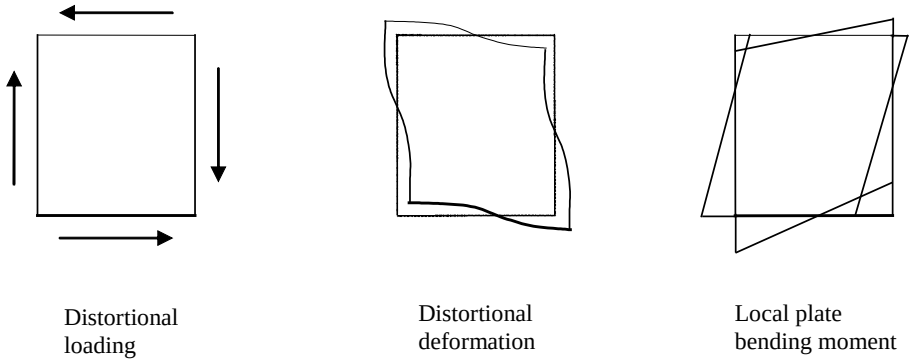

Figure 2.10 Distortional deformation and local plate bending moment

CHAPTER 3
Cross-sectional Forces

This chapter presents methods for calculating cross-sectional forces, including shear forces, support torque, and midspan bending moment, for straight and curved girders under a symmetrical uniform load. All methods presented in the first two sections in this chapter are limited to girders with the following characteristics:

- Simply supported for bending
- Pinned supports for torsion (i.e. warping deformation is permitted at the supports)
- Horizontal plane (i.e. no superelevation)
- Constant radius of curvature along the length

In addition to the exact method, which involves quite complicated expressions, this chapter presents an approximate method to calculate cross-sectional forces for a simply supported curved girder under uniform load. At the end of this chapter, the approximate method for estimating cross-sectional forces in a continuous girder is discussed briefly. In order to verify the approximate solutions, the results from UTRAP solutions were compared with the results obtained from the approximate methods.

3.1 STRAIGHT GIRDERS

Classical beam theory for a simply supported beam can be applied to analyze cross-sectional forces in a straight girder. In a straight girder, self-weight

of the girder and concrete weight, assuming the concrete pour is symmetric about the centerline of the girder, will not induce any torsional forces on the girder. The only possible source of torsional loading in a straight girder is the application of eccentric loading with respect to the girder centerline. The equivalent torsional loading M_T, due to load P, applied with an eccentricity e with respect to the girder centerline, can be expressed in Eq. 3.1.

$$M_T = P\ e \tag{3.1}$$

Figure 3.1 shows a torsional moment diagram T of a straight girder with a length l, under the torsional load M_T that is applied at a distance l_1 from the left end support (or at a distance l_2 from the right support). In general, boundary condition for torsional loading in a simply-supported girder can be assumed as a pinned-support in torsion (i.e. twisting is not permitted but warping deformation is permitted). Figure 3.1 shows that the left and the right end support torques are $(M_T\ l_2) / l$ and $(M_T\ l_1) / l$, respectively.

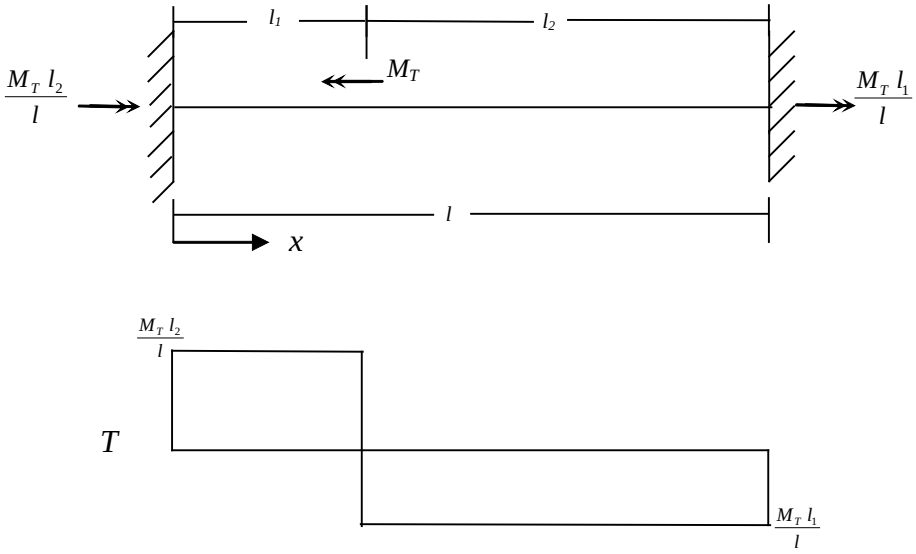

Figure 3.1 Torsional force diagram of a straight girder under a concentrated torsional loading

3.2 CURVED GIRDERS

In a curved girder, as shown in Figure 3.2, no matter where the gravity load is placed, there is always a component of torsional loading due to curvature. Before any external loads are applied to a curved girder, the dead weight of the girder itself produces a torsional loading. Primarily due to interaction between bending and torsion, the analysis for cross-sectional forces of a curved girder is, in general, more complicated than the analysis of a straight girder.

For a relatively small central angle Φ, Helwig and Fan (2000) indicated that the effect of curvature on bending behavior of a curved girder is negligible. Therefore, the cross-sectional force analysis of a curved girder can be approximated by a slight modification of the cross-sectional analysis of a straight girder. The most popular approximate method for the analysis of curved girders is the M/R method developed by Tung and Fountain (1970).

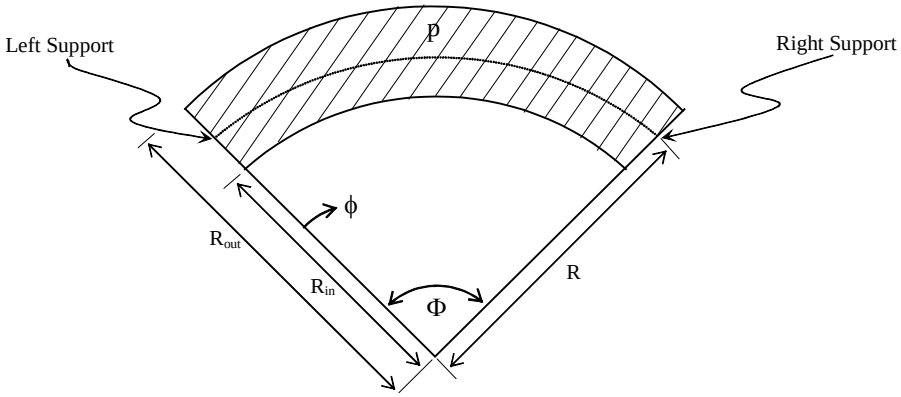

Figure 3.2 Simply supported curved girder under a uniformly distributed load p

Before the cross-sectional analysis of a curved girder is presented, it is important to understand the difference between torsional loading and torsional moment. In general, torsional loading refers to the externally applied torque while torsional moment, also known as internal torque, refers to the internal resistance forces developed in the structure due to torsional loading.

Section 3.2 presents the cross-sectional force analysis of a curved girder. Exact solutions from Nakai and Yoo (1988) were used to obtain the variation of shear force, bending moment, and total torsional moment along the length of the curved girder and equilibrium was used in order to find the support torque and midspan moment. Approximate solutions (section 3.2.2) using a modified straight girder approach are presented. The results from UTRAP solutions were compared with the results obtained from both the exact solutions and the approximate solutions (section 3.2.3).

3.2.1 Exact solution

Nakai and Yoo (1988) presented the closed form solutions for shear force, bending moment, and total torsional moment along the length of a simply-supported curved girder under a uniformly distributed load p over the girder surface shown in Figure 3.2 (Note: p is load per unit area). The curved girder has the radius of curvature R, and the radius of inside and outside edges of the uniformly distributed load R_{in} and R_{out}, respectively. The angle to define a position along the curved length, measured from the left support, is denoted as ϕ.

In deriving the solutions of cross-sectional forces, Nakai and Yoo used the following notations:

$$L_1 = \frac{1}{3}\left(R_{out}^3 - R_{in}^3\right) \tag{3.2}$$

$$L_2 = \frac{R_s}{2}\left(R_{out}^2 - R_{in}^2\right) \tag{3.3}$$

The shear force due to bending $V_{(\phi)}$, bending moment $M_{(\phi)}$, and total torsional moment $T_{T(\phi)}$, along the length of curved girder, are expressed in Eqs. 3.4, 3.5, and 3.6, respectively.

$$V_{(\phi)} = p\frac{L_2}{R_s}\left(\frac{\Phi}{2} - \phi\right) \tag{3.4}$$

$$M_{(\phi)} = pL_1\left[\frac{\sin(\phi) + \sin(\Phi - \phi)}{\sin(\Phi)} - 1\right] \tag{3.5}$$

$$T_{T(\phi)} = p\left[L_1\frac{\cos(\Phi - \phi) - \cos(\phi)}{\sin(\Phi)} + L_2\left(\frac{\Phi}{2} - \phi\right)\right] \tag{3.6}$$

where L_1 and L_2 are the notations introduced in Eqs.3.2 and 3.3, respectively. The total torsional moment $T_{T(\phi)}$ expressed by Eq.3.6 is the sum of the pure torsional moment and the warping torsional moment.

A simply supported curved girder defined by Model 1 shown in Figure 1.5, with a uniform load of 0.8 k/ft, was used as a case study to compare the exact calculation of shear force, bending moment, and total torsional moment along the length – Eqs.3.4, 3.5, and 3.6, respectively – to the results from UTRAP solutions. In order to study whether the accuracy of the closed-form solutions was sensitive to the variation in central angle, two different central angles were used in case studies. One case study used a 180-ft curved girder with a radius of 750 ft (central angle of 0.24 radian), and other used a 180-ft curved girder with a radius of 200 ft (central angle of 0.9 radian). The comparisons of shear forces, bending moment, and total torsional moment for those two case studies between the closed-form solutions and UTRAP outputs are shown in Figure 3.3, Figure 3.4, and Figure 3.5, respectively.

Figure 3.3 through Figure 3.5 show that the closed-form solutions from Nakai and Yoo can predict exactly the UTRAP solutions for shear forces, bending moment, and total torsional moment along the length. Herein, the closed form

solutions from Nakai and Yoo are called the exact solutions. In addition, the closed form solutions do not depend on the central angle. Figure 3.3 through Figure 3.5 show that the accuracy of the closed form solutions for a relatively small central angle (0.24 radian) is the same as that for a relatively large central angle (0.9 radian).

Figure 3.4 and Figure 3.5 shows that the maximum bending moment in a simply supported curved girder occurs at the midspan, and the maximum total torsional moment occurs at the supports. For the design process, it will be more convenient to estimate the maximum value using a simpler form of equation. The next discussion will present the derivation of maximum bending moment (midspan bending moment) and the support torque for a curved girder by using equilibrium, geometric relation, and integration processes.

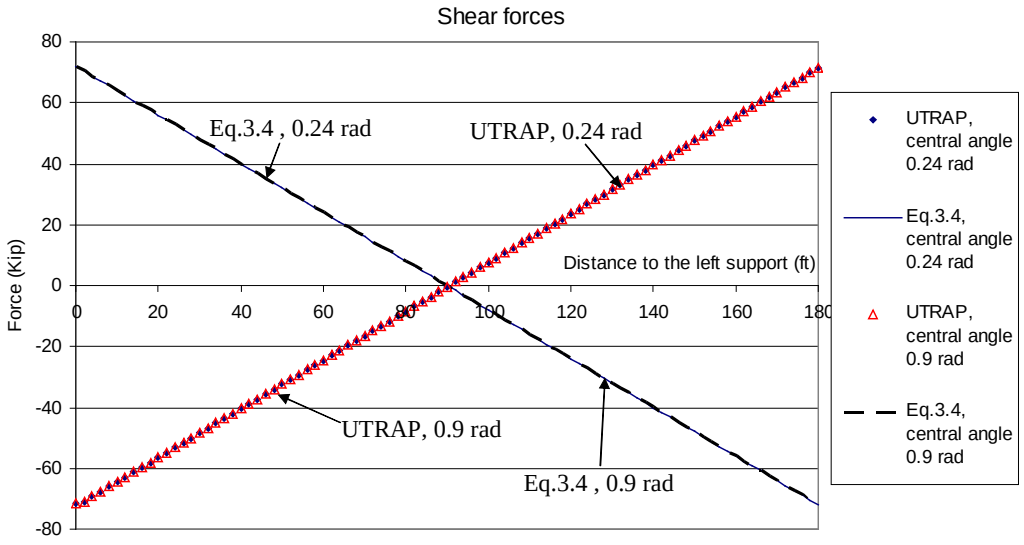

Figure 3.3 Comparison of shear force between UTRAP and closed-form solutions

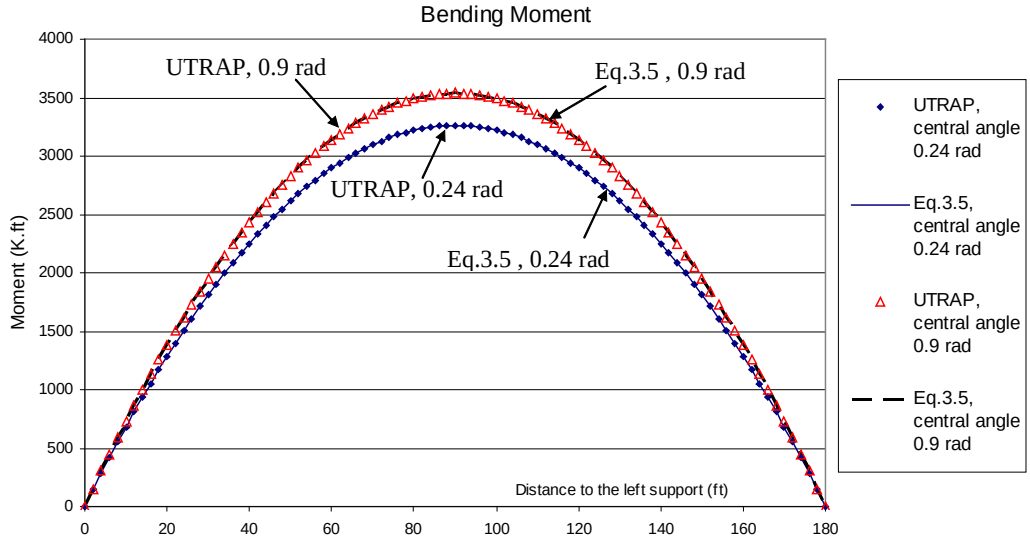

Figure 3.4 Comparison of bending moment between UTRAP and closed-form solutions

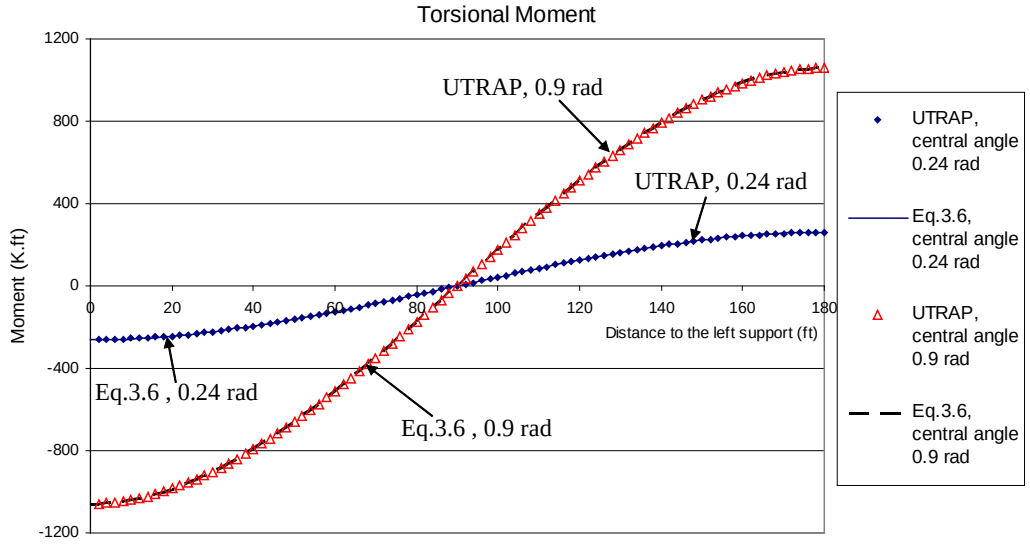

Figure 3.5 Comparison of total torsional moment between UTRAP and closed-form solutions

Figure 3.6 shows a simply supported curved girder under a uniform load per unit length *w*. By taking the sum of force in vertical direction, the reaction force on both ends can be derived as $\frac{wl}{2}$, where *l* is the curved length. A straight dashed line that connects the two ends of a curved girder is called the chord *c*.

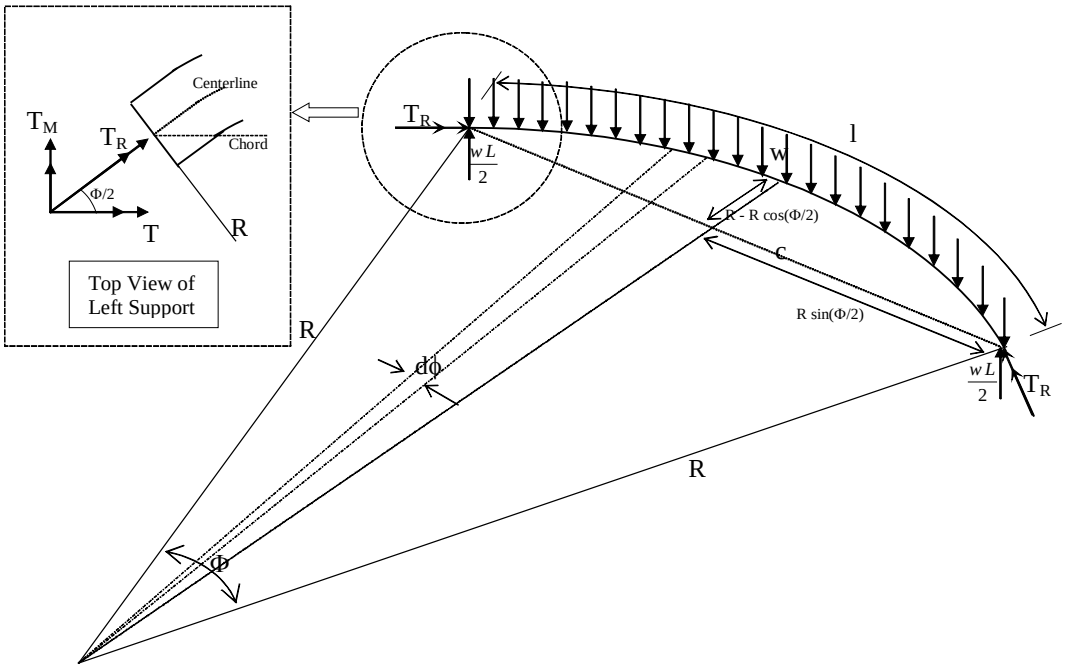

Figure 3.6 Simply supported curved girder under the uniform load

The box in Figure 3.6 shows that for a non-skewed support with respect to the girder centerline (support that is perpendicular to the girder centerline), the support torque T_R can be resolved into two components. The first component is *T*, which is parallel to the chord of curved girder, and the second component is T_M, which is perpendicular to the chord of the curved girder. T_M is the support torque component that is in the same direction (i.e. additive) with the midspan bending moment.

The first component of torque, *T*, can be obtained by taking the sum of torques at midspan. From torque equilibrium, the midspan torque is known to be zero, and therefore *T* can be expressed as in Eq.3.7. Refer to the Appendix C for a complete derivation of *T*.

$$T = \underbrace{\frac{wl}{2}}_{\text{Reaction}} \underbrace{R\left(1-\cos\left(\frac{\Phi}{2}\right)\right)}_{\text{Reaction Torque arm}} - \underbrace{\left[\int_0^{\frac{\Phi}{2}} \left(wR\overbrace{\left(R-R\cos\phi\right)}^{\text{Torque arm}}\right)\mathrm{d}\phi\right]}_{\text{Torque from uniform load}}$$

$$T = wR^2\left(\sin\left(\frac{\Phi}{2}\right) - \frac{\Phi}{2}\cos\left(\frac{\Phi}{2}\right)\right) \tag{3.7}$$

Having calculated the first component of torque *T* from Eq.3.7, the support torque T_R can be determined using geometry as expressed in Eq.3.8. It should be noted that T_R is the support torque given in the UTRAP output.

$$T_R = \frac{T}{\cos\frac{\Phi}{2}} = wR^2\left(\tan\left(\frac{\Phi}{2}\right) - \frac{\Phi}{2}\right) \tag{3.8}$$

The second component of the torque, T_M, can be calculated from geometry. As shown in the detailed view in Figure 3.6, T_M is the component of the support torque that is perpendicular to the chord and is expressed as follows:

$$T_M = T\tan\left(\frac{\Phi}{2}\right) = wR^2\left(\sin\left(\frac{\Phi}{2}\right) - \frac{\Phi}{2}\cos\left(\frac{\Phi}{2}\right)\right)\tan\left(\frac{\Phi}{2}\right)$$

$$T_M = wR^2\sin\left(\frac{\Phi}{2}\right)\left(\tan\left(\frac{\Phi}{2}\right) - \frac{\Phi}{2}\right) \tag{3.9}$$

Maximum bending moment in a simply supported curved girder under a uniform load occurs at the midspan. Midspan bending moment M_{mid} in a simply supported curved girder can be derived by taking the moment equilibrium about

midspan, as expressed in Eq.3.10. In order to correctly calculate the midspan bending moment, the second component of the support torque, $T_{M,}$ needs to be added in our moment equilibrium equation. Refer to Appendix C for a complete derivation of midspan bending moment.

$$M_{mid} = T_M + \underbrace{\frac{wl}{2}}_{\text{Reaction}} \underbrace{R\sin\left(\frac{\Phi}{2}\right)}_{\text{Ioment arm}} - \underbrace{\left[\int_0^{\frac{\Phi}{2}} w\,R\,\overbrace{(R\sin\phi)}^{\text{Moment arm}}\,d\phi\right]}_{\text{Moment from uniform load}}$$

$$M_{mid} = w\,R^2\left(\frac{1}{\cos\left(\frac{\Phi}{2}\right)} - 1\right) \tag{3.10}$$

As the radius of curvature R becomes infinity (i.e straight girder), the midspan bending moment expression shown in Eq.3.10 will become $\frac{wl^2}{8}$, which is the well-known midspan bending moment for a straight girder under a uniform load w.

The support torque calculated in Eq.3.8 is exactly the same as the one calculated using Nakai and Yoo's exact formula (by substituting ϕ = 0 (at left support) or $\phi = \Phi$ (at right support), as expressed in Eq.3.6). The midspan bending moment calculated in Eq.3.10 is also identical to the one calculated using Nakai and Yoo's exact formula (by substituting $\phi = \Phi/2$ (at midspan), as expressed in Eq.3.5).

3.2.2 Approximate solutions

Figure 3.3, Figure 3.4, and Figure 3.5 show that the maximum shear force due to bending in a simply-supported curved girder occurs at the support, the maximum bending moment occurs at the midspan, and the maximum total torsional moment occurs at the support. In the design process, predicting the maximum values by using the approximate method is convenient. This section will present an approximate solution for estimating the maximum shear force, midspan bending moment, and support torque.

3.2.2.1 Shear force

By taking the sum of forces in the vertical direction, the maximum shear force due to bending can be determined as $\frac{wl}{2}$, where *w* is the uniform load along the length and *l* is the arc length of the curved girder. In the example presented earlier (180-ft simply supported curved girder with 0.8 k/ft uniform load placed on it), the maximum shear force is 72 kip. This maximum shear force depends only on the magnitude of uniform load and the length of the curved girder.

3.2.2.2 Midspan bending moment

Midspan bending moment in non-skewed curved girder is not the same as that predicted by simply using classical beam theory for a straight girder, which is $\frac{wl^2}{8}$. One of the reasons is because in a curved girder, there is an interaction between support torque and midspan bending moment. From Figure 3.6, it can be observed that there is a component of support torque that is in the same direction and thus is additive with the midspan bending moment. This component of support torque is shown inside the box in Figure 3.6 and called T_M. Since the only

possible support condition in the UTRAP program is a non-skewed support, the effect of a skewed support is beyond the scope of this thesis.

Therefore, as long as the component of support torque T_M is added, the midspan bending moment can be estimated using a classical beam theory for a straight girder, which is $\frac{wc^2}{8}$. Instead of using the curved length, the length used in predicting midspan bending moment using classical beam theory for a straight girder is the chord length *c*. The approximate method to calculate midspan bending moment is

$$M_{mid,approx.} = \frac{wc^2}{8} + T_M \qquad (3.11)$$

where: c = chord length = $2R\sin\left(\frac{\Phi}{2}\right)$

T_M = Support torque component that is in the direction of midspan bending moment

$$= T_R \sin\left(\frac{\Phi}{2}\right)$$

$$= \left[wR^2 \left(\tan\left(\frac{\Phi}{2}\right) - \frac{\Phi}{2} \right) \right] \sin\left(\frac{\Phi}{2}\right)$$

R = radius of curvature

Φ= central angle = l/R , where l is the curved length

In addition to the Eq.3.11, Oleinik and Heins (1974, 1975) presented an approximate method to calculate midspan bending moment for curved girders with a ratio of the curved length to the radius of curvature (i.e central angle) smaller than or equal to 1.0 ($l/R \leq 1.0$). Their equation is expressed in Eq.3.12.

$$M\ curved = K \times \frac{wl^2}{8} \tag{3.12}$$

where w is uniform load along the length, l is the curved length, and K is a constant that depends on the type of loading. Constant for the uniform dead load, KD is expressed in Eq.3.13.

$$KD = 1 + \frac{1}{10\left(\frac{R}{l}\right)^2} \tag{3.13}$$

3.2.2.3 Support torque

Memberg (2002) presented an approximate method for dealing with torsion in curved girders. As discussed earlier, in curved girders, no matter where the load is placed, there is always a component of torsional loading due to curvature. Figure 3.7 shows a plan view of a curved girder.

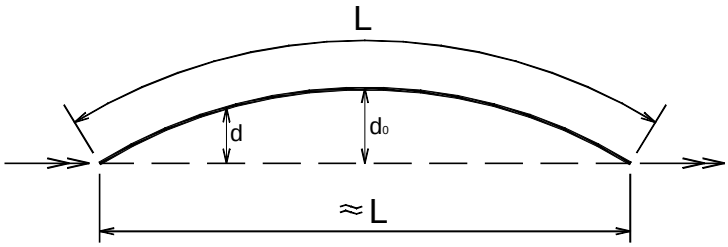

Figure 3.7 Plan view of curved girder (Memberg 2002)

In Figure 3.7, the straight perpendicular distance from any point on the chord to the curved girder is denoted by d. The maximum d occurs at the center of the arc--where it is denoted d_0 -- and it is expressed in Eq.3.14.

$$d_0 = R\left(1 - \cos\left(\frac{\Phi}{2}\right)\right) \tag{3.14}$$

where R is the radius of curvature and Φ is the central angle.

Assuming there is no eccentric load, the applied torque at any point along the girder is equivalent to the load at that point multiplied by *d* at that point. From a torsional point of view, the symmetrical loading on a curved girder whose curved length is *l* can be approximated with a parabolic torque distribution on a straight girder whose length is *l*. Figure 3.8 shows how the torsion due to curvature is applied to a straight girder of equal length.

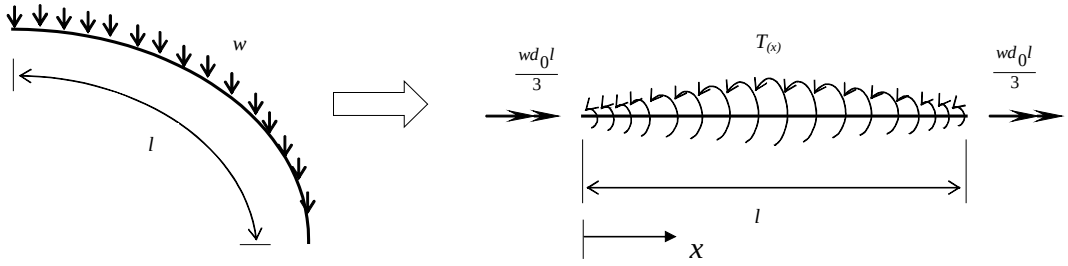

Figure 3.8 Approximating a curved girder with a straight girder from a torsional point of view

The torque at any point is calculated by multiplying the value of the distributed load *w* by *d* at that point, where *d* is defined as a parabolic function. Applied torque at any point along the straight line $T_{(x)}$ is

$$T_{(x)} = \frac{4wd_0}{l}x - \frac{4wd_0}{l^2}x^2 \qquad (3.15)$$

$$\text{for } \left\{0 \le x \le \frac{l}{2}\right\} \text{ symmetric}$$

Each support must resist half of the total applied torque. Since $T_{(x)}$ is symmetric with respect to the midspan, the approximate support torque in the direction of chord $T_{approx.}$ shown in Figure 3.8 can be found as follows:

$$T_{approx} = \int_0^{l/2} T_{(x)} dx = \int_0^{l/2} \left(\frac{4wd_0}{l} x - \frac{4wd_0}{l^2} x^2 \right) dx = \frac{wd_o l}{3} \qquad (3.16)$$

This expression of support torque in the direction of the chord is roughly equivalent to *T*, derived using equilibrium method (as expressed in Eq.3.7). Since the approximate support torque in the direction of chord is known, the approximation of real support torque $T_{R,approx.}$, which estimates UTRAP support torque, can be stated in as follows:

$$T_{R,approx.} = \frac{T_{approx}}{\cos\left(\frac{\Phi}{2}\right)} = \frac{wd_0 l}{3\cos\left(\frac{\Phi}{2}\right)} \qquad (3.17)$$

3.2.2.4 M/R Method

Tung and Fountain (1970) indicated that for a curved girder that has a central angle less than 30° (≈ 0.5 radian), the bending and torsional analysis of that curved girder can be uncoupled and investigated independently. This means that the bending moment of a curved girder can be found by straightening the curved girder to its full developed length (i.e. its arc length), and calculating the bending moment M using classical beam theory. Using the M/R Method, the midspan bending moment of a curved girder under a symmetrical uniform load is

$$M_{mid,approx.} = \frac{wl^2}{8} \qquad (3.18)$$

where *l* is the arc length of a curved girder. Eq.3.18 is different than Eq.3.11 in two aspects. First, the length used in Eq.3.18 is the arc length, whereas the length used in Eq.3.11 is the chord length. Second, Eq.3.18 does not consider the support torque component that is in the same direction as the midspan bending moment, whereas Eq.3.11 does.

The torsional analysis of a curved girder under a symmetrical uniform load using the M/R Method can then be performed by applying a distributed torsional loading of M/R to the straightened curved girder whose length is equal to its arc length. This analysis can be illustrated with a figure similar to Figure 3.9, except that the applied torque at any point along the straight line $T_{(x)}$ is

$$T_{(x)} = \frac{M_{(x)}}{R} = \frac{\frac{wx}{2}(l-x)}{R} \tag{3.19}$$

where w is the uniform load, x is the location along the length, measured from the left support, l is the arc length, and R is the radius of curvature. The approximate support torque in the direction of the chord, $T_{approx.}$, is

$$T_{approx.} = \int_0^{l/2} T_{(x)}\,dx = \int_0^{l/2} \left(\frac{\frac{wx}{2}(l-x)}{R} \right) dx = \frac{wl^3}{24R} \tag{3.20}$$

The approximation of real support torque $T_{R,approx.}$, is

$$T_{R,approx.} = \frac{T_{approx}}{\cos\left(\frac{\Phi}{2}\right)} = \frac{wl^3}{24R\cos\left(\frac{\Phi}{2}\right)} \tag{3.21}$$

3.2.3 Comparisons between approximate solution and exact solution

In order to examine the accuracy of the approximate solutions for different lengths and radii of curvature, the approximate solutions were compared to the exact solution.

The maximum shear force due to bending, which corresponds to the reaction force, can be predicted using $\frac{wl}{2}$. This maximum shear force exactly

matches the exact solution. As was discussed earlier, this maximum shear force depends only on the magnitude of the uniform load and the curved length.

The approximate method for calculating midspan bending moment for a relatively small central angle gives a reasonable prediction of the actual midspan bending moment. Table 3-1 compares result from UTRAP, the exact method (Eq.3.10) and the approximate methods (Eqs.3.11, 3.12 and 3.18). Table 3-1 shows that the percentages of error of the approximate methods depend only on the central angle. Figure 3.9 shows the percent error of the midspan bending moment obtained from approximate methods with respect to UTRAP solutions as a function of the central angle.

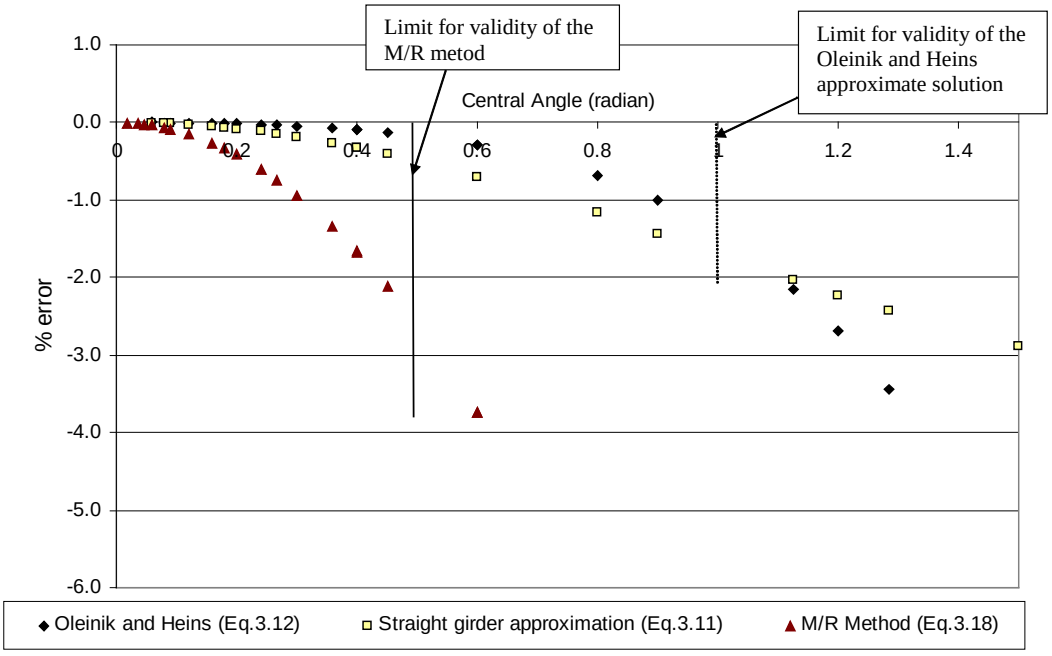

Figure 3.9 Percentage of error of the midspan bending moment obtained from approximate method

Table 3-1 Comparison of UTRAP results with exact and approximate method to estimate midspan bending moment

w	*l*	*R*	Central Angle	UTRAP	EXACT	APPROXIMATE METHOD					
				Midspan moment	Integration (Eqn.(3.10))	Straight girder approx. (Eqn.(3.11))	% Error	Oleinik, Heins (Eqn.(3.12))	% Error	M/R Method (Eqn.(3.18))	% Error
(K/ft)	ft	ft	rad	K.ft	K.ft	K.ft		K.ft		K.ft	
1.5	120	100	1.20	3174.4	3174.4	3103.8	-2.2	3088.8	-2.7 *	2700	-14.94 **
1.5	120	200	0.60	2805.1	2805.1	2785.5	-0.7	2797.2	-0.3	2700	-3.75 **
1.5	120	300	0.40	2745.7	2745.7	2736.9	-0.3	2743.2	-0.1	2700	-1.66
1.5	120	400	0.30	2725.5	2725.5	2720.5	-0.2	2724.3	0.0	2700	-0.94
1.5	120	500	0.24	2716.3	2716.3	2713.1	-0.1	2715.6	0.0	2700	-0.60
1.5	120	1000	0.12	2704.1	2704.1	2703.2	0.0	2703.9	0.0	2700	-0.15
0.8	180	120	1.50	4224.3	4224.4	4102.3	-2.9	3969.0	-6.0 *	3240	-23.30 **
0.8	180	140	1.29	3910.5	3910.5	3815.2	-2.4	3775.6	-3.4 *	3240	-17.15 **
0.8	180	160	1.13	3730.2	3730.2	3654.4	-2.0	3650.1	-2.1 *	3240	-13.14 **
0.8	180	200	0.90	3537.9	3537.9	3487.2	-1.4	3502.4	-1.0	3240	-8.42 **
0.8	180	300	0.60	3366.1	3366.1	3342.6	-0.7	3356.6	-0.3	3240	-3.75 **
0.8	180	400	0.45	3309.8	3309.8	3296.4	-0.4	3305.6	-0.1	3240	-2.11
0.8	180	500	0.36	3284.3	3284.3	3275.7	-0.3	3282.0	-0.1	3240	-1.35
0.8	180	1000	0.18	3251	3251.0	3248.8	-0.1	3250.5	0.0	3240	-0.34
0.8	180	2000	0.09	3242.7	3242.7	3242.2	0.0	3242.6	0.0	3240	-0.08
0.8	180	3000	0.06	3241.2	3241.2	3241.0	0.0	3241.2	0.0	3240	-0.04
0.8	180	4000	0.05	3240.7	3240.7	3240.5	0.0	3240.7	0.0	3240	-0.02
0.8	180	5000	0.04	3240.4	3240.4	3240.3	0.0	3240.4	0.0	3240	-0.01
0.8	180	10000	0.02	3240.1	3240.1	3240.1	0.0	3240.1	0.0	3240	0.00
3	80	100	0.80	2571.1	2571.1	2541.0	-1.2	2553.6	-0.7	2400	-6.65 **
3	80	200	0.40	2440.7	2440.7	2432.8	-0.3	2438.4	-0.1	2400	-1.67
3	80	300	0.27	2417.9	2417.9	2414.4	-0.1	2417.1	0.0	2400	-0.74
3	80	400	0.20	2410	2410.0	2408.0	-0.1	2409.6	0.0	2400	-0.41
3	80	500	0.16	2406.4	2406.4	2405.1	-0.1	2406.1	0.0	2400	-0.27
3	80	1000	0.08	2401.6	2401.6	2401.3	0.0	2401.5	0.0	2400	-0.07

*: Central angle is greater than 1 radian. Oleinik and Heins indicated that their method can only be used for the girder that has a central angle less than 1 radian.

**: Central angle is greater than 0.5 radian. Tung and Fountain indicated that the M/R method can only be used for the girder than has a central angle less than 0.5 radian.

Examining the percentage of error in Figure 3.9, it can be summarized that all three approximate methods underestimate the actual midspan bending moment. However, for a relatively small central angle (less than 1.2 radian), the percentage of error of Oleinik and Heins and the straight girder approximation methods are small (less than 3%). In general, for a central angle less than 1 radian, the Oleinik and Heins' method gives a smaller percentage of error than the straight girder approximation. However, its percentage of error increases dramatically for a central angle larger than 1 radian. Therefore, it is clear that as Oleinik and Heins recommended, their methods can only be used for the curved girder that has a central angle less than 1 radian. Among the three approximate methods, the percentage of error of the M/R method is the largest. However, as Tung and Fountain indicated, the M/R method is only appropriate for a curved girder that has a central angle less than 0.5 radians. For a central angle less than 0.5 radians, the percentage of error of the M/R method is less than 2.5%.

The approximate method for calculating support torque gives a good prediction of the actual support torque. Table 3-2 shows the results for UTRAP, the exact method (Eq.3.8) and the approximate methods (Eqs.3.17 and 3.21). Since UTRAP gives the torque at a location 2 feet away from the support, the UTRAP solution and the exact solution are slightly different. The percentages of error of the approximate methods also depend only on the central angle.

Table 3-2 shows that both approximate methods to predict the support torque slightly overestimate the actual support torque. However, the percentage of error is small (less than 1%). In general, the percentage of error of the M/R method is larger than the approximate method expressed in Eq.3.17. Tung and Fountain indicated that the M/R method is only appropriate for a curved girder that has a central angle less than 0.5 radians. For a central angle less than 0.5 radians, the percentage of error of the M/R method is less than 1%.

Table 3-2 Comparison of UTRAP results with exact and approximate method to estimate support torque

w	l	R	Central Angle	UTRAP Torque at 2 ft from support	Exact (using force equilibirum method)			Approximate Method			
					T (Eqn.(3.7))	T_M (Eqn.(3.9))	Support Torque (T_R) (Eqn.(3.8))	$T_{R,approx.}$ (Eqn.(3.17))	% error	$T_{R,approx.}$ (Use M/R Method) (Eqn.(3.21))	% error
(K/ft)	ft	ft	rad	K.ft	K.ft	K.ft	K.ft	K.ft		K.ft	
1.5	120	100	1.20	1260	1041.6	712.6	1262.1	1269.77	0.61	1308.56	3.68 **
1.5	120	200	0.60	559.3	535.2	165.5	560.2	561.02	0.15	565.25	0.91 **
1.5	120	300	0.40	365.3	358.6	72.7	365.9	366.10	0.07	367.32	0.40
1.5	120	400	0.30	272	269.4	40.7	272.5	272.55	0.04	273.07	0.23
1.5	120	500	0.24	216.9	215.7	26.0	217.3	217.30	0.02	217.56	0.14
1.5	120	1000	0.12	108	108.0	6.5	108.2	108.16	0.01	108.19	0.04
0.8	180	120	1.50	2090.6	1530.7	1426.0	2092.0	2112.20	0.97	2214.06	5.83 **
0.8	180	140	1.29	1663.1	1332.0	997.7	1664.2	1675.95	0.70	1734.88	4.24 **
0.8	180	160	1.13	1390.4	1177.0	742.0	1391.4	1398.82	0.54	1436.30	3.23 **
0.8	180	200	0.90	1057	952.5	460.1	1057.8	1061.37	0.34	1079.46	2.05 **
0.8	180	300	0.60	671.7	642.2	198.7	672.2	673.22	0.15	678.30	0.91 **
0.8	180	400	0.45	495.7	483.5	110.7	496.0	496.47	0.08	498.57	0.51
0.8	180	500	0.36	393.6	387.5	70.5	393.9	394.12	0.05	395.18	0.32
0.8	180	1000	0.18	194.9	194.2	17.5	195.0	195.06	0.01	195.19	0.08
0.8	180	2000	0.09	97.2	97.2	4.4	97.3	97.28	0.00	97.30	0.02
0.8	180	3000	0.06	64.8	64.8	1.9	64.8	64.82	0.00	64.83	0.01
0.8	180	4000	0.05	48.6	48.6	1.1	48.6	48.61	0.00	48.61	0.01
0.8	180	5000	0.04	38.9	38.9	0.7	38.9	38.89	0.00	38.89	0.00
3	80	100	0.80	681.3	629.8	266.3	683.8	685.64	0.27	694.85	1.62 **
3	80	200	0.40	324	318.7	64.6	325.2	325.42	0.07	326.51	0.40
3	80	300	0.27	214.1	213.0	28.6	214.9	214.93	0.03	215.24	0.18
3	80	400	0.20	160.1	159.8	16.0	160.6	160.67	0.02	160.80	0.10
3	80	500	0.16	127.9	127.9	10.3	128.3	128.34	0.01	128.41	0.06
3	80	1000	0.08	63.8	64.0	2.6	64.0	64.04	0.00	64.05	0.02

**: Central angle is greater than 0.5 radian. Tung and Fountain indicated that the M/R method can only be used for the girder than has a central angle less than 0.5 radian.

3.3 CONTINUOUS GIRDER

Predicting cross-sectional forces in a continuous girder is more complicated than that for a simply-supported girder, because a continuous girder is a statically indeterminate. In order to determine the cross-sectional forces in a continuous straight girder, one must use one of the methods of indeterminate analysis (i.e. stiffness method, flexibility method, moment distribution, etc). The problem in a continuous curved girder is much more complicated than in a continuous straight girder due to interaction between bending and torsion in curved girders. All simple formulas presented in sections 3.1 and 3.2 cannot be used for analysis of continuous girders. However, Tung and Fountain indicated that the M/R method can be applied to the analysis of continuous curved girders that satisfy the following limitations:

- The central angle of each span should not exceed 25° (0.44 radian) and the weighted average of ratio of bending rigidity to torsional rigidity *EI/GJ* in each span should not exceed 4.0, where *G* is the shear modulus of elasticity and *J* is the pure torsional constant.
- If all the supports are torsionally fixed, the central angle of the entire length of girder should not exceed 90° (1.6 radian).

Those limitations are based on a parametric study and subject to personal judgment about the acceptable accuracy of the approximate solutions.

This section presents cross-sectional forces of a three-span continuous girder based on UTRAP solutions and the effect of changing the central angle and the equivalent plate thickness on the cross-sectional forces. In addition, the effects of the central angle and the ratio of *EI/GJ* on the accuracy of the M/R method in predicting bending moment are discussed. The example of a continuous girder

presented in this section is the three-equal-span continuous girder that has a constant radius of curvature *R* and a centerline arc length of 480 ft under a symmetrical uniformly distributed load of 3.3 k/ft. That model is known as Model 2 and its cross-section dimensions are shown in Figure 1.5. An Alternating-Diagonal top lateral bracing system with a 10-ft panel length is used to represent a pseudo-closed section.

Different radii of curvature are used to examine the sensitivity of the cross-sectional forces to the central angle in a continuous girder. In addition, both the open-section and the pseudo-closed sections with the different equivalent plate thicknesses of Model 2 are used. Tables 3-3 and 3-4 shows the analysis cases studying the effect of the central angle and the ratio of *EI/GJ*, respectively, on the cross-sectional forces in a continuous girder. "Open" in Table 3-4 indicates that there is no lateral bracing system.

Table 3-3 Analysis cases to study the effect of the central angle on the cross-sectional forces

Radius of curvature, R	Total central angle	Central angle of each span
Straight	-	-
450 ft	61° (1.07 radian)	20.4° (0.356 radian)
225 ft	122° (2.13 radian)	40.7° (0.711 radian)

NOTE: Total length = 480 ft, each span length = 160 ft

Table 3-4 Analysis cases to study the effect of the ratio of EI/GJ on the cross-sectional forces

Equivalent plate thickness t_{eq}	Diagonal area	Moment of inertia, I	Pure torsional Constant, J	Ratio of EI/GJ
0.08 in	14.2 in^2	182198 in^4	121263 in^4	3.97
0.04 in	5.96 in^2	170104 in^4	67848 in^4	6.63
0.02 in	2.76 in^2	163804 in^4	36070 in^4	12
Open	-	157328 in^4	34.8 in^4	11948

NOTE: E=29600 ksi and G=11200 ksi

3.3.1 Shear force

Figure 3.10 shows the UTRAP solution for the shear force diagram for both straight and curved Model 2 girders. The shear force diagram is anti-symmetrical about midspan. Figure 3.10 shows that the shear forces along the length for both open sections and pseudo-closed sections in a continuous straight girder are the same. The shear force diagram for a curved girder that has a t_{eq} of 0.08 inches is the same as that for a straight girder. However, there will be slight discrepancies between the shear force diagram for the open-section curved girder and that for the straight girder.

3.3.2 Bending moment

Figure 3.11 shows the bending moment diagram for an open-section and pseudo-closed section continuous straight girder. Figure 3.11 shows that the bending moments along the length for both the open-section and the pseudo-closed section continuous straight girder are the same. The bending moment diagram is symmetrical about midspan, since the continuous girder is itself symmetric about midspan.

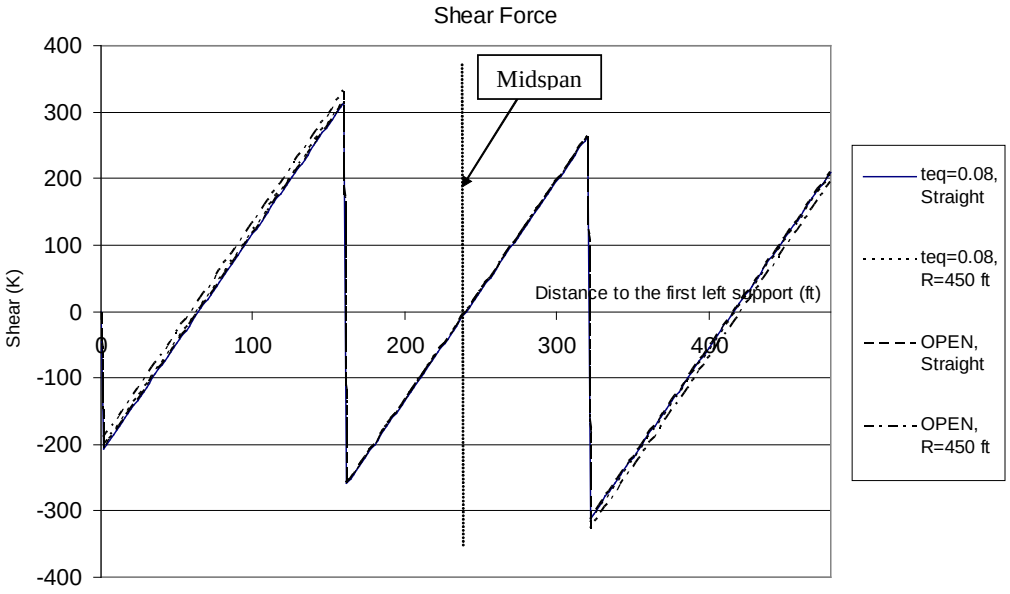

Figure 3.10 Shear force diagram of three-span continuous girder

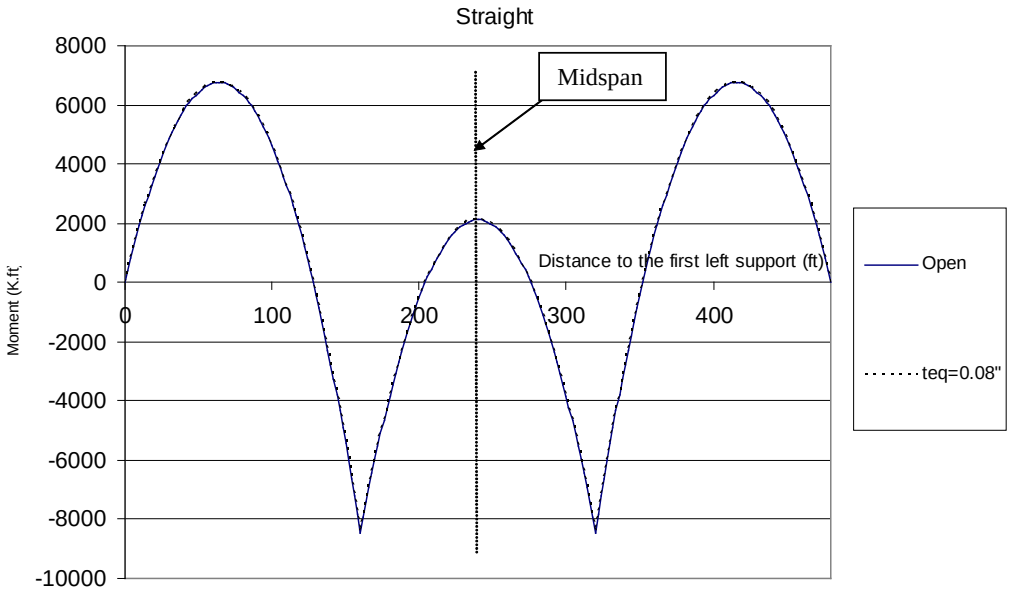

Figure 3.11 Bending moment diagram of a straight continuous girder

Tung and Fountain indicated that the M/R method can be applied to a continuous girder. Using the M/R method, the bending moment diagram for a continuous curved girder can be approximated with that of a continuous straight girder whose length is equal to the arc length of the curved girder. The accuracy of the approximate solution depends on the central angle of the span and the entire bridge and on the ratio of *EI/GJ*. In order to examine the effect of the central angle on the accuracy of approximate solutions, Figure 3.12 and Figure 3.13 show the comparison between the approximate and the exact bending moment diagrams for *EI/GJ* ratios of 3.96 and 12, respectively. Since the bending moment diagram is symmetric about midspan, the bending moment diagrams are shown for only half the girder length.

Figure 3.12 and Figure 3.13 show that the accuracy of representing bending moment diagram of a continuous curved girder with that of a continuous straight girder decreases as the central angle increases. The M/R method overestimates positive bending moment (i.e. compression on the top fiber) and underestimates negative bending moment (i.e. compression on the bottom fiber). Figure 3.12 and Figure 3.13 show that the accuracy of the approximate solution does not significantly change for different ratios of *EI/GJ*.

However, in order to examine the effect of the ratio of *EI/GJ* on the accuracy of approximate solutions in more detail, Figure 3.14 and Figure 3.15 show the comparisons between the approximate bending moment diagram and the bending moment diagram of a continuous curved girder for the central angle of 61° and 122°, respectively. Figure 3.14 and Figure 3.15 show that the accuracy of the approximate solutions is not significantly affected by the change in the ratio of *EI/GJ*, as long as that ratio is kept within the same order of magnitude. Certainly, the approximate method is not accurate for the girder that has a very large ratio of

EI/GJ (i.e. an open section). In general, it is easy to satisfy the limiting ratio of *EI/GJ* of around 10 by using a reasonable amount of top lateral bracing system.

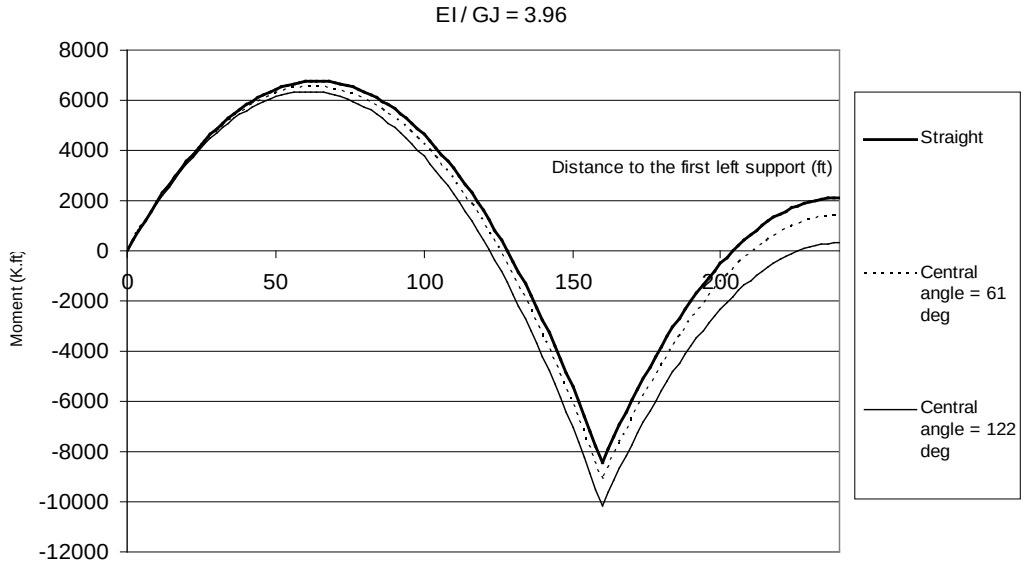

Figure 3.12 Bending moment diagram with EI/GJ=3.96

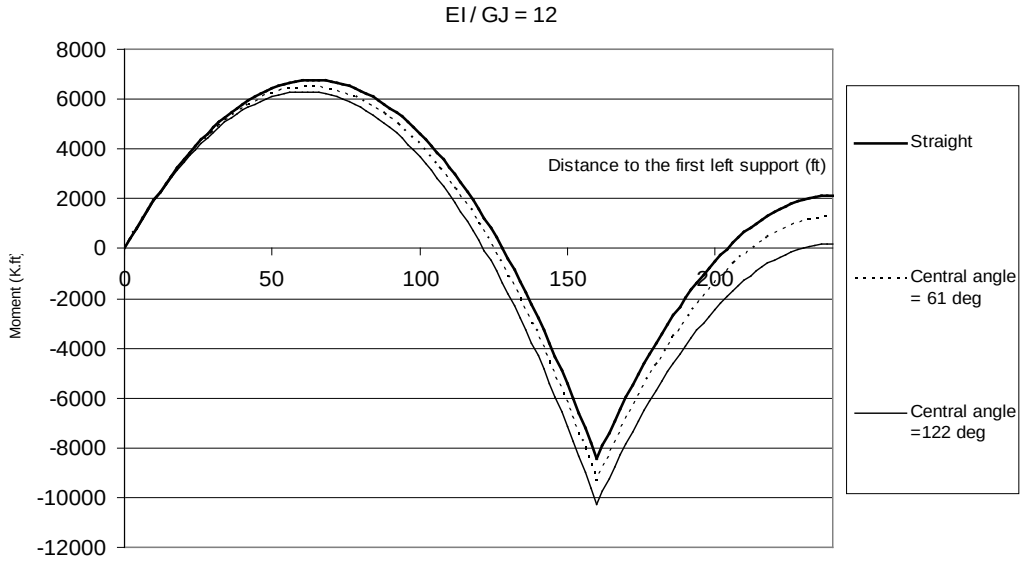

Figure 3.13 Bending moment with EI/GJ=12

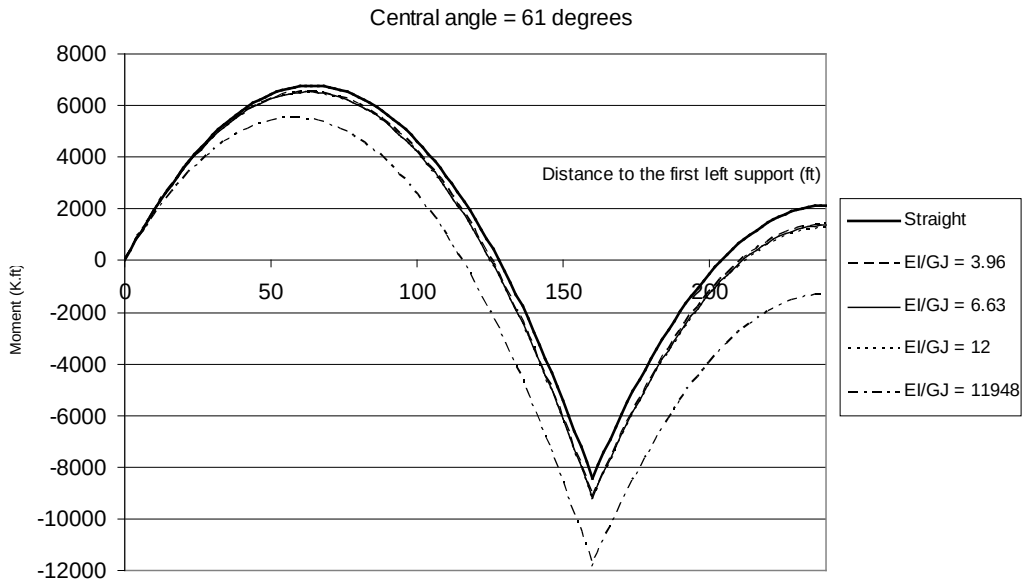

Figure 3.14 Bending moment diagram with central angle of 61°

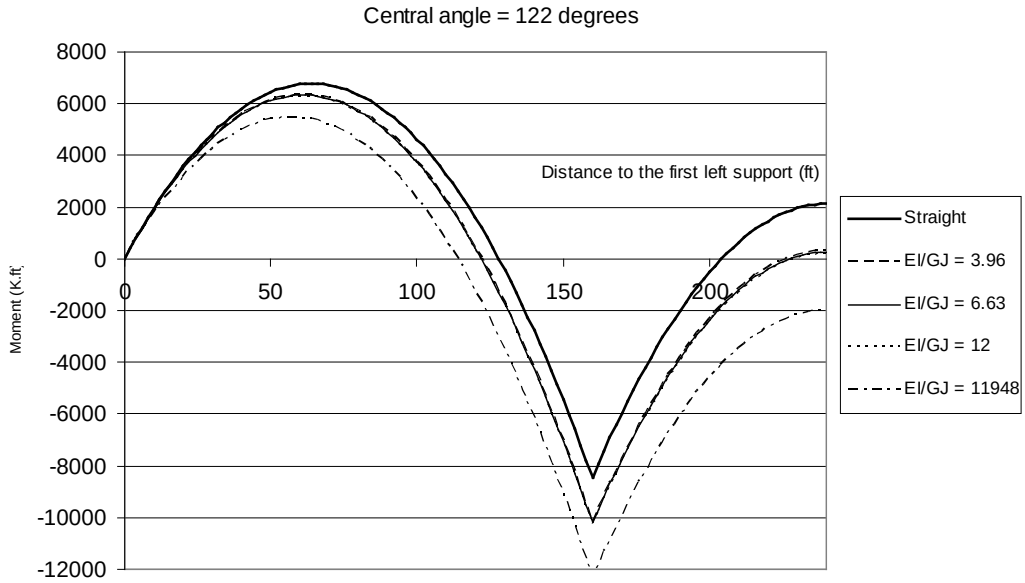

Figure 3.15 Bending moment diagram with central angle of 122°

Unlike the accuracy of the M/R method in predicting bending moment for a simply-supported curved girder, the accuracy of the M/R method in predicting bending moment for a continuous curved girder depends not only on the central angle, but also on the ratio of *EI/GJ*. The explanation for this is that the analysis of a continuous girder is a statically indeterminate. In a continuous curved girder, in addition to the static indeterminacy, there is an interaction between bending moment and torsional moment. Therefore, changes in the relative ratio between the bending rigidity and the torsional rigidity will definitely alter the cross-sectional force distribution, hence changing the bending moment diagram. It should be noted that for a simply supported curved girder, the accuracy of the M/R method to predict the bending moment of open-sections and pseudo-closed sections that have similar central angles is the same. Tung and Fountain stated that M/R method is applicable to a girder that has a total central angle of less than 90° and a ratio of *EI/GJ* of less than 4.0. However, Figures 13.12 through 13.15 show that the accuracy of the M/R method is much more sensitive to the total central angle than to the ratio of *EI/GJ*.

3.3.3 Torsional moment

Unlike the bending moment diagram, the torsional moment diagram is anti-symmetrical about midspan (like the shear diagram) even though the continuous girder is symmetrical about midspan. Figure 3.16 shows the torsional moment diagram for the three-equal-span continuous curved girder with a central angle of 122 degrees and an *EI/GJ* ratio of 3.96. Since the girder is symmetrical about midspan, the torsional moment diagram is shown for only half the girder length.

In order to study the effect of the central angle and the ratio of EI/GJ on the torsional moment diagram, Figures 3.17 and 3.18 show torsional moment diagrams for an open-section (corresponding to an *EI/GJ* ratio of 11948) and a pseudo-closed section of continuous curved girders with total central angles of 61 degrees and 122 degrees, respectively.

Figures 3.17 and 3.18 show that torsional moment diagrams are very sensitive to the central angle. Unlike the torsional moment diagram for a simply-supported curved girder that depends only on the central angle, torsional moment diagram for a continuous curved girder depends not only on the central angle, but also on the ratio of *EI/GJ*. The torsional moment diagram for the open-section (*EI/GJ* = 11948) is significantly different than that for the pseudo-closed sections. However, the torsional moment diagrams for pseudo-closed sections that have the same orders of magnitude of *EI/GJ* are not significantly different.

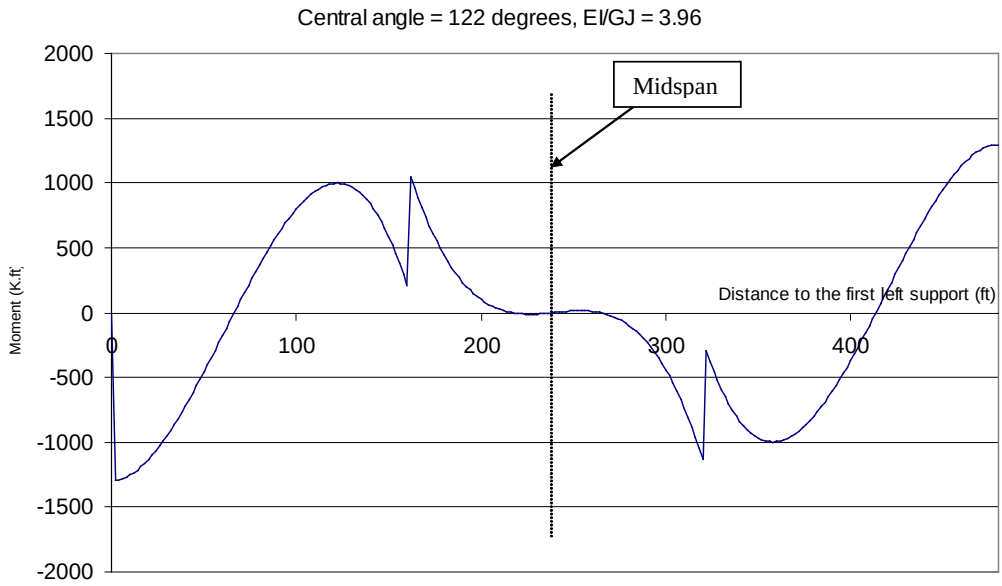

Figure 3.16 Torsional moment diagram

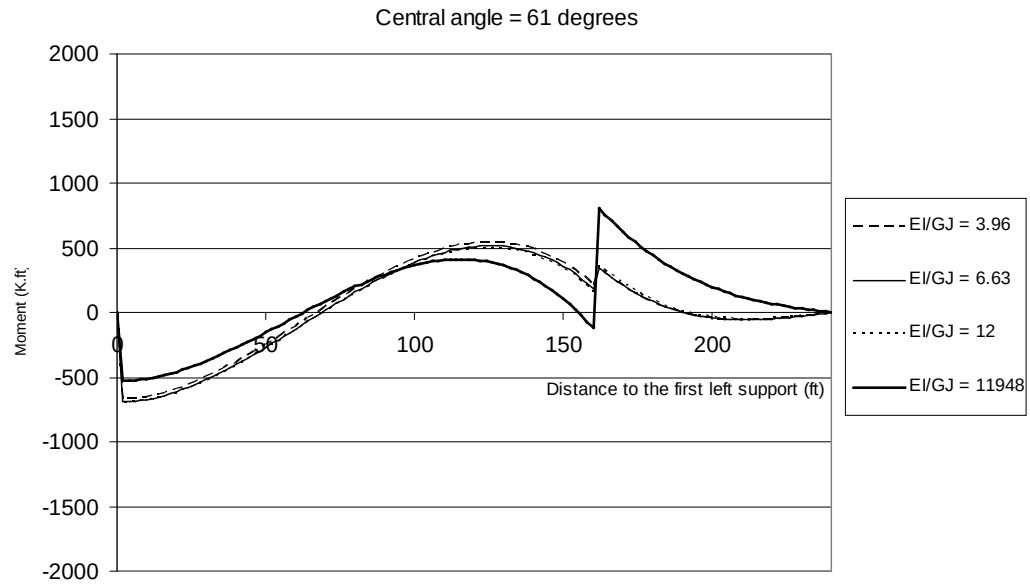

Figure 3.17 Torsional moment diagram with central angle of 61°

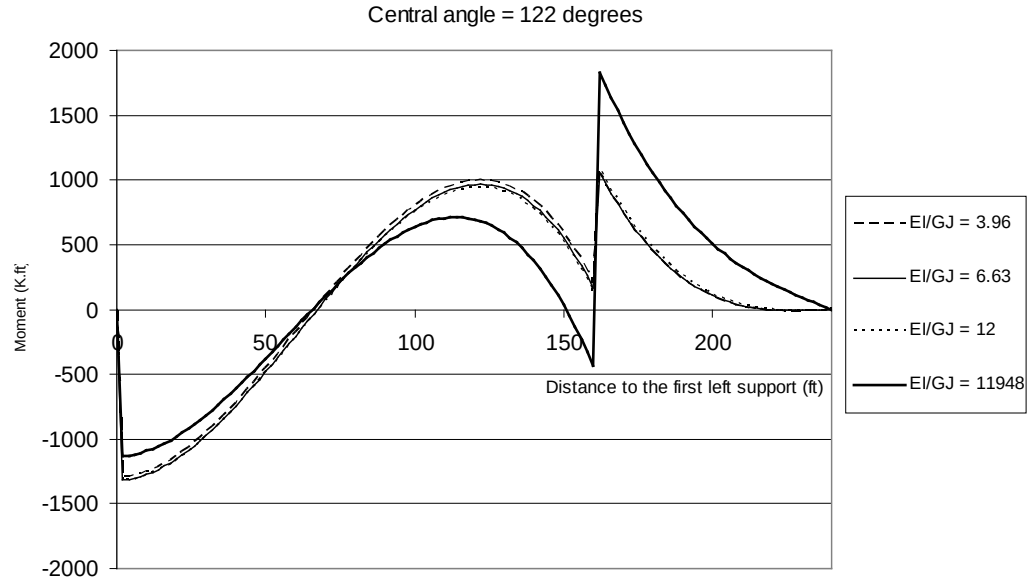

Figure 3.18 Torsional moment diagram with central angle of 122°

Tung and Fountain indicated that by using the M/R method, the torsional moment diagram for a continuous curved girder can be found by the following procedures:

- Determining bending moments M for the straightened girder.
- Applying the distributed torsional loading of M/R to each span of the straightened curved girder with the proper torsional boundary condition and determining the torsional moment in each span.

Figure 3.19 compares torsional moment for the three-equal-span of a Model 2 continuous girder with an equivalent plate thickness of 0.08 inches from the UTRAP solutions and the M/R method.

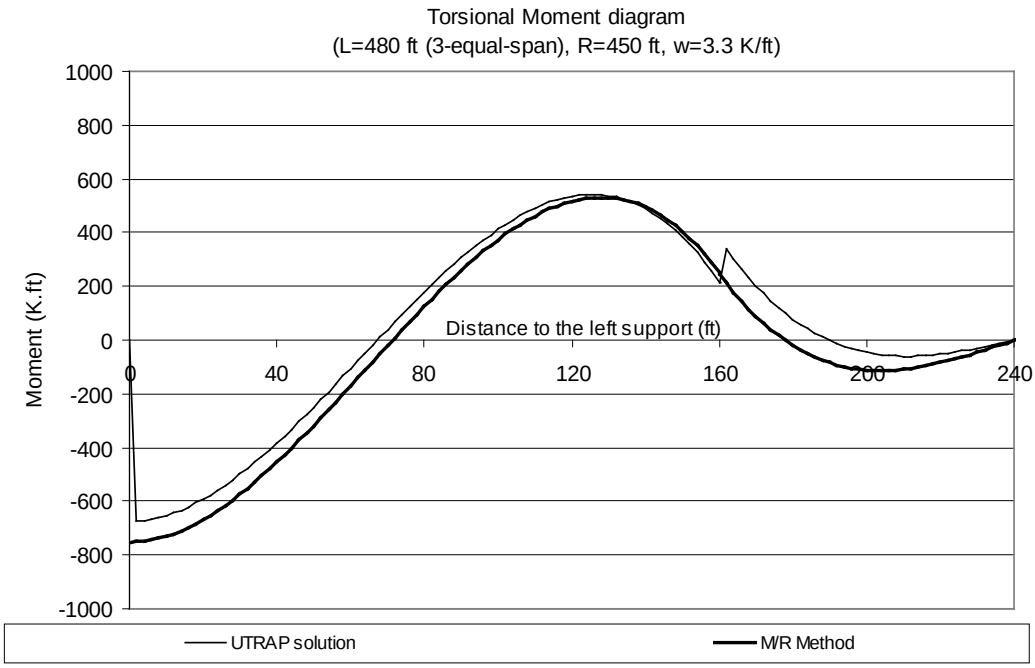

Figure 3.19 Approximate and real torsional moment diagram

Figure 3.19 shows that the M/R method can predict a torsional moment in a continuous curved girder well. The discrepancies of the torsional moments are

largest at the supports and reduce progressively toward the midspan. In addition, unlike the exact solutions for UTRAP, the predicted torsional moment at the interior support (at 160-ft from the left support) is smooth. The M/R method cannot capture the difference in torsional moments at both sides of the interior support. For a continuous girder with constant radius of curvature and bending rigidity, the M/R method gives only one set of torsional moments at an intermediate support, irrespective of the degrees of torsional restrains provided at the support. The algebraic difference of the two end torsional moments adjacent to an intermediate support is the torsional moment reaction at the support. Therefore, the M/R method cannot provide the torsional moment reactions at the intermediate support. The intermediate steps to determine torsional moments in a continuous curved girder using the M/R method are presented in Appendix C.

3.4 SUMMARY

Classical beam theory can be used to analyze the cross-sectional forces in a simply supported straight girder. The second section presented the exact method from Nakai and Yoo and approximate methods to analyze the cross-sectional forces in a simply supported curved girder. The exact method from Nakai and Yoo can predict the variation of cross-sectional forces along the length of a simply supported curved girder obtained from UTRAP solution exactly. By considering the interaction between bending moment and torsional moment, the exact-formulas to predict the midspan bending moment and the support torque can be derived using equilibrium and geometry.

In addition to the exact method, the approximate methods to calculate support torque and midspan bending moment were presented: the first one was

derived using the modification of classical beam theory for a straight girder and the second one using the M/R method, derived by Tung and Fountain. The accuracy of the approximate solutions depends only on the central angle. For a relatively small central angle, both approximate methods can predict the support torque and the midspan bending moment of a simply supported curved girder well. However, as the central angle becomes larger, the accuracies of the approximate solutions become smaller. It was shown that the closed-form formulas to predict the midspan bending moment by modifying classical beam theory (Eq.3.11) and derived by Oleinik and Heins (Eq.3.12) are slightly better than the M/R Method. In addition, the closed-form formula to predict the support torque by approximating a curved girder as a straight girder (Eq.3.17) is slightly better than the M/R Method.

The third section presented the cross-sectional forces in continuous straight and curved girders. Because of the static indeterminacy and an interaction between bending moment and torsional moment, the cross-sectional forces in a continuous curved girder depend not only on the central angle, but also on the ratio of bending rigidity to torsional rigidity (*EI/GJ*). However, the change of cross-sectional forces in a continuous is much more sensitive to the total central angle than to the ratio of *EI/GJ*. It can be concluded that the M/R method can predict the variation of bending moment and torsional moment in a continuous girder well, provided the girder satisfies the limitations recommended by Tung and Fountain. However, the M/R method cannot provide the torsional moment reactions at the intermediate support because it gives only one set of torsional moments at an intermediate support, irrespective of the degrees of torsional restrains provided at the support.

CHAPTER 4
Cross-section Properties

In general, trapezoidal box girders can be classified into three categories:

- open-sections (without any top lateral bracing system) } Construction phase
- pseudo-closed sections (with a top lateral bracing system) }
- closed-sections (after concrete deck has hardened) } Serviceability phase

Because the scope is limited to the behavior of trapezoidal steel box girders during the construction phase, behavior of the closed-section during the serviceability phase will not be considered. Also, only trapezoidal cross-sections symmetric about a vertical axis passing through a centroid subjected to bending and torsion will be discussed.

The bending and torsional cross-section properties of an open section and a pseudo-closed section are discussed in this chapter. Procedures for determining some of the torsional properties are not well known so methods for determining those properties are presented. Figure 4.1 gives the notation used for the cross-section properties calculations.

4.1 FLEXURAL PROPERTIES

The location of the horizontal centroidal axis below the centroid of top flange , y_C, for an open section is

$$y_C = \frac{\left(b_{bf} t_{bf} d + 2 r_{bw} t_w \left(0.5 t_{tf} + 0.5 r_d\right)\right)}{A} \qquad (4.1)$$

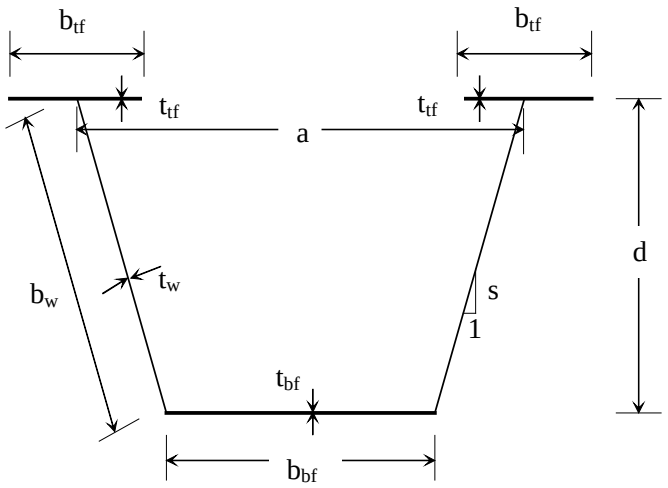

Notations:

a : Girder top width
b_{tf} : Top flange width
t_{tf} : Top flange thickness
s : Slope of web
b_w : Sloping web width, measured from centroid of top flange to centroid of bottom flange
t_w : Sloping web thickness
b_{bf} : Bottom flange width
t_{bf} : Bottom flange thickness
d : Girder depth, measured from centroid of top flange to centroid of bottom flange
A_{tf} : Area of top flange
A_w : Area of web
A_{bf} : Area of bottom flange

Figure 4.1 Notations for a trapezoidal box girder

where r_d : vertical web depth (measured from the bottom fiber of the top flange to the top fiber of the bottom flange)

$= d - 0.5\, t_{tf} - 0.5\, t_{bf}$

r_{bw} : width of the sloping web plate

$$= \sqrt{(r_d)^2 + \left(\frac{r_d}{s}\right)^2}$$

A : total cross-sectional area

$= \; 2\, b_{tf}\, t_{tf} + 2\, r_{bw}\, t_w + b_{bf}\, t_{bf}$

The moments of inertia with respect to the horizontal and vertical centroidal axes, I_{XC} and I_{YC}, respectively, for the open section shown in Figure 4.1 are

$$I_{XC} = 2\left(b_{tf} t_{tf} {y_C}^2 + \frac{1}{12} b_{tf} {t_{tf}}^3 \right) + 2 r_{bw} t_w \left[\frac{{r_d}^2}{12} + \left(\frac{r_d}{2} + \frac{t_{tf}}{2} - y_C \right)^2 \right] + \left(b_{bf} t_{bf} \left(d - y_C \right)^2 + \frac{1}{12} b_{bf} {t_{bf}}^3 \right) \tag{4.2}$$

$$I_{YC} = 2\left[t_{tf} b_{tf} \left(\frac{b_{bf}}{2} + \frac{d}{s} \right)^2 + \frac{1}{12} t_{tf} {b_{tf}}^3 \right] + 2\left[\frac{1}{12} t_w r_{bw} \left(\frac{r_d}{s} \right)^2 + t_w r_{bw} \frac{1}{4} \left(b_{bf} + \frac{d}{s} \right)^2 \right] + \frac{1}{12} t_{bf} {b_{bf}}^3 \tag{4.3}$$

For a pseudo-closed section, cross-section properties related to bending about the horizontal centroidal axis can be calculated either by considering or by neglecting the contribution of the top lateral bracing system into total bending stiffness.

Helwig and Fan (2000) proposed a simplified method for considering the contribution of the top lateral bracing system into the overall girder bending stiffness by adding the term A_{add} to the sum of the areas of the two top flanges. A_{add} depends on the geometry and member size of the top lateral system. Sample calculations for A_{add} are given later in this chapter. Including the contribution of the top lateral bracing system, y_C and I_{XC} for a pseudo-closed section are

$$y_C = \frac{\left(b_{bf} t_{bf} d + 2 r_{bw} t_w \left(0.5 t_{tf} + 0.5 r_d\right)\right)}{A} \tag{4.4}$$

where $A = 2\, b_{tf}\, t_{tf} + 2\, r_{bw}\, t_w + b_{bf}\, t_{bf} + A_{add}$ (4.5)

$$I_{XC} = 2\left(b_{tf} t_{tf} {y_C}^2 + \frac{1}{12} b_{tf} {t_{tf}}^3\right) + 2 r_{bw} t_w \left[\frac{{r_d}^2}{12} + \left(\frac{r_d}{2} + \frac{t_{tf}}{2} - y_C\right)^2\right] + \left(b_{bf} t_{bf} \left(d - y_C\right)^2 + \frac{1}{12} b_{bf} {t_{bf}}^3\right) + A_{add}\ {y_C}^2 \tag{4.6}$$

It is conservative and easier to neglect the contribution of the top lateral bracing system for determining stress in the steel girder.

4.2 SHEAR CENTER

The shear center is the point through which the applied loads must pass to produce bending without twisting. Under torsion, the shear center is center of rotation). Generally, the location of the shear center can be found by two techniques: the force method and the numerical method. The force method considers the resultant of the shear flow and equilibrium, and the numerical method directly employs numerical equations and uses the finite difference approach to locate a shear center. In the following sections, both methods will be used and the results will be compared.

4.2.1 Force method

The shear center of a singly symmetric section like a trapezoidal box girder is located on the y-axis (axis of symmetry). In order to determine location of the shear center along the y-axis, a shear force V_x is applied in the x-direction through the shear center at a distance e_y below bottom flange and the shear stress distribution is determined as shown in Figure 4.2. From the shear stress distribution, the equivalent shear force on each element is calculated. A complete derivation of the closed-form solution is given in section E.1 of Appendix E.

All seven equivalent shear forces (F_1 through F_7) shown in Figure 4.2(b) must be statically equivalent to the resultant force V_x acting through the shear center. Therefore, the moment of the shear force V_x about any point in the cross-section is equal to the moment of all seven equivalent shear force (F_1 through F_7) about that point. This moment relationship provides an equation from which the distance e_y to the shear center can be found. It is usually convenient to take the moment about the shear center, where the moment produced by V_x is zero.

The closed-form solution for e_y of an open-section trapezoidal box girder as measured from the centroidal axis of the bottom flange is

$$e_y = \frac{-2s\left\{db_{bf}\left[aA_{tf} + \frac{1}{2}\left(a - \frac{2}{3}\frac{d}{s}\right)A_w\right] - \frac{1}{4}db_{tf}{}^2A_{tf}\right\}}{sb_{bf}{}^2\left(A_w + \frac{A_{bf}}{3}\right) + 2asb_{bf}\left(A_{tf} + \frac{A_w}{2}\right) + 4\left[\left(ad + \frac{b_{tf}{}^2 s}{8}\right)A_{tf} + \frac{1}{2}\left(a - \frac{2}{3}\frac{d}{s}\right)dA_w\right]} \tag{4.7}$$

where all cross-section dimensions are shown in Figure 4.1. A negative value of e_y indicates that the shear center is located below the centroidal axis of bottom flange.

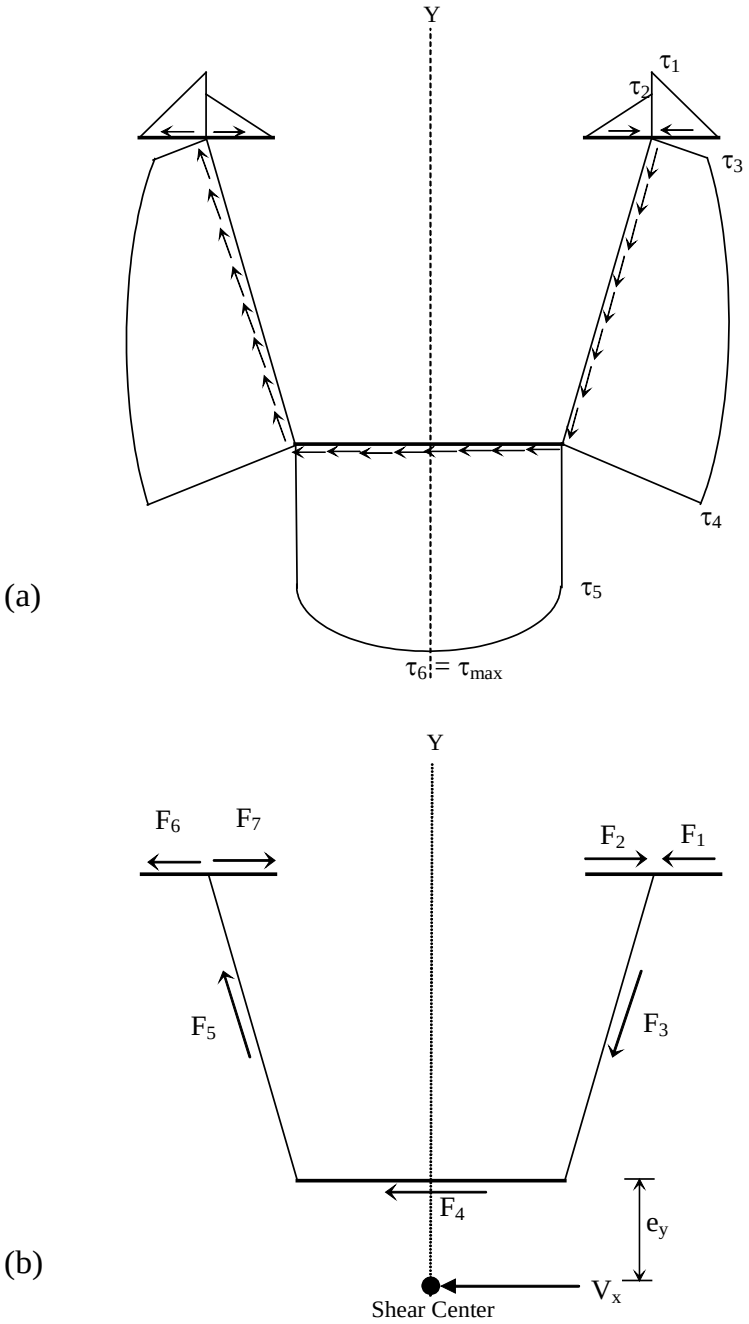

Figure 4.2 Shear stress distribution and shear flow in an open-section trapezoidal girder

4.2.2 Numerical method

Heins (1975) presented a numerical method using a finite difference approach. The y-coordinates of the shear center location relative to the centroid of the cross section is

$$y_0 = -\frac{I_{wx}}{I_y} \tag{4.8}$$

where I_{wx} is a geometric property.

$$I_{wx} = \frac{1}{3}\Sigma\left(w_i x_i + w_j x_j\right) t_{ij} L_{ij} + \frac{1}{6}\Sigma\left(w_i x_j + w_j x_i\right) t_{ij} L_{ij} \tag{4.9}$$

where x_i and x_j are the x-coordinates of points *i* and *j* of each straight line element on the cross-section, t_{ij} and L_{ij} are the thickness and length of element *ij*, and w_i , w_j are the absolute values of *w* at point i and j, respectively.

The w_{ij} between each point *i* and *j* is defined as $\rho_{ij}\ L_{ij}$, where ρ_{ij} is the perpendicular distance from centroid of the cross-section to a straight line through the end points of an element *ij*. The sign of ρ_{ij} is defined as positive if the centroid of cross-section is on the left side of the *ij* vector. The absolute value of *w* at each point is computed by summing the ρL starting from $w_1 = 0$ (where point 1 is called a reference point, which is the starting point of the element's flow vector for the entire cross-section). The choice and value of the reference point can be arbitrary, though the choice of zero is most convenient.

Section E.2 of Appendix E gives an example of how to apply this numerical method to locate shear center of an open-section trapezoidal box girder.

4.2.3 Comparison between force method and numerical method results

The shear center location for Model 1 was evaluated using both methods. From the force method (i.e. Eq.4.7)), the shear center location of Model 1 is 26.9

inches below the centroidal axis of the bottom flange, whereas the numerical method gave 26.8 inches. The difference between the two results is only about 0.4 %. In general, there is good agreement between the two methods.

4.2.4 Shear center location of thin-walled closed section

Determining the shear center location of a thin-walled closed section is not as easy as it is for an open section. Part of the reason is because in a closed section, the shear flow and shear stress are generally not known at any location, whereas in an open section, the values of the shear flow and shear stress at all edges of the cross section are zero. So, determining the shear flow in a closed section can be viewed as a statically indeterminate problem.

There are numerous methods available for determining the shear center of a thin-walled closed section. Heins (1975) describes a numerical method for locating the shear center of a thin-walled closed section. Bickford (1998) and Megson (1999) use a method similar to the force method to locate the shear center of a thin-walled closed section. Barber (2001) used an energy-based approach to locate the shear center of a thin-walled closed section. None of those methods considered a closed section that has a truss or some other lattice structure as part of the wall (i.e. pseudo-closed section).

However, Dabrowski (1968) presented a method for locating the shear center of a pseudo-closed section. The Dabrowski method will be used as a reference to locate the shear center of a pseudo-closed section. But, because his method involved integration of the torsional warping function, further discussion of shear centers of pseudo-closed sections will be presented when the torsional warping function is discussed later in this chapter.

4.3 PURE TORSIONAL CONSTANT

The pure torsional constant for open sections comprised of n narrow rectangular sections, J_{open}, can be approximated by:

$$J_{open} = \frac{1}{3}\sum_{i=1}^{n} b_i t_i^{\,3} \tag{4.10}$$

where b_i and t_i are the width and thickness of each element i, respectively.

For closed sections made up of n rectangular components, the pure torsional constant, J_{closed}, can be determined by:

$$J_{closed} = \frac{4A_o^{\,2}}{\sum_{i=1}^{n} \frac{b_i}{t_i}} \tag{4.11}$$

where A_o is the area enclosed by the centerline of the walls.

4.4 TORSIONAL WARPING FUNCTION

The torsional warping function for an open section $w(s)_{open}$, with origin s = 0 taken on the vertical axis that passes through shear center is

$$w(s)_{open} = -\int_0^s r\,ds \tag{4.12}$$

where r is the perpendicular distance from the ds element to the shear center. For the sign shown, it is assumed that the section is traversed in a counter-clockwise direction. It should be noted that r is positive whenever the shear center is located on the left side of an element when traversing from the beginning point to the ending point of that element. The advantage of taking s = 0 at the vertical axis that passes through shear center is that the torsional warping function diagram will be

anti-symmetrical about that axis. Therefore, only half of cross-section needs be considered. Table 4-1 illustrates how to use Eq.4.12 to construct the torsional warping function diagram for the open-section vertical web girder shown in Figure 4.3.

Figure 4.4 shows the torsional warping function diagram for the open section $w(s)_{open}$. which is anti-symmetrical with respect to the vertical axis that passes through the shear center. Using the same procedure, the torsional warping function diagram for an open-section trapezoidal box girder is shown in Figure 4.5.

In order to construct the torsional warping function diagram for a pseudo-closed section of trapezoidal box girder, its shear center location must first be determined. From Dabrowski (1968), the vertical distance e_{yA} between the initial pole A and the shear center S.C for a pseudo-closed section is

$$e_{yA} = \frac{1}{I_{YC}} \int_A \omega_A^{\wedge} x dA \tag{4.13}$$

where $\omega^{\wedge}_A$ is the reduced sectorial area with respect to an arbitrary pole A and x is the horizontal distance measured from the initial pole A. $\omega^{\wedge}_A$ defined by Eq.4.14 is basically a modified sectorial area to account for the fact that in a pseudo-closed section, the shear stress on the median surface is not zero.

$$\omega^{\wedge}{}_A = \omega_A - \frac{2A_o}{\sum_{i=1}^{n} \frac{b_i}{t_i}} \int_0^s \frac{ds}{t} \tag{4.14}$$

where ω_A is the sectorial area for an open section and A_o is the area enclosed by the shear flow.

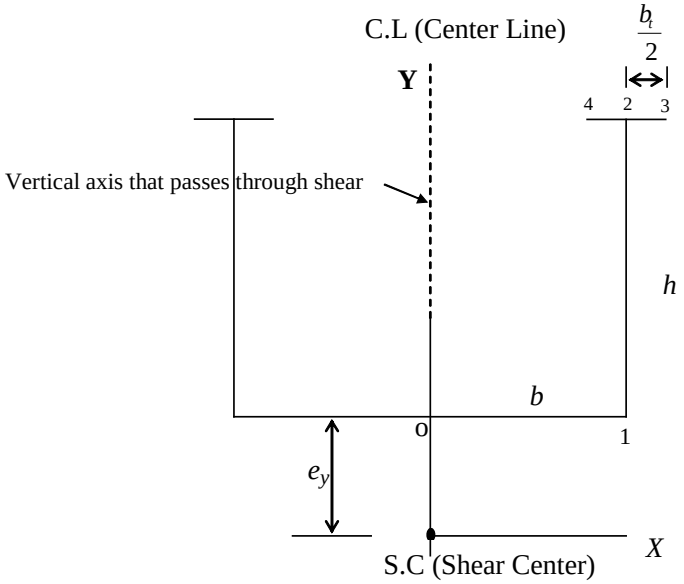

Figure 4.3 Representation of an open-section vertical web girder

Table 4-1 Tabular method for making the torsional warping function diagram

Segment	$-\int r\ ds$		i	w_i
	$x\,\Delta y$	$y\,\Delta x$		
0 - 1	---	$-(-e_y)\,b$	1	$0 + e_y\,b$ (Note: $w_0 = 0$)
1 - 2	$-b\,(h)$	---	2	$\underbrace{e_y\,b - b\,h}_{\text{from 1}}$
2 - 3	---	$-\left[-\left(e_y + h\right)\right]\frac{b_t}{2}$	3	$\underbrace{e_y\,b - b\,h}_{\text{from 2}} + \left(e_y + h\right)\frac{b_t}{2}$
2 - 4	---	$-\left(e_y + h\right)\frac{b_t}{2}$	4	$\underbrace{e_y\,b - b\,h + \left(e_y + h\right)\frac{b_t}{2}}_{\text{from 2}}$

r is negative because shear center is located on the right side of the element

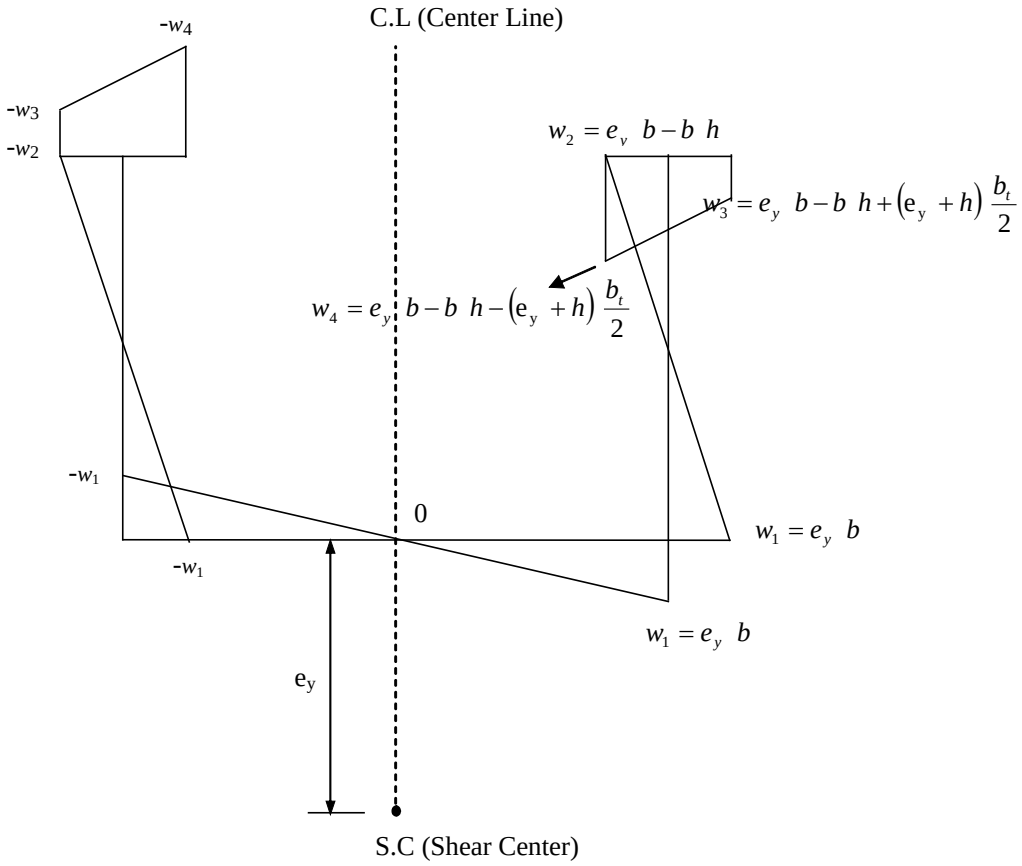

Figure 4.4 Torsional warping function diagram of an open-section vertical web girder

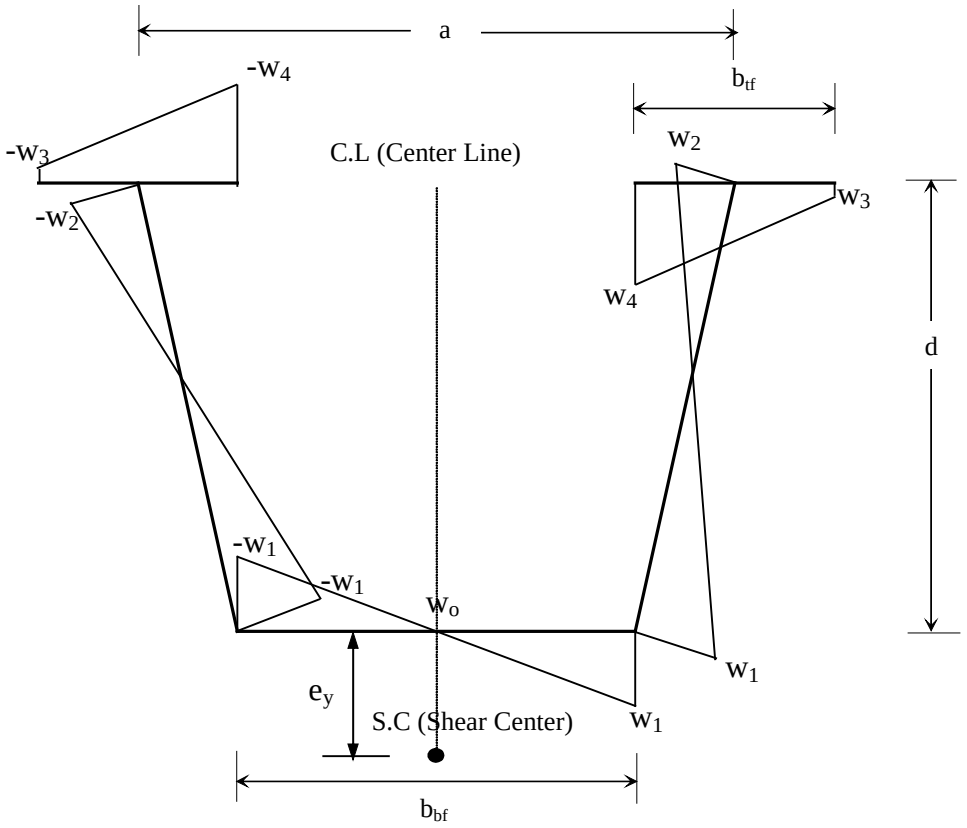

$w_o = 0$ (Because it lies on the vertical line that passes through shear center)

$$w_1 = w_o + e_y \frac{b_{bf}}{2}$$

$$w_2 = w_1 - \left(\frac{b_{bf}}{2} + \frac{a - b_{bf}}{4} \right) d + \left(e_y + \frac{d}{2} \right) \left(\frac{a - b_{bf}}{2} \right)$$

$$w_3 = w_2 + \left(e_y + d \right) \left(\frac{b_{tf}}{2} \right)$$

$$w_4 = w_2 - \left(e_y + d \right) \left(\frac{b_{tf}}{2} \right)$$

Figure 4.5 Torsional warping function diagram for an open-section trapezoidal box girder

With the pole *A* taken on the axis of symmetry and assuming the section is traversed in a clockwise direction from the pole *A*, ω_A is

$$\omega_A = \int_0^s r_A ds \tag{4.15}$$

where r_A is the perpendicular distance from the contour tangent to the pole *A*.

Figure 4.6 shows a simplified pseudo-closed section of a trapezoidal box girder with the pole *A* located on the y-axis, in the plane of the top lateral system. The perpendicular distance from web to the pole *A* is denoted r_{wA}. For simplification, the top flanges are assumed to only have areas (not length).

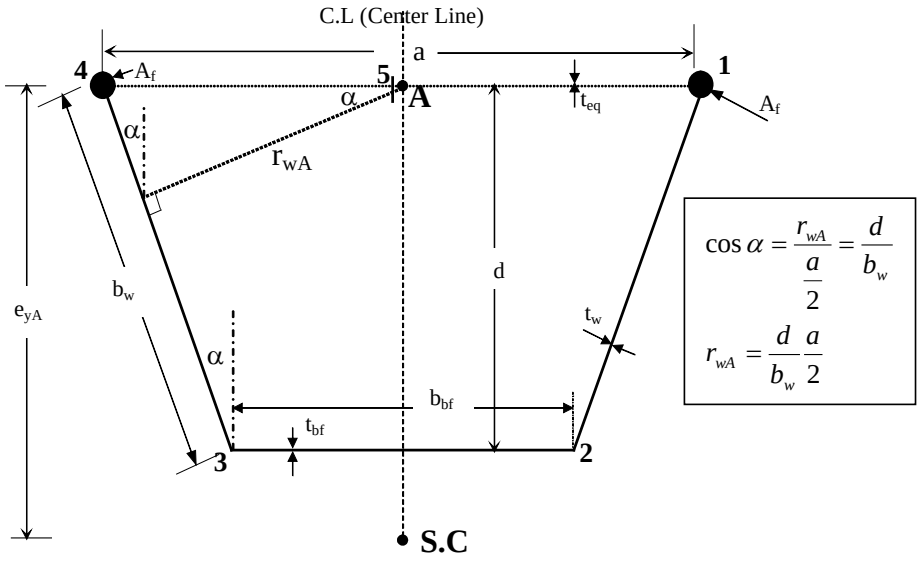

Figure 4.6 Simplified pseudo-closed section of trapezoidal box girder with pole A

An imaginary cut is assumed between pole *A* and point 5. Because of that cut, the section can be treated as an open section and ω_A is calculated with a procedure similar to the one shown in Table 4-1. The only differences are the procedure to calculate $w(s)_{open}$ shown in Table 4-1 is made with respect to the

shear center and the calculations are made proceeding counter-clockwise from point *o* at the center of the bottom flange.

Figure 4.7 shows the ω_A diagram. The section is traversed in a clockwise direction from the reference pole *A*. Using the ω_A diagram, the $\hat{\omega}_A$ diagram can be constructed using Eq.4.14, and is shown in Figure 4.8. Having both the $\hat{\omega}_A$ and *x* diagrams, $\int_A \hat{\omega}_A x dA$ can be readily calculated. For convenience, the area integration will be performed using visual integration with the aid of Table F-1 in Appendix F. Table 4-2 gives the integration details. Because both the $\hat{\omega}_A$ and *x* diagrams are anti-symmetric, only half of the cross section is considered.

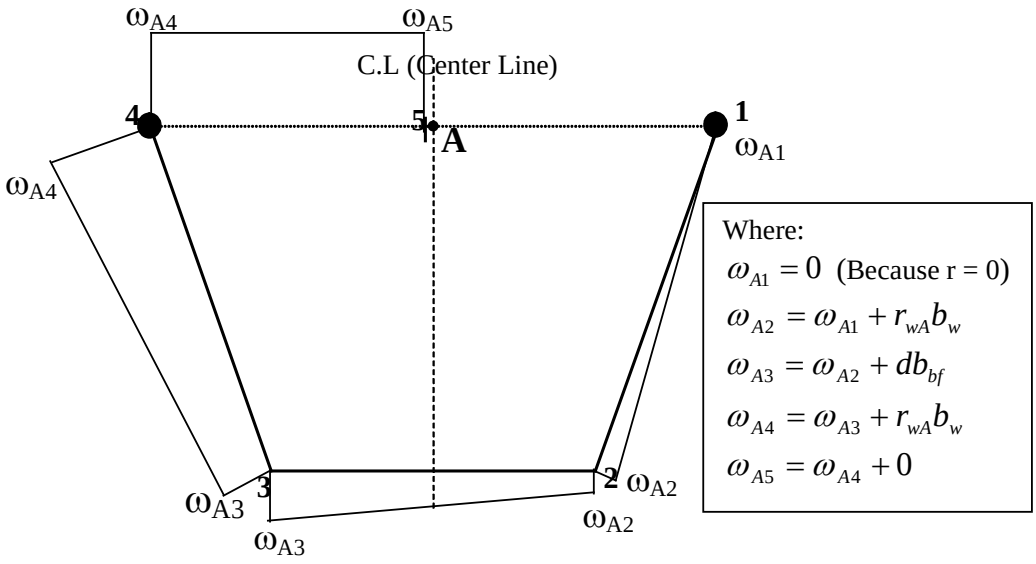

Figure 4.7 ω_A diagram for a pseudo-closed section

The shear center for a pseudo-closed trapezoidal box girder, expressed in Eq.4.13, can then be written as

$$e_{yA} = \frac{1}{I_{YC}} \times 2\left\{ \hat{\omega}_{A1}\left[\frac{(2a + b_{bf}) b_w t_w}{12} + \frac{aA_f}{2} \right] + \hat{\omega}_{A2}\left[\frac{{b_{bf}}^2 t_{bf} + (a + 2b_{bf}) b_w t_w}{12} \right] \right\} \quad (4.16)$$

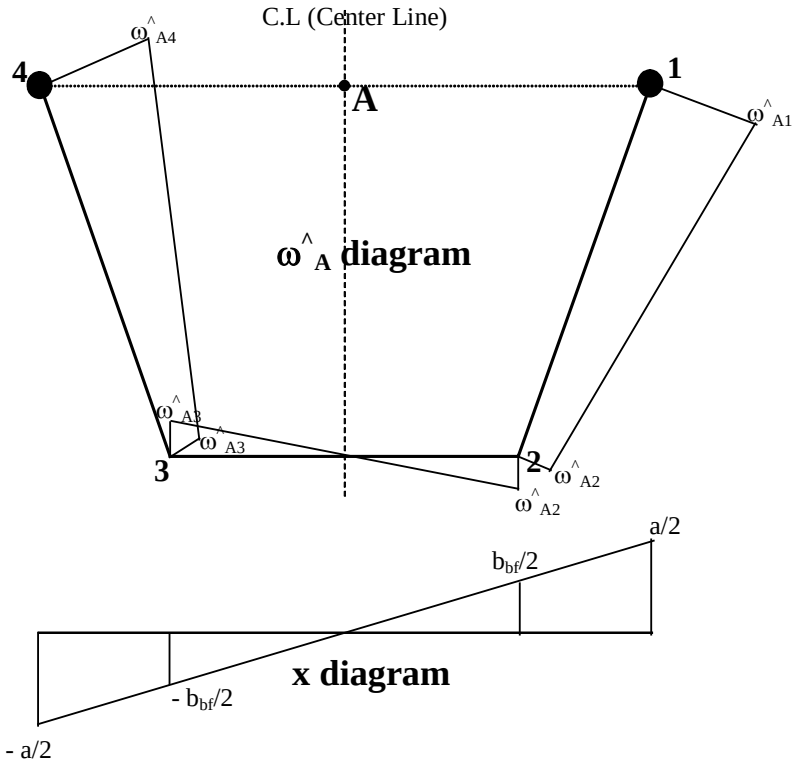

Where:

$$\hat{\omega}_{A1} = \omega_{A1} - \frac{2A_o}{\sum_{i=1}^{n}\frac{b_i}{t_i}}\left(\frac{a/2}{t_{eq}}\right) \qquad \hat{\omega}_{A2} = \omega_{A2} - \frac{2A_o}{\sum_{i=1}^{n}\frac{b_i}{t_i}}\left(\frac{a/2}{t_{eq}} + \frac{b_w}{t_w}\right)$$

$$\hat{\omega}_{A3} = \omega_{A3} - \frac{2A_o}{\sum_{i=1}^{n}\frac{b_i}{t_i}}\left(\frac{a/2}{t_{eq}} + \frac{b_w}{t_w} + \frac{b_{bf}}{t_{bf}}\right) \qquad \hat{\omega}_{A4} = \omega_{A4} - \frac{2A_o}{\sum_{i=1}^{n}\frac{b_i}{t_i}}\left(\frac{a/2}{t_{eq}} + \frac{b_w}{t_w} + \frac{b_{bf}}{t_{bf}} + \frac{b_w}{t_w}\right)$$

$$\frac{2A_o}{\sum_{i=1}^{n}\frac{b_i}{t_i}} = \frac{2\left[\frac{d}{2}\left(a + b_{bf}\right)\right]}{\frac{a}{t_{eq}} + 2\frac{b_w}{t_w} + \frac{b_{bf}}{t_{bf}}}$$

Noted that due to anti-symmetrical of $\hat{\omega}_A$ diagram:

$\hat{\omega}_{A3} = -\hat{\omega}_{A2}$ and $\hat{\omega}_{A4} = -\hat{\omega}_{A1}$

Figure 4.8 $\hat{\omega}_A$ diagram and x diagram of pseudo-closed trapezoidal box girder

Table 4-2 Visual integration technique for $\int_A \omega_A^{\wedge} x dA$

Part of Cross-section	Area	$\omega_A^{\wedge}$	x	$\int_A \omega_A^{\wedge} x dA$
One top flange	A_f	$\omega_{A1}^{\wedge}$	$\frac{a}{2}$	$\left(\omega_{A1}^{\wedge}\right)\left(\frac{a}{2}\right)\left(A_f\right)$
One web	$b_w t_w$	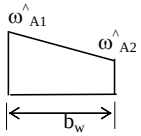	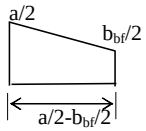	$\frac{1}{6}\left[\frac{a}{2}\left(2\omega_{A1}^{\wedge}+\omega_{A2}^{\wedge}\right)+\frac{b_{bf}}{2}\left(2\omega_{A2}^{\wedge}+\omega_{A1}^{\wedge}\right)\right]\left(b_w t_w\right)$
Half of bottom flange	$\frac{b_{bf}}{2} t_{bf}$	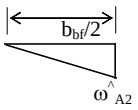	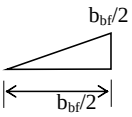	$\frac{1}{3}\left(\omega_{A2}^{\wedge}\right)\left(\frac{b_{bf}}{2}\right)\left(\frac{b_{bf}}{2} t_{bf}\right)$
Total area integration for half cross-section				$\omega_{A1}^{\wedge}\left[\frac{\left(2a+b_{bf}\right)b_w t_w}{12}+\frac{aA_f}{2}\right]+\omega_{A2}^{\wedge}\left[\frac{b_{bf}{}^2 t_{bf}+\left(a+2b_{bf}\right)b_w t_w}{12}\right]$

where $\omega_{A1}^{\wedge}$ and $\omega_{A2}^{\wedge}$ are the reduced sectorial areas with respect to pole *A* defined in Figure 4.8. Negative value of e_{yA} indicates that the shear center is located below pole *A*.

With the $\omega_A^{\wedge}$ diagram and shear center location having been determined, the torsional warping function $w(s)_{pseudo\text{-}closed}$ can be constructed. It should be pointed out that the torsional warping function for a pseudo-closed section is the same as the reduced sectorial area with respect to the shear center $\omega_{S.C.}^{\wedge}$. Dabrowski derived a relationship between the sectorial areas ω with respect to two different poles *A* and *S.C.* For a singly-symmetrical section, $\omega_{S.C.}^{\wedge}$ can be related to $\omega_A^{\wedge}$ as follows:

$$\omega^{\wedge}_{S.C.} = \omega^{\wedge}_{A} - e_{yA}x \qquad (4.17)$$

Figure 4.9 shows the reduced sectorial area of a pseudo-closed trapezoidal box girder with respect to its shear center $\omega^{\wedge}_{S.C.}$ diagram, which is exactly the same as the torsional warping function for a pseudo-closed section of a trapezoidal box girder $w(s)_{pseudo\text{-}closed}$. In order to simplify notation, $\omega^{\wedge}_{S.C}$ is denoted $w^{\wedge}$.

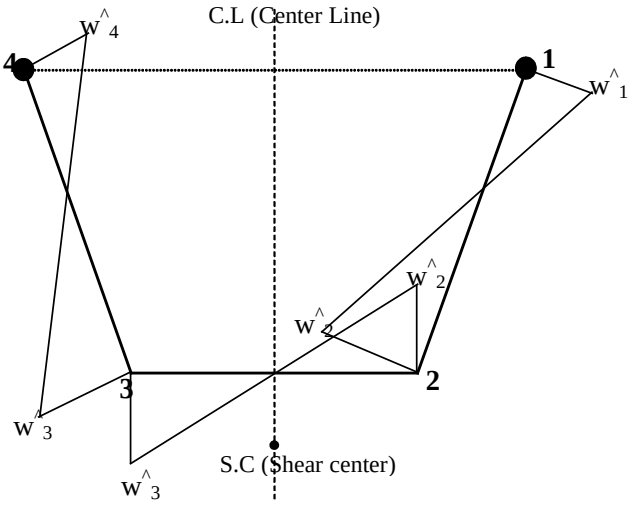

$$w^{\wedge}_1 = \omega^{\wedge}_{A1} - e_y\left(\frac{a}{2}\right)$$

$$w^{\wedge}_2 = \omega^{\wedge}_{A2} - e_y\left(\frac{b_{bf}}{2}\right)$$

$$w^{\wedge}_3 = \omega^{\wedge}_{A3} - e_y\left(\frac{-b_{bf}}{2}\right)$$

$$w^{\wedge}_4 = \omega^{\wedge}_{A4} - e_y\left(\frac{-a}{2}\right)$$

Because $w^{\wedge}$ diagram is anti-symmetrical with respect to the center-line,

$w^{\wedge}_3 = -w^{\wedge}_2$ and $w^{\wedge}_4 = -w^{\wedge}_1$

Figure 4.9 Torsional warping function of pseudo-closed section

4.5 WARPING MOMENT OF INERTIA

The warping moment of inertia I_w, also known as the torsional warping constant, is determined from

$$I_w = \int_A \left(w(s)\right)^2 dA \tag{4.18}$$

for both open and pseudo-closed sections. Table 4-3 illustrates the computation of I_w for an open-section trapezoidal box girder based on its $w(s)_{open}$ diagram shown in Figure 4.5. Because the $w(s)_{open}$ diagram is anti-symmetric, the integration only has to be performed over half the cross-section.

Based on the integration, the warping moment of inertia of an open-section trapezoidal box girder $I_{w,open}$ is

$$I_{w,open} = 2\left[\frac{1}{3}\left(w_3{}^2 + w_3 w_4 + w_4{}^2\right)A_f + \frac{1}{3}\left(w_1{}^2 + w_1 w_2 + w_2{}^2\right)\left(b_w t_w\right) + \frac{1}{3}w_1{}^2\left(\frac{b_{bf}}{2}t_{bf}\right)\right] \tag{4.19}$$

where w_1 through w_4 are defined in Figure 4.5.

Table 4-4 illustrates the computation of the warping moment of inertia of a pseudo-closed trapezoidal box girder based on its $w(s)_{pseudo\text{-}closed}$ diagram, shown in Figure 4.9. Again, because $w(s)_{pseudo\text{-}closed}$ diagram is anti-symmetric, only half of the cross section is integrated.

Based on the results of the integration, the warping moment of inertia of a pseudo-closed trapezoidal box girder $I_{w,pseudo\text{-}closed}$ is

$$I_{w,pseudo-closed} = 2\left\{\left(w_1^{\wedge}\right)^2 A_f + \frac{1}{3}\left[\left(w_1^{\wedge}\right)^2 + w_1^{\wedge} w_2^{\wedge} + \left(w_2^{\wedge}\right)^2\right]\left(b_w t_w\right) + \frac{1}{3}\left(w_2^{\wedge}\right)^2\left(\frac{b_{bf}}{2}t_{bf}\right)\right\} \tag{4.20}$$

where $w^{\wedge}_1$ and $w^{\wedge}_2$ are defined in Figure 4.9.

Table 4-3 Integration for $\int_A \left(w(s)_{open}\right)^2 dA$

Part of Cross-section	Area	$w(s)_{open}$	$w(s)_{open}$	$\int_A \left(w(s)_{open}\right)^2 dA$
One top flange	A_f	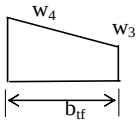	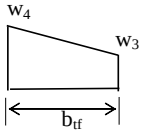	$\frac{1}{3}\left(w_3^{\,2} + w_3 w_4 + w_4^{\,2}\right)\left(A_f\right)$
One web	$b_w t_w$	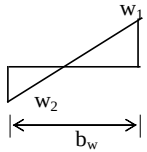	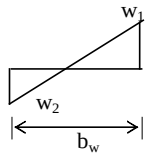	$\frac{1}{3}\left(w_1^{\,2} + w_1 w_2 + w_2^{\,2}\right)\left(b_w t_w\right)$
Half of bottom flange	$\frac{b_{bf}}{2} t_{bf}$	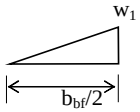	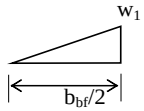	$\frac{1}{3}\left(w_1^{\,2}\right)\left(\frac{b_{bf}}{2} t_{bf}\right)$
Total area integration for half cross-section				$\frac{1}{3}\left(w_3^{\,2} + w_3 w_4 + w_4^{\,2}\right)A_f + \frac{1}{3}\left(w_1^{\,2} + w_1 w_2 + w_2^{\,2}\right)\left(b_w t_w\right) + \frac{1}{3} w_1^{\,2}\left(\frac{b_{bf}}{2} t_{bf}\right)$

Note: Integration over a top flange area of the following w(s) diagram can be calculated as follows:

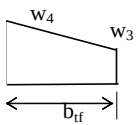

x

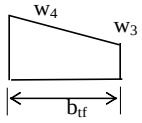

$$= \frac{1}{6}\left[w_3\left(2w_3 + w_4\right) + w_4\left(2w_4 + w_3\right)\right]\left(A_f\right) = \frac{1}{3}\left(w_3^{\,2} + w_3 w_4 + w_4^{\,2}\right)\left(A_f\right)$$

Table 4-4 Integration for $\int_A \left(w(s)_{\,pseudo-closed}\right)^2 dA$

Part of Cross-section	Area	$w(s)_{open}$	$w(s)_{open}$	$\int_A \left(w(s)_{\,pseudo-closed}\right)^2 dA$
One top flange	A_f	$\hat{w}_1$	$\hat{w}_1$	$\left(\hat{w}_1\right)^2 A_f$
One web	$b_w t_w$	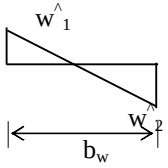	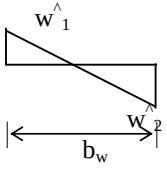	$\frac{1}{3}\left[\left(\hat{w}_1\right)^2 + \hat{w}_1\hat{w}_2 + \left(\hat{w}_2\right)^2\right]\left(b_w t_w\right)$
Half of bottom flange	$\frac{b_{bf}}{2} t_{bf}$	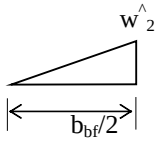	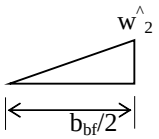	$\frac{1}{3}\left(\hat{w}_2\right)^2\left(\frac{b_{bf}}{2} t_{bf}\right)$
Total area integration for half cross-section				$\left(\hat{w}_1\right)^2 A_f + \frac{1}{3}\left[\left(\hat{w}_1\right)^2 + \hat{w}_1\hat{w}_2 + \left(\hat{w}_2\right)^2\right]\left(b_w t_w\right) + \frac{1}{3}\left(\hat{w}_1\right)^2\left(\frac{b_{bf}}{2} t_{bf}\right)$

4.6 WARPING SHEAR PARAMETER AND CENTRAL SECOND MOMENT OF AREA

The warping shear parameter μ is one of the required parameters for determining the bimoment derived by Dabrowski. For an open-section, μ_{open} = 1.0, and for a closed section, μ_{closed} is

$$\mu_{closed} = 1 - \frac{J_{closed}}{I_c} \tag{4.21}$$

where I_c is the central second moment of area defined as

$$I_c = \int_A \left(r_{S.C}\right)^2 dA \tag{4.22}$$

where $r_{S.C.}$ is the perpendicular distance from the contour tangent of each cross-section element to the shear center as shown in Figure 4.10. For the pseudo-closed trapezoidal girder I_c becomes

$$I_{c,pseudo-closed} = \left(e_{yA}\right)^2 \left(at_{eq}\right) + 2\left(r_{S.C.-web}\right)^2 \left(b_w t_w\right) + \left(e_{yA} - d\right)^2 \left(b_{bf} t_{bf}\right) \tag{4.23}$$

Dabrowski indicated that the flange area A_f should not be included in the $I_{c,pseudo-closed}$ calculation.

Generally, the warping shear parameter can be seen as a reduction factor to warping bimoment due to the presence of pure torsion. For an open section, because the pure torsion component is very small compared to warping torsion, μ_{open} can be taken as 1. In pseudo-closed and closed sections, pure torsion starts to dominate over warping torsion, and μ_{closed} will become smaller than 1.

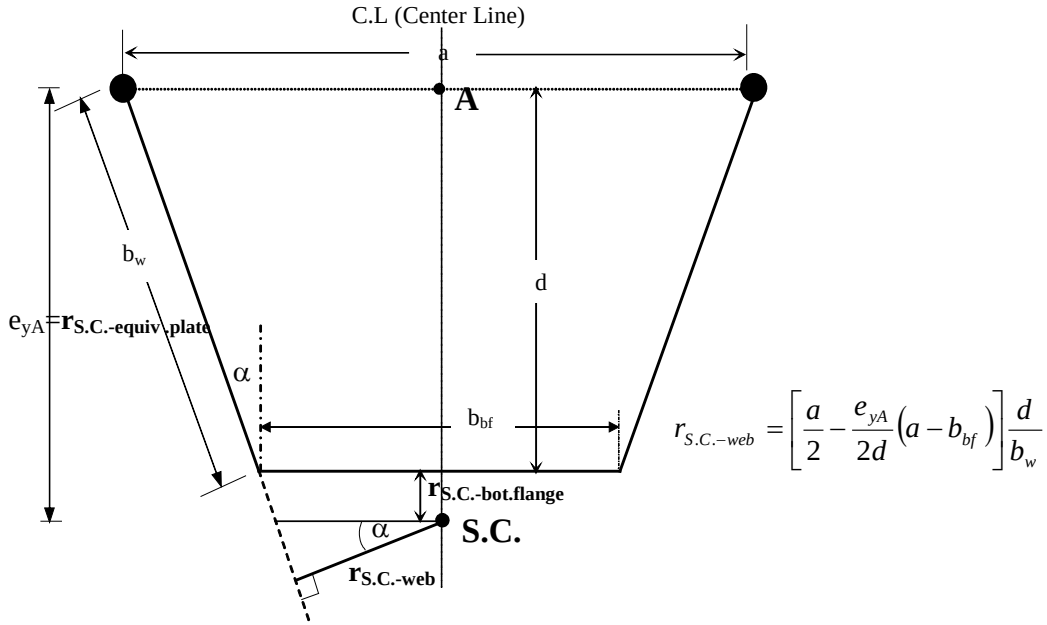

Figure 4.10 Perpendicular distance from a shear center to each element

4.7 SAMPLE CALCULATIONS OF CROSS-SECTION PROPERTIES

Sample calculations for the cross-section properties of Model 1, shown in Figure 4.11, are presented. Figure 4.11 also shows the dimensions of the pseudo-closed section of Model 1 and the configuration of the top lateral bracing system used in the pseudo-closed section.

From the dimensions of the open-section of the Model 1 girder shown in Figure 4.11, the vertical web depth r_d, the width of the sloping web plate r_{bw}, and the total cross-sectional area A are

$$r_d = \text{d} - 0.5\ t_{tf} - 0.5\ t_{bf} = 60 - 0.5(1.5) - 0.5(1.5) = 58.5 \text{ in}$$

$$r_{bw} = \sqrt{\left(r_d\right)^2 + \left(\frac{r_d}{s}\right)^2} = \sqrt{\left(58.5\right)^2 + \left(\frac{58.5}{4.615}\right)^2} = 59.86 \text{ in}$$

$$A = 2\, b_{tf}\, t_{tf} + 2\, r_{bw}\, t_w + b_{bf}\, t_{bf}$$

$$= 2(10)(1.5) + 2(59.86)(0.5) + (50)(1.5) = 164.86 \text{ in}^2$$

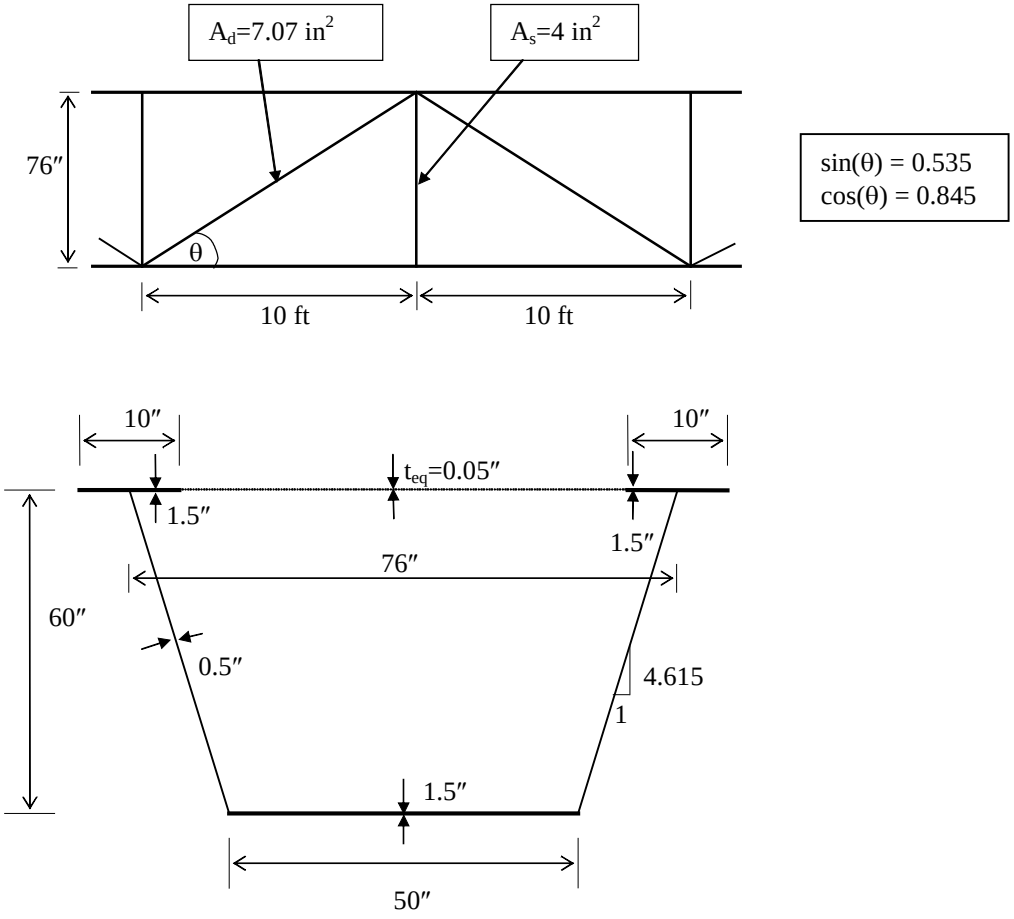

Figure 4.11 Top lateral bracing system configuration and dimensions Model 1

For a pseudo-closed section, cross-section properties related to the bending about the horizontal centroidal axis (i.e. the X-X axis) can be calculated either by considering or by neglecting the contribution of the top lateral bracing system. By ignoring the contribution of top lateral bracing system, the properties

of a pseudo-closed section are exactly the same as those of an open-section. However, if the contribution of the top lateral bracing system is included, an area $A_{add,each}$ is added to each top flange area, as derived by Helwig and Fan (2000). For the top lateral bracing system shown in Figure 4.11, $A_{add,each}$ can be calculated as follows:

$$A_{add,each} = \frac{\cos^3(\theta)}{2\left[\frac{1}{A_d} + \frac{s^2\cos(\theta)\sin(\theta)}{24I_{tf}} + \frac{\sin^3(\theta)}{A_s}\right]} \tag{4.24}$$

$$= \frac{(0.845)^3}{2\left[\frac{1}{7.07} + \frac{(120)^2(0.845)(0.535)}{24(125)} + \frac{(0.535)^3}{4}\right]} = 0.128 \text{ in}^2$$

where: $I_{tf} = \frac{1}{12} t_{tf} b_{tf}^{\ 3} = \frac{1}{12}(1.5)(10)^3 = 125 \text{ in}^3$

Using this simplified method, the total cross-sectional area A can be calculated as follows:

$$A = A_{open} + A_{add}$$

$$= 164.86 + 2(0.128) = 165.1 \text{ in}^2$$

More detailed discussions of the additional area calculation to account for the contribution of the top lateral bracing system will be presented in Chapter 9.

4.7.1 Centroidal axis and moment of inertia

From Eq.4.1, the location of the horizontal centroidal axis of the open-section Model 1 girder below the centroid of top flange is

$$y_C = \frac{\left(b_{bf} t_{bf} d + 2r_{bw} t_w \left(0.5t_{tf} + 0.5r_d\right)\right)}{A}$$

$$= \frac{(50)(1.5)(60) + 2(59.86)(0.5)[(0.5)(1.5) + 0.5(58.5)]}{164.86}$$

= 38.19 in

The moment of inertia with respect to the horizontal and vertical centroidal axes, I_{XC} and I_{YC}, respectively, are calculated using Eqs.4.2 and 4.3 as shown in Insert 4.1.

By including the contribution of the top lateral bracing system, y_C from Eq.4.4 is:

$$y_C = \frac{\left(b_{bf} t_{bf} d + 2 r_{bw} t_w \left(0.5 t_{tf} + 0.5 r_d\right)\right)}{A}$$

$$= \frac{(50)(1.5)(60) + 2(59.86)(0.5)[0.5(1.5) + 0.5(58.5)]}{165.1}$$

= 38.13 in

and I_{XC} from Eq.4.6 is

$$I_{XC} = 2\left(b_{tf} t_{tf} {y_C}^2 + \frac{1}{12} b_{tf} {t_{tf}}^3\right) + 2 r_{bw} t_w \left[\frac{{r_d}^2}{12} + \left(\frac{r_d}{2} + \frac{t_{tf}}{2} - y_C\right)^2\right]$$

$$+ \left(b_{bf} t_{bf} (d - y_C)^2 + \frac{1}{12} b_{bf} {t_{bf}}^3\right) + A_{add}\ {y_C}^2$$

$$= 2\left[(10)(1.5)(37.33)^2 + \frac{1}{12}(10)(1.5)^3\right] + 2(59.86)(0.5)\left[\frac{58.5^2}{12} + \left(\frac{58.5}{2} + \frac{1.5}{2} - 37.33\right)^2\right]$$

$$+ \left[(50)(1.5)(60 - 37.33)^2 + \frac{1}{12}(50)(1.5)^3\right] + 2(0.128)(38.13)^2$$

= 100900 in^4

By including the contribution of the top lateral bracing system, the I_{XC} increases from 100535 in^4 to 100900 in^4, or only about 0.4 percent.

$$I_{XC} = 2\left(b_{tf} t_{tf} {y_C}^2 + \frac{1}{12} b_{tf} {t_{tf}}^3 \right) + 2 r_{bw} t_w \left[\frac{{r_d}^2}{12} + \left(\frac{r_d}{2} + \frac{t_{tf}}{2} - y_C \right)^2 \right] + \left(b_{bf} t_{bf} (d - y_C)^2 + \frac{1}{12} b_{bf} {t_{bf}}^3 \right)$$

$$= 2\left[(10)(1.5)(38.19)^2 + \frac{1}{12}(10)(1.5)^3 \right] + 2(59.86)(0.5)\left[\frac{58.5^2}{12} + \left(\frac{58.5}{2} + \frac{1.5}{2} - 38.19 \right)^2 \right] + \left[(50)(1.5)(60 - 38.19)^2 + \frac{1}{12}(50)(1.5)^3 \right]$$

$= 100535 \text{ in}^4$

$$I_{YC} = 2\left[t_{tf} b_{tf} \left(\frac{b_{bf}}{2} + \frac{d}{s} \right)^2 + \frac{1}{12} t_{tf} {b_{tf}}^3 \right] + 2\left[\frac{1}{12} t_w r_{bw} \left(\frac{r_d}{s} \right)^2 + t_w r_{bw} \frac{1}{4} \left(b_{bf} + \frac{d}{s} \right)^2 \right] + \frac{1}{12} t_{bf} {b_{bf}}^3$$

$$= 2\left[(1.5)(10)\left(\frac{50}{2} + \frac{60}{4.615} \right)^2 + \frac{1}{12}(1.5)(10)^3 \right] + 2\left[\frac{1}{12}(0.5)(59.86)\left(\frac{58.5}{4.615} \right)^2 + (0.5)(59.86)\frac{1}{4}\left(50 + \frac{60}{4.615} \right)^2 \right] + \frac{1}{12}(1.5)(50)^3$$

$= 119390 \text{ in}^4$

Insert 4.1 Calculations of flexural properties of Model 1

4.7.2 Shear center location

The shear center location measured from the centroid of the bottom flange of an open-section trapezoidal box girder is given by Eq.4.7 [see Insert 4.2]. So the shear center of an open-section Model 1 girder is located 26.9 inches below the centroidal axis of the bottom flange.

In order to determine the shear center location of a pseudo-closed section, the $\hat{\omega}$ diagram of a pseudo-closed section must first be determined. Before the $\hat{\omega}$ diagram can be constructed, the sectorial area diagram of an open-section must be constructed. It should be noted that in constructing both sectorial area and reduced sectorial area for a pseudo-closed section, top flanges are assumed to only have areas (not length). The shear center location of a pseudo-closed section is determined using the following procedures:

1. Construct a sectorial area diagram with respect to an arbitrary pole A (ω_A diagram) for an open-section. It should be noted that Dabrowski indicated that for a singly-symmetric section, an arbitrary pole A can be advantageously located on the y-axis. Figure 4.12 shows the ω_A diagram of an open-section of Model 1 girder.

2. Calculate the area enclosed by the wall A_o and the value of $\dfrac{2A_o}{\sum_{i=1}^{n}\dfrac{b_i}{t_i}}$, then construct a reduced sectorial area diagram with respect to the pole A ($\hat{\omega}_A$ diagram) and x diagram where x is the horizontal distance from the pole A.

$$A_o = \frac{d}{2}\left(a + b_{bf}\right) = \frac{60}{2}\left(76 + 50\right) = 3780 \text{ in}^2$$

$$e_y = \frac{-2s\left\{db_{bf}\left[aA_{tf} + \frac{1}{2}\left(a - \frac{2}{3}\frac{d}{s}\right)A_w\right] - \frac{1}{4}db_{tf}{}^2A_{tf}\right\}}{sb_{bf}{}^2\left(A_w + \frac{A_{bf}}{3}\right) + 2asb_{bf}\left(A_{tf} + \frac{A_w}{2}\right) + 4\left[\left(ad + \frac{b_{tf}{}^2s}{8}\right)A_{tf} + \frac{1}{2}\left(a - \frac{2}{3}\frac{d}{s}\right)dA_w\right]}$$

$$e_y = \frac{-2(4.615)\left\{(60)(50)\left[(76)(15) + \frac{1}{2}\left(76 - \frac{2}{3}\frac{60}{4.615}\right)(30.696)\right] - \frac{1}{4}(60)(10)^2(15)\right\}}{4.615(50)^2\left(30.696 + \frac{75}{3}\right) + 2(76)(4.615)(50)\left(15 + \frac{30.696}{2}\right) + 4\left[\left((76)(60) + \frac{(10)^2(4.615)}{8}\right)15 + \frac{1}{2}\left(76 - \frac{2}{3}\frac{60}{4.615}\right)(60)(30.696)\right]}$$

e_y = - 26.9 inches

Insert 4.2 Shear center of an open-section Model 1 girder

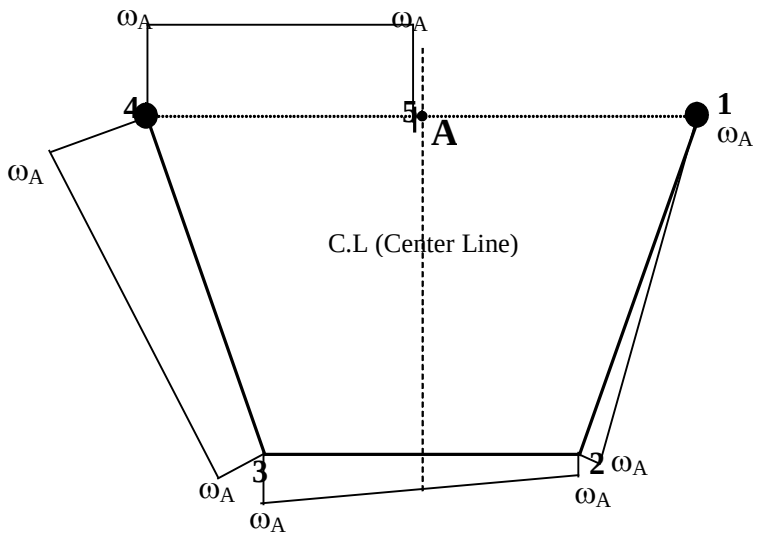

Where:

$\omega_{A1} = 0$ (Because r = 0)

$$\omega_{A2} = \omega_{A1} + r_{wA} b_w \quad ; \quad r_{wA} = \frac{d}{b_w}\frac{a}{2} = \frac{60}{61.39}\frac{76}{2} = 37.14 \text{ in}$$

$$\omega_{A2} = 0 + (37.14)(61.39) = 2280 \text{ in}^2$$

$$\omega_{A3} = \omega_{A2} + d b_{bf} \Rightarrow \omega_{A3} = 2280 + (60)(50) = 5280 \text{ in}^2$$

$$\omega_{A4} = \omega_{A3} + r_{wA} b_w \Rightarrow \omega_{A4} = 5280 + (37.14)(61.39) = 7560 \text{ in}^2$$

$$\omega_{A5} = \omega_{A4} + 0 \Rightarrow \omega_{A5} = 7560 + 0 = 7560 \text{ in}^2$$

Figure 4.12 Sectorial area diagram for the open-section

$$\frac{2A_o}{\sum_{i=1}^{n}\frac{b_i}{t_i}} = \frac{2\left[\frac{d}{2}\left(a + b_{bf}\right)\right]}{\frac{a}{t_{eq}} + 2\frac{b_w}{t_w} + \frac{b_{bf}}{t_{bf}}} = \frac{2(3780)}{\frac{76}{0.05} + 2\left(\frac{61.39}{0.5}\right) + \frac{50}{1.5}} = 4.2$$

Figure 4.13 shows both the $\hat{\omega}_A$ diagram and the *x* diagram for a pseudo-closed section.

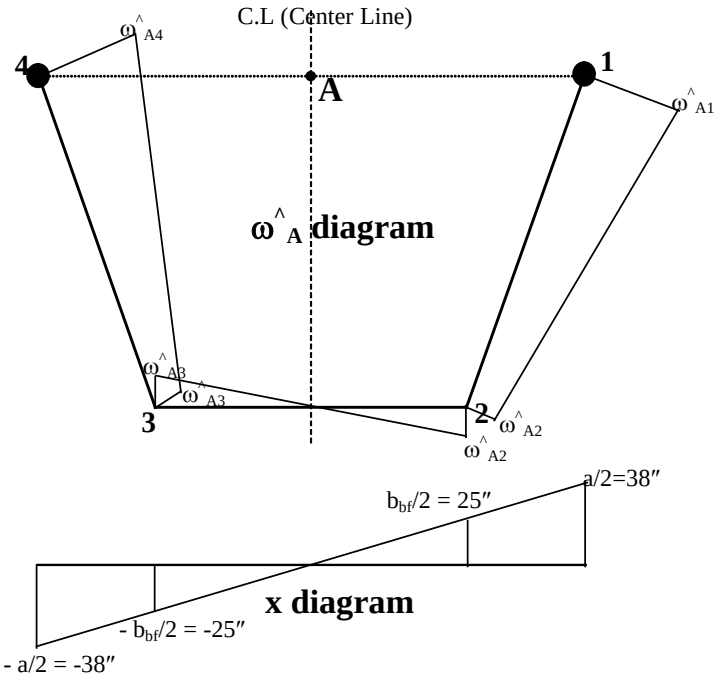

$$\omega_{A1}^{\wedge} = \omega_{A1} - \frac{2A_o}{\sum_{i=1}^{n}\frac{b_i}{t_i}}\left(\frac{a/2}{t_{eq}}\right) = 0 - 4.2\left(\frac{76/2}{0.05}\right) = -3194 \text{ in}^2$$

$$\omega_{A2}^{\wedge} = \omega_{A2} - \frac{2A_o}{\sum_{i=1}^{n}\frac{b_i}{t_i}}\left(\frac{a/2}{t_{eq}} + \frac{b_w}{t_w}\right) = 2280 - 4.2\left(\frac{76/2}{0.05} + \frac{61.39}{0.5}\right) = -1430 \text{ in}^2$$

$$\omega_{A3}^{\wedge} = \omega_{A3} - \frac{2A_o}{\sum_{i=1}^{n}\frac{b_i}{t_i}}\left(\frac{a/2}{t_{eq}} + \frac{b_w}{t_w} + \frac{b_{bf}}{t_{bf}}\right) = 5280 - 4.2\left(\frac{76/2}{0.05} + \frac{61.39}{0.5} + \frac{50}{1.5}\right) = 1430 \text{ in}^2$$

$$\omega_{A4}^{\wedge} = \omega_{A4} - \frac{2A_o}{\sum_{i=1}^{n}\frac{b_i}{t_i}}\left(\frac{a/2}{t_{eq}} + \frac{b_w}{t_w} + \frac{b_{bf}}{t_{bf}} + \frac{b_w}{t_w}\right) = 7560 - 4.2\left(\frac{76/2}{0.05} + \frac{61.39}{0.5}(2) + \frac{50}{1.5}\right) = 3194 \text{ in}^2$$

Figure 4.13 Reduced sectorial area diagram and x diagram for the pseudo-closed section

3. Determine the shear center location measured from the pole *A*, as follows:

$$e_{yA} = \frac{1}{I_{YC}} \times 2\left\{ \hat{\omega}_{A1} \left[\frac{(2a + b_{bf}) b_w t_w}{12} + \frac{aA_f}{2} \right] + \hat{\omega}_{A2} \left[\frac{{b_{bf}}^2 t_{bf} + (a + 2b_{bf}) b_w t_w}{12} \right] \right\}$$

$$e_{yA} = \frac{1}{119390} \times$$

$$2\left\{ (-3194) \left[\frac{(2(76) + 50)(61.39)(0.5)}{12} + \frac{(76)(15)}{2} \right] + (-1430) \left[\frac{(50)^2 (1.5) + (76 + 2(50))(61.39)(0.5)}{12} \right] \right\}$$

e_{yA} = -76.4 inches

So the shear center of the pseudo-closed section is located 76.4 inches below the pole *A* or 16.4 inches below the centroidal axis of the bottom flange. The shear center of the open section is located 26.9 inches below the centroidal axis of the bottom flange. In general, the shear center location of an open-section trapezoidal box girder is located below its bottom flange and is located inside the box for a closed section. As the equivalent plate thickness increases, the shear center location moves upward closer to the inside box.

4.7.3 Pure torsional constant

The pure torsional constant of the open-section Model 1 girder comprised of *5* narrow rectangular sections, J_{open}, is

$$J_{open} = \frac{1}{3} \sum_{i=1}^{5} b_i {t_i}^3$$

$$J_{open} = \frac{1}{3} \left\{ 2\left[(10)(1.5)^3 \right] + 2\left[(59.86)(0.5)^3 \right] + (50)(1.5)^3 \right\} = 83.74 \text{ in}^4$$

The pure torsional constant of the pseudo-closed section can be calculated as a closed section. $J_{pseudo\text{-}closed}$ of Model 1 is

$$J_{pseudo-closed} = \frac{4A_o^{\,2}}{\sum_{i=1}^{4}\frac{b_i}{t_i}}$$

$$J_{pseudo-closed} = \frac{4(3780)^2}{2\left(\frac{61.39}{0.5}\right)+\frac{50}{1.5}+\frac{76}{0.05}} = 31772 \text{ in}^4$$

The pure torsional constant of the pseudo-closed section is 210 times greater than that of the open section.

4.7.4 Torsional warping function

Figure 4.14 shows the torsional warping function of the open section. Figure 4.15 shows the torsional warping function of the pseudo-closed Model 1 girder. In order to construct the torsional warping function, the value of the reduced sectorial area at each point ($\hat{\omega}$) must first be calculated as shown in Figure 4.13.

4.7.5 Warping moment of inertia

The $I_{w,open}$ from Eq.4.19 is

$$I_{w,open} = 2\left[\frac{1}{3}\left(w_3^{\,2}+w_3w_4+w_4^{\,2}\right)A_f+\frac{1}{3}\left(w_1^{\,2}+w_1w_2+w_2^{\,2}\right)\left(b_wt_w\right)+\frac{1}{3}w_1^{\,2}\left(\frac{b_{bf}}{2}t_{bf}\right)\right]$$

$$= 2\left\{\begin{array}{l}\frac{1}{3}\left[(-43.3)^2+(-43.3)(-912.3)+(-912.3)^2\right](15)\\ +\frac{1}{3}\left[(672.5)^2+(672.5)(-477.8)+(-477.8)^2\right](61.39)(0.5)+\frac{1}{3}(672.5)^2\left(\frac{50}{2}(1.5)\right)\end{array}\right\}$$

= 2.74 x 10^7 in^6.

It should be noted that w_1 through w_4 are the torsional warping functions of the open section shown in Figure 4.14.

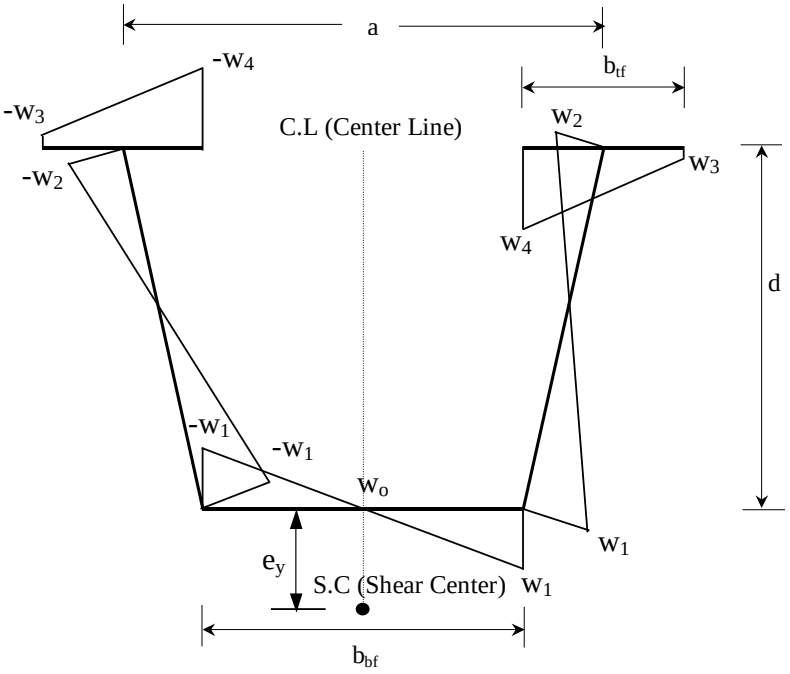

$w_o = 0$ (Because it lies on the vertical line that passes through shear center)

$$w_1 = w_o + e_y \frac{b_{bf}}{2} = 0 + (26.9)\frac{(50)}{2} = 672.5 \text{ in}^2$$

$$w_2 = w_1 - \left(\frac{b_{bf}}{2} + \frac{a - b_{bf}}{4}\right)d + \left(e_y + \frac{d}{2}\right)\left(\frac{a - b_{bf}}{2}\right)$$

$$= 672.5 - \left(\frac{50}{2} + \frac{76 - 50}{4}\right)60 + \left(26.9 + \frac{60}{2}\right)\left(\frac{76 - 50}{2}\right) = -477.8 \text{ in}^2$$

$$w_3 = w_2 + \left(e_y + d\right)\left(\frac{b_{tf}}{2}\right) = -477.8 + (26.9 + 60)\left(\frac{10}{2}\right) = -43.3 \text{ in}^2$$

$$w_4 = w_2 - \left(e_y + d\right)\left(\frac{b_{tf}}{2}\right) = -477.8 - (26.9 + 60)\left(\frac{10}{2}\right) = -912.3 \text{ in}^2$$

Figure 4.14 Torsional warping function of the open-section

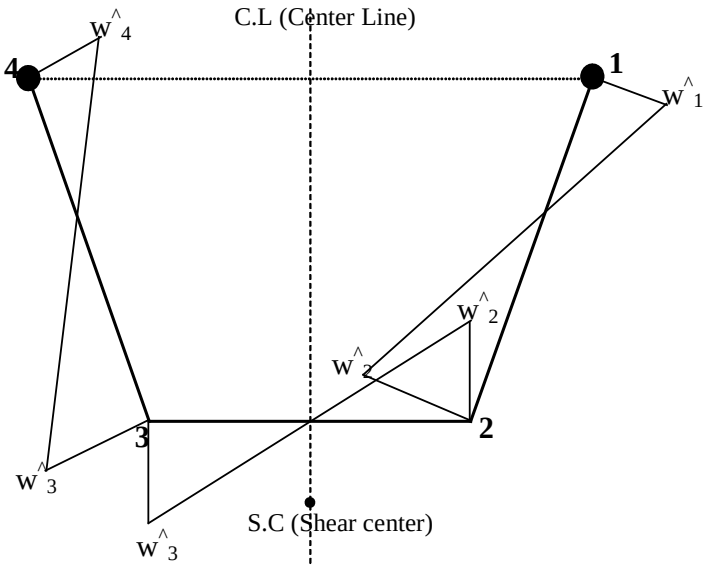

$$w_1^{\wedge} = \omega_{A1}^{\wedge} - e_y\left(\frac{a}{2}\right) = -3194 - (-76.4)(38) = -290.2 \text{ in}^2$$

$$w_2^{\wedge} = \omega_{A2}^{\wedge} - e_y\left(\frac{b_{bf}}{2}\right) = -1430 - (-76.4)(25) = 480.4 \text{ in}^2$$

$$w_3^{\wedge} = \omega_{A3}^{\wedge} - e_y\left(\frac{-b_{bf}}{2}\right) = 1430 - (-76.4)\left(\frac{-50}{2}\right) = -480.4 \text{ in}^2$$

$$w_4^{\wedge} = \omega_{A4}^{\wedge} - e_y\left(\frac{-a}{2}\right) = 3194 - (-76.4)\left(\frac{-76}{2}\right) = 290.2 \text{ in}^2$$

Figure 4.15 Torsional warping function of the pseudo-closed

The $I_{w,pseudo\text{-}closed}$ from Eq.4.20 is

$$I_{w,\,pseudo-closed} = 2\left\{\left(w_1^{\wedge}\right)^2 A_f + \frac{1}{3}\left[\left(w_1^{\wedge}\right)^2 + w_1^{\wedge} w_2^{\wedge} + \left(w_2^{\wedge}\right)^2\right]\left(b_w t_w\right) + \frac{1}{3}\left(w_2^{\wedge}\right)^2\left(\frac{b_{bf}}{2} t_{bf}\right)\right\}$$

$$= 2\left\{\begin{array}{l}(-290.2)^2(15) \\ +\frac{1}{3}\left[(-290.2)^2 + (-290.2)(480.4) + (480.4)^2\right](61.39)(0.5) + \frac{1}{3}(480.4)^2\left(\frac{50}{2}(1.5)\right)\end{array}\right\}$$

= 1.19 x 10^7 in^6

The $\hat{w}_1$ and $\hat{w}_2$ values were determined in Figure 4.15.

Clearly, $I_{w,pseudo\text{-}closed}$ is smaller than $I_{w,open}$. This indicates that under the same total torsional moment, the pseudo-closed section torsional warping resists a smaller portion of the total torsional moment than that in the open-section.

4.7.6 Warping shear parameter and central second moment of area

The warping shear parameter for an open-section μ_{open} is 1.0. The warping shear parameter for the pseudo-closed Model 1 girder $\mu_{pseudo\text{-}closed}$ is calculated using the following procedures:

1. Calculate the perpendicular distance from the shear center to the web $r_{S.C.\text{-}web}$ (see Figure 4.10)

$$r_{S.C.-web} = \left[\frac{a}{2} - \frac{e_{yA}}{2d}\left(a - b_{bf}\right)\right]\frac{d}{b_w}$$

$$= \left[\frac{76}{2} - \frac{76.4}{2(60)}(76 - 50)\right]\frac{60}{61.39} = 21.0 \text{ in}$$

2. Calculate the central second moment of area for the pseudo-closed section $I_{c,pseudo\text{-}closed}$ using Eq.4.23.

$$I_{c,pseudo-closed} = (e_y)^2(at_{eq}) + 2(r_{S.C.-web})^2(b_w t_w) + (e_y - d)^2(b_{bf} t_{bf})$$

$$= (76.4)^2(76)(0.05) + 2(21.0)^2(61.39)(0.5) + (76.4 - 60)^2(50)(1.5)$$

$$= 69360 \text{ in}^4$$

3. Calculate the warping shear parameter for the pseudo-closed section of Model 1 girder using Eq.4.21

$$\mu_{pseudo-closed} = 1 - \frac{J_{pseudo-closed}}{I_c}$$

$$= 1 - \frac{31772}{69360} = 0.542$$

4.7.7 Parameter *X*

Parameter *X* was presented in Chapter 2. It does not only depend on the cross-section dimension, but also on the girder length. Having calculated both the pure torsional constant *J* and the warping moment of inertia I_w, the parameter *X*, which indicates whether pure torsion or warping torsion is dominant, can be calculated. For the open-section 180-ft Model 1 girder, the parameter *X* is

$$X = l\sqrt{\frac{GJ}{EI_w}}$$

$$X = (180x12)\sqrt{\frac{(11200)(83.74)}{(29600)(2.74x10^7)}} = 2.32$$

and for the pseudo-closed Model 1 girder

$$X = (180x12)\sqrt{\frac{(11200)(31772)}{(29600)(1.19x10^7)}} = 68.7$$

As Chen (1999) indicated, the parameter *X* of 2.32 indicates that both pure torsion and warping torsion resist the total torsional moment (i.e. mixed torsion), while a value of 68.7 indicates that almost all torsional moment is resisted by pure torsion (i.e. only pure torsion is present). It can be concluded that in order to analyze the behavior of the open section properly, the contribution of both pure torsion and warping torsion must be considered, whereas for the pseudo-closed section, warping torsion can be ignored.

CHAPTER 5
Behavior of a straight girder

This chapter discusses the general behavior of an open-section and a pseudo-closed section straight girder under uniform symmetrical loading. The first section discusses the application of classical beam theory to predict the vertical deflection of a straight girder. The second and third sections present the general behavior of an open section and a pseudo-closed section straight girder, respectively.

5.1 VERTICAL DEFLECTION PREDICTION USING CLASSICAL BEAM THEORY

In general, it is desirable to have a trapezoidal box girder perform within its elastic range during the construction and serviceability stages. This section studies the applicability of classical beam theory for predicting the vertical deflection of a straight trapezoidal box girder. Using classical beam theory, the elastic vertical deflection along girder length $\delta_{(x)}$ and the elastic vertical deflection at midspan δ_{mid} of a simply-supported straight girder with length l under uniform load w are

$$\delta_{(x)} = \frac{wx}{24EI}\left(l^2 - 2lx + x^3\right) \tag{5.1}$$

$$\delta_{mid} = \frac{5wl^4}{384EI} \tag{5.2}$$

where x is the coordinate along the girder length, E is the modulus of elasticity, and I is the moment of inertia about the horizontal axis.

Eqs.5.1 and 5.2 can be used for both open sections and pseudo-closed sections, provided that I is calculated appropriately. In order to verify the applicability of these formulas to trapezoidal box girders, UTRAP was used to analyze a simply-supported Model 1 straight girder for both the open section and the pseudo-closed section. The cross-section dimensions of Model 1 were shown in Figure 1.5. Figure 5.1 shows the analysis cases and top lateral bracing systems used throughout this chapter.

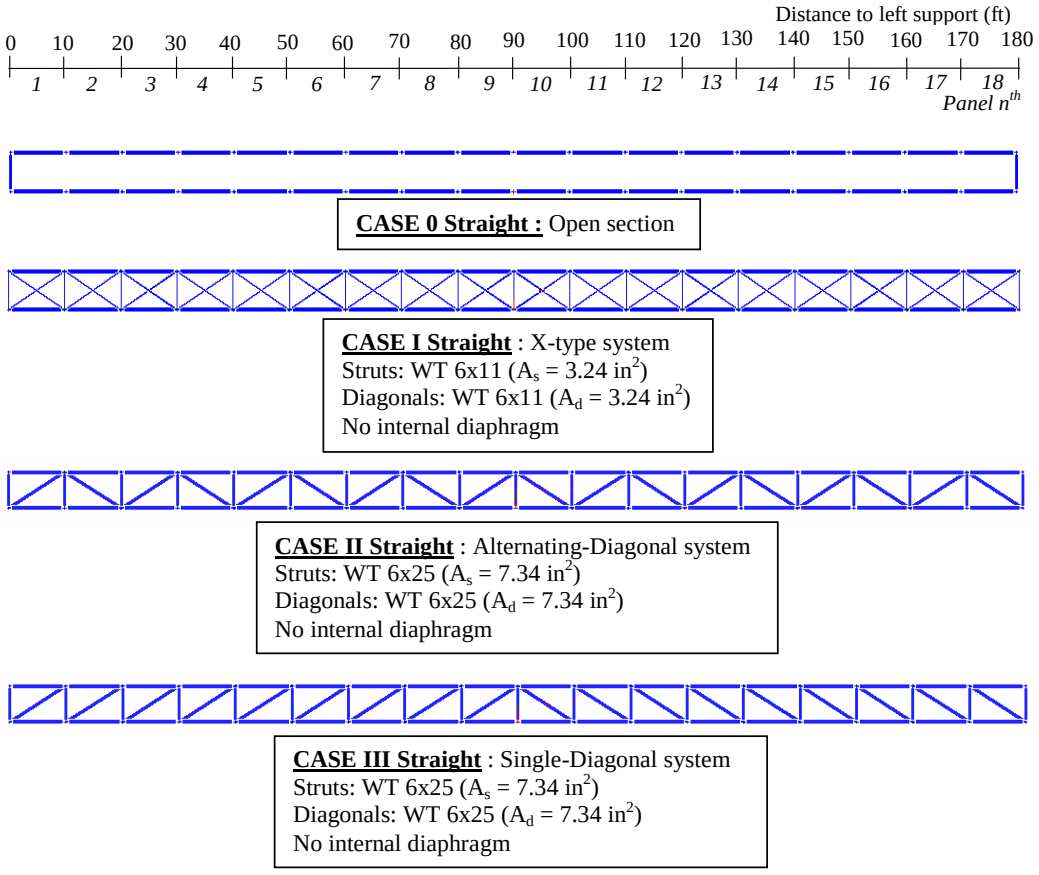

Figure 5.1 Type of top lateral bracing system used in each analysis case

Figure 5.2 shows comparisons between the predicted vertical deflections along the length (using Eq.5.1) and UTRAP solutions for both the open section and the pseudo-closed section with the X-type top lateral bracing system under a uniformly distributed load of 1 k/ft.

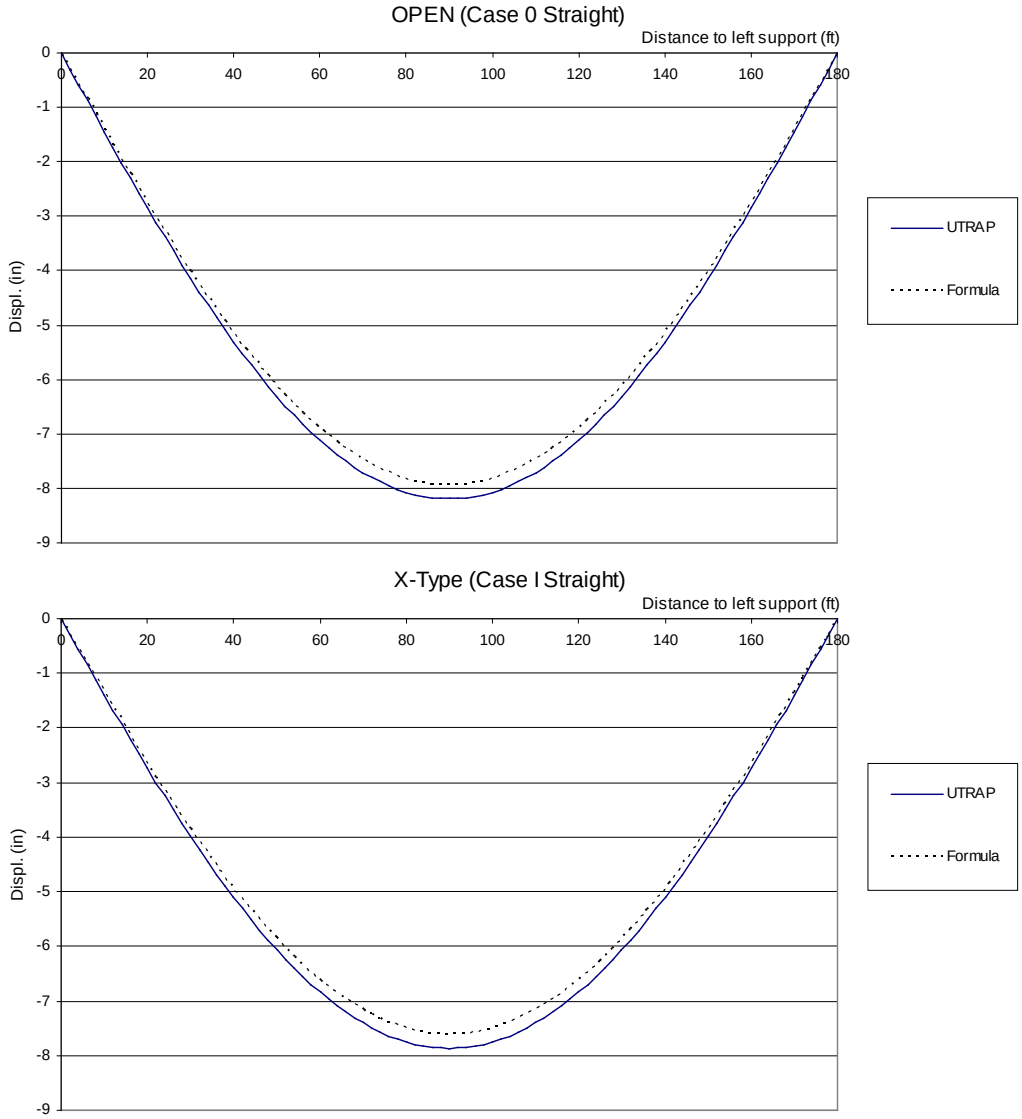

Figure 5.2 Predicted vertical deflections and UTRAP solutions

There is good agreement between the predicted vertical displacements using classical beam theory and the UTRAP solutions. However, the predicted vertical deflections are smaller than the UTRAP solutions for both the open and the pseudo-closed sections.

5.1.1 Shear deformation

The formulas to predict vertical deflections expressed in both Eqs.5.1 and 5.2 neglect vertical deflections due to shear deformation. Total vertical deflections δ_{TOT} including the effect of shear deformation can be calculated as follows:

$$\delta_{TOT} = \delta_{B.M} + \delta_S \tag{5.3}$$

where δ_{BM} is the component of vertical deflection due to bending moment, expressed in Eqs.5.1 and 5.2, and δ_S is the component of vertical deflection due to shear deformation. Using the Virtual Work Method (Castigliano's 1st Theorem), δ_S of a straight girder with length l is

$$\delta_S = \int_0^l \alpha \frac{V_{(x)} v_{(x)}}{GA} dx \tag{5.4}$$

where α is the shear deformation coefficient that depends on the cross-section shape and the assumptions about the distribution of shear stress across the cross-section, G is the shear modulus of elasticity (for steel G = 11200 ksi), A is the cross-sectional area, $V_{(x)}$ is the shear force along the length due to the applied load, and $v_{(x)}$ is the shear force along the length due to a unit load applied at the location where the deflection is to be calculated.

Figure 5.3 shows $V_{(x)}$ and $v_{(x)}$ for a girder under a uniformly distributed load w with the midspan vertical deflection as the deflection of interest (i.e. applying a unit load at the midspan).

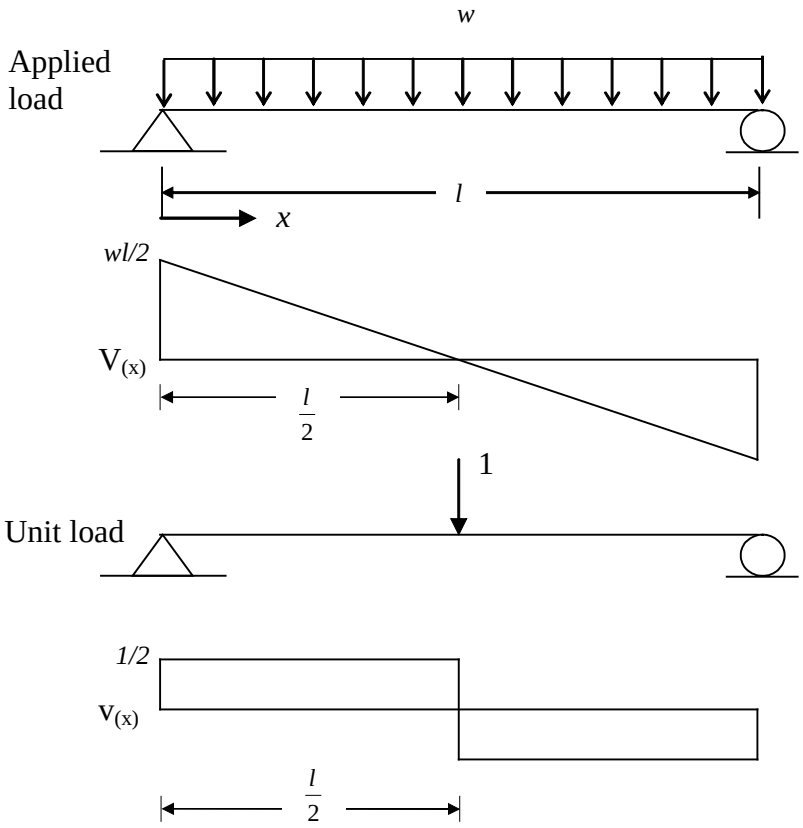

Figure 5.3 Shear force diagram

Based on Figure 5.3, Eq.5.4 can be modified as follows:

$$\delta_S = \frac{\alpha}{GA}\int_0^l V_{(x)} v_{(x)} dx$$

$$\delta_S = \frac{\alpha}{GA}\left\{2\left[\frac{1}{2}\left(\frac{wl}{2}\right)\left(\frac{l}{2}\right)\left(\frac{1}{2}\right)\right]\right\}$$

$$\delta_S = \frac{\alpha}{GA}\frac{(wl)l}{8} \qquad (5.5)$$

The shear deformation coefficient α for a trapezoidal box girder is not well established, whereas the α for an I-section is given in Young and Budynas (2002). Therefore, in order to study the effect of shear deformation on the vertical deflection, Model 1 is modified to Model 4, which is analogous to two identical I-girders. Figure 5.4 shows the cross-section dimensions of Model 4; Figure 5.5 shows the analysis cases for the hand calculations and UTRAP.

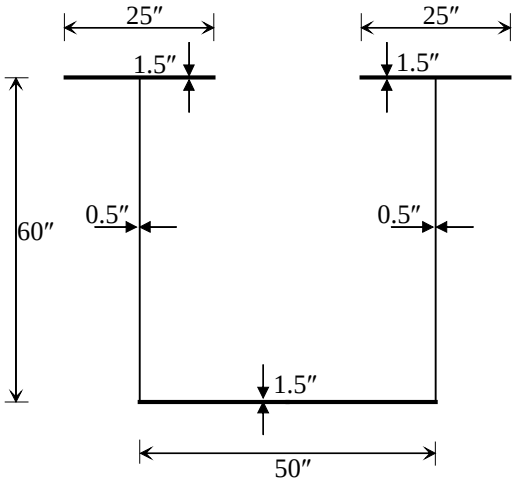

Figure 5.4 Cross-section dimensions of Model 4 girder

Young and Budynas indicated that for the I-section shown in Figure 5.6, the shear coefficient α is

$$\alpha = \left[1 + \frac{3\left(d_2^{\,2} - d_1^{\,2}\right)d_1}{2d_2^{\,3}}\left(\frac{t_2}{t_1} - 1\right)\right]\frac{4d_2^{\,2}}{10r^2} \qquad (5.6)$$

where r is the radius of gyration of the section with respect to the neutral axis. The shear coefficient α for Model 4 is 3.98.

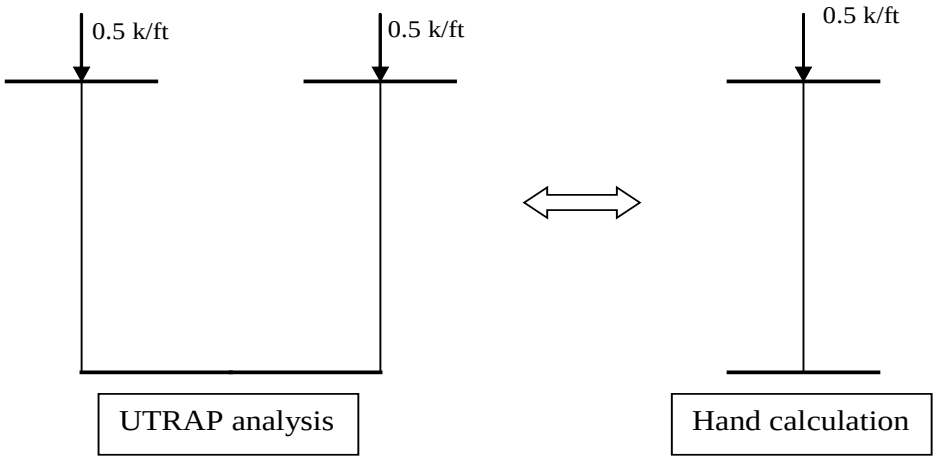

Figure 5.5 Analysis case for UTRAP and hand calculation

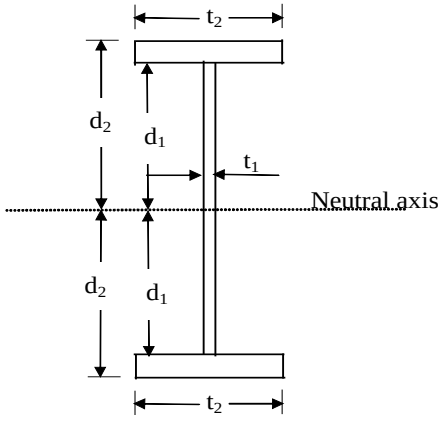

Figure 5.6 Dimension of I girder

The UTRAP solution for the midspan deflection of an open-section Model 4 straight girder under a uniformly distributed load of 1 k/ft is 5.44 inches. The components of the midspan vertical deflection of Model 4 using the hand-calculation are:

$$\delta_{B.M} = \frac{5wl^4}{384EI} = \frac{5\left(\frac{0.5}{12}\right)(180\times12)^4}{384(29600)(7.585\times10^4)} = 5.26 \text{ inches}$$

$$\delta_S = \frac{\alpha}{GA}\frac{(wl)l}{8} = \frac{3.98}{(11200)(104.25)}\frac{(0.5)(180)(180\times12)}{8} = 0.083 \text{ inches}$$

The predicted midspan vertical deflection neglecting shear deformation is 5.26 inches (3.3% difference from the UTRAP solution) and the predicted midspan vertical deflection including shear deformation is 5.34 inches (1.8% difference from the UTRAP solution).

Figure 5.7(a) shows the midspan deflection for seven different lengths of a Model 4 straight girder from UTRAP and the calculated deflection due to bending moment only, and the total deflection including both elastic components due to both bending moment and shear deformation. Figure 5.7(b) shows the percent discrepancies between the UTRAP solutions and the predicted midspan deflections neglecting and including shear deformation. Figure 5.7(a) shows that there is good agreement between the predicted midspan deflections and the UTRAP solutions. Usually, the deflection component from shear deformation is very small compared to the elastic deflection due to bending moment. Figure 5.7(b) shows that for a relatively short girder, the discrepancies between the UTRAP solutions and the predicted deflections using only the bending component can be large. On the other hand, for a short girder, deflection usually will not control the design, and the additional precision in predicting the deflection is not justified from a fabrication perspective. The percent discrepancies between the specified camber and the final product are usually more than those of neglecting shear deformation in predicting deflections. Moreover, steel box girders are not

generally used for short spans. Based on all of these facts, it can be concluded that neglecting shear deformation in predicting deflections is acceptable from a design standpoint.

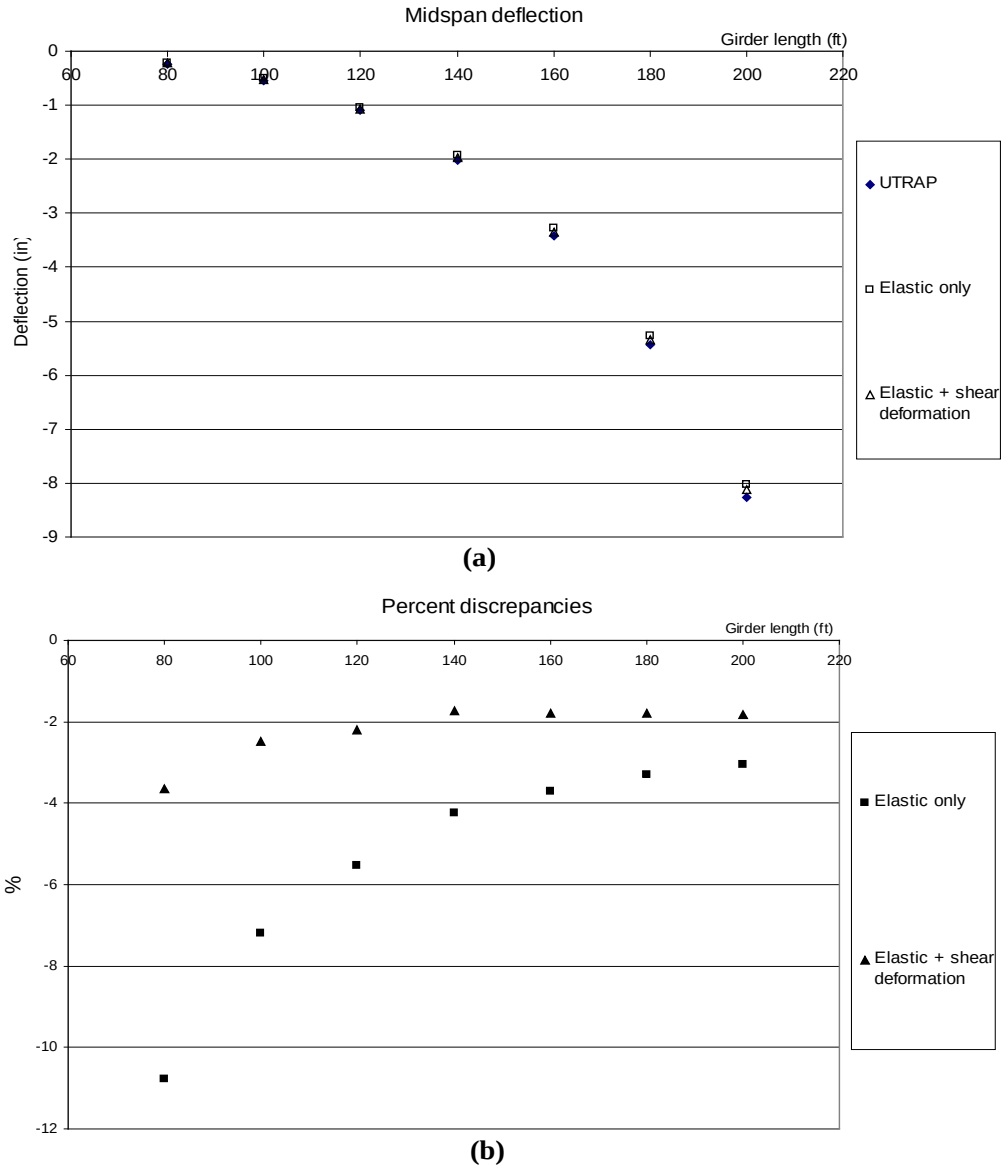

Figure 5.7 Midspan deflection and percent discrepancies between the predicted midspan deflection and the UTRAP solution

5.2 BEHAVIOR OF AN OPEN-SECTION STRAIGHT GIRDER

Branco (1981) indicated that an open-section straight girder under a symmetrical uniformly distributed load will experience a bending distortion, as shown in Figure 5.8.

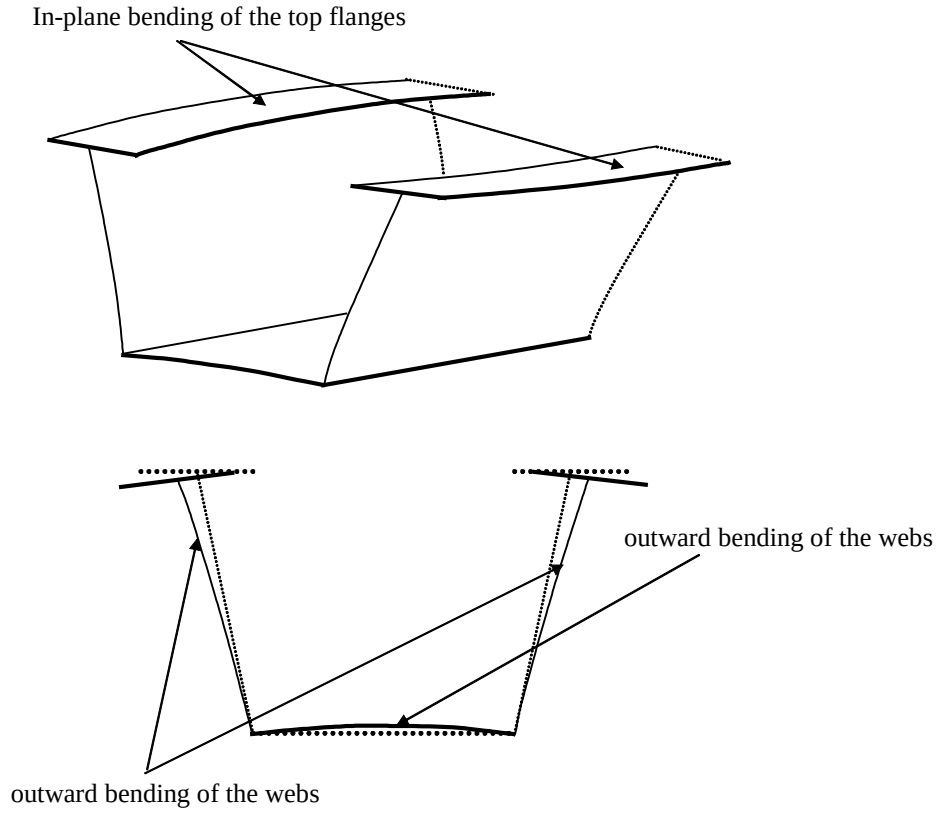

Figure 5.8 Bending distortion of an open-section trapezoidal box girder

Bending distortion involves the outward bending of the webs, the upward bending of the bottom flange, and the in-plane (lateral) bending of the top flanges. This bending distortion is caused by the horizontal load component w_H due to the sloping webs as shown in Figure 5.9.

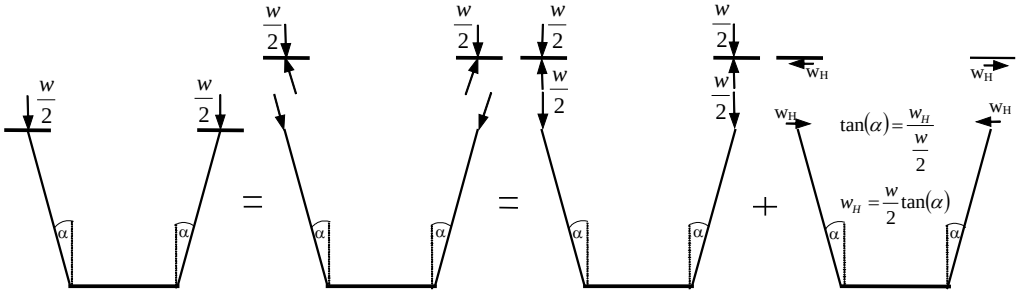

Figure 5.9 Horizontal load component due to sloping webs

The horizontal load component w_H is directly proportional to tan(α), so a trapezoidal box girder with a larger web angle α is more prone to bending distortion than one with a smaller α.

In order to verify the presence of bending distortion in an open-section trapezoidal box girder, UTRAP was used to analyze "Case 0 Straight" of a Model 1 girder. It should be noted that both vertical and horizontal deflections of all seven nodes shown in Figure 5.10 can be obtained from the UTRAP output.

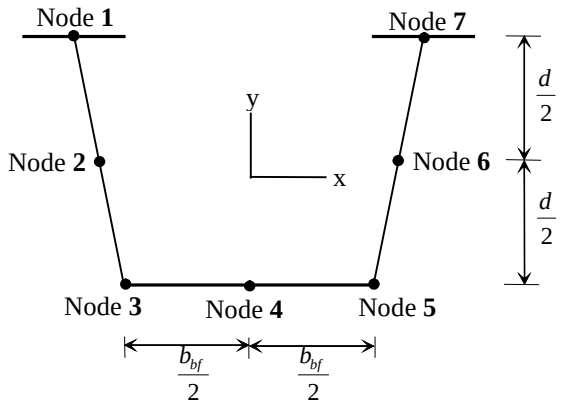

Figure 5.10 Nodes locations where deflections can be extracted from the UTRAP output

Figure 5.11 shows UTRAP solutions for horizontal deflections of the "Case 0 straight" Model 1 girder under a uniform load of 1 k/ft. Positive and negative horizontal displacements indicate the horizontal displacement in the positive and the negative x-direction, respectively. Nodes 1 and 2 move in the negative x-direction and nodes 6 and 7 move in the positive x-direction. In an open-section straight girder under a symmetrical uniform load, the movement of nodes 1 and 7 and the movement of nodes 2 and 6 are symmetrical with respect to the girder centerline. The horizontal displacement is fairly constant over the center portion of the span. There is no horizontal deflection at the supports because UTRAP assumes there is a rigid diaphragm at each support.

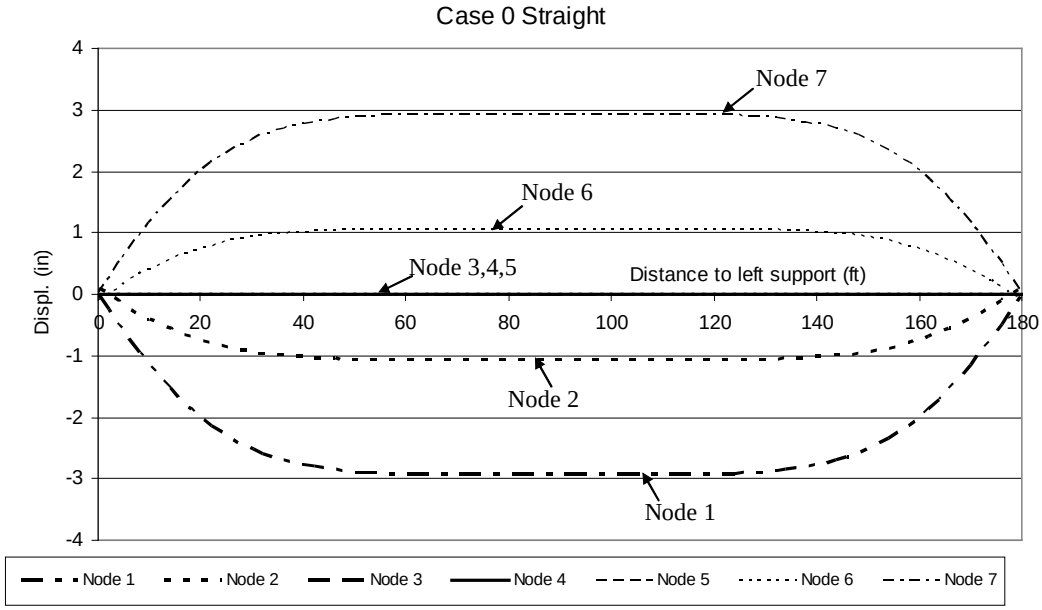

Figure 5.11 Horizontal deflection of the open-section

In order to provide a more detailed illustration of bending distortion, Figure 5.12 shows the deformed position of an open-section Model 1 straight girder at midspan. Figure 5.12 shows that under a symmetrical uniform loading,

there is a cross-section deformation in an open-section straight girder in addition to its rigid body motion. Vertical deflection data shows the upward bending of the bottom flange.

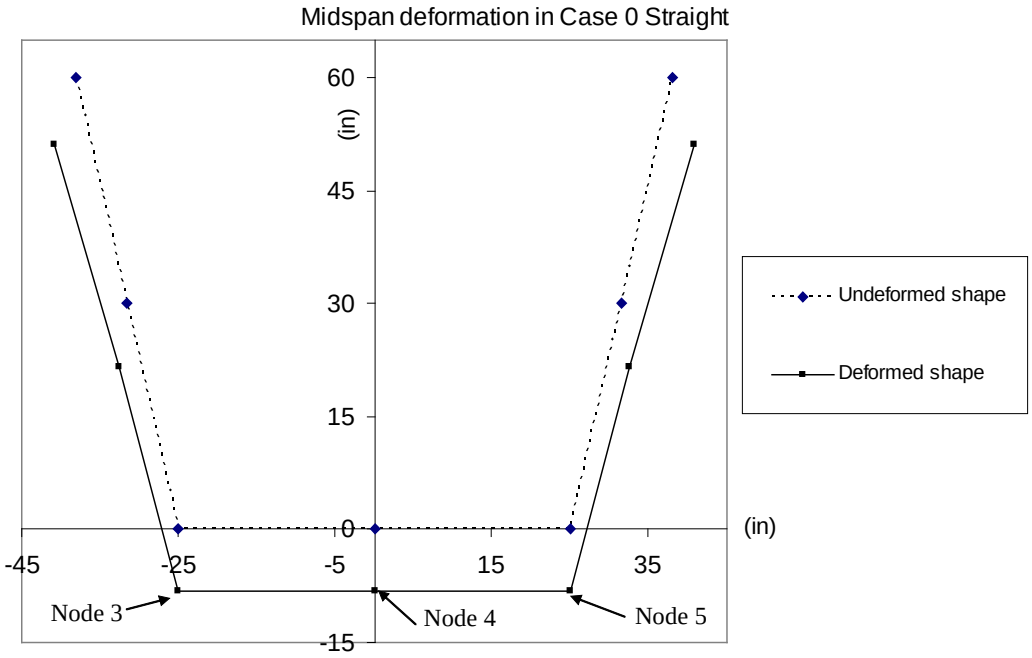

	Node 3	Node 4	Node 5
Vertical deflections	-8.21”	-8.19”	-8.21”

Figure 5.12 Deformed position at the midspan of an open-section

Figure 5.13 shows the normal stress variation along the length. The average normal stress represents the normal stress due to bending assuming a rigid cross-section (i.e. without bending distortion). The bending distortion does not change the maximum normal stress at the midspan. The explanation for this is that the deviance of total normal stress from the bending normal stress is caused by the in-plane bending of the top flanges. Figure 5.11 shows that there is no in-plane bending of the top flanges near the midspan (i.e. horizontal displacements

of nodes 1 and 7 near the midspan are constant). Therefore, there is no additional normal stress due to bending distortion near the midspan.

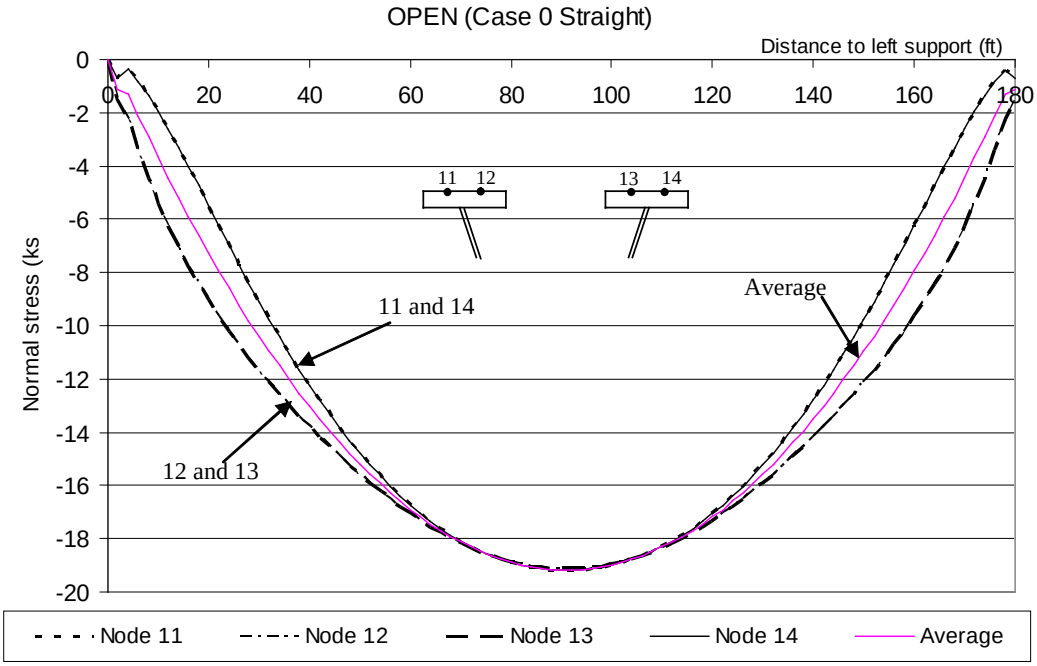

Figure 5.13 Normal stress in the open-section of Model 1 straight girder

Figure 5.13 also shows that the normal stresses at nodes 11 and 14 are the same, as are those at nodes 12 and 13. Therefore in all the subsequent plots of normal stress variation, only nodes 13 and 14 are shown.

5.2.1 Preventing Bending Distortion

Bending distortion shown in Figure 5.8 can easily be prevented by using struts that will prevent the spreading of the web, as shown in Figure 5.14. The struts used in the following example are WT 6x11 (Area = 3.24 in^2).

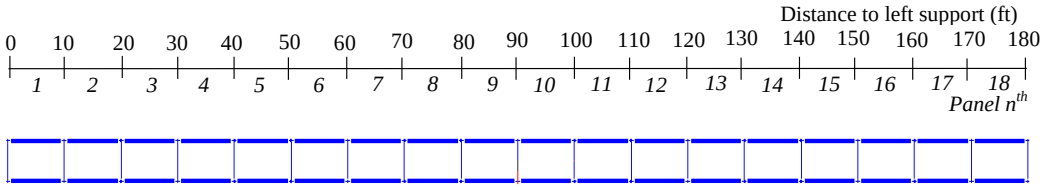

Figure 5.14 Using struts with 10-ft spacing to prevent bending distortion

Struts only prevent the spreading of the web. They do not contribute to the overall bending or torsional stiffness of the girder. For this reason, a girder with struts must be treated as an open section.

Figure 5.15 shows the total normal stress variation along the length of a Model 1 girder with struts under a uniform load of 1 k/ft, which can be compared to that without struts, shown in Figure 5.13. Figure 5.15 shows that the total normal stress in nodes 11 through 14 in top flanges of an open-section girder with struts is approximately the same as the bending normal stress. However, there is jaggedness in the total normal stress variation along the length, as compared to the smooth variation shown in Figure 5.13. This indicates that there are localized normal stresses in addition to the bending normal stress due to the presence of the struts.

Figure 5.16 shows the horizontal displacements of the right top flange. The horizontal displacement of the top flanges in the open-section straight girder with struts is almost zero, compared to that without struts (i.e. Figure 5.11). However, as can be seen from Figure 5.16, there is a repetitive pattern of in-plane bending of the top flanges between struts. This in-plane bending of the top flanges causes the additional normal stress, which is called the localized normal stress. The horizontal displacement is flat over a 2-foot increment at maximum displacement. The reason for this is that the UTRAP output is in 2-ft increments, so there is no data point between the two points to make a smooth plot.

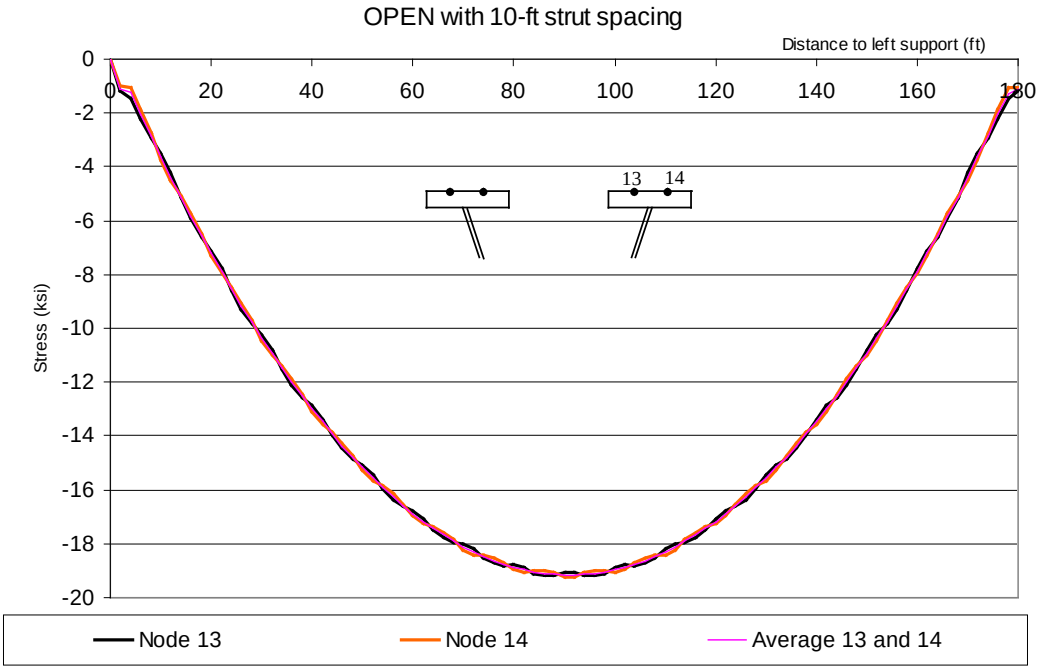

Figure 5.15 Total normal stress in the top flanges of the open-section

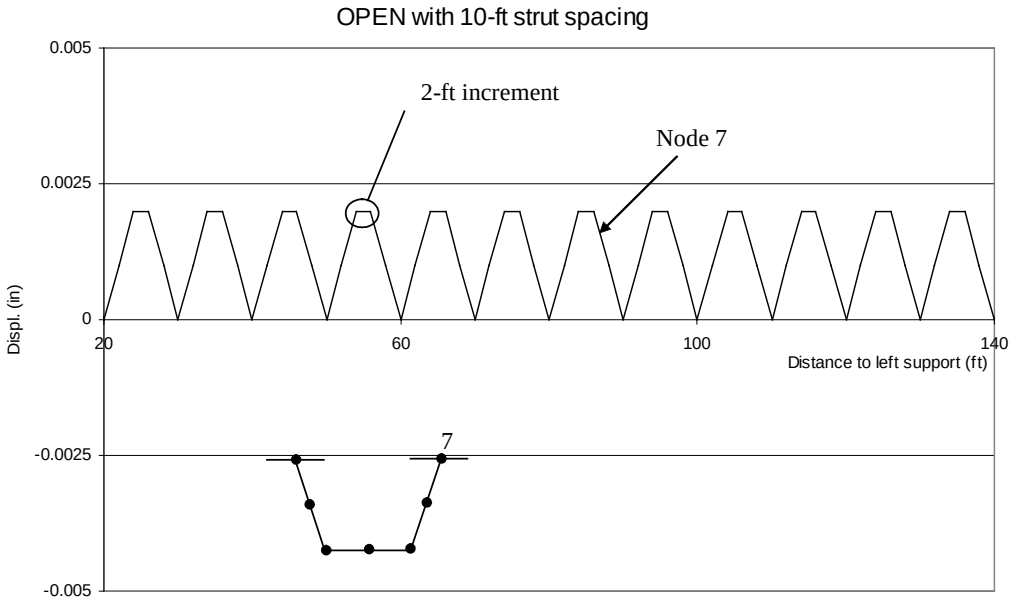

Figure 5.16 Horizontal displacement of the top flange of the open-section

Figure 5.17 shows a comparison of the deformed shape of Model 1 with and without struts at a location 86 ft from the left support. This location is arbitrarily chosen because there is no strut at that location (strut spacing is 10 ft). Even though there is no strut in that location, there is no bending distortion in the Model 1 girder with a 10-ft strut spacing. It can be concluded that struts are effective for preventing the cross-section deformation due to bending distortion.

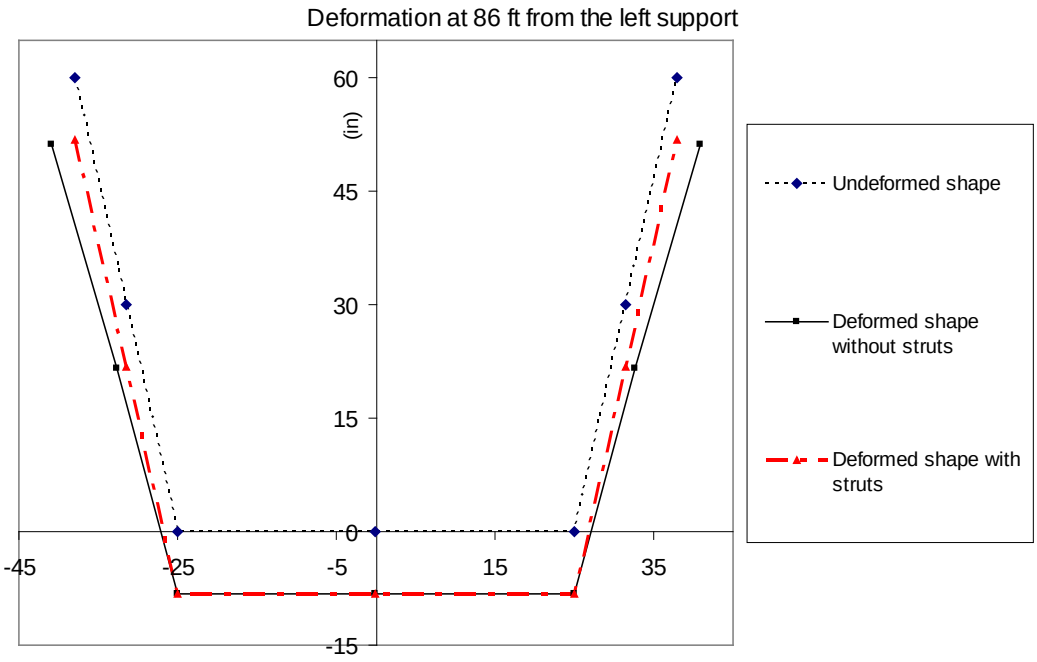

Figure 5.17 Deformed position 86 ft from the left support of the open-section

5.2.2 Required strut spacing

In-plane bending of the top flanges will occur between struts and thus induces localized normal stress in addition to the bending normal stresses. Figure 5.18 shows the total normal variation in the right top flange of the open-section Model 1 girder with a 30-ft strut spacing, under a uniform load of 1 k/ft. The

maximum total normal stress in the girder with 30-ft strut spacing can be 2 ksi more than that in the girder without struts

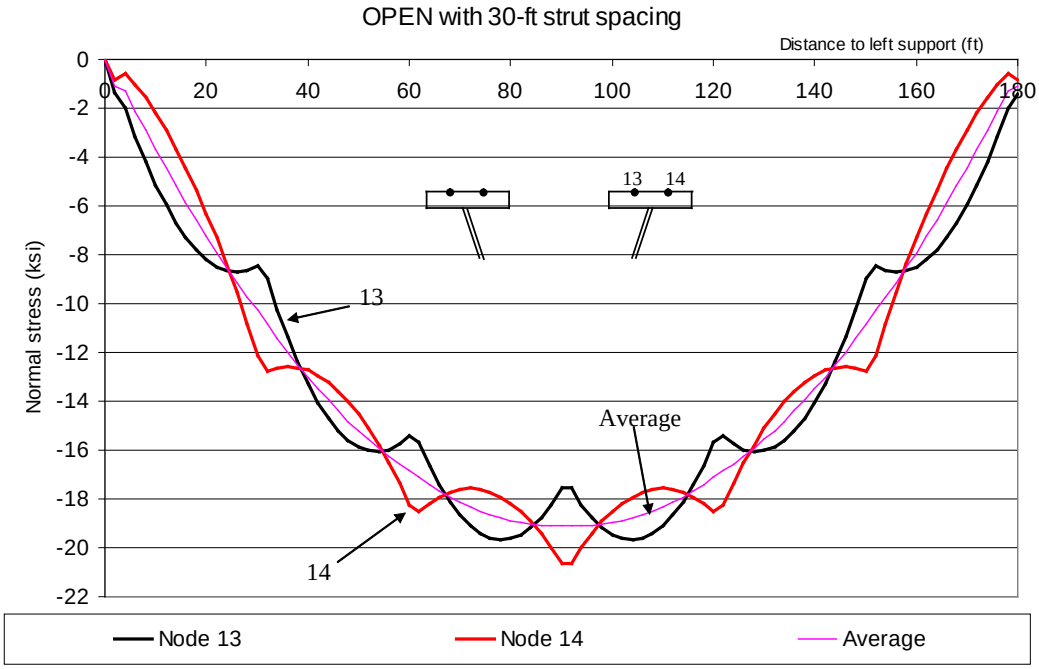

Figure 5.18 Total normal flange stress with a 30-ft strut spacing

As seen in Figure 5.16, the horizontal displacement of the top flanges due to the horizontal component of the applied load in a straight trapezoidal box girder with struts can be simplified as the displacement of a continuous girder. In order to calculate the additional normal stress conservatively, each panel (between two adjacent struts) can be simplified as a fixed-fixed beam. The maximum localized bending moment is $\frac{1}{12} w_H s^2$ at the strut locations, where s is the strut spacing. The additional normal stress σ_{add} at the tip of the top flanges due to lateral bending of the top flanges is

$$\sigma_{add} = \frac{Mc}{I} = \frac{\left(\frac{w_H s^2}{12}\right)\left(\frac{b_{tf}}{2}\right)}{\left(\frac{1}{12} t_{tf} {b_{tf}}^3\right)}$$

$$\sigma_{add} = \frac{w_H s^2}{2 t_{tf} {b_{tf}}^2} \tag{5.7}$$

t_{tf} and b_{tf} are the thickness and width of the top flanges, respectively. From Eq.5.7, the required s to limit σ_{add} due to lateral bending of the top flange is

$$s = \sqrt{\frac{2\sigma_{add} t_{tf} {b_{tf}}^2}{w_H}} \tag{5.8}$$

In order to verify the analytical formula, UTRAP was used to analyze Model 1 straight girders with different strut spacings. It should be pointed out that UTRAP can only give the total normal stresses at nodes 11 through 14 on the top flanges, which do not correspond to the maximum total normal stresses that occur at the tip of the top flanges. The total normal stresses at the tip of the left top flange and right top flange can be found by using a linear interpolation based on those at nodes 11 and 12 and nodes 13 and 14, respectively. The maximum additional normal stress due to lateral bending of the top flange is found by subtracting the bending normal stress from the total normal stresses at the tip of the top flange. The bending normal stresses on the top flange were obtained by averaging the total normal stresses at nodes 11 through 14.

Figure 5.19 shows the variation of the maximum additional normal stresses due to lateral bending of the top flange for a Model 1 girder with a 30-ft strut spacing, under a uniform load of 1 k/ft. The maximum additional normal stress due to bending occurs at the strut location. The maximum stresses in the first and last panel are greater than those in the other panels. The explanation for this is that the first panel is analogous to a propped cantilever beam, whereas all

the other panels are analogous to a fixed-fixed beam. Since the maximum bending moment in a propped cantilever beam is larger than that in a fixed-fixed beam, the maximum bending stress is also larger. From a design perspective, the maximum additional normal stress in the first panel will not be a concern, because the bending normal stresses near a support are very small. Therefore, the analytical formula to predict the additional normal stresses due to lateral bending of the top flanges is derived based on a fixed-fixed beam.

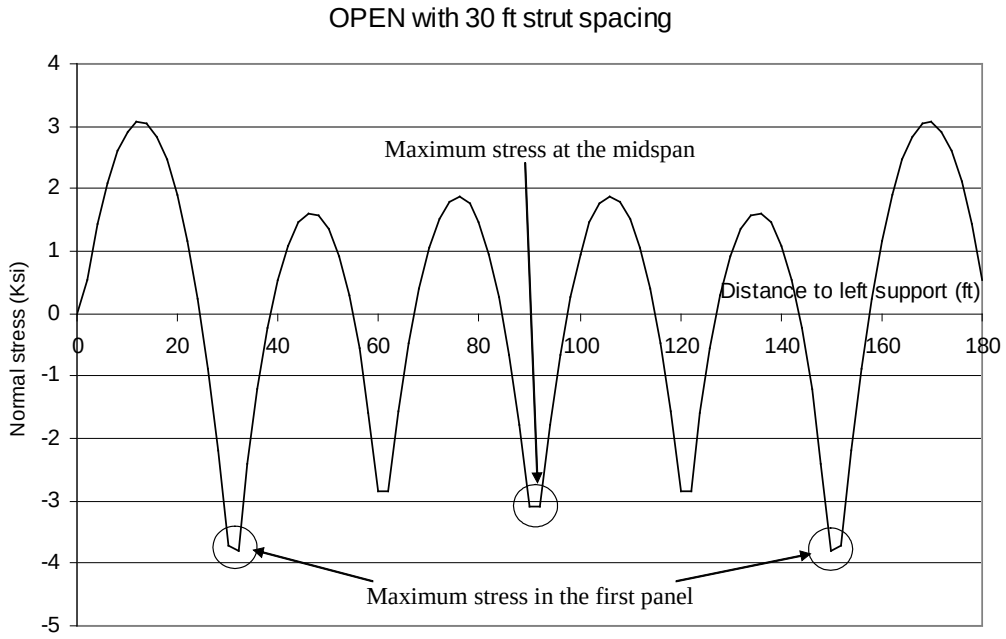

Figure 5.19 Additional normal stress at the tip of the top flanges

Figure 5.20 shows an example of the additional normal stress at the tip of the top flanges due to lateral bending of the top flanges as a function of the strut spacing. Model 1 girder under a uniform load of 1k/ft was used in this analysis. The analytical solution was calculated using Eq.5.7. The analytical formula can conservatively predict the additional normal stress due to lateral bending of the

top flanges. The discrepancies between the analytical formula and the UTRAP solution are caused by modeling error. The analytical formula is derived using a fixed-fixed beam model, whereas the real condition at the strut location is less stiff than a fixed support.

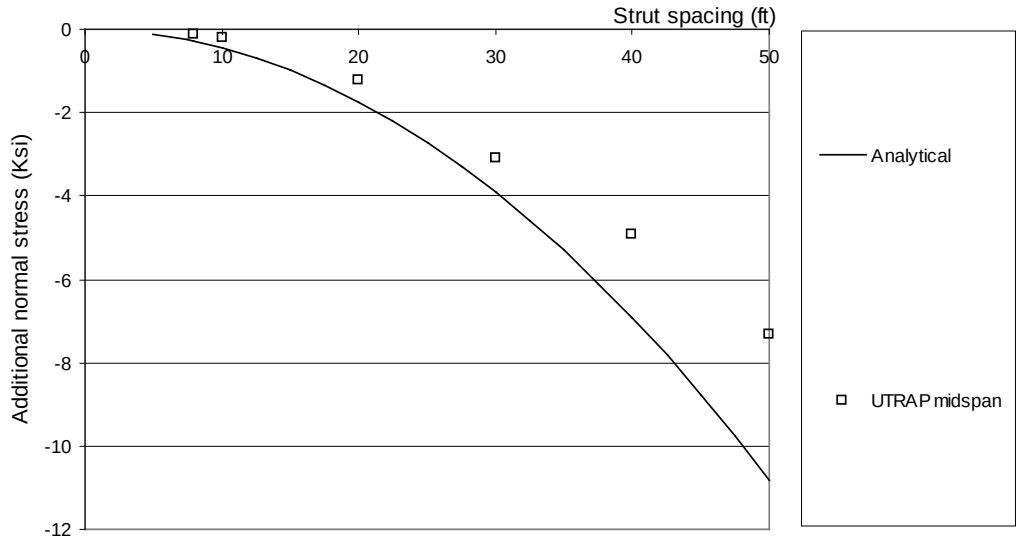

Figure 5.20 Additional normal stress at the tip of the top flanges

5.3 BEHAVIOR OF A PSEUDO-CLOSED SECTION STRAIGHT GIRDER

Figure 5.21 shows UTRAP solutions for the vertical deflections along the length of a Model 1 straight girder under a uniformly distributed load of 1 k/ft for an open section with three different top lateral bracing systems, shown in Figure 5.1. Figure 5.21 shows that the vertical deflections of the open-section, Alternating-Diagonal, and Single-Diagonal top lateral bracing systems are almost identical. The vertical deflections of the X-type system are slightly smaller than those for the other systems. These observations agree with the fact that

Alternating-Diagonal and Single-Diagonal systems are less effective than the X-type system in resisting vertical bending.

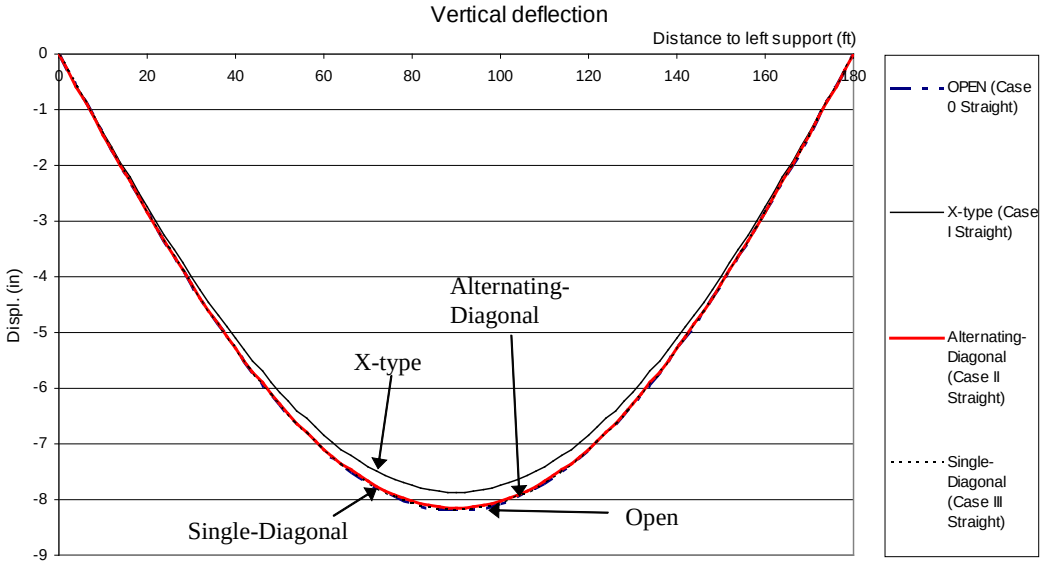

Figure 5.21 UTRAP solutions for vertical deflections

Figure 5.22 shows the normal bending stress among the open section and the pseudo-closed section using three different top lateral bracing systems under a uniform load of 1 k/ft. The variation of normal bending stress in both the open-section and the pseudo-closed section Model 1 straight girder follows the same trend as noted for the vertical deflection. From both vertical deflection and bending normal stress perspectives, there is no advantage for using either the Alternating-Diagonal or the Single-Diagonal system in a straight girder. On the other hand, using the X-type system can reduce the vertical deflection and bending normal stress, although only slightly.

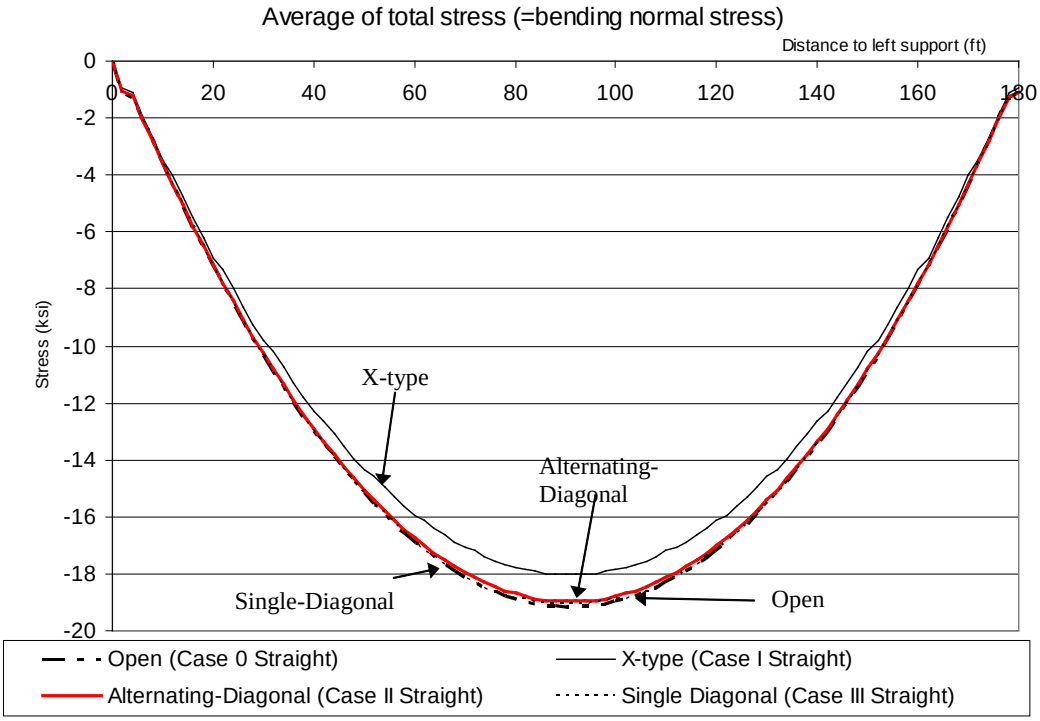

Figure 5.22 Bending normal stress of the open and pseudo-closed sections

Even though the variations of the bending normal stresses in the three different top lateral bracing systems are identical as shown in Figure 5.22, the variations of total normal stresses are significantly different because of the localized normal stress. The following sections present the localized normal stresses in Model 1 with the three different top lateral bracing systems under a uniformly distributed load of 1 k/ft.

5.3.1 Localized normal stress in the X-type system

Figure 5.23 shows the total normal stress variation along the length of the pseudo-closed section with an X-type system.

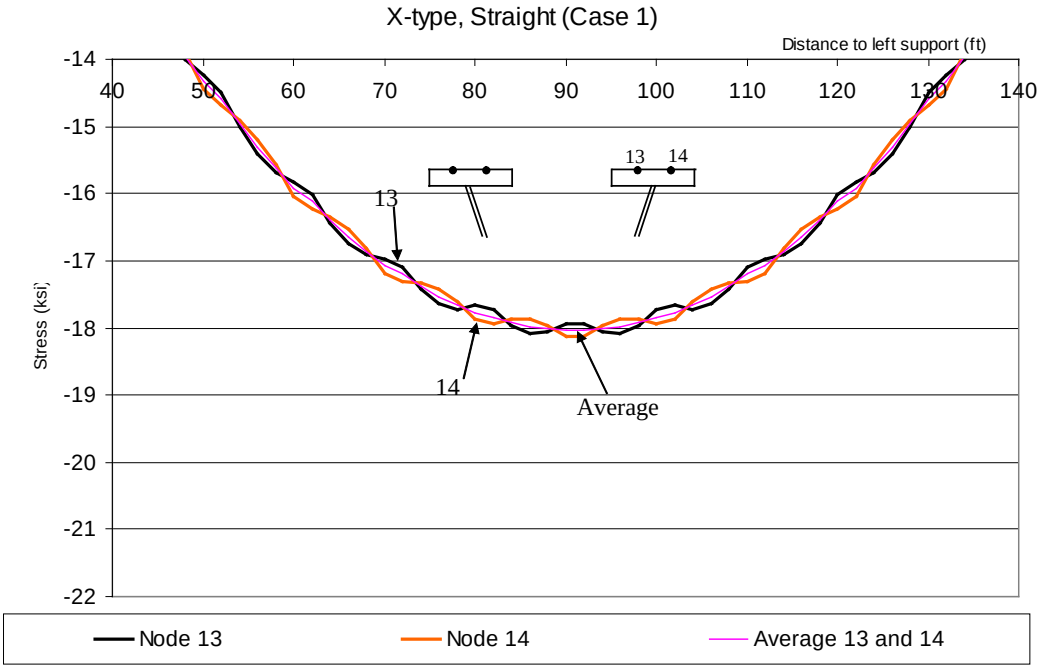

Figure 5.23 Total normal stress variation on the top flange - X-type system

Using an X-type top lateral bracing system instead of using only struts will not affect the localized normal stress. The only difference is that the total stress in a pseudo-closed section using X-type system is smaller than that in an open section because the X-type system provides some contribution to the overall bending stiffness of the girder.

5.3.2 Localized normal stress in Alternating-Diagonal system

In addition to the lateral bending of top flanges due to spreading of the webs, the localized normal stress in a pseudo-closed section using Alternating-Diagonal top lateral system can be caused by the lateral bending of the flanges due to the interactive forces between top lateral bracing members and top flanges,

as will be discussed in Chapter 9. Figure 5.24 shows the total normal stress variation along the length of the pseudo-closed section with the Alternating-Diagonal system. In this case, the localized normal stress is about 15 percent of the bending normal stress. This ratio is fairly constant within each panel. The maximum localized normal stress of about 2.5 ksi is also fairly constant within each panel.

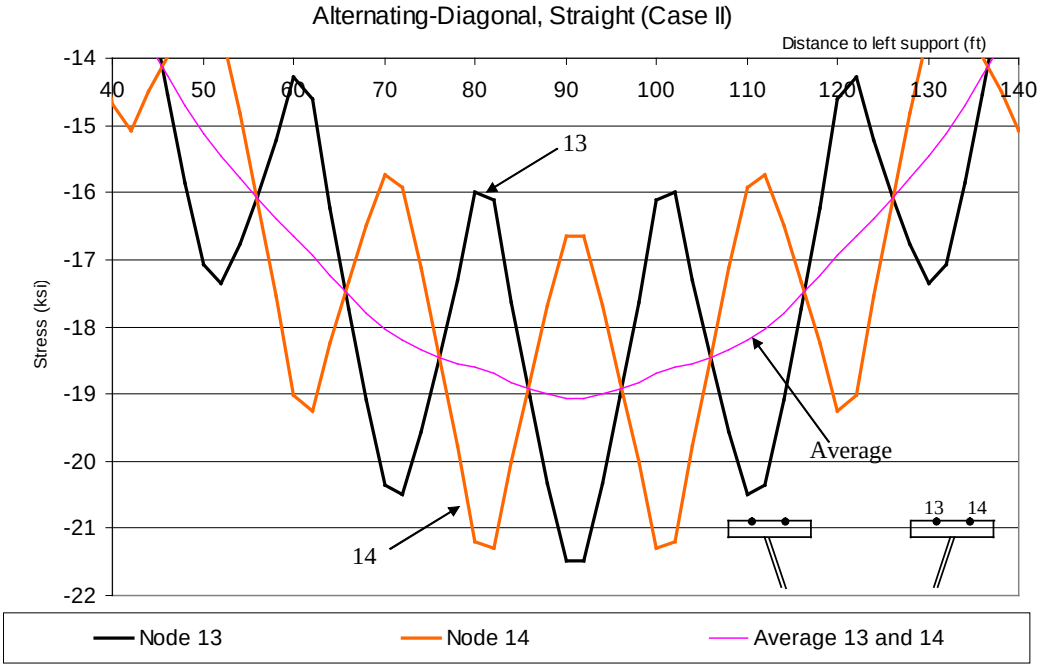

Figure 5.24 Total normal stress variation on the top flange - Alternating-Diagonal

Comparing Figure 5.23 and Figure 5.24 shows that the localized normal stresses in a girder with an Alternating-Diagonal top lateral bracing system are significantly higher than that with X-type system because in an X-type system, there are no interactive forces between top lateral bracing members and top flanges, as presented in Chapter 9. In addition, Figure 5.25 shows that the top flanges of a girder with an Alternating-Diagonal system laterally bend like a

continuous beam between panels, whereas those in a girder with X-type system do not.

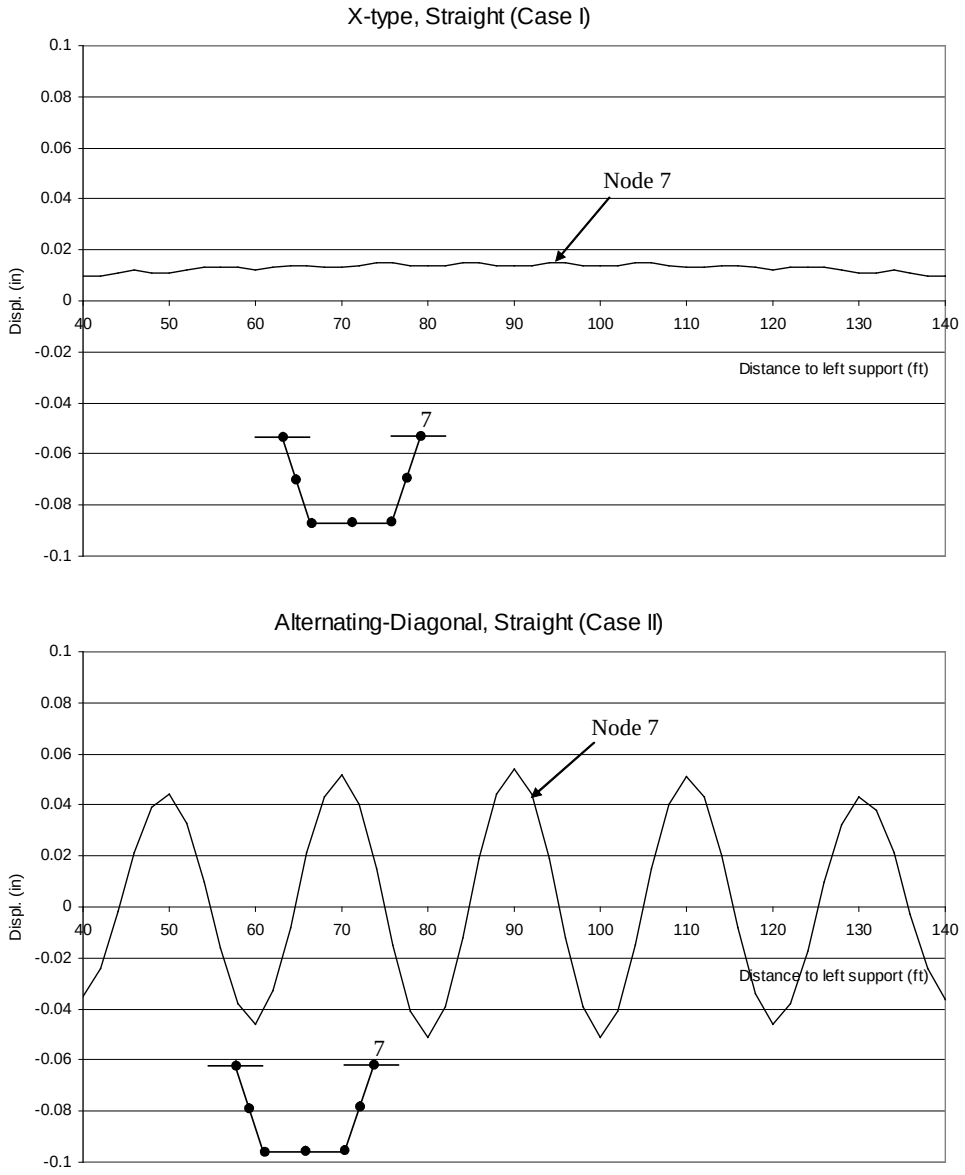

Figure 5.25 Horizontal displacement of the right top flange with X-type and Alternating-Diagonal systems

5.3.3 Localized normal stress in the Single-Diagonal system

Unlike the top flanges in a girder with an Alternating-Diagonal system, those in a girder with a Single-Diagonal system do not bend like a continuous beam as shown in Figure 5.26. Also, there is a kink at the midspan. Obviously, this kink will induce significantly high localized normal stress. Figure 5.27 shows the total normal stress variation along the length with the Single-Diagonal system. The total normal stress variation in the top flanges of a girder with the Single-Diagonal top lateral bracing system is generally similar to that with the X-type system. However, there is a significantly high localized normal stress at midspan due to the kink in horizontal displacement of its top flange. In this case, the localized normal stress at midspan is about 10 percent of the bending normal stress.

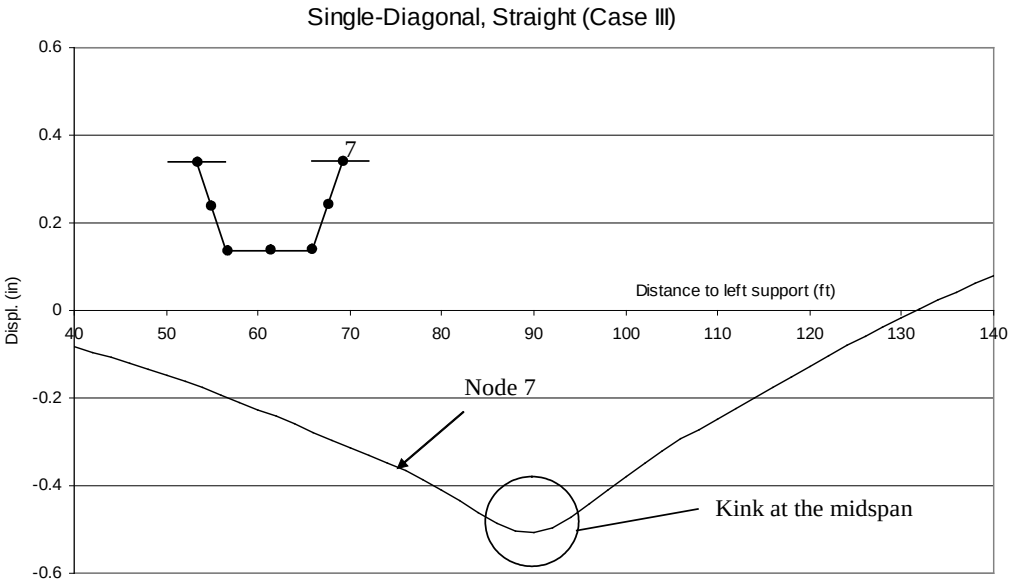

Figure 5.26 Horizontal displacement of the top flange - Single-Diagonal

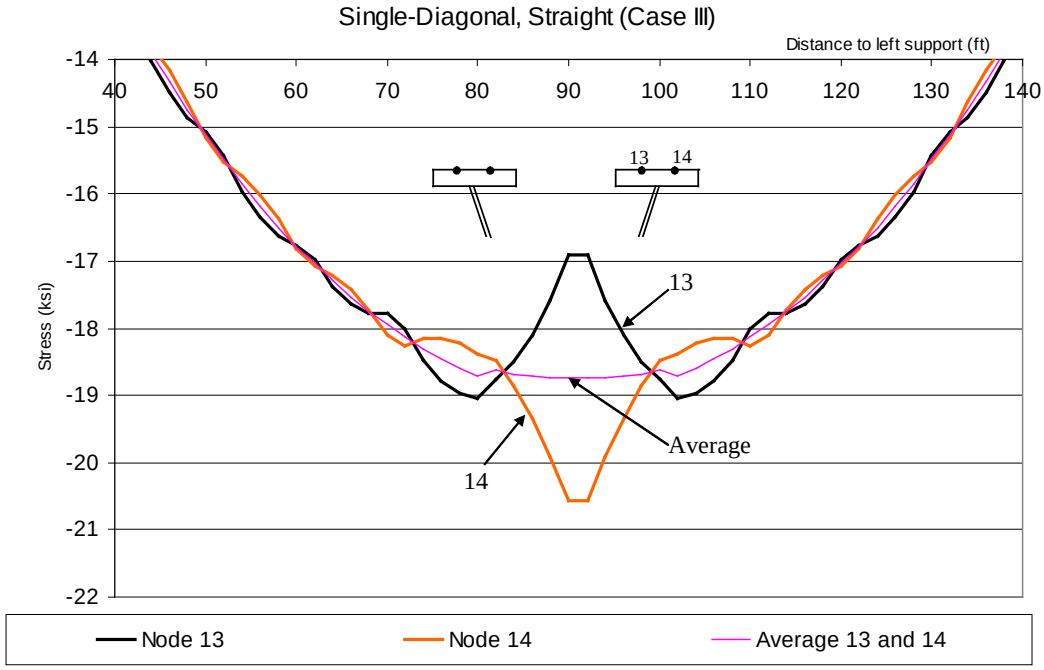

Figure 5.27 Total normal stress variation on the top flange - Single-Diagonal

5.4 SUMMARY

Classical beam theory can be used to predict the vertical deflection of a straight trapezoidal box girder. For a typical steel box girder used in practice, there is a good agreement between the vertical deflections obtained from classical beam theory neglecting shear deformation and those obtained from UTRAP.

Due to the horizontal component of the applied load (because of the sloping web), the cross-section of an open section trapezoidal box girder will distort under vertical bending. This bending distortion involves the outward bending of the webs, the upward bending of the bottom flange, and the lateral bending of the top flanges. The lateral bending of the top flanges causes deviation of the total normal stresses from the bending normal stresses in the top flanges.

The struts are very effective in preventing bending distortion because they prevent the spreading of the webs. However, the lateral bending of the top flanges can still occur between struts and cause additional normal stresses (i.e. localized normal stresses), which reach their maximum magnitude at the strut location. Depending upon the spacing of the struts, this localized normal stress can be significant, causing the maximum total normal stresses in a girder with struts to be greater than the maximum bending normal stress. This chapter presented an analytical formula for determining the required strut spacing in order to limit these additional normal stresses.

The vertical deflections and the bending normal stresses in a pseudo-closed girder with the Alternating-Diagonal or the Single-Diagonal top lateral bracing system are the same as those in an open-section girder. However, both the vertical deflections and the bending normal stresses in a pseudo-closed girder with the X-type system are slightly less than those in an open-section girder. From both vertical bending and bending normal stress perspectives, there is no benefit in using the Alternating-Diagonal or the Single-Diagonal top lateral bracing system in a straight girder.

The total normal stress in a simply-supported straight girder consists of bending and localized normal stresses. The localized normal stress depends on the type of top lateral bracing system and generally caused by a lateral bending of the top flanges. The magnitudes of the localized normal stresses in an open section with the struts and in a pseudo-closed section with an X-type system are about the same and those in an Alternating-Diagonal system are significantly larger. The localized normal stresses in a girder with a Single-Diagonal system are significantly high near the midspan where the top flanges experience a kink. However, the maximum localized normal stress in a girder with a Single-Diagonal system is still smaller than that with an Alternating-Diagonal system.

CHAPTER 6
Behavior of a Curved Girder

This chapter discusses the general behavior of a horizontally curved girder. The most important difference between a curved girder and a straight girder is that in a curved girder, regardless of load placement, there is always a torsional loading component due to curvature. Consequently, the deformation of a curved girder involves rotations and horizontal displacements in addition to the vertical displacements. Generally, the cross-sections of a curved girder will also distort from the original profile due to the distortional component of the torsional loading.

The first two sections in this chapter discuss vertical deflection, rotation, and lateral displacement of a curved girder. In those sections, the cross-section is assumed to be rigid (i.e. the original profile of cross-section is maintained). In order to make this assumption valid, closely-spaced internal diaphragms (2-ft spacing) are used. The third section discusses cross-section distortion. In that section, the significance of various parameters on cross-section distortion is discussed and recommendations for the spacing of internal diaphragms to control distortion are presented.

6.1 VERTICAL DEFLECTION AND ROTATION

6.1.1 Analytical

Nakai and Yoo (1988) presented closed-form solutions for the vertical deflection and the rotation of a simply-supported curved girder under uniformly

distributed and concentrated loads. The distributed load *p* used in the Nakai and Yoo formulation is over the girder surface (i.e. load per unit area). The formulas were obtained by solving the differential equation related to the torsional warping theory and are applicable to both open and pseudo-closed sections. The general Nakai and Yoo formulations have been simplified for the singly symmetric sections considered herein.

Figure 6.1 shows a simply supported curved girder under a uniformly distributed load *p* over the girder surface with the notations used by Nakai and Yoo in the closed-form solutions. The curved girder has a central angle Φ, a radius of centroidal axis R_o, and radii of the inside and outside edges of the uniformly distributed load R_{in} and R_{out}, respectively. The angle defining a position along the curved length, measured from the left support, is denoted ϕ.

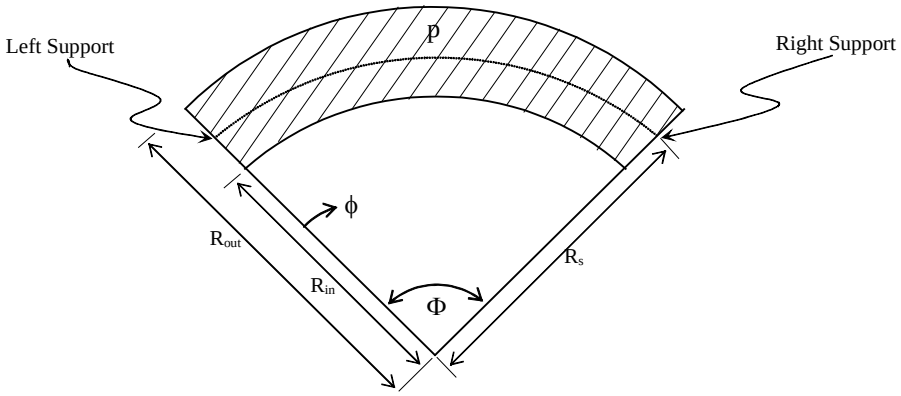

Figure 6.1 Simply supported curved girder under a uniform load p

For a uniformly distributed load *p*, Nakai and Yoo used the following notations in their formulation.

$$L_1 = \frac{1}{3}\left(R_{out}^3 - R_{in}^3\right) \tag{6.1}$$

$$L_2 = \frac{R_o}{2}\left(R_{out}^2 - R_{in}^2\right) \tag{6.2}$$

The differential equation related to the torsional warping theory is

$$\frac{d^2\delta}{d\phi^2} + \delta = -R_o{}^2\left(\frac{M_X}{EI_X} - \frac{\theta}{R_o}\right) \tag{6.3}$$

where M_X and I_X are the bending moment and the bending moment of inertia with respect to the horizontal centroidal axis, respectively, and θ is the torsional angle. The analytical formulas for predicting the deflection along the length of a simply supported curved girder under a uniformly distributed load *p*, obtained by solving Eqn.(3), is

$$\delta_{(\phi)} = pR_o{}^2\left\{\begin{array}{l} -\dfrac{\kappa_2}{\alpha^2}\dfrac{\sinh(\alpha\phi)+\sinh(\alpha(\Phi-\phi))}{\sinh(\alpha\Phi)} - \omega_1\dfrac{\sin(\phi)+\sin(\Phi-\phi)}{\sin(\Phi)} \\ +\dfrac{1}{GJ}\left[\dfrac{L_2}{\alpha^2}\left(\dfrac{\alpha^2\Phi\phi}{2} - \dfrac{\alpha^2\phi^2}{2} - 1\right) + L_1\right] \\ -\kappa_1\left[\dfrac{1-\cos(\Phi)}{\sin(\Phi)}\left(\Phi\cos(\Phi)\dfrac{\sin(\phi)}{\sin(\Phi)} - \phi\cos(\phi)\right) + (\phi-\Phi)\sin(\phi)\right] + \kappa_3 \end{array}\right\} \tag{6.4}$$

where:

$$\omega_1 = \frac{L_1\alpha^2}{GJ\left(\alpha^2+1\right)} + \kappa_2 + \kappa_3 \tag{6.5}$$

$$\kappa_1 = \left[\frac{R_o{}^2}{EI_w\left(\alpha^2+1\right)} + \frac{1}{EI_X}\right]\frac{L_1}{2} \tag{6.6}$$

$$\kappa_2 = \frac{R_o{}^2}{EI_w\left(\alpha^2+1\right)}\left(\frac{L_1}{\alpha^2+1} - \frac{L_2}{\alpha^2}\right) \tag{6.7}$$

$$\kappa_3 = \frac{R_o{}^2 L_2}{EI_w\alpha_2} + \frac{L_1}{EI_X} \tag{6.8}$$

$$\alpha = R_o \sqrt{\frac{GJ}{EI_w}} \tag{6.9}$$

E: Young's modulus of elasticity

G: Shear modulus of elasticity

J: Pure torsional constant

I_w: Warping moment of inertia

Figure 6.2 shows the cross-section rotation of a girder. The analytical formula for predicting the torsional angle θ along the length of a simply-supported curved girder under a uniformly distributed load p is

$$\theta_{(\phi)} = \frac{pR_o}{GJ}\left[\begin{array}{l}\left(\frac{L_2}{\alpha^2} - \frac{L_1}{\alpha^2+1}\right)\frac{\sinh(\alpha\phi)+\sinh(\alpha(\Phi-\phi))}{\sinh(\alpha\Phi)} \\ -\frac{L_1}{\alpha^2+1}\alpha^2\frac{\sin(\phi)+\sin(\Phi-\phi)}{\sin(\Phi)} + \frac{L_2}{\alpha^2}\left(\frac{\alpha^2\phi\Phi}{2} - \frac{\alpha^2\phi^2}{2} - 1\right) + L_1\end{array}\right] \tag{6.10}$$

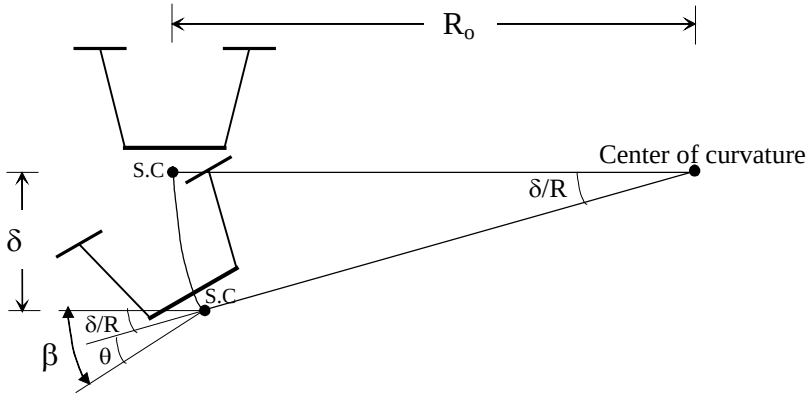

Figure 6.2 Cross-section rotation

Having calculated both the torsional angle and the vertical deflection, the rotation along the length of a simply supported curved girder $\beta_{(\phi)}$ is

$$\beta_{(\phi)} = \theta_{(\phi)} - \frac{\delta_{(\phi)}}{R_o} \tag{6.11}$$

6.1.2 Verification

In order to determine the accuracy of the analytical formulas, UTRAP was used to analyze a 180-ft simply supported Model 1 girder, shown in Figure 1.5, under a uniformly distributed load of 0.8 k/ft. An X-type top lateral bracing system with a 2-ft panel spacing was used as shown in Figure 6.3. In order to eliminate the cross-section distortion, a 2-ft spacing of the internal diaphragms with 4-in^2 member sizes was used. The area of the strut A_s was 4 in^2 and the area of the diagonal A_d was varied to produce different equivalent plate thicknesses. In order to study whether the accuracy of the analytical formulas is sensitive to the equivalent plate thickness, an open section and a pseudo- closed section with equivalent plate thicknesses of 0.05 inches (A_d=2.63 in^2) and 0.01 inches (A_d=0.525 in^2) were used. Three different radii of curvature were used.

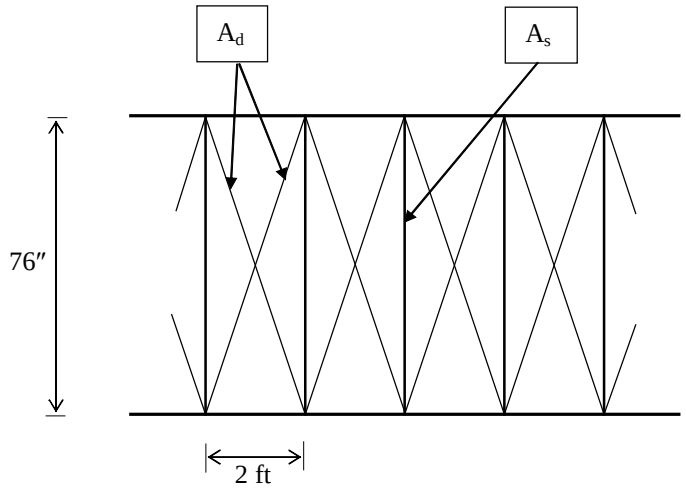

Figure 6.3 X-type top lateral bracing system

Figure 6.4 shows the vertical deflections along the length of the curved girder obtained from Eq.6.4 and the UTRAP solutions. The UTRAP vertical

deflections plotted are those of the node located at the middle of the bottom flange.

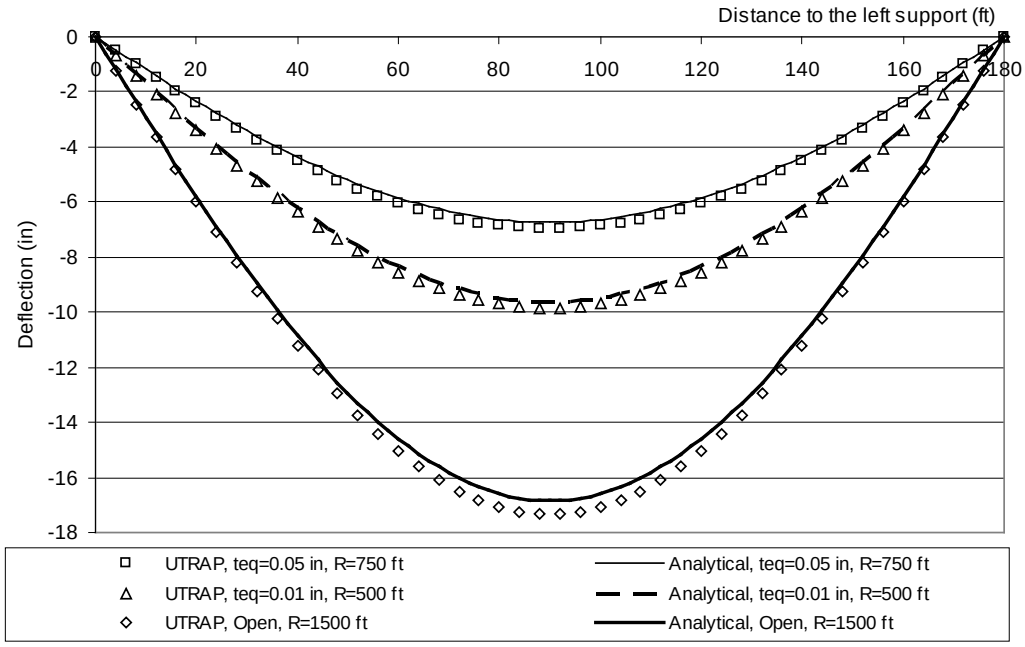

Figure 6.4 Vertical deflections of Model 1 curved girder

There is good agreement between the UTRAP solution and the analytical formula. The UTRAP deflections are slightly greater than those from the analytical formulas. These small discrepancies may be caused by ignoring the shear deformation in the derivation of the analytical formulas. Figure 6.4 suggests that the accuracy of the analytical formulas for predicting the vertical deflection is not sensitive to the central angle or the equivalent plate thickness.

Figure 6.5 shows the rotations along the length of the two pseudo-closed section and Figure 6.6 presents the rotation for the open section. The UTRAP rotations shown are the rotations of the bottom flange. A negative rotation indicates a counter-clockwise rotation when viewed from the origin, as shown in

Figure 6.2. Because the rotation of an open section is much larger than that of a pseudo-closed section, the rotation of the open section is plotted separately.

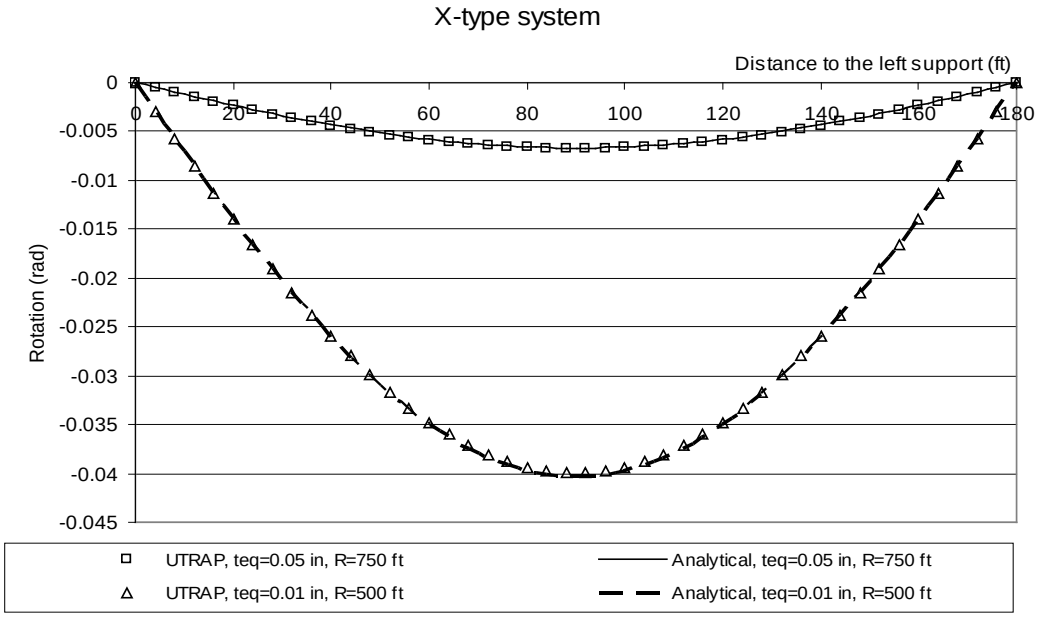

Figure 6.5 Rotations of a pseudo-closed section curved girder

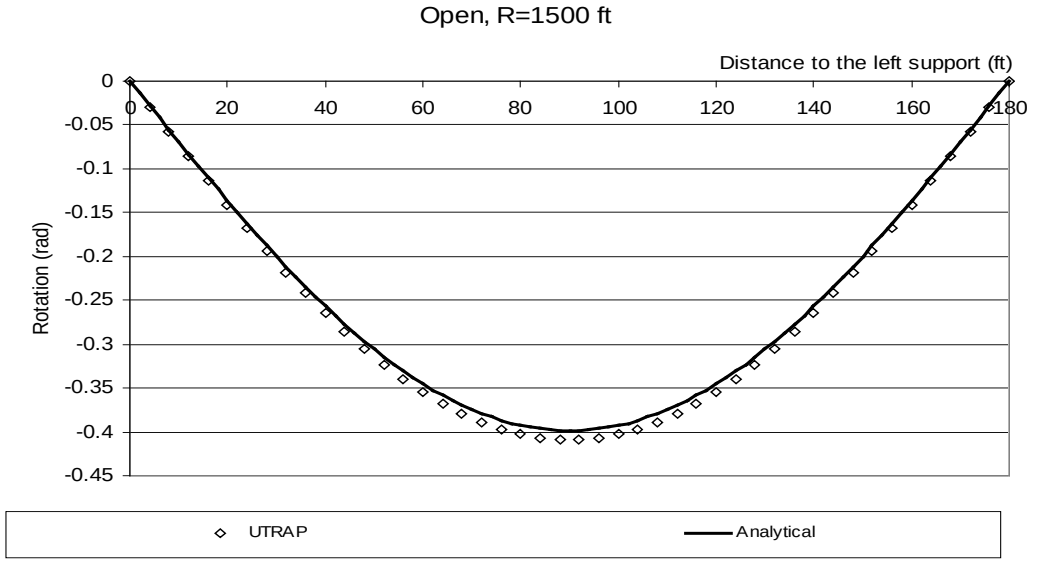

Figure 6.6 Rotations of an open-section curved girder

Figure 6.5 and Figure 6.6 show that there is a good agreement between the rotations obtained from the UTRAP solution and the analytical formula. The accuracy of the analytical formula for predicting rotation is not sensitive to the central angle or the equivalent plate thickness.

6.1.3 Parametric study

A parametric study was performed to study the effect of the equivalent plate thickness on the maximum vertical displacement and the maximum rotation. Figure 6.7 and Figure 6.8 show the maximum vertical displacement of the node located at the middle of the bottom flange and the cross-section rotation, respectively. These results were obtained from the UTRAP solution for the 180-ft Model 1 curved girder with a radius of curvature of 600 ft, under a uniformly distributed load of 1 k/ft. An X-type top lateral bracing system with a 2-ft panel, with the diagonal areas corresponding to each equivalent plate thickness shown in Table 6-1, was used in the analysis. As before, a 2-ft spacing of internal diaphragms with 4-in^2 members was used to eliminate the cross-section distortion.

For equivalent plate thicknesses greater than 0.03 inches, the maximum deflection and the maximum rotation are not very sensitive to the equivalent plate thickness. It can be concluded that with an equivalent plate thickness greater than 0.03 inches, the changes in the maximum deflection and rotation will be insignificant to the changes in the top lateral bracing member size.

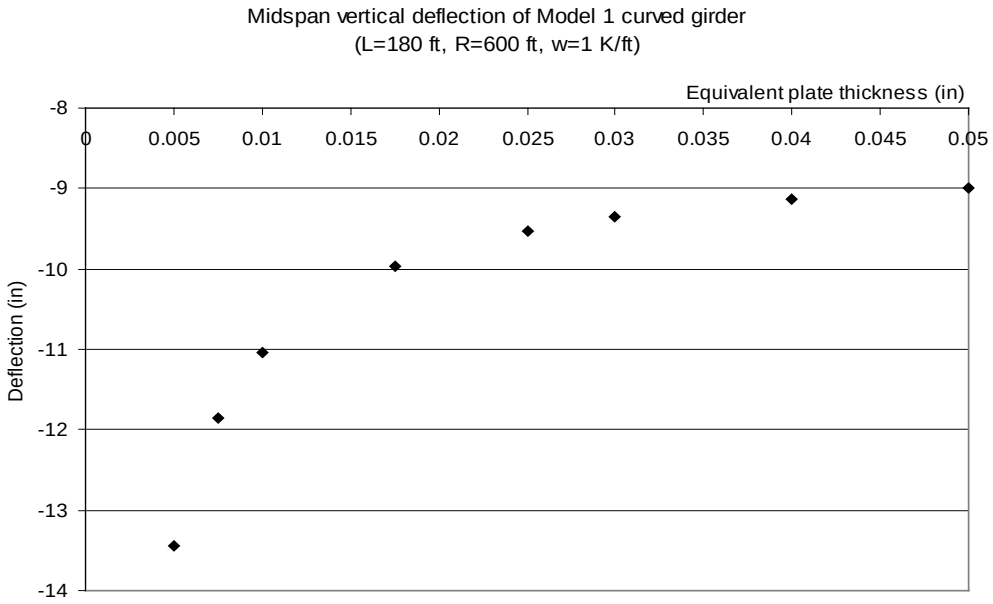

Figure 6.7 Effects of equivalent plate thickness on maximum vertical deflection

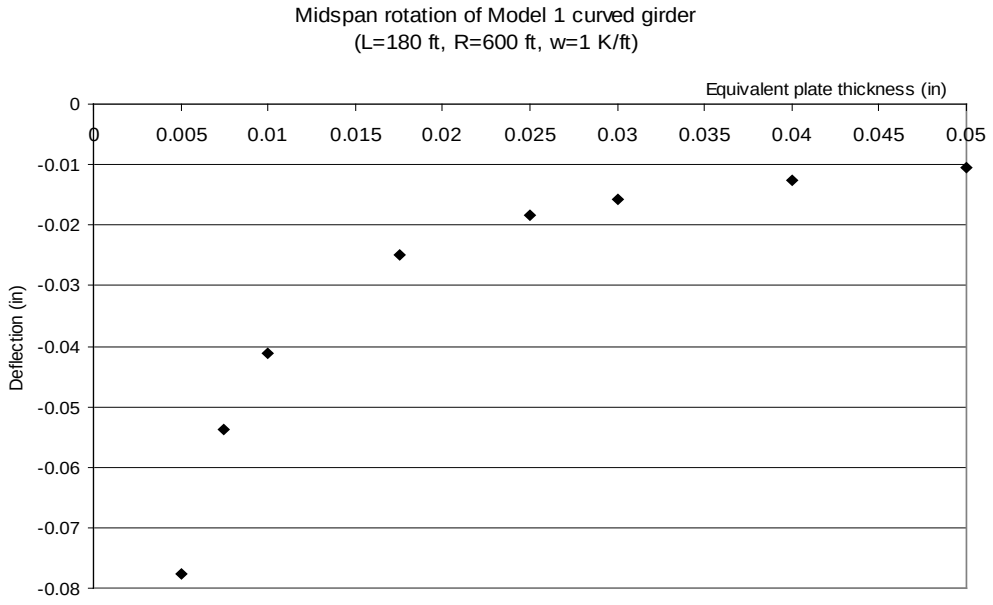

Figure 6.8 Effects of equivalent plate thickness on maximum rotation

Table 6-1 Diagonal area of the 2-ft panel the X-type system and the corresponding equivalent plate thickness

Equivalent plate thickness (inch)	Diagonal area (in^2)
0.005	0.263
0.0075	0.394
0.01	0.525
0.0175	0.919
0.025	1.31
0.03	1.58
0.04	2.10
0.05	2.63

A second parametric study evaluated the effect of the type of top lateral bracing system on vertical deflection and rotation. Figure 6.9 and Figure 6.10 show the vertical deflections and the rotations along the length of the curved girder with different top lateral bracing systems. The diagonal cross-sectional areas used in each top lateral bracing system are summarized in Table 6-2. The strut spacing and properties of the internal diaphragm were the same as those used in the earlier studies.

Table 6-2 Diagonal area for each top lateral bracing system and the corresponding equivalent plate thickness

Equivalent plate thickness	Cross-sectional area of diagonal member		
	X-type	Alternating-Diagonal	Single-Diagonal
0.01 in	0.525 in^2	1.05 in^2	1.36 in^2
0.03 in	1.58 in^2	3.16 in^2	9.97 in^2

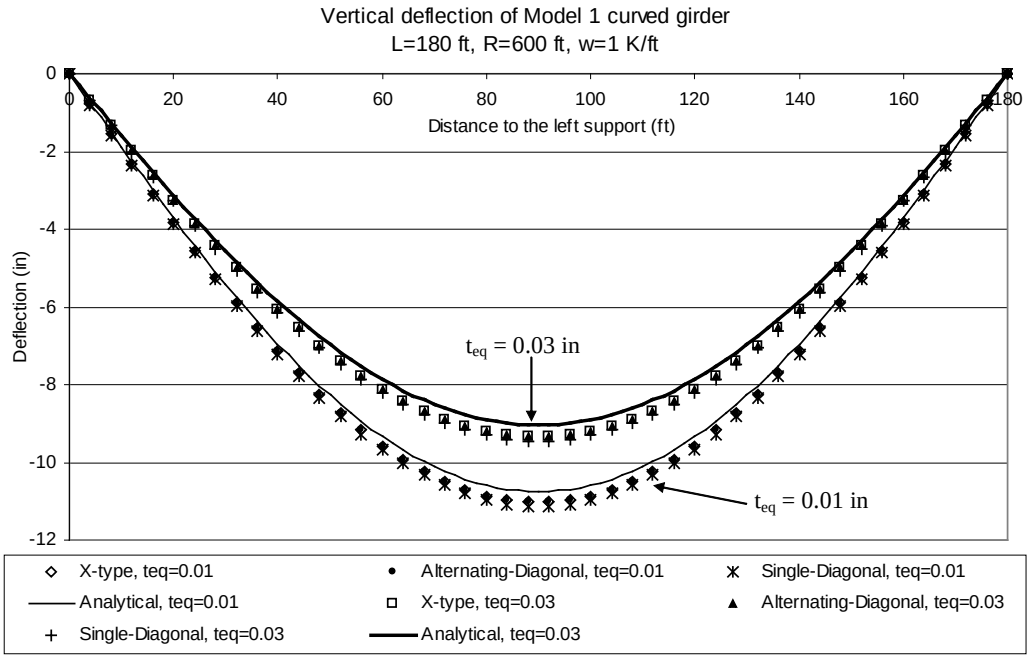

Figure 6.9 Vertical deflection with different top lateral bracing systems

Figure 6.9 shows that the vertical deflections for the three different top lateral bracing systems that have the same equivalent plate thickness are the same. This observation is true for equivalent plate thicknesses of 0.01 and 0.03 inches. The vertical deflections predicted by the analytical formula are slightly smaller than those from the UTRAP solution, since the analytical formula neglects shear deformation. It should be noted that in this case, the bending properties used in the analytical formula are calculated without considering the presence of the top lateral bracing system because the panel geometry shown in Figure 6.3 gives a low effective stiffness.

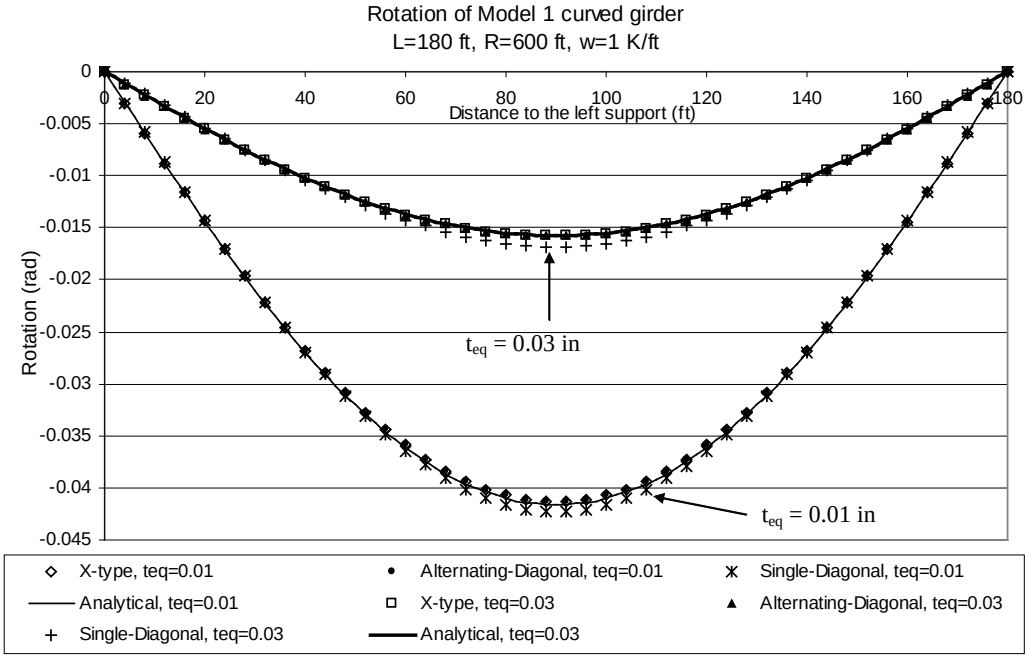

Figure 6.10 Rotation with different top lateral bracing systems

Figure 6.10 shows that the rotation is also not sensitive to the type of top lateral bracing system. However, the rotations of the Single-Diagonal system are slightly larger than those in the X-type and the Alternating-Diagonal systems. As shown in Figure 5.26, the lateral displacement of the top flanges near the midspan is several times greater than that of the X-type and the Alternating-Diagonal systems. In a curved girder, the lateral displacement of the top flanges is larger than that of a straight girder due to a second order effect as follows: Under bending, the top flanges are in compression and want to move away from the center of curvature, whereas the bottom flange is in tension, wanting to straighten up and move toward the center of curvature. As a result, the lateral movement of the top flanges is accompanied by additional rotation. As the lateral displacement

of the top flanges becomes larger, the additional rotation due to the second order effect will also be larger.

Using a longer panel length, the lateral displacements of the top flanges near the midspan of a girder with the Single-Diagonal system will be significantly larger that those with the X-type and the Alternating-Diagonal system. Consequently, due to the second order effect, the rotations near the midspan of the simply-supported curved girder with the Single-Diagonal system will also be significantly larger. Figure 6.11 shows rotations along the length of the 180-ft Model 1 curved girder. All systems have an equivalent plate thickness of 0.03 inches, but the panel length and the internal diaphragm spacing are 10 ft. The cross-sectional area of the strut is 4 in^2 and the cross-sectional areas of the diagonals in the X-type, the Alternating-Diagonal, and the Single-Diagonal systems are 1.83 in^2, 3.94 in^2, and 4.25 in^2, respectively.

Figure 6.11 shows that the rotations of Model 1 with the X-type and the Alternating-Diagonal systems are the same and they are similar to those for the 2-ft panel spacing given in Figure 6.10. However, the rotations with the Single-Diagonal system are very sensitive to the panel length. Even though the equivalent plate thicknesses are kept the same (i.e. 0.03 inches), the rotations with a 10-ft panel Single-Diagonal system are significantly larger than those with a 2-ft panel. In general, cross-section distortion due to curvature effects is not affected by the type of top lateral system as will be shown in section 6.3. Choosing the panel length that maintains a top lateral bracing member angle of 45 degrees will result in a maximum total rotation of a Single-Diagonal system 50 percent larger than that of the X-type or the Alternating-Diagonal system.

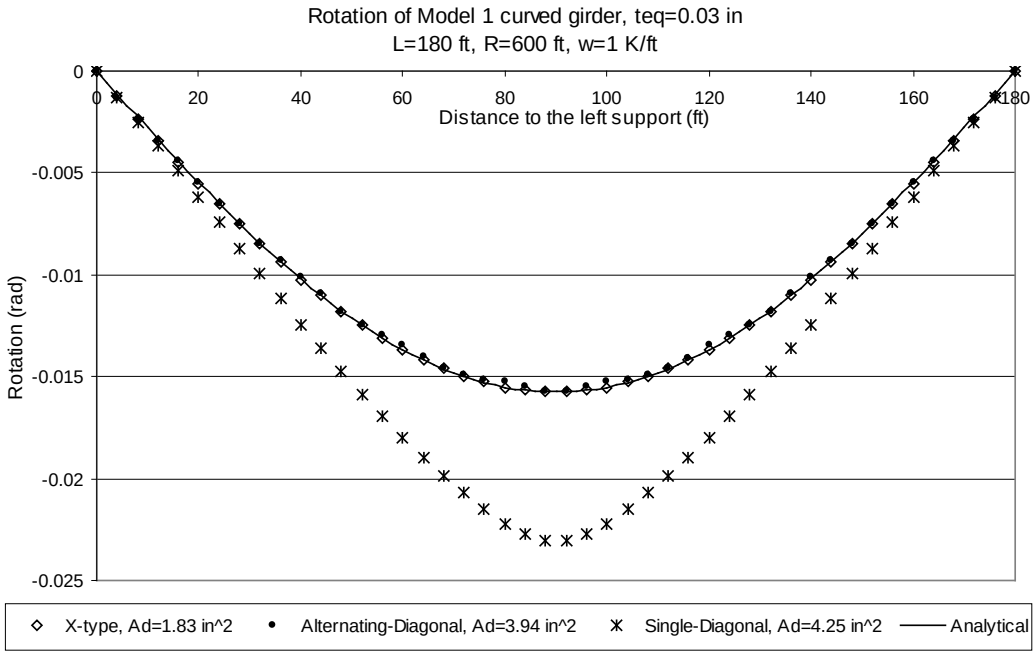

Figure 6.11 Rotation with the equivalent plate thickness of 0.03 in and using 10-ft panel

6.2 LATERAL DISPLACEMENT

Unlike in a straight girder, there can be significant lateral displacements in a curved girder. Figure 6.12 shows the lateral displacement of the top and the bottom flanges of a simply-supported Model 1 curved girder with 2-ft panels of the X-type system from UTRAP solutions. Positive and negative lateral displacements indicate displacement toward and away from the center of curvature, respectively. The lateral displacement values have been plotted on a reverse scale in order to physically correlate displacements with the plan view of a curved-girder in UTRAP.

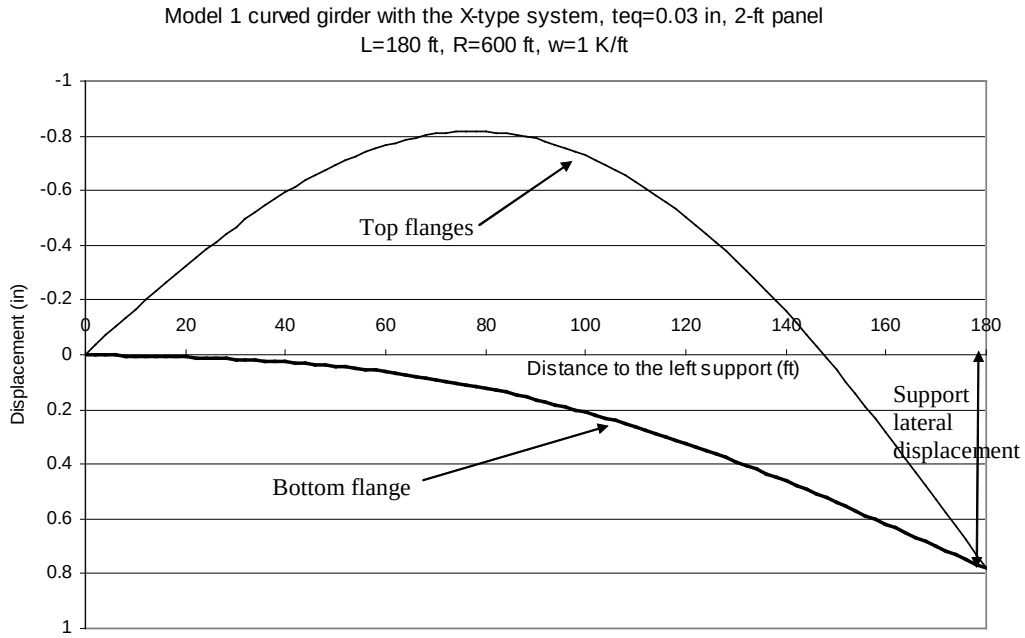

Figure 6.12 Lateral displacements of the top and the bottom flanges from UTRAP

Figure 6.12 shows that the lateral displacements of the bottom flange along the length of a curved girder are different than those of the top flanges. Since UTRAP assumes that there is a rigid diaphragm at each support that prevents cross-section distortion, the lateral displacement of all nodes at the support location must be the same. Since the lateral boundary conditions in UTRAP supports are fixed and free, Figure 6.12 shows that there is rigid body lateral movement at the right support, which is a free support. Even though the girder is a pseudo-closed section, there is some warping of cross-section. The laterally fixed support prevents warping displacements and consequently, the rigid body movement is induced. In practice, the lateral movement in a simply-supported curved girder is not permitted. Therefore, all the subsequent lateral displacement plots are

corrected for the rigid body movement so that there is no support lateral movement.

Figure 6.13 shows the corrected lateral displacements of the top and bottom flanges. Since the girder is symmetrical about midspan, the corrected lateral displacements are also symmetrical about midspan. Both of the top and bottom flanges move away from the center of curvature. This indicates that the shear center is located under the bottom flange, which agrees with the calculation shown in Chapter 4. More detailed discussions of the lateral displacement of the top flanges, the bottom flange and the support are presented in the following sections.

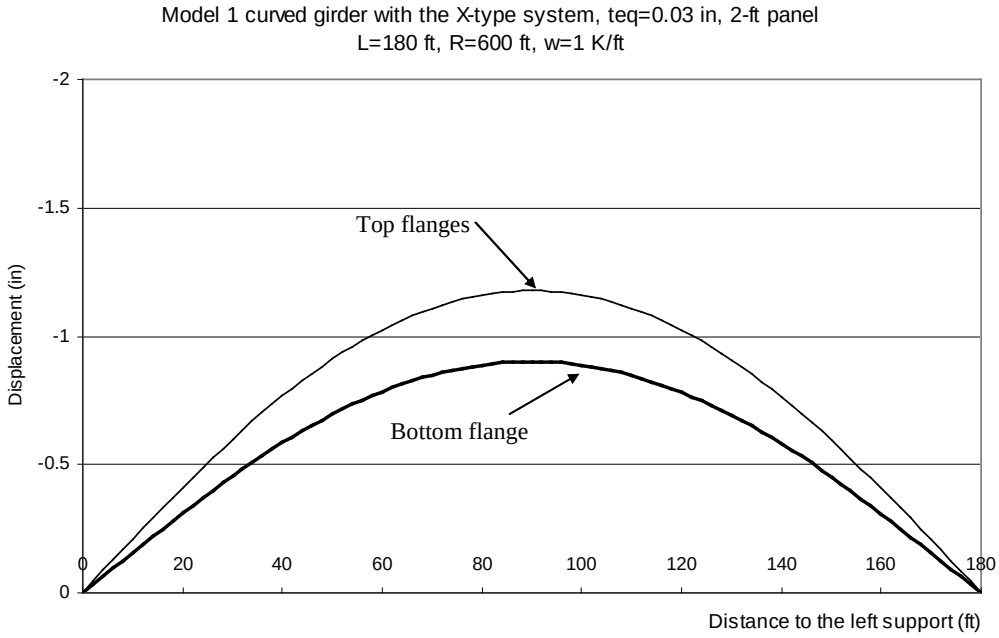

Figure 6.13 Corrected lateral displacements of the top and bottom flanges

6.2.1 Lateral displacement of the top flanges

The lateral displacements of the top flanges in a girder with the Single-Diagonal system are larger than those with the X-type and the Alternating-Diagonal systems. In addition, even for the same equivalent plate thickness, as the panel length in the Single-Diagonal system gets longer, the lateral displacements become larger. Figure 6.14 shows the corrected lateral displacements of the top flanges of Model 1 with different top lateral bracing systems. A 2-ft panel length is used and the equivalent plate thicknesses for all systems are 0.03 inches.

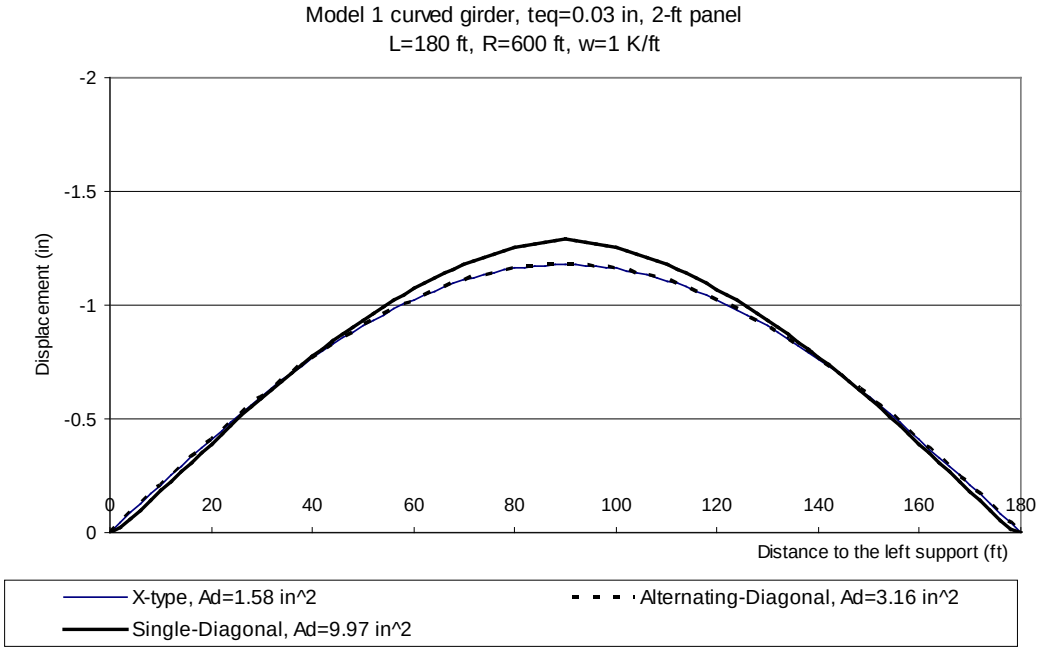

Figure 6.14 Lateral displacements of the top flanges

Figure 6.14 shows that the lateral displacements of the top flanges of Model 1 with the X-type and the Alternating-Diagonal systems are the same and those with the Single-Diagonal system are slightly larger. Figure 6.15 compares the lateral

displacements of Model 1 with the 2-ft panel and the 10-ft panel of the Single-Diagonal system. Both of them have the same equivalent plate thickness of 0.03 inches.

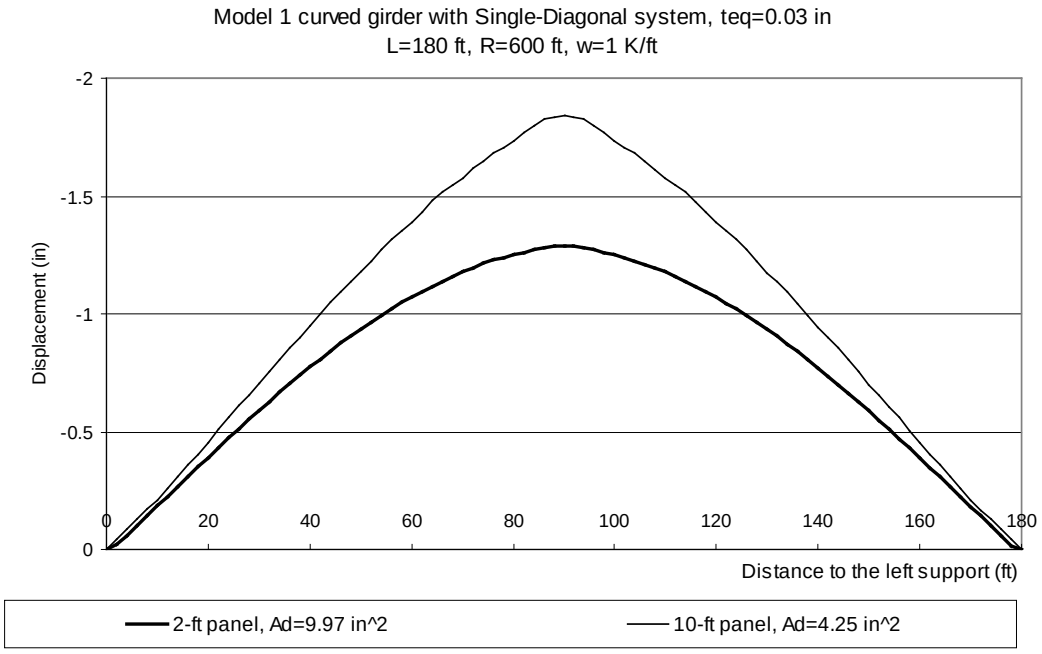

Figure 6.15 Lateral displacements with the 2-ft panel and the 10-ft panel of the Single-Diagonal system

Figure 6.15 shows that the lateral displacements with the 10-ft panel Single-Diagonal system are larger than those with the 2-ft panel. These additional lateral displacements cause the rotations with the 10-ft panel to be larger than those with the 2-ft panel. Therefore, if one wants to use a Single-Diagonal system instead of an X-type or an Alternating-Diagonal system, he must be careful in determining the panel length in addition to selecting the member sizes to produce the same equivalent plate thickness. As the panel length of the Single-Diagonal system increases, the lateral displacements and rotations become significantly larger than

those in a girder with the X-type or the Alternating-Diagonal system, even though the equivalent plate thicknesses are the same. In order to limit the additional lateral displacements and rotations of the Single-Diagonal system to 50 percent of those of the X-type and Alternating-Diagonal systems, the maximum recommended panel length is equal to the top width of the girder.

6.2.2 Lateral displacements of the bottom flange

In order to study the sensitivity of the top lateral bracing systems on the lateral displacements of the bottom flange, Figure 6.16 shows the corrected lateral displacement of the bottom flange of Model 1 with different top lateral bracing systems. A 2-ft panel top lateral bracing system is used, while the equivalent plate thickness for all systems used in this analysis is reduced to 0.01 inches.

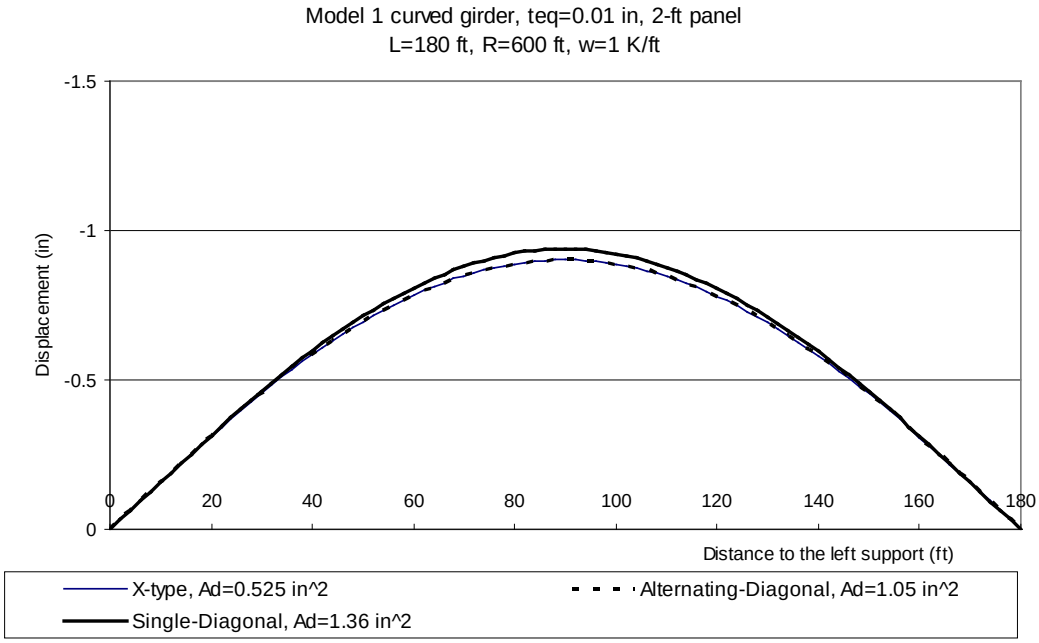

Figure 6.16 Lateral displacements of the bottom flange

Figure 6.16 shows that the lateral displacements of the bottom flange are not sensitive to the type of the top lateral bracing system. No matter what type of top lateral bracing system is used, as long as the equivalent plate thicknesses are the same, the lateral displacements of the bottom flange are the same. Comparing the lateral displacement of the bottom flange for Model 1 with equivalent plate thicknesses of 0.01 inches and 0.03 inches (Figure 6.16 and Figure 6.12), it can be observed that those for Model 1 with an equivalent plate thickness of 0.01 inches are larger. The maximum lateral displacement of the bottom flange in a simply supported curved girder occurs at the support.

6.2.3 Lateral displacement of the support

Simply-supported curved girder rests on one pin and one roller support. In UTRAP, the pin support prevents both lateral and longitudinal displacements, whereas the roller support allows both lateral and longitudinal displacement. Depending on the equivalent plate thickness, the uncorrected UTRAP solutions for support lateral displacement can be significant. The UTRAP solution for the support lateral displacement of the open-section Model 1 curved girder used in the previous analysis (i.e. L=180 ft, R=600 ft, w=1 k/ft) is 108 inches. Figure 6.17 shows the uncorrected UTRAP support lateral displacements of the pseudo-closed Model 1 with different equivalent plate thicknesses. In order to prevent cross-section distortion, a 2-ft internal diaphragm spacing is used. Figure 6.17 shows that the magnitude of the support lateral displacement depends on the equivalent plate thickness. For an equivalent plate thicker than 0.03 inches, the support lateral displacement is not very sensitive to the equivalent plate thickness, whereas for an equivalent plate thickness less than 0.03 inches, it becomes very

sensitive. It should be noted that all support lateral displacements are positive, which means the support tends to move laterally toward the center of curvature.

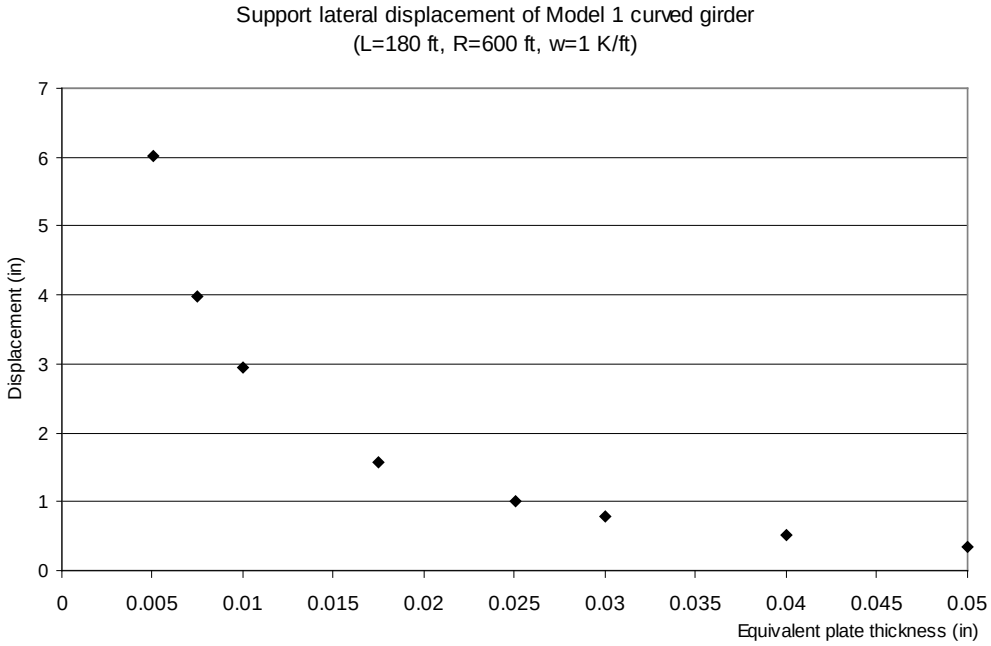

Figure 6.17 UTRAP solutions for support lateral displacements

In practice, support lateral displacement in simply-supported curved girders is not permitted. However, in a continuous curved girder, there is a support lateral displacement. As seen from UTRAP solutions, the support lateral displacement can be significant depending on the equivalent plate thickness. Figure 6.18 shows the lateral displacement at an end support of the three-spans continuous U.S 290 Bridge in Austin, Texas.

Figure 6.18 Lateral displacement of an end support of the "U.S 290-Bridge"

6.2.3.1 Analytical prediction of support lateral displacement

Since cross-section distortion is prevented, the only source of the support lateral displacement is warping deformation. As discussed in Chapter 2, warping deformation involves an out-of-plane displacement. Figure 6.19 shows a plan view of an out-of-plane warping displacement of the bottom flange with the width of b_{bf}. Warping deformation involves the rotation κ of the edge of the bottom flange. The coordinate and the out-of-plane displacement along the width of the

bottom flange are denoted as *s* and $u_{(s)}$, respectively. The maximum out-of-plane displacements occur at the edges of the bottom flange and are denoted u_{max}.

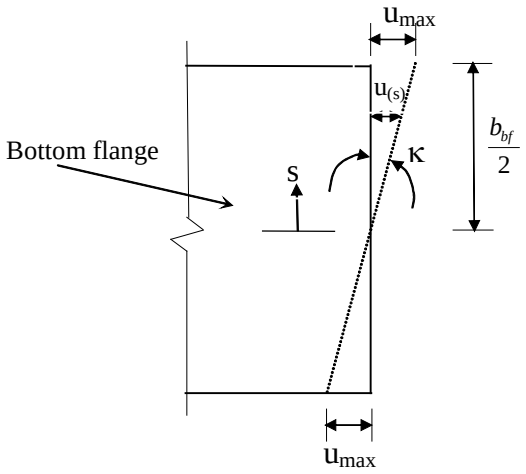

Figure 6.19 Plan view of an out-of-plane warping displacement of the bottom flange

The torsional warping function *w(s)*, discussed in Chapter 2, is linearly proportional to the warping axial displacement $u_{(s)}$. Mathematically, the relation between the warping axial displacement and the torsional warping function at the edge is

$$u_{\max} = w_{edge} \frac{d\theta}{dz} \tag{6.12}$$

where w_{edge} is the torsional warping function at the edge of the bottom flange and $\frac{d\theta}{dz}$ is the rate of change of twist along the girder length (torsional curvature).

From Figure 6.19, u_{max} can also be expressed as

$$u_{\max} = \kappa \frac{b_{bf}}{2} \tag{6.13}$$

Combining Eqs.6.12 and 6.13, the rotation of the edge of the bottom flange κ is

$$\kappa = \frac{2w_{edge}\dfrac{d\theta}{dz}}{b_{bf}} \tag{6.14}$$

Figure 6.20(a) shows a plan view of the lateral displacement of the bottom flange δ_H. For clarity, a line representing the bottom flange is shown in Figure 6.20(b). Due to the warping deformation, a chord of a curved girder rotates κ radians and the roller support laterally moves δ_H closer to the center of curvature. The final and the initial chord lengths are assumed to be the same. From the box shown in Figure 6.20(b), the support lateral displacement δ_H of a curved girder with the chord length c and the central angle Φ is

$$\delta_H = \kappa(c)\cos\left(\frac{\Phi}{2}\right) \tag{6.15}$$

Combining Eqs.6.14 and 6.15, δ_H becomes

$$\delta_H = \frac{2w_{edge}\dfrac{d\theta}{dz}}{b_{bf}}(c)\cos\left(\frac{\Phi}{2}\right) \tag{6.16}$$

It should be noted that $\dfrac{d\theta}{dz}$ shown in Eq.6.16 is the rate of change of twist at the support.

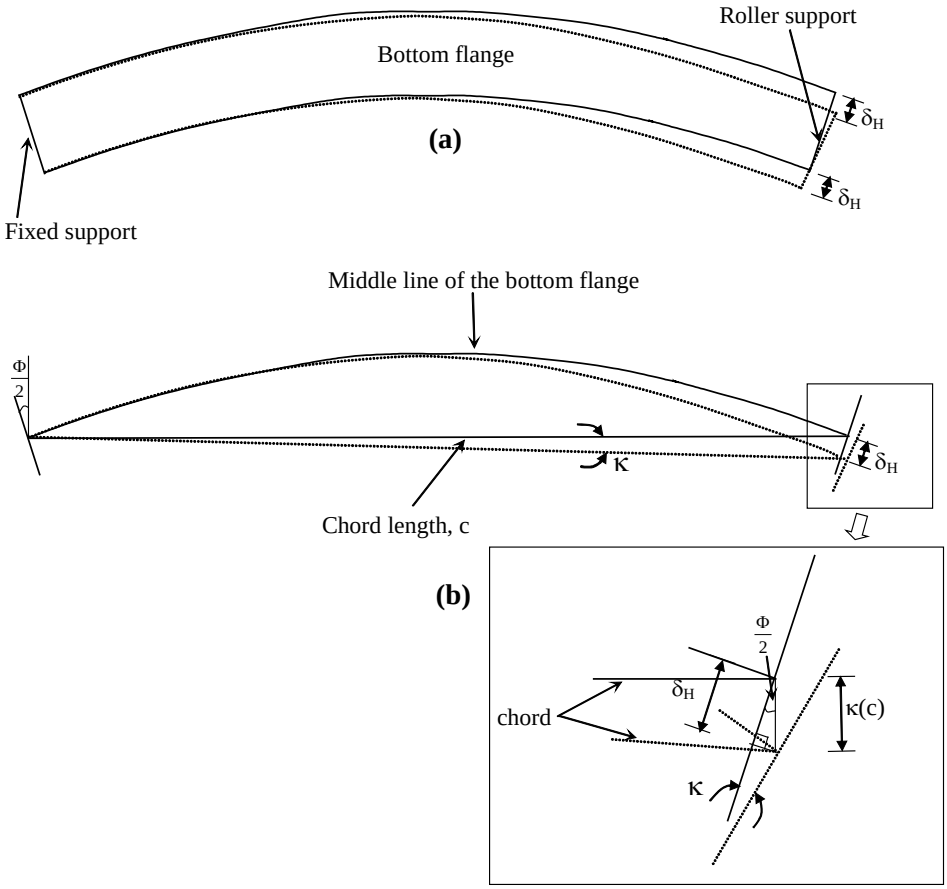

Figure 6.20 Plan view of the lateral displacement of the bottom flange

6.2.3.2 Verification

In order to verify the analytical formula for predicting a support lateral displacement, UTRAP was used to analyze a 180-ft Model 1 curved girder with a radius of curvature of 600 ft, under a uniform load of 1 k/ft. The central angle of the girder Φ is 0.3 radians and the chord length c is

$$c = 2R\sin\left(\frac{\Phi}{2}\right) = 2(600)\sin\left(\frac{0.3}{2}\right) = 179.3 \text{ ft}$$

The UTRAP solutions for the support lateral displacement of an open section and a pseudo-closed section with an equivalent plate thickness of 0.01 inches are 108 inches and 2.92 inches, respectively. Having calculated the twist at 2 ft from the support using Eq.6.11, the rate of change of twist within 2 ft of the support of the open-section and the pseudo-closed section are 0.001845 in^{-1} and 0.000062 in^{-1}, respectively.

From the cross-section properties calculations shown in Chapter 4, the torsional warping function at the edge of the bottom flange w_{edge} for the open section and the pseudo-closed section are 672.5 in^2 and 649.4 in^2, respectively. Using Eq.6.16, δ_H of the open section is:

$$\delta_H = \frac{2(672.5)(0.001845)}{50}(179.3\times 12)\cos\left(\frac{0.3}{2}\right) = 105.6 \text{ inches}$$

Similarly, support lateral displacement of the pseudo-closed section is 3.43 inches. The discrepancy between the UTRAP solution and the analytical solution for the support lateral displacement of the open section and the pseudo-closed section are 2.2 percent and 17.5 percent. Even though the percent discrepancy with the pseudo-closed section is much larger than with the open-section, the support lateral displacement of a pseudo-closed section is significantly smaller. It can be concluded that the lateral support displacement given by UTRAP is caused by warping displacement.

6.3 CROSS-SECTION DISTORTION

The previous sections discussed the behavior of a curved girder with the assumption of a non-deformable cross section. In order to prevent cross-section distortion, closely-spaced internal diaphragms must be used along the length.

This section discusses the distortion of the cross section due to curvature and the effect of the internal diaphragms on cross-section distortion. Section 6.3.1 discusses some existing recommendations for the internal diaphragm spacing. Sections 6.3.2 through 6.3.4 presents the effect of different parameters on distortional deformation in simply supported girders. Section 6.3.5 briefly discusses the distortional deformation in a continuous girder.

In order to aid the physical understanding of cross-section deformation, Figure 6.21 shows the deformed position at the midspan of a Model 1 girder with both a 2-ft internal diaphragm spacing and without any internal diaphragms. The girder used in this example is a 180-ft simply-supported girder with a 2-ft panel of the X-type system under a uniformly distributed load of 1 k/ft. The radius of curvature is 600 ft and the equivalent plate thickness is 0.01 inches.

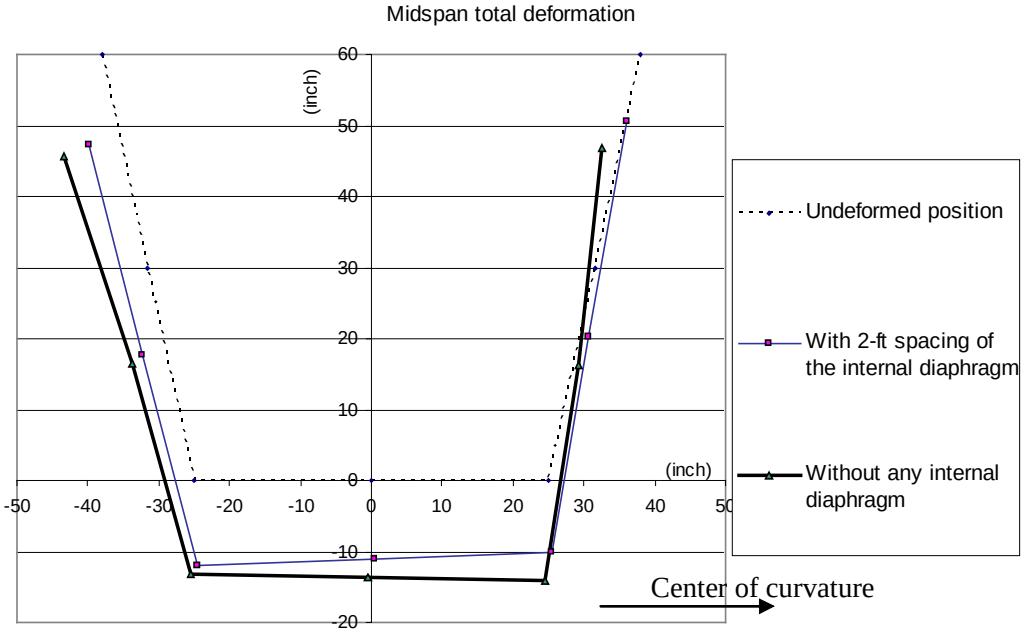

Figure 6.21 Total deformation at the midspan

Figure 6.21 shows that the total deformations of the girder using a closely-spaced internal diaphragm and without any internal diaphragms are significantly different. With a closely-spaced internal diaphragm, the girder only experiences rigid body rotation, whereas without any internal diaphragms, it experiences cross-section distortion in addition to rigid body rotation. The deformation due to distortion, shown in Figure 6.22, can be found by subtracting the deformation of the girder with closely-spaced internal diaphragms (rigid body rotation) from that without any internal diaphragms.

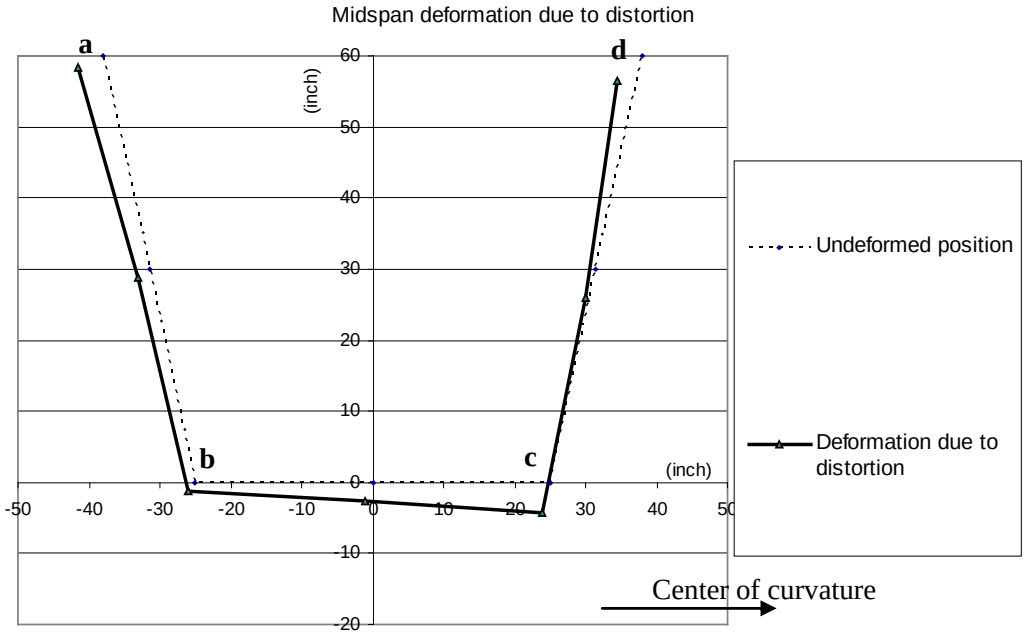

Figure 6.22 Deformation at midspan due to distortion

Figure 6.21 and Figure 6.22 show that cross-section distortion involves bottom flange rotation opposite to the rigid body rotation, a change in the diagonal lengths *a*-*c* and *b*-*d*, and web distortion.

6.3.1 Existing recommendations for internal diaphragm spacing and area

Internal diaphragms are effective in preventing cross-section distortion. Heins (1978) recommended that in order to limit the distortional normal stress to 10 percent of the bending normal stress, the required internal diaphragm spacing *s* should satisfy the following requirement:

$$s \le L\sqrt{\left(\frac{R}{200L-7500}\right)} \le 25 \text{ ft} \tag{6.17}$$

where *L* and *R* are the span length and the radius of curvature, respectively, in feet. Eq.6.17 is based on limiting the distortional normal stresses in the bottom flange so it was developed for application to the completed bridge. The recommended internal diaphragm spacing shown in Eq.6.17 assumes that all cross frames and diaphragms are rigid. In order to satisfy this assumption, Heins suggested that the required minimum area of X-type cross-frames A_b should be

$$A_{b,\min} = 75\frac{sb}{d^2}\frac{t_w^{\,3}}{(b+d)} \tag{6.18}$$

where *d*, *b*, and t_w are the girder depth, width, and web thickness, respectively.

Green (1978) indicated that a distortional brace spacing of one-quarter of the span length was appropriate for the majority of spans with length greater than 30 m (98.4 ft).

Nakai and Yoo (1988) presented guidelines that limit the distortional normal stress to less than 5 percent of the bending normal stress. The required internal diaphragm spacing *s* in meters for a straight girder should be:

$$s < 6 \text{ m} \qquad \text{for } L < 60 \text{ m} \tag{6.19}$$

$$s \le 0.14L - 2.4 \qquad \text{for } 60 \text{ m} \le L \le 160 \text{ m} \tag{6.20}$$

$$s = 20 \text{ m} \qquad \text{for } L > 160 \text{ m} \tag{6.21}$$

For a curved girder, the required internal diaphragm spacing must be decreased by the reduction factors ξ as follows:

$$\xi = 1.0 \qquad \text{for } L < 60 \text{ m} \tag{6.22}$$

$$\xi = 1 - \frac{\sqrt{\frac{L}{R}}(L-60)}{100\sqrt{2}} \qquad \text{for } 60 \text{ m} \le L \le 200 \text{ m} \tag{6.23}$$

It should be noted that 1 meter is equal to 3.28 feet.

Based on experimental works performed using 46-inch scaled models, Siddiqui and Ng (1988) recommended that an internal diaphragm spacing of $L/4$ should be used in box girder bridges with rectangular or trapezoidal cross-sections. This recommendation was based on the observation that the maximum decrease in the distortional normal stress occurs when an internal diaphragm spacing of $L/4$ was used and any further decrease in spacing did not reduce the stress appreciably.

Based on parametric studies performed on rectangular box girders without lattice walls, under vertically eccentric loading, using the Beam on Elastic Foundation analogy, Yabuki and Arizumi (1989) recommended ratios of span length to internal diaphragm spacing. Table 6-3 shows the recommended ratios for limiting the vertical deflection due to distortion to less than 1/1000 of the internal diaphragm spacing and the distortional stress to less than 5 percent of the design bending stress. Their recommendations are a function of the *L/b* and *L/R* ratios.

The 2003 AASHTO Guide Specifications for Laterally Curved Steel Girder Highway Bridges states that spacing of the internal diaphragms should not exceed 30 feet. This recommendation is based on the criteria that the longitudinal distortional normal stress should be less than 10 percent of the bending stress.

Table 6-3 Required ratio of span length to internal diaphragm spacing recommended by Yabuki and Arizumi (1989)

Span length to width ratio (L/b)	Central angle (L/R) (radian)										
	0	0.1	0.2	0.3	0.4	0.5	0.6	0.7	0.8	0.9	1.0
10	5	6	6	7	8	8	9	9	10	10	10
20	5	6	7	8	9	10	11	11	12	13	13
30	5	7	8	9	11	11	12	13	14	15	15
40	5	7	9	10	12	13	14	15	15	16	17
50	5	8	10	11	13	14	15	16	17	18	19

Figure 6.23 summarizes all existing recommendations. In one case, the radius of curvature is kept constant at 600 ft and in the other case, the length is kept constant at 180 ft. Yabuki and Arizumi recommendations result in the smallest spacing. Green, Siddiqui and Ng recommendations are similar and they result in the largest spacing for the girder longer than 120 ft. Heins' recommendation is about 50 percent larger than Yabuki and Arizumi's recommendation. Figure 6.23 shows that there are significant variations among the recommendations. These variations indicate that cross-section distortion has not been well understood.

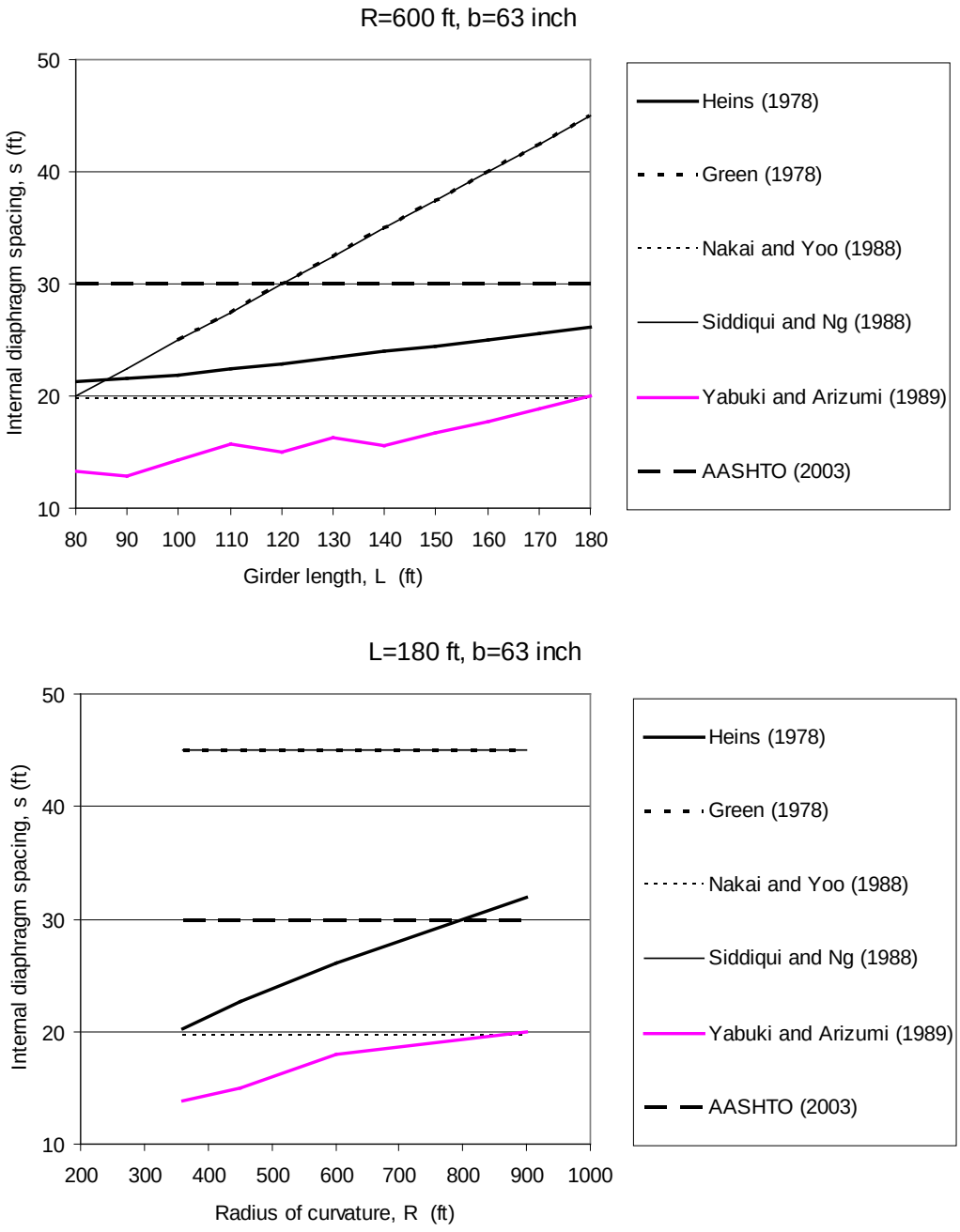

Figure 6.23 Existing recommendations for internal diaphragm spacing

6.3.2 Effect of internal diaphragms on total rotation

As seen in Figure 6.22, the cross-section distortion involves a distortional rotation opposite to the rigid body rotation. Unlike rigid body rotation, the distortional rotation of the bottom flange is not the same as that of the top flanges. Figure 6.24 shows the total rotation of the bottom and the top flanges of a 180-ft long Model 1 girder with a 30-ft internal diaphragm spacing and with no internal diaphragms.

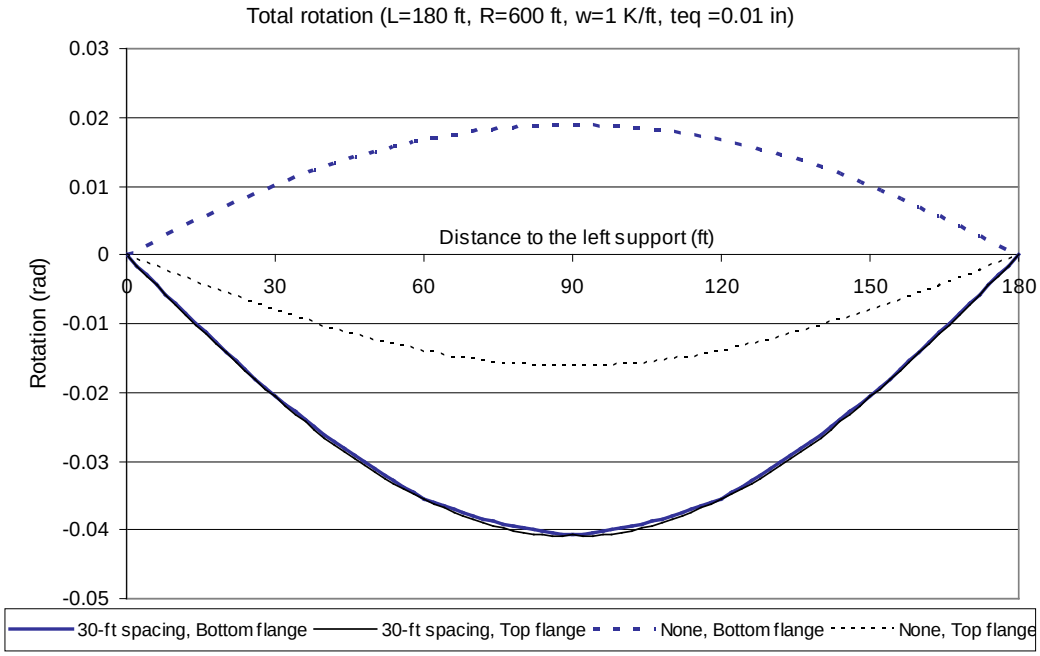

Figure 6.24 Total rotations of the bottom and the top flanges

The total rotations of the bottom flange and the top flanges with a 30-ft internal diaphragm spacing are about the same, whereas those without any internal diaphragms are tremendously different. The maximum magnitude of the total rotation without internal diaphragms is significantly smaller than that with a 30-ft internal diaphragm spacing. However, as seen in Figure 6.21, the webs of a girder

without any internal diaphragms experience significant distortion. Since the total rotations of the bottom and top flanges in a girder with a reasonable internal-diaphragm spacing are about the same, the rotation of the bottom flange will be reported.

In order to observe the effect of internal diaphragms on cross-section distortion, Figure 6.25 shows the total rotation of the bottom flange with different internal-diaphragm spacings. The top lateral bracing system was a 2-ft panel of the X-type system with an equivalent plate thickness of 0.01 inches. Negative and positive rotations indicate counter-clockwise and clockwise rotations, respectively, with the center of curvature on the right side of the girder as shown in Figure 6.21. There is no distortional rotation with a 2-ft internal-diaphragm spacing (i.e. only rigid body rotation). The 30-ft spacing and 2-ft spacing give almost the same total rotation indicating that the 30-ft spacing is sufficient to control distortion. As the internal-diaphragm spacing gets larger, the total rotation becomes less negative. From the total rotation of Model 1 with a 90-ft internal diaphragm spacing, it can be seen that the presence of just one internal diaphragm brings the total rotation closer to the rigid body rotation.

The distortional rotation can be obtained by subtracting the rigid body rotation from the total rotation. Figure 6.26 shows distortional rotations with 18-ft and 30-ft internal diaphragm spacings. Two different internal diaphragms areas A_{id}, 4 in^2 and 20 in^2, are also used. These values will be compared to Eq.6.18 later. The maximum distortional rotation with a 30-ft internal diaphragm spacing is more than double that with an 18-ft spacing. However, the distortional rotation is very small. The maximum rotation at midspan is less than 0.001 radians (0.057 degrees). The distortional rotation decreases as the internal diaphragm area increases. Even though the percentage reductions in the distortional rotation due to increased internal diaphragm area can be significant, from a total rotation

perspective, as long as a reasonable internal diaphragm spacing is used, there is little difference in total rotation due to the change in a change in diaphragm area.

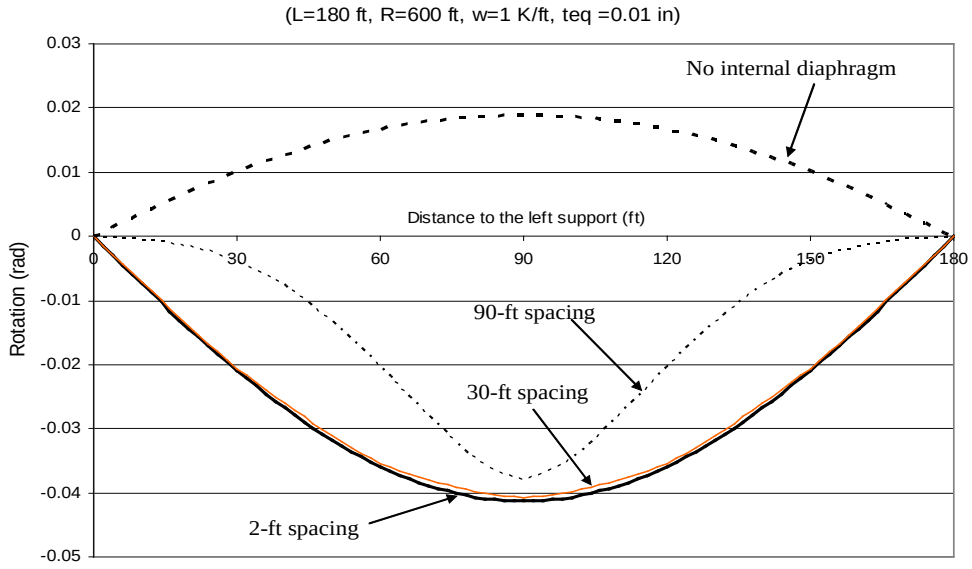

Figure 6.25 Effect of internal diaphragm spacing on total rotation

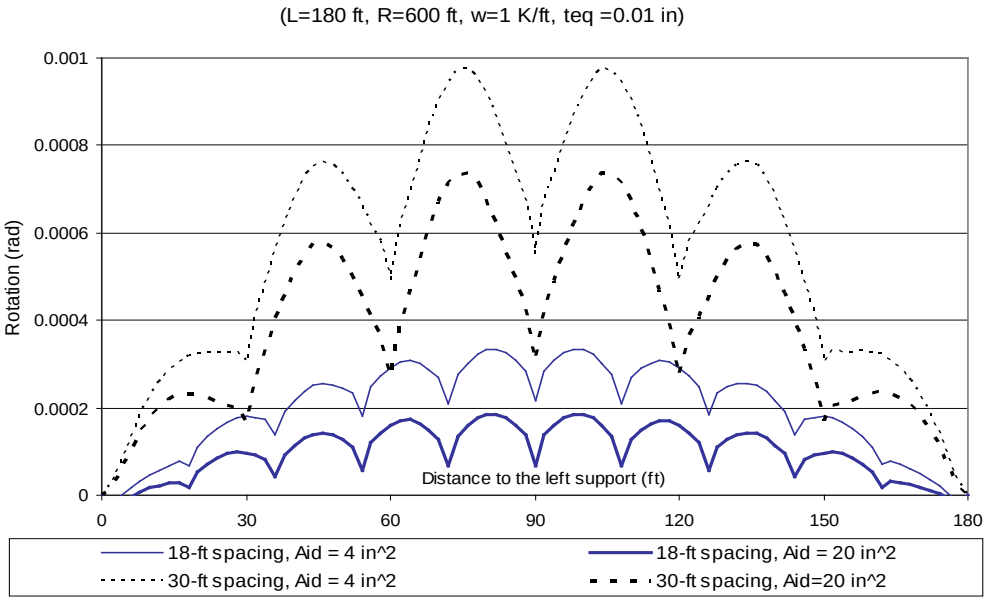

Figure 6.26 Distortional rotations

The required internal diaphragm areas based on Eq.6.18 for 18-ft and 30-ft internal diaphragm spacing are 0.26 in^2 and 0.43 in^2, respectively. The maximum forces in the internal diaphragm diagonal member with an 18-ft spacing are 12.3 k in both tension and compression. With a 30-ft spacing, the maximum forces are 20.3 k in both tension and compression. These forces were obtained from UTRAP. The forces predicted by the formulation developed by Helwig and Fan (2000) are 12.7 k and 21.1 k for the two spacing. From a strength standpoint, a WT 5x6 (1.77 in^2) is required indicating Eq.6.18 is unrealistic. It can be concluded that the required internal diaphragm area is controlled by the strength requirement. The strength requirements and the design equations for evaluating brace forces in internal diaphragms are discussed in Helwig and Fan (2000).

6.3.2.1 Parametric studies

A parametric study was conducted to determine the effect of the equivalent plate thickness on the magnitude of distortional rotation. Figure 6.27 shows the distortional stress as a function of the internal diaphragm spacing for Model 1 with an equivalent plate thicknesses of 0.01 inches and 0.03 inches. The maximum distortional rotation is insensitive to the equivalent plate thickness. However, the rigid body rotation of a girder with a larger equivalent plate thickness is smaller. The maximum rigid body rotations for the Model 1 curved girder (L=180 ft, R=600 ft, w=1 k/ft) with equivalent plate thicknesses of 0.01 inches and 0.03 inches are -0.0413 radian and -0.0158 radian, respectively.

Figure 6.28 shows that the ratio of the maximum distortional rotation to the maximum rigid body rotation is sensitive to the equivalent plate thickness. Since the direction of the distortional rotation is opposite to the rigid body

rotation, the ratio shown in Figure 6.28 is negative. Depending on the equivalent plate thickness, the distortional rotation can be larger than the rigid body rotation.

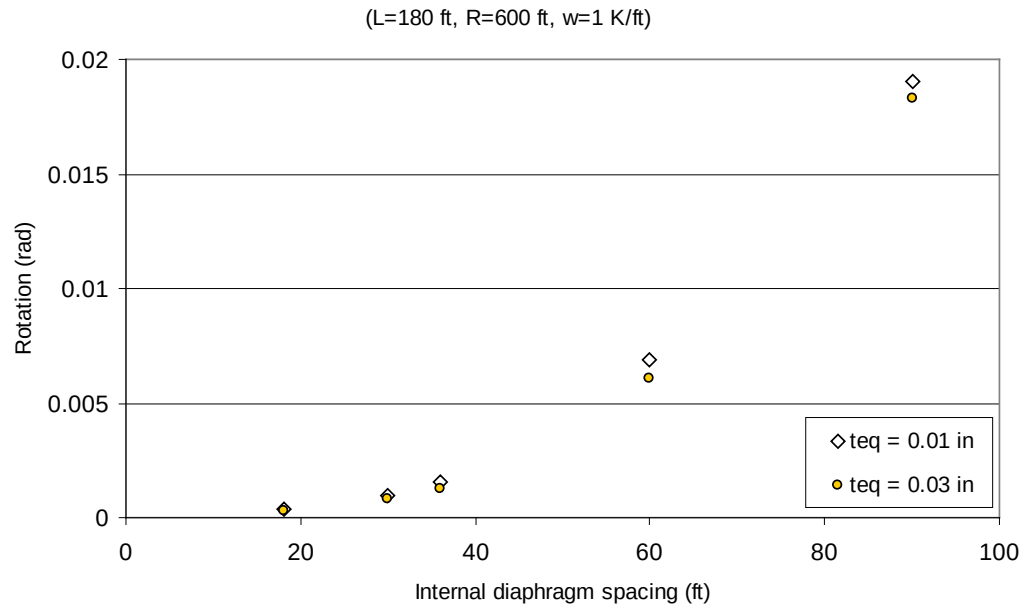

Figure 6.27 Maximum distortional rotation as a function of an internal diaphragm spacing

Another parametric study was performed to examine the effect of the internal diaphragm spacing on the ratio of the distortional to the rigid body rotations (θ_D/θ_T). In this study, both lengths and radii of curvature were varied to produce the same central angle of 0.3 radians. However, the ratio of the midspan total rotation to the span length and the midspan bending normal stress are kept about the same. Table 6-4 shows all analysis cases used in this study and shows θ_D/θ_T for Model 1 with an equivalent plate thickness of 0.03 inches. The existing recommendations for the internal diaphragm spacing are summarized in Table 6-5.

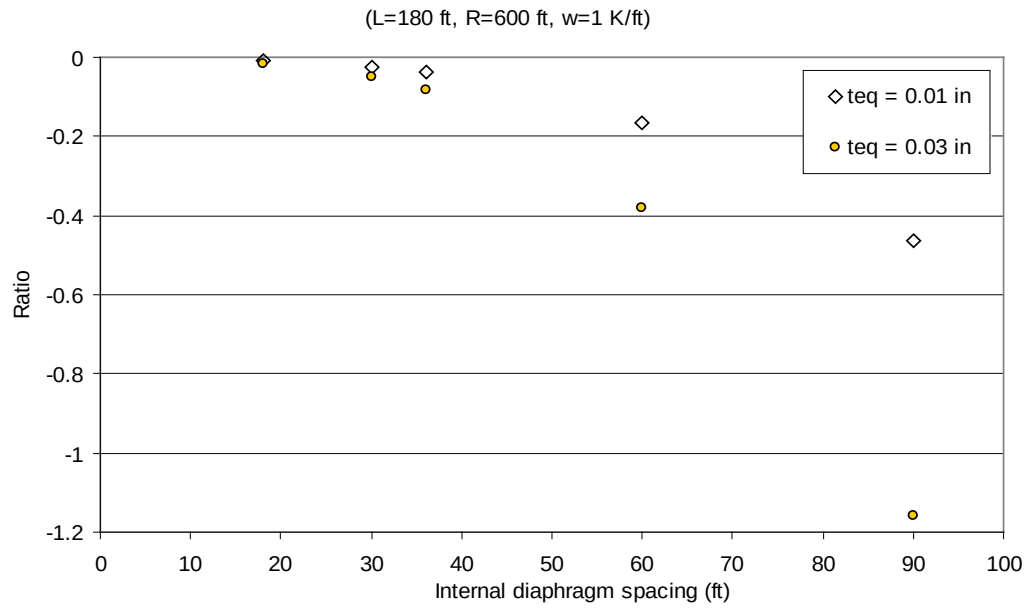

Figure 6.28 Ratio of the maximum distortional rotation to the maximum rigid body rotation

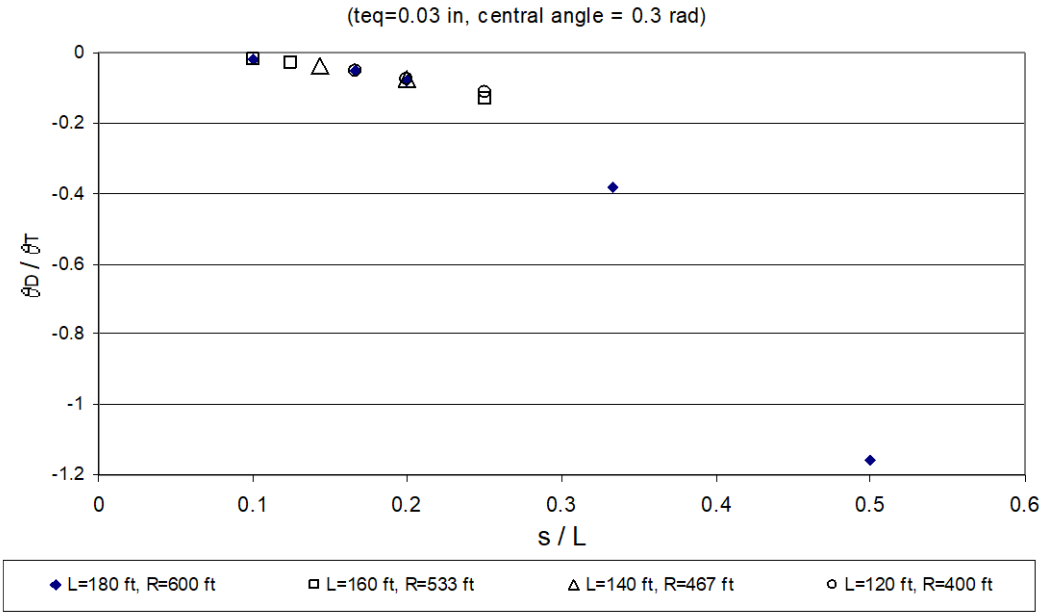

Figure 6.29 Effect of s/L on distortional rotation

Table 6-4 Analysis cases to study internal diaphragm spacing

Length, L (ft)	Radius of curvature (ft)	Load (k/ft)	Midspan rotation, θ_T (rad)*	Midspan Deflection, Δ_m (in)*	Midspan bending normal stress, σ (Ksi)*	Ratio of θ_T / L (ft^{-1})	Ratio of Δ_m / L	Internal diaphragm spacing, s (ft)	Ratio of s / L
180	600	1	0.0158	9.36	19.5	8.78 E-5	4.33 E-3	18	1/10
								30	1/6
								36	1/5
								60	1/3
								90	1/2
160	533	1.27	0.0140	7.41	19.8	8.75 E-5	3.86E-3	16	1/10
								20	1/8
								40	1/4
140	467	1.65	0.0123	5.70	19.6	8.78 E-5	3.39 E-3	20	1/7
								28	1/5
120	400	2.25	0.0105	4.22	19.6	8.77 E-5	2.93 E-3	20	1/6
								24	1/5
								30	1/4

Note:
***** Value for a girder with 2-ft internal diaphragm spacing (i.e. no distortion)

Table 6-5 Existing recommendations for the maximum internal diaphragm spacing

Length, L (ft)	Radius of Curvature, R (ft)	Recommended minimum ratio of the internal diaphragm spacing to the span length (s / L)					
		AASHTO (2003)	Yabuki & Arizumi (1989)	Nakai & Yoo (1988)	Siddiqui & Ng (1988)	Heins (1978)	Green (1978)
180	600	0.17	0.10	0.11	0.25	0.14	0.25
160	533	0.19	0.11	0.12	0.25	0.15	0.25
140	467	0.21	0.11	0.14	0.25	0.15	0.25
120	400	0.25	0.11	0.16	0.25	0.16	0.25

Figure 6.29 shows that as long as the ratio of θ_T/L and the midspan bending normal stress are kept about the same, the ratio of θ_D/θ_T for girders with similar central angles and s/L are about the same. If distortional rotation is equal to the rigid body rotation, the total rotation of the bottom flange is zero. In order to avoid a total rotation in the opposite direction to the rigid body rotation, at least one internal diaphragm must be used.

To examine the sensitivity of the ratio of θ_D/θ_T for different central angles, a third parametric study was performed. In this study, a 180-ft Model 1 girder with an equivalent plate thickness of 0.06 inches is used. In order to produce different central angles, three different radii of curvature were utilized. Figure 6.30 shows the ratio of θ_D/θ_T with central angles of 0.2, 0.3, and 0.4 radians. As the central angle increases (i.e. R decreases for L=constant), the ratio of θ_D/θ_T also increases. The explanation for this is that the lateral load component on a girder due to curvature ($M/(hR)$) that causes the distortion becomes larger as the central angle increases. The change in the ratio of θ_D/θ_T is not linearly proportional to the change of the lateral load component due to curvature. Using an internal diaphragm spacing requirement for a larger central angle is conservative.

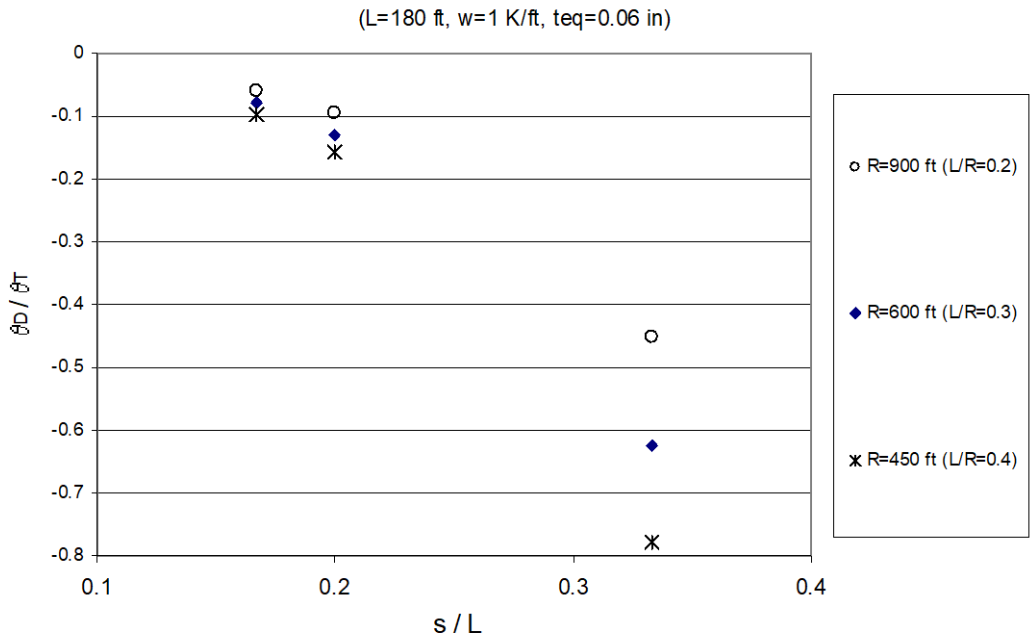

Figure 6.30 Effect of central angle on the ratio of the distortional rotation to the rigid body rotation

6.3.3 Effect of internal diaphragm on the diagonal lengths

As shown in Figure 6.22, cross-section distortion changes both diagonal lengths. Figure 6.31 shows the diagonal lengths of a trapezoidal box girder. The diagonal lengths from the left and right top flanges are called the left and the right diagonal lengths, respectively. The center of curvature is located on the right side of the girder. The undeformed diagonal length in a Model 1 girder is 87 inches.

Figure 6.32 shows the change in diagonal lengths due to distortion δ_D of a 180-ft Model 1 with one internal diaphragm at the midspan (4-in^2 member size) and without any internal diaphragms. Figure 6.32 shows that the maximum distortion always occurs midway between any two internal diaphragms. The changes in both diagonal lengths due to distortion are equal in magnitude and opposite in direction.

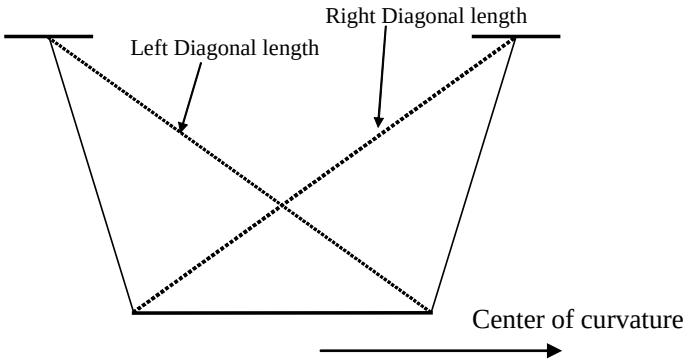

Figure 6.31 Diagonal lengths of a trapezoidal box girder

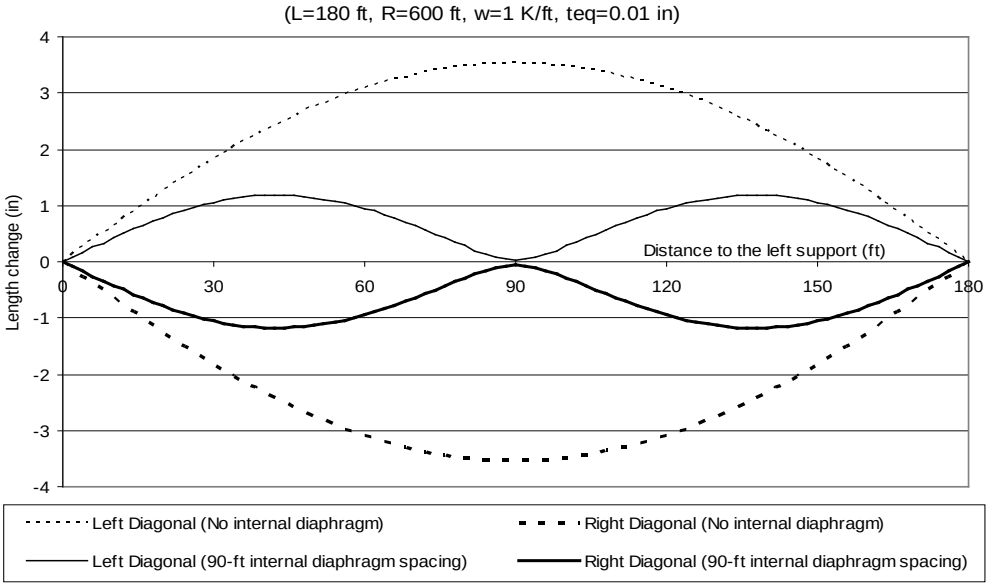

Figure 6.32 Change in diagonal lengths due to distortion

Figure 6.33 shows the effect of internal diaphragm area on δ_D. The internal diaphragm areas A_{id} used in this analysis were 1 in^2, 4 in^2, and 20 in^2 and the spacing of the internal diaphragm was 30 ft. Since δ_D of the left and right

diagonals are equal in magnitude and opposite in direction, only δ_D of the right diagonal is shown. Figure 6.33 shows that the internal diaphragm area affected δ_D. The length change decreases as the internal diaphragm area increases. However, with a reasonable internal diaphragm area (i.e. 4 in^2), increasing the internal diaphragm area will not affect δ_D appreciably.

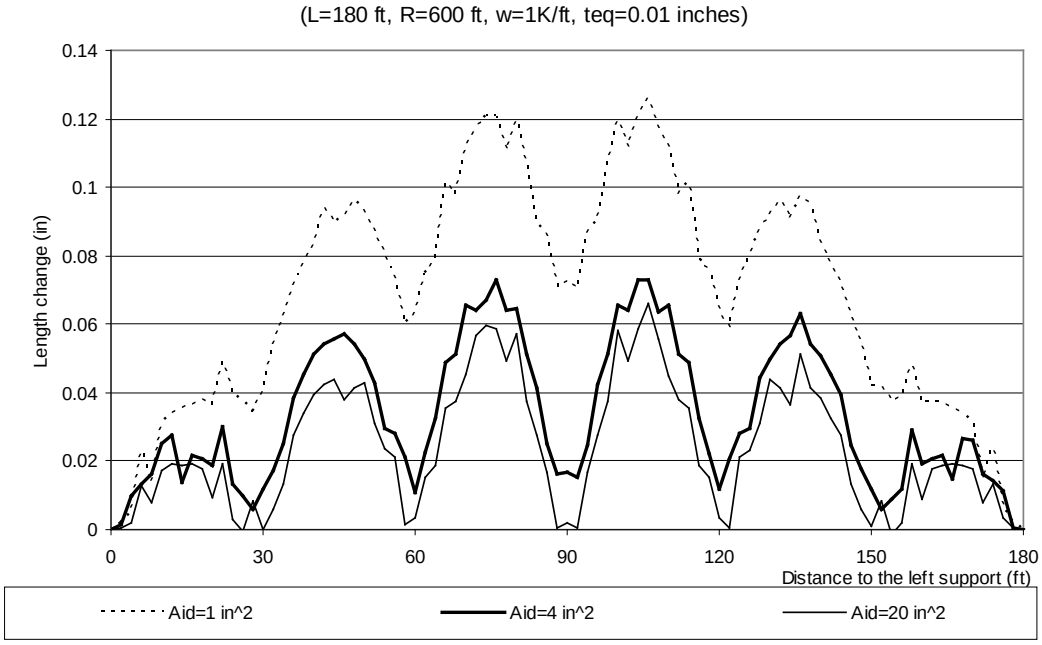

Figure 6.33 Change in right diagonal length due to distortion

6.3.3.1 Parametric studies

A parametric study examined the effect of the equivalent plate thickness on the magnitude of δ_D. Figure 6.34 shows the maximum δ_D in Model 1 with a 2-ft panel of the X-type system as a function of the internal diaphragm spacing. The internal diaphragm area used in this study is 4 in^2. It should be noted that the initial diagonal length in Model 1 is 87 inches. The maximum δ_D increases as the internal diaphragm spacing increases. For a certain internal diaphragm spacing, δ_D

decreases as the equivalent plate thickness increases, but the effect is not significant for spacing less than 50 ft.

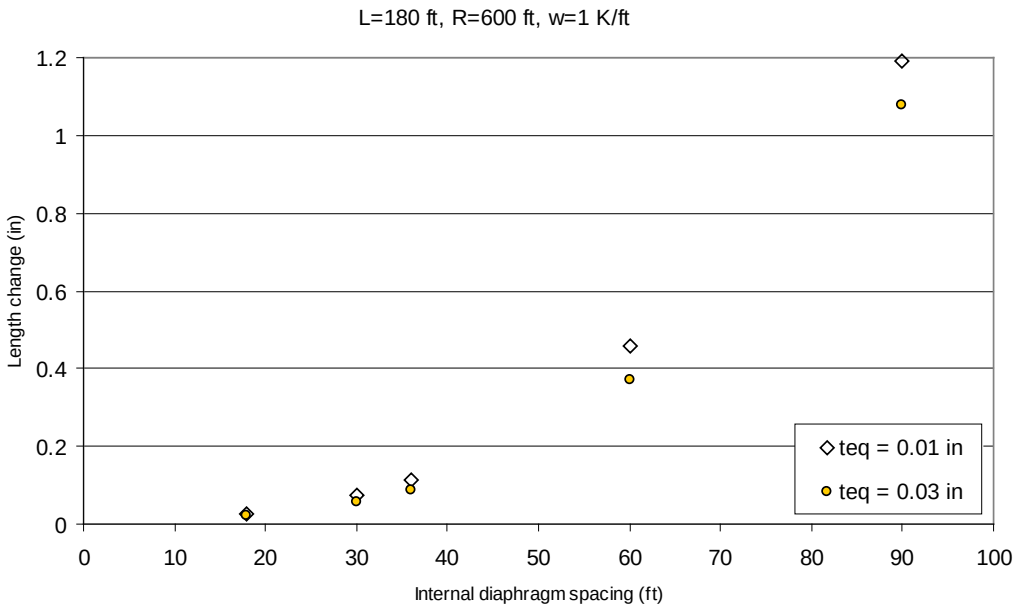

Figure 6.34 Effect of diaphragm spacing on change in diagonal length

A second parametric effort studied the effect of internal diaphragm spacing on δ_D of girders with different lengths and radii of curvature. In order to summarize all results in one graph, the change in a diagonal length is normalized by the midspan vertical deflection Δ_m. All analysis cases used in this study are shown in Table 6-4 where all the girders have the same central angle of 0.3 radians and equivalent plate thicknesses of 0.03 inches. Figure 6.35 summarizes the results of this parametric study. Figure 6.35 shows that the ratio of δ_D/Δ_m of girders with similar central angles and ratios of s/L are about the same. In order to limit the ratio of δ_D/Δ_m to less than 2 percent, the maximum recommended ratio of s/L is 1/4. The maximum proposed ratio of 1/4 is the same as the existing maximum

recommended ratio shown in Table 6-5. Since the magnitude of the maximum change in a diagonal length is not very sensitive to the equivalent plate thickness (refer to Figure 6.34), the ratio shown in Figure 6.35 will likewise not be sensitive.

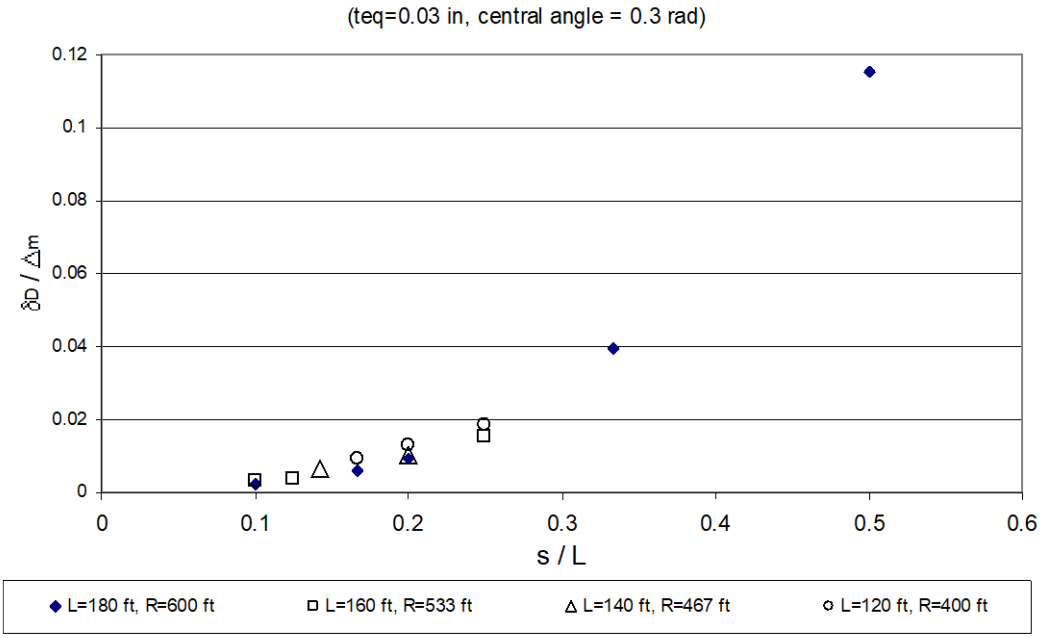

Figure 6.35 Ratio of the maximum change in diagonal length change due to distortion to the midspan vertical deflection

A third parametric study observed the effect of changing the central angle on the maximum change in diagonal length due to distortion. Figure 6.36 shows ratios of the maximum change in diagonal length due to distortion to the midspan vertical deflection for central angles of 0.2, 0.3, and 0.4 radians. In this case, the girder length and the equivalent plate thickness are kept constant. As the central angle increases, the ratio of δ_D/Δ_m also increases. Using an internal diaphragm spacing requirement for a larger central angle will therefore be conservative.

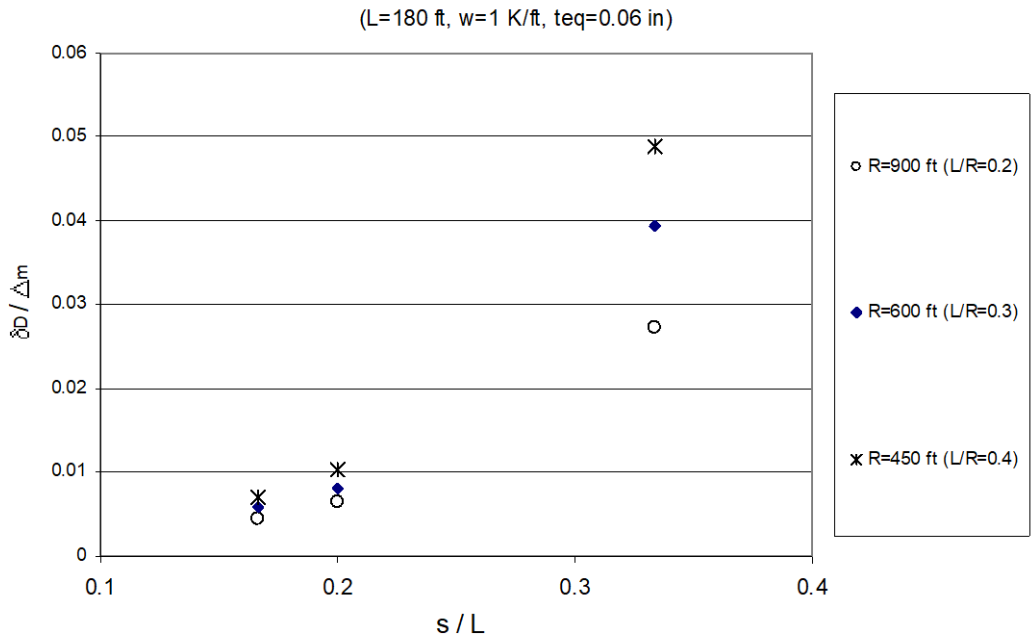

Figure 6.36 Effect of central angle on the ratio of the maximum change in a diagonal length to the midspan vertical deflection

6.3.4 Effect of changing plate thickness and cross-section dimensions

Figure 6.37 shows the effect of increasing the web thickness t_w on the maximum θ_D and the maximum δ_D of Model 1 with an equivalent plate thickness of 0.03 in. Figure 6.37 shows that generally, increasing the web thickness results in a smaller distortion. The reductions of both the maximum θ_D and δ_D because of the increase of the web thickness are more significant as the internal diaphragm spacing increases. The rationalization for this is that generally, cross-section distortion is controlled by cross-section distortion stiffness and internal diaphragm stiffness. In a girder with closely-spaced internal diaphragms, the contribution of cross-section distortional stiffness to the overall girder distortional stiffness is negligible compared to the contribution of the internal diaphragm. Therefore,

increasing the cross-section distortional stiffness does not affect the cross-section distortion in such cases. However, as the internal diaphragm spacing becomes larger, increasing the distortional stiffness will reduce cross-section distortion considerably.

The parametric study was conducted to examine the effect of changing the cross-section dimensions on the maximum θ_D and δ_D. Two different cross-sections, Model 1 and Model 3 (shown in Figure 1.5) are used. The length, radius of curvature, and equivalent plate thickness are the same in both models. In order to keep the midspan bending normal stresses the same in both models, uniform loads of 1 k/ft and 1.4 k/ft are applied to Model 1 and Model 3, respectively. Since the depths of the girders are not the same, the lateral load components due to curvature ($M/(hR)$) are different (1.36 k/ft in Model 1 and 0.908 k/ft in Model 3). Figure 6.38 shows the distortional rotation and the maximum change in diagonal length due to distortion in both models. Figure 6.38 shows that the maximum θ_D and δ_D of Model 3 are larger. As the internal diaphragm spacing gets larger, the differences in the maximum θ_D and δ_D become more significant.

Figure 6.39 shows the ratios of θ_D/θ_T and δ_D/Δ_m for both Model 1 and Model 3. Figure 6.39 shows that those ratios are practically insensitive to cross-section dimensions. Therefore, it can be concluded that an internal diaphragm spacing requirement established based on the parametric study using Model 1 can be extended to different cross-sections.

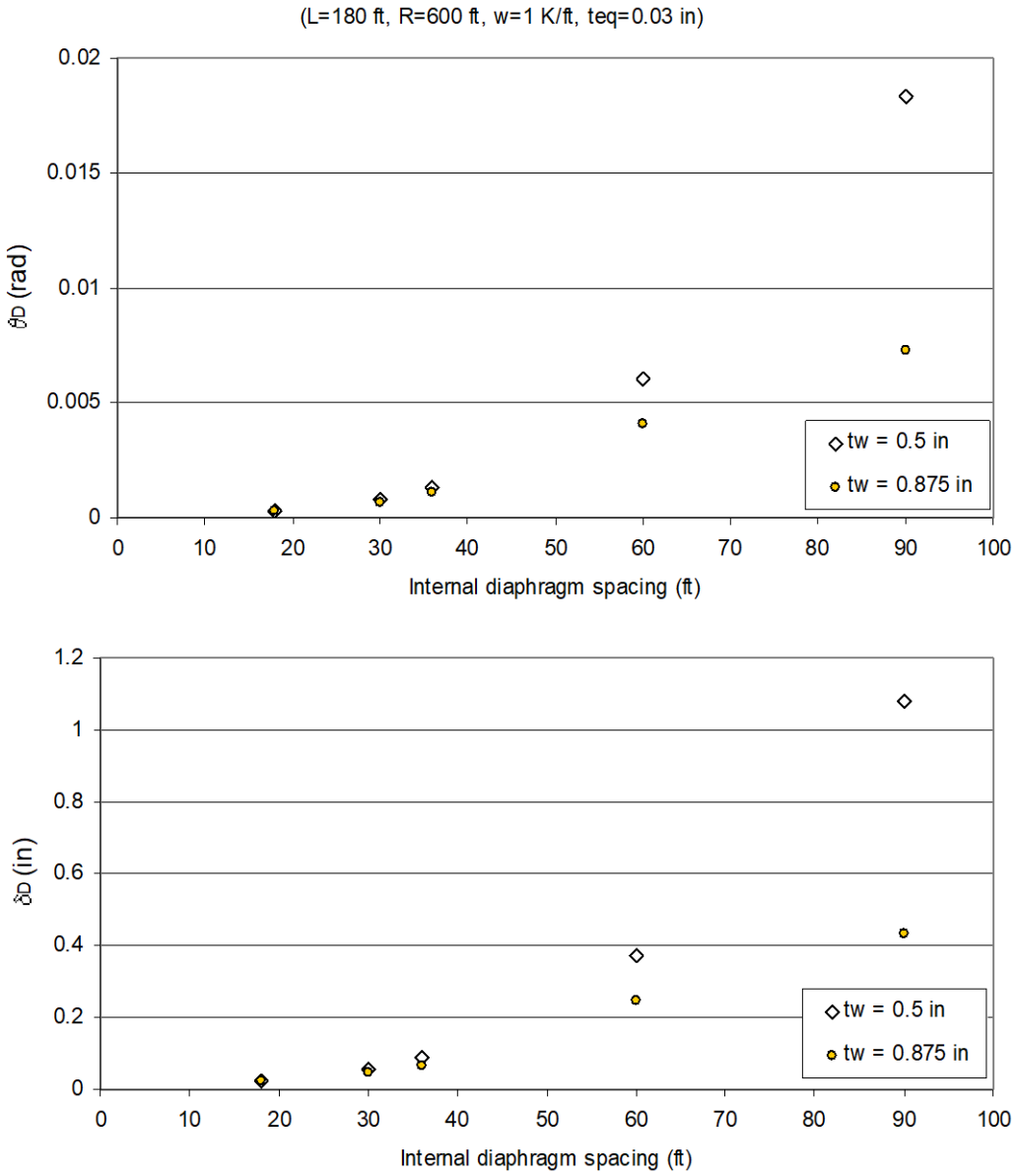

Figure 6.37 Effect of changing the web thickness on the maximum distortional rotation and the maximum change in diagonal length

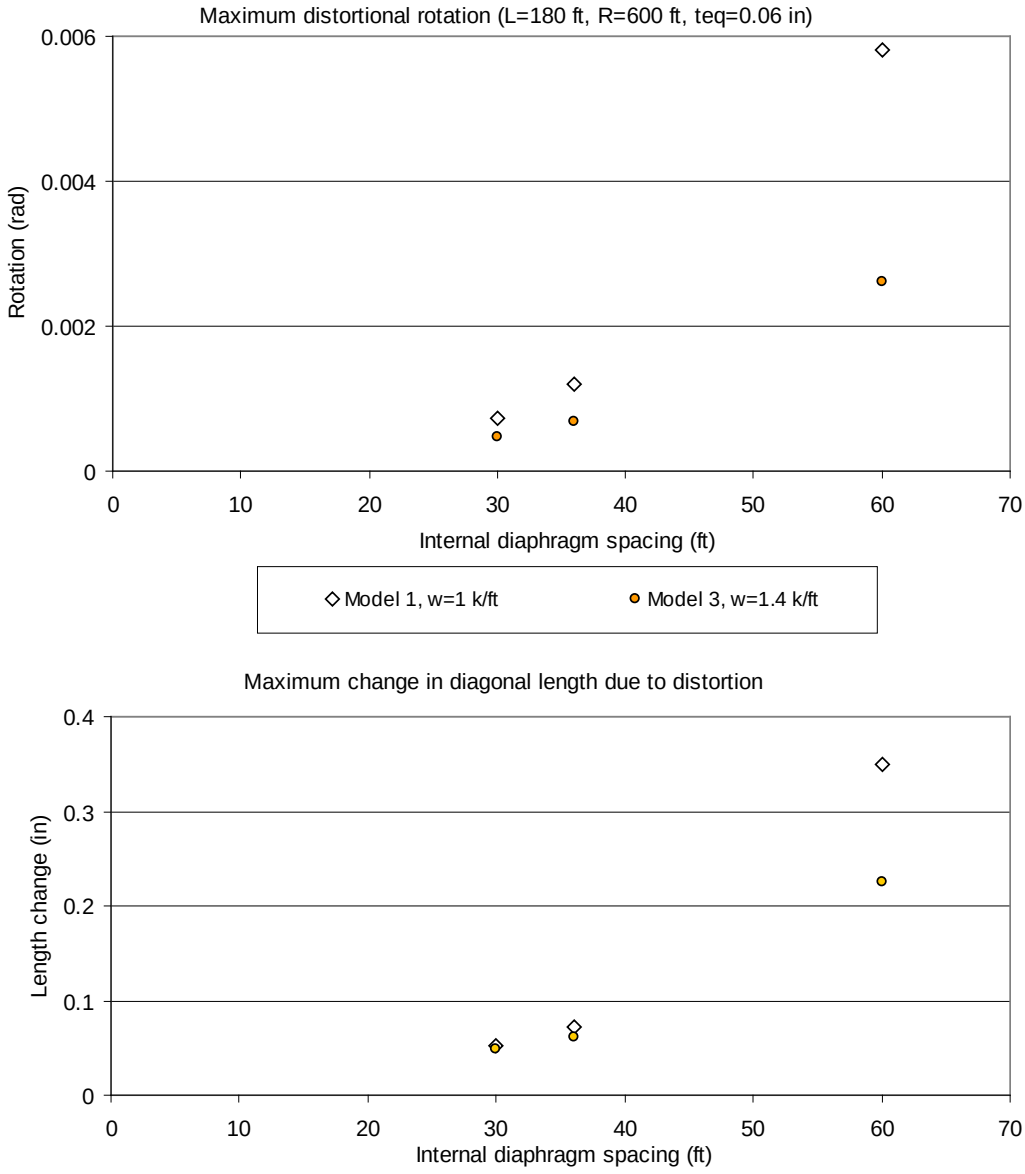

Figure 6.38 Maximum distortional rotation and maximum change in a diagonal length due to distortion for Model 1 and Model 3

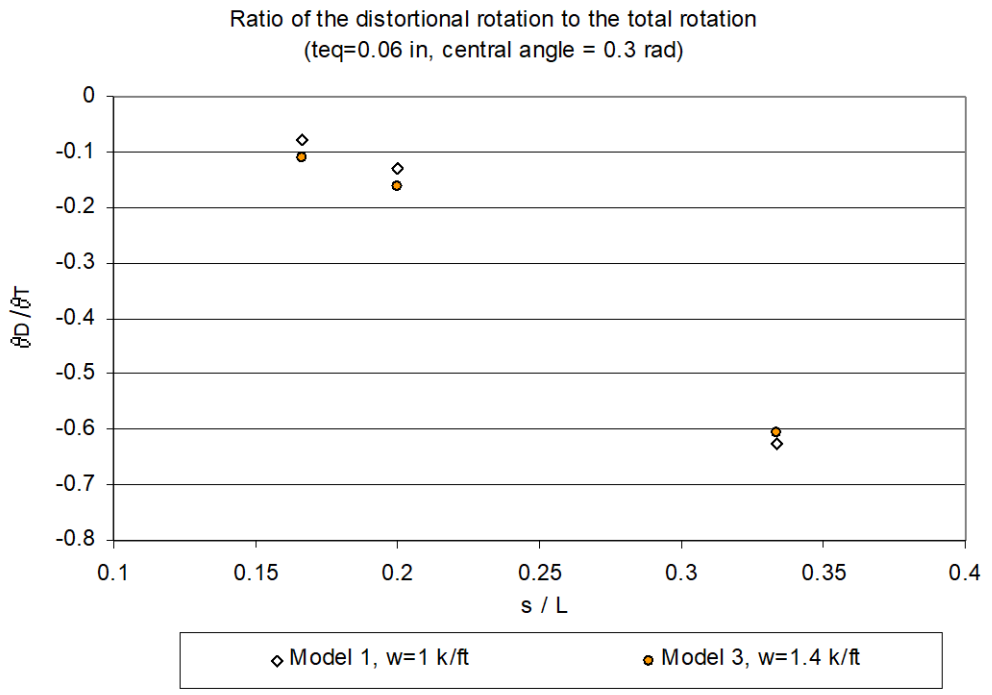

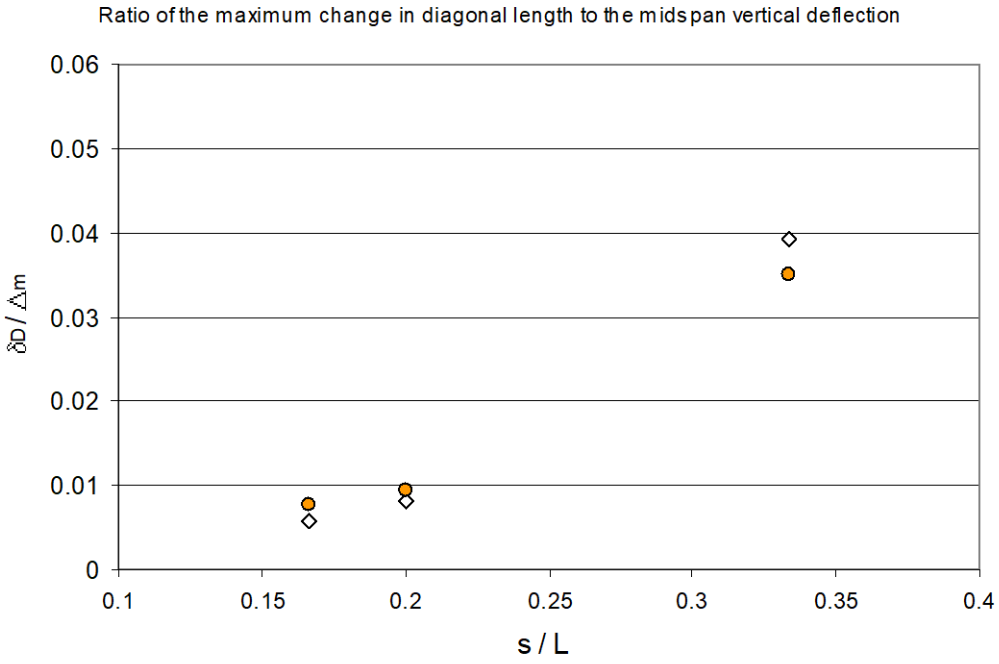

Figure 6.39 Effect of changing the cross-section dimensions

6.3.5 Cross-section distortion in a continuous girder

This section discusses distortional rotation and change in diagonal length due to distortion in a continuous girder. The purpose of this section is to study whether the results of the parametric studies conducted for a simply-supported girder can be extended to a continuous girder. The girder used in this section is a two-equal-span Model 1 girder, in which the length and the radius of curvature of each span are the same as those in the simply-supported girder.

Figure 6.40 shows both the rigid body and the distortional rotations of the bottom flange in a two-equal-span 180-ft Model 1 continuous curved girder. The central angle of each span is 0.3 radians.

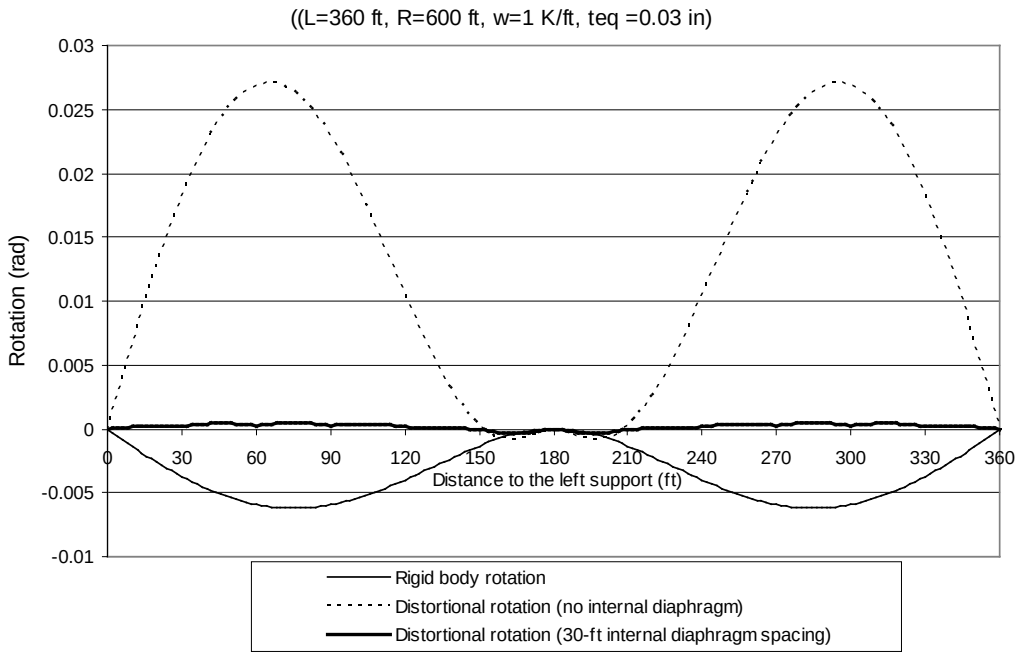

Figure 6.40 Rigid body and distortional rotation of a two-equal-span 180-ft continuous curved girder

As in a simply supported girder, the distortional rotation in a continuous girder is opposite to the rigid body rotation. The maximum rigid body rotation in a continuous girder is significantly smaller than the rotation in a simple span. Moreover, the maximum distortional rotation in a continuous girder that has the same internal diaphragm spacing is smaller. Figure 6.41 shows the ratio of θ_D/θ_T as a function of the ratio of *s/L* for both a simply-supported and a continuous girder.

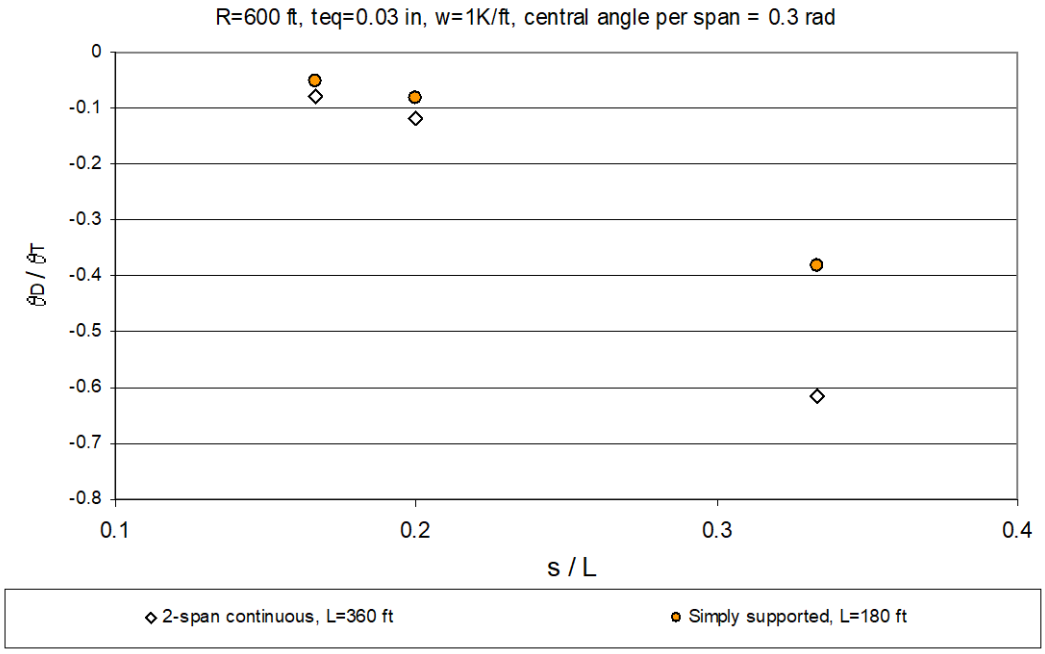

Figure 6.41 Ratio of the distortional rotation to the rigid body rotation

Since the rigid body rotation in a continuous girder is significantly smaller than that in a simply-supported girder, the ratio of the distortional rotation to the rigid body rotation in a continuous girder is larger. In order to keep the distortional rotation less than the rigid body rotation, it is recommended that the ratio of *s/L* be kept smaller than 1/3. In this particular example, using a 60-ft internal diaphragm spacing is satisfactory from a distortional rotation perspective.

The maximum change in a diagonal length δ_D in a continuous girder in which the central angle of each span is the same as that in a simply-supported girder is smaller than that in the simply supported girder. In addition, the maximum vertical deflection Δ_m in a continuous girder is also smaller. Figure 6.42 shows the ratio of δ_D/Δ_m as a function of the ratio of s/L.

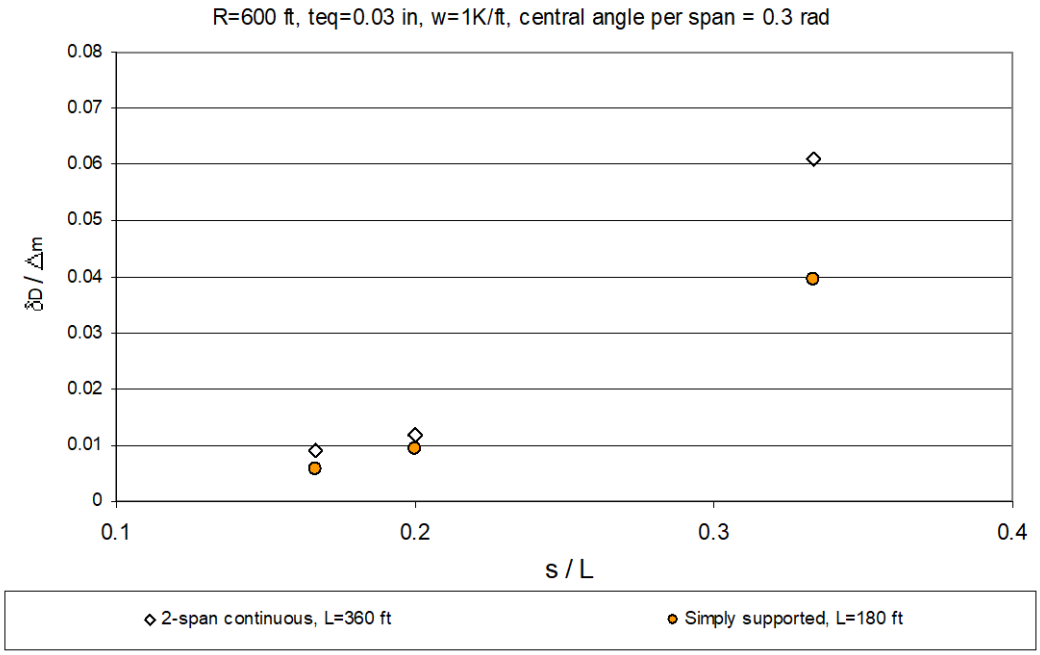

Figure 6.42 Ratio of the maximum change in a diagonal length to the maximum vertical deflection

Figure 6.42 shows that the ratio of δ_D/Δ_m in a continuous girder is larger than that in a simply-supported girder. The explanation for this is that the percent reduction in Δ_m, going from a simply-supported to a continuous girder, is larger than that in δ_D. Using a ratio of s/L of 1/5 or smaller, one can keep δ_D less than 2 percent of Δ_m. However, since Δ_m in a continuous girder is significantly smaller, the

reduction in the recommendation for the maximum *s/L* from 1/4 to 1/5 in a continuous girder is not warranted.

The maximum θ_D and δ_D in an equal-span continuous girder is smaller than those in a simply-supported girder whose length and central angle are the same as those for each span of the continuous girder. However, with a ratio of s/L smaller than 1/4, the ratios of θ_D/θ_T and δ_D/Δ_m between the two girders are about the same. Therefore, the internal diaphragm spacing requirement developed based on the studies of a simply-supported girder can be extended to a continuous girder. As the central angle of each span of the continuous girder decreases, those ratios will also decrease. For that reason, it is conservative to determine an internal diaphragm spacing requirement based on the parametric studies done with a girder with a larger central angle.

6.4 SUMMARY

This chapter presented the general behavior of a curved girder. There is good agreement between the vertical deflections and rotations obtained from the UTRAP solution and the analytical formulas. The vertical deflections and rotations of a curved girder are not very sensitive to a change in the equivalent plate thickness for thicknesses greater than 0.03 inches. The vertical deflection is not sensitive to the type of top lateral bracing system, whereas the rotation is. The rotation of a girder with the X-type and the Alternating-Diagonal systems are the same and independent of the panel length, whereas the rotation with the Single-Diagonal system is larger. In order to limit the additional maximum rotation of the Single-Diagonal system to 50 percent of those of the X-type and Alternating-

Diagonal system, the maximum recommended panel length is equal to the top width of the girder.

The lateral displacement of the top flange is sensitive to the type of top lateral bracing system, whereas that of the bottom flange is not. The magnitude of support lateral displacement obtained from UTRAP depends on the equivalent plate thickness. From a support lateral displacement perspective, the minimum recommended equivalent plate thickness is 0.03 inches.

Cross-section distortion involves the distortional rotation of the bottom flange opposite to the rigid body rotation, the change of both diagonal lengths, and web distortion. The required internal diaphragm area is controlled by strength, not stiffness. In order to keep the maximum distortional rotation less than the maximum rigid body rotation and the ratio of δ_D/Δ_m less than 2 percent, the maximum recommended ratio of s/L is 1/4.

The internal diaphragm spacing requirement developed based on the studies of a simply-supported girder can be extended to a continuous girder. It should be pointed out that the recommended internal diaphragm spacing is based on the parametric study done of a simply supported girder and a continuous girder with a central angle of each span of 0.3 radians. This recommendation is conservative for a girder with a central angle of each span less than 0.3 radians.

The recommended ratio of s/L of 1/4 is the same as the ratio proposed by Green, Siddiqui, and Ng. However, for a span longer than 120 ft, the recommended internal diaphragm spacing is larger than the maximum spacing permitted by AASHTO 2003. This chapter shows that relaxing the AASHTO maximum internal diaphragm spacing requirement and the recommended spacing from Yabuki, Arizumi, Nakai, Yoo, and Heins does not adversely affect the cross-section distortion.

CHAPTER 7
Warping Normal Stresses

An analytical method for predicting the warping normal stress in a simply supported curved girder is presented in this section. The results from the analytical method are then compared with UTRAP solutions for an open and a pseudo-closed sections. The Model 1 girder whose cross-section dimensions are shown in Figure 1.5 is used for both the open section and pseudo-closed cross-sections. For the pseudo-closed section, an X-type top lateral bracing system with an equivalent plate thickness of 0.05 inches, shown in Figure 7.1, is used. This equivalent plate thickness was also used in the sample calculations of the cross-sectional properties in Chapter 4. For convenience, the cross-sectional properties from those sample calculations are presented in this section. In order to eliminate the localized normal stress due to lateral bending of the top flange, a 2-ft panel spacing is adopted. Moreover, in order to minimize any distortional warping normal stresses, internal diaphragms are closely spaced at 2 ft intervals.

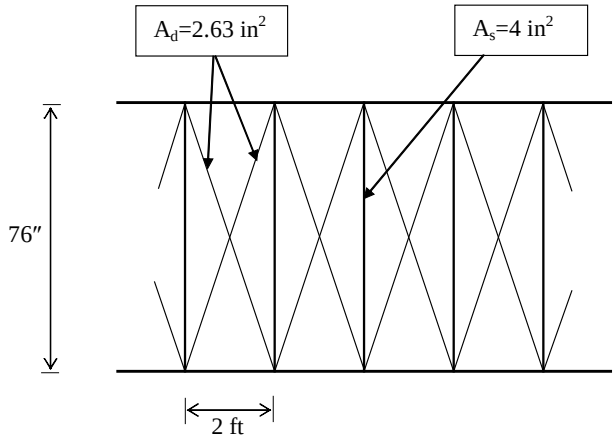

Figure 7.1 X-type top lateral bracing system

7.1 ANALYTICAL METHOD

The warping normal stress σ_W can be predicted using Eq.2.17. Analytically, σ_W in a trapezoidal box girder can be calculated using the following procedures.

1. Calculate the shear center location.
2. Calculate the pure torsional constant J
3. Construct the torsional warping function diagram $w(s)$
4. Calculate the warping moment of inertia I_w
5. Calculate the warping shear parameter μ and the central second moment of area for the pseudo-closed section I_c

   The open and pseudo-closed Model 1 cross-section properties are shown in Figure 7.2 and Figure 7.3, respectively. The detailed calculations were given in Chapter 4.
6. Determine B (bimoment) for a simply supported curved girder

The distribution of the bimoments along the length of the simply-supported, uniformly loaded curved girder with a constant cross-section is shown in Figure 7.4. From Eq. 2.18 derived by Dabrowski, the maximum magnitude of the bimoments for the open and pseudo-closed sections of a 180-ft, simply-supported Model 1 curved girder with 600-ft radius of curvature under 1 k/ft loading are 14840 k.ft^2 and 46.7 k.ft^2, respectively. The bimoment in the open-section is much higher (about 300 times) than that in the pseudo-closed section because a significant portion of the torsional moment is resisted by warping torsion. In a pseudo-closed section, the portion resisted by warping is almost negligible. Since the maximum bimoment occurs at midspan, the maximum σ_W

will also occur at midspan. For many other loading and support conditions, the location of the maximum σ_W has been derived (Dabrowski, 1968, Seaburg and Carter, 1997).

Having calculated the bimoments and all cross-sectional properties of the open and pseudo-closed sections, the σ_W distribution on the cross-section can be determined using Eq.2.17. Figure 7.5 shows the predicted σ_W at the midspan of the open-section and the pseudo-closed section of the 180-ft simply supported Model 1 curved girder with a 600-ft radius of curvature under a symmetric uniformly-distributed load of 1 k/ft. The σ_W distribution is anti-symmetrical about the vertical centroidal axis. A negative sign indicates a compressive stress. The warping normal stress is added to the bending normal stress. The maximum σ_W in the open section is much higher than that in the pseudo-closed section. It should be noted that in the simplified analytical model for the pseudo-closed section, the top flanges are assumed to be concentrated at one point and located at the top of the web. Therefore, only the σ_W at the junction between the top flange and the web can be predicted analytically.

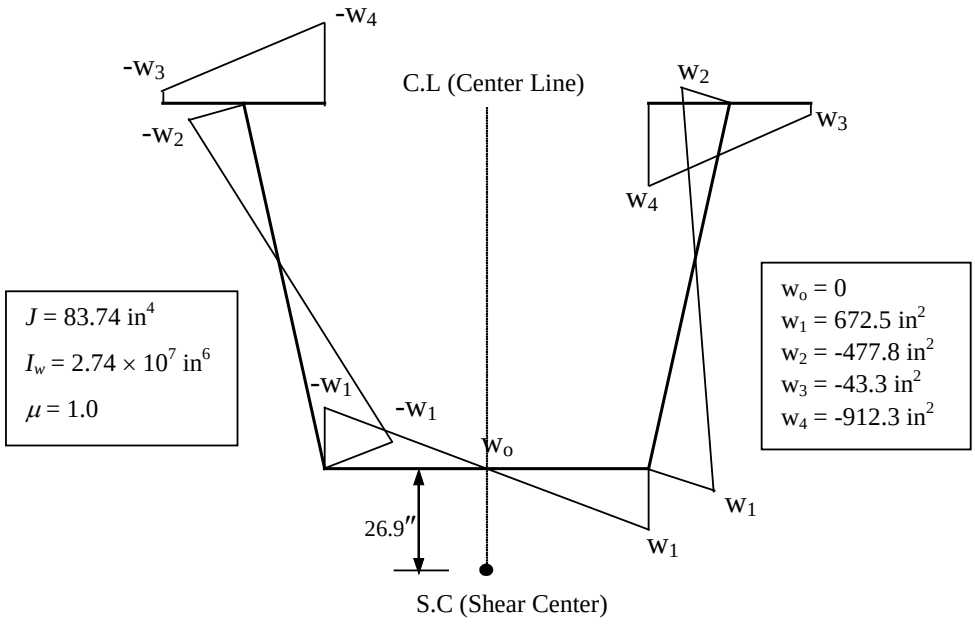

Figure 7.2 Model 1 torsional properties - open section

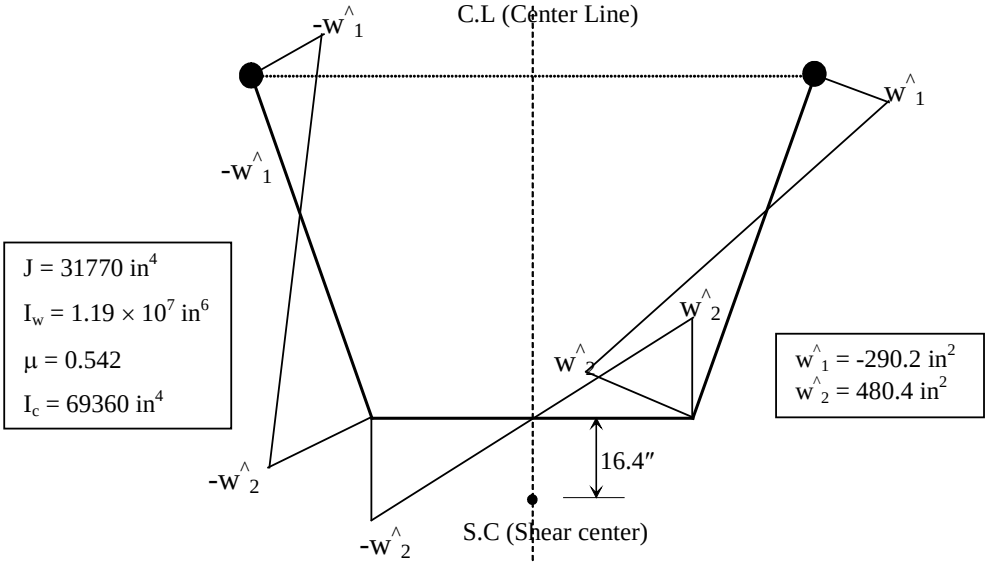

Figure 7.3 Model 1 torsional properties - pseudo-closed section

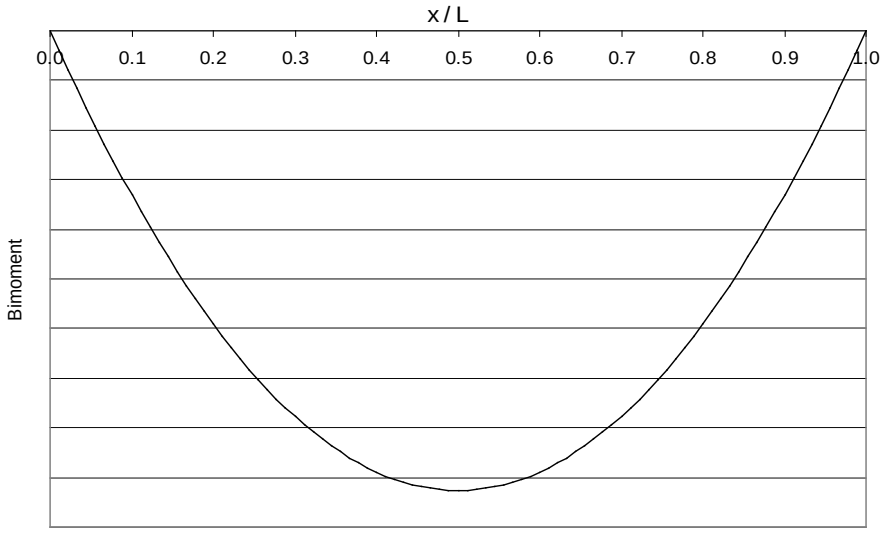

Figure 7.4 Bimoment distribution for a simply supported curved girder

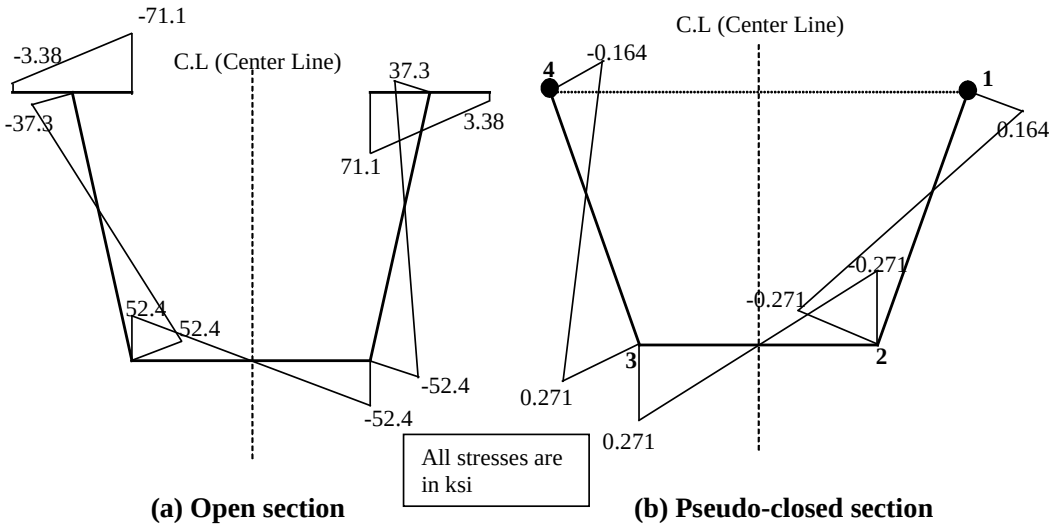

Figure 7.5 Predicted warping normal stress distribution

7.2 VERIFICATION

In order to verify the analytical prediction of the warping normal stresses σ_W, the UTRAP program was used to analyze the same problem as discussed in Section 7.1. Figure 7.6 shows the node locations where the total normal stress can be obtained from UTRAP outputs.

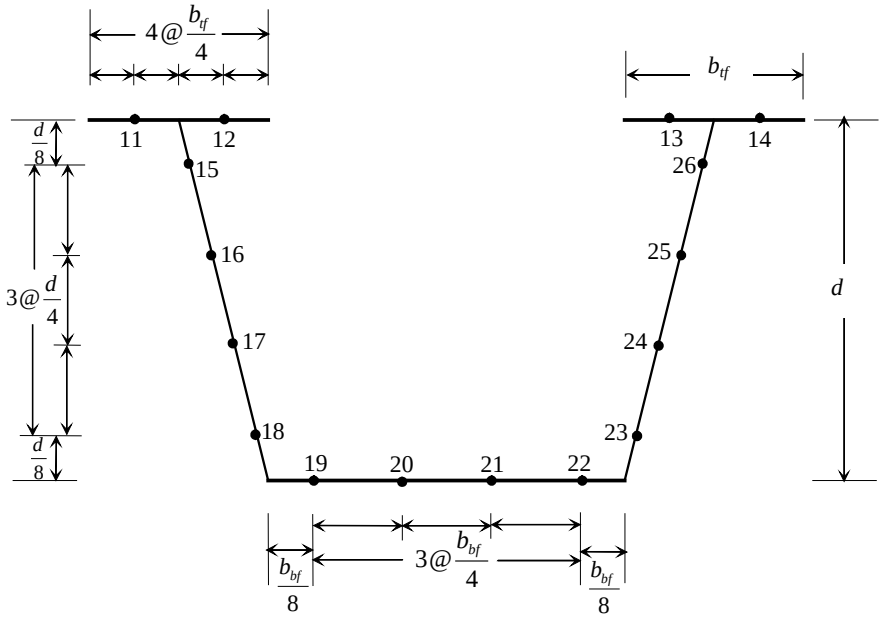

Figure 7.6 Node locations from UTRAP

7.2.1 Open section

In general, one is more concerned with the top flanges than the bottom flange because the top flanges are much smaller and experience larger normal bending stresses because the centroidal axis is closer to the bottom flange. Figure 7.7 shows the variation of the total normal stresses on nodes 11 through 14 and the bending normal stresses on the top flanges. The bending normal stresses σ_B were obtained by taking the average of the total normal stresses on nodes 11

through 14. Figure 7.7 shows that the total normal stress is significantly different than σ_B. Since a closely spaced k-frame internal diaphragm is used, there is no distortional normal stress. The warping normal stress is the only normal stress causing the significant deviation of the total normal stresses from σ_B. The magnitude of σ_W can then be found by subtracting σ_B from the total normal stresses.

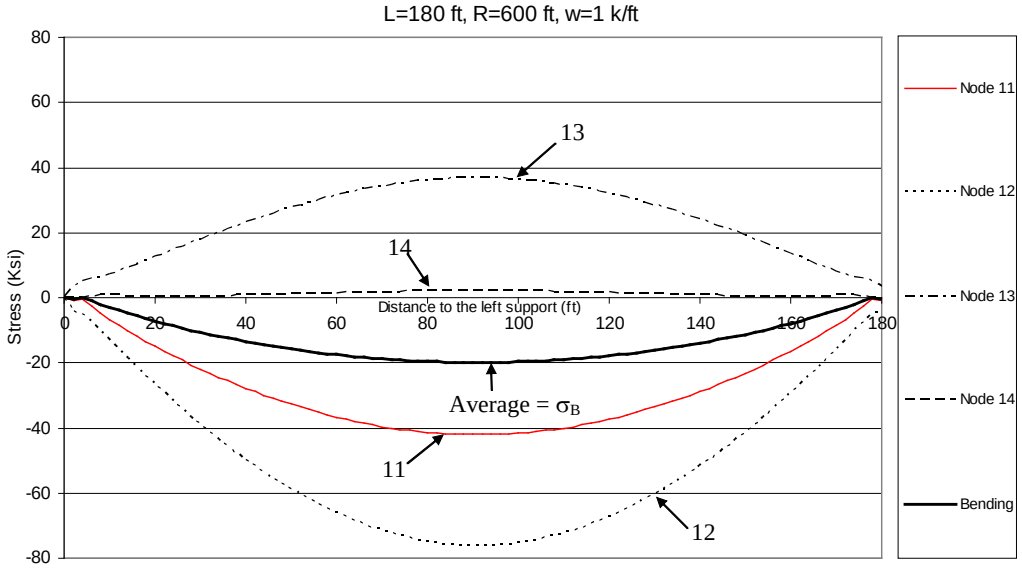

Figure 7.7 Total and bending normal stress variation - open section

Figure 7.8 compares the σ_W variation obtained from UTRAP and that obtained from Eq.2.17. For clarity, the UTRAP solutions are shown for every 8-ft interval. There is good agreement between the σ_W obtained from the UTRAP solution and that predicted using the analytical method. Figure 7.8 also shows the anti-symmetrical nature of the warping normal stress (i.e. σ_W at nodes 12 and 13 are equal in magnitude but opposite in sign, as are those at nodes 11 and 14). Comparing the σ_B shown in Figure 7.7 and the warping σ_W shown in Figure 7.8

shows that the σ_W for an open-section can be three times higher than the σ_B. In a simply supported curved girder, the maximum σ_W occurs at the midspan, where the σ_B is also maximum. The σ_W in Figure 7.8 are for nodes 11 through 14, which do not correspond to the maximum σ_W location, which occurs at the tip of the top flanges as shown in Figure 7.5.

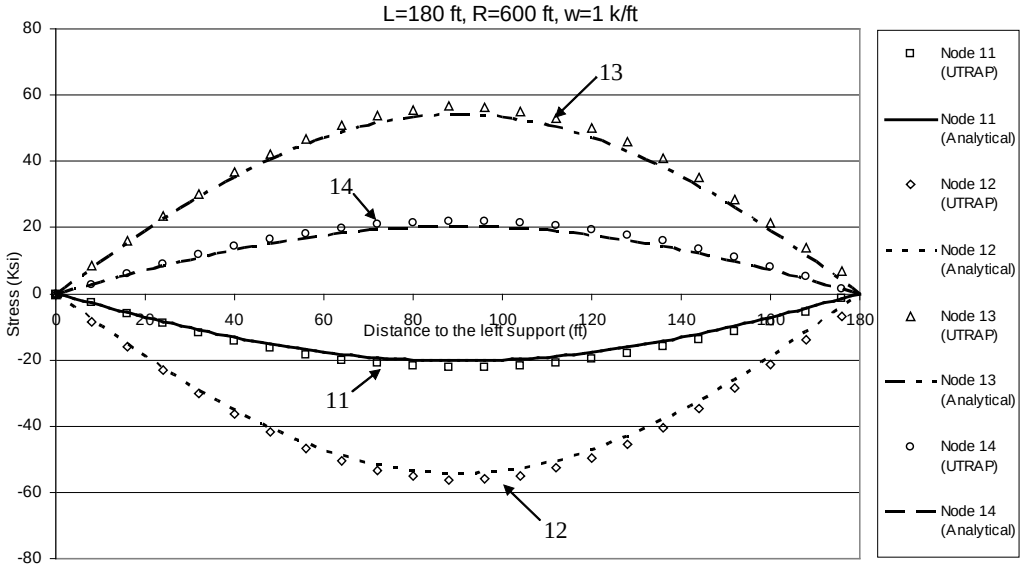

Figure 7.8 Warping normal stress variation – Open section

Figure 7.9 shows the distribution of the σ_W on the midspan cross-section of the open-section Model 1 girder obtained from the UTRAP output and the analytical method. Because of the anti-symmetry of the σ_W, only stresses for the left top flange and the left web are shown. There is good agreement between the UTRAP output and the analytical method.

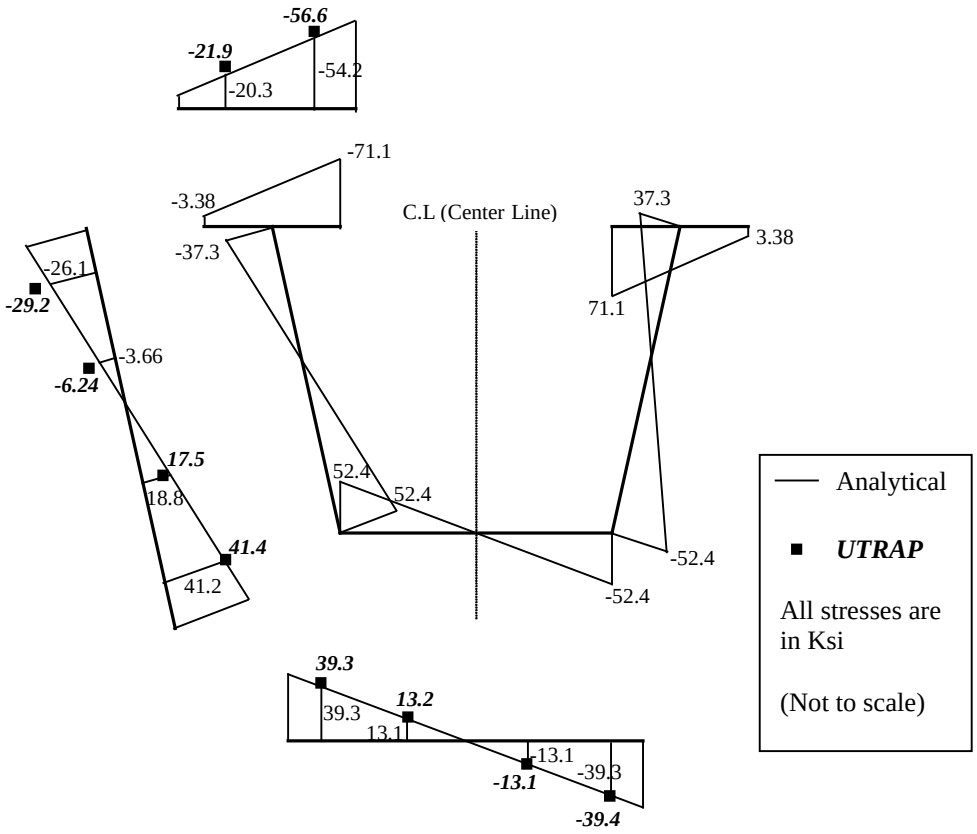

Figure 7.9 Distribution of warping normal stresses at midspan – open section

7.2.2 Pseudo-closed section

Figure 7.10 shows the total and bending normal stress variations along the length of the pseudo-closed section. Unlike the total and the bending normal stresses for the open-section, those for the pseudo-closed section are about the same. However, they are not exactly identical. The total normal stresses at nodes 13 and 12 are slightly smaller and larger, respectively, than the bending normal stress and the total normal stress at nodes 11 and 14, and the bending normal stresses are identical. The deviation of the total normal stress from the bending normal stress is caused by the warping normal stress.

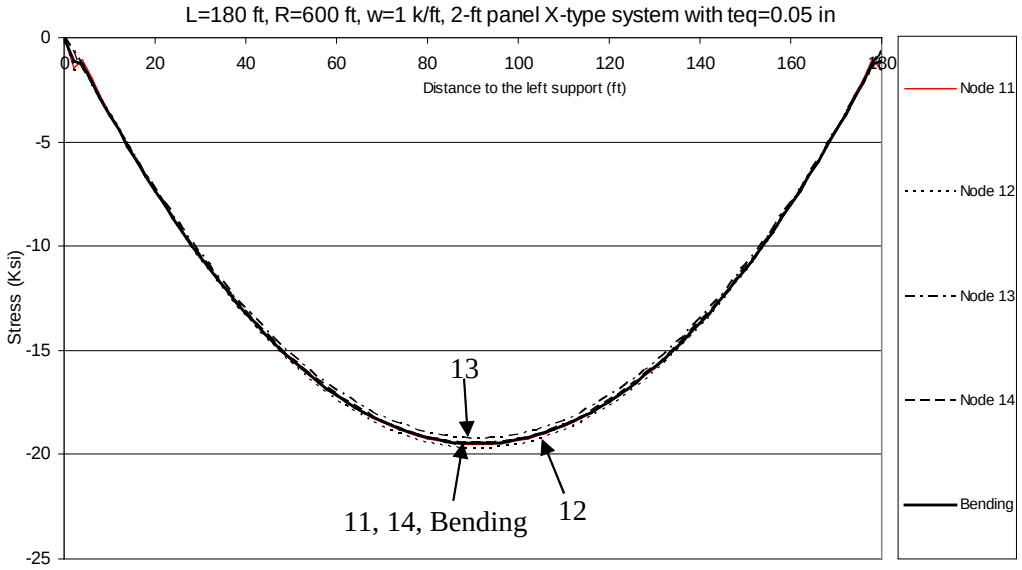

Figure 7.10 Total and bending normal stress variations - pseudo-closed

Figure 7.11 compares the σ_W at the junction of the left web and the left top flange along the length of the open section and the pseudo-closed section, obtained from UTRAP. σ_W in a pseudo-closed section is almost zero.

Figure 7.12 shows the σ_W at the junction of the web and the top flange obtained from UTRAP and from Eq.2.17. There is good agreement between the UTRAP and the analytical solutions. The σ_W in the two flanges are equal in magnitude but opposite in sign. The σ_W near the supports obtained from the UTRAP output deviate from the analytical prediction. However, since the bending normal stress near the supports is almost zero, the total normal stress is very small and of no concern.

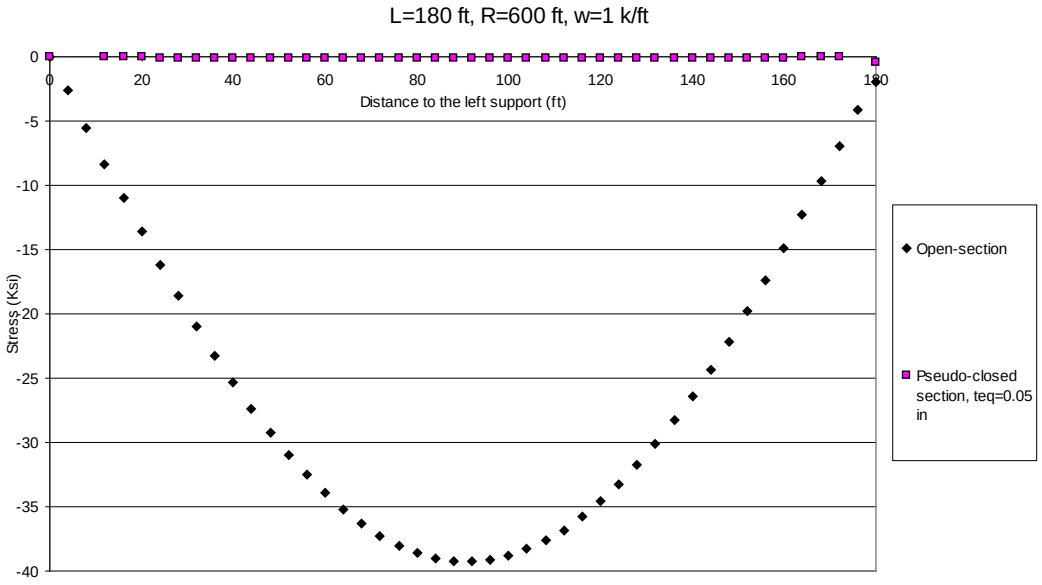

Figure 7.11 Warping normal stress for the open and pseudo-closed sections

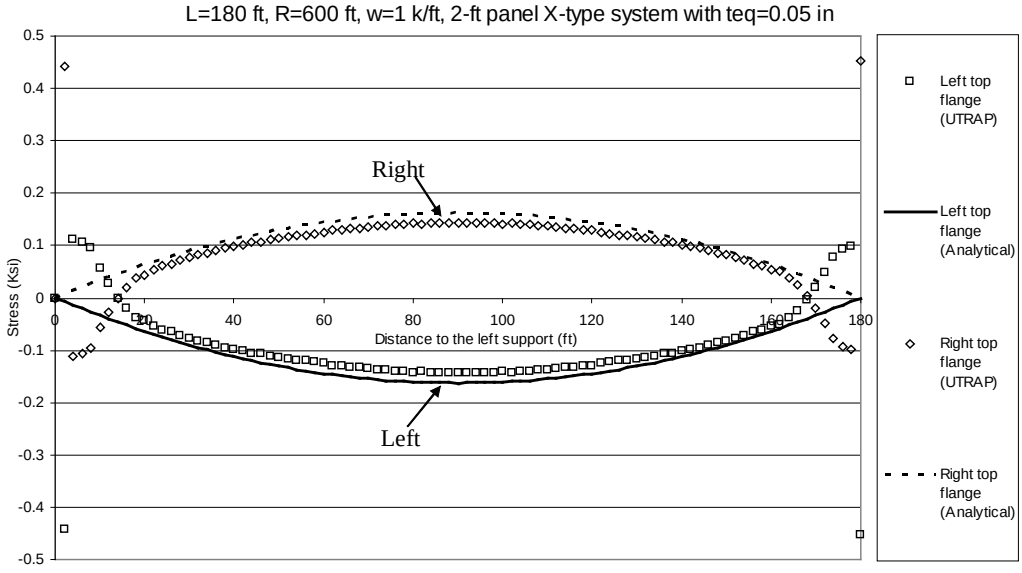

Figure 7.12 Warping normal stress variation - pseudo-closed section

Figure 7.13 shows the σ_W distribution at the midspan cross-section of a pseudo-closed-section with an equivalent plate thickness of 0.01 in because the σ_W in the pseudo-closed section with an equivalent plate thickness of 0.05 inches are very small. Unlike the small discrepancies between the predicted distribution of the σ_W and the UTRAP output for the open-section shown in Figure 7.9, those for this pseudo-closed section are quite large, especially in the web. However, the discrepancy between the predicted σ_W and the UTRAP output at the junction of the web and the top flange is not large (about 10 percent). Since the σ_W in a pseudo-closed section are generally very small, the discrepancies between the predicted distribution of the σ_W and the UTRAP output are of minor concern.

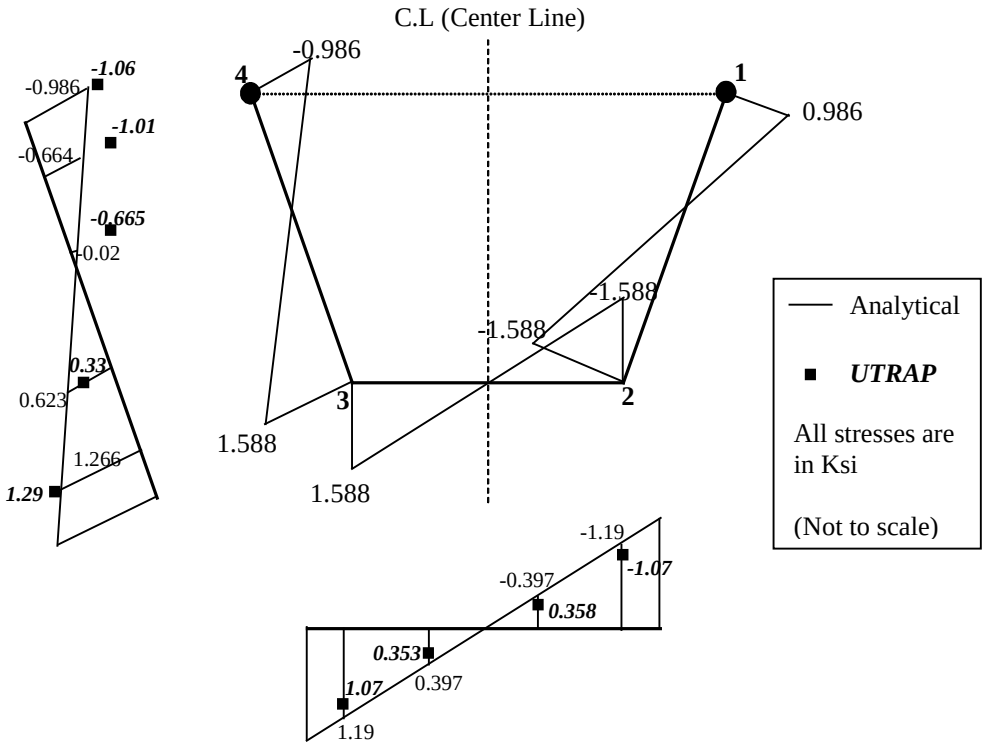

Figure 7.13 Distribution of the warping normal stresses at midspan – pseudo-closed section

7.3 PARAMETRIC STUDIES

The warping normal stresses σ_W for an open-section can be several times larger than the bending normal stresses σ_B, whereas those for a pseudo-closed section with a sufficient equivalent plate thickness are generally so small that they may be neglected. Based on studies performed on rectangular box girders with the width to depth ratio between 1 and 3, Heins (1978) concluded that in order to keep the σ_W less than 10 percent of σ_B, the required minimum equivalent plate thickness is 0.05 inches. Heins' parametric studies indicated that as the width to depth ratio increases, the ratio of σ_W/σ_B increases. In a girder with the width to depth ratio of 1, the minimum required equivalent plate thickness to keep the ratio of σ_W/σ_B less than 10 percent is 0.03 inches.

This section presents the effect of equivalent plate thickness on the magnitude of the σ_W obtained from UTRAP and the analytical method. The parametric studies presented in this section focus on the σ_W at the junction of the web and the top flange. The analyses are conducted on a Model 1 curved girder with the same configuration as that in the previous sections.

Figure 7.14 shows the variation of the σ_W along the length for several different equivalent plate thicknesses t_{eq}. Since the absolute magnitudes of the σ_W in a singly-symmetric trapezoidal box girder at both web-top flange junctions are the same (refer to Figure 7.12), only the σ_W at the left junction are shown. The sizes of the diagonal members used in the X-type top lateral bracing system corresponding to each equivalent plate thickness were shown in Table 6.1. Figure 7.14 shows that there is good agreement between the variation of the σ_W along the length obtained from UTRAP and the analytical method. The values near each end support are not included because they are not meaningful. Even though the

accuracy of the analytical method depends on the equivalent plate thickness, the maximum discrepancy between the two results is generally less than 10 percent. For the equivalent plate thicknesses that are relatively thick (e.g. 0.04”), the predicted σ_W are larger than the UTRAP solution, whereas for equivalent plate thicknesses that are relatively thin, the predicted values are smaller than the UTRAP solution.

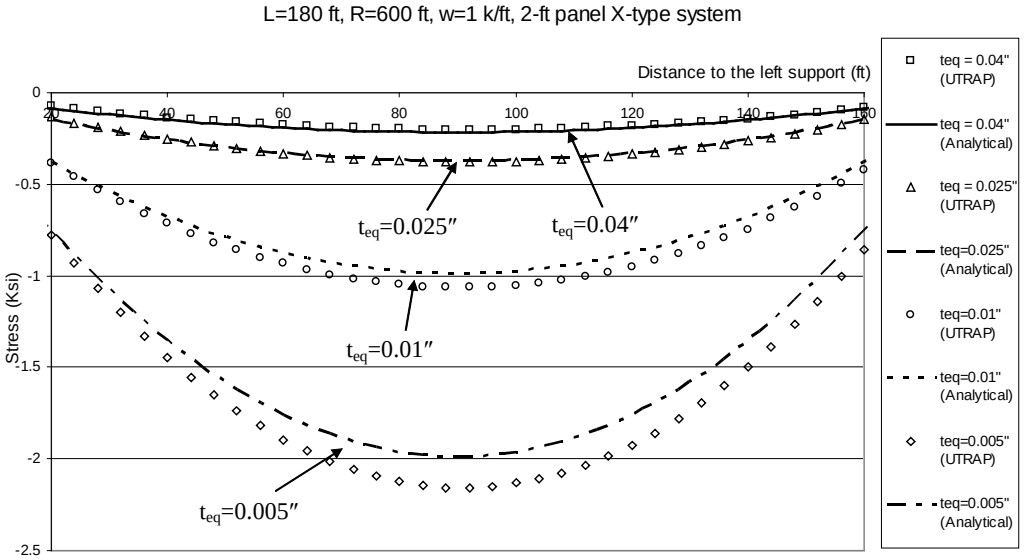

Figure 7.14 Warping normal stresses for different equivalent plate thicknesses

Figure 7.15, Figure 7.16, and Figure 7.17 show the effect of t_{eq} on the midspan bimoment, the torsional warping function at the junction between the left web and the left top flange, and the warping moment of inertia, respectively. Figure 7.15 shows that in the curved girder with t_{eq} greater than 0.02 inches, changing t_{eq} does not affect the magnitude of the bimoment significantly, whereas with a t_{eq} less than 0.02 inches, the bimoment is very sensitive to t_{eq}. As t_{eq} becomes smaller, the bimoment increases dramatically. Figure 7.16 and Figure

7.17 show that assuming the torsional warping function and the warping moment of inertia to be inversely proportional to t_{eq} is reasonable.

Figure 7.15 shows that the midspan bimoment for the open-section is very close to that for the pseudo-closed section with an equivalent plate thickness approaching zero. On the other hand, there are noticeable discrepancies (about 10 percent) between the torsional warping function and the warping moment of inertia for the open-section and those for the pseudo-closed section with an equivalent plate thickness approaching zero. These discrepancies indicate that the analytical formulas used to predict the cross-sectional properties related to torsional warping are not perfect, which accounts for the deviation of the predicted warping normal stresses from the UTRAP solution, especially when the equivalent plate thickness becomes extremely thin. However, due to the complexity of warping torsion, a ten percent discrepancy between the analytical method and the UTRAP solution is acceptable, particularly since in a typical curved girder with a reasonable amount of top lateral bracing, the warping normal stresses are so small that they can be neglected.

Figure 7.18 and Figure 7.19 show the variation of the σ_W along the length of the pseudo-closed section with three different top lateral bracing systems, with t_{eq} of 0.05 inches and 0.01 inches, respectively. Table 7-1 shows the areas of the diagonal members used in the top lateral bracing systems corresponding to each t_{eq}. Figure 7.18 through Figure 7.19 show that the σ_W are generally not sensitive to the type of top lateral bracing system, as long as the t_{eq} is kept the same. The variations of the σ_W along the length of the girder using the X-type and the Alternating-Diagonal systems are exactly the same. For the t_{eq} of 0.05 inches, the σ_W using the Single-Diagonal system are close to those using both the X-type and the Alternating Diagonal systems, except near the midspan where the stresses increase significantly.

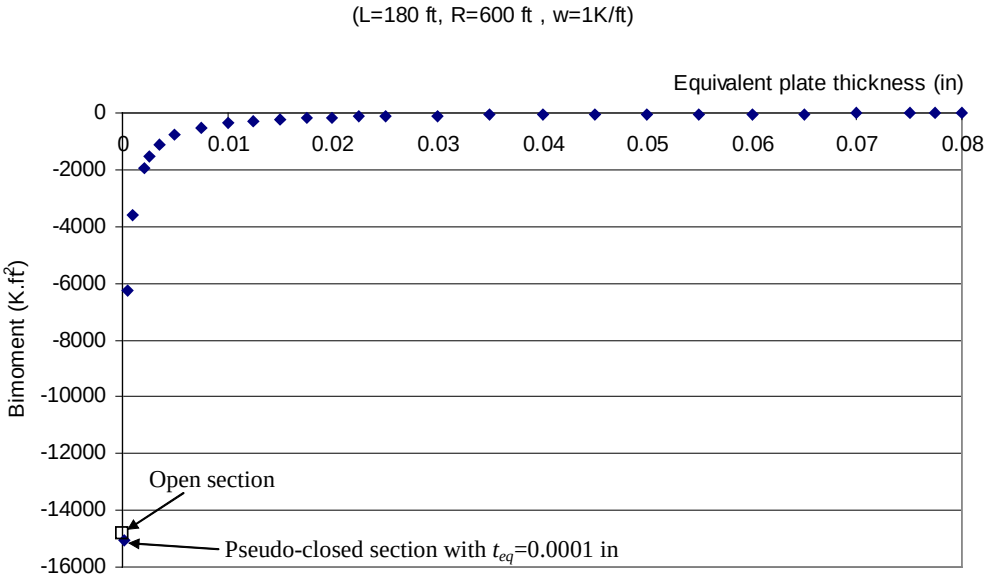

Figure 7.15 Midspan bimoment

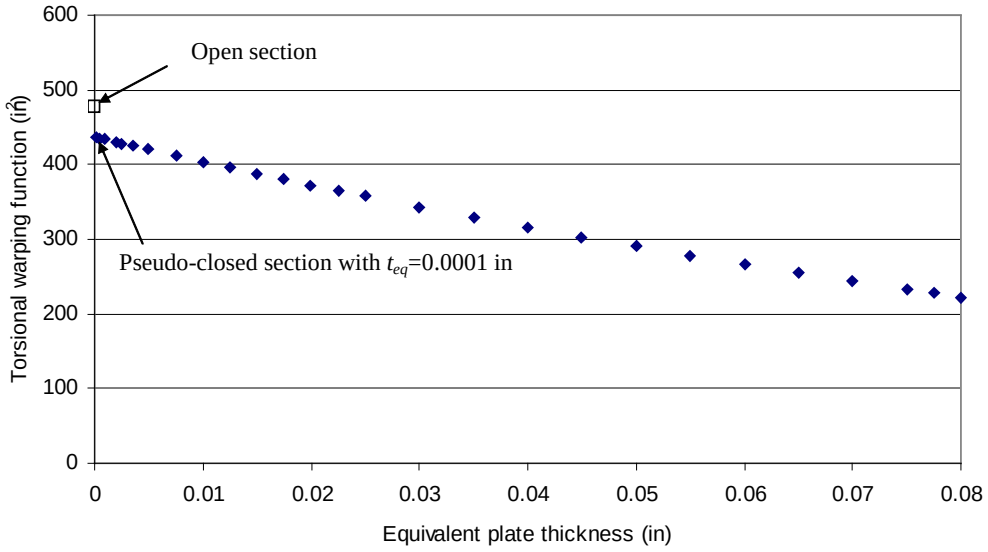

Figure 7.16 Torsional warping function

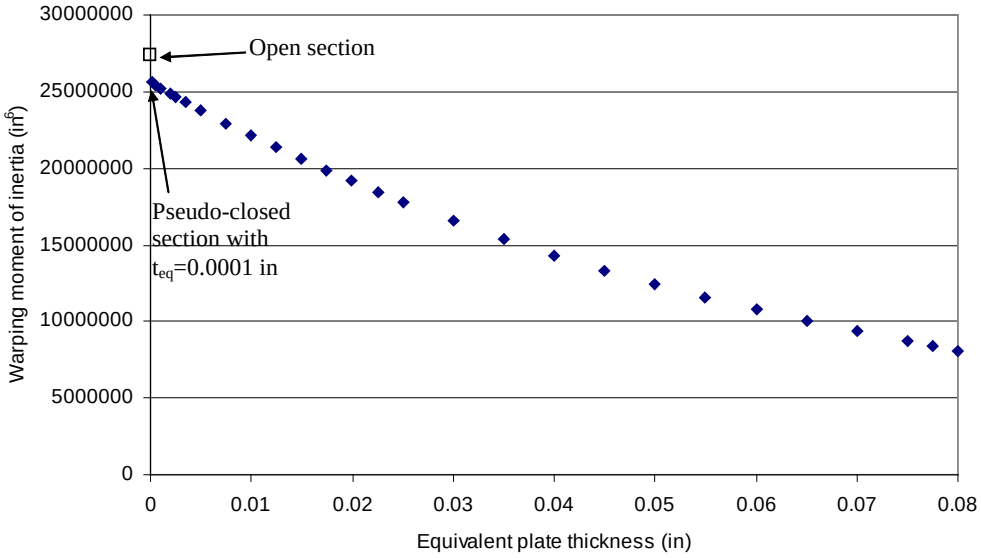

Figure 7.17 Warping moment of inertia

The jump in the σ_W near the midspan of the girder using the Single-Diagonal system is partly due to the kink in the horizontal displacement discussed in Chapter 5 that induces the concentrated localized normal stresses. The magnitude of the σ_W near the midspan of the girder using the Single-Diagonal system becomes closer to those of the girder using both the X-type and the Alternating-Diagonal systems as the t_{eq} becomes smaller. For an extremely thin equivalent plate thickness (0.01 inches), the σ_W with a Single-Diagonal system are smaller than those in a girder using either the X-type or the Alternating-Diagonal system. Therefore, for a curved girder with a typical equivalent plate thickness, the results of parametric studies using the X-type system can be extended to the Alternating-Diagonal and Single-Diagonal systems.

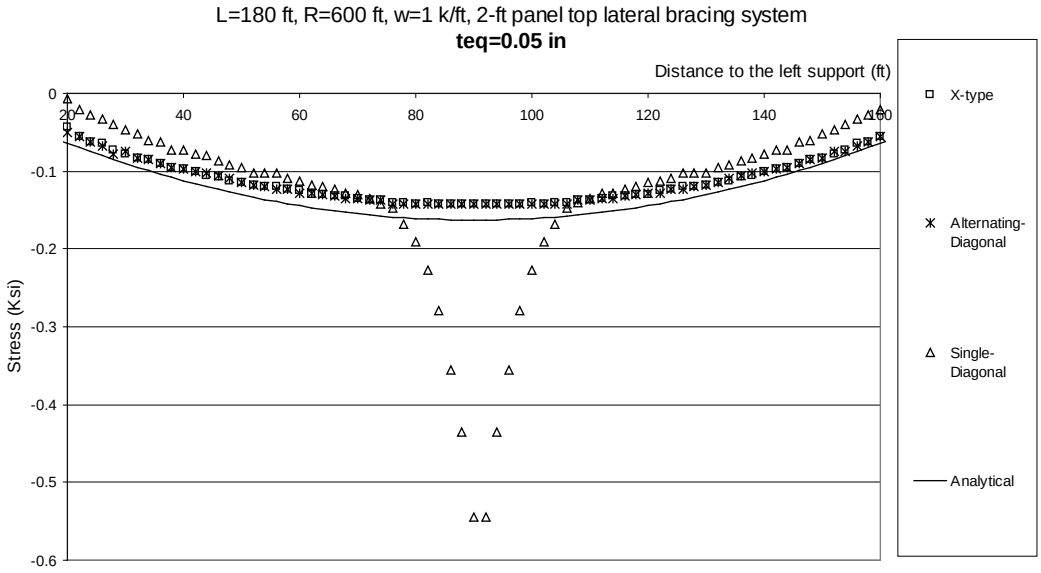

Figure 7.18 Effect of different top lateral bracing systems – t_{eq}=0.05 in

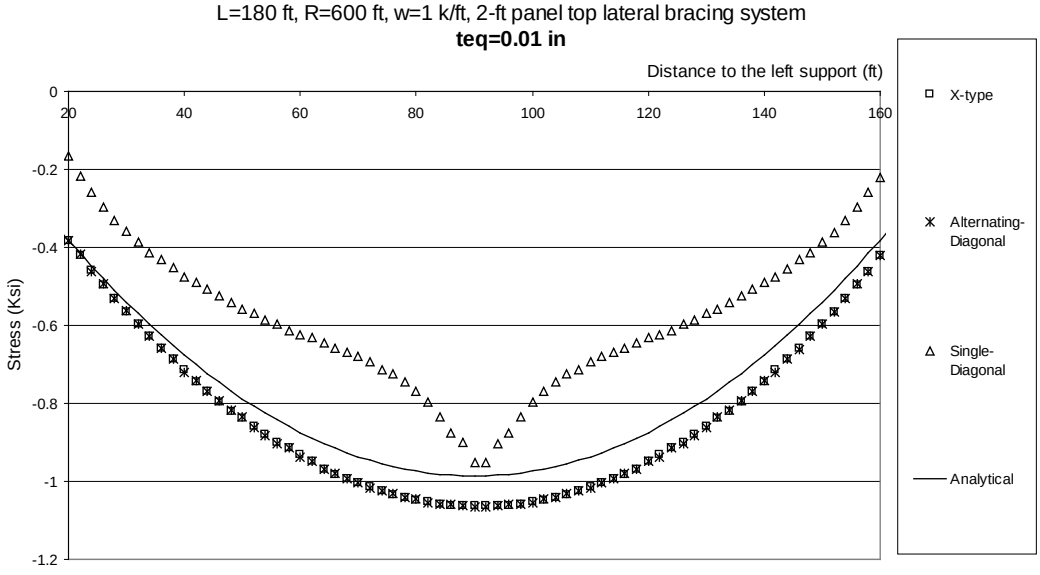

Figure 7.19 Effect of different top lateral bracing systems – t_{eq}=0.01 in

Table 7-1 Areas of diagonal members corresponding to equivalent plate thicknesses

Equivalent plate thickness (in)	Size of diagonal member in top lateral bracing system (in^2)		
	X-type	Alternating-Diagonal	Single-Diagonal*
0.05	2.63	5.28	9.82
0.025	1.31	2.63	4.91
0.01	0.525	1.05	1.96

*** *Note:*** Assume the area of the struts is 4 in^2 (same as the area of the internal diaphragms)

Figure 7.20 shows the midspan warping normal stresses at the junction of the web and the top flange as a function of the equivalent plate thickness. The maximum σ_W increases as the t_{eq} decreases. The maximum σ_W approaches zero as the t_{eq} becomes greater than 0.05 inches. For a typical t_{eq} (between 0.02 and 0.05 inches), the stresses are not sensitive to the t_{eq}. Figure 7.20 also shows that there is good agreement between the maximum σ_W obtained from UTRAP and from the analytical method.

Figure 7.21 shows the UTRAP solutions for the variation of the maximum warping normal stress at the junction of the web and flange in a simply-supported Model 1 curved girder with an equivalent plate thickness of 0.01 inches as a function of the central angle. In addition to the magnitude of the σ_W, Figure 7.21 also shows the ratio of the maximum warping normal stresses to the maximum bending normal stresses. In Figure 7.21(a) and (b), the radius of curvature is kept constant at 600 ft, whereas in Figure 7.21(c) and (d), the length is kept constant at 180 ft. Changing the central angle for a constant radius of curvature was done by altering the length; for a constant length, the radius of curvature was varied. Figure 7.21(a) and (c) show that the maximum σ_W is sensitive to the central angle, the length L, and the radius of curvature R. In general, as the central angle increases, the maximum σ_W also increases. However, the change of the maximum

σ_W is more sensitive to the change of the length than to the change of the radius of curvature. For a constant radius of curvature of 600 ft, the maximum σ_W increases with the square of the central angle. For example, the maximum σ_W with the length *2L* is roughly four times higher than with the length *L*. For a constant length of 180 ft, the change of maximum σ_W is approximately inversely proportional to the change of central angle.

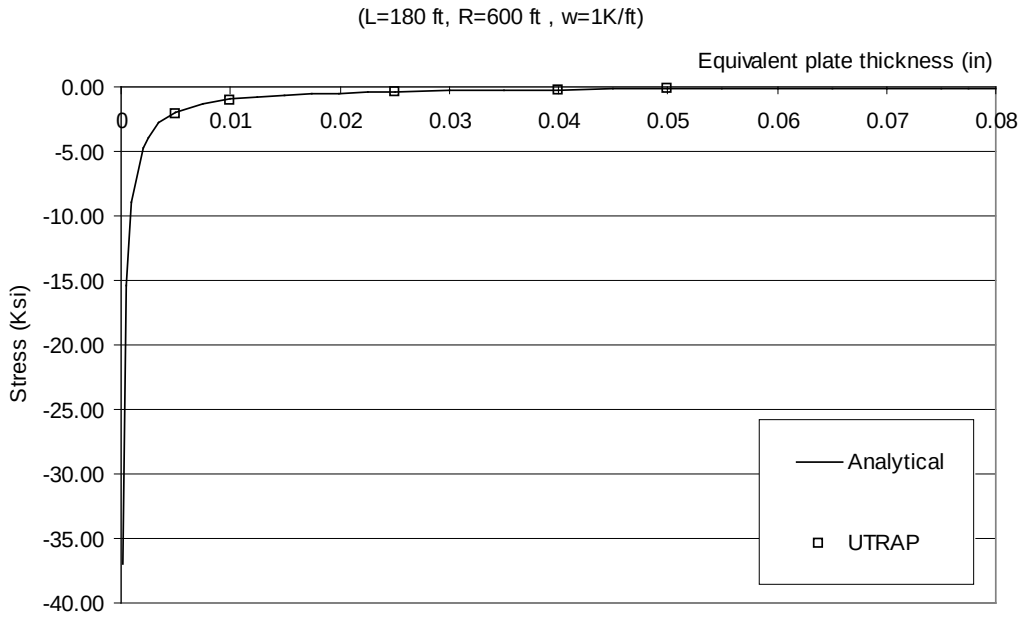

Figure 7.20 Maximum warping normal stress as a function of the equivalent plate thickness

Even though the change in the maximum σ_W is more sensitive to the change in girder length than to the change in the radius of curvature, the ratio of the maximum warping normal stress to the maximum bending normal stress for a constant radius of curvature of 600 ft is about the same for different central angles, as shown in Figure 7.21(b). On the other hand, Figure 7.21(d) shows that

the change of that ratio for a constant length of 180 ft is linearly proportional to the change of the central angle. For a central angle less than 0.4 radians, the maximum σ_W is less than 2 ksi and the ratio of the maximum warping normal stress to the bending normal stress is less than 8 percent.

The maximum σ_W for different combination of length and radius of curvature vary. However, the parametric studies for a constant radius of curvature and the constant length coincide at the central angle of 0.3 radians, since the 180-ft girder with a radius of curvature of 600 ft is used in both parametric studies.

Figure 7.22 shows the variation of the ratio of the midspan warping normal stress to the midspan bending normal stress (σ_W/σ_B) as a function of an equivalent plate thickness. In this parametric study, the sensitivity of the σ_W/σ_B to the pair of length and radius of curvature, and to the cross-section dimensions are examined. The cross-section dimensions of the Model 3 girder are shown in Figure 1.5. The central angle of 0.3 radians and the maximum bending normal stress are kept constant. Figure 7.22 shows that the ratio σ_W/σ_B for a certain t_{eq} are sensitive to L and R and to the cross-section dimensions. For the same central angle, σ_W/σ_B in a girder with a shorter length is larger. In order to limit the σ_W to less than 2.5 percent of the σ_B, the minimum recommended t_{eq} is 0.05 inches. The limit of 2.5 percent is selected because the ratio shown in Figure 7.22 is based on the warping normal stress at the junction of the web and the top flange, which is not the maximum warping normal stress in a cross-section. The recommended minimum equivalent plate thickness is the same as Heins' recommendation with the criterion to limit the ratio of the warping to bending normal stress less than 10 percent in a relatively shallow girder (depth to width ratio of 1/3).

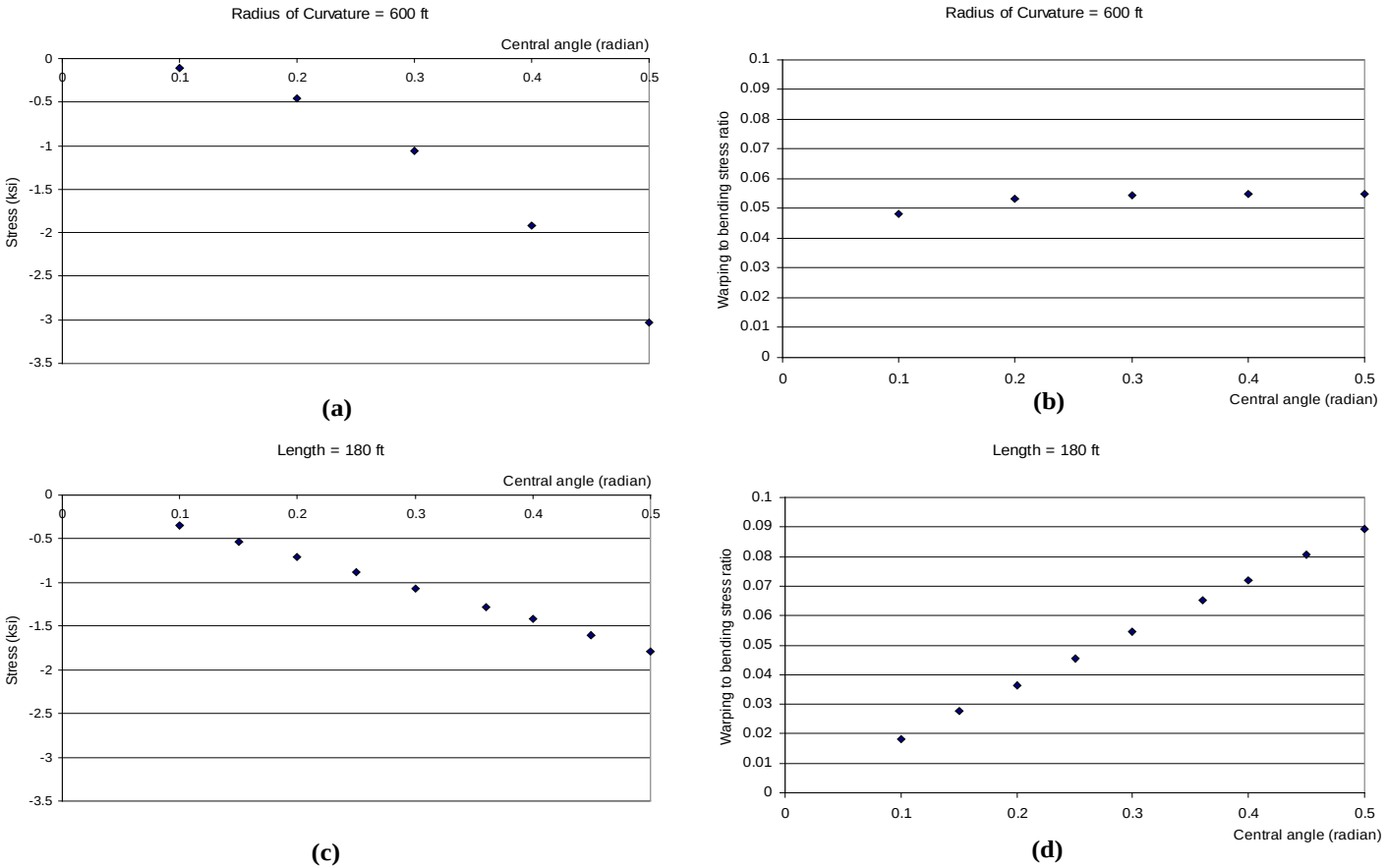

Figure 7.21 Variation of the maximum warping normal stress as a function of the central angle

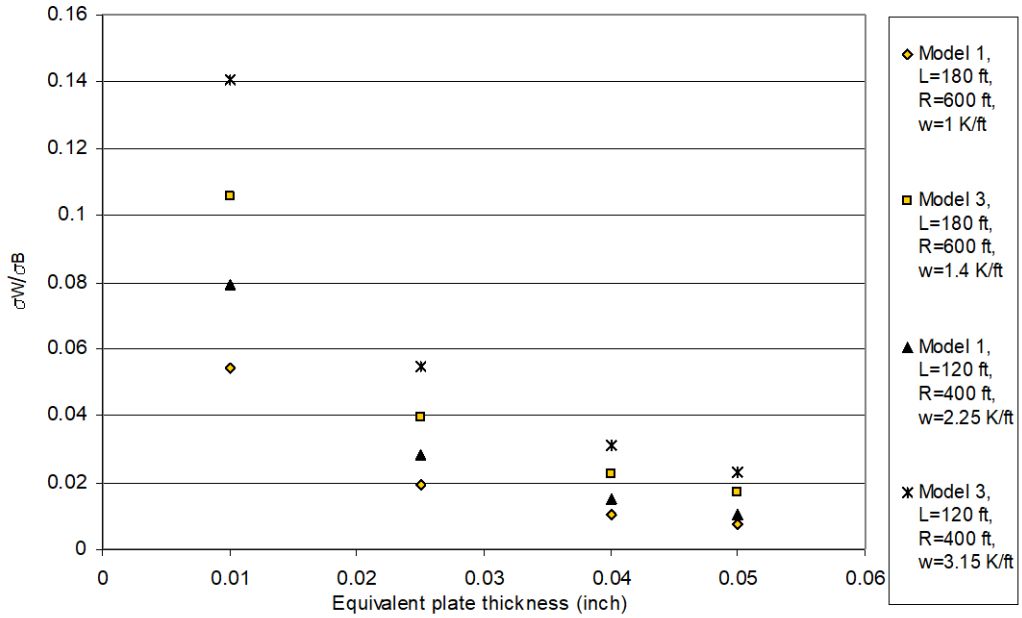

Figure 7.22 Ratio of midspan warping normal stress to midspan bending normal stress

7.4 WARPING NORMAL STRESS IN A CONTINUOUS GIRDER

The analytical method to predict the warping normal stress is limited to a simply-supported curved girder because there is no simple expression available for predicting the bimoment in a continuous curved girder. To study the variation of the σ_W in a continuous curved girder, this section presents the UTRAP solutions for the σ_W in a two-equal-span and a three-equal-span continuous curved girder. A Model 1 girder with the 2-ft panel of the X-type system was used again as a representative pseudo-closed section. The diagonal area used in this section is 0.525 in^2, which corresponds to an equivalent plate thickness of 0.01 inches. In order to eliminate cross-section distortion, a 2-ft spacing of internal diaphragms

consisting of a k-frame with 4-in^2 member sizes was used. A symmetrical uniform load of 1 k/ft was applied to the girder.

Figure 7.23 and Figure 7.24 show the variation of the bending and the warping normal stresses, respectively, in a two-equal-span 180-ft continuous curved girder for central angles of 0.3 radians (R=1200 ft) and 0.6 radians (R=600 ft). Only the σ_W at the junction of the left web and the left top flange is presented. Figure 7.24 shows that the maximum σ_W in a two-equal-span continuous curved girder is smaller than that in a simply-supported girder. For the same total central angle of 0.3 radians, the maximum magnitude of the σ_W in the continuous girder is only 0.37 ksi, as opposed to about 1 ksi in the simply-supported girder (refer to Figure 7.21). Even if the radius of curvature is kept at 600 ft, so that the central angle of each span is the same that of the simply supported girder, the maximum magnitude of the σ_W is only 0.6 ksi, which is still significantly less than that in the simply-supported girder. In addition, for the total central angle of 0.3 radians (R=1200 ft), the compressive σ_W in the continuous girder is only about 2.7 percent of the maximum compressive bending normal stress, as opposed to 5.4 percent in the simply-supported girder. However, if the central angle of each span is 0.3 radians (R=600 ft), the ratio of the maximum compressive warping normal stress to the compressive bending normal stress in the continuous girder is the same as that in the simply supported girder with the same central angle and span. The maximum warping normal stress occurs at the intermediate support, where the tensile bending normal stress is generally maximum. The additional tensile σ_W is not as detrimental as the additional compressive σ_W, due to a potential buckling problem. In addition, the ratio of the maximum tensile σ_W to the maximum tensile σ_B is smaller than the ratio of the maximum compressive σ_W to the maximum compressive σ_B.

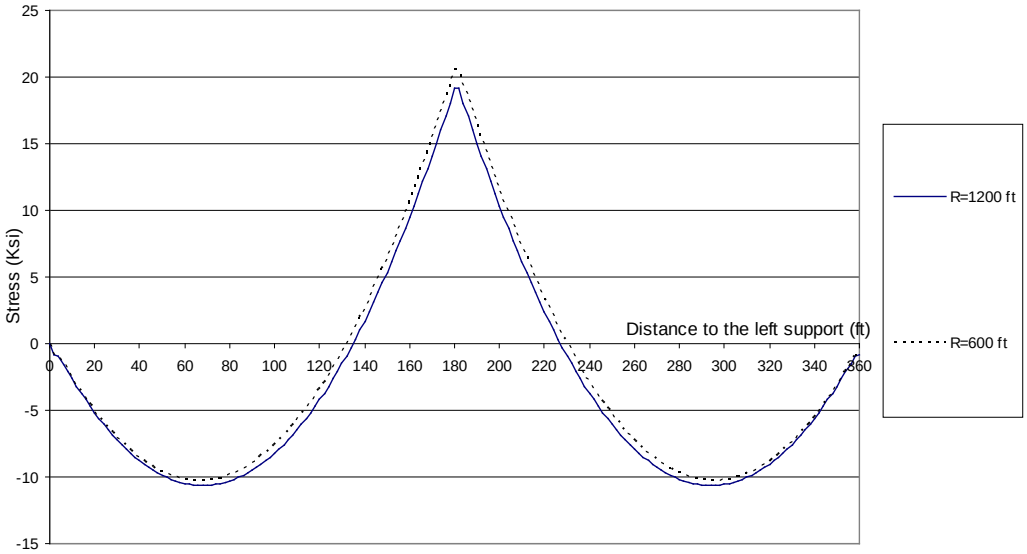

Figure 7.23 Bending normal stress - two-equal-span 180-ft continuous girder

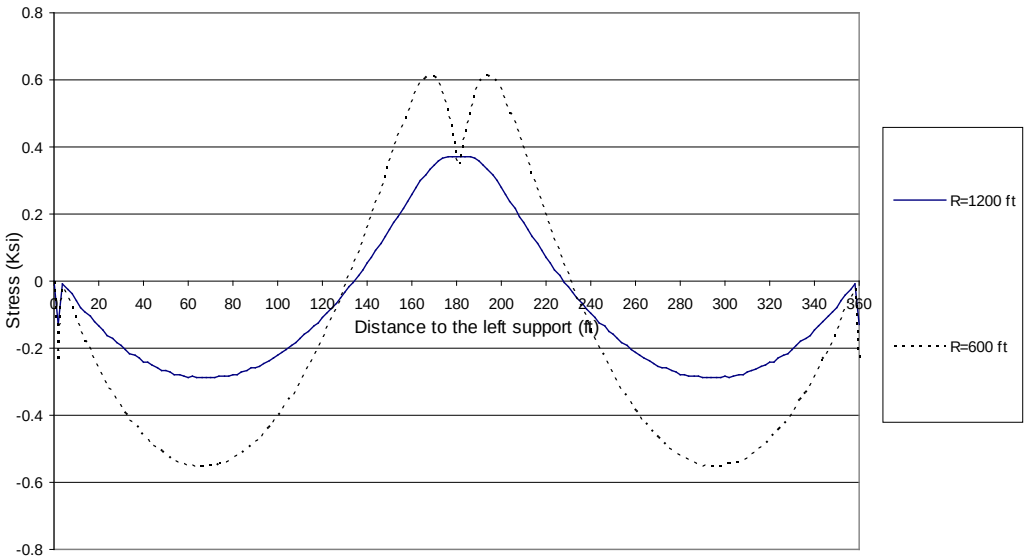

Figure 7.24 Warping normal stress - two-equal-span 180-ft continuous girder

Figure 7.25 and Figure 7.26 show the variation of σ_B and σ_W, respectively, in a three-equal-span 180-ft continuous curved girder for central angles of 0.3 radians (R=1800 ft) and 0.9 radians (R=600 ft). As in the two-equal-span continuous girder example, the maximum magnitudes of the σ_W in a three-equal-span continuous girder with a central angle of 0.3 radians are also smaller than those in a simply-supported girder with the same central angle. However, the ratio of the maximum compressive σ_W to the maximum σ_B in a three-equal-span continuous curved girder with an individual span central angle of 0.3 radians is 5.4 percent, which is the same as that in a simply-supported girder with the same central angle and length. The maximum magnitude of the σ_W in a three-equal-span continuous girder occurs near the midspan of the exterior spans.

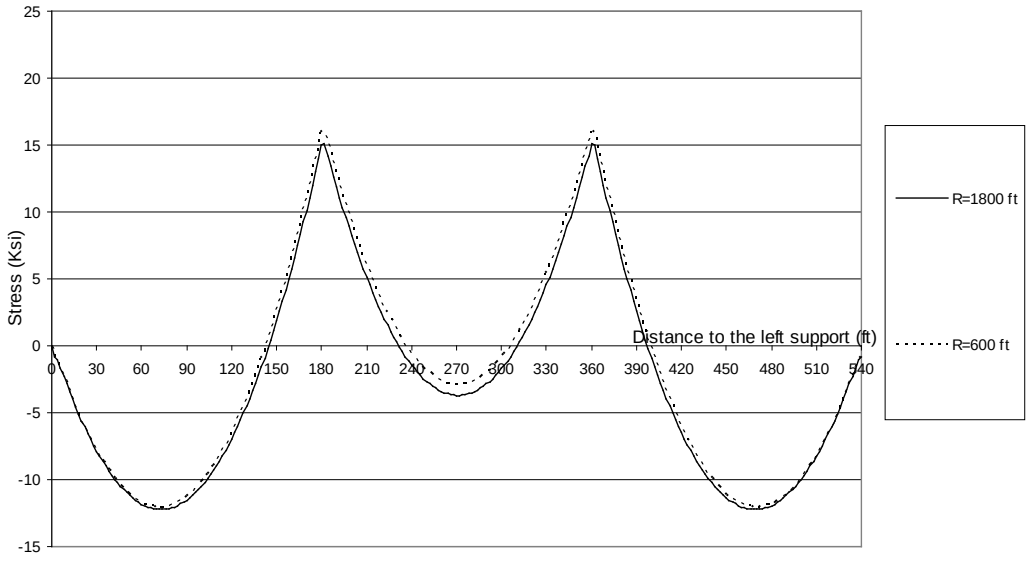

Figure 7.25 Bending stress - three-equal-span 180-ft continuous girder

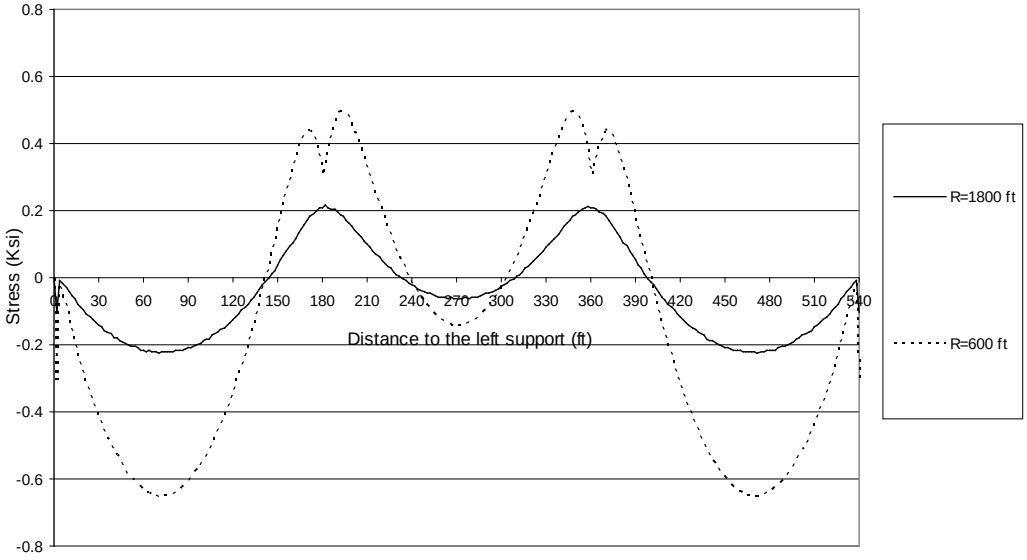

Figure 7.26 Warping stress - three-equal-span 180-ft continuous girder

The trend of the maximum σ_W as a function of the central angle in a continuous girder is the same as in a simply-supported girder. As the total central angle increases, the maximum magnitude of the σ_W in a continuous girder also increases. The maximum magnitude of the σ_W in an equal-span continuous girder is smaller than that in a simply-supported girder whose length and central angle are the same as those for each span of the continuous girder. In addition, the ratio of the maximum compressive σ_W to the compressive σ_B in an equal-span continuous girder is the same as that in a simply supported girder with the same length and central angle as those in each span of the continuous girder. Therefore, for warping normal stress calculations, it is conservative to analyze each span of a continuous curved girder as being simply-supported.

7.5 SUMMARY

This chapter presented an analytical method for predicting the warping normal stress in a simply-supported curved girder. There was good agreement between the results from the analytical method and the UTRAP solution for both an open section and a pseudo-closed section. In a simply-supported curved girder, the maximum warping normal stress σ_W occurs at the midspan. The σ_W in an open-section can be several times higher than the bending normal stresses σ_B, whereas those in a pseudo-closed section with a relatively thick equivalent plate thickness are negligible compared to σ_B. The maximum σ_W increases as the equivalent plate thickness decreases. In order to σ_W in the junction of the web and the top flange to less than 2.5 percent of σ_B, the minimum recommended equivalent plate thickness is 0.05 inches.

The maximum σ_W is sensitive to the central angle and the combination of length L, and radius of curvature, R. Based on the parametric studies, the maximum σ_W increases with the square of the central angle for a constant R, whereas with a constant L, that change is approximately inversely proportional to the change of central angle. However, for a constant R, the ratio of σ_W/σ_B is about the same for different central angles; for a constant length, the change of that ratio is linearly proportional to the change in the central angle.

The maximum magnitude of σ_W in an equal-span continuous girder is smaller than that in a simply-supported girder whose length and central angle are the same as those for each span of the continuous girder. However, the ratio of the maximum compressive σ_W/σ_B in an equal-span continuous girder is the same as that in a simply supported girder with the same length and central angle as those of each span of a continuous girder.

CHAPTER 8
Distortional Normal Stress

In Chapter 6, the distortion of a curved pseudo-closed box sections was discussed with a focus on the distortional deformations. In this chapter, the normal stresses that develop in the flange from the distortion will be discussed. These stresses will be called distortional normal stresses. A general discussion of the source of the distortional normal stresses is given first, followed by a presentation of UTRAP results on a simply supported girder subjected to a symmetrical uniform load. The model used in the analysis is the same model that was used to discuss distortional deformation in Chapter 6. The use of internal diaphragm to control distortional stresses is discussed along with other parameters that may affect distortion. After the parametric study on simply supported girders, a brief discussion of distortional normal stresses in continuous girders is presented. A method for predicting the distortional normal stress is then developed and the results compared with UTRAP and some existing recommendations.

8.1 SOURCE OF DISTORTIONAL NORMAL STRESS

The distortional component of torsional loading in a curved girder under a symmetrical uniform load develops as a result of a second order effect. Figure 8.1 shows bending normal stresses in the top and bottom flanges of a curved girder. Under bending, the top flanges that are in compression move away from the center of curvature, whereas the bottom tension flange moves toward the center of

curvature. Since this lateral movement is caused by internal normal bending stresses that act on a curved member, the source of this lateral movement is a second order (P-δ) effect.

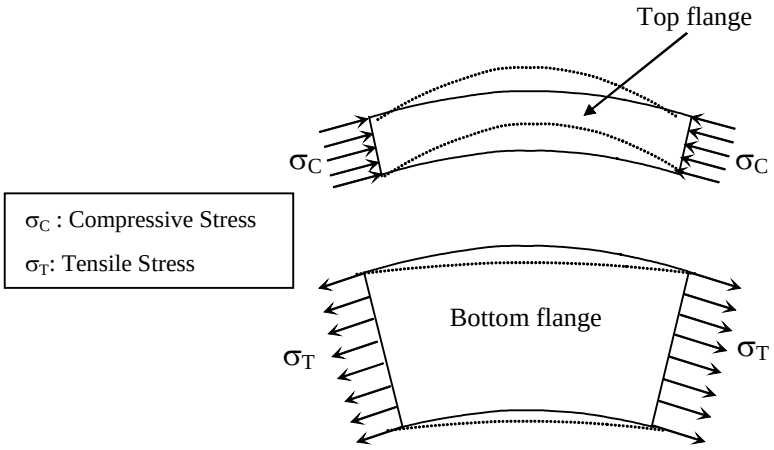

Figure 8.1 Bending normal stresses in the flanges of a curved girder

The second order effect can be approximated by applying imaginary horizontal loads as shown in Figure 8.2. Helwig and Fan (2000) indicated that the imaginary horizontal load can be approximated by $M/(hR)$, where M is the bending moment, h is the girder depth, and R is the radius of curvature.

Figure 8.3 shows the distribution of the distortional normal stress. It can be seen from Figure 8.3 that the distribution of the distortional normal stress σ_D is anti-symmetrical about the vertical centroidal axis and is similar to the warping normal stress. For this reason, σ_D is called the distortional warping normal stress in some literature. Even though the distributions of the distortional and warping normal stresses are similar, the sources of the two stresses are completely different. The distortional normal stress occurs because the lateral movements of the top and bottom flanges due to the curvature, whereas the warping normal stress develops because warping (i.e. out-of-plane displacement) is restrained.

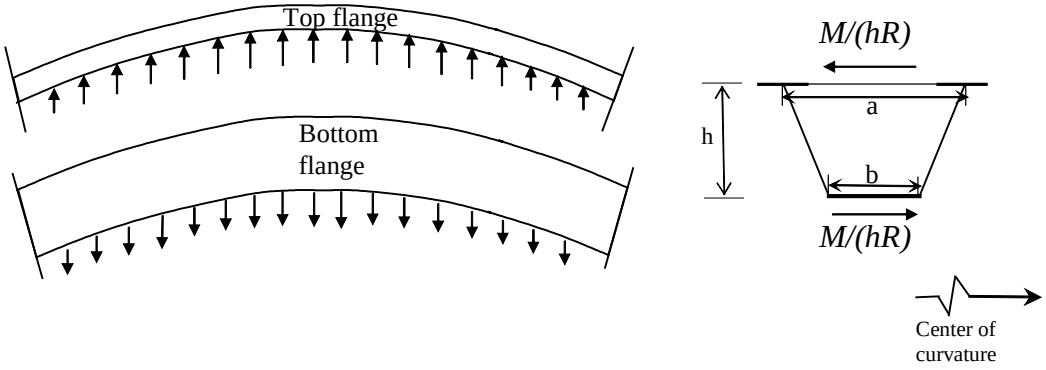

Figure 8.2 Imaginary horizontal loads due to curvature

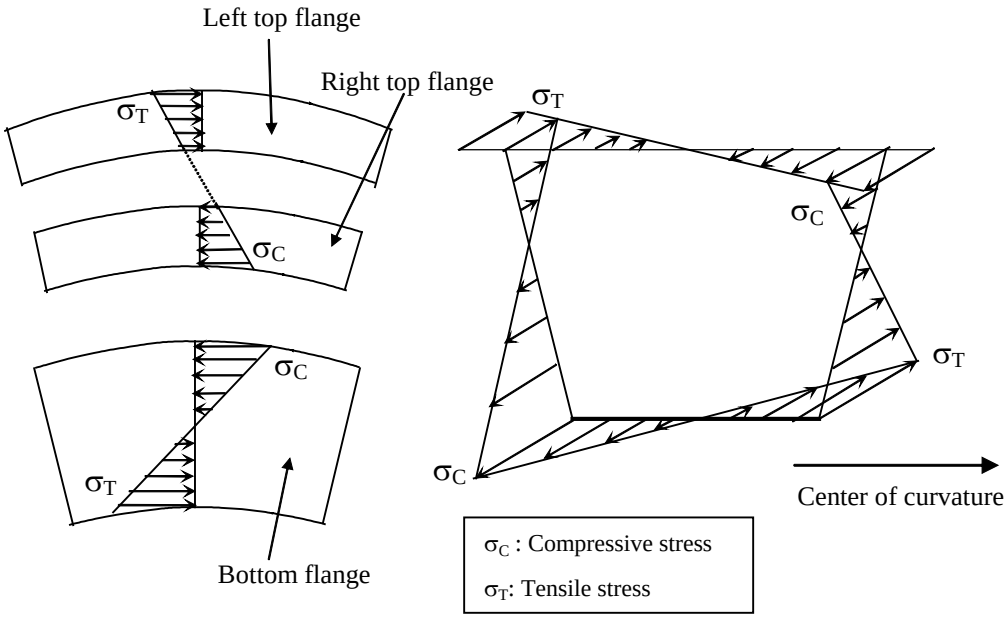

Figure 8.3 Distribution of distortional normal stress

8.2 UTRAP SOLUTION FOR DISTORTIONAL NORMAL STRESS

Total normal stresses in a curved girder consist of bending, localized, warping, and distortional normal stresses. The distortional normal stress can be determined by subtracting the bending, localized, and warping normal stresses from the total normal stresses.

Figure 8.4 shows the variation of total normal stresses along a 180-ft Model 1 girder with the radius of curvature of 600 ft, under a uniform load of 1 k/ft. The diagonal and strut areas used in this case are 0.525 in^2 and 4 in^2, corresponding to an equivalent plate thickness of 0.01 inches. In order to clearly show the distortional normal stress, no internal diaphragms are used in this case. Only total normal stresses at the junction of the web and the top flanges are shown. Normal bending stress σ_B is determined by taking the average of the total normal stresses in the left and the right flanges. Since a very close X-type panel spacing is used, the localized normal stress can be assumed to be negligible. The smooth variation of the total normal stresses shown in Figure 8.4 supports this assumption. Therefore, the deviation of the total normal stresses from the bending normal stress shown in Figure 8.4 is caused by the warping normal stress σ_W and the distortional normal stress σ_D.

Figure 8.5 shows the variations of σ_W and σ_D. The warping normal stress was obtained by subtracting σ_B from the total normal stress in the analysis using 2-ft diaphragm spacing, and σ_D was determined by subtracting σ_W from the total normal stress. Figure 8.5 shows that both the maximum σ_W and σ_D occur at the midspan. However, at any location, the sense (i.e. compression or tension) of σ_D is opposite to that of σ_W. Without using any internal diaphragms, it can be seen from Figure 8.5 that σ_D is significantly higher than σ_W and is 9.4 percent of the

bending normal stress. Since the sense of σ_D and σ_W are opposite to one another, the maximum additional stresses from both of those stresses to σ_B are only about 0.7 Ksi (as seen in Figure 8.4).

It should be emphasized that σ_D at the junction of the web and the top flange is not the largest. The maximum σ_D usually occurs at the junction of the web and the bottom flange. However in the construction stage, the top flanges are of more concern than the bottom flange because they are much smaller. For simplicity, only σ_D at the top flanges is presented. In the top flanges, σ_W at the junctions of the web and the top flanges can be predicted theoretically and verified by the UTRAP solutions as shown in Chapter 7. For simplicity, only σ_D at the junctions of the web and the top flanges is presented.

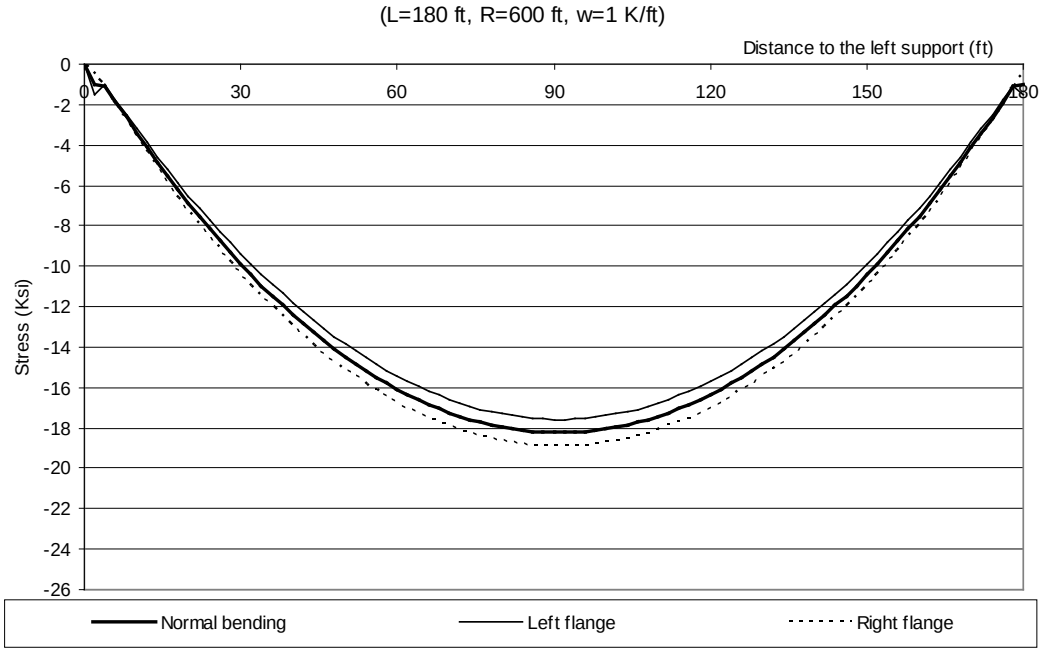

Figure 8.4 Variation of total and bending normal stresses - No internal diaphragm

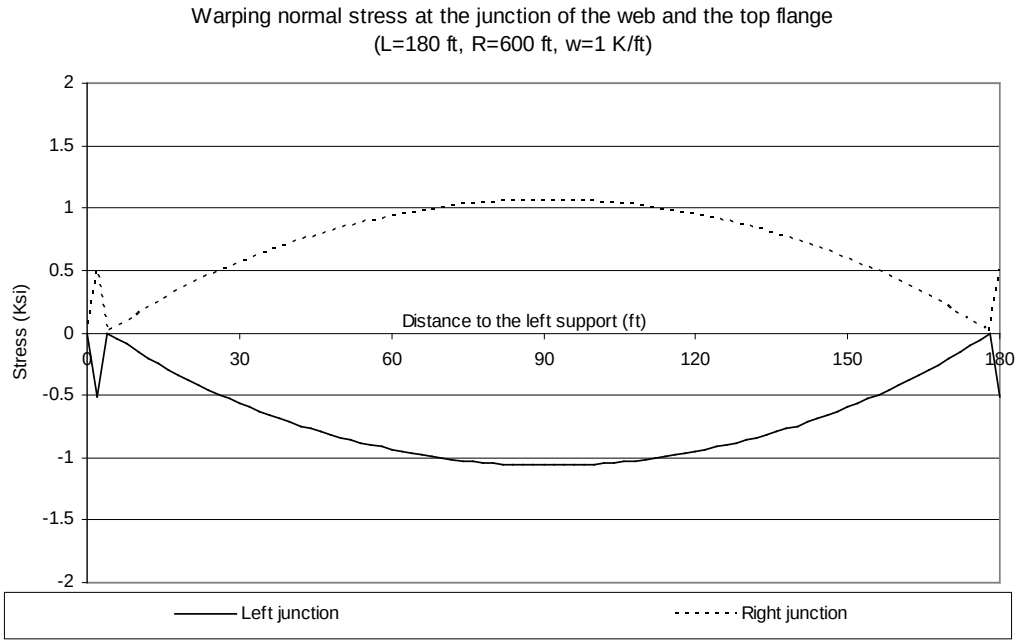

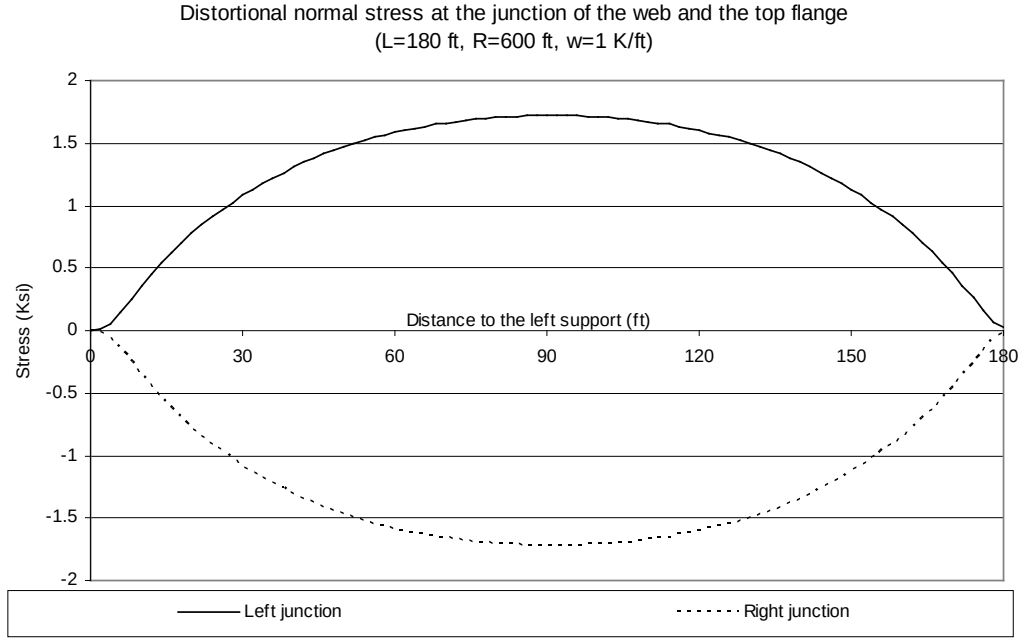

Figure 8.5 Variations of warping and distortional normal stresses - No internal diaphragm

8.3 EFFECT OF THE INTERNAL DIAPHRAGM

Figure 8.6 shows the variation of total normal stresses along the length with one internal diaphragm at the midspan. The top lateral bracing system and the equivalent plate thickness are kept the same as before (i.e. 2-ft panel X-type system with an equivalent plate thickness of 0.01 inches).

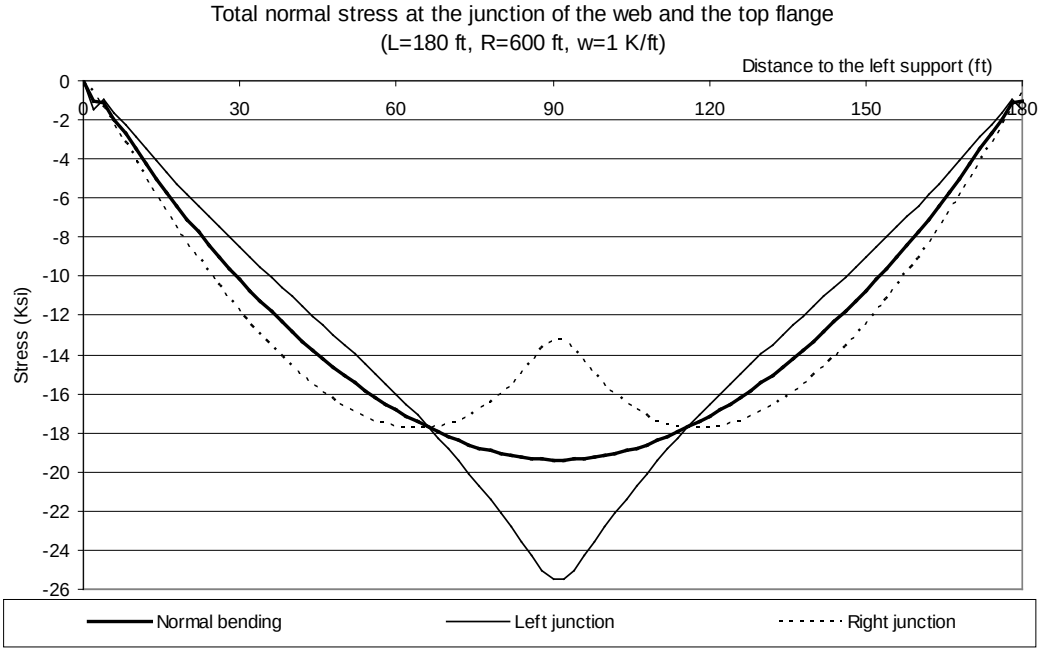

Figure 8.6 Variation of total and bending normal stresses - one internal diaphragm

Comparing the maximum total normal stresses in a girder without diaphragms (18.9 ksi) and with one internal diaphragm (25.5 ksi) shown in Figure 8.4 and Figure 8.6, respectively, the stress with one internal diaphragm is larger. It can also be observed that the presence of one internal diaphragm increases the maximum σ_B from 18.2 ksi to 19.4 ksi. However, the reason for this increase has not been resolved. Figure 8.7 shows variations of σ_W and σ_D. Since the top lateral

bracing systems are the same, σ_W shown in Figure 8.7 are the same as that shown in Figure 8.5 ; just the scale is different. From a lateral bending perspective, the top flanges in a girder with internal diaphragms behave as continuous girders, where the internal diaphragms serve as intermediate supports. Similar to the bending stress in a continuous girder, the maximum σ_D occurs at the internal diaphragm location, as shown in Figure 8.7. Unlike the case without any internal diaphragms, shown in Figure 8.5, the maximum σ_D with one internal diaphragm has the same sense (i.e. additive) as σ_W. The presence of the internal diaphragm generally reverses the sense of σ_D at its location. However, the deformation of a girder with an internal diaphragm is smaller than that without any internal diaphragm.

In order to study the effect of internal diaphragm area A_{id} on the σ_D, Figure 8.8 shows σ_D when there is one internal diaphragm at the midspan. Three different internal diaphragm areas, 1 in^2, 4 in^2, and 20 in^2, were used. Figure 8.8 shows that σ_D is not sensitive to the area of the internal diaphragm. The required minimum internal diaphragm area recommended by Heins (Eq.6.18) is 1.28 in^2.

8.4 PARAMETRIC STUDIES

Internal diaphragms are effective in reducing cross-section distortion. The maximum σ_D in the flanges occurs at the location of the internal diaphragm for girders with constant cross-section properties over the length. Therefore, it is important to determine internal diaphragm spacing that is effective in limiting cross-section distortion without inducing significant σ_D. This section studies the effect of equivalent plate thickness, web thickness, span length, radius of curvature, the central angle and cross-sectional dimensions at different diaphragm

spacing. Spacing recommendations from various sources were presented in Chapter 6.

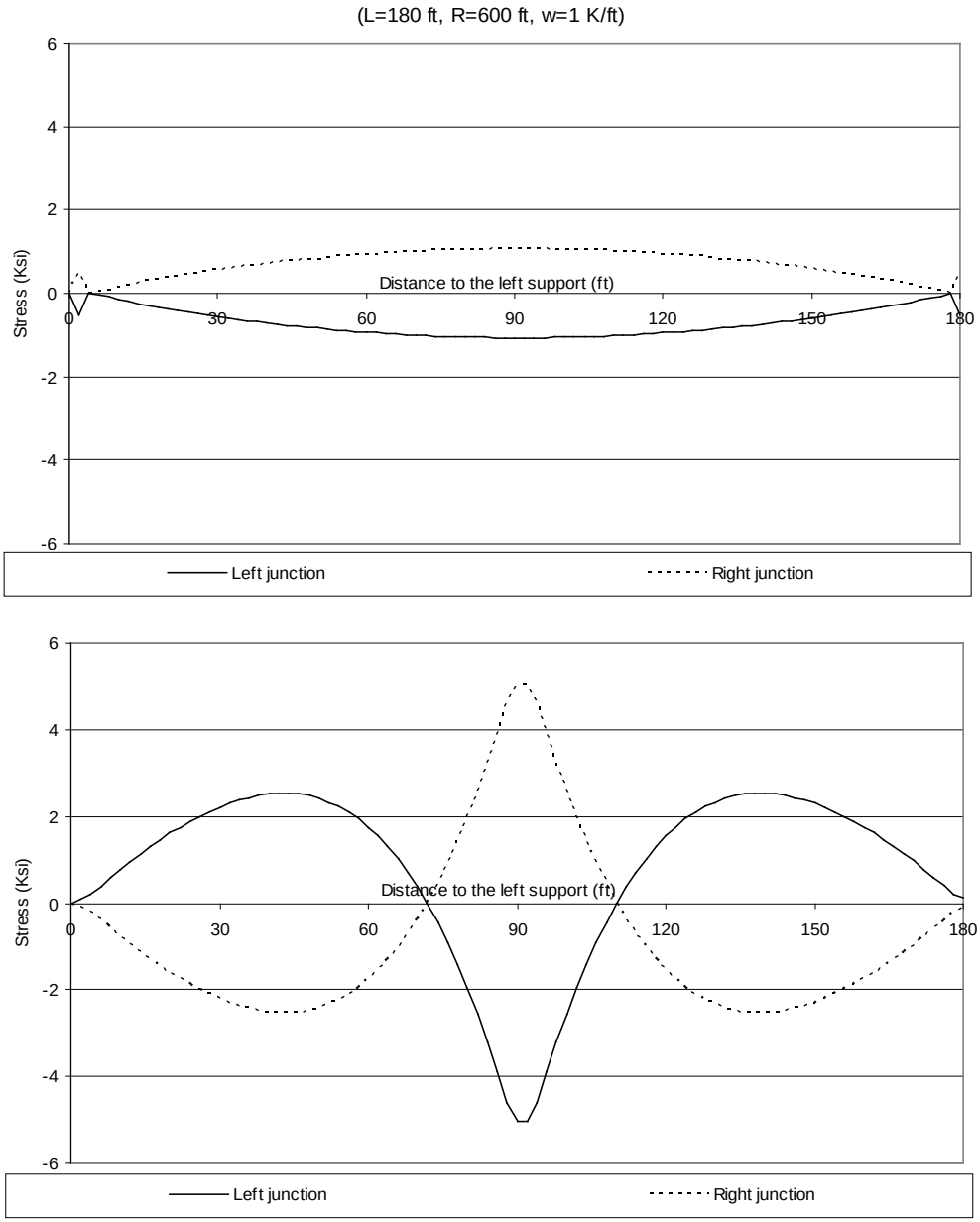

Figure 8.7 Variations of warping and distortional normal stresses - one internal diaphragm

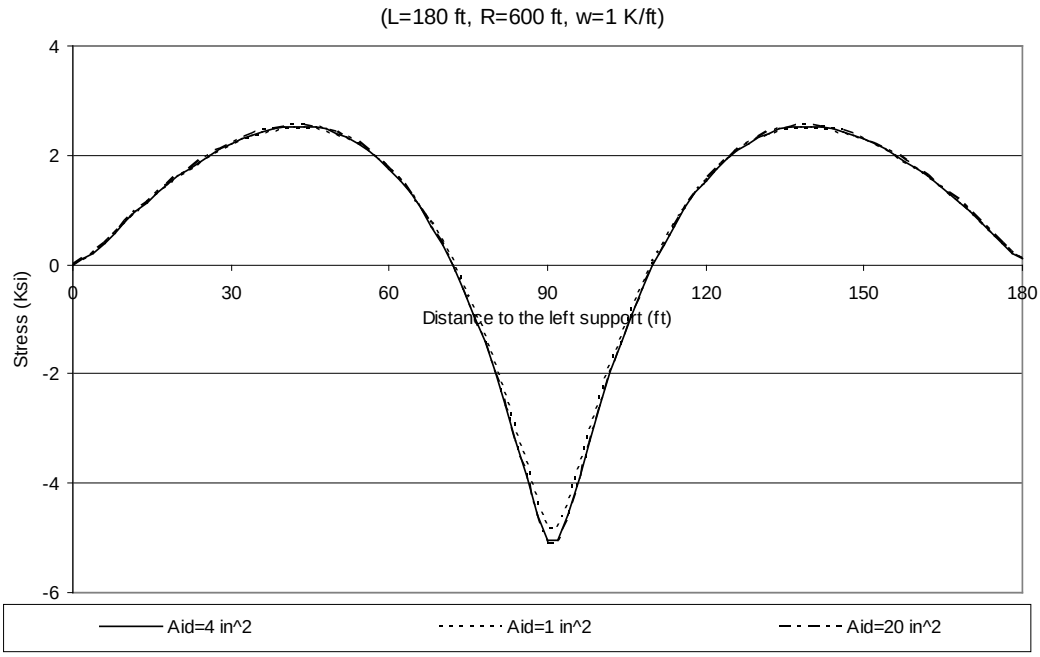

Figure 8.8 Effect of internal diaphragm area on the distortional normal stress

A parametric study investigated the effect of equivalent plate thickness t_{eq} on σ_D in a simply supported girder. Figure 8.9 shows the midspan σ_D (σ_D is maximum at midspan) as a function of internal diaphragm spacing. Figure 8.9 shows that σ_D is not sensitive to equivalent plate thickness.

The effect of changing the web thickness (i.e. changing the cross-section distortional stiffness) on σ_D was studied. Since increasing the web thickness will slightly change σ_B, the midspan distortional normal stress shown in Figure 8.10 is normalized by the midspan σ_B. The ratio of σ_D/σ_B decreases as a web thickness increases. The effect of changing the web thickness is only significant in a girder with a relatively large internal diaphragm spacing.

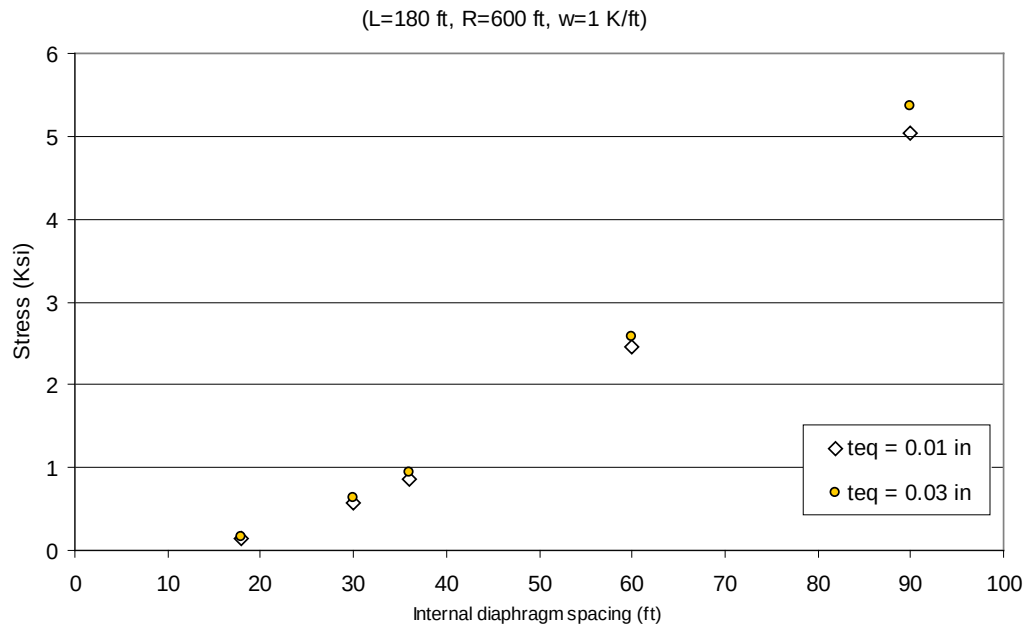

Figure 8.9 Effect of t_{eq} on the midspan distortional normal stress

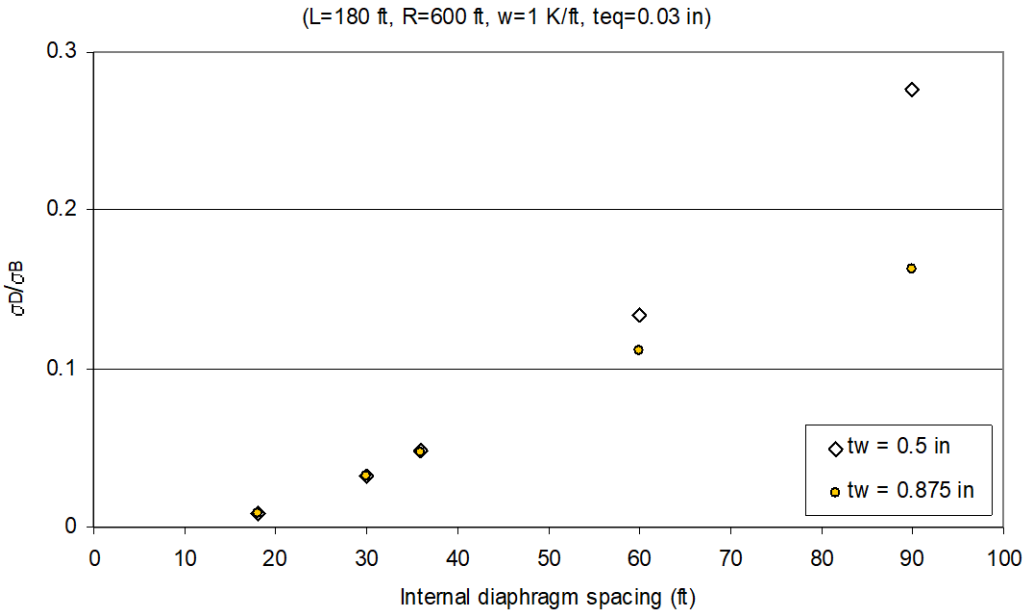

Figure 8.10 Effect of web thickness on the midspan distortional normal stress

The effects of changes in span length L and radius of curvature R on σ_D are shown in Figure 8.11. The same central angle was kept constant at 0.3 radians. The midspan total rotation to the span length and the midspan bending normal stress are kept about the same. Table 6-4 shows all analysis cases used in this study and Figure 8.11 shows the ratio of the midspan σ_D to the midspan σ_B for Model 1 with an equivalent plate thickness of 0.03 inches. The existing recommendations for the maximum ratio of the span length to the internal diaphragm spacing s/L are summarized in Table 6-5. Figure 8.11 shows that the ratio of σ_D/σ_B in the girders having similar central angles and s/L are similar, but the longer spans show slightly higher ratio. However, for $s/L \leq 0.15$, σ_D is insignificant. For $s/L \leq 0.20$, σ_D will be less than 5 percent of σ_B. For girders with $L \leq 120$ ft, an $s/L \leq 0.25$ will control the ratio of σ_D/σ_B to the 5 percent limit.

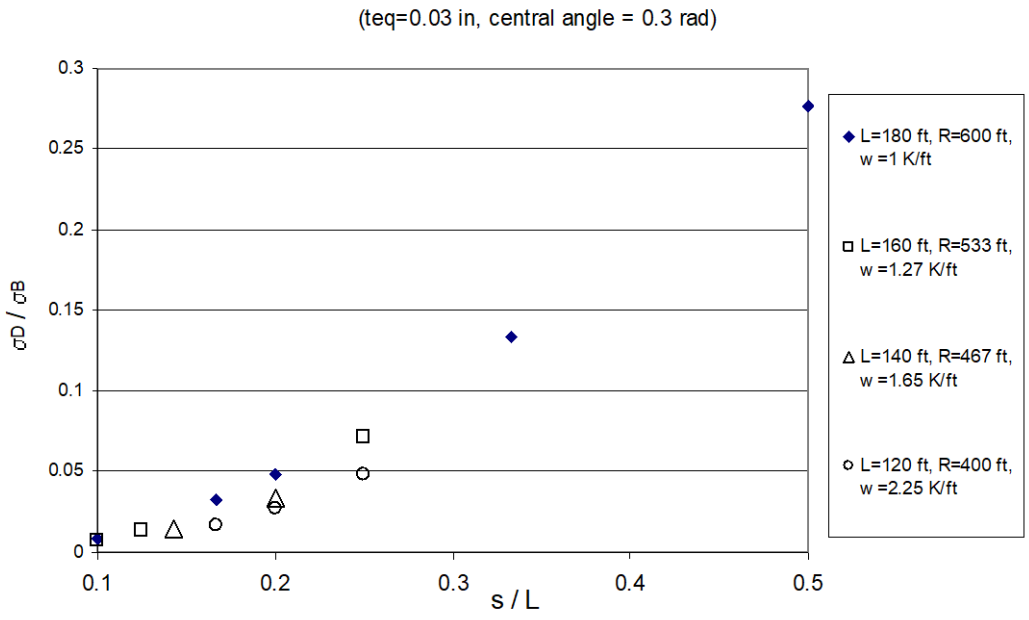

Figure 8.11 Ratio of the midspan distortional normal stress to the midspan bending normal stress

A fourth parametric study was performed to examine the effect of central angle on the ratio of σ_D/σ_B. Figure 8.12 shows ratios of σ_D/σ_B for a 180-ft Model 1 girder with central angles of 0.2, 0.3, and 0.4 radians. The trendline of each data set is also shown in Figure 8.12. Figure 8.12 shows that each data set can be best fitted using a second order equation. As the central angle increases, the ratio of σ_D/σ_B also increases. The explanation for this is that the lateral load component on a girder due to curvature ($M/(hR)$) becomes larger as the central angle increases, as shown in Table 8-1.

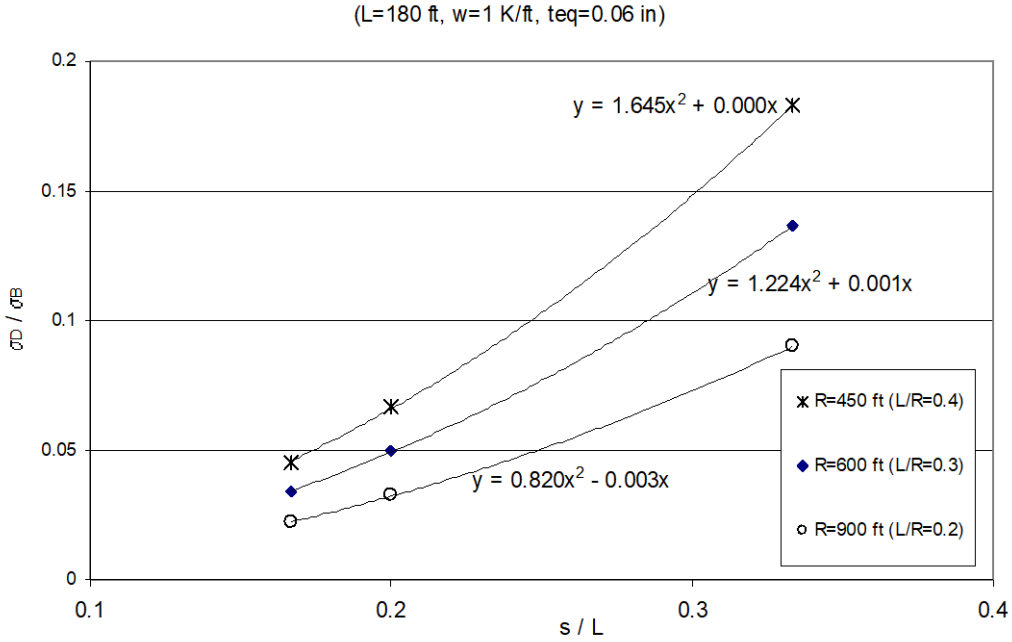

Figure 8.12 Effect of central angle on the ratio of distortional normal stress to bending normal stress

Decreasing the radius of curvature from 600 ft to 450 ft causes a 35% increase in the midspan lateral load due to curvature (from 1.36 to 1.83). As seen in Figure 8.12, the trendline equation for the 450-ft radius of curvature is 1.34 times larger than that for the 600-ft radius of curvature. In addition, the midspan lateral load in

a girder with the 900-ft radius of curvature is only 66% of that with the 600-ft radius of curvature. The trendline equation for the 900-ft radius of curvature is 0.67 of that for the 600-ft radius of curvature. The change in the ratio of σ_D/σ_B is linearly proportional to the change in the lateral load due to curvature. This suggests that the recommended internal diaphragm spacing developed based on parametric studies performed using a central angle of 0.3 radians can be modified by the ratio of the *M/(hR*) for other central angles. However, it is conservative to apply the recommendation for a girder with a larger central angle to that with a smaller central angle.

Table 8-1 Lateral load component due to curvature

Length, *L* (ft)	Radius, *R* (ft)	*L/R* (radian)	Midspan moment, *M* (k.ft)	Midspan lateral load due to curvature *(M/(hR))* (k/ft)
180	450	0.4	4118.4	1.83
	600	0.3	4088.2	1.36
	900	0.2	4066.8	0.904

A fifth parametric study considered cross-section dimensions. For this purpose, two different cross-sections, Model 1 and Model 3 (shown in Figure 1.5), are analyzed. The length, radius of curvature, equivalent plate thickness, and midspan bending normal stresses of both models are the same. Figure 8.13 shows the ratio of σ_D/σ_B in both Model 1 and Model 3. Figure 8.13 shows that the ratio of σ_D/σ_B is sensitive to the cross-section dimensions. The difference of the ratio between different girders increases as the internal diaphragm spacing becomes larger. Using an internal diaphragm spacing of 36 ft (s/L = 0.2), the ratio for Model 1 is not tremendously different than that for Model 3, and both are still less than 5 percent.

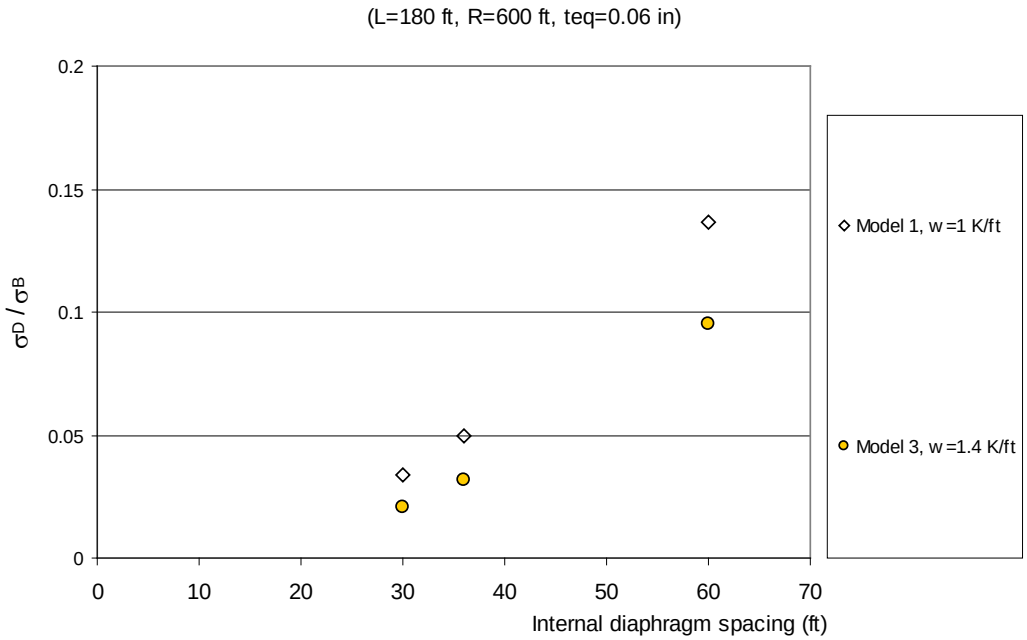

Figure 8.13 Ratio of the distortional normal stress to the bending normal stress in Model 1 and Model 3

8.5 DISTORTIONAL NORMAL STRESS IN A CONTINUOUS GIRDER

This section discusses distortional normal stress in a continuous girder and the applicability of the parametric study results of a simply-supported girder to a continuous girder. Figure 8.14 shows both σ_W and σ_D in a two-equal-span Model 1 girder. Since σ_W and σ_D are anti-symmetrical about the vertical centroidal axis, only the stresses at the junction of the left web and the left top flange are presented. The central angle of each span is 0.3 radians. The maximum compressive σ_B in this continuous girder is 10.6 ksi, as opposed to 19.5 ksi in a simply supported girder with the same length and central angle as those in each span of the continuous girder.

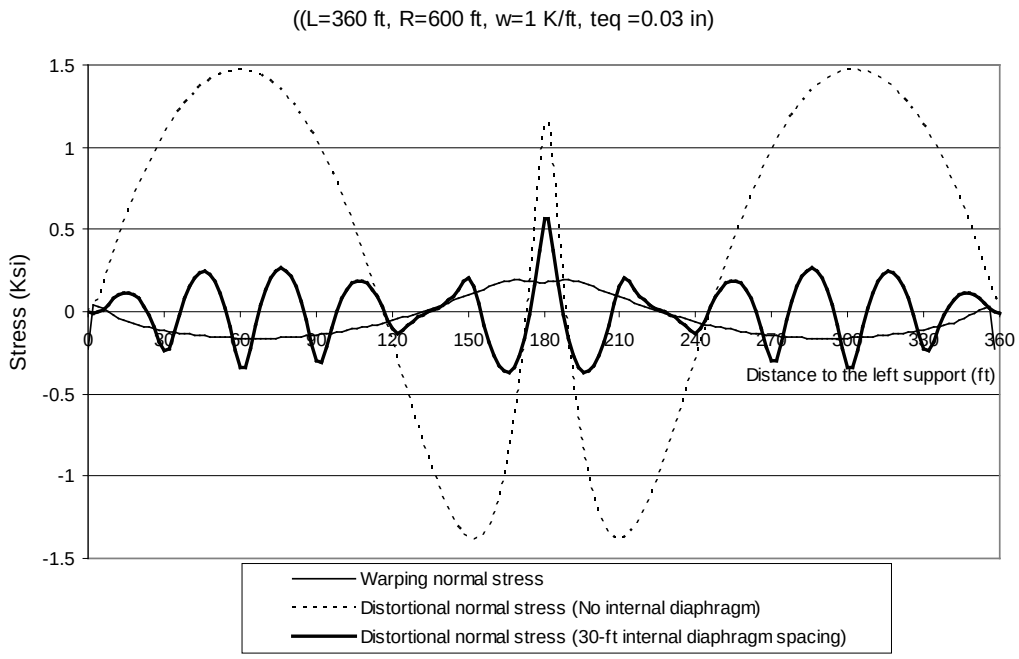

Figure 8.14 Warping and distortional normal stress in a two-equal-span continuous girder

Like in a simply-supported girder, the sense of σ_D in a continuous girder without any internal diaphragm is generally opposite to that of σ_W. It can be seen from Figure 8.14 that the maximum σ_D in a girder without any internal diaphragms is several times larger than the maximum σ_W. The presence of the internal diaphragms significantly reduces the maximum σ_D. However, at the locations of the internal diaphragms, the sense of the σ_D is the same as that of σ_W.

Figure 8.14 shows that the maximum σ_D in a continuous girder with 30-ft internal diaphragm spacing is 0.37 ksi. This stress is significantly smaller than the maximum σ_D of 0.63 ksi in a simply supported girder with the same length and central angle as those in each span of the continuous girder. Since the maximum

bending normal stress in a continuous girder is also smaller, the ratios of σ_D / σ_B in both girders are the same.

Figure 8.15 shows σ_D and the ratio of σ_D/σ_B in a two-equal-span continuous girder and a simply-supported girder. The length and central angle of each span in the continuous girder are the same as those in the simply-supported girder. Figure 8.15 shows that the maximum σ_D in a continuous girder is smaller than that in a simply-supported girder. However, with a reasonable internal diaphragm spacing, the ratios of σ_D/σ_B in both girders are practically the same. The parametric study results of a simply-supported girder can then be extended to a continuous girder, provided that the length and central angle of each span of the continuous girder are the same as those of the simply-supported girder. As the central angle increases, the ratio of σ_D/σ_B also increases. Therefore, it is conservative to apply the results of the parametric studies performed on a girder with a larger central angle to that with a smaller central angle.

8.6 DEVELOPMENT OF DESIGN RECOMMENDATION

8.6.1 Analytical modeling

As seen in Figure 8.14, the variation of distortional normal stress between two internal diaphragms can be simplified as that in a fixed-fixed beam. Figure 8.16 shows simplification of the top and bottom flanges of a curved girder between two internal diaphragms under the distortional load due to curvature w_T and w_B, respectively. Each top flange is assumed to carry half of w_T. Even though the variations of w_T and w_B follow the variation of bending moment diagram, herein, the variations are assumed to be constant.

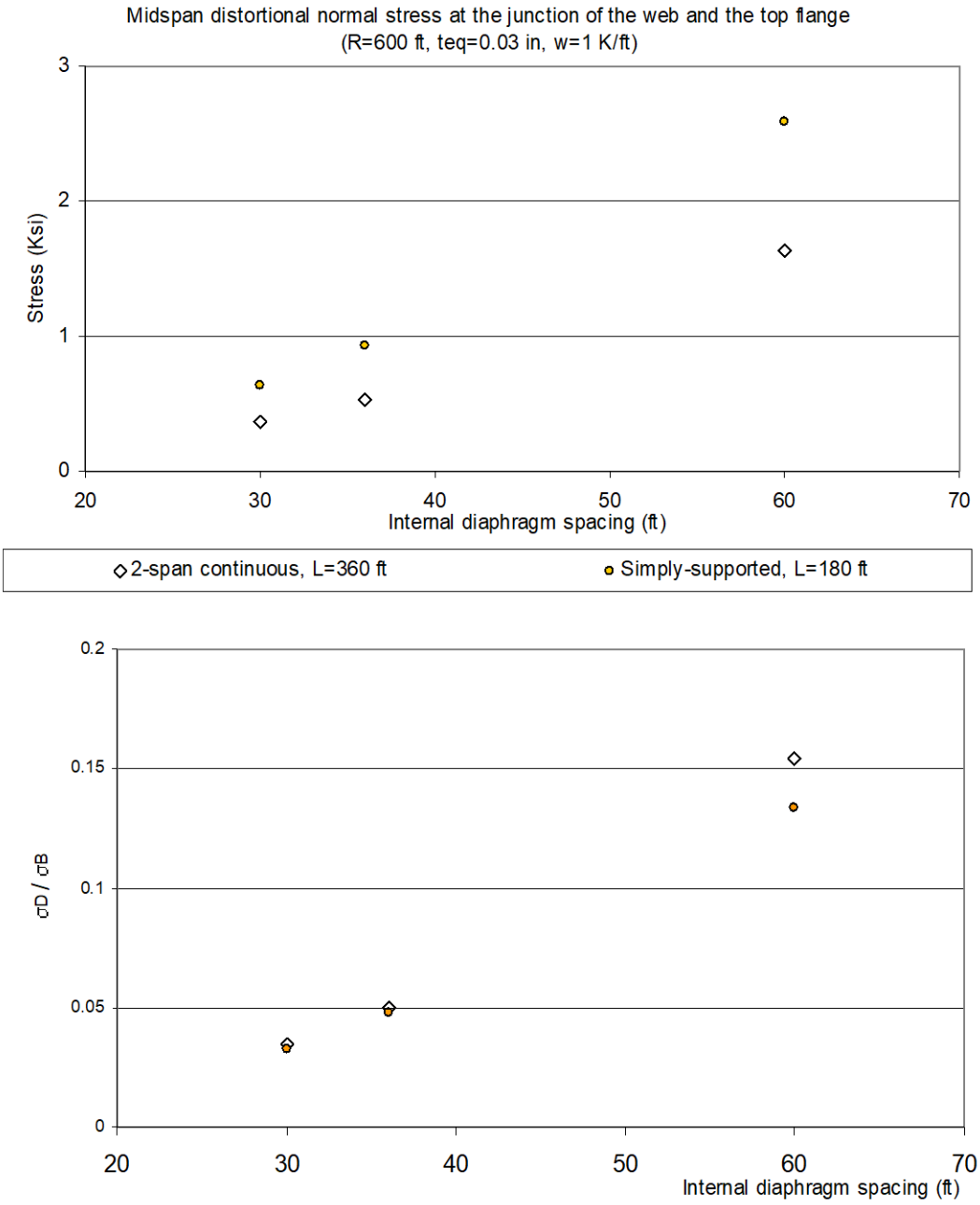

Figure 8.15 Distortional normal stress and the ratio of distortional to bending normal stresses in a continuous and a simply-supported girder

The maximum lateral bending moment in the top and bottom flanges are $\frac{1}{12} w_T s^2$ and $\frac{1}{12} w_B s^2$, respectively, at the internal diaphragm locations. The distortional normal stress due to this bending moment is denoted σ_D *global*. On the top flanges, there is an additional stress σ_D *local* because the w_T can bend the top flanges between strut locations. The distortional normal stresses at the internal diaphragm location at the tip of the top and bottom flanges $\sigma_{D,T}$ and $\sigma_{D,B}$, respectively, can be derived as follows:

$$\sigma_{D,T} = \sigma_D \textit{ global} + \sigma_D \textit{ local}$$

$$\sigma_{D,T} = \frac{\left(\frac{1}{12} w_T s^2\right)\left(\frac{a}{2} + \frac{b_{tf}}{2}\right)}{2\left(\frac{1}{12} t_{tf} b_{tf}^{\ 3} + \left(t_{tf} b_{tf}\right)\left(\frac{a}{2}\right)^2\right)} + \frac{\left(\frac{1}{12}\frac{w_T}{2} s_p^{\ 2}\right)\left(\frac{b_{tf}}{2}\right)}{\frac{1}{12} t_{tf} b_{tf}^{\ 3}} \tag{8.1}$$

$$\sigma_{D,B} = \frac{\left(\frac{1}{12} w_B s^2\right)\left(\frac{b}{2}\right)}{\frac{1}{12} t_{bf} b^3} \tag{8.2}$$

where t_{tf} and t_{bf} are the thickness of the top and bottom flanges, respectively.

Figure 8.17 shows UTRAP solutions for σ_D on the top and bottom flanges of a 180-ft Model 1 girder with a 6-ft panel of the X-type system and a 30-ft internal diaphragm spacing. UTRAP solutions for σ_D were obtained by subtracting the total normal stresses with a 2-ft internal diaphragm spacing from those with a 30-ft spacing. Since the girder is symmetrical about the midspan, the stresses are shown for only half of the girder length. Node locations are shown in Figure 7.6. Figure 8.17 shows that the variations of σ_D on the top flanges are much more complex due to the presence of the top lateral bracing system. From

the σ_D at nodes 11 through 14 and at nodes 19 through 22, σ_D at the tips of the top flanges and at the edge of the bottom flange can be calculated by assuming a linear stress distribution.

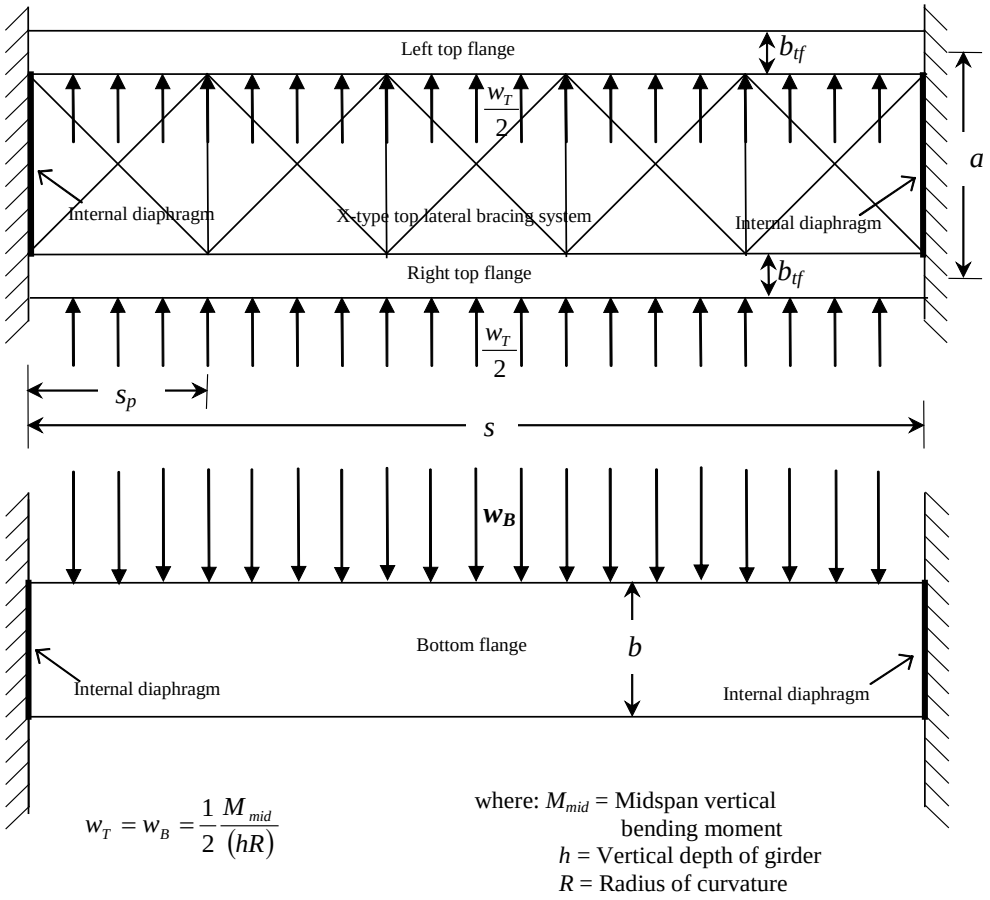

Figure 8.16 Simplified model of top and bottom flanges between two internal diaphragms

Figure 8.18 shows the magnitude of σ_D at the junction of the top flange and the web obtained from the analytical formula and the UTRAP solutions. Eq.8.1 was modified to predict σ_D at the junction of the top flange and the web by

ignoring the σ_D *local* and eliminating the $b_{tf}/2$ term in the numerator of σ_D *global*. Figure 8.18 shows that the analytical formula can predict the magnitude of σ_D at the junction of the top flange and the web well.

Figure 8.19 shows σ_D at the tip of the top flanges obtained from Eq.8.1 and the UTRAP solutions. Even though the maximum σ_D at the tip of the left top flange is compressive, only the absolute value is presented. The analytical solutions accounting for only σ_D *global* and both σ_D *global* and σ_D *local* are presented. The distortional normal stress at the tip of the top flanges can be more than double that at the junction of the top flange and the web. Figure 8.19 shows that the magnitudes of σ_D at the tip of the left top flange are larger than those in the right top flange. The difference in magnitudes between the two is approximately constant for different internal diaphragm spacings. Figure 8.19 also shows that the analytical formula underestimates the magnitude of the distortional stress. The analytical formula including the global and local effects can only account for 60 percent of the maximum σ_D at the tip of the top flange. Since the σ_D *global* analytical formula can predict the σ_D at the junction of the top flange and the web well as shown in Figure 8.18, the additional σ_D at the tip of the top flange that cannot be calculated analytically must be due to the local effect. With an internal diaphragm spacing of less than 40 feet, the unknown source of σ_D is small (i.e. less than 1.5 ksi).

Figure 8.20 shows σ_D at the edge of the bottom flanges obtained from Eq.2 and the UTRAP solutions. The senses of σ_D at both edges of the bottom flange are opposite, whereas the magnitudes are the same. Figure 8.20 shows that the analytical formula can predict the stress well. The distortional normal stress at the edge of the bottom flange is smaller than that at the tip of the top flange.

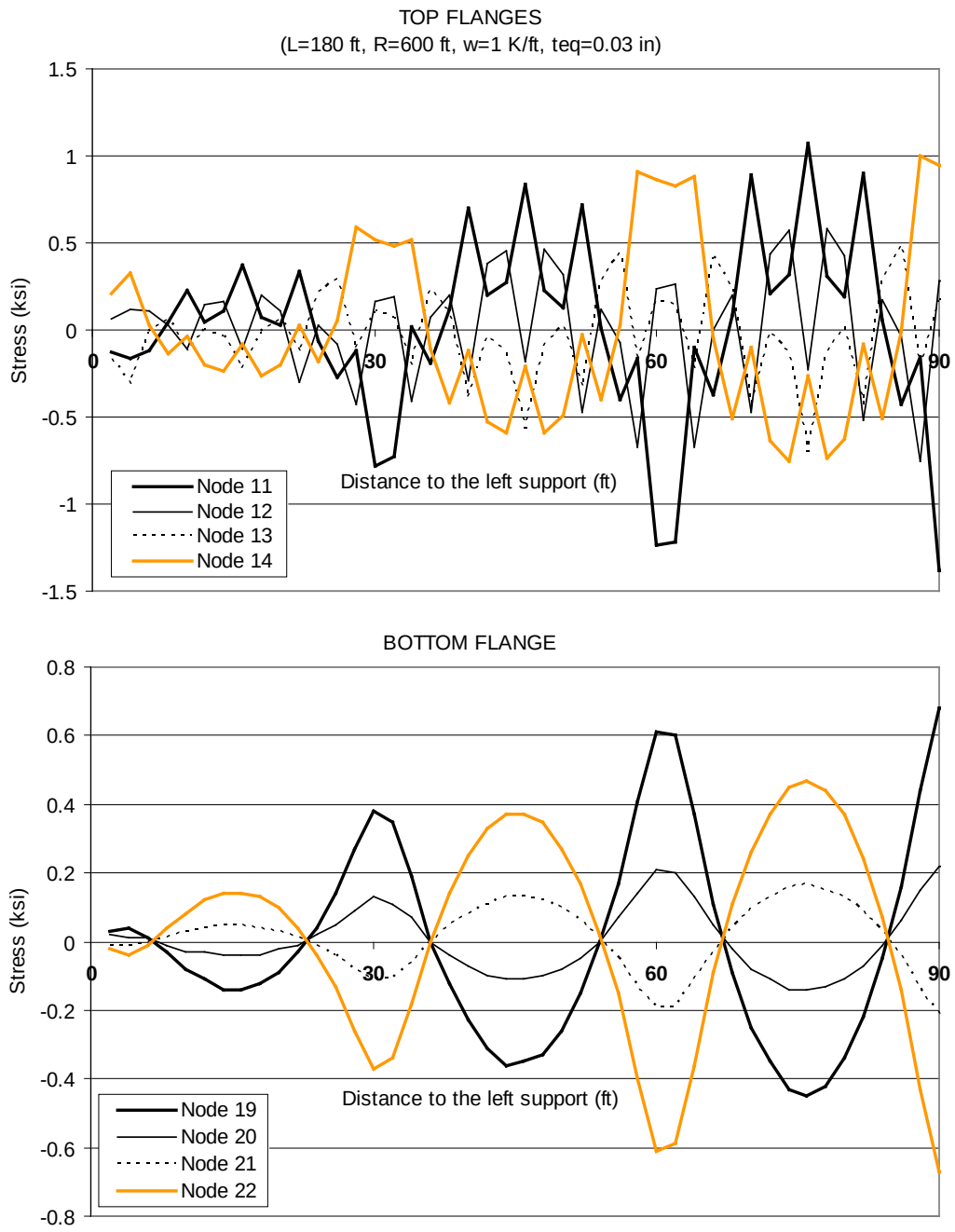

Figure 8.17 Distortional normal stresses on the top and bottom flanges

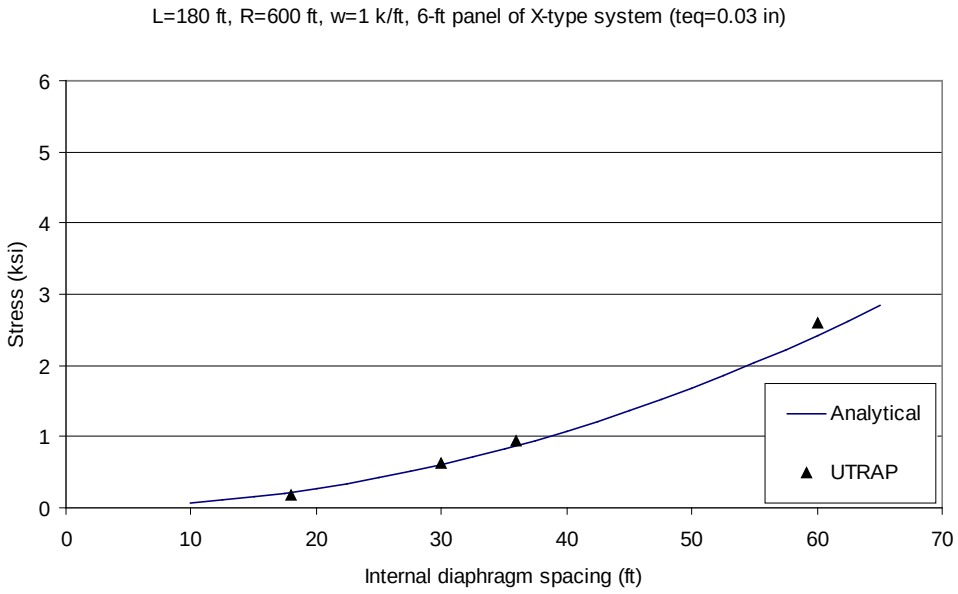

Figure 8.18 Distortional normal stress at the junction of the top flange and the web

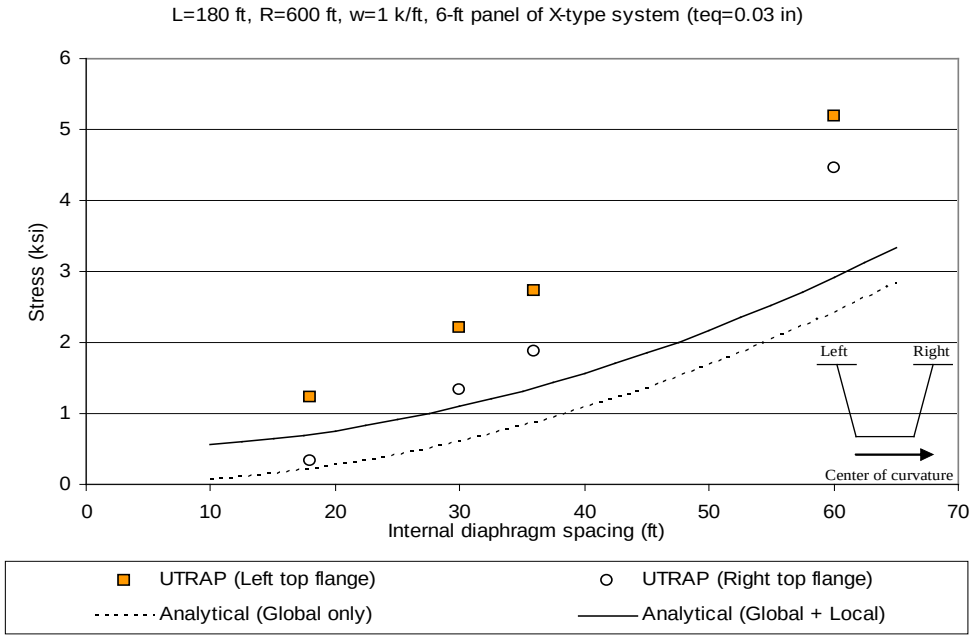

Figure 8.19 Distortional normal stresses at the tip of the top flange

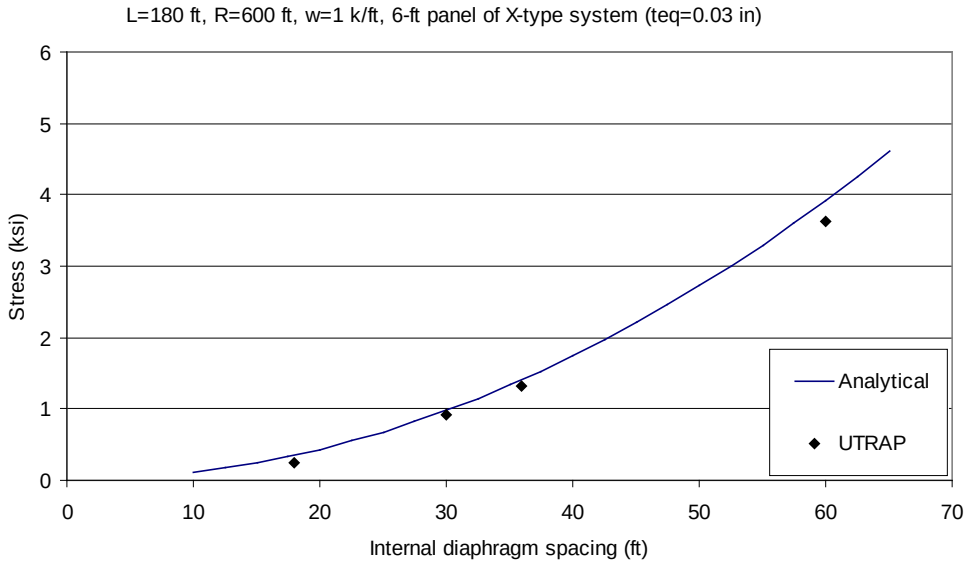

Figure 8.20 Distortional normal stress at the edge of the bottom flange

As shown in Figure 8.19, Eq.8.1 can predict only 60 percent of σ_D at the tip of the top flange. Figure 8.21 shows σ_D at nodes 11 though 14 that cannot be predicted analytically. The line connecting each data point is only for clarity and it does not suggest that the stress varies linearly. Those σ_D were obtained by subtracting the analytical prediction (using σ_D *global* and σ_D *local*) from the UTRAP solution for σ_D shown in Figure 8.17. Figure 8.21 shows that the variation of σ_D that cannot be predicted analytically is complicated and the mechanism or forces causing that variation cannot be explained.

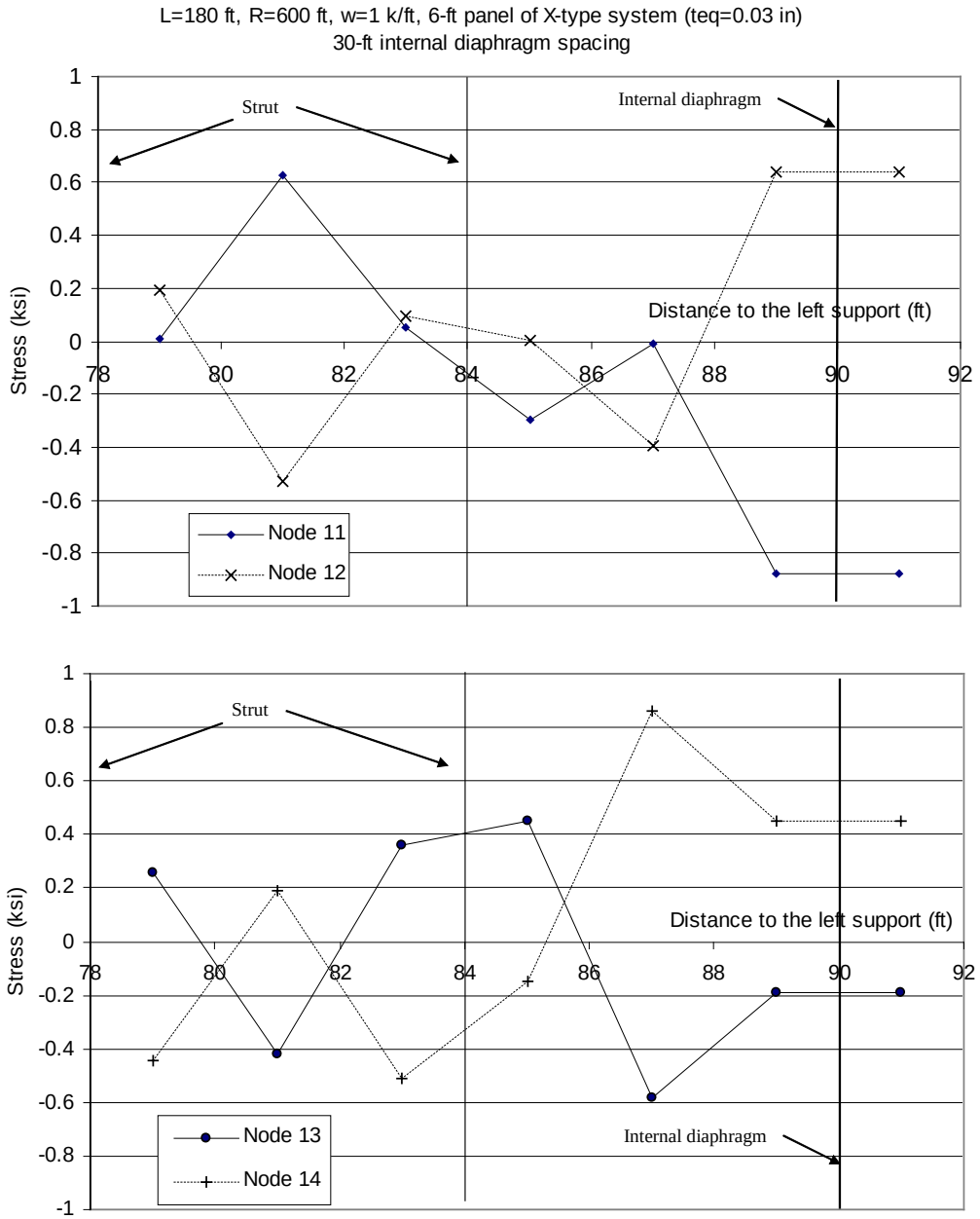

Figure 8.21 Variation of distortional normal stresses that cannot be predicted analytically

8.6.2 Design recommendation and comparison to the existing recommendation

Based on the results of parametric studies presented in this chapter, the maximum recommended ratio of s/L to control σ_D at the junction of the web and the top flange to less than 5 percent of σ_B is 1/5. For girders with $L \leq 120$ ft, an $s/L \leq 1/4$ will control the ratio of σ_D/σ_B to the 5 percent limit. These recommendations can be applied to a girder within the limit of parametric studies performed in this chapter (i.e. the maximum length and central angle are 180-ft and 0.3 radians, respectively, and the width to depth ratio is about 1). For a girder outside the limit of the parametric study, this chapter presented a simplified analytical method to calculate the distortional normal stress as a function of internal diaphragm spacing and cross-section dimensions. In order to use the analytical formula for predicting σ_D at the tip of the top flange, the additional stress of 1 to 2 ksi must be added to account for the distortional normal stress that cannot be predicted analytically.

Comparing the existing recommendation shown in Table 6.5 to the parametric study results shown in this chapter, the s/L = 1/4 recommended by Green, Siddiqui, and Ng results in a σ_D larger than 5 percent of σ_B for longer spans. The recommended ratio of 1/5 will result in an internal diaphragm spacing in a girder longer than 150 ft that is larger than the maximum spacing of 30 feet recommended by AASHTO 2003. However, as seen in Figure 8.11, relaxing the AASHTO maximum spacing requirement and the recommended spacing from Yabuki, Arizumi, Nakai, Yoo, and Heins will not adversely affect the ratio of σ_D/σ_B. For a girder with a span of 120 feet, the recommended internal diaphragm spacing is 30 feet, which is the same as the AASHTO maximum spacing requirement.

One of the reasons why Yabuki, Arizumi, Nakai, Yoo, and Heins recommended a closer internal diaphragm spacing is that they used the maximum σ_D at the bottom flange, which is larger than that in the junction of the web and the top flange. One must realize that the maximum σ_B in a typical trapezoidal girder occurs at the top flange. Therefore, herein the ratio of σ_D/σ_B is taken at the junction of the web and the top flange, instead of at the bottom flange. This way, the recommended internal diaphragm spacing is larger than that proposed by other authors.

A maximum ratio of σ_D/σ_B of 5 percent, as opposed to 10 percent in the current specification, is selected in order to account for the fact that the maximum σ_D is higher than the σ_D at the junction of the web and the top flange. In the top flange, the maximum σ_D occurs at the tip. It should be noted that the Japanese Specification for Highway Bridges also limits the distortional stress to 5 percent of the bending stress (Nakai and Yoo 1988).

Figure 8.22 shows the required internal diaphragm spacing *s* in a 180-ft Model 1 girder with different radius of curvature from the proposed recommendation, analytical methods, and several existing recommendations. The proposed recommendation of the maximum ratio *s/L* of 1/5 is valid when the central angle is less than 0.3 radians. The required *s* based on the proposed recommendation is smaller than that based on the formulas to limit σ_D/σ_B at the junction of the top flange and the edge of the bottom flange to 5 percent and 10 percent, respectively. The required *s* based on the analytical formula to limit σ_D at the junction of the top flange to 5 percent of σ_B is about 45 percent larger than Heins' recommendation and 10 percent smaller than the requirement to limit σ_D/σ_B at the edge of bottom flange to 10 percent. For the radius of curvature less than 650 ft, the required s based on the analytical formula to limit σ_D/σ_B at the

junction of the top flange to 5 percent is smaller than Green, Siddiqui and Ng's recommendation.

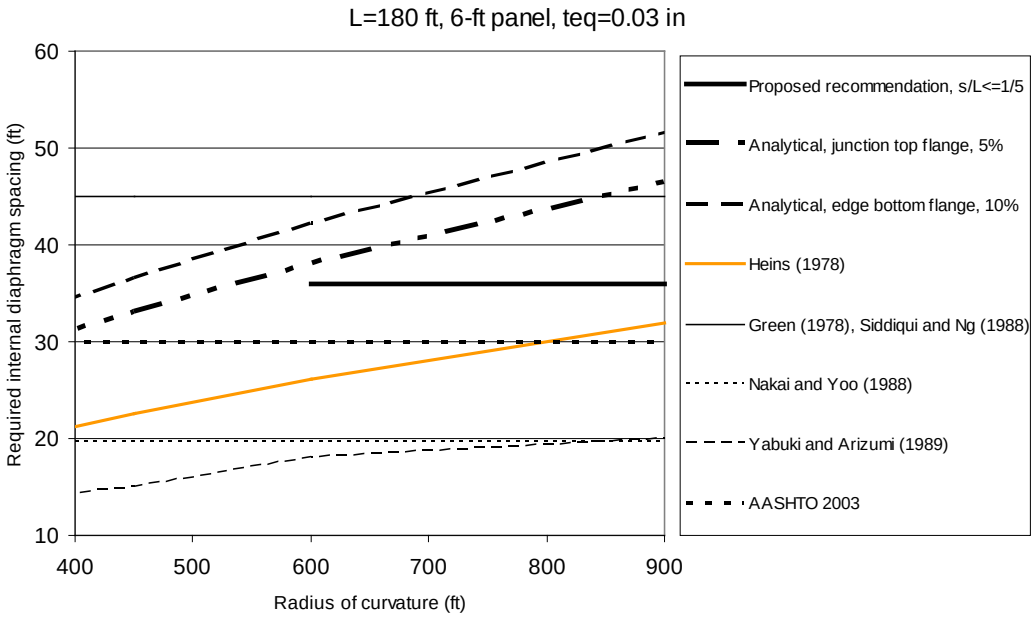

Figure 8.22 Proposed and existing recommendations for diaphragm spacing

8.7 SUMMARY

This chapter showed that the distortional normal stress in a curved girder under a symmetrical uniform load occurs because of the lateral movement of the top and bottom flanges (i.e. second order effect). The distribution of the distortional normal stress is anti-symmetrical with respect to the vertical centroidal axis.

In a girder without any internal diaphragms, the sense of the distortional normal stress is opposite to that of the warping normal stress. The presence of an internal diaphragm generally reverses the sense of the distortional normal stress at

its location. In addition, the maximum distortional normal stress occurs at the internal diaphragm location. The distortional normal stress is not sensitive to the area of the internal diaphragm or to the equivalent plate thickness.

In order to keep the distortional normal stress at the junction of the web and the top flange to less than 5 percent of the bending normal stress, the recommended maximum ratio of s/L is 1/5. Since the ratio of σ_D/σ_B in a shorter girder is smaller, it is not necessary to use an internal diaphragm spacing less than 30 feet. The recommended internal diaphragm spacing can be extended to a continuous girder, provided that the length and central angle of each span are the same as those of the simply-supported girder. This recommendation is valid for a girder with a maximum length and central angle of 180 ft and 0.3 radians, respectively, and a width to depth ratio of about 1. For a girder outside these limits, a simplified analytical method to calculate the distortional normal stress as a function of internal diaphragm spacing and cross-section dimensions was developed. The analytical formula can very accurately predict σ_D at the junction of the web and the edge of the bottom flange. However, in order to use the analytical formula for predicting σ_D at the tip of the top flange, an additional stress of 1 to 2 ksi must be added to account for the distortional normal stress that cannot be predicted analytically.

CHAPTER 9
Top Lateral Bracing Force

Helwig and Fan (2000) indicated that forces developed in the top lateral bracing system result from three components:

- Horizontal component of the applied load due to sloping webs
- Vertical bending
- Torsional moment

This chapter presents methods to estimate the force developed in top lateral bracing system due to each component. In order to calculate total forces in the top lateral bracing system, the force developed from each component can then be added together using principal of superposition.

The magnitude of force developed in top lateral bracing system depends on the type of system. Three different top lateral bracing systems, X-type, Alternating-Diagonal, and Single-Diagonal, are examined in this chapter. In order to verify all analytical formulas to predict top lateral bracing forces, UTRAP was used to analyze a simply supported straight and curved girder with the three different top lateral bracing systems. Results from UTRAP will be compared to those from Helwig and Fan.

9.1 TOP LATERAL BRACING FORCE FROM THE HORIZONTAL COMPONENT OF THE APPLIED LOAD

Sloping webs of a trapezoidal box girder induce a horizontal component acting on the top flange, as shown in Figure 5.9, which then induces forces on top lateral bracing system. The horizontal component of the applied load w_H is found to be $\frac{w}{2}\tan(\alpha)$. Helwig and Fan indicated that the top flanges carries the entire horizontal component of the applied load, instead of the top and bottom flanges carrying half of the horizontal component of the applied load.

Under a uniform loading *w*, the total horizontal component of the applied load in each panel of the top lateral bracing system with length *s* (strut spacing) is $w_H s$. Which truss member carries this total horizontal component depends on the type of top lateral bracing system.

9.1.1 X-type top lateral bracing system

In an X-type lateral bracing system, both the struts and the diagonals work together to carry the horizontal component of the applied load w_H. Figure 9.1 shows an elongation of both struts and diagonals due to w_H. For simplicity, it is assumed that the only movement is A-A'.

Neglecting longitudinal deformation of top flanges, the elongation of strut is Δ_s and the elongation of diagonal is Δ_d. Their relation can be expressed as:

$$\Delta_d = \Delta_s \sin(\theta) \tag{9.1}$$

Due to elongation Δ_s and Δ_d, the axial force in the struts $F_{s,H}$ and the axial force in the diagonals $F_{d,H}$ can be found as follows:

$$F_{s,H} = \frac{EA_s}{a}\Delta_s \tag{9.2}$$

$$F_{d,H} = \frac{EA_d}{d}\Delta_d = \frac{EA_d}{d}\Delta_s \sin(\theta) \tag{9.3}$$

where E is modulus of elasticity. Writing equilibrium equation in y-direction at joint A will yield the following equations:

$$F_{s,H} + 2F_{d,H}\sin(\theta) = w_H s$$

$$\frac{EA_s}{a}\Delta_s + 2\frac{EA_d}{d}\Delta_s \sin(\theta)\sin(\theta) = w_H s$$

$$\Delta_s = \frac{w_H s}{\frac{EA_s}{a} + \frac{2EA_d}{d}\sin^2(\theta)} \tag{9.4}$$

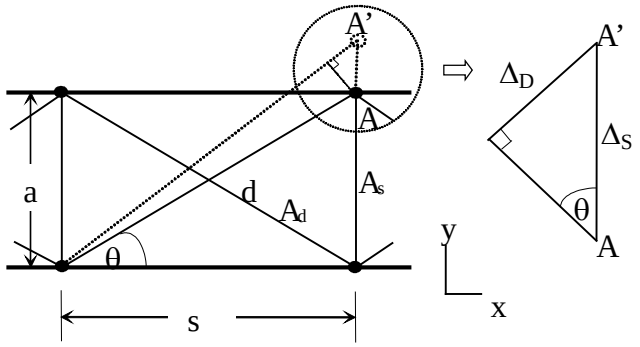

Figure 9.1 Elongation of both struts and diagonals

Final expressions of axial force in the struts and diagonals due to the horizontal component of the applied load can be found by substituting Eq.9.4 into Eqs.9.2 and 9.3 and they are expressed as follows:

$$F_{s,H} = \frac{A_s}{A_s + 2A_d \sin^3(\theta)} w_H s \tag{9.5}$$

$$F_{d,H} = \frac{A_d \sin^2(\theta)}{A_s + 2A_d \sin^3(\theta)} w_H s \tag{9.6}$$

9.1.2 Alternating-Diagonal top lateral bracing system

In an Alternating-Diagonal top lateral bracing system, the diagonal forces due to the sloping web are usually significantly smaller than strut forces that resist the horizontal component. As a result, struts are assumed to carry the entire horizontal component of the load and there will be no force induced in diagonal. Mathematically, this can be expressed as:

$$F_{s,H} = w_H s \tag{9.7}$$

$$F_{d,H} = 0 \tag{9.8}$$

9.1.3 Single-Diagonal top lateral bracing system

Strut and diagonal forces induced in a Single-Diagonal top lateral bracing system due to the horizontal component of the applied load can be assumed similar to those in an Alternating-Diagonal top lateral bracing system (i.e. Eqs.9.7 and 9.8 apply).

9.2 TOP LATERAL BRACING FORCE DUE TO VERTICAL BENDING

In a simply supported girder under uniformly applied gravity load, a top fiber will shorten and a bottom flange will lengthen. The force developed in top lateral bracing system is due to shortening of top fiber and compatibility between top flanges and top lateral bracing system. The magnitude of the induced force is

a function of the stiffness of the top lateral bracing system and the bending strain at the level of top lateral bracing system. Herein, top lateral bracing members are conservatively assumed to be connected directly to the top flanges. A more general solution to predict the top lateral bracing forces for cases where the top lateral bracing system is located significantly below top flanges can be found in Helwig and Fan.

In order to observe the deflected shape of each system, SAP 2000 computer software was used to analyze each top lateral bracing system under the loading that mimics the vertical bending moment diagram. Figure 9.2 shows the boundary conditions and loading conditions of a planar truss model of the top flanges and top lateral bracing system of a trapezoidal box girder. The flanges are represented by the chords of the truss. Joints 1, 18, 19, and 36 (at girder ends) can only move in the Y-direction and joints 10 and 28 (at midspan) can only move in the X-direction. All loads are applied as a concentrated load at a joint, except loads between joints 9 and 11 and between joints 27 and 29, which are applied as a uniform load. These loads can be calculated by taking a cut at joint location, determining the bending moment at that location, calculating the force at that location by dividing bending moment at that location by the girder depth, and determining what incremental load needed to be applied at that joint to develop total force at that joint. In modeling, all bracing member connections are assumed to be pin-connections (i.e. all diagonals and struts have moment releases at both ends of each member). The two-dimension analysis option in SAP 2000 was used in analyzing the model.

Figure 9.3 shows an example of the required loading conditions to simulate the effect of vertical bending for the 180-foot simply-supported straight girder of Model 1, under a uniformly distributed load of 1 k/ft.

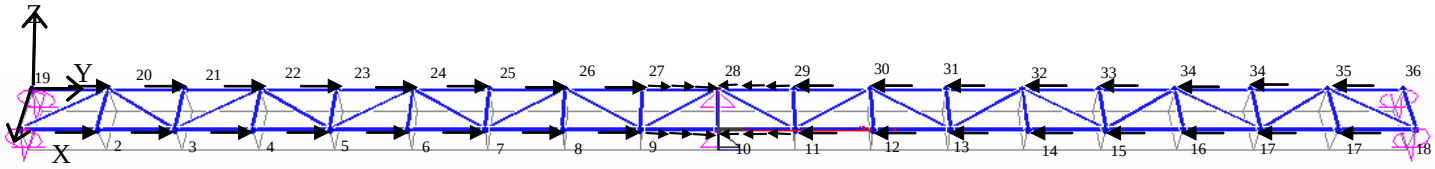

Figure 9.2 SAP 2000 Model of top flanges and top lateral bracing system

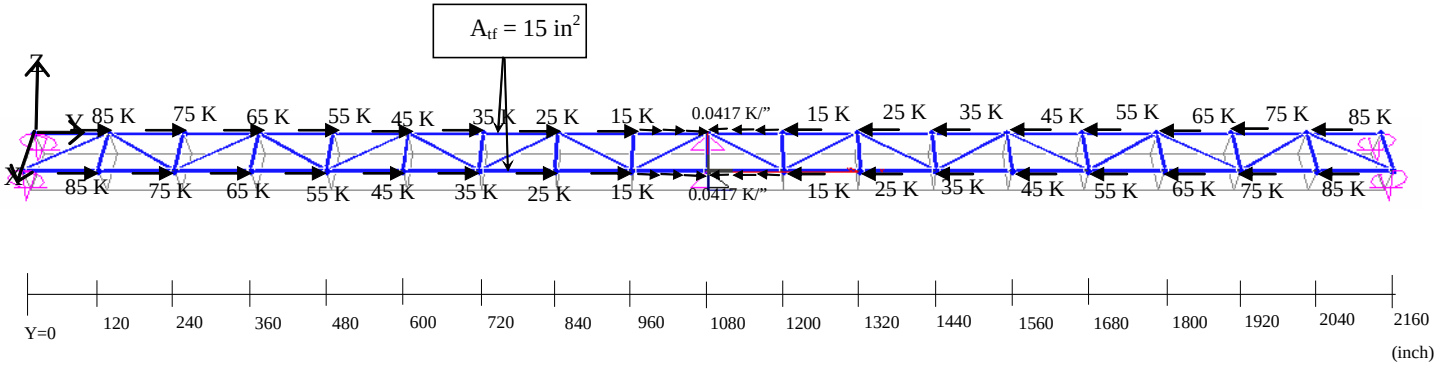

Figure 9.3 Loading conditions to simulate the effect of vertical bending in a straight girder

Figure 9.4 shows the SAP 2000 results for deflected shapes of three different top lateral bracing systems. A WT 6x11 was used as diagonals and struts in X-type lateral bracing system and WT 6x25 was used as diagonals and struts in both Alternating-Diagonal and Single-Diagonal systems.

Figure 9.4 shows that among the three top lateral bracing systems, the X-type system experienced the smallest amount of axial deformation and lateral displacement, while the Single-Diagonal system experienced the largest amount of axial deformation and lateral displacement. Based on these observations, the hypothesis can be made that under the effect of vertical bending only, the bracing forces in X-type system will be the largest and bracing forces in Single-Diagonal systems will be the smallest.

In order to verify this hypothesis, further study was conducted using both SAP 2000 and UTRAP. Figure 9.5 shows the forces in the top lateral bracing members for three different systems from both SAP 2000 and UTRAP outputs. In order to eliminate the effects of sloping webs, the Model 1 trapezoidal box girder is converted into the vertical web girder by modifying the bottom flange width of Model 1 to 76 inch (similar to the top width). Figure 9.5 shows that there are some discrepancies between SAP 2000 and UTRAP results for top lateral bracing forces. In general, top lateral bracing forces obtained from the model shown in Figure 9.3 analyzed using SAP 2000 are larger than those obtained from straight girder, vertical webs of Model 1, analyzed using UTRAP. However, the trend of force variation along the length of the girder is approximately the same for both analysis results.

For the X-type system under vertical bending, diagonal bracing forces are shown as if there is only one diagonal per panel since axial forces developed in both diagonals located in one panel are always similar in magnitude and direction.

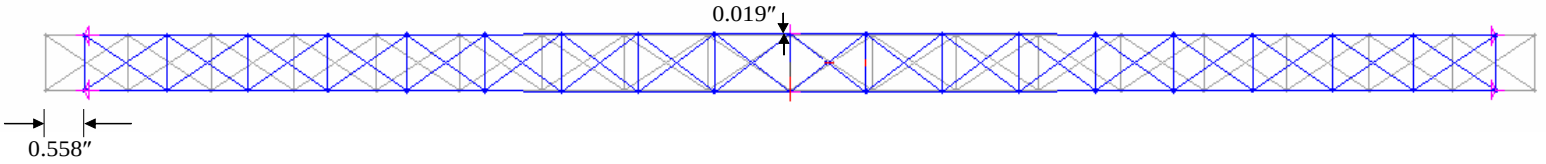

X-type lateral bracing system

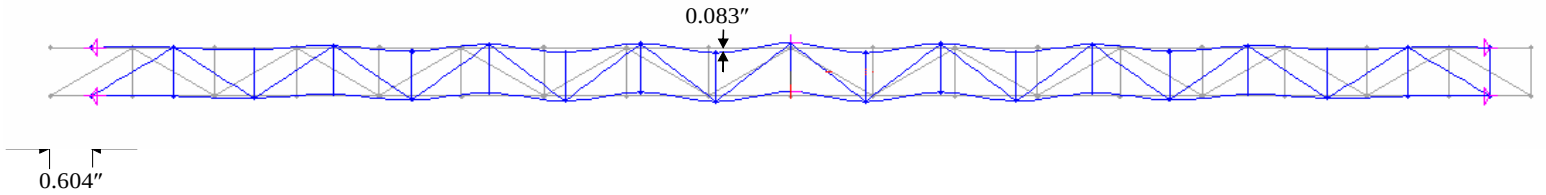

Alternating-Diagonal lateral bracing system

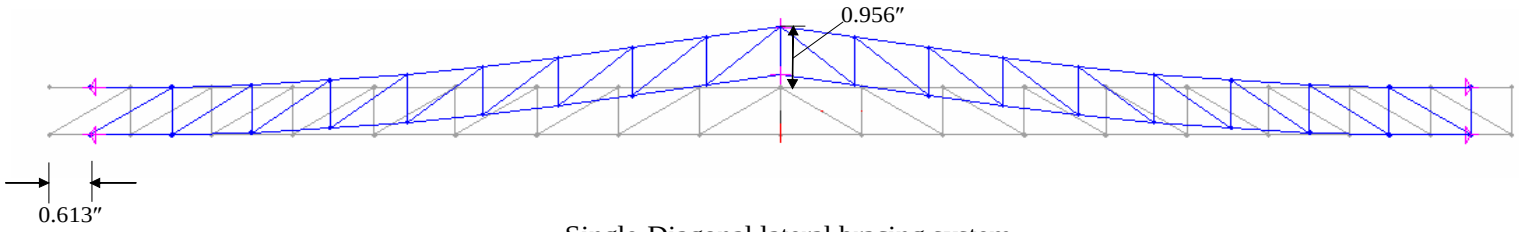

Single-Diagonal lateral bracing system

Figure 9.4 Deflected shapes of top lateral bracing system under loading shown in Figure 9.3 (Scale factor : 100)

Figure 9.5 shows that the bracing members in X-type systems have the largest forces and those in Single-Diagonal system have negligible forces. The bracing forces in the Single-Diagonal system are approximately zero, except near the midspan location, where there is the largest lateral displacement. These observations are consistent with the deflected shapes shown in Figure 9.4 and support the previous hypothesis. Based on the deflected shape shown in Figure 9.4 and top lateral bracing forces shown in Figure 9.5, it can be concluded that the X-type system provides the largest stiffness contribution to the overall bending stiffness of the girder, the Alternating-Diagonal system provides the second largest contribution, and the Single-Diagonal system provides the smallest (almost negligible) contribution. In order to satisfy equilibrium, top flanges in Single-Diagonal and Alternating-Diagonal systems have to carry higher compressive forces due to vertical bending than those are in X-type system.

Helwig and Fan derived a formula to predict top lateral bracing forces due to vertical bending in both X-type and Alternating-Diagonal systems. For convenience, those derivations are reproduced in the following section. In the derivation of top lateral bracing forces due to vertical bending Helwig and Fan assumed that the girder is prismatic and under uniform moment, the web provides no lateral resistance to the top flanges, and the effects of horizontal curvature on bending behavior are negligible.

9.2.1 X-Type lateral bracing system

Figure 9.6 shows the interactive forces Q between top lateral bracing members and top flanges in X-type system. F_B is the total force due to bending moment. Because the web is assumed to provide no lateral resistance to the top flanges, Q must be zero in order to satisfy equilibrium of top flanges.

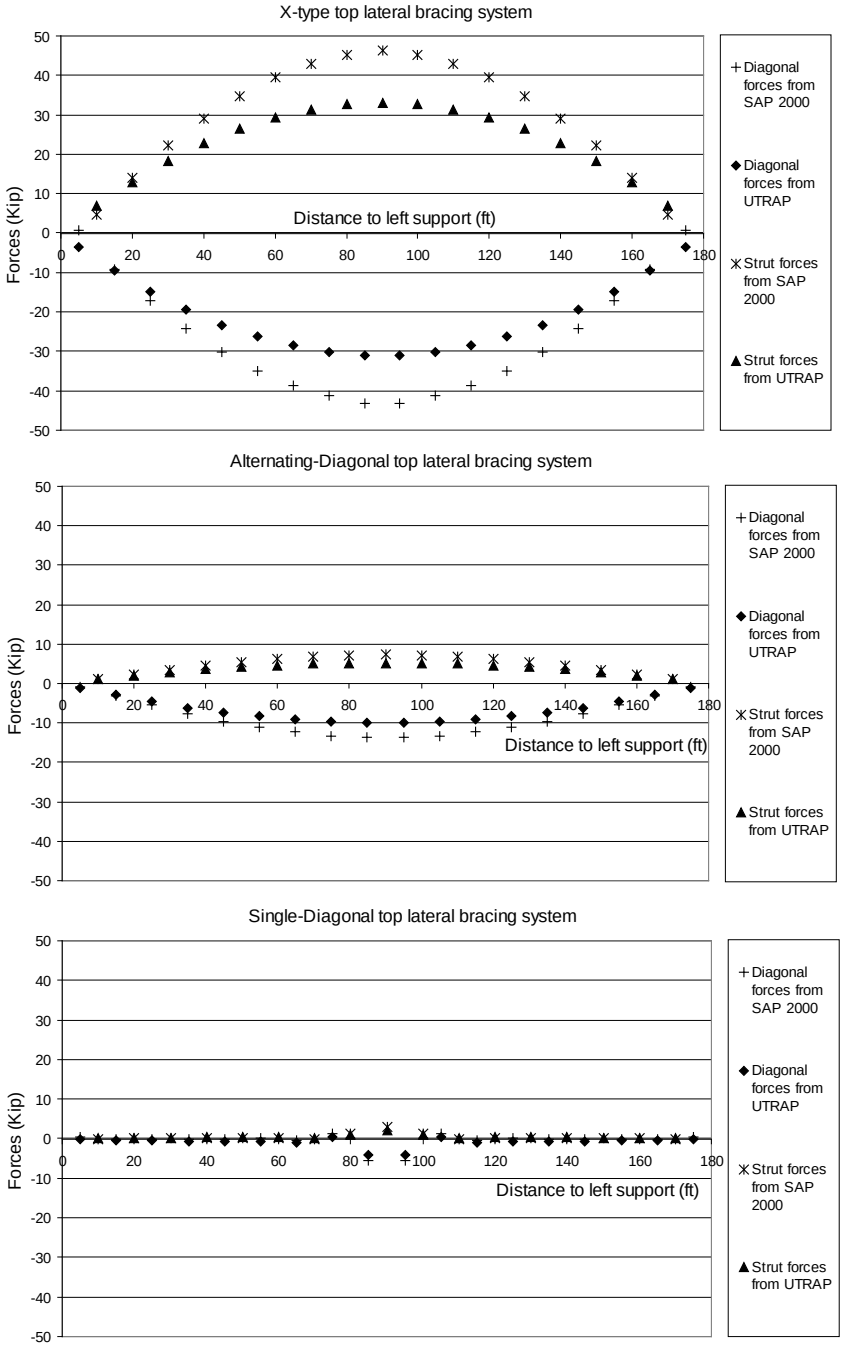

Figure 9.5 Top lateral bracing forces due to vertical bending

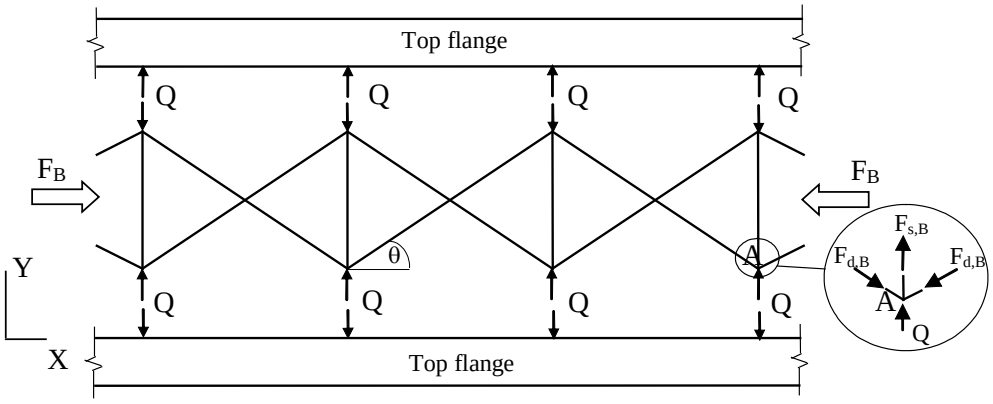

Figure 9.6 Interactive forces Q between top lateral bracing members and top flanges in X-type system

By enforcing equilibrium in the Y-direction at joint A, the relationship between the strut force due to bending $F_{s,B}$ and diagonal force due to bending $F_{d,B}$ is

$$F_{s,B} = -2F_{d,B}\sin(\theta) \tag{9.9}$$

If the moment is not uniform, $F_{d,B}$ in two adjacent panel will not be equal (i.e. $F_{d,B}$ left $\neq$ $F_{d,B}$ right), so Eq.9.9 would need to be modified by replacing (-$2F_{d,B}$) with (-($F_{d,B}$ left + $F_{d,B}$ right)). Left and right refer to the panel locations adjacent to the strut under consideration.

In order to develop the expression for $F_{d,B}$, the axial elongation of diagonal needed to be considered first. Figure 9.7 shows the elongation of diagonal in a panel of X-type system. u is a displacement in X-direction and v is a displacement in Y-direction.

The axial elongation of diagonal Δ_d is

$$\Delta_d = u\cos(\theta) + v\sin(\theta) \tag{9.10}$$

where v is the axial elongation of strut Δ_s , expressed as

$$v = \Delta_s = F_{s,B}\frac{a}{EA_s} = -2F_{d,B}\sin(\theta)\frac{a}{EA_s} \tag{9.11}$$

Using the relation between force and deformation, Δ_d becomes

$$\Delta_d = F_{d,B}\frac{d}{EA_d} \tag{9.12}$$

Axial deformation of top flange u (for one panel) using Hook's Law is

$$u = \frac{\sigma_{tf,B}}{E}s \tag{9.13}$$

where s is the panel length (i.e. spacing of strut) and $\sigma_{tf,B}$ is the axial stress in the top flange due to vertical bending.

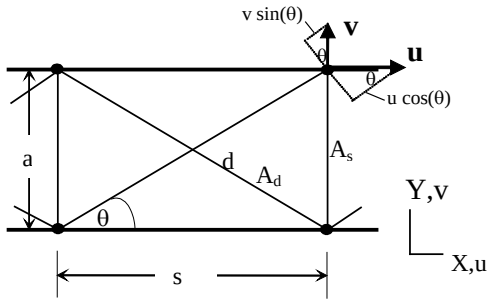

Figure 9.7 Elongation of diagonal in a panel of X-type system

The force in the diagonal due to vertical bending $F_{d,B}$, found by substituting Eqs.9.11, 9.12, and 9.13 into Eq.9.10, is

$$F_{d,B} = \frac{\sigma_{tf,B}\cos^2(\theta)}{\frac{1}{A_d} + \frac{2}{A_s}\sin^3(\theta)} \tag{9.15}$$

where $\sin(\theta) = \frac{a}{d}$ and $\cos(\theta) = \frac{s}{d}$ as can be seen in Figure 9.7. The diagonal forces due to bending in the X-type system are a function of the axial stiffness of the diagonals, struts, and top flanges.

9.2.1.1 Modification of top flange areas

The X-type system provides a significant stiffness contribution to the overall bending stiffness of the girder. Consequently, the actual axial stress in top flange due to vertical bending $\sigma_{tf,B}$ is less than the predicted stress by bending theory without including the presence of the X-type system. It is conservative to neglect the presence of the X-type system in calculating $\sigma_{tf,B}$. However, Fan and Helwig indicated that a modification to the $\sigma_{tf,B}$ can be made by adding the additional area $A_{add,each}$ to a top flange. For convenience, the derivation of the equivalent increase in each top flange area due to the presence of the X-type top lateral bracing system $A_{add,each}$ is reproduced in this section.

Figure 9.8, which is similar to the one shown in Helwig and Fan, shows a free body diagram of the top flange and the X-type system under vertical bending.

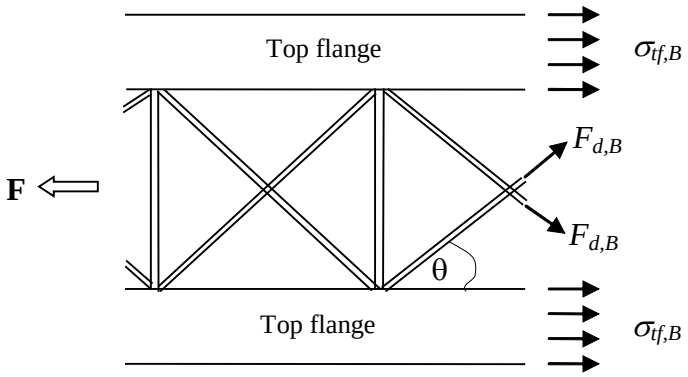

Figure 9.8 Resistance to the bending moment

The contributions of the top flanges and the X-type system in resisting bending moment M_{Top} are

$$M_{Top} = F\, y_C = 2\, \sigma_{tf,B}\, A_{tf}\, y_C + 2\, F_{d,B}\, cos(\theta)\, y_C \qquad (9.16)$$

where y_C is the distance from the centroid of the top flanges to the neutral axis and A_{tf} is the cross-sectional area of each top flange. Treating the X-type system as the additional area of each top flange $A_{add,each}$, Eq.9.16 can be written as follows:

$$M_{Top} = 2\ \sigma_{tf,B}\ (A_{tf} + A_{add,each})\ y_C \tag{9.17}$$

Eq.9.17 assumes that the X-type system is connected directly to the top flanges. From Eqs.9.16 and 9.17, $A_{add,each}$ is

$$A_{add,each} = \frac{F_{d,B}\cos(\theta)}{\sigma_{tf,B}} \tag{9.18}$$

Substituting Eq.9.15 to Eq.9.18 results in the following expression:

$$A_{add,each} = \frac{\cos^3(\theta)}{\frac{1}{A_d} + \frac{2}{A_s}\sin^3(\theta)} \tag{9.19}$$

9.2.2 Alternating-Diagonal top lateral bracing system

Figure 9.9 shows the interactive forces Q between top lateral bracing members and the top flanges in the Alternating-Diagonal system. F_B is the total force due to the bending moment. In the Alternating-Diagonal system, there are two types of joints. Joint type I is the connection between the strut and the top flange only, whereas joint type II is the connection between the strut, the two diagonals, and the top flange. Unlike the X-type system where Q is zero, in the Alternating-Diagonal system, Q must be equal in magnitude and opposite in direction with $F_{s,B}$, in order to satisfy equilibrium of top flanges. Again it is assumed that the web provides no lateral resistance to the top flanges.

The relationship between the strut force due to bending $F_{s,B}$ and the diagonal force due to bending $F_{d,B}$ is, by enforcing equilibrium in the Y-direction at joint type II,

$$F_{s,B} = -F_{d,B}\sin(\theta) \tag{9.20}$$

Eq.9.20 is obtained using the fact that in the Alternating-Diagonal system, Q = $F_{s,B}$.

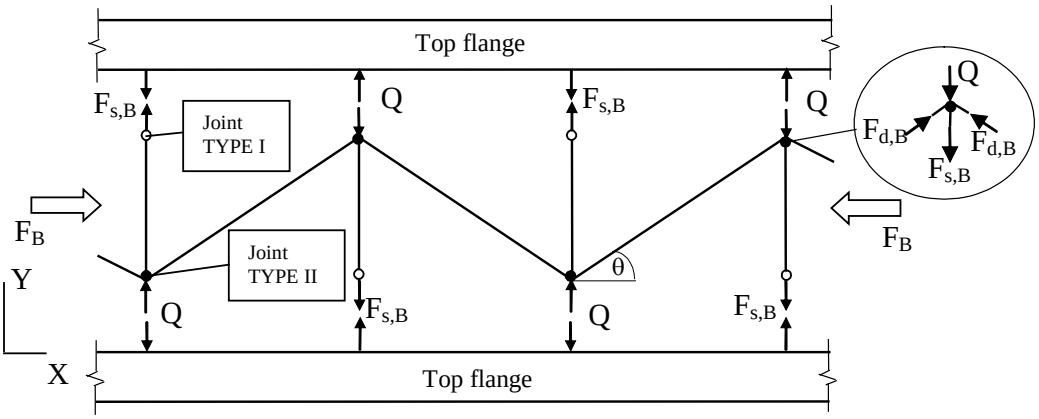

Figure 9.9 Interactive forces Q between top lateral bracing members and top flanges in Alternating-Diagonal system

Figure 9.4 shows that there is a displacement pattern that always repeated every two panels where the top flanges bend like a continuous beam between panel points. Figure 9.10 shows a relative deflection between two consecutive panels in the Alternating-Diagonal system. v_1 is a relative lateral displacement of top flanges at the strut location, u is a displacement in the X-direction and v is a displacement in the Y-direction.

Vertical bending causing the shortening of the top fiber will induce forces in the diagonals and struts. As can be seen in Figure 9.9, at joint type I, there are no other members framing to that joint to pick up strut forces. As the result, top flanges must carry the strut forces, causing lateral bending of the top flanges as shown in Figure 9.10. Figure 9.10 shows that v_1 is analogous to the midspan

deflection of fixed-fixed beam with length 2*s* under a concentrated load $F_{s,B}$ applied at the midspan, which is expressed as follows:

$$v_1 = \frac{F_{s,B}(2s)^3}{192EI_{tf}} = \frac{-F_{d,B}\sin(\theta)s^3}{24EI_{tf}} \tag{9.21}$$

where I_{tf} is the lateral flange moment of inertia.

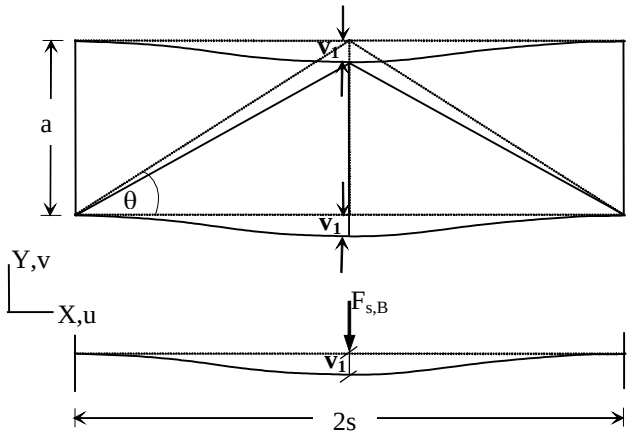

Figure 9.10 Relative deflection between two consecutive panels in Alternating-Diagonal system

Using the same approach as for the X-type system, the axial elongation of diagonal Δ_d for the Alternating-Diagonal system is

$$\Delta_d = u\cos(\theta) + (v_1 + v_2)\sin(\theta) \tag{9.22}$$

where *u* is the axial deformation of top flange *u* (for one panel), expressed in Eq.9.13, and v_2 is the axial elongation of the struts defined by:

$$v_2 = F_{s,B}\frac{a}{EA_s} = -F_{d,B}\sin(\theta)\frac{a}{EA_s} \tag{9.23}$$

The force in the diagonal due to vertical bending $F_{d,B}$, found by substituting Eq.9.12, 9.13, 9.21, and 9.23 into Eq.9.22, is

$$F_{d,B} = \frac{\sigma_{tf,B}\cos^2(\theta)}{\frac{1}{A_d} + \frac{s^2\cos(\theta)\sin^2(\theta)}{24I_{tf}} + \frac{\sin^3(\theta)}{A_s}} \tag{9.24}$$

where $\sin(\theta) = \frac{a}{d}$ and $\cos(\theta) = \frac{s}{d}$. The forces developed in the diagonals of the Alternating-Diagonal system are a function of the axial stiffnesses of the diagonals, struts, and top flanges, and the lateral stiffness of the top flanges. The lateral stiffness of the top flanges does not affect the forces developed in the diagonals in the X-type system.

Using the same procedure as that for the X-type system, the equivalent increase in each top flange area due to the presence of the Alternating-Diagonal top lateral bracing system $A_{add,each}$ is

$$A_{add,each} = \frac{\cos^3(\theta)}{2\left[\frac{1}{A_d} + \frac{s^2\cos(\theta)\sin^2(\theta)}{24I_{tf}} + \frac{\sin^3(\theta)}{A_s}\right]} \tag{9.25}$$

9.2.3 Single-Diagonal top lateral bracing system

The Single-Diagonal system provides almost negligible stiffness contribution to the overall bending stiffness of the girder. It is assumed that the top lateral bracing forces in Single-Diagonal system due to vertical bending are negligible. In addition, the bending properties of a pseudo-closed section with the Single-Diagonal system are assumed to be the same as those of an open-section.

9.2.4 Verifications of top lateral bracing forces formulas

In order to verify the top lateral bracing formulas, UTRAP was used to analyze a simply supported straight girder of Model 1, shown in Figure 1.5, under

a uniform load of 1 k/ft with the top lateral bracing configurations shown in Figure 9.11.

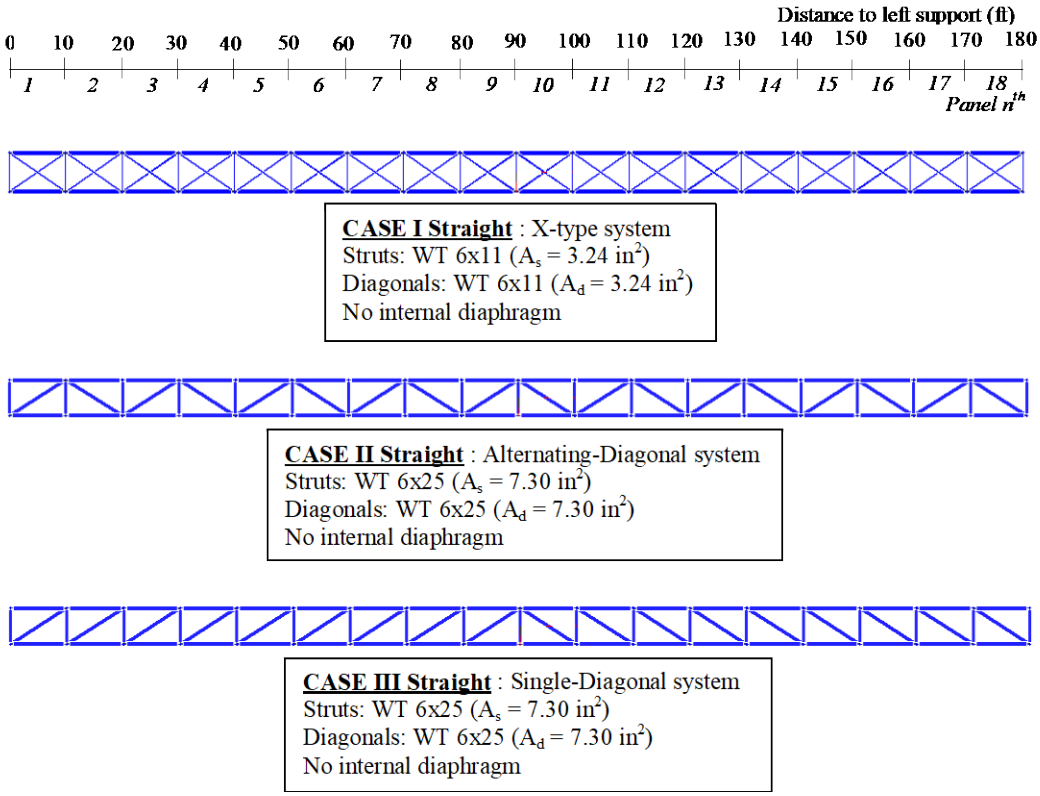

Figure 9.11 UTRAP analysis cases and top lateral bracing systems

Figure 9.12 shows comparisons between top lateral bracing forces obtained from UTRAP and the predicted top lateral bracing forces for three different systems. Figure 9.12 shows that the top lateral bracing force formulas predict the force in the top lateral bracing members of a straight-trapezoidal box girder very well. It should be noted that the scales used for the y-axis among all top lateral bracing systems are not the same. For the X-type system under vertical bending, diagonal bracing forces are shown as if there is only one diagonal per

panel since axial forces developed in both diagonals located in one panel are always identical in magnitude and direction.

Figure 9.12 shows that analytically, there is no diagonal force induced in Single-Diagonal top lateral bracing system due to the horizontal component and vertical bending. However, there are still some strut forces induced by the horizontal load component due to sloping webs. The bracing forces in the Single-Diagonal top lateral bracing system are predicted quite well, except near midspan, where the lateral displacement is the largest as can be seen in Figure 9.4.

The X-type system provides a significant stiffness contribution to the overall bending stiffness of the girder, whereas the Alternating-Diagonal system provides an insignificant contribution to the overall bending stiffness of the girder. Thus, when determining the axial stress in the top flange due to vertical bending $\sigma_{tf,B}$ for the X-type system, one needs to take into account the increase of overall bending stiffness due to the presence of top lateral bracing system (i.e. calculate neutral axis location and moment of inertia for a pseudo-closed section). Helwig and Fan indicated that one simplified method for accounting the contribution of the top lateral bracing system to the overall bending stiffness is by adding the equivalent area of the top lateral bracing system to the top flanges. The additional area for each top flange due to the presence of the X-type system shown in Figure 9.11 is 1.50 in^2, or 10% from the total top flange area. The presence of top lateral bracing system will change the location of the neutral axis location y_c and the moment of inertia about horizontal centroidal axis I. Table 9-1 shows the vertical bending property comparisons between Model 1 open-section and pseudo-closed section with the X-type system. If an open-section value of y_c and I (i.e. neglect the presence of X-type lateral system) are used, there will be an additional error in predicting the top lateral bracing forces. Figure 9.13 shows an increase in discrepancies between the predicted forces and the UTRAP solution

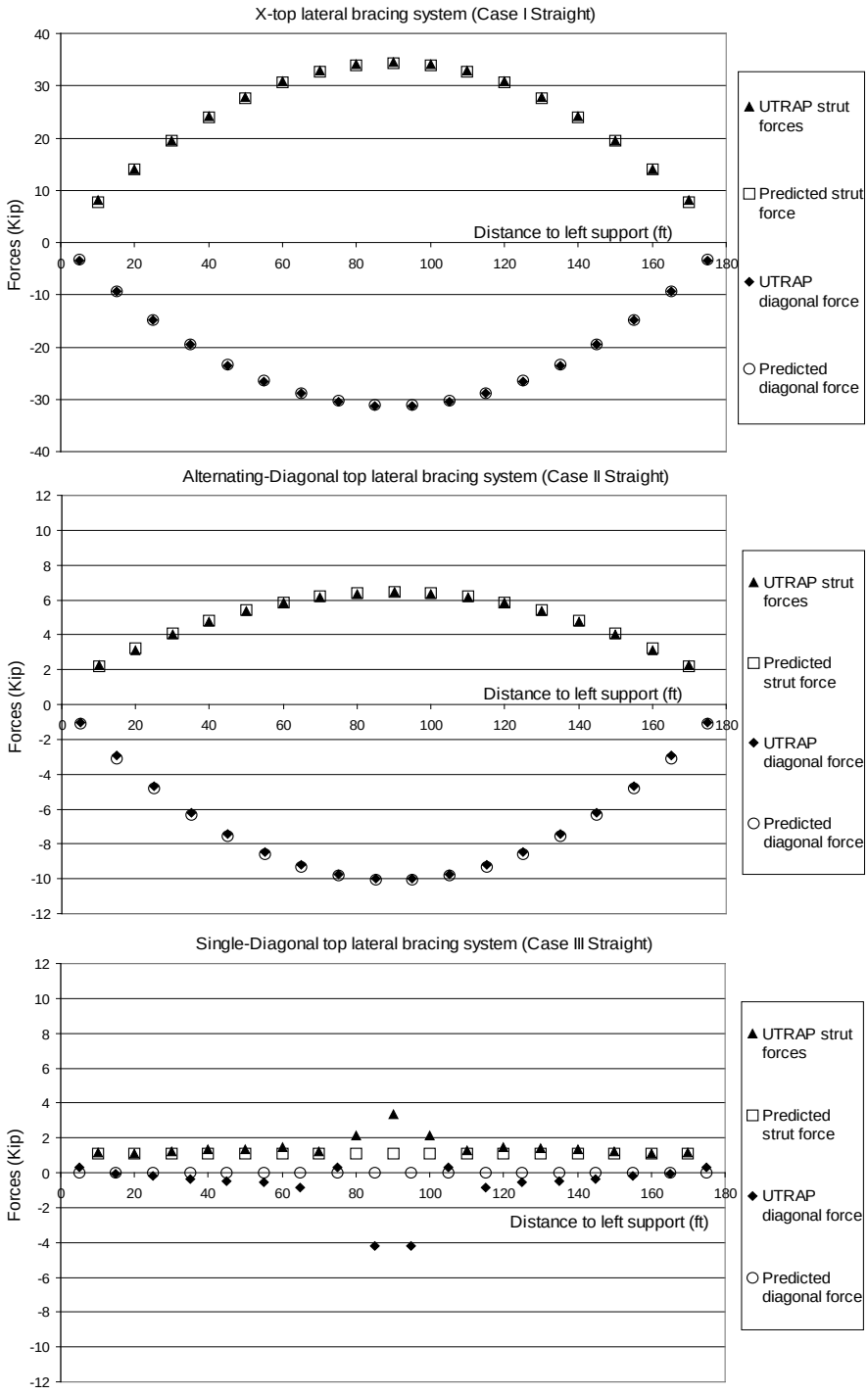

Figure 9.12 Top lateral bracing forces in a straight trapezoidal box girder

due to neglecting the presence of the X-type system in calculating bending properties.

Table 9-1 Vertical bending properties for the X-type system

Vertical bending properties	Open-section	Pseudo-closed section
y_c	38.2 in	37.5 in
I	100530 in^4	104810 in^4

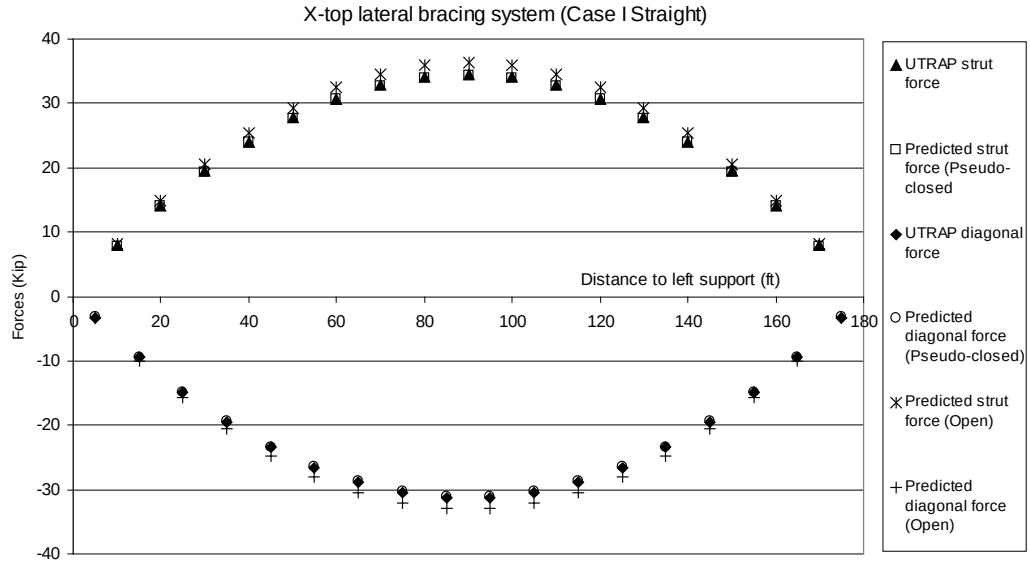

Figure 9.13Top lateral bracing forces in the X-type system

Figure 9.13 shows that the predicted top lateral bracing forces obtained by treating a girder as an open section (i.e. neglecting the contribution of the top lateral bracing system) in calculating the bending properties are slightly larger than those obtained by treating a girder as a pseudo-closed section. Treating a girder as an open-section is conservative and the percent discrepancies in this example are less than 5 percent.

On the other hand, the Alternating-Diagonal system does not provide as much bending stiffness contribution as the X-type system does. The additional area for each top flange by including the presence of the Alternating-Diagonal system shown in Figure 9.11 is only 0.23 in^2, or only about 1.5 percent of the total top flange area. Table 9-2 shows the vertical bending properties between the Model 1 open section and pseudo-closed section for Alternating-Diagonal system. The vertical bending properties calculated by treating a girder as an open section are about the same as those obtained by treating a girder as a pseudo-closed section. Consequently, the predicted top lateral bracing forces calculated by treating a girder as an open-section are about the same as those calculated by treating a girder as a pseudo-closed section.

Table 9-2 Vertical bending properties for the Alternating-Diagonal system

Vertical bending properties	Open-section	Pseudo-closed section
y_c	38.2 in	38.1 in
I	100530 in^4	101200 in^4

9.3 TOP LATERAL BRACING FORCES DUE TO TORSIONAL MOMENT

Adding a top lateral bracing system into an open-section girder increases its torsional stiffness significantly and makes the section pseudo-closed rather than open. Torsional analysis of a pseudo-closed section is usually performed using the equivalent plate method (EPM) developed by Kollbrunner and Basler (1969). Using the EPM, the top lateral bracing system is converted into a fictitious plate that has a thickness of $t_{eq.}$ Part of the reason that the section is called a pseudo-closed section instead of a closed-section is because the thickness of the fictitious plate is typically much thinner than the web or flange thickness

which could develop significant warping stresses. However, the EPM assumes that the pseudo-closed section can be treated as a closed-section in determining the torsional stiffness, the torsional moment resistance, and the shear flow due to pure torsion. Figure 9.14 shows a trapezoidal box girder with top lateral bracing system (pseudo-closed section) with total torsional moment *T*. Treating a pseudo-closed section as a closed section, the resulting shear flow *q* can be calculated simply using Bredt's formula,

$$q = \frac{T}{2A_o} \tag{9.26}$$

where A_o is the area enclosed by shear flow (i.e. area of trapezium).

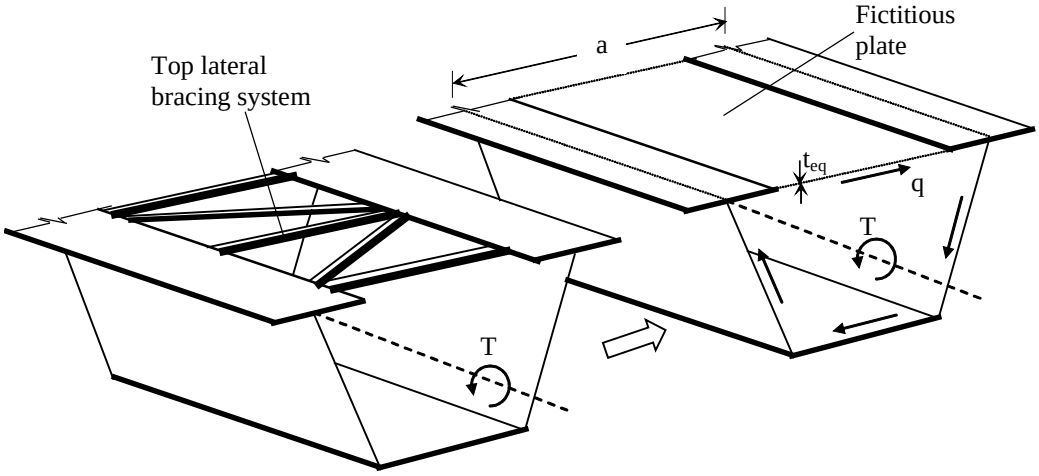

Figure 9.14 Torsional analysis of a pseudo-closed section using the Equivalent Plate Method

Having determined the shear flow in the fictitious plate using Eq.9.26, the equivalent shearing force acting on the fictitious plate F_{plate} is

$$F_{plate} = q\,a \tag{9.27}$$

where a is the assumed width of the fictitious plate shown in Figure 9.14. The equivalent shear force on the fictitious plate F_{plate} can be converted to axial forces in the top lateral bracing members. The magnitude and direction of those axial forces depends on geometry and orientation of bracing members and can be calculated using force resolution. Figure 9.15 shows the forces on diagonal F_d and the struts F_s due to uniform torsional moment for three different bracing systems. Double arrows indicate that the force depends upon the direction of the torsional moment.

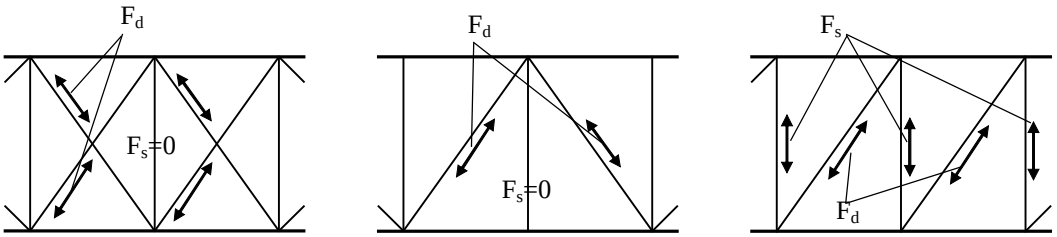

X-type system | Alternating – Diagonal top system | Single – Diagonal top system

Figure 9.15 Forces on top lateral bracing members due to uniform torsional moment

Figure 9.15 shows that under a uniformly applied torsional moment there is no force developed in the struts due to torsional moment for both X-type and alternating-diagonal top lateral bracing systems. However, some force develops in the struts for the single-diagonal top lateral bracing system. These observations agree with the fact that the area of the strut does not appear in Eqs.D.1 through D.4 to determine t_{eq} in both X-type and alternating-diagonal top lateral bracing systems, but does appear in Eqs.D.5 and D.6 for the single-diagonal top lateral bracing system. If the torsional moment varies along the length, the forces developed in diagonals in adjacent panels will not be equal. These unbalanced

forces between diagonals in adjacent panels will induce strut forces in the Alternating-Diagonal system to satisfy joint equilibrium. However, for an X-type system, there will not be any strut forces induced by unbalanced diagonal forces because of the symmetry of top lateral system. The strut forces induced by unbalanced diagonal forces due to non-uniform torsion are discussed in more detail in the following sections.

The force prediction in the top lateral bracing system due to torsional moment using EPM can be summarized as follows:

1. Calculate the equivalent plate thickness t_{eq} for a given top lateral bracing system using Table D-1.
2. Calculate the cross-section torsional properties and the total torsional moment T resisted by a cross-section. Technically, T consists of pure torsion and warping torsion components. However, for a typical pseudo-closed section, warping torsion component is small compared to pure torsion component, so total torsional moment can be simplified using the pure torsion component only.
3. Calculate shear flow q develops along the contour of the box using Eq.9.26.
4. Calculate the equivalent shear force acting on the fictitious plate F_{plate} based on the shear flow developed on the fictitious plate calculated in step 4.
5. Calculate the force in the top lateral bracing system based on the geometry and the orientation of the bracing member (i.e. force resolution) as shown in Figure 9.15.

For a simply supported curved girder, the torsional moment T can be calculated directly using Eq.3.6.

In general, there are two possible orientations for diagonal members used as top lateral bracing, called diagonal type 1 and diagonal type 2, as shown in Figure 9.16. Axial force in diagonal type 1 and 2 are denoted as F_{d1} and F_{d2}, respectively. The orientations of both diagonal types 1 and 2 are consistent with those used in UTRAP.

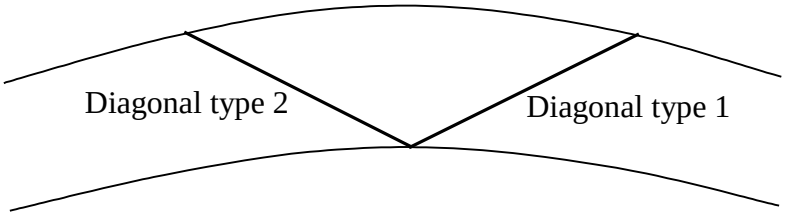

Figure 9.16 Orientations of diagonal type 1 and diagonal type 2

The following section presents the derivation of formulas to predict the forces in a top lateral bracing system due to torsion using the EPM for three different top lateral bracing systems. In order to predict the diagonal forces at a certain panel, it is satisfactory to use the torsional moment in the middle of that panel.

9.3.1 X-type top lateral bracing system

Figure 9.17 shows the top lateral bracing forces in an X-type system due to uniform torsional moment. The diagonal forces due to torsional moment $F_{d1,T}$ and $F_{d2,T}$, found by resolving the equivalent shearing force acting on the fictitious plate F_{plate} , is

$$F_{d1,T}\sin(\theta)+F_{d2,T}\sin(\theta)=F_{plate} \tag{9.28}$$

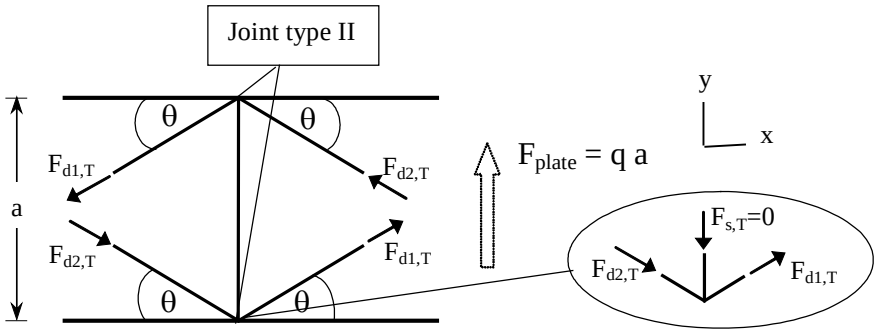

Figure 9.17 Top lateral bracing forces in X-type system due to uniform torsional moment

Under a uniform torsional moment, both diagonal forces $F_{d1,T}$ and $F_{d2,T}$ in all panels must be equal in magnitude and opposite in direction. Based on this fact, Eq.9.28 can be written as follows:

$$F_{d1,T} = -F_{d2,T} = \frac{F_{plate}}{2\sin(\theta)} \tag{9.29}$$

Enforcing equilibrium in the y-direction at joint type II, the strut force due to torsional moment $F_{s,T}$ can be expressed as follows:

$$F_{d1,T}\sin(\theta) - F_{d2,T}\sin(\theta) - F_{s,T} = 0$$

$$F_{s,T} = 0 \tag{9.30}$$

For non-uniform torsion, $F_{d1,T}$ and $F_{d2,T}$ for diagonals located on one panel are still always the same in magnitude and opposite in direction. However, due to non-uniform torsion, $F_{d1,T}$ and $F_{d2,T}$ in each panel will be different. Figure 9.18 shows two adjacent panels of X-type lateral system, which are called left panel and right panel, relative to the strut under consideration (in this case strut *AB*). It is assumed that the torsional moment in the middle of the left panel T_{LEFT} is greater than torsional moment in the middle of the right panel T_{RIGHT}. As a result,

the diagonal forces due to torsional moment in the left panel, $F_{d1LEFT,\ T}$ and $F_{d2LEFT,\ T}$, are higher than diagonal forces $F_{d1RIGHT,\ T}$ and $F_{d2RIGHT,\ T}$.

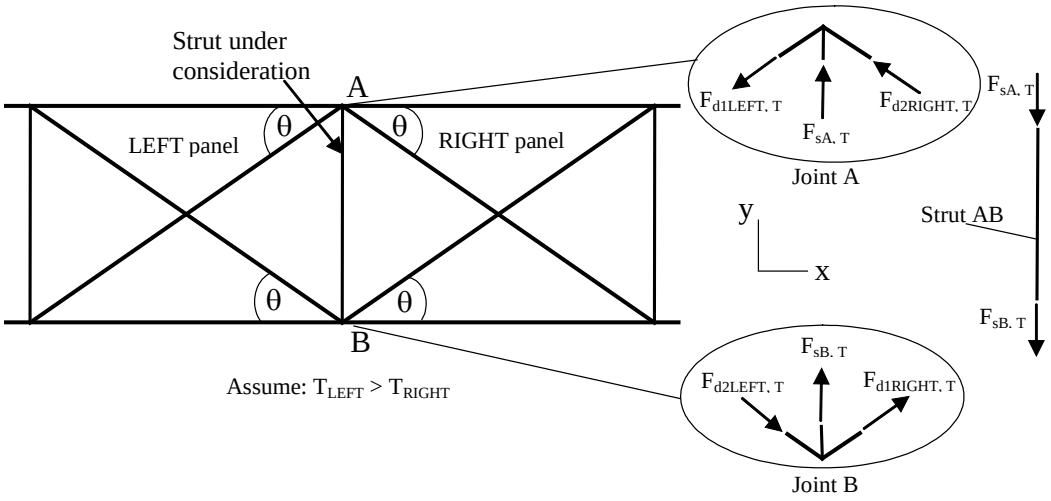

Figure 9.18 Unbalanced diagonal forces in two-adjacent panels of X-type system

Enforcing equilibrium in the y-direction at joints A and B, as shown in Figure 9.18, the strut forces due to the non-uniform torsional moment at both joints A and B, $F_{sA,T}$ and $F_{sB,T}$, respectively, are

$$F_{sA,T} = \left(F_{d1LEFT,\mathrm{T}} - F_{d2RIGHT,\mathrm{T}}\right)\sin(\theta) \tag{9.31}$$

$$F_{sB,T} = \left(F_{d2LEFT,\mathrm{T}} - F_{d1RIGHT,\mathrm{T}}\right)\sin(\theta) \tag{9.32}$$

Using the fact that the magnitude of the diagonal forces are always the same in one panel, it can be shown from Eqs.9.31 and 9.32 that both $F_{sA,T}$ and $F_{sB,T}$ are equal in magnitude and direction. This indicates that there will not be any axial force induced in strut AB due to unbalanced diagonal forces, so theoretically, struts are not required in X-type system to resist torsional moment. The y-component of unbalanced diagonal forces will induce lateral forces in both top flanges and cause lateral bending of the top flanges and localized stress

concentrations. Therefore, top flanges must be designed to have sufficient lateral bending stiffness (i.e. sufficient width) to carry lateral forces due to the unbalanced diagonal forces.

9.3.2 Alternating-Diagonal top lateral bracing system

Figure 9.19 shows the top lateral bracing forces in an Alternating-Diagonal system due to uniform torsional moment. The forces in the diagonal type 2, $F_{d2,T}$, found by resolving the equivalent shearing force acting on the fictitious plate F_{plate} , is

$$F_{d2,T}\sin(\theta) = F_{plate} \tag{9.33}$$

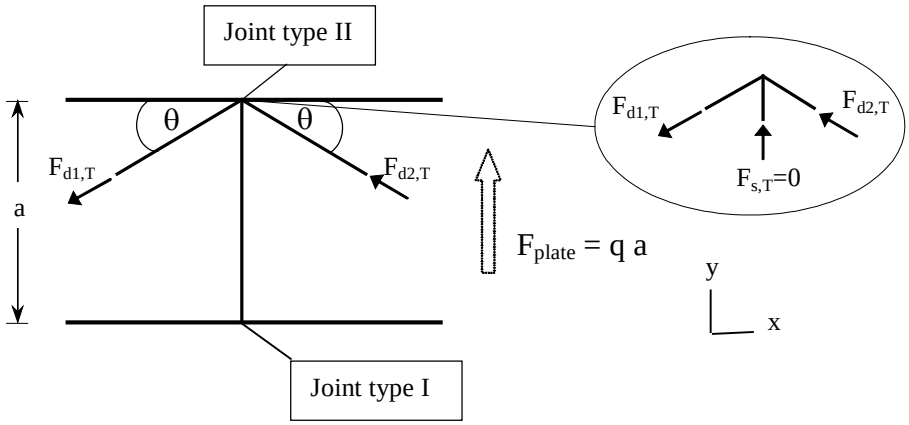

Figure 9.19 Top lateral bracing forces in Single-Diagonal system due to torsional moment

Under uniform torsional moment, all diagonal forces due to torsional moment have to be the same (i.e. $F_{d1,T}$ = - $F_{d2,T}$ in all panels, where the negative sign indicates opposite in direction). Based on this fact, Eq.9.33 can be written as follows:

$$F_{d1,T} = -F_{d2,T} = \frac{F_{plate}}{\sin(\theta)} \tag{9.34}$$

Enforcing equilibrium in the y-direction at joint type II, the strut force due to torsional moment $F_{s,T}$ can be expressed as follows:

$$F_{d2,T}\sin(\theta) - F_{d1,T}\sin(\theta) + F_{s,T} = 0$$

$$F_{s,T} = 0 \tag{9.35}$$

Under non-uniform torsional moment, $F_{d1,T}$ will not be equal with $F_{d2,T}$, so there will be unbalanced diagonal forces at joints. Figure 9.20 shows a model of two adjacent panels in the Alternating-Diagonal system under the y-component of the unbalanced diagonal forces P applied at the joint type II. For practical purposes, the lateral bending stiffness of both top flanges are assumed to be the same. In addition, the top flanges are assumed continuous so the strut can carry axial force.

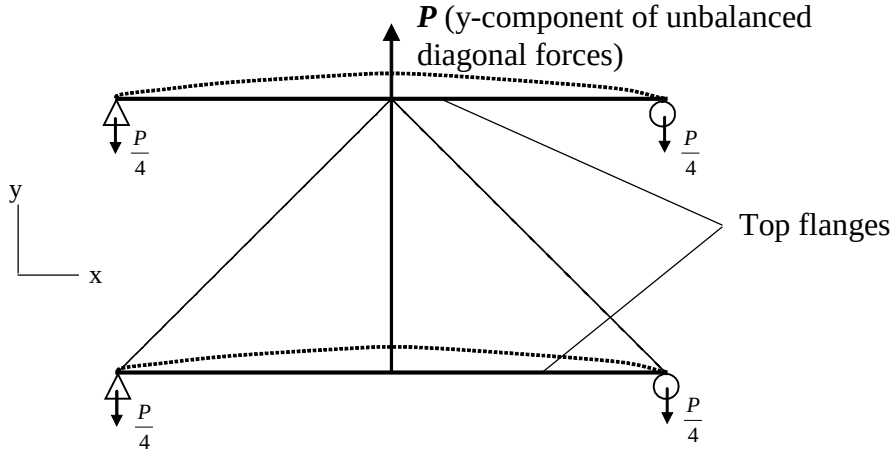

Figure 9.20 Simplified model of two-adjacent panels in Alternating-Diagonal system under the y-component of unbalanced diagonal forces

Figure 9.20 shows that half of the load P is taken by each of the top flanges. The strut will carry half of the unbalanced diagonal forces. Strut forces due to non-uniform torsional moment $F_{s,T}$ can be expressed as:

$$F_{s,T} = -\frac{1}{2}\left(F_{d1,T} + F_{d2,T}\right)\sin(\theta) \tag{9.36}$$

Diagonal forces $F_{d1,T}$ and $F_{d2,T}$ must have opposite signs. The negative sign in Eq.9.36 indicates that the force in the strut is opposite to the unbalanced diagonal forces.

Unlike the X-type system, struts are required in the Alternating-Diagonal system to carry part of the unbalanced diagonal forces due to non-uniform torsional moment. In addition, top flanges must be designed to have sufficient lateral bending stiffness (i.e. sufficient width) to carry lateral forces due to the unbalanced diagonal forces.

9.3.3 Single-Diagonal top lateral bracing system

Figure 9.21 shows the top lateral bracing forces in the Single-Diagonal system due to uniform torsional moment. The forces in diagonal type 1 due to torsional moment $F_{d1,T}$ is

$$F_{d1,T}\sin(\theta) = F_{plate} \Rightarrow F_{d1,T} = \frac{F_{plate}}{\sin(\theta)} \tag{9.37}$$

Unlike the X-type and the Alternating-Diagonal systems, under uniform torsional moment, strut forces $F_{s,T}$ will develope in Single-Diagonal top lateral system. The strut force $F_{s,T}$ can be found by enforcing equilibrium in the y-direction at joint type III and is expressed as:

$$F_{s,T} = -F_{d1,T}\sin(\theta) \tag{9.38}$$

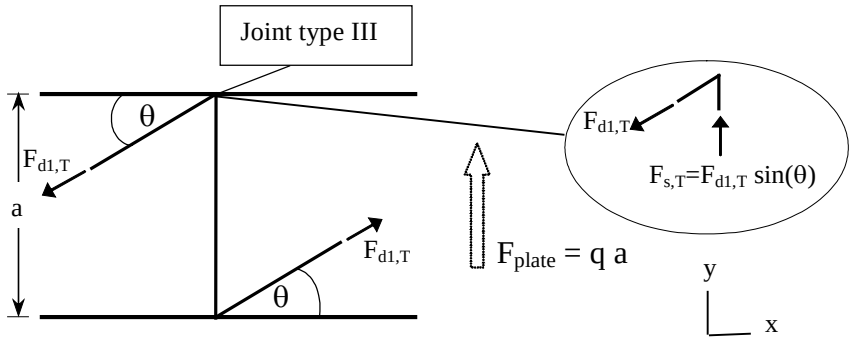

Figure 9.21 Top lateral bracing forces in Single-Diagonal system due to uniform torsional moment

The negative sign in Eq.9.38 indicates that $F_{s,T}$ is opposite to $F_{d1,T}$ (i.e. if $F_{d1,T}$ is in tension, $F_{s,T}$ must be in compression).

Under non-uniform torsional moment, $F_{d1,T}$ in adjacent panels is not the same, so there will be an unbalanced diagonal forces at the joints. As with struts in the Alternating-Diagonal system, struts in a Single-Diagonal system will also carry half of the y-component of unbalanced diagonal forces and Eq.9.38 can be modified as follows:

$$F_{s,T} = -\frac{1}{2}\left(F_{d1LEFT,T} + F_{d1RIGHT,T}\right)\sin(\theta) \qquad (9.39)$$

where $F_{d1LEFT,\,T}$ and $F_{d1RIGHT,\,T}$ are the diagonal forces in the left and right sides of the strut under consideration. Unlike $F_{d1,T}$ and $F_{d2,T}$ that have the opposite signs in the Alternating-Diagonal system, both $F_{d1LEFT,\,T}$ and $F_{d1RIGHT,\,T}$ have the same signs in the Single-Diagonal system. This fact causes the strut in Single-Diagonal system to carry much higher axial forces than those in the Alternating-Diagonal system.

9.4 TOTAL AXIAL FORCES IN TOP LATERAL BRACING MEMBERS OF A SIMPLY-SUPPORTED CURVED TRAPEZOIDAL BOX GIRDER

This section presents comparisons between the predicted top lateral bracing forces and the UTRAP solutions for a simply supported 180 ft curved girder with Model 1 and a radius of curvature of 750 ft, under a uniform load of 1 k/ft with the top lateral bracing systems shown in Figure 9.11. The equivalent plate thickness of the three top lateral bracing systems are the same, therefore, all systems shown in Figure 9.11 have the same torsional characteristics as predicted by the EPM.

For a curved trapezoidal girder, the total forces developed in the top lateral bracing system result from the horizontal component of the applied load due to sloping webs, vertical bending, and torsional moment. Figure 9.22 shows the torsional moment diagram for the simply supported curved girder. The torsional moment diagram indicates the torsional resistance from the cross-section. It is not the same as externally applied torsional loading due to curvature, in which the variation along the member follows the shape of a bending moment diagram (i.e. *M/R* method).

Figure 9.23 shows comparisons between the predicted top lateral bracing forces and the UTRAP solution for three different top lateral systems. It should be noted that the y-axis scale for the X-type system is different than the y-axis scale for the Alternating-Diagonal and Single-Diagonal systems. In general, the predicted forces are in good agreement with the UTRAP forces. Figure 9.23 shows that even though all top lateral bracing systems have the same equivalent plate thickness, the top lateral bracing forces in are significantly different. In general, the maximum diagonal forces in a simply supported curved girder occur at the end-supports, where the torsional moment is the greatest (refer to Figure

9.22). For the X-type system, the maximum compressive forces in the diagonals occur some distance from the end-span because vertical bending induces significant compressive forces at top lateral bracing system (refer to Figure 9.12). At the end-span, vertical bending moment is zero, so the only component inducing diagonal forces is torsional moment. At some distance away from end-supports, vertical bending starts to induce a significant compressive force in diagonals. Because Alternating-Diagonal and Single-Diagonal systems provide smaller contributions to the overall bending stiffness than the X-type system, the effect of vertical bending on the total forces in both Alternating-Diagonal and Single-Diagonal systems is very small compared to the effect of torsional moment. It can clearly be seen from Figure 9.23 that the variations of diagonal forces along the length in both Alternating-Diagonal and Single-Diagonal systems are approximately the same as the variation of torsional moment along the length, shown in Figure 9.22.

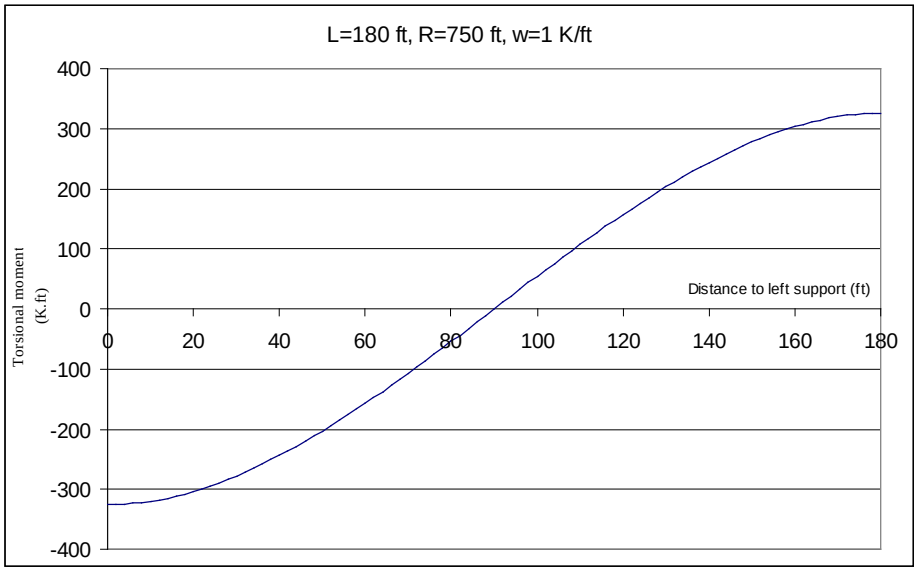

Figure 9.22 Torsional moment diagram

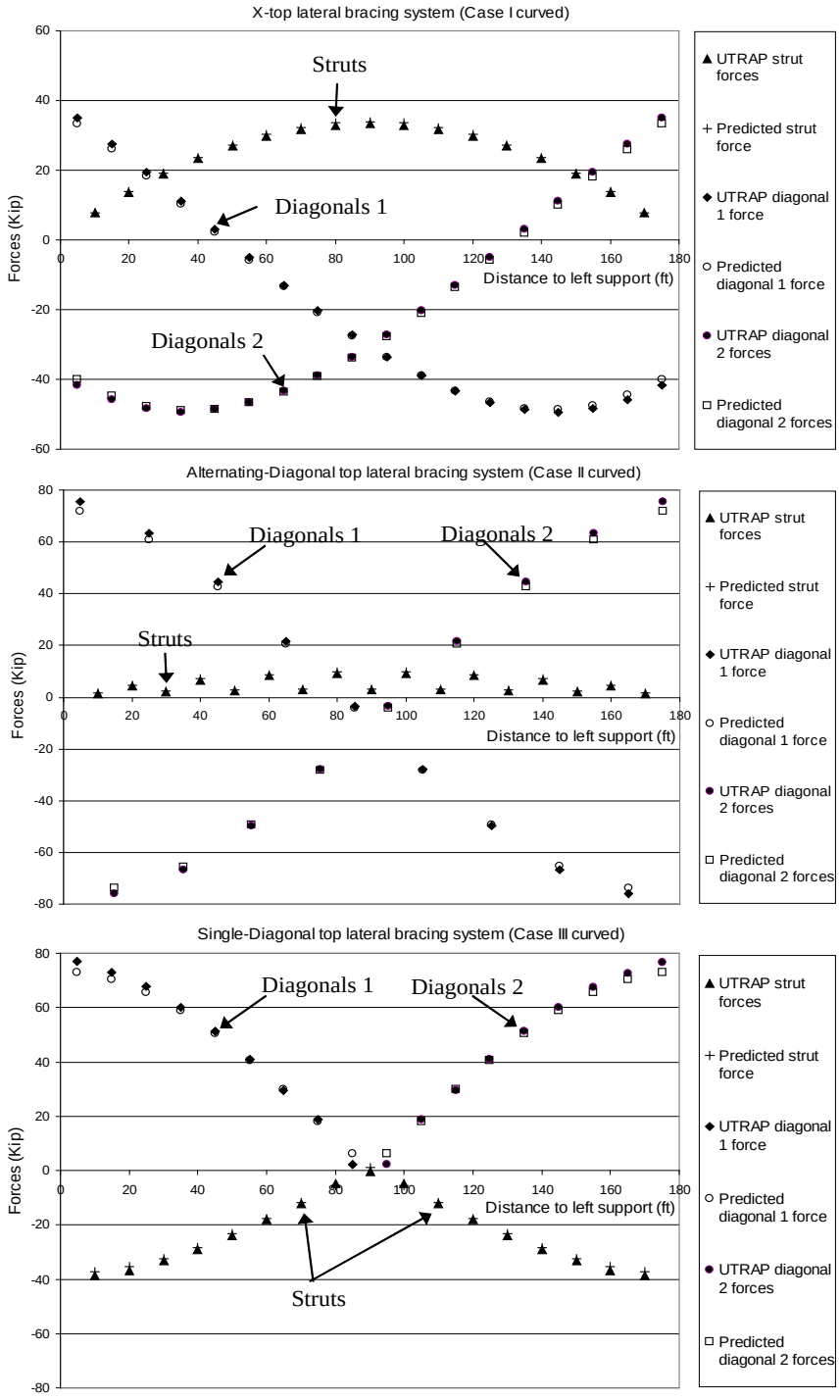

Figure 9.23 Top lateral bracing forces in a curved trapezoidal box girder

Comparing the X-type system with the Alternating-Diagonal system in Figure 9.23, the maximum diagonal forces in both tension and compression for the X-type system are smaller than those for the Alternating-Diagonal system. The explanation for this is that in a curved girder, the largest component of diagonal forces near the end-supports results from torsional moment. In the X-type system, there are two diagonals resisting torsional moment, whereas in the Alternating-Diagonal system, there is only one diagonal resisting the same magnitude of torsional moment. However, the strut forces in the X-type system are larger than those in the Alternating-Diagonal system because vertical bending induces significant strut forces (i.e. struts carry unbalanced diagonal forces due to non-uniform bending moment). This explanation is supported by the fact that the variation of struts forces in the X-type system is approximately the same as the variation of vertical bending moment along the length. In addition, variations of strut forces in the X-type system are smooth, whereas those in the Alternating-Diagonal system are irregular. The jaggedness of strut forces in the Alternating-Diagonal system is caused by the unbalanced diagonal forces in adjacent panels, due to non-uniform torsional moment.

Observing the sign of the torsional moment and the forces in diagonals due to torsional moment, diagonals type 1 located in the negative torsional moment region will experience tensile forces and diagonals type 2 will experience compressive forces. As can be seen from Figure 9.23, placing diagonals type 1 in the negative torsional moment region and diagonals type 2 in the positive torsional moment region will cause all diagonals to experience tensile forces. The magnitude of the diagonal forces for both systems are approximately the same. However, the magnitude, sign, and variation of strut forces in both systems are significantly different. All strut forces in the Alternating-Diagonal system are tensile, whereas all strut forces in the Single-Diagonal system are compressive,

and the maximum magnitude of the strut forces in the Alternating-Diagonal system is significantly smaller than in Single-Diagonal system.

From a design perspective, the diagonal member size in an Alternating-Diagonal system will be larger than in a Single-Diagonal since the member must be designed for compression rather than tension. However, strut members in the Single-Diagonal system will be larger than they are in the Alternating-Diagonal system. One must also realize that using a smaller diagonal member in a Single-Diagonal system will result in a thinner equivalent plate thickness, which can cause greater deformation.

9.5 SUMMARY

The forces in the top lateral bracing system have three components: the horizontal component of the applied load due to sloping webs, the vertical bending of a girder, and the torsional moment. There is good agreement between the predicted forces in the top lateral bracing system using the analytical method and those from the UTRAP solutions for both a straight girder and a curved girder.

Analytically, the horizontal component of the applied load due to sloping web is assumed to be carried by both struts and diagonals in the X-type system, whereas it is assumed to be carried only by the struts in both the Alternating-Diagonal and the Single-Diagonal systems.

Only the X-type system provides significant contribution to the overall bending stiffness of a girder. Both the Alternating-Diagonal and the Single-Diagonal systems can be assumed to not contribute to the overall bending stiffness of a girder. Thus, there are significant forces induced in bracing members

of the X-type system due to vertical bending, whereas there are only small forces induced in those of the Alternating-Diagonal and the Single-Diagonal systems. In addition, it can be concluded that ignoring the presence of the top lateral bracing system in calculating bending properties is acceptable. For the X-type system, the additional percent discrepancies between the predicted top lateral bracing forces obtained by treating a girder as an open section in calculating the bending properties and the UTRAP solutions are very small (in the example presented in this chapter is less than 5 percent). Under torsional moment, diagonals in the Alternating-Diagonal system carry significantly higher forces than those in the X-type system because there is only one diagonal resisting the forces as opposed to two. Diagonals in the Single-Diagonal system carry approximately the same forces as those in the Alternating-Diagonal system, except that all of the diagonals are in tension, allowing smaller member sizes. However, all forces carried by struts in the Single-Diagonal system are compressive forces that are significantly larger than those in the Alternating-Diagonal system.

CHAPTER 10
Continuous Curved Girder Behavior under a Uniform Load

This chapter focuses on the top lateral bracing forces in a continuous curved girder under a symmetric uniformly distributed load. Sample calculations for predicting the diagonal and strut forces in the X-type, Alternating-Diagonal, and Single-Diagonal top lateral bracing systems using the analytical method discussed in Chapter 9 are presented. In order to aid the understanding of the effect of using different top lateral bracing systems on the behavior of a continuous curved girder, this chapter also presents comparisons of the deformations and the total normal stresses. Three different analyses are performed. For the first analysis, the member sizes in each top lateral bracing system are selected so that all three top lateral bracing systems have the same equivalent plate thickness. For the second analysis, the member sizes in each system are chosen based on the required member size to carry the axial forces in each member based on the result of the first analysis. A third analysis was done to study the consequence of modifying the direction of diagonal members from the Alternating-Diagonal to the Single-Diagonal system. For this purpose, all member sizes in both systems are chosen to be the same.

The cross-section dimensions of the Model 3 continuous girder used for the examples are shown in Figure 10.1. Two different cross-sections are used along the girder length. Section P ("Positive") is used where the positive bending moment is dominant and section N ("Negative") is used where the negative bending moment is dominant. The radius of curvature of the girder is 955 ft.

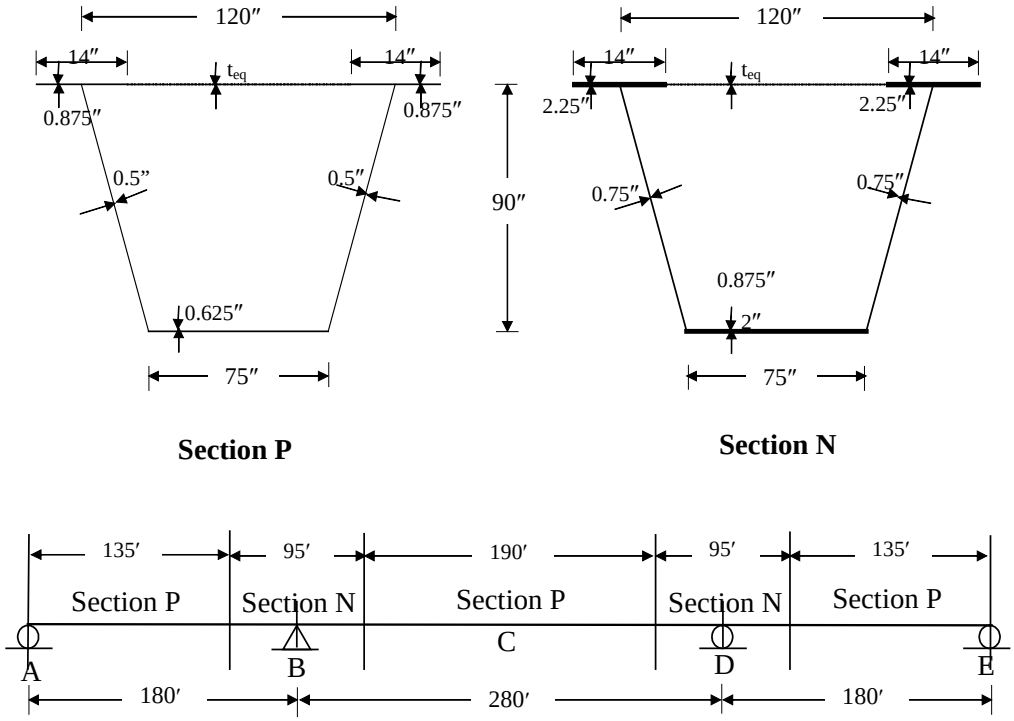

Figure 10.1 Cross-section dimension of Model 3 girder

The nodes at the bottom flange at supports A,D, and E the are only prevented from moving vertically, whereas those at support B are prevented from moving vertically, laterally and longitudinally. The bottom flange at support B cannot rotate in the horizontal plane. Support B is similar to the fixed support in a grid analysis. Herein, it is called a pinned support. As can be seen in Figure 10.1, the girder is symmetric about point C.

Figure 10.2 shows the top lateral bracing systems that were used. A 10-ft panel length (distance between struts) and a 20-ft internal diaphragm spacing are used in all top lateral bracing systems. Figure 10.3 and Figure 10.4 show the bending and torsional moment diagrams under a uniformly distributed load of 3.3 k/ft. Since the girder is symmetrical about the midspan, the diagrams are shown

for only half of the girder length. The bending moment and the torsional moment in the middle of both the 24th and the 25th panels are shown explicitly. Those values will be used in the sample calculations of calculating forces in the top lateral bracing members.

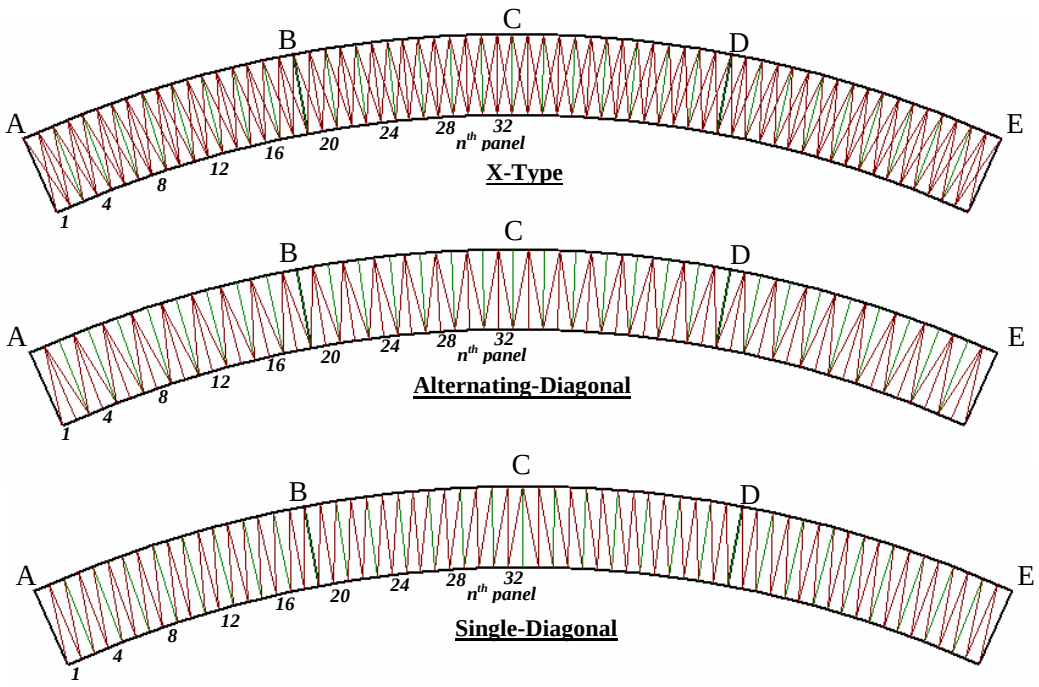

Figure 10.2 Top lateral bracing systems used in the analyses

10.1 ANALYSIS I

Analysis I was performed using the same equivalent plate thickness for all the three top lateral bracing systems. All member sizes in the top lateral bracing system were kept the same for both sections P and N. Since the areas of the top flanges in the two sections are different, the equivalent plate thickness will be different. Therefore, in Analysis I, the member sizes in all top lateral bracing

systems were chosen so that the equivalent plate thickness of section P is the same. Table 10-1 summarizes the member sizes used in each top lateral bracing system and the corresponding equivalent plate thickness for both sections P and N.

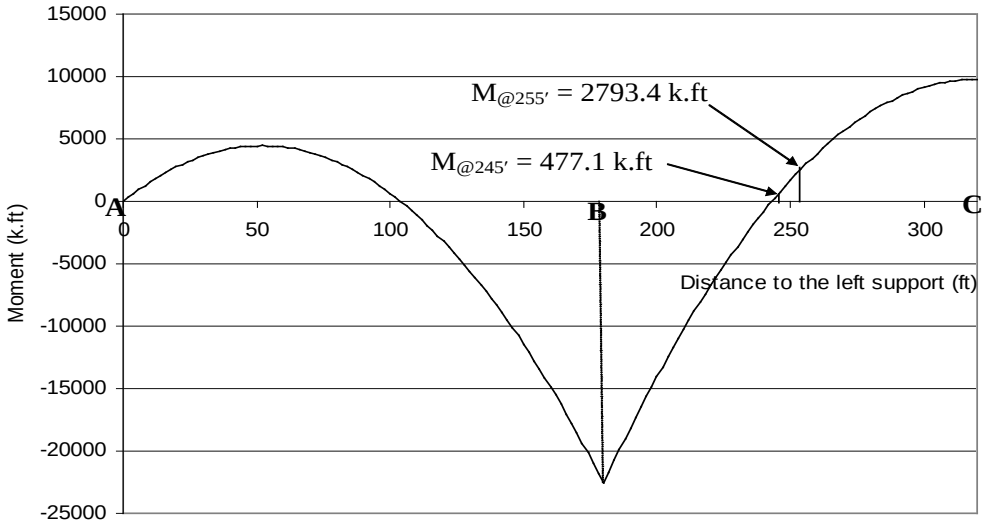

Figure 10.3 Bending moment diagram

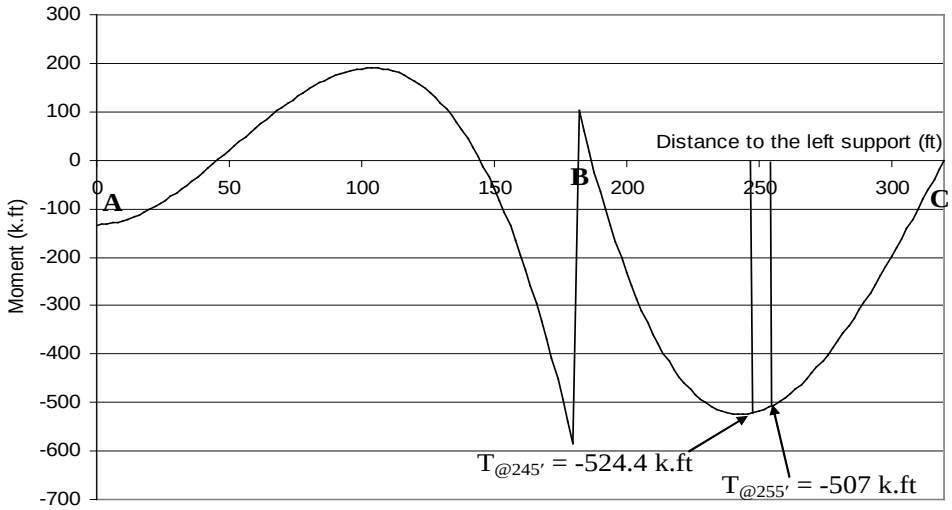

Figure 10.4 Torsional moment diagram

Table 10-1 Member size and the corresponding equivalent plate thickness used in Analysis I

	X-type	Alternating-Diagonal	Single-Diagonal
Diagonal area	3.82 in^2	8.59 in^2	10.3 in^2
Strut area	2.4	2.4	10.3
t_{eq} section P	0.05738 in	0.05738 in	0.05738 in
t_{eq} section N	0.05865 in	0.06282 in	0.05865 in

All internal diaphragms are the same with a member area of 2.4 in^2.

10.1.1 Top lateral bracing forces

Figure 10.5 shows the diagonal forces. For the length between A and C, there is no diagonal type 2 for the Single-Diagonal system. Therefore, in the graph showing the force in diagonal type 2, only the X-type and the Alternating-Diagonal systems are shown. The line connecting each data point is only for clarity purposes.

The maximum tensile force in a diagonal occurs at support B, where the magnitude of the torsional moment is also maximum. Table 10-2 summarizes the maximum diagonal forces in both tension and compression for each top lateral bracing system. The diagonal members in the Alternating-Diagonal system experience the largest compressive forces, so that from a design standpoint, these members will require a larger size than those in the two other systems. The maximum diagonal tensile forces in both the Alternating-Diagonal and the Single-Diagonal are not significantly different (i.e. from a design perspective, the same member size can be used to carry the diagonal tensile forces in both systems).

However, the maximum diagonal compressive force in the Single-Diagonal system is several times smaller than that in the Alternating-Diagonal system.

Table 10-2 Summary of the maximum diagonal forces

Top lateral bracing system	Maximum tensile force	Maximum compressive force
X-type	71.3 K	-41.5 K
Alternating-Diagonal	61.5 K	-60.8 K
Single-Diagonal	69.4 K	-16.6 K

The diagonal type 1 located in the negative torsional moment region will experience a tensile force. Unlike the diagonal forces in a simply-supported girder with a Single-Diagonal top lateral bracing system, due to the complexity of the torsional moment diagram in a continuous girder, there are some diagonals that experience a compressive force in the Single-Diagonal system. Technically, one can avoid having the diagonal member in compression by orienting the diagonal such that there are only type 1 diagonals in the negative torsional moment region and only type 2 diagonals in the positive torsional moment region. However, this approach is not justified from a construction perspective. In addition, due to the pouring sequence and moving loads, the torsional moment inflection point will move so that no matter how one orients the diagonals, there will always be a compressive force in some diagonal in a continuous curved girder.

Figure 10.6 shows the strut forces in each top lateral bracing system. The maximum tensile and compressive forces in the struts of each top lateral bracing system are summarized in Table 10-3. The struts in the Alternating-Diagonal system experience the smallest force. It should be noted that the strut forces in Figure 10.6 are shown every 20 ft (at 10 ft, 30 ft, 50 ft, etc. from the left support).

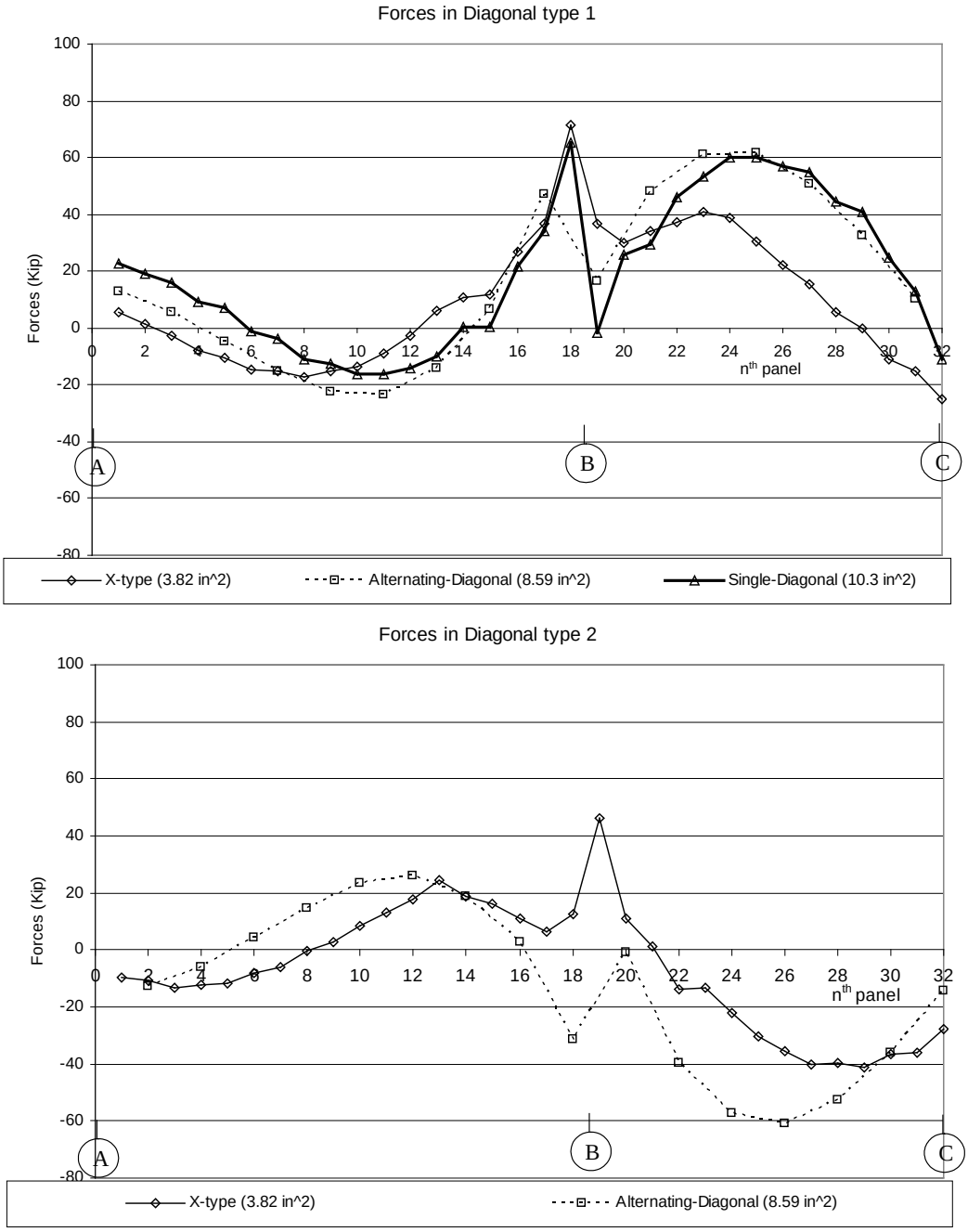

Figure 10.5 Diagonal forces – Analysis I

This does not mean there are no struts at 20 ft, 40 ft, etc. At those locations, the internal diaphragm consisting of a k-frame serves as the strut. However, the forces in that internal diaphragm are not shown, due to the fact that UTRAP solution for the top horizontal member of the k-frame includes components from the k-diagonals.

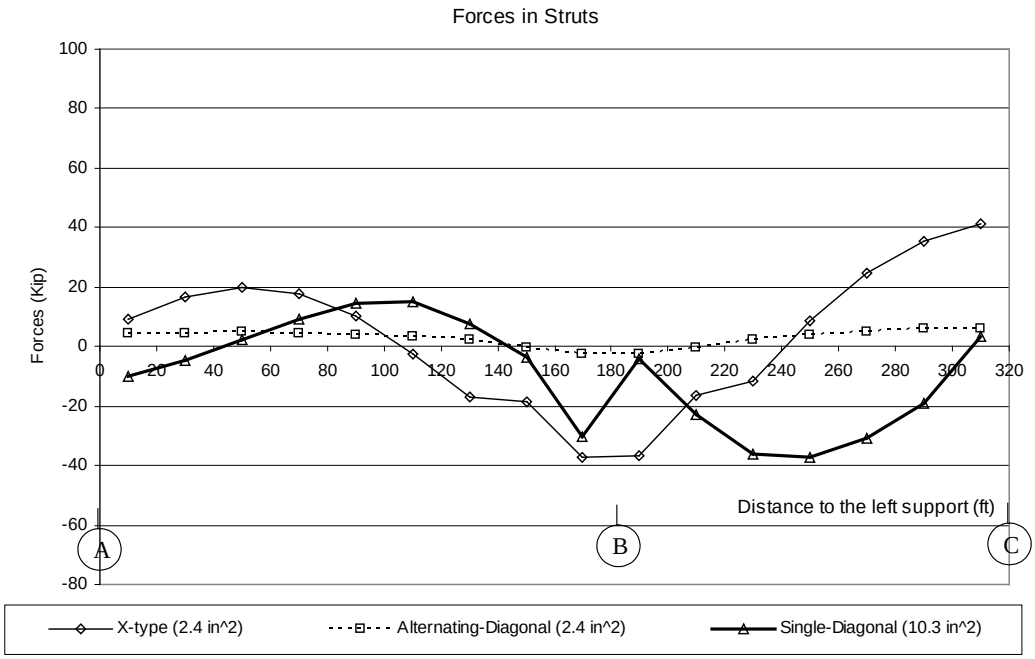

Figure 10.6 Strut Forces – Analysis I

Table 10-3 Summary of the maximum strut forces

Top lateral bracing system	Maximum tensile force	Maximum compressive force
X-type	41.0 K	-37.3 K
Alternating-Diagonal	6.13 K	-2.46 K
Single-Diagonal	15.0 K	-37.4 K

As can be seen in Table 10-3, the struts in the Single-Diagonal system will carry much higher compressive forces than those in the Alternating-Diagonal system. From a design standpoint, the struts are much shorter than the diagonals so the effect of the magnitude of force on the strut is not as significant compared to the longer diagonal. Therefore, from a bracing member perspective, the Single-Diagonal system is better than the Alternating-Diagonal system.

10.1.2 Sample calculations of the forces in top lateral bracing member

This section presents sample calculations for estimating the forces in the diagonals and struts located in the 25th and the 26th panels from the left support. Those two panels are arbitrarily chosen. The UTRAP solutions for the forces in the diagonals and the struts are shown in Figure 10.5 and Figure 10.6, respectively. The total forces developed in the top lateral bracing members result from three components: the horizontal component of the applied load due to sloping webs, vertical bending moment, and torsional moment. The horizontal component of the applied load in Model 3 under the uniform vertical load of 3.3 k/ft is 0.4125 k/ft. From Figure 10.3 and Figure 10.4 the bending moments in the middle of the 25th and the 26th panels are 477.1 k.ft and 2793.4 k.ft, and the corresponding torsional moments are –524.4 k.ft and –507.7 k.ft, respectively.

10.1.2.1 X-type top lateral bracing system

Figure 10.7 shows the properties of the X-type panel and the areas of the diagonal and the strut A_d and A_s, respectively.

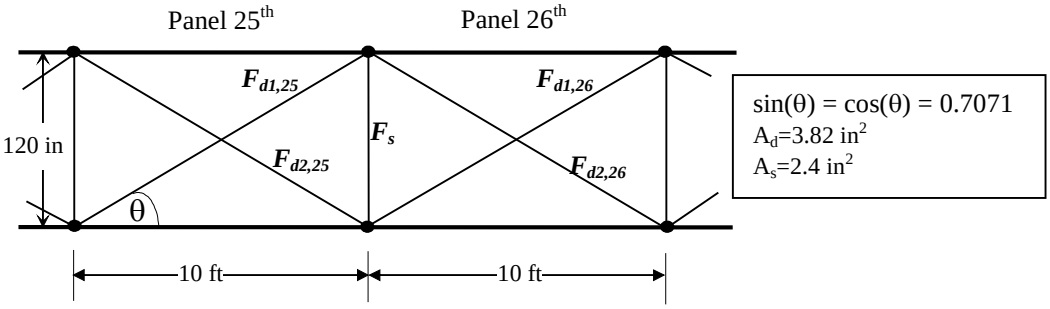

Figure 10.7 Properties of the X-type top lateral bracing system

The diagonal forces due to the horizontal component $F_{d,H}$ can be found from Eq.9.3:

$$F_{d,H} = \frac{A_d \sin^2(\theta)}{A_s + 2A_d \sin^3(\theta)} w_H s = \frac{(3.82)(0.7071)^2}{2.4 + 2(3.82)(0.7071)^3}(0.4125)(10) = 1.54\,\text{k}$$

The diagonal forces due to the horizontal component $F_{d,H}$ are the same for both the diagonal type 1 and type 2, and are the same in all panels.

In order to calculate the forces due to vertical bending, the cross-sectional properties of section P must first be calculated. The equivalent increase in each top flange area due to the presence of the X-type top lateral bracing system $A_{add,each}$ from Eq.9.19 is

$$A_{add,each} = \frac{\cos^3(\theta)}{\frac{1}{A_d} + \frac{2}{A_s}\sin^3(\theta)} = \frac{(0.7071)^3}{\frac{1}{3.82} + \frac{2}{2.4}(0.7071)^3} = 0.64 \quad \text{in}^2$$

The axial stress in top flange due to vertical bending in the middle of each panel can be calculated as follows:

$$\sigma_{tf,B,25} = M_{25}\frac{y_c}{I} = (477.1 \times 12)\frac{(50.803)}{202632} = -1.44 \text{ ksi}$$

$$\sigma_{tf,B,26} = M_{26}\frac{y_c}{I} = (2793.4 \times 12)\frac{(50.803)}{202632} = -8.40 \text{ ksi}$$

The diagonal forces due to vertical bending $F_{d,B}$ in both panels from Eq.9.15 are:

$$F_{d,B,25} = \frac{\sigma_{tf,B,25}\cos^2(\theta)}{\frac{1}{A_d}+\frac{2}{A_s}\sin^3(\theta)} = \frac{(-1.435)(0.7071)^2}{\frac{1}{3.82}+\frac{2}{2.4}(0.7071)^3} = -1.29 \text{ k}$$

$$F_{d,B,26} = \frac{\sigma_{tf,B,26}\cos^2(\theta)}{\frac{1}{A_d}+\frac{2}{A_s}\sin^3(\theta)} = \frac{(-8.404)(0.7071)^2}{\frac{1}{3.82}+\frac{2}{2.4}(0.7071)^3} = -7.55 \text{ k}$$

Due to vertical bending, both the type 1 and type 2 diagonals located in the same panel experience the same force, and thus:

$F_{d1,B,25} = F_{d2,B,25} = -1.29$ k and $F_{d1,B,26} = F_{d2,B,26} = -7.55$ k.

In order to calculate the forces due to torsional moment using the equivalent plate method (EPM), the shear flow q and the equivalent shearing force acting on the fictitious plate F_{plate} must first be determined. Both the magnitudes of q (Eq.9.26) and F_{plate} (Eq.9.27) in the middle of each panel can be calculated as follows:

$$q_{25} = \frac{T_{25}}{2A_o} = \frac{524.4\times 12}{2(8775)} = 0.359 \text{ k/in}$$

$$q_{26} = \frac{T_{26}}{2A_o} = \frac{507\times 12}{2(8775)} = 0.347 \text{ k/in}$$

$$F_{plate,25} = q_{25}\, a = (0.3586)(120) = 43.0 \text{ k}$$

$$F_{plate,26} = q_{26}\, a = (0.3466)(120) = 41.6 \text{ k}$$

The negative sign has been abandoned at this point in order to avoid confusion. The diagonal forces due to torsional moment in both panels can then be calculated using Eq.9.29.

$$F_{d,T,25} = \frac{F_{plate,25}}{2\sin(\theta)} = \frac{43.03}{2(0.7071)} = 30.4 \text{ k}$$

$$F_{d,T,26} = \frac{F_{plate,26}}{2\sin(\theta)} = \frac{41.6}{2(0.7071)} = 29.4 \text{ k}$$

The diagonal type 1 that is located on the negative torsional moment will experience a tensile force, whereas the diagonal type 2 will experience a compressive force. Using this convention, the forces in both the diagonal types 1 and 2 in both panels can be expressed as follows:

$$F_{d1,T,25} = 30.4 \text{ k} \quad \text{and} \quad F_{d2,T,25} = -30.4 \text{ k}$$

$$F_{d1,T,26} = 29.4 \text{ k} \quad \text{and} \quad F_{d2,T,26} = -29.4 \text{ k}$$

Having calculated the forces due to each component, the total diagonal force in each diagonal located in the 25th and 26th panels can be determined as follows:

$$F_{d1,25} = F_{d1,H,25} + F_{d1,B,25} + F_{d1,T,25} = 1.54 + (-1.29) + 30.4 = 30.7 \text{ k}$$

$$F_{d2,25} = F_{d2,H,25} + F_{d2,B,25} + F_{d2,T,25} = 1.54 + (-1.29) + (-30.4) = -30.2 \text{ k}$$

$$F_{d1,26} = F_{d1,H,26} + F_{d1,B,26} + F_{d1,T,26} = 1.54 + (-7.55) + 29.4 = 23.4 \text{ k}$$

$$F_{d2,26} = F_{d2,H,26} + F_{d2,B,26} + F_{d2,T,26} = 1.54 + (-7.55) + (-29.4) = -35.4 \text{ k}$$

Table 10-4 summarizes the total diagonal forces in the 25th and 26th panels obtained from the analytical formulas and the UTRAP solutions. It can be seen that there is good agreement between the two methods.

Table 10-4 Accuracy of analytical solution for diagonal forces- X-type system

Bracing member	Analytical formula	UTRAP solution	% discrepancy
$F_{d1,25}$	30.7 K	30.56 K	0.46 %
$F_{d2,25}$	-30.2 K	-30.28 K	-0.26 %
$F_{d1,26}$	23.4 K	22.43 K	4.3 %
$F_{d2,26}$	-35.4 K	-35.34 K	0.17 %

The strut forces due to the horizontal component $F_{s,H}$ from Eq.9.5 is:

$$F_{s,H} = \frac{A_s}{A_s + 2A_d \sin^3(\theta)} w_H s = \frac{2.4}{2.4 + 2(3.82)(0.7071)^3}(0.4125)(10) = 1.94 \text{ k}$$

The strut forces due to vertical bending are caused by the fact that the diagonal forces in the 25th and 26th panels are different because of non-uniform bending moment. The strut forces due to vertical bending $F_{s,B}$ can be calculated from Eq.9.9.

$$F_{s,B} = -(F_{d,B,25} + F_{d,B,26})\sin(\theta) = -(-1.29 - 7.55)(0.7071) = 6.25 \text{ k}$$

There is no force developed in the strut of the X-type system due to torsional moment (i.e. $F_{s,T} = 0$). So, the total strut force is:

$$F_s = F_{s,H} + F_{s,B} + F_{s,T} = 1.94 + 6.25 + 0 = 8.19 \text{ k.}$$

The UTRAP solution for that strut force is 8.57 k, about 4.4 percent higher.

10.1.2.2 Alternating-Diagonal top lateral bracing system

Figure 10.8 shows the properties of the Alternating-Diagonal panel and the areas of the diagonal and the strut A_d and A_s, respectively. The diagonals located in the 25th and the 26th panels are type 1 and type 2, respectively.

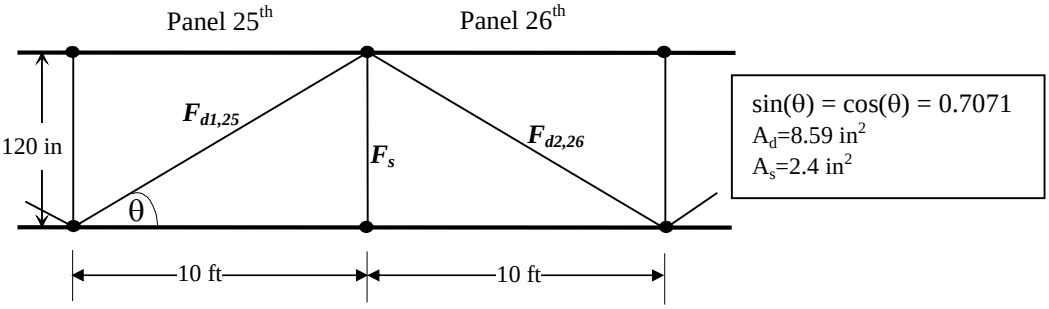

Figure 10.8 Properties of the Alternating-Diagonal top lateral bracing system

The diagonal forces due to the horizontal component $F_{d,H}$ in the Alternating-Diagonal system are assumed to be negligible. The equivalent increase in each top flange area due to the presence of the Alternating-Diagonal top lateral bracing system $A_{add,each}$ from Eq.9.25 is:

$$A_{add,each} = \frac{\cos^3(\theta)}{2\left[\frac{1}{A_d} + \frac{s^2\cos(\theta)\sin^2(\theta)}{24I_{tf}} + \frac{\sin^3(\theta)}{A_s}\right]}$$

$$= \frac{(0.7071)^3}{2\left[\frac{1}{8.59} + \frac{120^2(0.7071)(0.7071)^2}{24(200)} + \frac{(0.7071)^3}{2.4}\right]} = 0.13 \text{ in}^2$$

Even though both the X-type and the Alternating-Diagonal systems have the same equivalent plate thickness, $A_{add,each}$ in the Alternating-Diagonal system is only about 20 percent of that in the X-type system. The axial stress in the top flange due to vertical bending in the middle of each panel can be calculated as follows:

$$\sigma_{tf,B,25} = M_{25}\frac{y_c}{I} = (477.1\times 12)\frac{(51.115)}{200026} = -1.46 \text{ ksi}$$

$$\sigma_{tf,B,26} = M_{26}\frac{y_c}{I} = (2793.4\times 12)\frac{(51.115)}{200026} = -8.57 \text{ ksi}$$

For panels 25th and 26th in the X-type system, the bending stresses calculated previously were -1.44 ksi and -8.40 ksi, respectively. The bending stresses in the Alternating-Diagonal system are slightly larger.

The diagonal force due to vertical bending $F_{d,B}$ in both panels can be found from Eq.9.24.

$$F_{d,B,25} = \frac{\sigma_{tf,B,25}\cos^2(\theta)}{\frac{1}{A_d} + \frac{s^2\cos(\theta)\sin^2(\theta)}{24I_{tf}} + \frac{\sin^3(\theta)}{A_s}}$$

$$= \frac{(-1.463)(0.7071)^2}{\frac{1}{8.59} + \frac{(120)^2(0.7071)(0.7071)^2}{24(200)} + \frac{(0.7071)^3}{2.4}} = -0.553 \text{ k}$$

$$F_{d,B,26} = \frac{\sigma_{tf,B,26}\cos^2(\theta)}{\frac{1}{A_d} + \frac{s^2\cos(\theta)\sin^2(\theta)}{24I_{tf}} + \frac{\sin^3(\theta)}{A_s}}$$

$$= \frac{(-8.566)(0.7071)^2}{\frac{1}{8.59} + \frac{(120)^2(0.7071)(0.7071)^2}{24(200)} + \frac{(0.7071)^3}{2.4}} = -3.23 \text{ k}$$

The diagonal forces due to vertical bending in the Alternating-Diagonal system are only about 43 percent of those previously calculated for the X-type system. This supports the fact that the Alternating-Diagonal system is not as effective as the X-type system from a vertical bending standpoint.

Since there is only one diagonal per panel in the Alternating-Diagonal system, as opposed to two in the X-type system, the diagonal force due to torsional moment $F_{d,T}$ in the Alternating-Diagonal system is double of that in the X-type system. Mathematically, $F_{d,T}$ in the 25th and the 26th panels are:

$$(F_{d1,T,25})_{Alternating\text{-}Diagonal} = 2\,(F_{d1,T,25})_{X\text{-}type} = 2\,(30.43) = 60.86 \text{ k}$$

$$(F_{d2,T,26})_{Alternating\text{-}Diagonal} = 2\,(F_{d2,T,26})_{X\text{-}type} = 2\,(-29.4) = -58.8 \text{ k}$$

Having calculated the forces due to each component, the total diagonal forces in the 25th and 26th panels can be determined as follows:

$$F_{d1,25} = F_{d1,H,25} + F_{d1,B,25} + F_{d1,T,25} = 0 + (-0.553) + 60.86 = 60.3 \text{ k}$$

$$F_{d2,26} = F_{d2,H,26} + F_{d2,B,26} + F_{d2,T,26} = 0 + (-3.23) + (-58.8) = -62.0 \text{ k}$$

Table 10-5 shows the comparison between the predicted total diagonal forces and the UTRAP solutions. The discrepancies between the two results are only about two percent.

Table 10-5 Accuracy of analytical solution for diagonal forces – Alternating-Diagonal system

Bracing member	Analytical formula	UTRAP solution	% discrepancy
$F_{d1,25}$	60.3 K	61.52 K	-2 %
$F_{d2,26}$	-62.03 K	-60.75 K	2.1 %

Unlike in the X-type system, the struts in the Alternating-Diagonal system carry the entire horizontal component of the applied load. The strut force due to the horizontal component from Eq.9.7 is:

$$F_{s,H} = w_H s = (0.4125)(10) = 4.125 \text{ k}$$

The strut force due to the horizontal component in the Alternating-Diagonal system is more than double that in the X-type system.

From a bending perspective, the strut must carry the unbalanced diagonal forces due to non-uniform bending moment. In the Alternating-Diagonal system, the strut only carries half of the unbalanced diagonal forces because the top flanges carry the other half due to their lateral bending rigidity. The strut force due to vertical bending from Eq.9.20 is:

$$F_{s,B} = -\frac{1}{2}\left(F_{d,B,25} + F_{d,B,26}\right)\sin(\theta) = -\frac{1}{2}(-0.553 - 3.23)(0.7071) = 1.337 \text{ k.}$$

This strut force due to vertical bending in the Alternating-Diagonal system is much smaller than that in the X-type system.

The strut in the Alternating-Diagonal system has to pick up a portion of the unbalanced diagonal forces due to non-uniform torsional moment as given by Eq.9.36.

$$F_{s,T} = -\frac{1}{2}\left(F_{d1,T,25} + F_{d2,T,26}\right)\sin(\theta) = -\frac{1}{2}(60.86 - 58.8)(0.7071) = -0.728 \text{ k}$$

The total strut force is:

$$F_s = F_{s,H} + F_{s,B} + F_{s,T} = 4.125 + 1.337 + (-0.726) = 4.73 \text{ k.}$$

The UTRAP solution for this strut force is 3.92 k, giving a 21 percent difference between the solutions.

10.1.2.3 Single-Diagonal top lateral bracing system

Figure 10.9 shows the properties of the Single-Diagonal panel and the areas of the diagonal and the strut A_d and A_s, respectively. Both diagonals located in the 25th and the 26th panels are type 1.

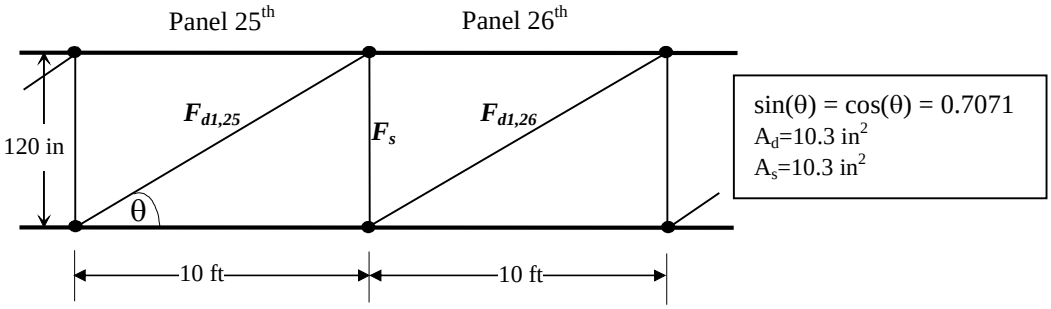

Figure 10.9 Properties of the Single-Diagonal top lateral bracing system

The diagonal forces in the Single-Diagonal system due to the horizontal component $F_{d,H}$ and due to vertical bending $F_{d,B}$ are negligible ($F_{d1,H,25} = F_{d1,H,26} = F_{d1,B,25} = F_{d1,B,26} = 0$). Therefore, only the torsional moment develops diagonal forces in the Single-Diagonal system. The magnitudes of the diagonal forces are determined from Eq.9.37, which are the same as those in the Alternating-Diagonal system, and are shown in Table 10-6.

Table 10-6 summarizes the predicted total diagonal forces, the UTRAP solutions, and the discrepancies between the results.

Table 10-6 Accuracy of analytical solution for diagonal forces – Single-Diagonal system

Bracing member	Analytical formula	UTRAP solution	% discrepancy
$F_{d1,25}$	60.86 K	59.96 K	1.5 %
$F_{d2,26}$	58.8 K	57.09 K	3 %

Comparing the total diagonal forces in the Alternating-Diagonal and the Single-Diagonal systems (Table 10-5 and Table 10-6), it can be seen that the magnitudes are about the same. However, both diagonal forces in the 25th and the 26th panels in the Single-Diagonal system are tensile, whereas those in the Alternating-Diagonal system are tensile and compressive, respectively.

The strut forces due to the horizontal component of the applied load in both the Single-Diagonal and the Alternating-Diagonal systems are the same and are expressed as follows:

$$(F_{s,H})_{Single\text{-}Diagonal} = (F_{s,H})_{Alternating\text{-}Diagonal} = w_H s = 4.125 \text{ k}$$

Since there are no diagonal forces due to vertical bending, the strut force due to vertical bending is also zero ($F_{s,B} = 0$). For torsional loading, the strut force from Eq.9.39 is

$$F_{s,T} = -\frac{1}{2}\left(F_{d1,T,25} + F_{d1,T,26}\right)\sin(\theta) = -\frac{1}{2}(60.86 + 58.8)(0.7071) = -42.3 \text{ k}$$

Since the diagonal forces due to torsional moment in both the 25th and the 26th panels of the Single-Diagonal system are tensile, as opposed to having one strut in tension and one in compression in the Alternating-Diagonal system, the strut forces due to torsional moment in the Single-Diagonal system are much larger than those in the Alternating-Diagonal system.

The total strut force can then be calculated as follows:

$$F_s = F_{s,H} + F_{s,B} + F_{s,T} = 4.125 + 0 + (-42.3) = -38.2 \text{ k}.$$

The UTRAP solution for this strut force is –37.35 k (2.3 percent discrepancy).

10.1.3 Deformation

This section presents the rotation and the vertical and horizontal displacements of Model 3 with the three different top lateral bracing systems using the member sizes shown in Table 10-1. Figure 10.10 shows the rotation of the bottom flange along the length of Model 3 continuous curved girder obtained from the UTRAP. It should be noted since the rotation is very small, the rotation plot is not smooth.

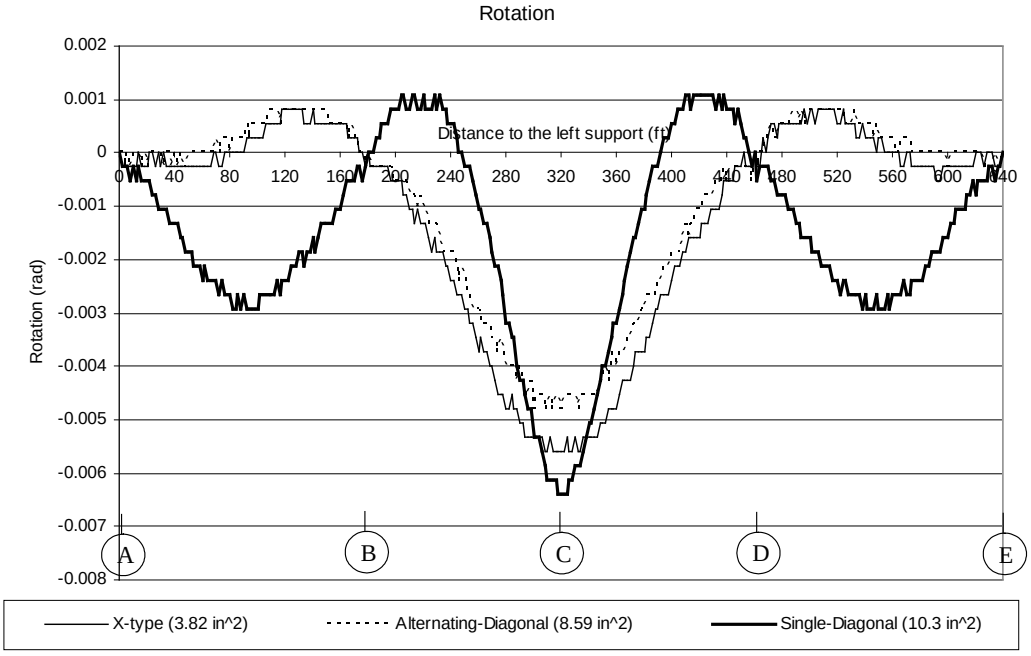

Figure 10.10 Rotation – Analysis I

Figure 10.10 shows that even though the equivalent plate thicknesses of section P in the three top lateral bracing systems are the same, the rotations are not the same. Although the maximum rotation of the girder with the X-type

system is larger than with the Alternating-Diagonal system, the rotation variation along the length is generally similar. The girder with the Single-Diagonal system experiences the largest midspan rotation, while the girder with the Alternating-Diagonal system experiences the smallest midspan rotation. In addition, it can be seen that the rotation variations along the length with Single and Alternating-Diagonal systems are significantly different.

Figure 10.11 shows the vertical and horizontal deflections along the length. The vertical and horizontal deflections of the node located in the middle of the bottom flange are shown. The positive and negative horizontal deflections indicate the lateral movement toward and farther away from the center of curvature, respectively. The support B, located at 180 ft from the left support, is pinned (i.e. cannot move laterally). The horizontal displacements have been plotted on a reverse scale in order to physically correlate displacements with the plan view of the girder shown in Figure 10.2. The vertical displacements of a Model 3 girder are independent of the top lateral bracing system, whereas the horizontal displacements are not. The horizontal displacements with the X-type and the Alternating-Diagonal systems are about the same, while the horizontal displacements with the Single-Diagonal system are in the opposite direction and have a much larger magnitude.

In order to study the effect of changing the location of the pinned support on the horizontal displacements, Figure 10.12 shows the horizontal displacements of Model 3 with the exterior support (support A) pinned.

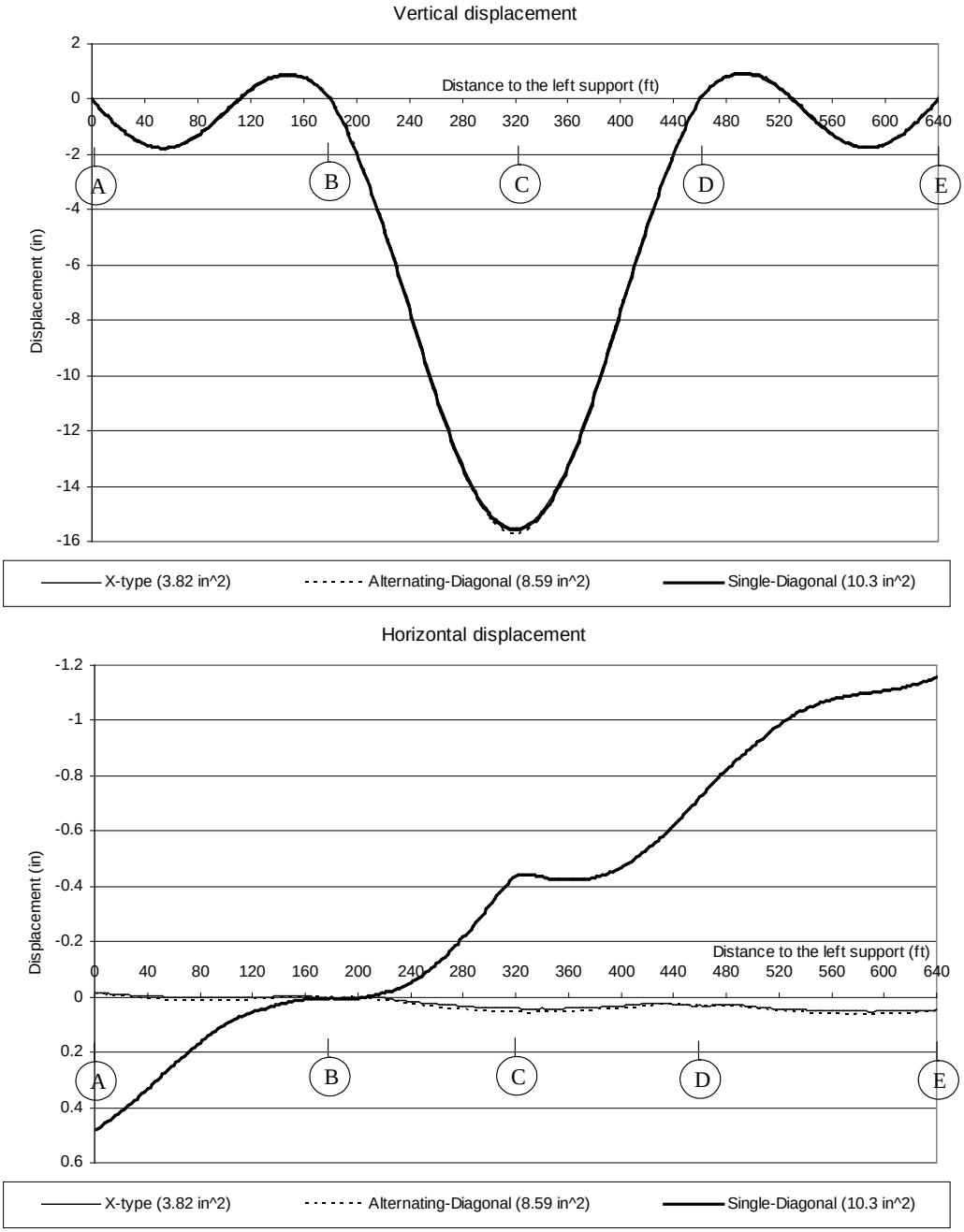

Figure 10.11 Deflections - Analysis I

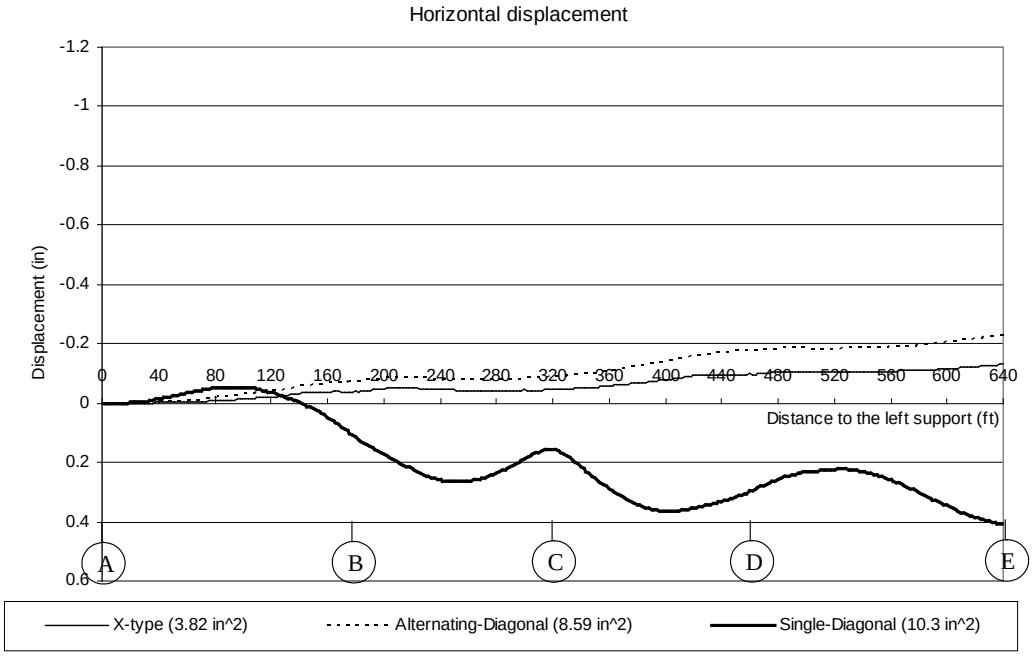

Figure 10.12 Horizontal displacements with the exterior support pinned

Comparing the horizontal displacements in Figure 10.11 and Figure 10.12, shows that the horizontal displacement variations along the length are very sensitive to the support conditions. The horizontal displacements with an interior support pinned are opposite to those with an exterior support pinned. For both the X-type and the Alternating-Diagonal systems, the maximum horizontal displacement with the interior support pinned is approximately half of that with the exterior support pinned. However, with the Single-Diagonal system, the maximum horizontal displacement with the interior support pinned is approximately double that with the exterior support pinned. Pinning the exterior support instead of the interior support cause the X-type and the Alternating-Diagonal systems to laterally move away from the center of curvature (i.e. (-) horizontal displacement)

and causes the girder with the Single-Diagonal system to move toward the center of curvature.

10.1.4 Total normal stresses

This section discusses the maximum tensile and compressive total normal stresses in a girder with the different top lateral bracing systems using the member sizes shown in Table 10-1. The maximum total normal stresses are found from the total normal stresses on the entire cross-section along the length of the girder. Because the equivalent plate thicknesses and the spacing of the internal diaphragms for all three top lateral bracing systems are the same, both the maximum ordinary and distortional warping normal stresses must be the same. It should be noted, though, that the maximum bending normal stresses in a girder with the X-type system are slightly smaller than those in the Alternating-Diagonal and the Single-Diagonal systems. And the maximum bending normal stresses in girders with the Alternating-Diagonal and the Single-Diagonal systems are about the same.

Table 10-7 summarizes the maximum total normal stresses for the Model 3 continuous curved girder under a uniform load of 3.3 k/ft with the interior support (support B) pinned. The maximum compressive stress in the X-type system is smaller than that in the Alternating-Diagonal and the Single-Diagonal systems. This observation agrees with the fact that the bending normal stresses in a girder with the X-type system are slightly smaller than those with the Alternating-Diagonal or the Single-Diagonal systems. The maximum tensile and compressive total normal stresses with the Alternating-Diagonal system are larger than those with the Single-Diagonal system. These observations suggest that the localized normal stresses in the Alternating-Diagonal system are larger than those

in the Single-Diagonal system, since the bending normal stresses, the ordinary and the distortional warping normal stresses in both systems are practically the same.

Table 10-7 Maximum total normal stresses

Type of stresses	X-type	Alternating-Diagonal	Single-Diagonal
Compressive	-32.35 Ksi	-35.99 Ksi	-35.31 Ksi
Tensile	35.13 Ksi	38.53 Ksi	35.23 Ksi

Table 10-8 shows the total normal stress in Model 3 with the exterior support pinned. Comparing the maximum total normal stress with the interior and with the exterior support pinned (Table 10-7 and Table 10-8) shows that changing the location of the pinned support does not affect the total normal stress

Table 10-8 Maximum total normal stresses in Model 3 with support A pinned

Type of stresses	X-type	Alternating-Diagonal	Single-Diagonal
Compressive	-32.35 Ksi	-35.99 Ksi	-35.31 Ksi
Tensile	35.12 Ksi	38.53 Ksi	35.22 Ksi

10.2 ANALYSIS II

Having calculated the axial forces in each member of the top lateral bracing system in Analysis I, the members in each top lateral bracing system can be designed appropriately. Analysis II was performed using the required member sizes for each top lateral bracing system to carry the axial forces as determined from Analysis I.

10.2.1 Designing top lateral bracing members

The third edition of the Manual of Steel Construction (LRFD) specification was used to determine the required member sizes. The unbraced length of the diagonals and the struts in all top lateral bracing systems are 14.1 ft and 10 ft, respectively. As compression members, both the diagonals and the struts are assumed to be pin-ended columns (k=1.0) in bending about both principal axes. Design of the diagonals in the X-type system is controlled by the compressive force. An effective length equal to the actual length of the diagonal (14.1 ft) was used in determining the column capacity. If the other diagonal is always in tension, an effective length equal to one half the diagonal length could be used. All connections are assumed to be bolted in single shear with the bolt threads excluded from the shear plane. Two rows of ¾ inch diameter A325 bolts are used. All members are assumed to be WT shapes. summarizes the required member sizes of each top lateral bracing system based on the maximum tensile and compressive forces obtained from the Analysis I results. The corresponding equivalent plate thicknesses are also shown.

The Single-Diagonal system requires the smallest diagonals, whereas the Alternating-Diagonal system requires the largest. However, the Alternating-Diagonal system requires the smallest struts, whereas the Single-Diagonal system requires the same struts as the X-type. Using the member size shown in , the total weight of all bracing members in Model 3 with the X-type, the Alternating-Diagonal, and the Single-Diagonal systems are 30.4 kip, 17.3 kip, and 16.9 kip, respectively. It should be noted that from a construction cost standpoint, the X-type system is more expensive than the two other systems because it requires more connections.

Table 10-9 Properties of the top lateral system used in Analysis II

	X-type	Alternating-Diagonal	Single-Diagonal
Diagonals	WT 6x13 (3.82 in^2)	WT 6x15 (4.40 in^2)	WT 5x11 (3.24 in^2)
Struts	WT 5x11 (3.24 in^2)	WT 5x6 (1.77 in^2)	WT 5x11 (3.24 in^2)
t_{eq} section P	0.05738 in	0.03378 in	0.01843 in
t_{eq} section N	0.05865 in	0.03407 in	0.01856 in

The member sizes in the internal K-frames were kept the same as those used in Analysis I.

10.2.2 Top lateral bracing forces

Figure 10.13 shows the diagonal forces in the three top lateral bracing systems for both Analysis I and Analysis II. Because the diagonal size in the X-type system for both Analysis I and II are similar, only one result is presented for diagonal forces in the X-type system. Figure 10.13 shows that the diagonal forces in each top lateral bracing system for both Analysis I and Analysis II are about the same. Changing the member size does not affect the force in the member significantly. Therefore, the diagonal sizes shown in are satisfactory.

Figure 10.14 shows the strut forces in each top lateral bracing system for both Analysis I and Analysis II. Like the diagonal forces, the strut forces in Analysis II are not significantly different that those in Analysis I.

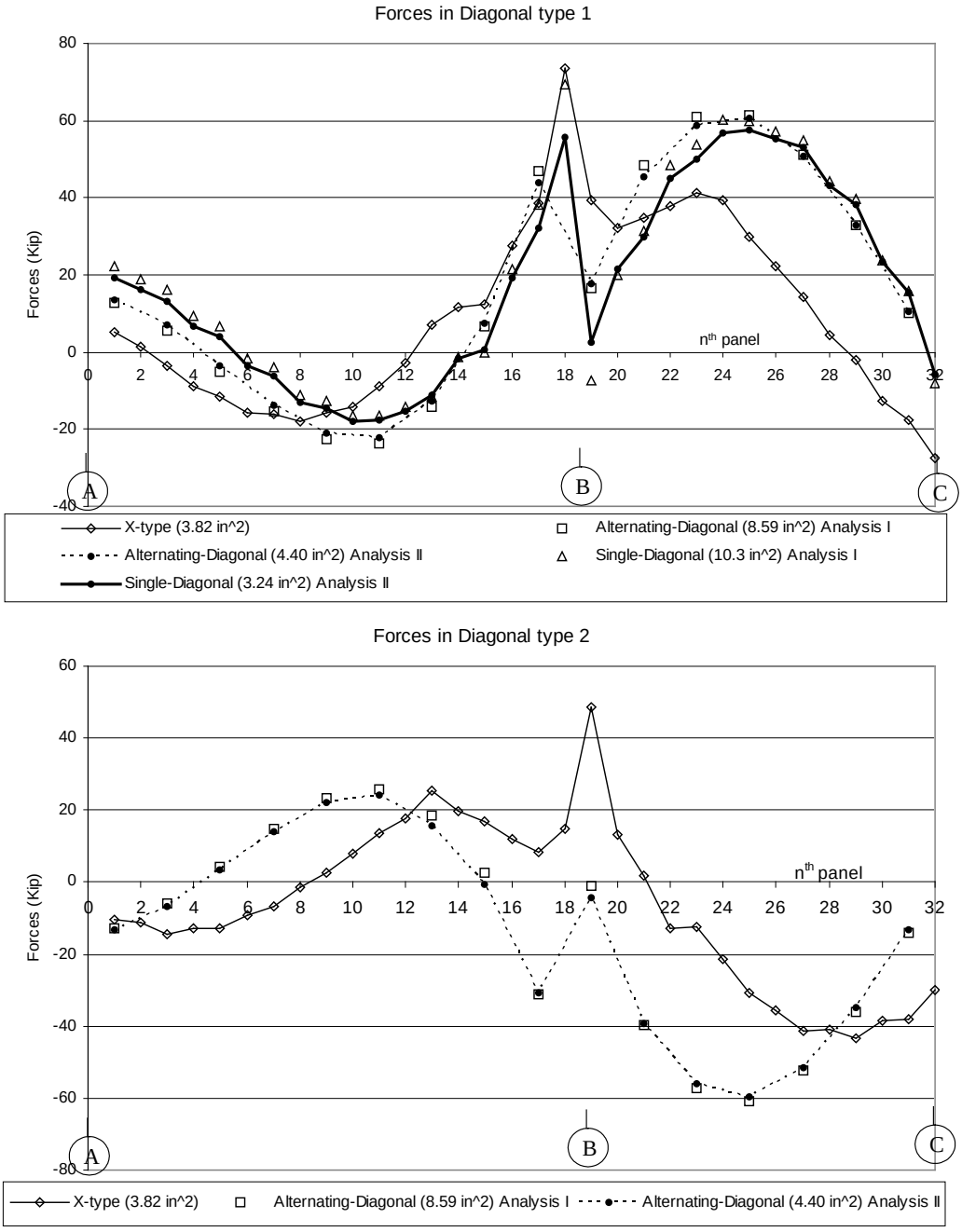

Figure 10.13 Diagonal forces for Analysis I and II

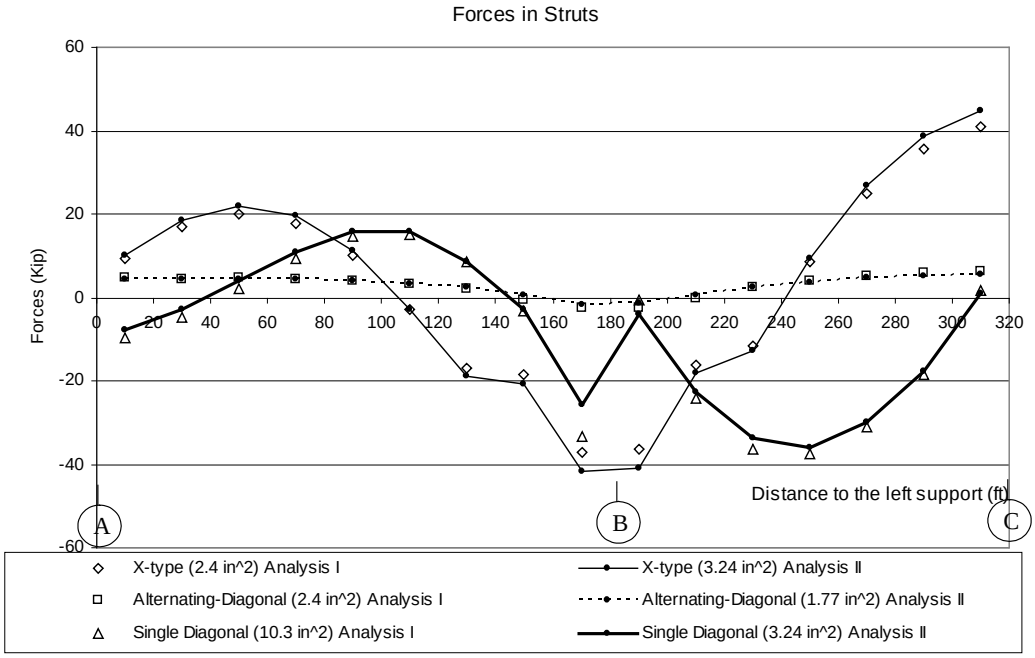

Figure 10.14 Strut forces for Analysis I and II

10.2.3 Deformation

This section presents the effect of changing member size in the top lateral bracing system on the girder deformations. Figure 10.15 shows the twist along the length from Analysis II. Table 10-10 summarizes the maximum rotations of Model 3 in Analysis I and Analysis II.

Comparing the maximum rotations for each top lateral bracing system in both Analysis I and Analysis II shows that the maximum rotation is very sensitive to the equivalent plate thickness. Increasing the strut area in the X-type system from 2.4 in^2 in Analysis I to 3.24 in^2 in Analysis II does not affect the equivalent plate thickness, and thus does not change the maximum rotation. In the Alternating- Diagonal system, decreasing the diagonal area by 49% causes a 67% increase in the maximum rotation. In the Single-Diagonal system, a 69%

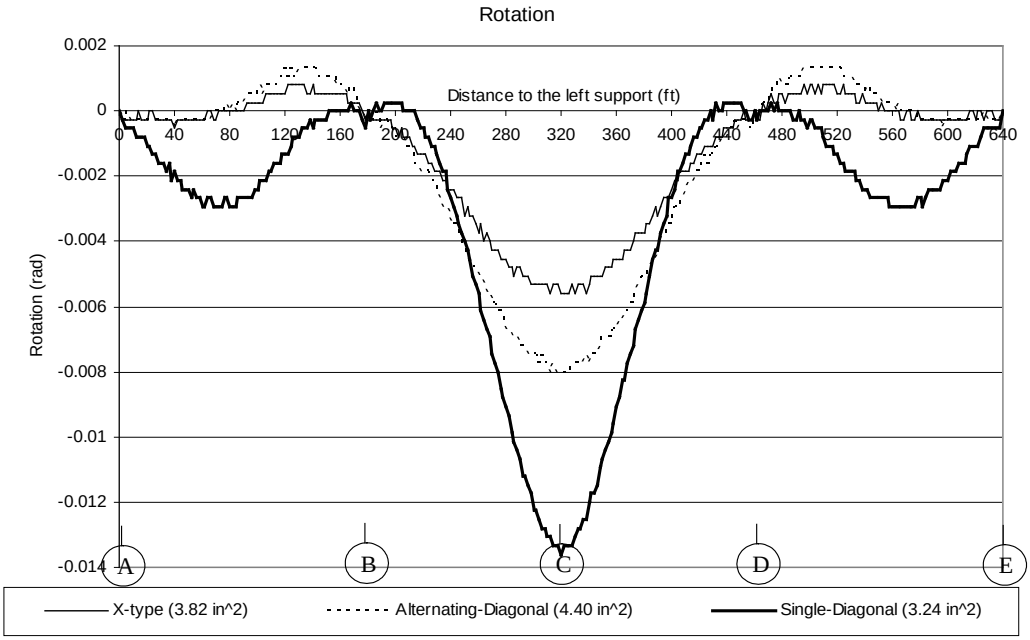

Figure 10.15 Rotation - Analysis II

Table 10-10 Maximum rotation in Analysis I and Analysis II

Top lateral bracing system	Analysis	Maximum rotation *
X-type	Analysis I (A_d=3.82 in^2)	0.0056 rad
	Analysis II (A_d=3.82 in^2)	0.0056 rad
Alternating-Diagonal	Analysis I (A_d=8.59 in^2)	0.0048 rad
	Analysis II (A_d=4.40 in^2)	0.008 rad
Single Diagonal	Analysis I (A_d=10.3 in^2)	0.0064 rad
	Analysis II (A_d=3.24 in^2)	0.0136 rad

* **Note:** Only the absolute value is presented. The actual value of the largest rotation is negative, which means counter-clockwise rotation.

decrease in diagonal area results in a 210% increase in the maximum rotation. The additional rotation is not linearly proportional to the reduction in the diagonal area. The difference in the equivalent plate thickness among the three top lateral bracing systems is not the only factor causing the difference in the maximum rotation. As presented in Analysis I, the maximum rotations of Model 3 with the three different top lateral bracing systems are different even though the equivalent plate thickness are the same.

Figure 10.16 shows both the vertical and the horizontal deflections. In this case, the interior support (support B) is pinned. Comparing the deflections between Analysis I and Analysis II (Figure 10.11 and Figure 10.16) shows that changing the top lateral bracing member sizes does not alter the vertical displacement. However, it does alter the horizontal displacement. With the smaller equivalent plate thickness, the magnitude of the horizontal deflection with the Alternating-Diagonal system in Analysis II is larger (more positive) than that in Analysis I. However, the magnitude of the horizontal deflection with the Single-Diagonal system in Analysis II is smaller (less negative) than that in Analysis I.

As seen in Figure 10.15 and Figure 10.16, the largest rotation and vertical displacement occur at the midspan (point C). In order to provide a better physical understanding of the cross-section deformation, Figure 10.17 shows the deformed position at the midspan for the three different top lateral bracing systems. The deformed positions with the three different top lateral bracing systems are not significantly different. Even though the rotation with the Single-Diagonal system is more than double that with the X-type and Alternating-Diagonal systems, from an overall girder dimension perspective, one can hardly see the difference in the deformed position. This observation suggests that in evaluating the advantages and disadvantages of the top lateral bracing systems from the deformation

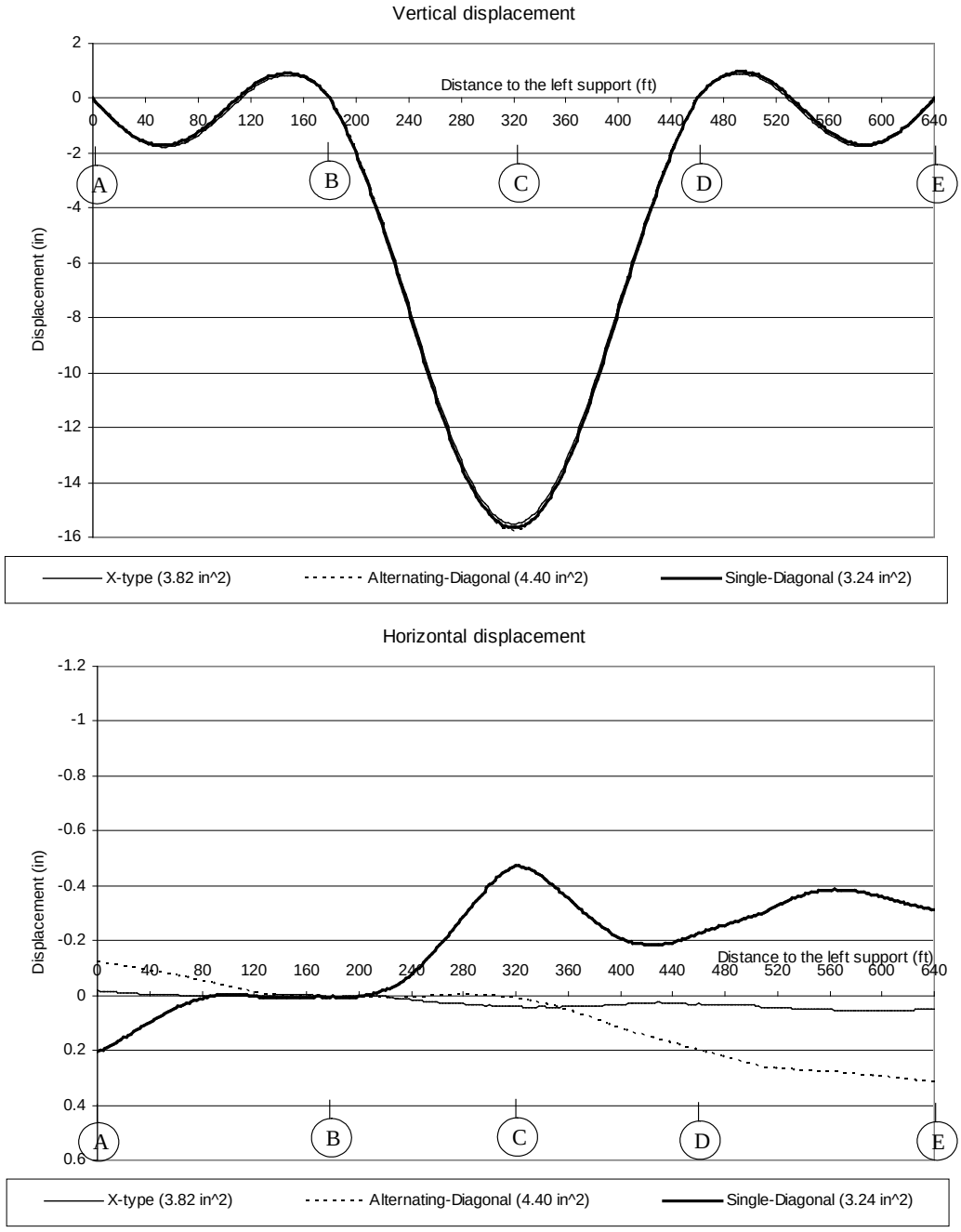

Figure 10.16 Deflections – Analysis II

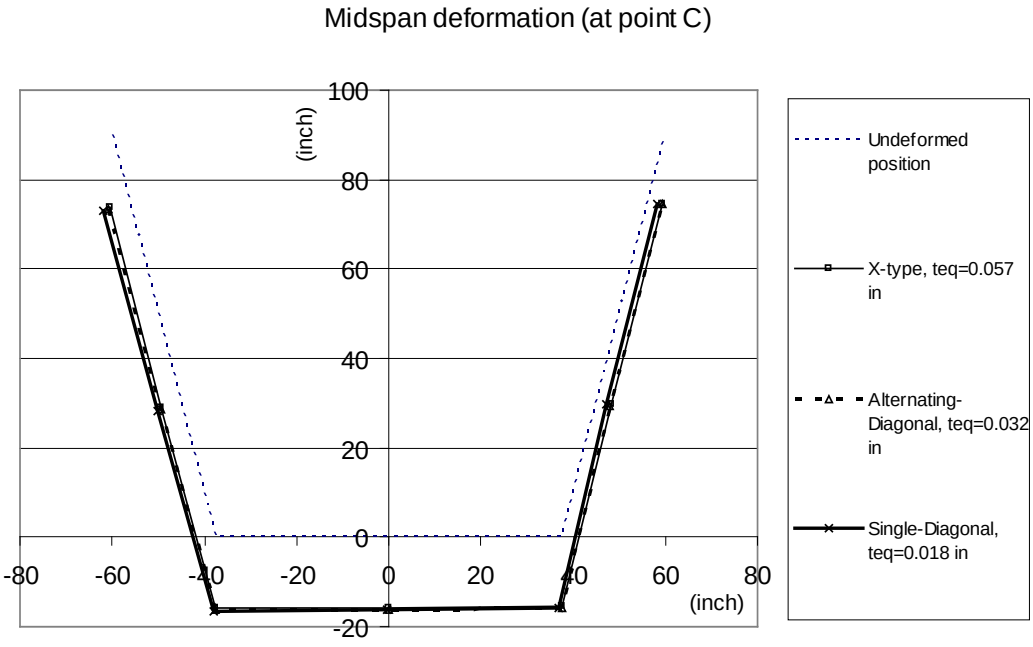

Figure 10.17 Deformed position at the midspan (at 320 ft from support A)

standpoint, percent difference should not be the sole criterion. Solely based on this criterion, the Single-Diagonal system is less suitable than the other systems. However, since the magnitudes of the rotations are very small, any of the three lateral bracing systems can be acceptable with regard to rotations.

Figure 10.18 shows the horizontal displacements for the exterior support (support A) pinned. Comparing the horizontal displacements with the exterior support pinned between Analysis I and Analysis II (Figure 10.12 and Figure 10.18) shows that as the equivalent plate thickness decreases, the girder moves laterally toward the center of curvature (more positive horizontal displacement). Unlike in Analysis I, pinning the exterior support with the Alternating-Diagonal system decreases the magnitude of the horizontal displacement. So, the

advantages and disadvantages of having the exterior support pinned instead of the interior support depends on the equivalent plate thickness.

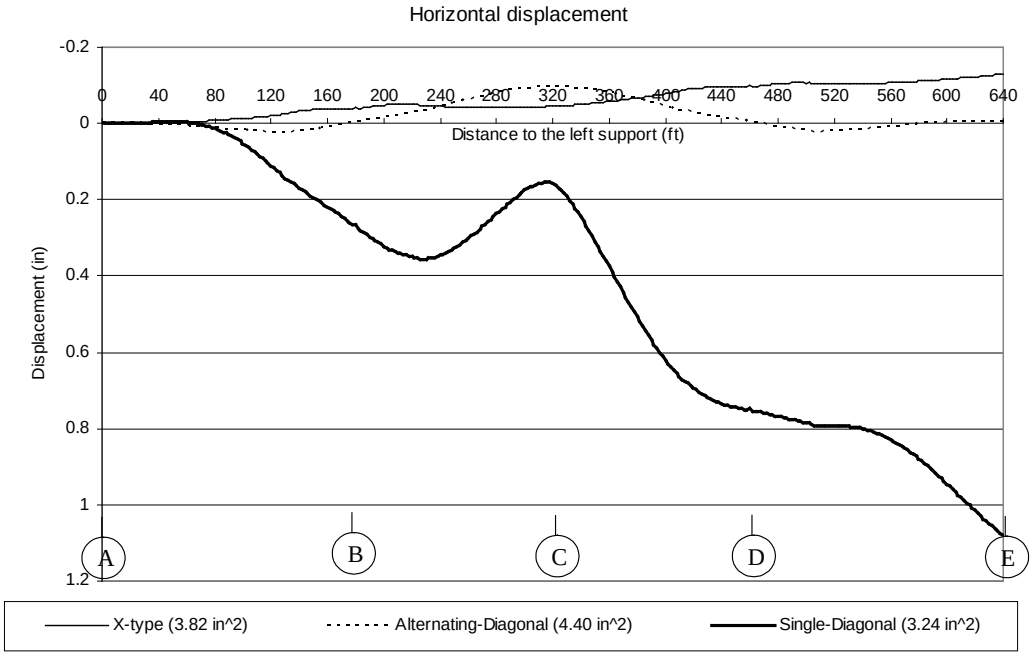

Figure 10.18 Horizontal displacements with the exterior support pinned

10.2.4 Total normal stresses

In Analysis II, since the equivalent plate thicknesses of the three top lateral bracing systems are different, the ordinary warping normal stresses are not the same. However, the distortional warping normal stresses in all systems are the same because the spacing and member sizes of the internal diaphragms are the same. The maximum final total tensile and compressive normal stresses in each system are presented in Figure 10.19. The continuous curved girder has the interior support (support B) pinned. Analysis I results are also shown. Changing the top lateral bracing member sizes does not affect the maximum total normal stresses significantly. Girders with the X-type system and the Alternating-

Diagonal system in Analysis II experience the smallest and the largest total normal stresses, respectively.

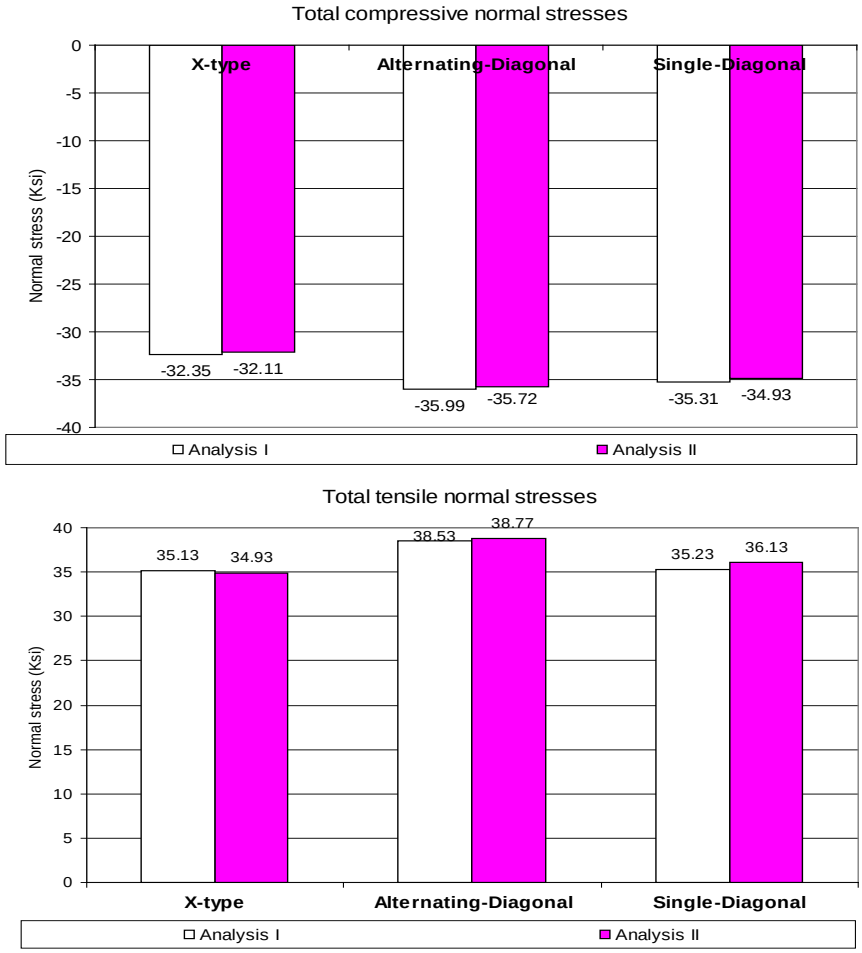

Figure 10.19 Comparison of total normal stresses from Analysis I and II

10.3 ANALYSIS III

Analysis III studied the effect of modifying the direction of the diagonal members from the Alternating-Diagonal to the Single-Diagonal system. For this

purpose, all member sizes in both systems are chosen to be the same. The diagonal and strut areas used in this analysis are 4.40 in^2 and 3.24 in^2, respectively. The internal diaphragms, consisting of a k-frame with 3.24 in^2 members, are used every 2 ft. It should be noted that the equivalent plate thicknesses of the systems are not the same. The equivalent plate thickness of section P and N in the Alternating-Diagonal system are 0.03159 in and 0.03317 in, respectively, whereas those in the Single-Diagonal system are 0.02282 in and 0.02302 in, respectively. In this case, changing the direction of the diagonal members from the Alternating-Diagonal to the Single-Diagonal system without altering the member size decreases the equivalent plate thickness.

10.3.1 Top lateral bracing forces

Figure 10.20 and Figure 10.21 show the diagonal and strut forces, respectively, for a half length of Model 3. The diagonal forces are shown in both real and absolute terms. Figure 10.20 shows that changing the direction of diagonals from the Alternating-Diagonal to the Single-Diagonal system causes the forces in some diagonals to flip from compressive to tensile. However, from the absolute value comparison, it can be observed that changing the diagonal direction does not affect the magnitude of diagonal forces significantly. Since the Alternating-Diagonal system is more effective from a vertical bending perspective, there are small discrepancies between the absolute value of the diagonal forces in the systems. Changing the diagonal direction has significant effect on the strut forces as shown in Figure 10.21. The strut forces in the Single-Diagonal system are much larger than those in the Alternating-Diagonal system.

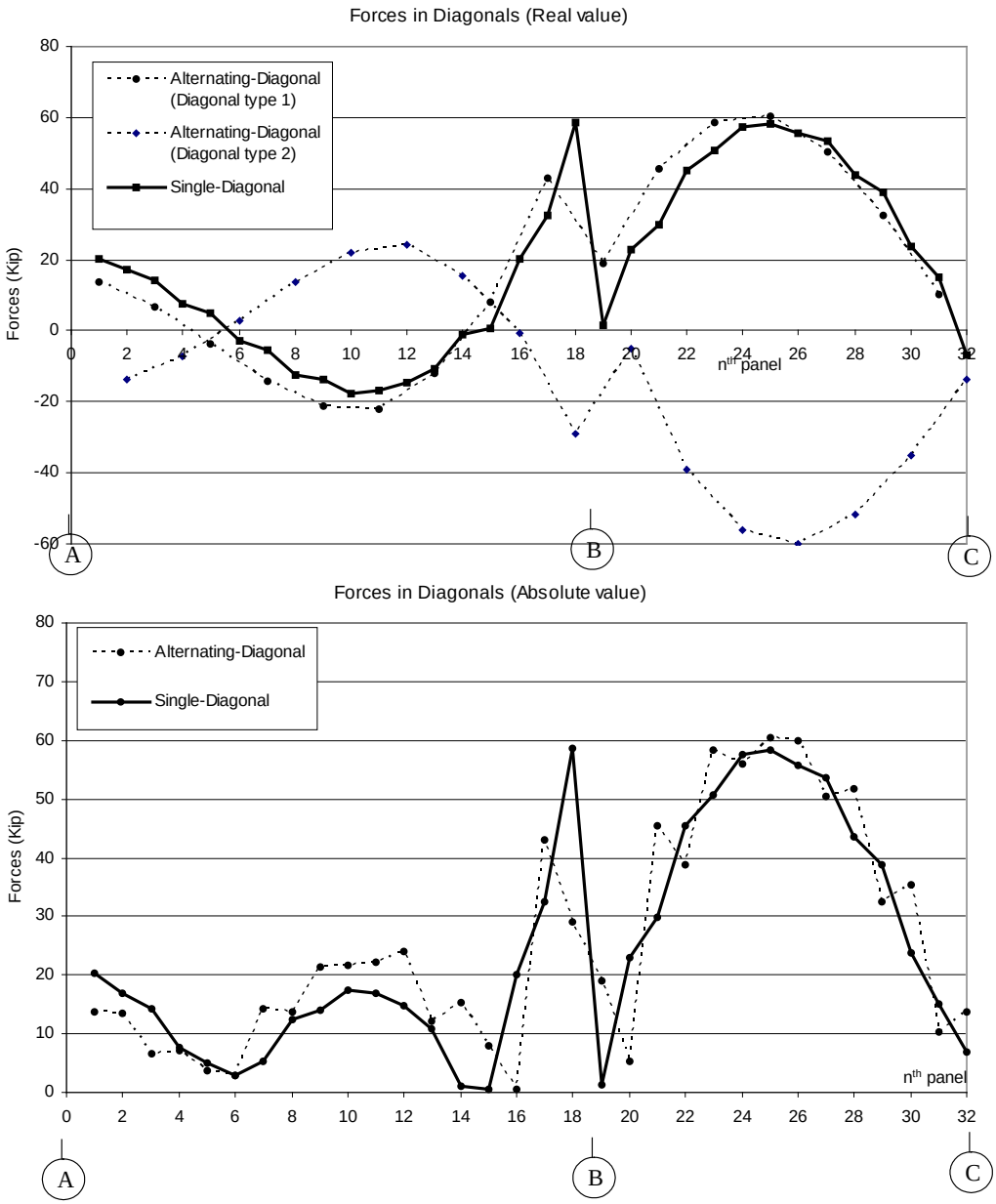

Figure 10.20 Diagonal forces – Analysis III

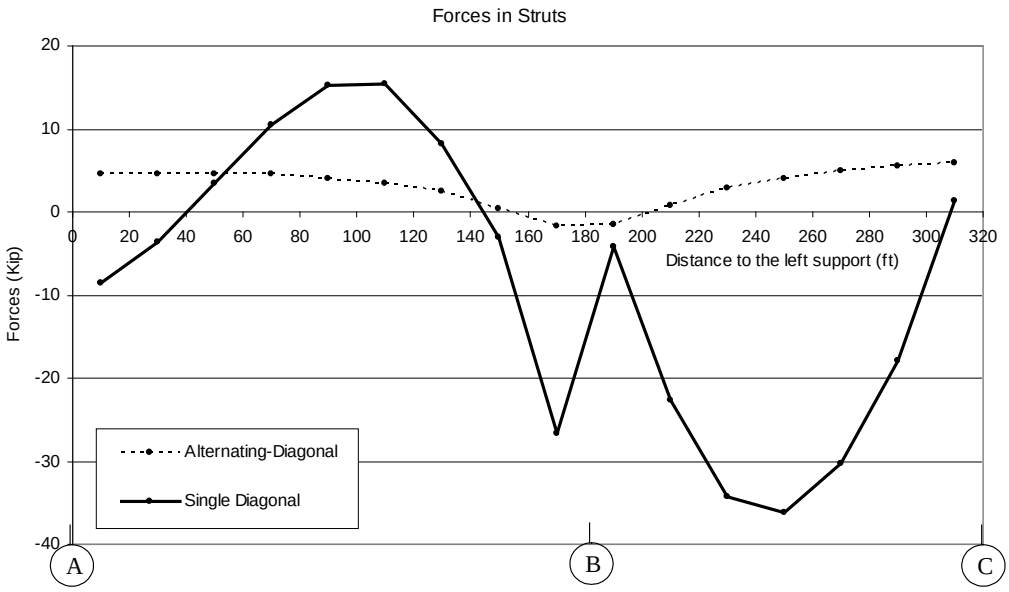

Figure 10.21 Strut forces – Analysis III

10.3.2 Deformation

To aid the understanding of the effect of changing the diagonal direction on girder deformation, rotation and horizontal displacement between Model 3 girders with the Alternating-Diagonal and the Single-Diagonal systems are presented. The vertical deflections are insensitive to the type of top lateral bracing system so will not be discussed. Figure 10.22 shows the rotations along the length. Figure 10.22 shows that the maximum rotation with the Single-Diagonal system is larger than that with the Alternating-Diagonal. Since all bracing members in both systems are the same, the difference in the maximum rotation between the Single-Diagonal and the Alternating-Diagonal systems is solely due to the difference in the diagonal direction. The lateral displacements of the top flanges in a girder with a Single-Diagonal system are significantly larger than those in a girder with an Alternating-Diagonal system as discussed in Chapter 6.

However, the bottom flange does not want to move laterally as much as the top flanges. Consequently, the larger lateral displacements of the top flanges are accompanied by larger rotations.

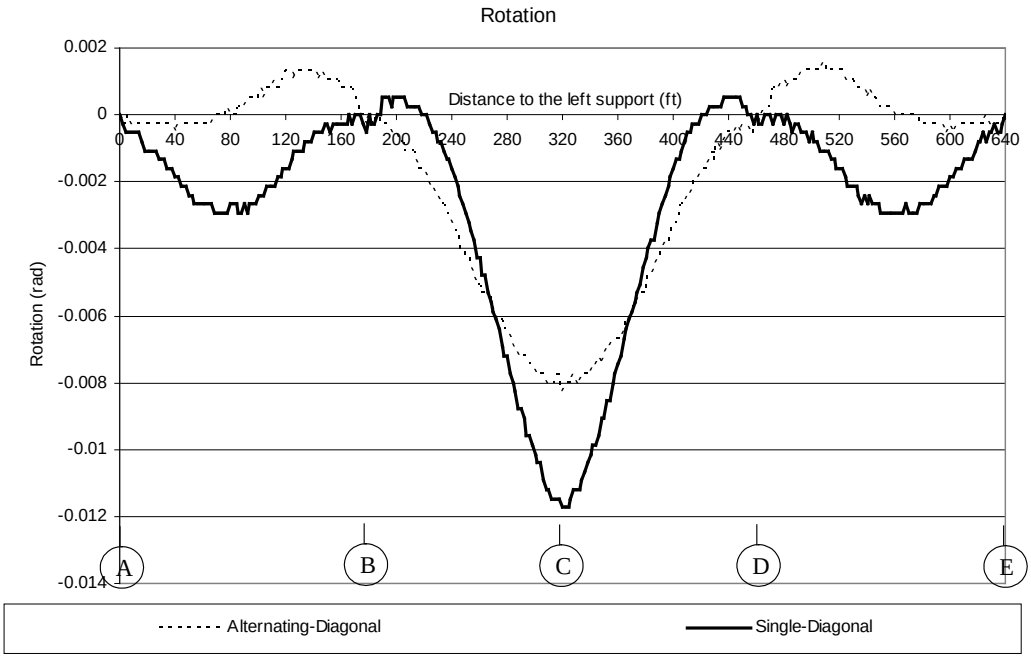

Figure 10.22 Rotation – Analysis III

Figure 10.23 shows a comparison of horizontal displacements of the node located in the middle of the bottom flange of Model 3 between the Alternating-Diagonal and the Single-Diagonal systems. Figure 10.23 shows that changing the orientation of diagonals from the Alternating-Diagonal to the Single-Diagonal system causes the bottom flange to move in the opposite direction. In addition, the magnitude of the horizontal displacement in a girder with the Single-Diagonal system is larger than in that with the Alternating-Diagonal system.

10.3.3 Total normal stress

Table 10-11 shows the maximum compressive and tensile normal stresses with the Alternating-Diagonal and the Single-Diagonal systems.

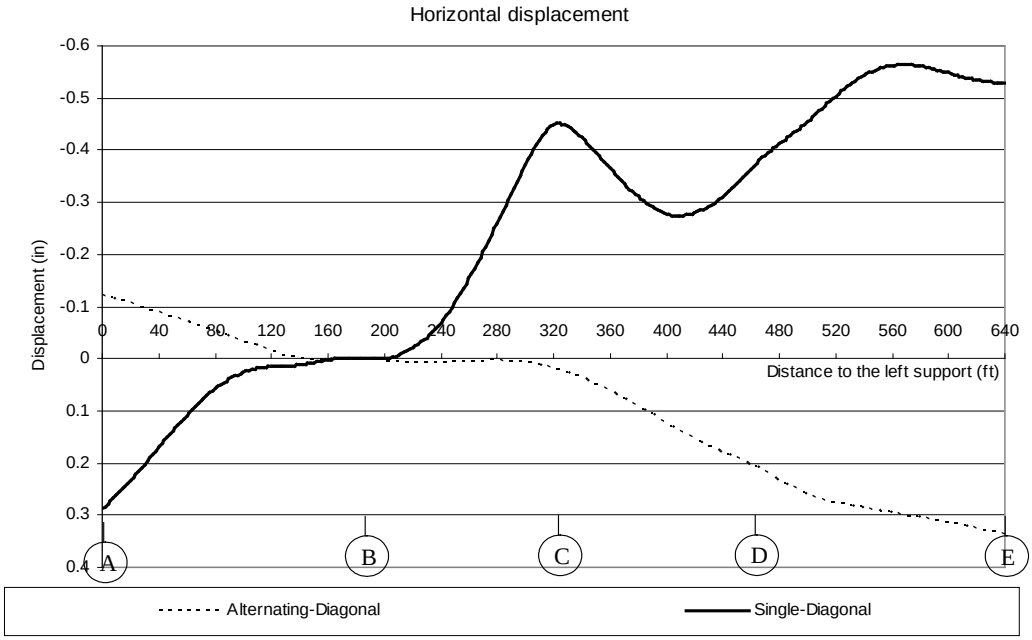

Figure 10.23 Horizontal displacements – Analysis III

Table 10-11 Maximum total normal stresses

Type of stresses	Alternating-Diagonal	Single-Diagonal
Compressive	-35.86 Ksi	-35.06 Ksi
Tensile	38.82 Ksi	35.74 Ksi

Both the compressive and tensile stresses with the Single-Diagonal system are slightly smaller than those with the Alternating-Diagonal system. In general, changing the diagonal direction from the Alternating-Diagonal to the Single-Diagonal system has a very small effect on the total normal stress.

10.4 SUMMARY

This chapter presented an examination of the top lateral bracing forces in a continuous curved girder under a symmetric uniformly distributed load. There was good agreement between the predicted top lateral bracing forces and the UTRAP solutions for the three different top lateral bracing systems.

The diagonals in the Single-Diagonal system can be designed with a smaller member size because the maximum compressive force is smaller than those in the X-type or Alternating-Diagonal systems. For systems with the same equivalent plate thickness, the X-type and Alternating-Diagonal systems show a similar torsional response, whereas the response of the Single-Diagonal system is quite different. Vertical displacements are similar for all three bracing systems. The maximum tensile and compressive total normal stresses in the X-type system are the smallest and those with the Alternating-Diagonal system are the largest.

Changing the bracing member sizes does not affect the member forces significantly. In addition, both the vertical deflection and the total normal stress are generally insensitive to the member size. However, changing the member sizes does affect the rotation and the horizontal displacement. Using a smaller bracing member decreases the equivalent plate thickness and leads to a larger rotation.

Changing the direction of the diagonal members from the Alternating-Diagonal system to the Single-Diagonal system without altering the member size decreases the equivalent plate thickness. Consequently, the maximum rotation and the maximum horizontal displacement in a girder with the Single-Diagonal system are larger than that with the Alternating-Diagonal system. However, the maximum compressive and tensile total normal stresses in a girder with the Single-Diagonal system are slightly smaller than those in a girder with the Alternating-Diagonal system.

CHAPTER 11
Continuous Curved Girder Behavior during the Pouring Sequence

This chapter focuses on the top lateral bracing forces, girder deformations, and total normal stresses developed in a continuous girder during the pouring sequence. The Alternating-Diagonal and Single-Diagonal arrangements as shown in Figure 10.2 are evaluated for the Model 3 continuous curved girder with three different deck pouring sequences, denoted as A,B, and C. The only difference between the pouring sequences is the length of each concrete pour. Each pouring sequence consists of five consecutive pours; the pour order in all cases is the same. The first and second pours place concrete at the beginning and end of the spans AB and DE, respectively. The third pour places concrete near the midspan of the span BD. The fourth and fifth pours place concrete in the vicinity of supports B and D, respectively. Between each pour, the concrete modulus and the shear stud stiffness are assumed to be increased by 1000 ksi and 250 k/in, respectively. However, during the entire pour, the concrete modulus and the shear studs stiffness are assumed to be not greater than 2000 ksi and 500 k/in, respectively. All of these values are based on the example problem shown in the UTRAP manual (Topkaya et.al., 2002). The details of each pouring sequence are presented in the following sections.

11.1 POURING SEQUENCE A

Figure 11.1 shows details of pouring sequence A. There are two different cases, A-1 and A-2, used in this pouring sequence. In A-1, the member sizes in both the Alternating-Diagonal and the Single-Diagonal systems are the same. In A-2, the member sizes in each system are designed to carry the maximum forces in that member. The third edition of the Manual of Steel Construction (LRFD) specification is used as a guideline to determine the required member sizes.

UTRAP can perform multiple analyses corresponding to each pour independently. In this case, the analyses corresponding to the order of pouring are denoted Analysis 1 through Analysis 5. The uniform load used in this pouring sequence is 3.3 k/ft. The results from each analysis are summed up sequentially to determine the maximum values.

11.1.1 Case A-1

In this case, a WT 6x20 was used for the diagonals and struts for both the Alternating-Diagonal and the Single-Diagonal systems.

11.1.1.1 Diagonal forces

Figure 11.2 and Figure 11.3 show the total diagonal forces in the 2^{nd} and 20^{th} panels, respectively, after each concrete pour. There is concrete above the 2^{nd} panel since the first pour, whereas there is no concrete above the 20^{th} panel until the last pour. Figure 11.2 shows that the diagonal forces in the locations where the concrete has gained stiffness do not change significantly during subsequent pours. Figure 11.3 shows that the diagonal forces during concrete pour can change significantly. And the maximum forces can occur before the final pouring.

DECK	LENGTH (ft)	ANALYSIS 1			ANALYSIS 2			ANALYSIS 3			ANALYSIS 4			ANALYSIS 5		
		Coc.Mod*	Std.Stiff**	Load***	Coc.Mod	Std.Stiff	Load	Coc.Mod	Std.Stiff	Load	Coc.Mod	Std.Stiff	Load	Coc.Mod	Std.Stiff	Load
1	85	0	0	3.3	1000	250	0	2000	500	0	2000	500	0	2000	500	0
2	180	0	0	0	0	0	0	0	0	0	0	0	3.3	1000	250	0
3	110	0	0	0	0	0	0	0	0	3.3	1000	250	0	2000	500	0
4	180	0	0	0	0	0	0	0	0	0	0	0	0	0	0	3.3
5	85	0	0	0	0	0	3.3	1000	250	0	2000	500	0	2000	500	0

Note:

* Coc.Mod : Concrete modulus in ksi

** Std. Stiff : Shear stud stiffness in k/in

*** Load : Magnitude of the uniform load in k/ft

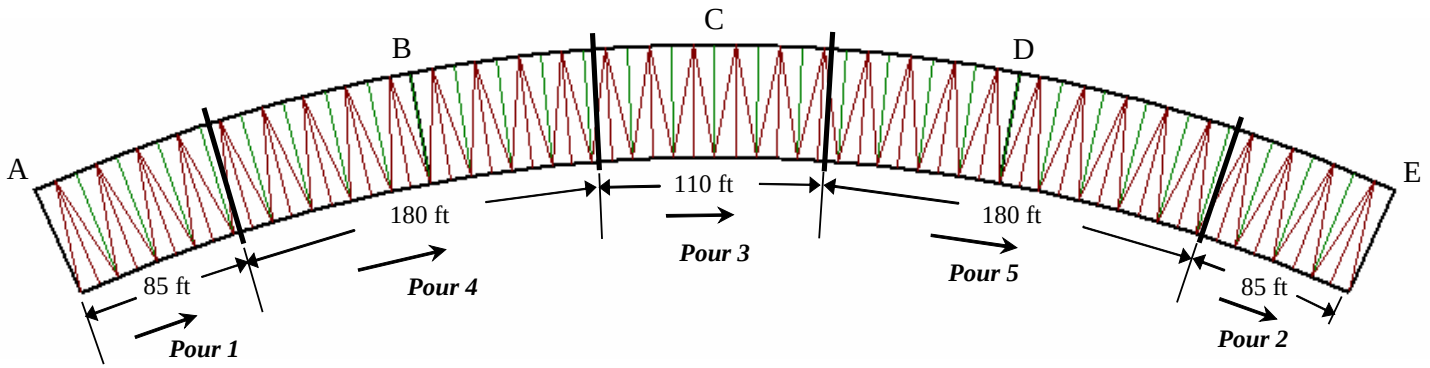

Figure 11.1 Pouring sequence A

From the history of the forces in particular panel similar to the ones shown in Figure 11.2 and Figure 11.3, the maximum tensile and compressive forces can be obtained.

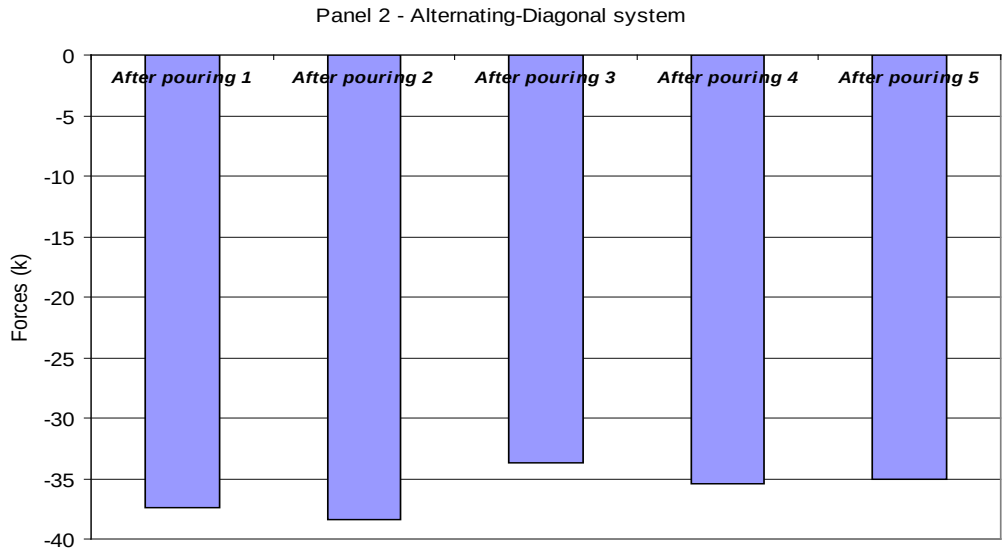

Figure 11.2 Total diagonal forces after each pour – effect of concrete stiffness

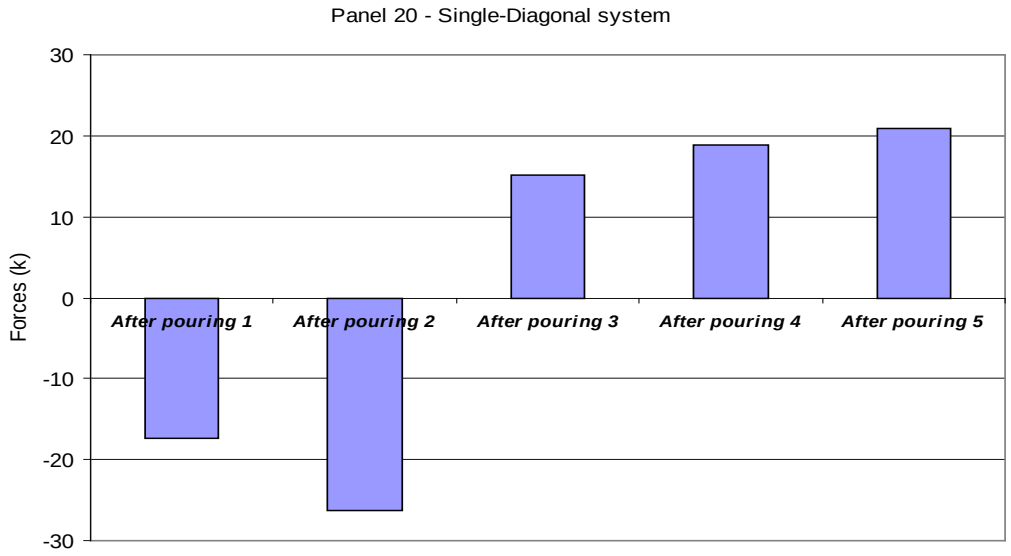

Figure 11.3 Total diagonal forces after each pour

Figure 11.4 and Figure 11.5 show the envelopes of tensile-compressive diagonal forces due to pouring sequence and the diagonal forces due to the monolithic pour in the Alternating-Diagonal and the Single-Diagonal systems, respectively. Those envelopes were constructed by plotting the maximum tensile and compressive forces that the diagonal experiences during the entire pouring sequence. The number on the top of each bar graph indicates the pour order that produces the maximum forces. In the monolithic pour, a uniform load of 3.3 k/ft is applied to the entire girder at one time (i.e. similar with the analysis shown in Chapter 10). Some diagonals (e.g. diagonals in panel 1 through 5) will only experience tensile or compressive forces. In this case, only the maximum magnitude is of interest. The envelopes of the tensile and compressive diagonal forces in the Alternating-Diagonal system are like a mirror image to one another. The maximum tensile diagonal force with the Single-Diagonal system is about the same as that with the Alternating-Diagonal system, whereas the maximum compressive diagonal force with the Single-Diagonal system is significantly smaller. From a design standpoint, WT 6x15 and WT 5x13 can be used as a diagonal with the Alternating-Diagonal and Single-Diagonal systems.

Figure 11.4 shows that the maximum tensile and compressive diagonal forces in the Alternating-Diagonal system due to pouring sequence A are slightly smaller than those due to a monolithic pour. However, under pouring sequence A, the diagonals near the exterior supports (supports A and E) experience larger tensile and compressive forces than those under a monolithic pour. From a design standpoint, WT 6x15 can be used as a diagonal member under both pouring sequence A and the monolithic pour.

Figure 11.5 shows that the maximum tensile diagonal force under pouring sequence A is only slightly smaller than that due to a monolithic pour. On the other hand the maximum compressive diagonal force under pouring

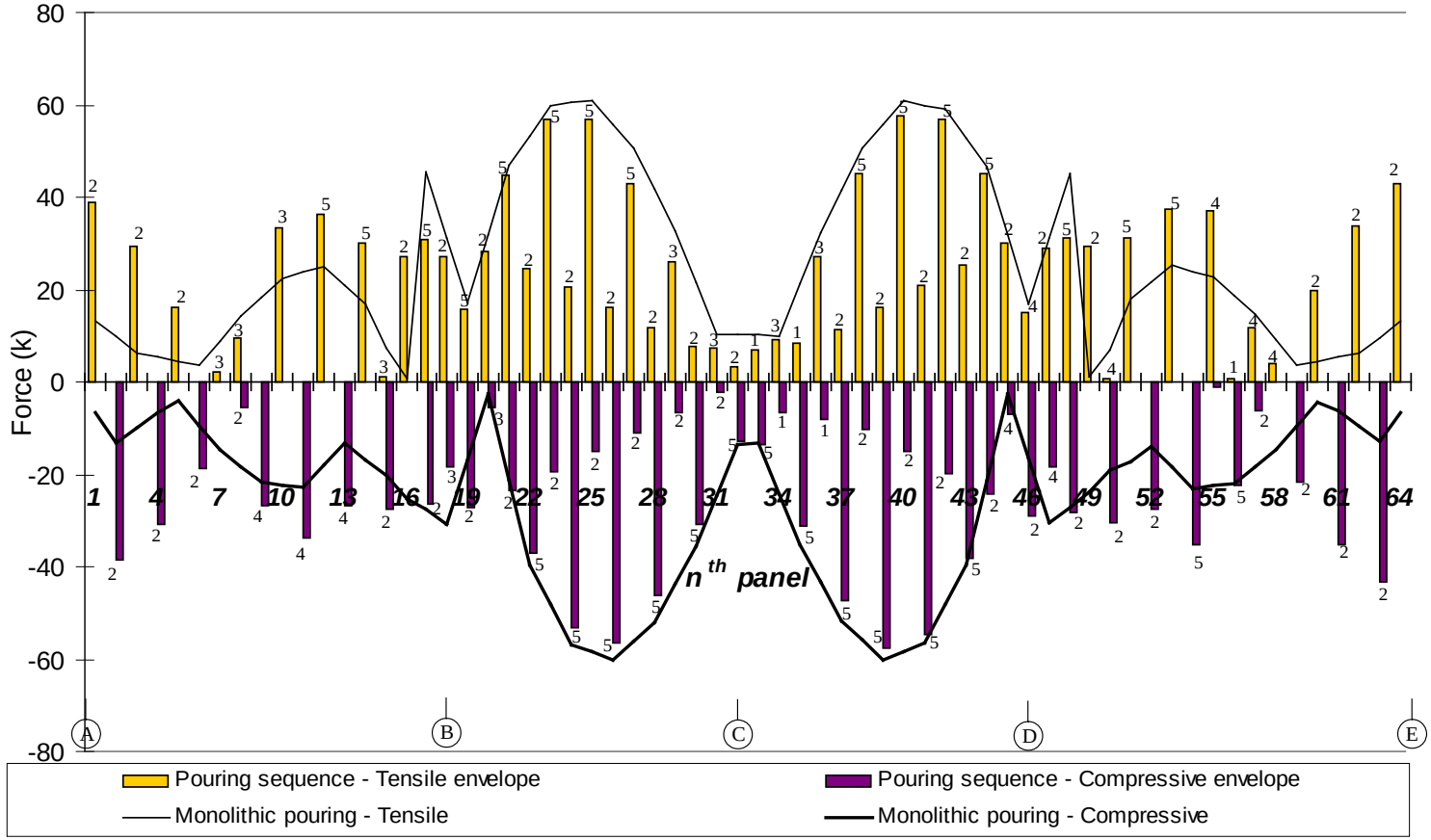

Figure 11.4 Diagonal force envelopes – Alternating-Diagonal

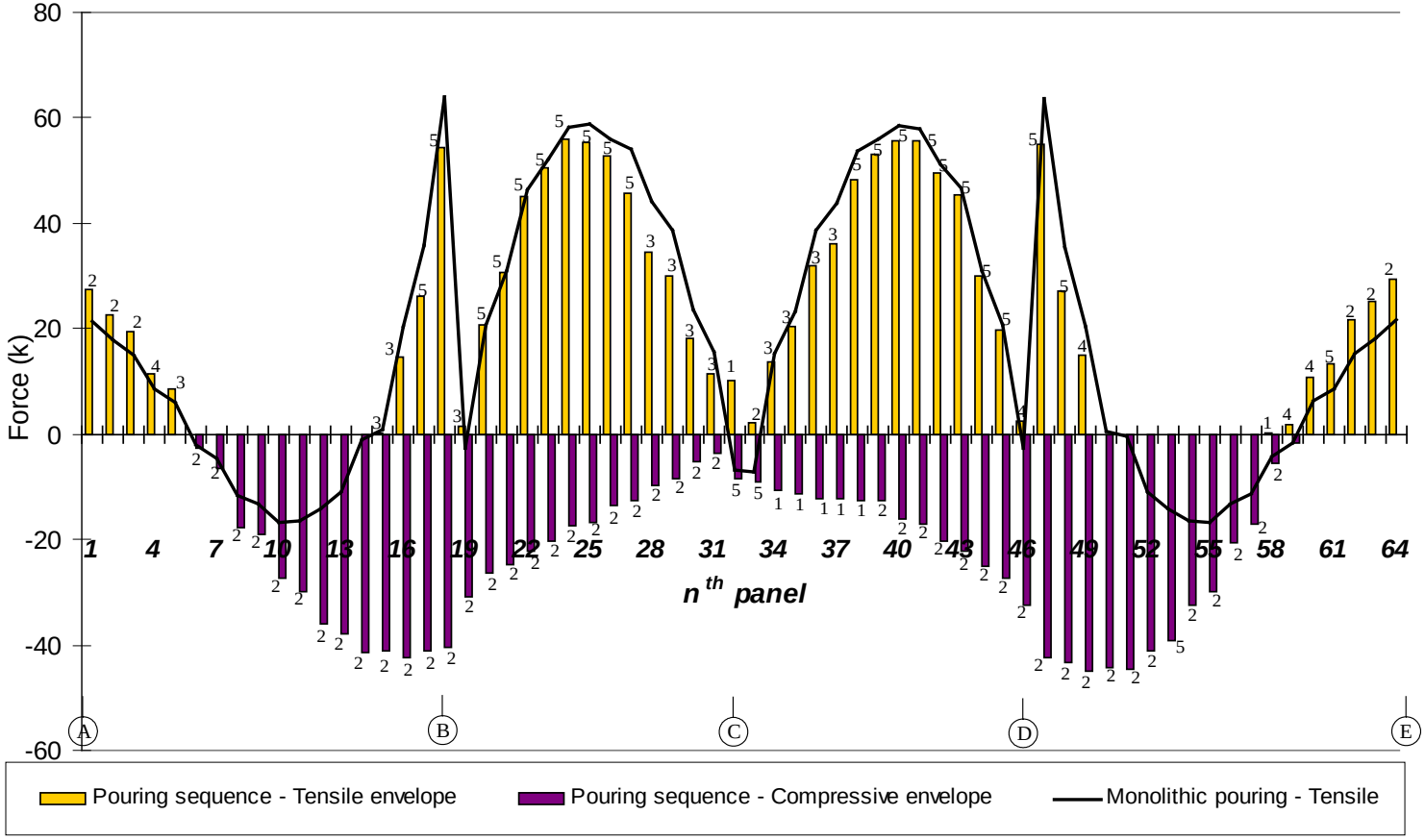

Figure 11.5 Diagonal force envelopes – Single-Diagonal

sequence A is about two times larger than that due to a monolithic pour. From a design standpoint, a WT 5x11 can be used for the diagonals under a monolithic pour, and a WT 5x13 should be used with pouring sequence A. Comparing the diagonal sizes in the Alternating-Diagonal and the Single Diagonal systems shows that modifying the diagonal direction from the Alternating-Diagonal to the Single-Diagonal system results in a smaller diagonal member.

In addition, an analysis of the data shows that largest tensile diagonal force resulted from the third concrete pour. This indicates that the length of the third pour will determine the maximum tensile diagonal force. As the length increases, the maximum tensile diagonal force becomes larger. In addition, most of the diagonal compressive forces in the Single-Diagonal system are developed after the first and second concrete pours. This observation suggests that changing the length of the first and second concrete pours may change the maximum compressive diagonal force due to the pouring sequence. The modification of pouring sequence A is discussed in Section 11.3.

11.1.1.2 Strut forces

Figure 11.6 shows the envelopes of tensile and compressive strut forces due to pouring sequence A in Alternating-Diagonal and Single-Diagonal systems. During the entire concrete pour, the struts in the Single-Diagonal system experience an abrupt change from tension to compression, whereas the struts in the Alternating-Diagonal system do not experience significant forces. The strut forces in the Alternating-Diagonal are several times smaller than those in the Single-Diagonal system.

Figure 11.7 shows a comparison between the tensile-compressive strut force envelopes due to pouring sequence A and the strut forces due to a monolithic loading for the Alternating-Diagonal system. The maximum tensile

and compressive strut forces in the Alternating-Diagonal system due to the pouring sequence are slightly larger than those due to a monolithic pour. However, since all the forces are small (less than 8 kip in both tension and compression), the same member size (i.e. WT 5x6) can be used for struts in both a monolithic pour and pouring sequence A.

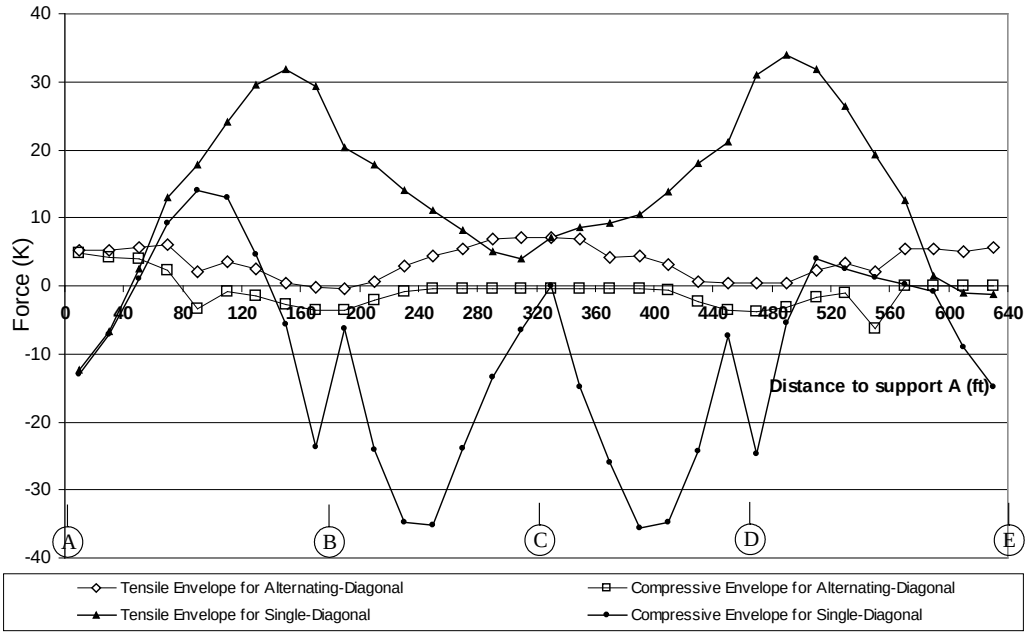

Figure 11.6 Envelope of tensile and compressive strut forces

Figure 11.8 compares the strut force envelopes due to pouring sequence A and the strut forces due to a monolithic loading for the Single-Diagonal system. Figure 11.8 shows that the maximum tensile strut forces due to a pouring sequence is about two times larger than that due to a monolithic pour. However, the maximum compressive strut forces due to a pouring sequence are slightly smaller. From a design standpoint, a WT 5x11 can be used as a strut under pouring sequence A and a monolithic pour. Modifying the diagonal direction from

the Alternating-Diagonal to the Single-Diagonal system results in larger struts (from a WT 5x6 to a WT 5x11).

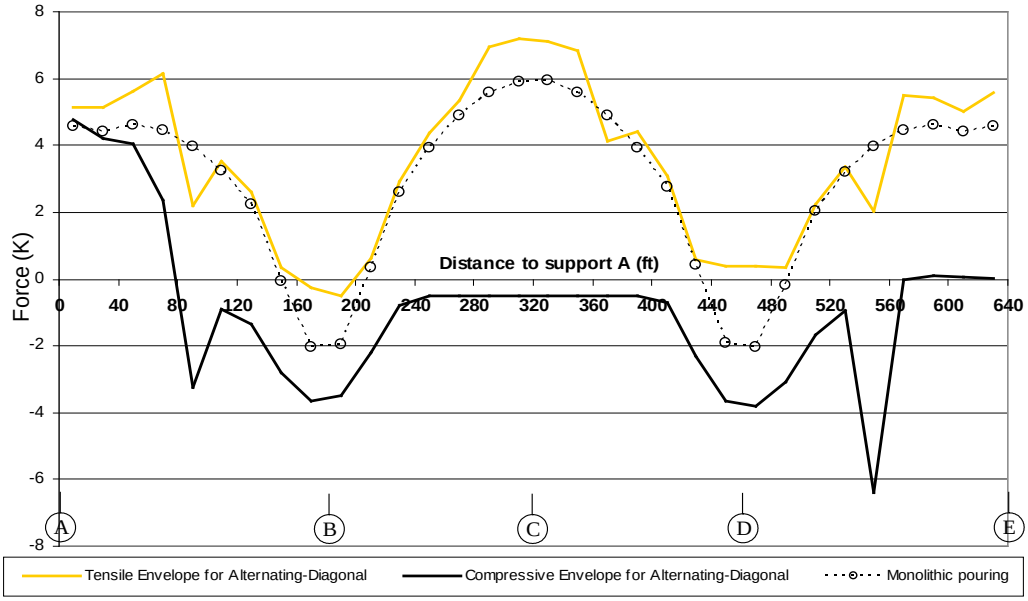

Figure 11.7 Strut force envelopes - Alternating-Diagonal

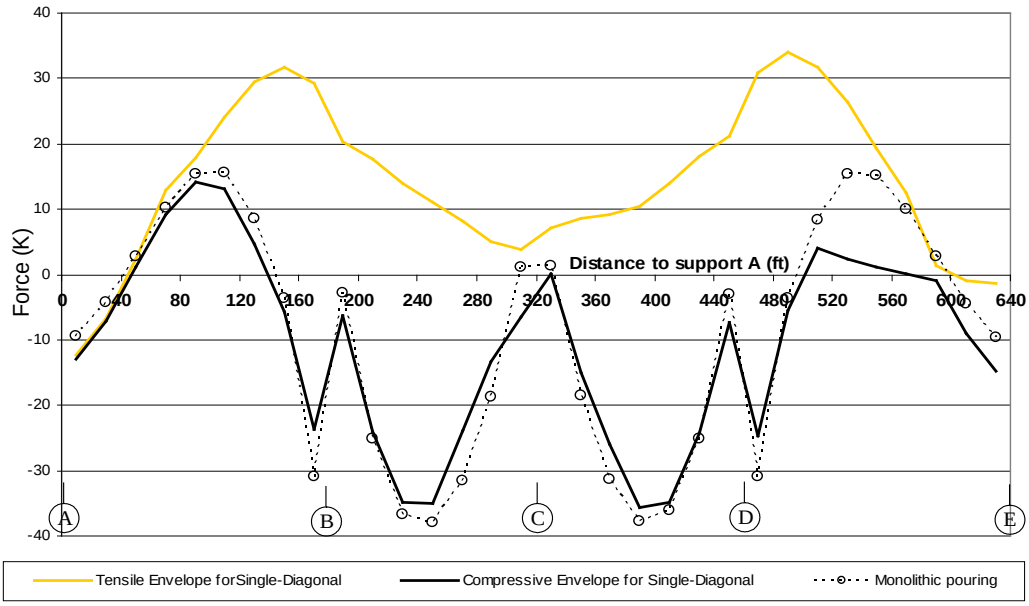

Figure 11.8 Strut force envelopes - Single-Diagonal

11.1.1.3 Deformation

Figure 11.9 shows the rotations of the bottom flange along the length after each concrete pour and the rotation due to a monolithic loading. Even though the member sizes of both the diagonal and the strut in both top lateral bracing systems are the same, the maximum rotation with the Single-Diagonal system is larger. For both top lateral bracing systems, the maximum rotation after the last concrete pour (after pour 5) is smaller than that due to a monolithic loading.

Figure 11.10 shows the vertical deflections along the length after each concrete pour and those due to a monolithic loading. Vertical deflections are insensitive to the type of top lateral bracing system. The total vertical deflections after the last concrete pour are smaller than those due to a monolithic pour. This is one of the consequences of using a pouring sequence as opposed to a monolithic pour.

Figure 11.11 shows the horizontal displacements under pouring sequence A and a monolithic loading. The positive and negative horizontal deflections indicate the lateral movement toward and away from the center of curvature, respectively. Support B, located 180 ft from the left support, acts as laterally fixed support (no horizontal rotation at support B). Since the displacements with the Alternating-Diagonal system are much smaller than those with the Single-Diagonal system, the displacement scales in the plots are different. The horizontal displacement values have been plotted on a reverse scale in order to physically correlate displacements with the plan view of the girder shown in Figure 10.2. With the Alternating-Diagonal system, the final horizontal displacements under pouring sequence A are smaller than those under a monolithic pour. However, the maximum magnitude of horizontal displacement during the entire pouring sequence exceeds that under a monolithic pour. The final horizontal displacements with the Single-Diagonal system under pouring sequence A and a

monolithic pour are about the same, while the maximum magnitudes during the pouring sequence are smaller than those under a monolithic pour. Therefore, the consequences of the pouring sequence from a horizontal displacement perspective depend on the type of top lateral bracing system.

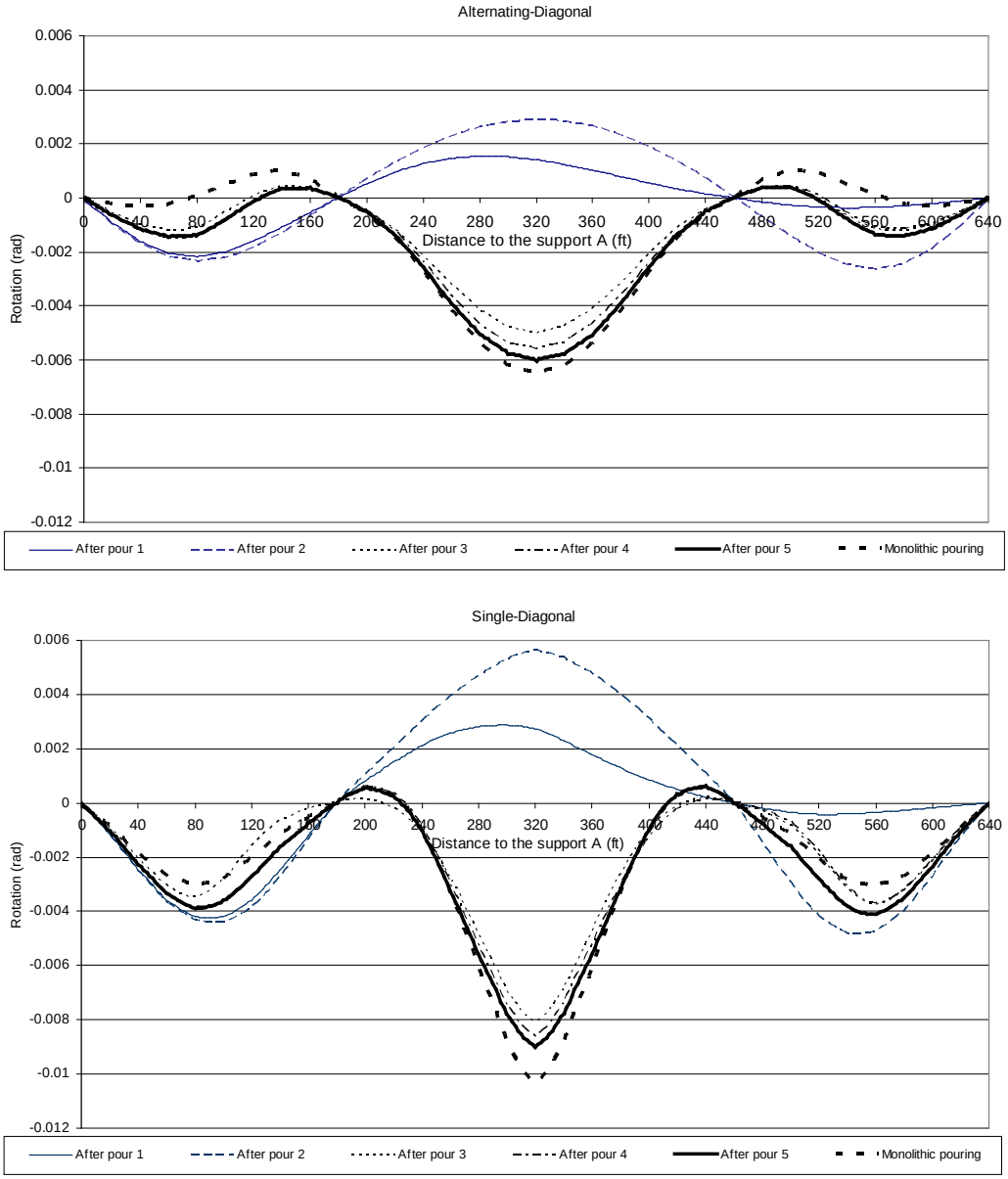

Figure 11.9 Rotations of the bottom flange along the length

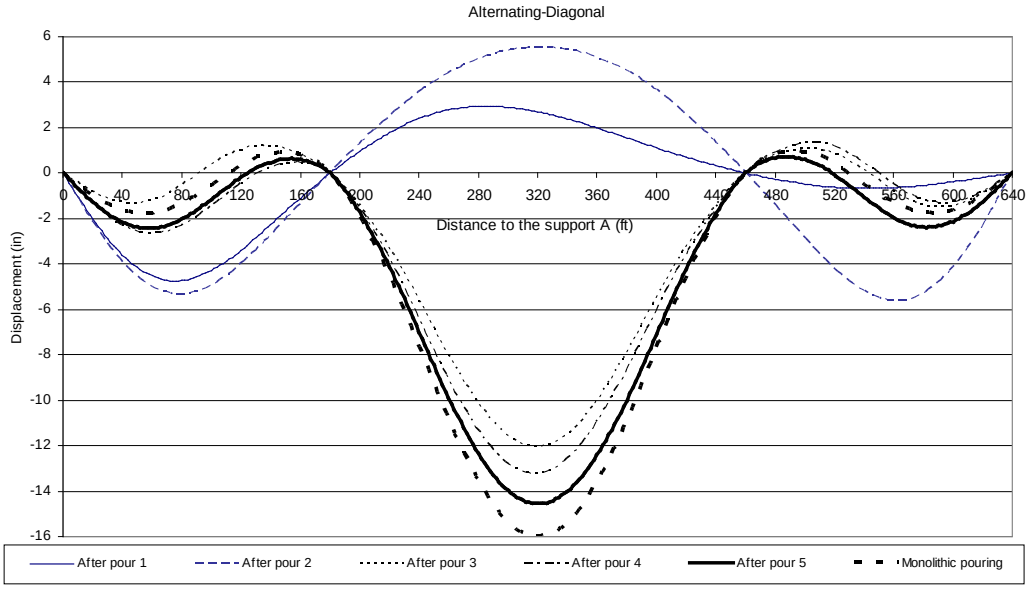

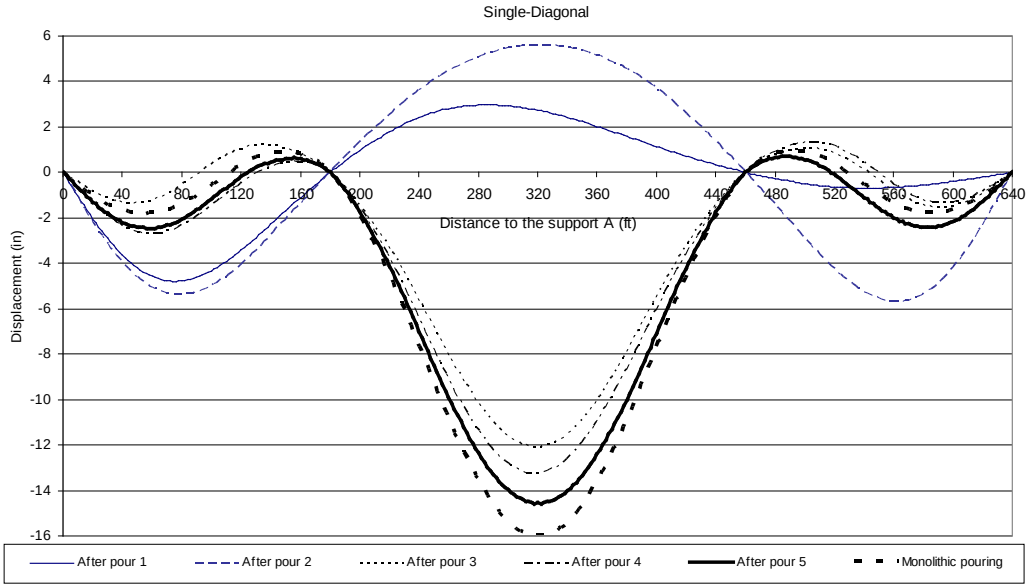

Figure 11.10 Vertical deflections along the length

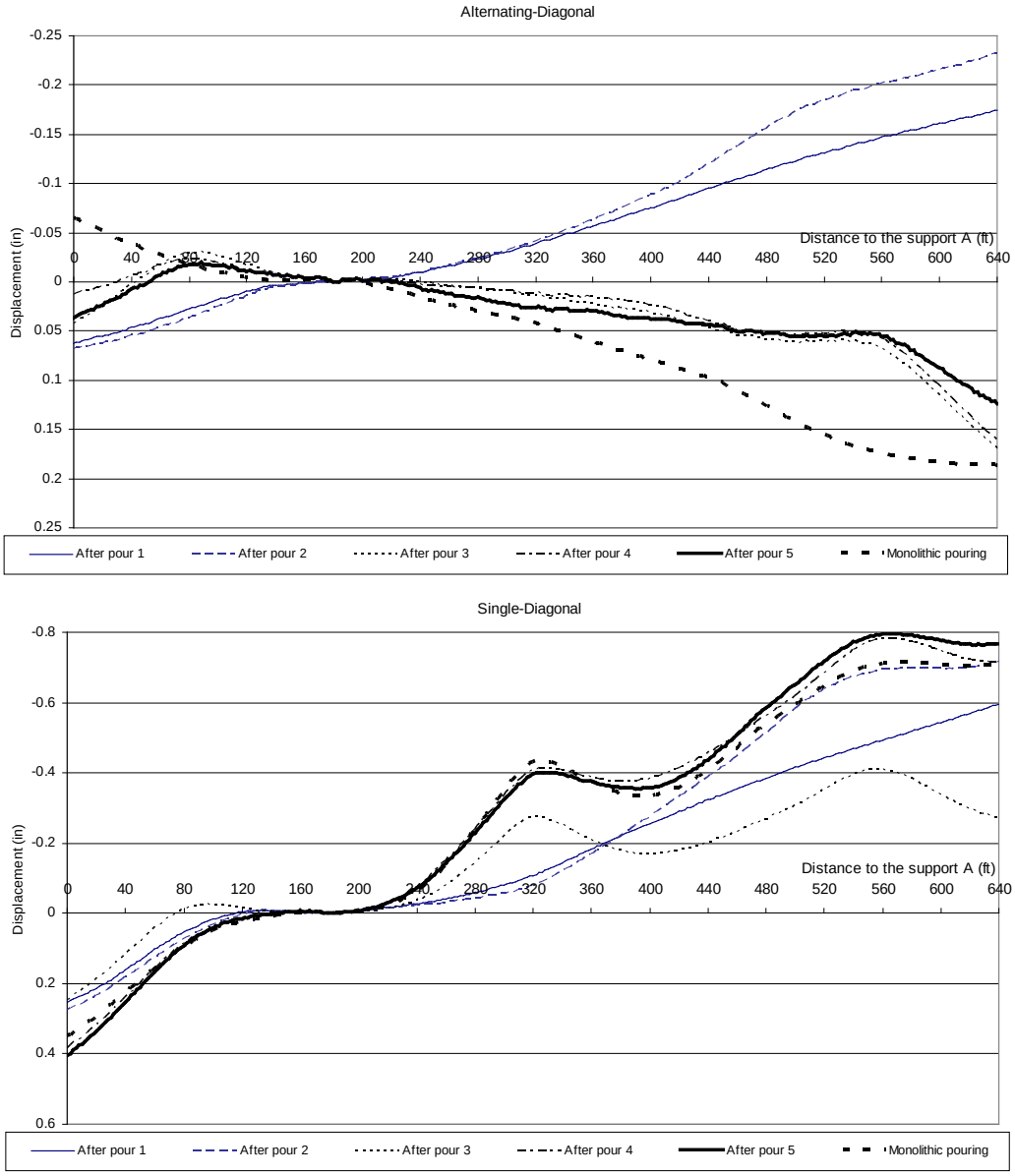

Figure 11.11 Horizontal displacement along the length

11.1.1.4 Total normal stress

Figure 11.12 shows the maximum compressive and tensile total normal stresses after each concrete pour and under a monolithic pour for the Alternating-Diagonal system. The maximum stresses are obtained from the examination of total normal stresses in all nodes on the cross-section and along the length of the girder. For example, the maximum tensile stress after pour 1 occurs in the bottom flange at 60 ft from support A, whereas that after pour 5 occurs in the top flange at 462 ft from support A. Figure 11.12 shows that both the maximum tensile and compressive total normal stresses during pouring sequence A occur after the last pour. The maximum compressive and tensile total normal stresses after the last concrete pour are about 14 % and 2.8 % smaller, respectively, than those due to monolithic pouring.

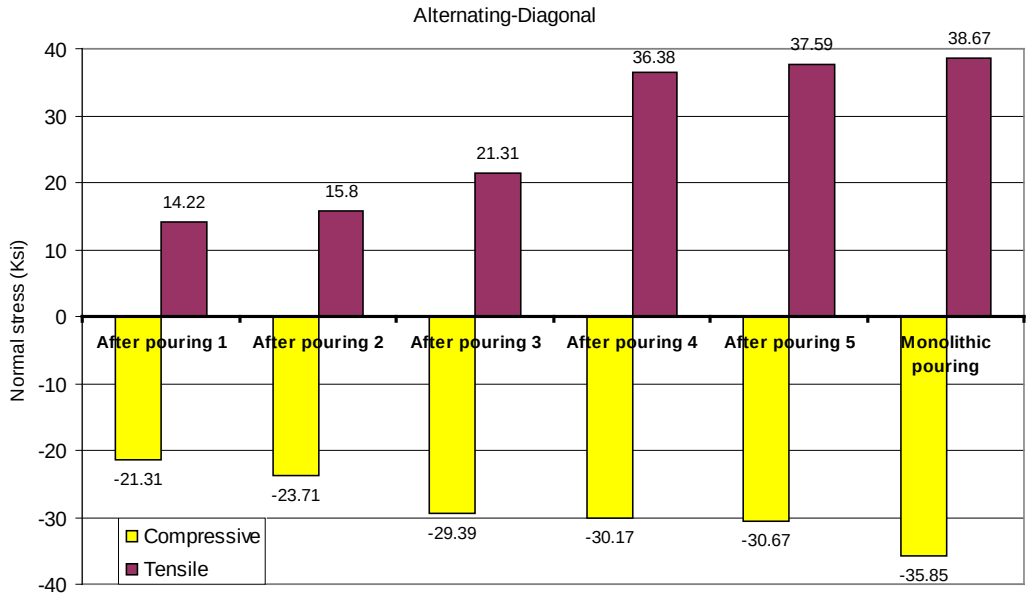

Figure 11.12 Maximum total normal stresses with Alternating-Diagonal system

Figure 11.13 shows the maximum compressive and tensile total normal stresses with the Single-Diagonal system after each concrete pour and under a monolithic pour. The maximum compressive and tensile total normal stresses with the Single-Diagonal system occur after the fifth concrete pour. The maximum compressive and tensile total normal stresses during pouring sequence A are 14.5 % and 1.9 % smaller, respectively, than those due to a monolithic pour.

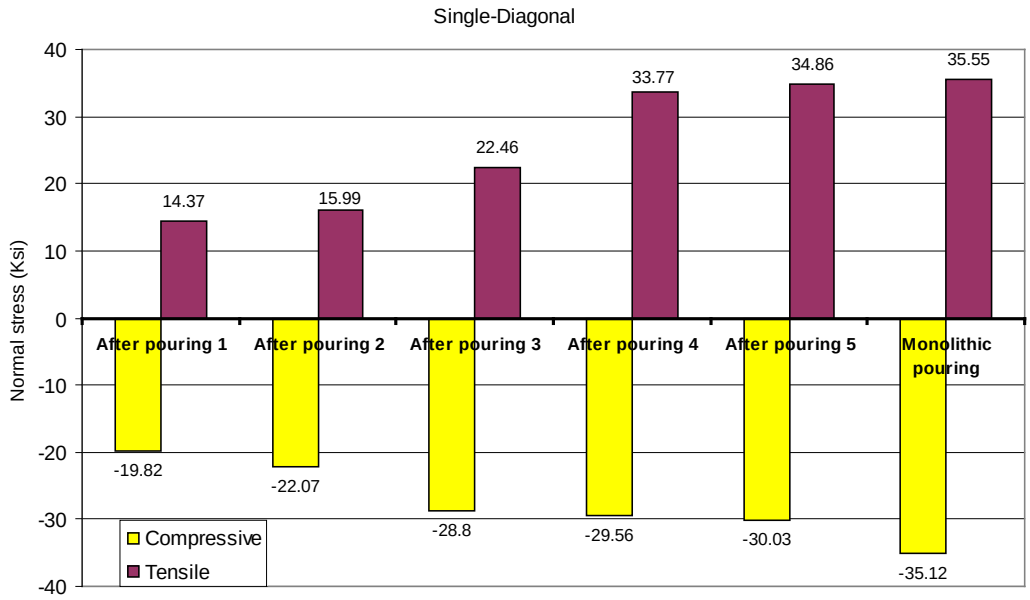

Figure 11.13 Maximum total normal stresses with Single-Diagonal system

The maximum total normal stresses with the Alternating-Diagonal are larger than those with the Single-Diagonal. This observation is true for both a pouring sequence and a monolithic loading.

11.2 CHANGE IN TOP DIAGONAL SIZE

Case A-2 studies the effect of changing member size on girder rotations and horizontal displacements. Since changing the top lateral bracing member size does not affect top lateral bracing forces, girder vertical deflections, and the total normal stresses significantly, this section will not discuss these parameters. The only difference between Case A-2 and Case A-1 is the member size used in the top lateral bracing system. The member size used in Case A-2 is selected based on the area required to carry the force in that member as shown in Table 11-1.

Table 11-1 Member sizes used in Case A-2

Member type	Alternating-Diagonal		Single-Diagonal	
	Pouring sequence A	Monolithic pouring	Pouring sequence A	Monolithic pouring
Diagonal	WT 6x15 (A_d=4.40 in^2)	WT 6x15 (A_d=4.40 in^2)	WT 5x13 (A_d=3.81 in^2)	WT 5x11 (A_d=3.24 in^2)
Strut	WT 5x6 (A_s=1.77 in^2)	WT 5x6 (A_s=1.77 in^2)	WT 5x11 (A_s=3.24 in^2)	WT 5x11 (A_s=3.24 in^2)

Figure 11.14 shows rotations of the bottom flange along the length of Model 3 with pouring sequence A and a monolithic pour. Comparing the rotations in Case A-1 and Case A-2 shows that using a smaller member size results in a larger rotation in Case A-2. The additional rotation is not linearly proportional to the area reduction of top lateral bracing member. Since the diagonal sizes used in both pouring sequence A and a monolithic pour are the same, the difference between the maximum rotation with the Alternating-Diagonal system due to pouring sequence A and a monolithic loading is not as large as that with the Single-Diagonal system.

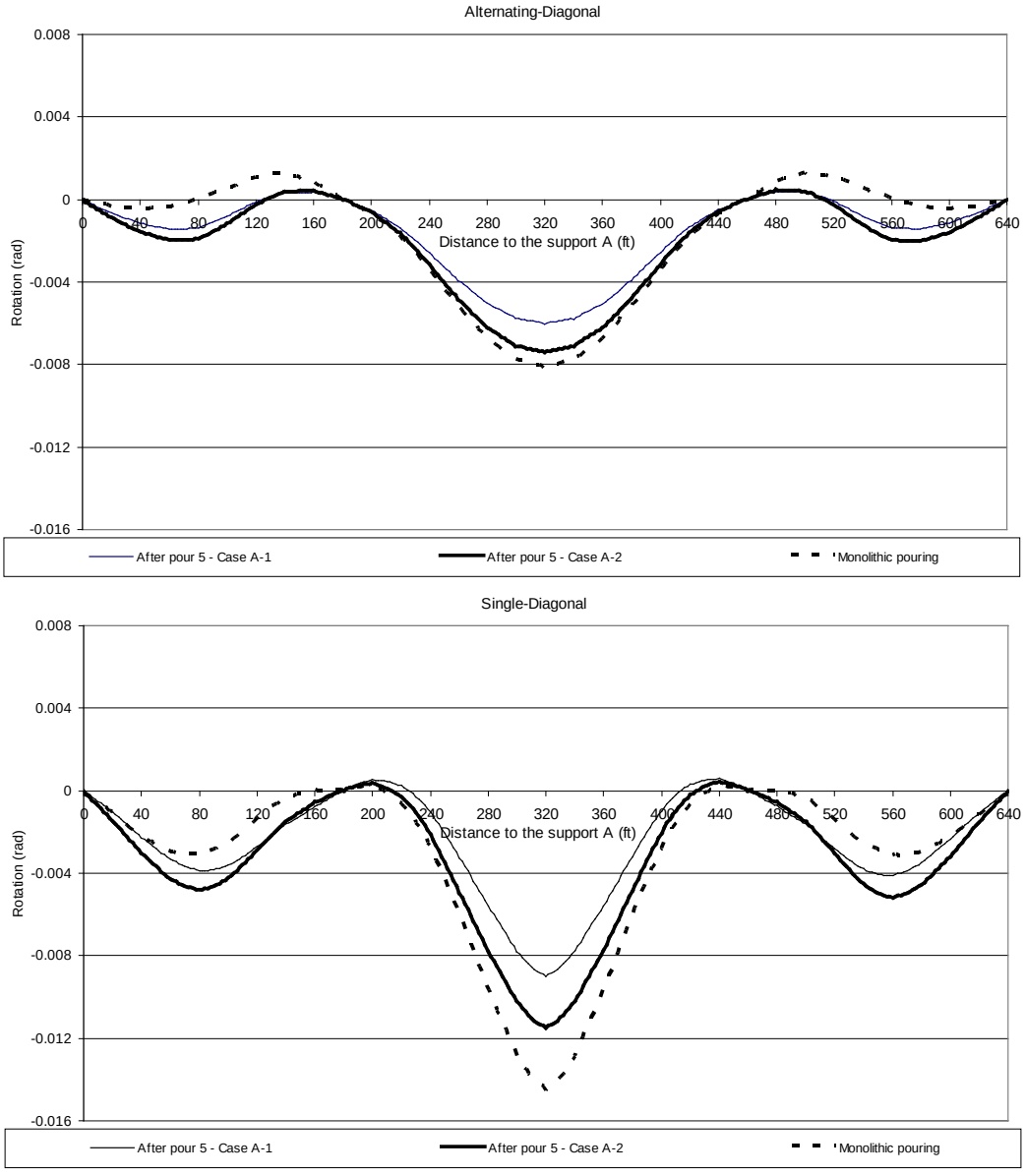

Figure 11.14 Rotation of the bottom flange along the length

Figure 11.15 shows horizontal displacements of the node located in the middle of the bottom flange during pouring sequence A and due to a monolithic pour. Figure 11.15 shows that the horizontal displacements of the bottom flange with the Alternating-Diagonal and the Single-Diagonal systems after the fifth concrete pour and under a monolithic pour are opposite. The maximum horizontal displacement with the Alternating-Diagonal system after the fifth concrete pour is slightly smaller than that due to a monolithic pour. However, with the Single-Diagonal system, the maximum horizontal displacement after the fifth concrete pour is larger. Comparing the horizontal displacements in Case A-1 and Case A-2 shows that the area reduction of the top lateral bracing member results in a more positive horizontal displacement. This observation agrees with the fact that as the equivalent plate thickness decreases, a girder moves laterally toward the center of curvature (more positive horizontal displacement). Since the horizontal displacement becomes more positive as the top lateral bracing members get smaller, the maximum magnitude of the horizontal displacement with the Alternating-Diagonal system in Case A-2 is larger than that in case A-1, whereas with the Single-Diagonal system, the maximum magnitude of the horizontal displacement in Case A-2 is smaller.

11.3 CHANGE IN POURING SEQUENCE

This section focuses on the effect of changing the pouring sequence on top lateral bracing forces. Two different pouring sequences, denoted B and C and shown in Figure 11.16 and Figure 11.17, respectively, are studied. The only difference between pouring sequences A, B, and C is the length of each concrete pour. Pouring sequence B examines the effect of reducing the length of the first and second pours, and pouring sequence C studies the effect of reducing the

length of the third pour. The length of the third pour in pouring sequence B is kept about the same as in pouring sequence A. The only difference between pouring sequences B and C is the length of the third, fourth, and fifth concrete pours. WT 6x20 is used for the diagonals and struts in both the Alternating-Diagonal and Single-Diagonal systems, in both pouring sequences B and C.

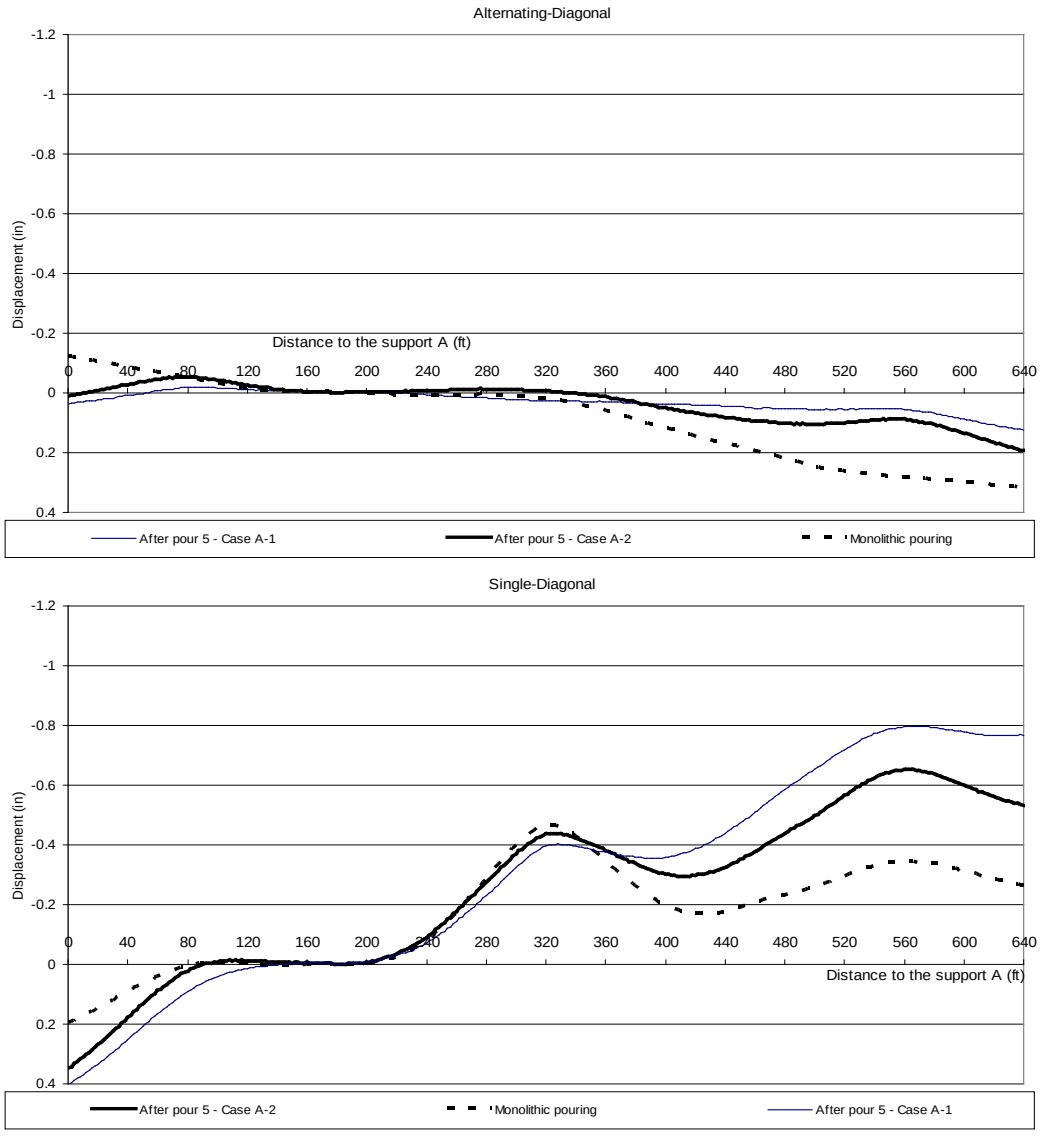

Figure 11.15 Horizontal displacement along the length

DECK	LENGTH (ft)	ANALYSIS 1			ANALYSIS 2			ANALYSIS 3			ANALYSIS 4			ANALYSIS 5		
		Coc.Mod*	Std.Stiff**	Load***	Coc.Mod	Std.Stiff	Load	Coc.Mod	Std.Stiff	Load	Coc.Mod	Std.Stiff	Load	Coc.Mod	Std.Stiff	Load
1	50	0	0	3.3	1000	250	0	2000	500	0	2000	500	0	2000	500	0
2	210	0	0	0	0	0	0	0	0	0	0	0	3.3	1000	250	0
3	120	0	0	0	0	0	0	0	0	3.3	1000	250	0	2000	500	0
4	210	0	0	0	0	0	0	0	0	0	0	0	0	0	0	3.3
5	50	0	0	0	0	0	3.3	1000	250	0	2000	500	0	2000	500	0

Note:

* Coc.Mod : Concrete modulus in ksi

** Std. Stiff : Shear stud stiffness in k/in

*** Load : Magnitude of the uniform load in k/ft

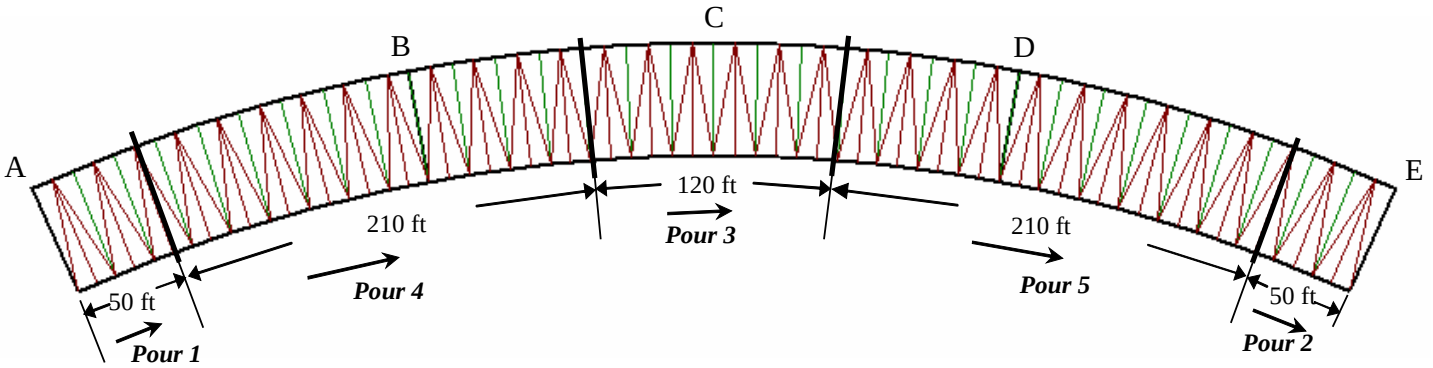

Figure 11.16 Pouring sequence B

DECK	LENGTH (ft)	ANALYSIS 1			ANALYSIS 2			ANALYSIS 3			ANALYSIS 4			ANALYSIS 5		
		Coc.Mod*	Std.Stiff**	Load***	Coc.Mod	Std.Stiff	Load	Coc.Mod	Std.Stiff	Load	Coc.Mod	Std.Stiff	Load	Coc.Mod	Std.Stiff	Load
1	50	0	0	3.3	1000	250	0	2000	500	0	2000	500	0	2000	500	0
2	230	0	0	0	0	0	0	0	0	0	0	0	3.3	1000	250	0
3	80	0	0	0	0	0	0	0	0	3.3	1000	250	0	2000	500	0
4	230	0	0	0	0	0	0	0	0	0	0	0	0	0	0	3.3
5	50	0	0	0	0	0	3.3	1000	250	0	2000	500	0	2000	500	0

Note:

* Coc.Mod : Concrete modulus in ksi

** Std. Stiff : Shear stud stiffness in k/in

*** Load : Magnitude of the uniform load in k/ft

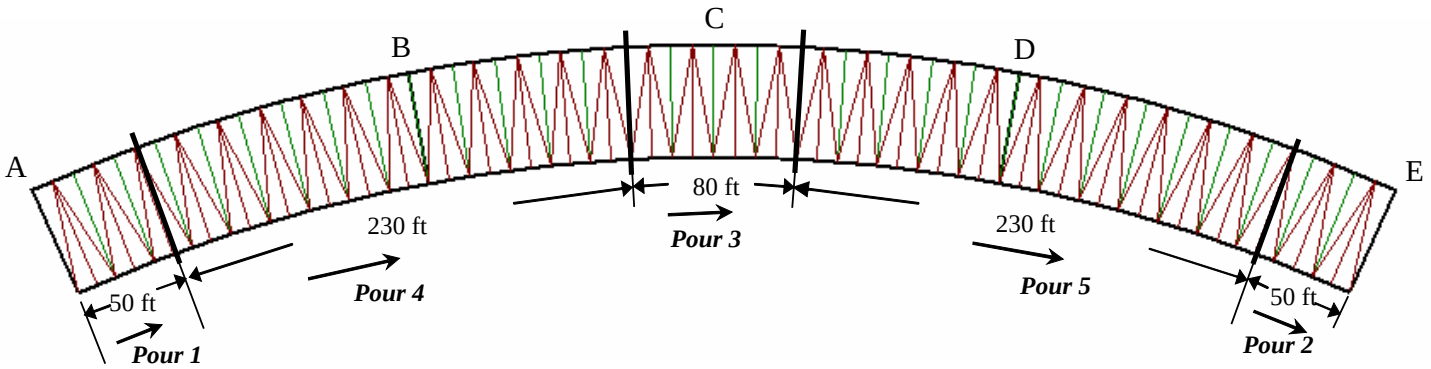

Figure 11.17 Pouring sequence C

11.3.1 Diagonal forces

Figure 11.18 and Figure 11.19 show the envelope for both tensile and compressive diagonal forces in the Alternating-Diagonal and Single-Diagonal systems, under pouring sequences B and C, respectively. Generally, diagonals in the Single-Diagonal system experience much smaller compressive forces than those in the Alternating-Diagonal system, whereas diagonals located in span BD (panels 19 through 46) in both systems experience about the same maximum tensile forces. The maximum total compressive diagonal force in the Single-Diagonal system is clearly much smaller than that in the Alternating-Diagonal system. However, the maximum total tensile diagonal force in the Single-Diagonal system, which occurs near the intermediate supports (Supports B and D), is slightly larger than that in the Alternating-Diagonal system. WT 6x15 and WT 5x11 can be used for diagonals in the Alternating-Diagonal and the Single-Diagonal systems, respectively. However, in order to use a WT 5x11 in the Single-Diagonal system, a 3-inch bolt spacing must be used in the connection to prevent tension rupture, whereas when using a WT 6x15 in the Alternating-Diagonal system, a 2.5-inch bolt spacing can be used.

The envelope of compressive diagonal force in the Single-Diagonal system under pouring sequence B is significantly smaller than that under pouring sequence A. An analysis of forces after each concrete pour indicates that compressive diagonal forces after the first and second concrete pours in pouring sequence B are significantly smaller than those in pouring sequence A. Since the compressive diagonal forces in the Single-Diagonal system are developed during the first and second pour, reducing the length of the first and second pour in pouring sequence B results in a significantly smaller compressive envelope. And

since the length and second pour in both pouring sequence B and C are the same, the compressive envelopes under both pouring sequences are the same.

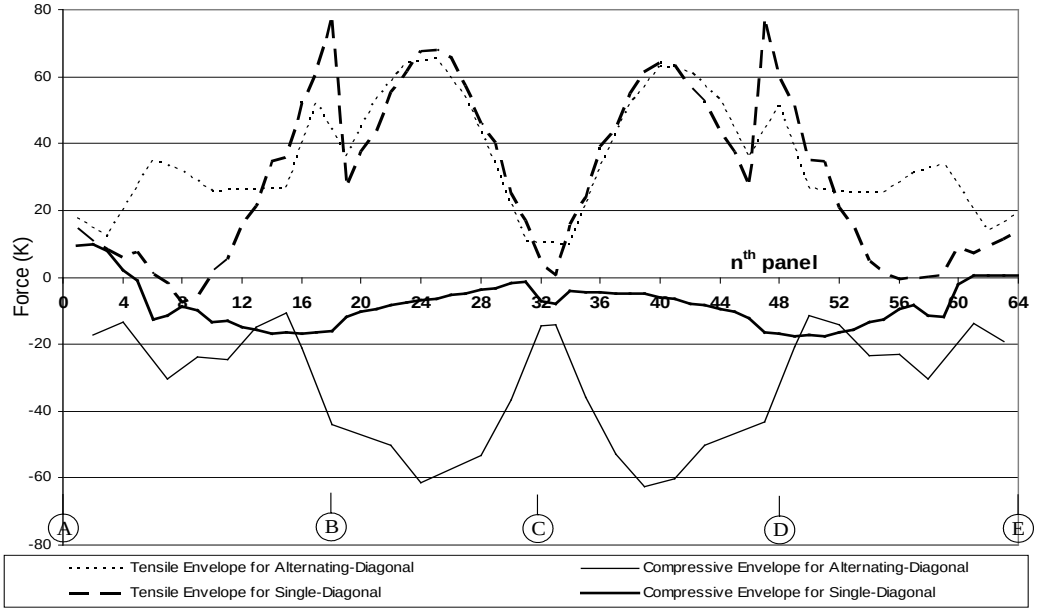

Figure 11.18 Envelope of tensile and compressive diagonal forces – Sequence B

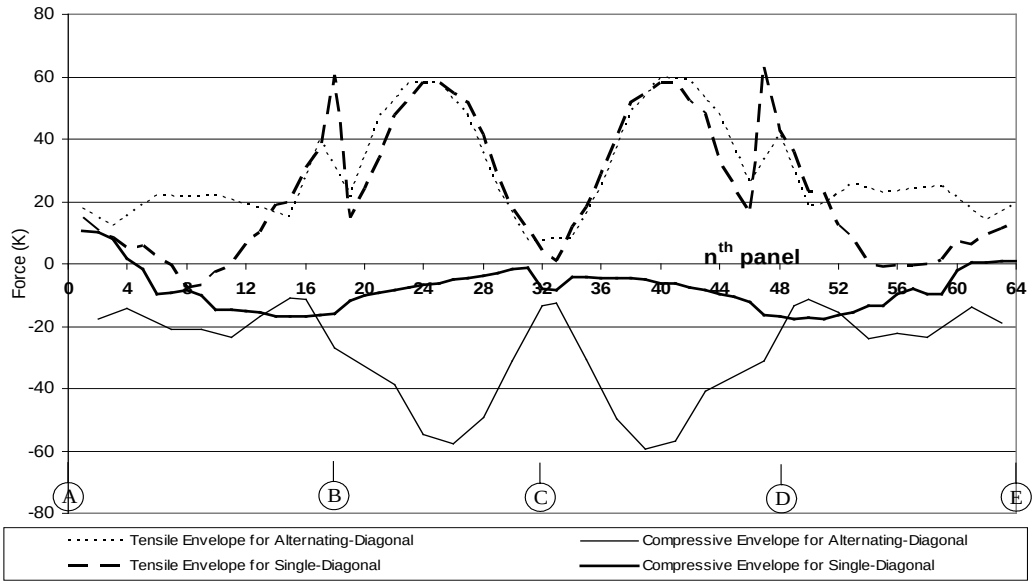

Figure 11.19 Envelope of tensile and compressive diagonal forces – Sequence C

An analysis of forces after each concrete pour indicates that significant tensile diagonal forces are developed after the third concrete pour in both systems. Since the length of the third concrete pour in pouring sequence B are larger than that in pouring sequence C, the envelopes of tensile forces in both systems under pouring sequence B are larger.

11.3.2 Strut forces

Figure 11.20 and Figure 11.21 show the envelope for both tensile and compressive strut forces in the Alternating-Diagonal and Single-Diagonal systems, under pouring sequence B and C, respectively. The envelopes for the Alternating-Diagonal system under pouring sequences A, B, and C are about the same. The tensile envelope for the Single-Diagonal system under pouring sequences B and C are about the same, whereas the compressive envelope under pouring sequence B is significantly larger. Comparing the envelopes for the Single-Diagonal under pouring sequences A and B shows that the tensile envelope under pouring sequence B is smaller and the compressive envelope under pouring sequence B is larger. Comparing the envelopes for the Single-Diagonal system under pouring sequences A and C shows that the compressive envelopes are about the same, whereas the tensile envelope under pouring sequence C is smaller. The strut forces in the Single-Diagonal system are more sensitive to the length of concrete pour than those in the Alternating-Diagonal system.

11.3.3 Summary

Table 11-2 summarizes the maximum results under monolithic pouring and pouring sequences A, B, and C. In all cases, the maximum magnitudes of

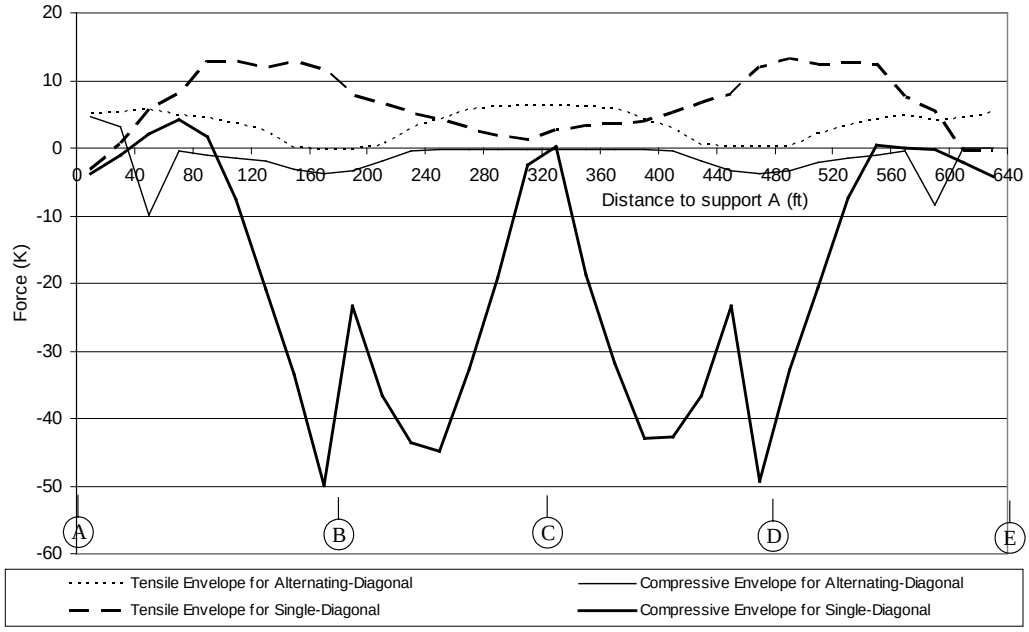

Figure 11.20 Envelope of tensile and compressive strut forces – Sequence B

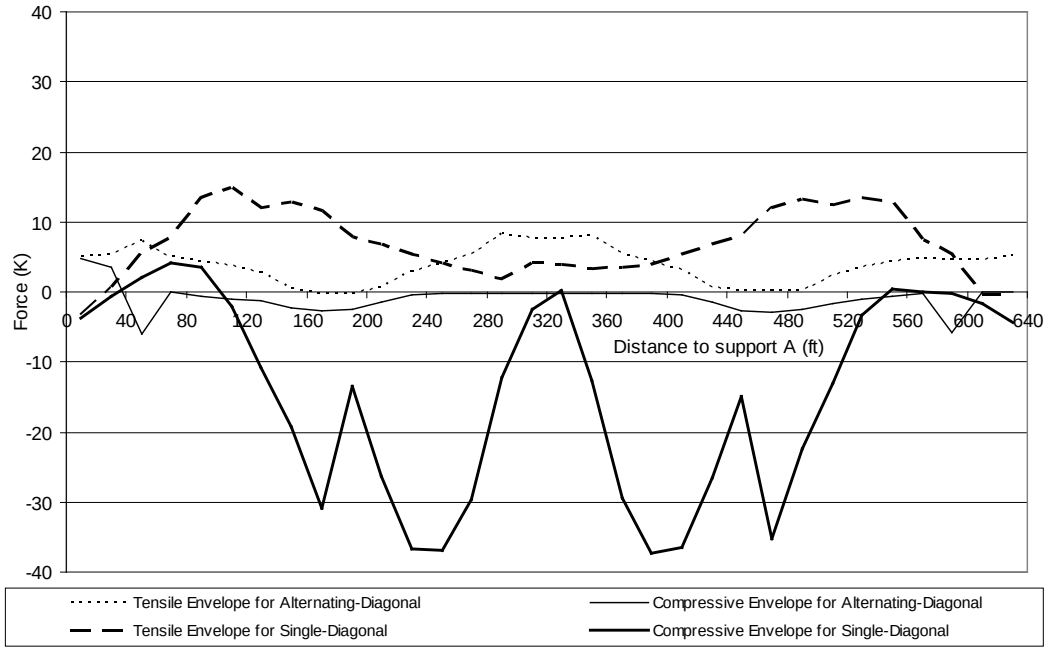

Figure 11.21 Envelope of tensile and compressive strut forces – Sequence C

compressive diagonal forces in the Alternating-Diagonal system are about the same as the maximum magnitudes of tensile forces, whereas the maximum magnitudes of compressive diagonal forces in the Single-Diagonal system are smaller than the maximum magnitudes of tensile forces. The maximum compressive diagonal force in the Single-Diagonal system is sensitive to the length of the first and second pours. As the length decreases, the maximum compressive force decreases. The maximum tensile diagonal forces in both systems are sensitive to the length of the third pour. As the length increases, the maximum tensile diagonal force increases. Depending on the pouring sequence, the maximum diagonal forces in both systems can be larger or smaller than those due to a monolithic pouring.

In all cases, the maximum strut forces in the Alternating-Diagonal system are significantly smaller than those in the Single-Diagonal system. Reducing the length of the first and second pour decreases the maximum tensile strut forces in the Single-Diagonal system and reducing the length of the third pour decreases the maximum compressive strut forces.

The maximum total normal stresses in both systems during pouring sequence can be larger or smaller than those under a monolithic pouring. Shortening the third pour reduces the maximum compressive total normal stresses in both systems. The maximum tensile total normal stresses are not as sensitive to the pouring sequence as the maximum compressive total normal stresses are. The maximum vertical displacement and rotation in both systems during pouring sequence can be larger or smaller than those under a monolithic pouring. In general, increasing the length of the third pour results in larger vertical deflections and rotations. With a short third pour, the maximum rotation and vertical deflection during pouring sequence are smaller than those under a monolithic loading

Table 11-2 Summary of maximum results

Analysis Cases	Alternating-Diagonal top lateral bracing system								Single-Diagonal top lateral bracing system							
	Diagonal forces (k)		Strut forces (k)		Total normal stress (ksi)		Vert. displ. (inch)	Rotation (radian)	Diagonal forces (k)		Strut forces (k)		Total normal stress (ksi)		Vert. displ. (inch)	Rotation (radian)
	+	-	+	-	+	-			+	-	+	-	+	-		
Monolithic pouring	61.0	-60.2	5.9	-2.0	38.7	-35.9	16.0	0.0065	63.9	-16.8	15.5	-37.9	35.6	-35.1	16.0	0.0103
Pouring sequence A-1	57.8	-57.7	7.2	-6.4	37.6	-30.7	14.6	0.0060	56.0	-45.1	33.9	-35.6	34.9	-30.0	14.6	0.0090
Pouring sequence B	65.5	-64.9	6.4	-10.0	39.0	-36.2	17.3	0.0076	78.6	-17.5	13.2	-49.8	36.0	-35.3	17.4	0.0132
Pouring sequence C	59.6	-59.4	8.3	-6.0	37.7	-28.9	14.8	0.0061	63.7	-17.5	15.0	-37.2	34.7	-28.2	14.8	0.0095

Note: (+) : Tensile forces / stresses
(−) : Compressive forces / stresses

11.4 SUMMARY

This chapter presented the effect of the pouring sequence on the top lateral bracing forces, deformations, and total normal stresses in a three-span bridge with the Alternating-Diagonal and the Single-Diagonal systems. The results due to the pouring sequence are compared with those due to a monolithic pour. Depending on the length of each concrete pour, the maximum top lateral bracing forces, deformations, and total normal stresses during pouring sequence can be larger or smaller than those under a monolithic pouring.

The maximum diagonal compressive forces in the Single-Diagonal system occur in the exterior spans and are sensitive to the length of the first and second pour. As the first and second pours get longer, the maximum diagonal compressive forces in the Single-Diagonal system become larger. From this perspective, the recommended pouring sequence is the one with short first and second pours. Unlike in the Single-Diagonal system, the maximum compressive force in the Alternating-Diagonal system occurs near the midspan of the middle span and is insensitive to the length of the first and second pour. The maximum tensile diagonal forces in both systems are sensitive to the length of the third pour. As the length increases, the maximum tensile diagonal force becomes larger. For this reason, the recommended pouring sequence is the one with a short third pour.

The maximum rotation and vertical deflection of a girder are sensitive to the length of the third pour. As the length of the third pour increases, the maximum rotation and vertical deflections become larger. As long as the third pour is kept short, the maximum rotation and vertical deflection due to a pouring sequence are smaller than those due to a monolithic loading.

The maximum compressive total normal stresses in a girder are sensitive to the length of the third pour, whereas the maximum tensile total normal stresses are not. As the length of the third pour gets longer, the maximum compressive total normal stress increases.

It can be concluded that in order to get a positive consequence from a pouring sequence, one needs to keep the first, second, and third pours short.

CHAPTER 12
Conclusions and Future Research

12.1 CONCLUSIONS

The purpose of this research was to study the general behavior of steel trapezoidal box girders during construction. Parametric studies using the UTRAP program were performed to examine the effect of different parameters on top lateral bracing forces, stresses, and deformations of a single trapezoidal box girder system. Whenever possible, hand methods were presented to predict the UTRAP solutions. More detailed findings and recommendations are summarized in the following sections.

12.1.1 Cross-sectional forces

In a curved girder, there is an interaction between support torque and midspan bending moment. This thesis presented derivations of the exact formulas to predict the midspan bending moment and the support torque using equilibrium and geometry. The final forms of the formulas are simple. In addition, the approximate formulas were also shown, and it can be concluded that for a simply-supported curved girder, the approximate formulas presented in this thesis are slightly better than the M/R method in predicting the support torque and midspan bending moment. However, it was shown that the M/R method can be applied very well in a continuous curved girder, for which no simple closed-form formula can be derived.

12.1.2 Internal diaphragm spacing

In order to limit the distortional normal stress at the junction of the web and the top flange to less than 5 percent of the bending normal stress, the ratio of the maximum distortional rotation less than the maximum rigid body rotation, and the maximum change in a diagonal length due to distortion to less than 2 percent of the maximum vertical deflection, the recommended maximum internal diaphragm spacing is 1/5 of the span length. It is not necessary to use an internal diaphragm spacing less than 30 feet. This recommendation is conservative for a girder within the limit of the parametric studies (i.e. maximum length and central angle of 180 ft and 0.3 radians, respectively, and a width to depth ratio of about 1). For a girder outside these limits, a simplified analytical method to calculate the distortional normal stress as a function of internal diaphragm spacing and cross-section dimensions was developed.

12.1.3 Top lateral bracing system

In evaluating different top lateral bracing systems, one needs to consider member force, girder deformation, and normal stress aspects. The following sections provide more detailed discussions of these issues.

12.1.3.1 Member forces

The forces in the top lateral bracing system result from three components: the horizontal component of the applied load due to sloping webs, the vertical bending of the girder, and the torsional moment. Most of the horizontal component of the applied load due to sloping webs is carried by the strut. Compared to the forces from the other components, this force is the smallest.

From a vertical bending standpoint, only the X-type system makes a significant contribution to the overall girder bending stiffness. Both the

Alternating-Diagonal and the Single-Diagonal systems can be assumed to not contribute to the overall girder bending stiffness. Consequently, there are significant forces induced in the X-type system due to vertical bending, whereas there are only small forces induced in the Alternating-Diagonal and Single-Diagonal systems.

From a torsional moment perspective, diagonals in the Alternating-Diagonal system carry significantly higher forces than those in the X-type system because there is only one diagonal resisting the forces as opposed to two. Diagonals in the Single-Diagonal system carry approximately the same forces as those in the Alternating-Diagonal system, except that all of the diagonals are in tension, allowing smaller member sizes. This observation is only true in a simply supported curved girder. In a continuous curved girder, some diagonals will experience a compressive force in a Single-Diagonal system due to the complexity of the torsional moment diagram. However, the maximum compressive diagonal force in a Single-Diagonal system is significantly smaller than that in an Alternating-Diagonal system. Therefore, a smaller member size can be used as the diagonal in a Single-Diagonal system. It should be noted that all strut forces in the Single-Diagonal system are compressive that are significantly larger than those in the Alternating-Diagonal system.

12.1.3.2 Girder deformations

In a straight girder, the vertical deflections of a pseudo-closed section with the Alternating-Diagonal or the Single-Diagonal top lateral bracing system are the same as those of an open section. However, the vertical deflections in a pseudo-closed section with the X-type system are slightly smaller. In addition, it was demonstrated that struts are very effective in preventing bending distortion because they prevent the spreading of the webs.

In a curved girder, the vertical deflections and rotations of a pseudo-closed section are several times smaller than those of an open section. It was shown that the changes in the maximum vertical deflection and rotation of a girder with an equivalent plate thickness larger than 0.03 inches are not very sensitive to the change in equivalent plate thickness. From vertical deflection and rotation standpoints, the minimum recommended equivalent plate thickness is 0.03 inches.

This thesis showed that the vertical deflection is not sensitive to the type of top lateral bracing system, whereas the rotation is sensitive. The rotation variation along the length of a girder with the X-type and the Alternating-Diagonal systems having the same equivalent plate thickness are generally the same. Depending on panel length, changing the diagonal orientation from the Alternating-Diagonal to the Single-Diagonal system results in different rotation variation and larger maximum rotation. As the panel length increases, the difference of the maximum rotation in the two systems becomes larger. For this reason, the maximum recommended panel length in a Single-Diagonal system is equal to the top width of the girder.

Horizontal displacement in a curved girder is also sensitive to equivalent plate thickness. Using a smaller member size will cause the girder to move laterally toward the center of curvature. From a support lateral displacement perspective, the minimum recommended equivalent plate thickness is 0.03 inches.

12.1.3.3 Normal stresses

This thesis presented an analytical formula for determining the required strut spacing in order to limit the additional normal stresses due to lateral bending of the top flanges. It was shown that the required strut spacing depends on the applied load and the dimensions of the top flanges.

The maximum tensile and compressive total normal stresses in a girder with the X-type system are the smallest and those with the Alternating-Diagonal system are the largest. Bending normal stresses in a girder with the X-type system are smaller than those with the Alternating-Diagonal or the Single-Diagonal system. It was shown that changing the diagonal direction from the Alternating-Diagonal to the Single-Diagonal systems results in slight reductions of the maximum tensile and compressive total normal stresses.

The top lateral bracing system is effective in reducing warping normal stresses. In order to limit the ordinary warping normal stress at the junction of the web and the top flange to less than 2.5 percent of the bending normal stress, the minimum recommended equivalent plate thickness is 0.05 inches.

12.1.3.4 Recommendation

The best top lateral bracing system for a straight girder under a symmetrical uniform loading (i.e. no torsional loading) is the strut-only system (i.e. open section). The required strut spacing to limit additional normal stress can be determined using the closed-form formulas given in this thesis.

The best top lateral bracing system for a curved girder is the X-type system. Unfortunately, it usually costs more because it requires more connections. The second best system is the Single-Diagonal system. If the X-type system is undesirable, the recommended design procedure for selecting a top lateral bracing system is as follows:

1. Try Single-Diagonal system with panel length approximately the same as girder top width and equivalent plate thickness greater than 0.05 inches.
2. Check girder rotation and bracing forces.
3. If the rotation is too large, increase the member size or change to Alternating-Diagonal system that automatically reduces rotation.

Changing to Alternating-Diagonal system will result in a significant increase in the maximum compressive force.

12.1.4 Pouring sequence

It is important to evaluate the pouring sequence because the maximum top lateral bracing forces and deformations during the concrete pour can be larger than those after the pour. The recommended pouring sequence with the pour order shown in this thesis is the one with short first, second, and third pours.

12.2 FUTURE RESEARCH

The recommended internal diaphragm spacing presented in this thesis was developed based on the assumption that there is no web stiffener. Previous research indicates that web stiffeners are very effective in controlling cross-section distortion and distortional normal stress. A new recommendation for internal diaphragm spacing with the presence of web stiffeners should be studied. It was shown that the presence of internal diaphragms increases bending normal stress. However, the reason behind this behavior has not been resolved in this thesis. In addition, the analytical formula cannot predict the distortional normal stress at the tip of the top flange. Therefore, further research is required to develop an analytical formula that can predict the distortional normal stress at the top flange tip.

Currently, UTRAP lateral boundary conditions are fixed and free. The fixed boundary condition prevents warping displacements. As a result, there is a rigid body lateral movement even in a simply supported curved girder as shown in Chapter 6. The real girder has elastomeric bearings at its supports. These bearings

have some lateral stiffness and permit warping displacements. In order to imitate the real support, further research is needed to modify UTRAP program so that it can offer a support with some lateral stiffness (i.e. spring support).

APPENDIX A

Determination of Local Plate Bending Stress

Appendix A presents the derivation of local plate bending stress due to distortional loading in a simplified model of a rectangular box section. The distortional loading component on a general box section causes the distortional deformation and the local plate bending moment M_{plate} shown in Figure A.1.

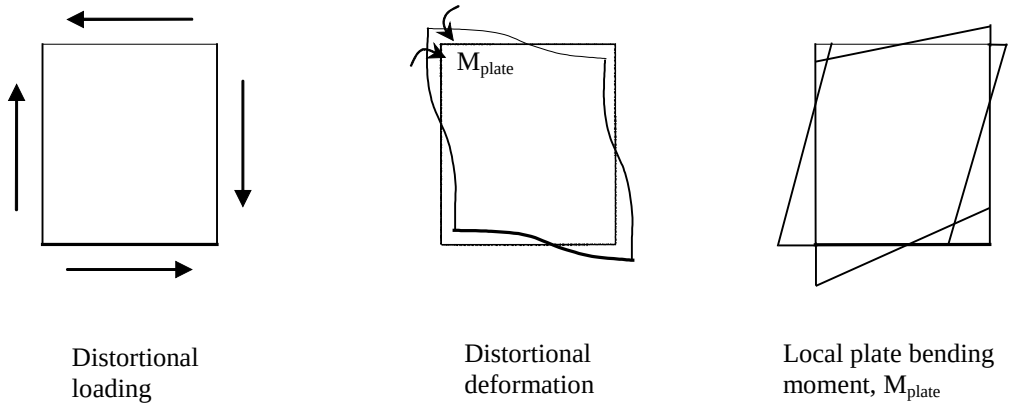

Figure A.1 Distortional deformation and local plate bending moment

The derivations in this appendix deal with open-section rectangular box girders, which have no top plate. Since the equivalent plate thickness in this model is zero, the inflection point of the web is located at the junction of the web and the top flange. Figure A.2 shows the model under a horizontal load *V*, turned upside down for familiarity. The depth and width of the model are *h* and *b*, respectively. The moment of inertias of the web and the bottom flange are I_w and I_{bf}.

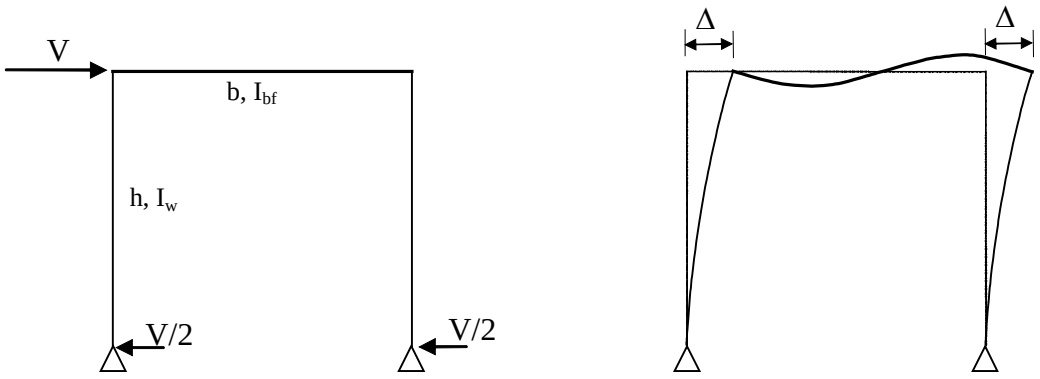

Figure A.2 Simplified model under a horizontal load

Total horizontal displacement Δ of the model is the sum of the horizontal displacement due to cantilever bending of the column (web) $\Delta_{cantilever}$ and that due to bending of the beam (bottom flange) Δ_{beam} as follows:

$$\Delta = \Delta_{cantilever} + \Delta_{beam}$$

$$= \frac{Vh^3}{6EI_w} + \frac{Vbh^2}{12EI_{bf}}$$

$$= \frac{Vh^2}{6E}\left(\frac{h}{I_w} + \frac{b}{2I_{bf}}\right)$$

$$= \frac{Vh^2}{6E}\frac{h}{I_w}\left(1 + \frac{\frac{b}{h}}{\frac{2I_{bf}}{I_w}}\right)$$

$$= \frac{Vh^3}{6EI_w}\left(1 + \frac{G}{2}\right) \qquad \text{(A.1)}$$

where E is the Young's modulus and G is the ratio of the web stiffness to the bottom flange stiffness ($G = \frac{\left(I/L\right)_{web}}{\left(I/L\right)_{bottom\ flange}} = \frac{I_w/h}{I_{bf}/b}$). From Eq.A.1, V can be solved as follows:

$$V = \frac{\Delta}{h}\frac{6EI_w}{h^2\left(1+\frac{G}{2}\right)} \tag{A.2}$$

In the simplified model, the maximum local plate bending moment occurs at the junction of the web and the bottom flange and is denoted $M_{plate,b.}$ This moment is

$$M_{plate,b} = \frac{V}{2}h \tag{A.3}$$

Since the web thickness t_w is smaller than the bottom flange thickness t_{bf} , the maximum local plate bending stress occurs in the web and is denoted $\sigma_{plate,w.}$ This stress is

$$\sigma_{plate,w} = \frac{\frac{V}{2}h}{I_w\frac{2}{t_w}} = \frac{Vht_w}{4I_w} \tag{A.4}$$

Substituting Eq.A.2 into Eq.A.4 results in the following expression:

$$\sigma_{plate,w} = \frac{3}{2}\frac{E}{\frac{h}{t_w}\left(1+\frac{G}{2}\right)}\frac{\Delta}{h} \tag{A.5}$$

Normalizing $\sigma_{plate,w}$ to the yield stress F_y and assuming the bottom flange is very stiff compared to the web (i.e. G=0) results in the following equation:

$$\frac{\sigma_{plate,w}}{F_y} = \frac{\frac{E}{F_y}}{\frac{h}{t_w}} \frac{\Delta}{h} \tag{A.6}$$

If the distortional deformation is limited so that Δ is smaller than 2.5 percent of the midspan vertical deflection δ_{mid} and the yield stress F_y is 50 ksi, Eq.A.6 can be written as follows:

$$\frac{\sigma_{plate,w}}{F_y} = \frac{15}{\left(\frac{h}{t_w}\right)} \frac{\left(\frac{\delta_{mid}}{L}\right)}{\left(\frac{h}{L}\right)} \tag{A.7}$$

where L is the girder length. Eq.A.7 shows that the local plate bending stress is proportional to (δ_{mid}/L) and inversely proportional to (h/t_w) and (h/L). For even extreme values for these variables, $\sigma_{plate,w}$ is less than 0.1 percent of F_y, and can thus be safely ignored.

APPENDIX B
Derivation of Support Torque and Midspan Bending Moment

Appendix B gives a complete derivation of support torque and midspan bending moment presented in Chapter 3 by using force equilibrium, geometric relation, and integration process.

B.1 SUPPORT TORQUE

Figure B. 1 shows all notations used in a complete derivation of support torque and midspan bending moment.

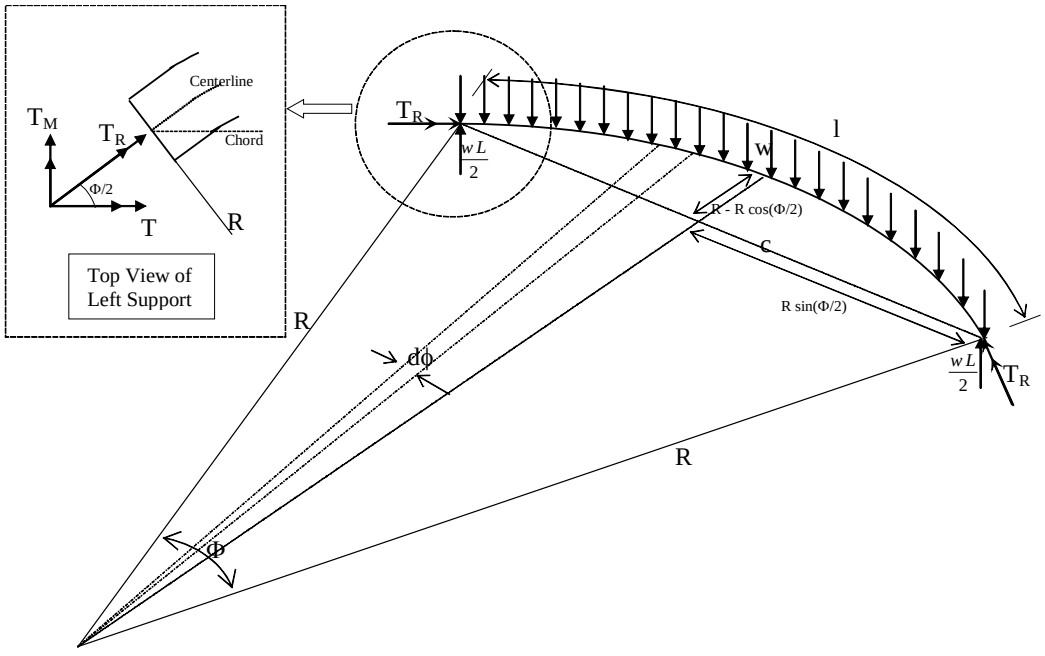

Figure B. 1 Simply-supported curved girder under the uniform load

The first component of torque, *T*, can be found by taking sum of torque at midspan. From torque equilibrium, the midspan torque is known to be zero and *T* is

$$T = \underbrace{\frac{w\,l}{2}}_{\text{Reaction}}\ \underbrace{R\left(1-\cos\left(\frac{\Phi}{2}\right)\right)}_{\text{Reaction Torque arm}} - \underbrace{\left[\int_0^{\frac{\Phi}{2}} \left(w\,R\overbrace{\left(R-R\cos\phi\right)}^{\text{Torque arm}}\right)\mathrm{d}\phi\right]}_{\text{Torque from uniform load}} \qquad \text{(B.1)}$$

Integral of "*Torque from uniform load*" in Eq. B.1 can be evaluated as follows:

$$\begin{aligned}\int_0^{\frac{\Phi}{2}} \left(w\ R\left(R-R\cos\phi\right)\right)\,d\phi &= \int_0^{\frac{\Phi}{2}} w\ R^2\ d\phi - \int_0^{\frac{\Phi}{2}} w\ R^2\cos\phi\ \ d\phi \\ &= w\ R^2\left(\frac{\Phi}{2}\right) - w\ R^2\sin\left(\frac{\Phi}{2}\right) \\ &= w\ R^2\left[\frac{\Phi}{2} - \sin\left(\frac{\Phi}{2}\right)\right] \qquad \text{(B.2)}\end{aligned}$$

Substituting Eq.B.2 to Eq.B.1, *T* can be written as follows:

$$\begin{aligned}T &= \frac{w\ l}{2}\ R\left(1-\cos\left(\frac{\Phi}{2}\right)\right) - w\ R^2\left(\frac{\Phi}{2}-\sin\left(\frac{\Phi}{2}\right)\right) \\ &= \underbrace{\frac{w\ l}{2}\ R\left(1-\cos\left(\frac{\Phi}{2}\right)\right) - w\ R\ \underbrace{R\ \frac{\Phi}{2}}_{\frac{l}{2}} + w\ R\ R\ \sin\left(\frac{\Phi}{2}\right)}_{\frac{w\ l}{2}\ R\left(1-\cos\left(\frac{\Phi}{2}\right)-1\right)}\end{aligned}$$

$$= \frac{w\ l}{2}\ R\left(-\cos\left(\frac{\Phi}{2}\right)\right) + w\ R\ \underbrace{R\left(\frac{\Phi}{2}\right)}_{\frac{l}{2}} \frac{\sin\left(\frac{\Phi}{2}\right)}{\left(\frac{\Phi}{2}\right)}$$

$$= w\ R\ \frac{l}{2}\left(\frac{\sin\left(\frac{\Phi}{2}\right)}{\frac{\Phi}{2}} - \cos\left(\frac{\Phi}{2}\right)\right)$$

$$= w R^2\left(\sin\left(\frac{\Phi}{2}\right) - \frac{\Phi}{2}\cos\left(\frac{\Phi}{2}\right)\right) \qquad \text{(B.3)}$$

Eq.B.3 is the expression of *T*, as can be seen in Eq.3.7.

For a non-skewed support, support torque T_R can be found from geometry as follows:

$$T_R = \frac{T}{\cos\left(\frac{\Phi}{2}\right)}, \text{ where } T \text{ is expressed in Eq.B.3}$$

$$= \frac{w R^2\left(\sin\left(\frac{\Phi}{2}\right) - \frac{\Phi}{2}\cos\left(\frac{\Phi}{2}\right)\right)}{\cos\left(\frac{\Phi}{2}\right)}$$

$$= w\ R^2\left(\tan\left(\frac{\Phi}{2}\right) - \frac{\Phi}{2}\right) \qquad \text{(B.4)}$$

Eq.B.4 is the expression T_R, as seen in Eq.3.8.

B.2 MIDSPAN BENDING MOMENT

Midspan bending moment M_{mid} in a simply supported curved girder can be found by taking the moment equilibrium about midspan and is

$$M_{mid} = \underbrace{T_M}_{\text{Reaction}} + \underbrace{\frac{wl}{2} R \sin\left(\frac{\Phi}{2}\right)}_{\text{Moment arm}} - \underbrace{\left[\int_0^{\frac{\Phi}{2}} w R \overbrace{\left(R \sin\phi\right)}^{\text{Moment arm}} d\phi\right]}_{\text{Moment from uniform load}} \qquad \text{(B.5)}$$

Integral of "*Moment from uniform load*" in Eq.B.5 can be evaluated as follows:

$$\int_0^{\frac{\Phi}{2}} w\ R\left(R\sin\phi\right)\ d\phi = w\ R^2 \int_0^{\frac{\Phi}{2}} \sin\phi\ \ d\phi$$

$$= w\ R^2\left(-\cos\left(\frac{\Phi}{2}\right)+1\right) \qquad \text{(B.6)}$$

Substituting Eqn.(A.6) into Eqn.(A.5), midspan bending moment M_{mid}, can be written as follow:

$$M_{mid} = T_M + \frac{w\ l}{2}\ R\ \sin\left(\frac{\Phi}{2}\right) - \int_0^{\frac{\Phi}{2}} w\ R\left(R\sin\phi\right)\ d\phi$$

$$= w\ R\ \frac{l}{2}\left(\frac{\sin\left(\frac{\Phi}{2}\right)}{\frac{\Phi}{2}} - \cos\left(\frac{\Phi}{2}\right)\right) \tan\left(\frac{\Phi}{2}\right) + \frac{w\ l}{2}\ R\ \sin\left(\frac{\Phi}{2}\right) - w\ R^2\left(1-\cos\left(\frac{\Phi}{2}\right)\right)$$

$$= w\ R\ \frac{l}{2}\left(\frac{\sin\left(\frac{\Phi}{2}\right)}{\frac{\Phi}{2}} - \cos\left(\frac{\Phi}{2}\right)\right)\tan\left(\frac{\Phi}{2}\right) + \frac{w\ l}{2}\ R\ \sin\left(\frac{\Phi}{2}\right) + w\ R^2\cos\left(\frac{\Phi}{2}\right) - w\ R^2$$

$$= w\ R\ \frac{l}{2}\left(\frac{\sin\left(\frac{\Phi}{2}\right)}{\frac{\Phi}{2}}\tan\left(\frac{\Phi}{2}\right) - \underbrace{\cos\left(\frac{\Phi}{2}\right)\tan\left(\frac{\Phi}{2}\right) + \sin\left(\frac{\Phi}{2}\right)}_{0}\right) + w\ R^2\cos\left(\frac{\Phi}{2}\right) - w\ R^2$$

$$\frac{l}{2} = R\left(\frac{\Phi}{2}\right)$$

$$= w\ R^2\ \frac{\Phi}{2}\left(\frac{\sin\left(\frac{\Phi}{2}\right)}{\frac{\Phi}{2}}\tan\left(\frac{\Phi}{2}\right)\right) + w\ R^2\cos\left(\frac{\Phi}{2}\right) - w\ R^2$$

$$= w\ R^2\left(\sin\left(\frac{\Phi}{2}\right)\tan\left(\frac{\Phi}{2}\right) + \cos\left(\frac{\Phi}{2}\right) - 1\right)$$

$$= w\ R^2\left(\frac{\sin\left(\frac{\Phi}{2}\right)\sin\left(\frac{\Phi}{2}\right) + \cos^2\left(\frac{\Phi}{2}\right)}{\cos\left(\frac{\Phi}{2}\right)} - 1\right) \quad \text{(1)}$$

$$= w\ R^2\left(\frac{1}{\cos\left(\frac{\Phi}{2}\right)} - 1\right) \qquad \text{(B.7)}$$

Eq.B.7 is the expression of midspan bending moment M_{mid}, as can be seen in Eq.3.10.

APPENDIX C

Determination of Torsional Moments in Continuous Curved Girder using the M/R Method

Appendix C shows all intermediate steps to determine torsional moment in a continuous curved girder using the M/R Method (Tung and Fountain, 1970), shown in Figure 3.22. The required procedures to determine torsional moment in a continuous curved girder are as follows:

1. Straighten the entire curved girder to its full developed length and determining the bending moments of the girder. Figure C. 1 shows the bending moment of a three-equal-span Model 2 straight girder shown in Figure 3.11.
2. Consider one span at a time, apply the distributed M/R loads on the simply supported straight conjugate beam. Figure C. 2 shows the M/R loadings on the left exterior and interior spans. The radius of curvature in this example is 450 ft.
3. Determine the shear forces in each span of the conjugate beam under the M/R loading. These shear forces correspond to the torsional moments in the real girder. For simplification in determining the shear forces, the M/R loading can be decomposed into parabolic and straight line components as shown in Figure C. 3. The shear forces in each span of the conjugate beam are shown in Figure C. 4.
4. Calculate the total torsional moments in the girder by superimposing the torsional moments due to parabola and straight line components of the M/R loading. Figure C. 5 shows the torsional moment in the left exterior

and interior spans of Model 2 continuous curved girder. For comparison, the UTRAP solution is also shown.

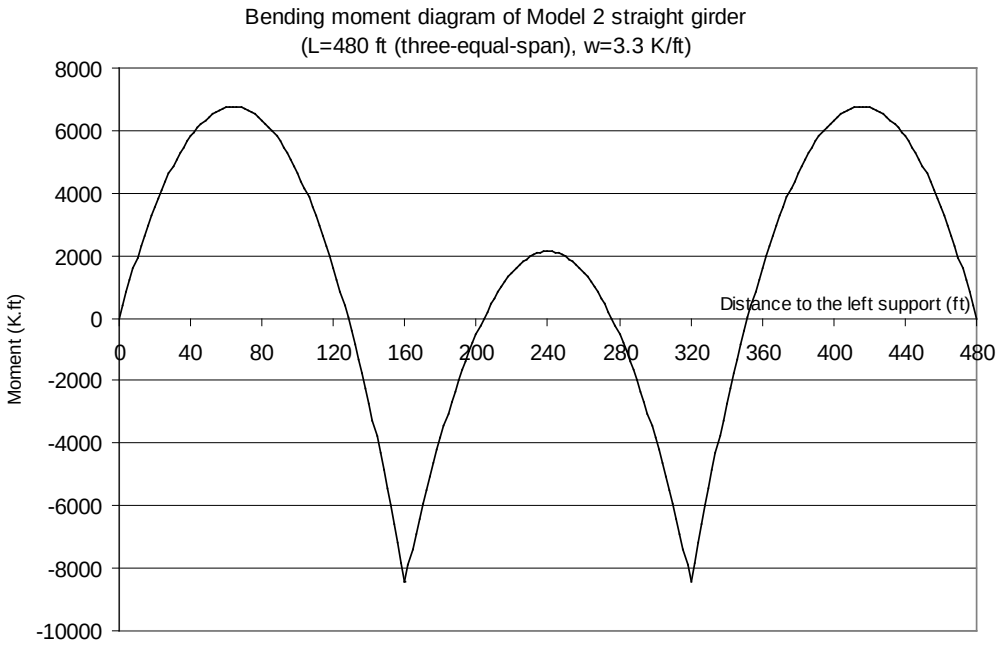

Figure C. 1 Bending moment diagram

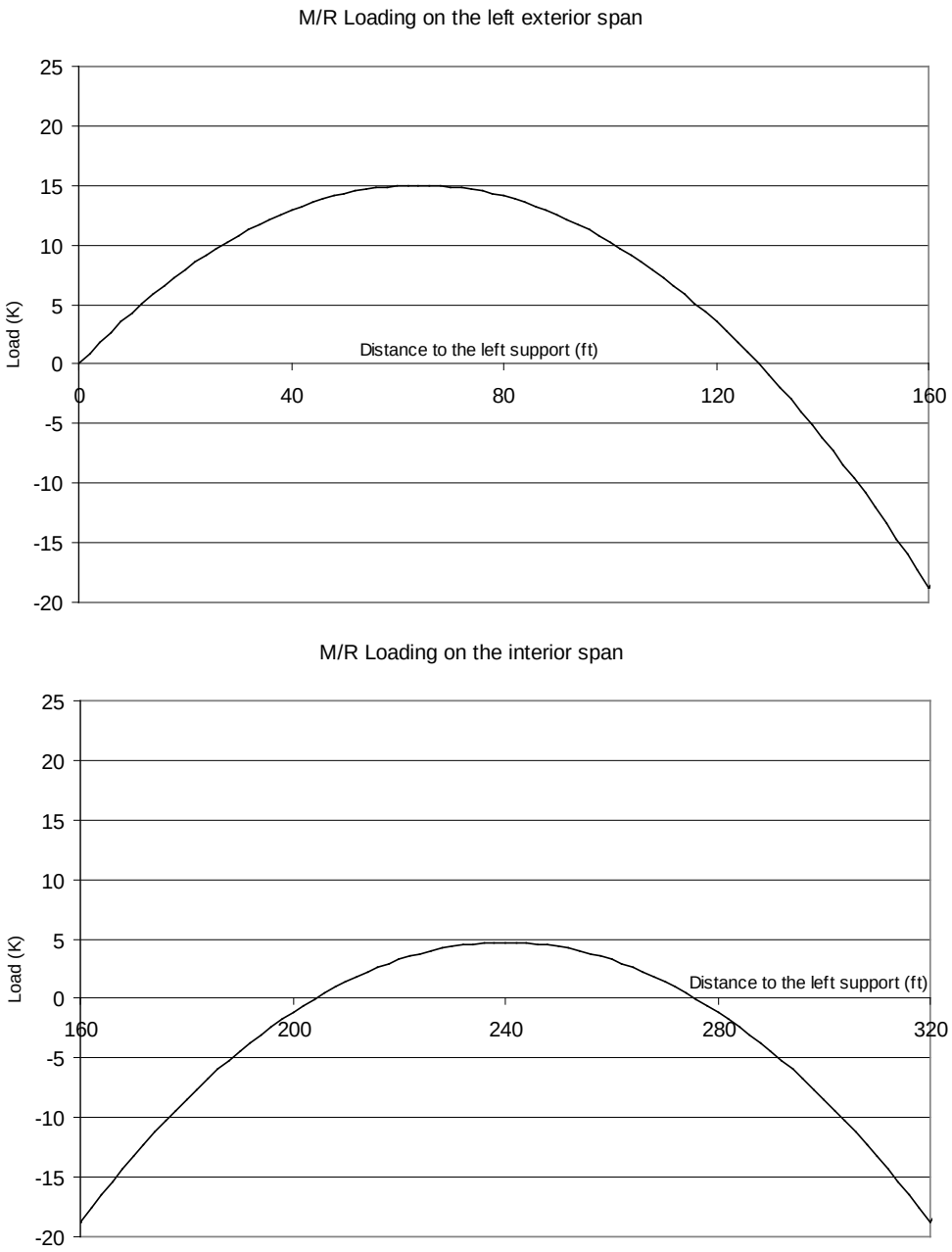

Figure C. 2 M/R loadings on the left exterior and interior spans

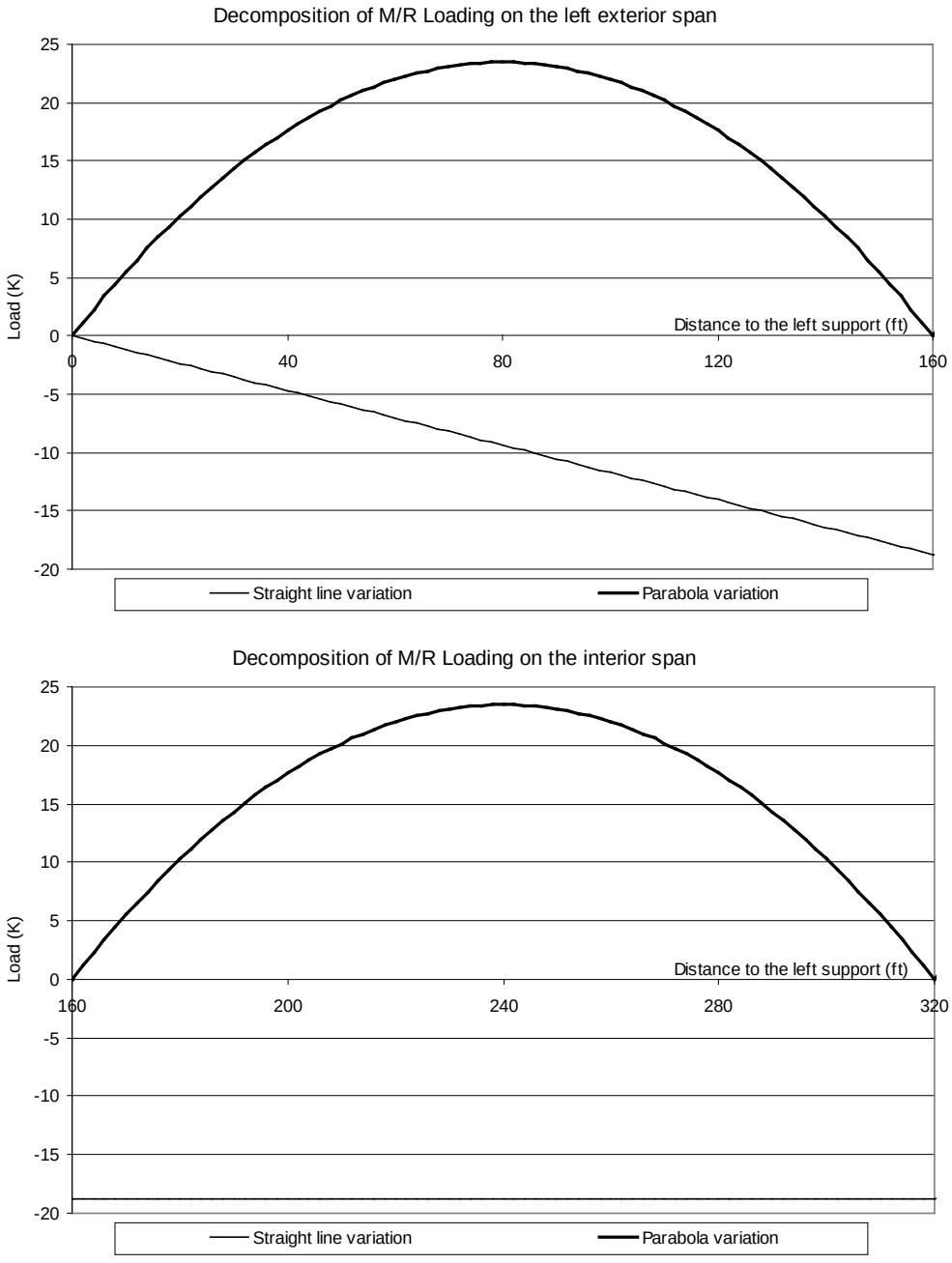

Figure C. 3 Decomposition of the M/R loading into parabolic and straight line components

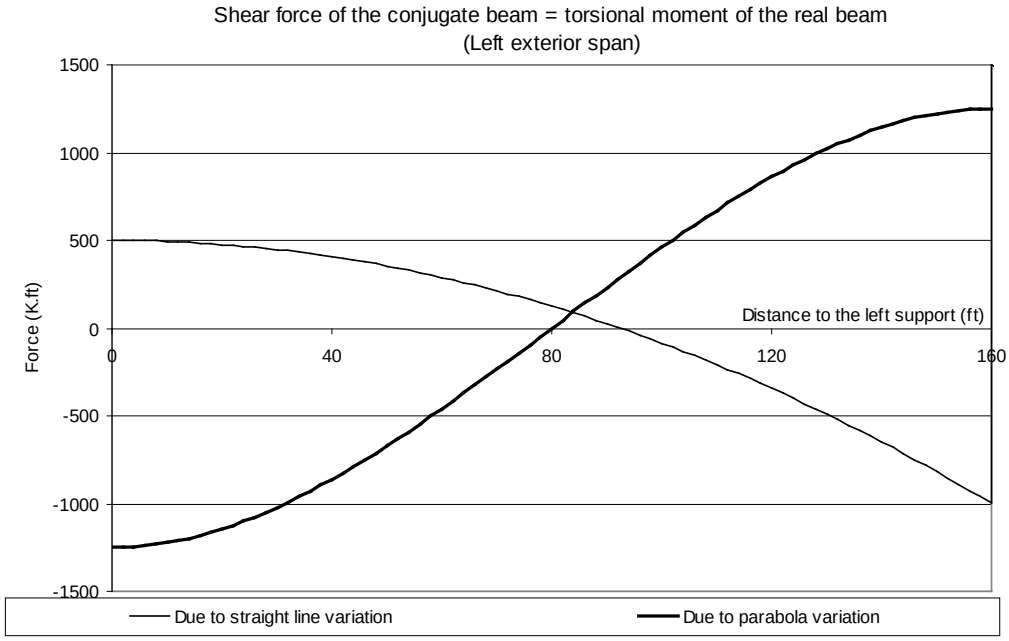

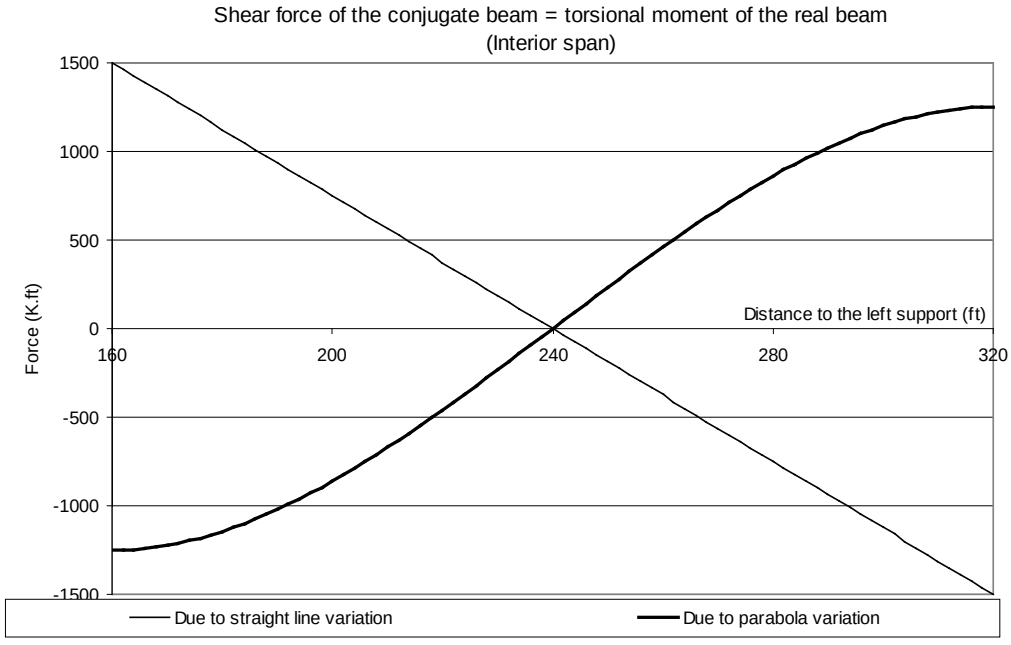

Figure C. 4 Torsional moments of the girder

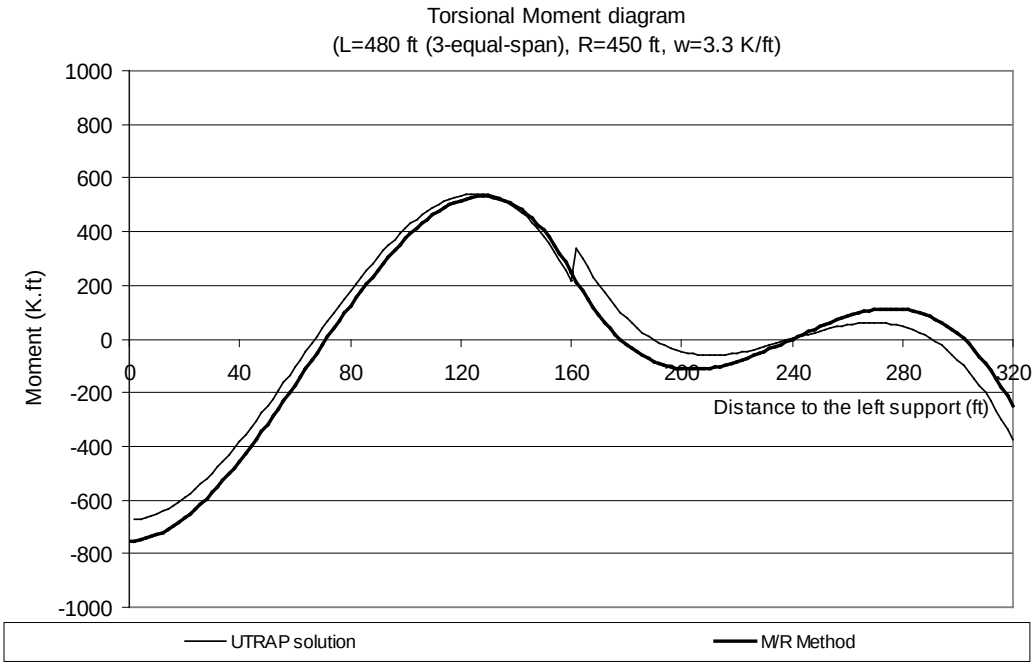

Figure C. 5 Torsional moments in the left exterior and interior spans

APPENDIX D
Equivalent Plate Thickness Formulas

The torsional analysis of a quasi-closed section is usually performed using the Equivalent Plate Method (EPM). Based on the EPM, top lateral bracing system may be replaced by an equivalent wall element of constant thickness t_{eq} in the analysis. This thickness is determined by comparing the angle of shear in the panel of equivalent wall element, shown in Figure D. 1(a), with the angle of shear in the panel of bracing, shown in Figure D. 1(b), due to same loading. It should be noted that *s* and *a* shown in Table D- 1 are panel length (i.e. strut spacing) and top width of girder, respectively.

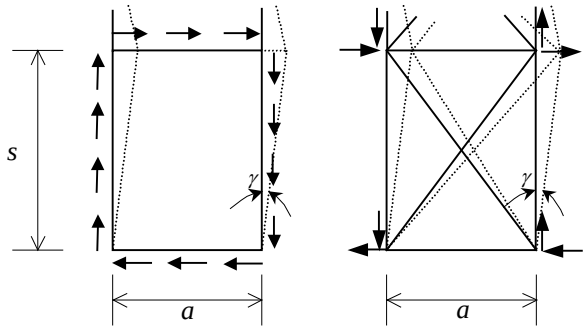

(a) **(b)**

Figure D. 1 Angle of shear in the panel of equivalent wall element and panel of bracing

Based on strain energy equivalency, Kollbrunner and Basler (1969) derived the formulas to determine the equivalent plate thickness t_{eq} for different types of top lateral bracing system. Those formulas are shown in Table D- 1.

Table D- 1 Equivalent plate thickness for different types of top lateral bracing systems

Type of top lateral bracing system	Equivalent plate thickness
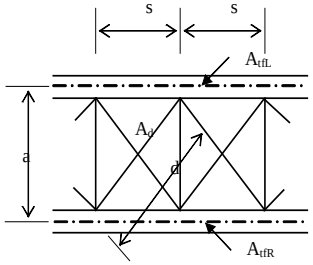 **X-type system**	$t_{eq} = \frac{E}{G} \times \frac{a.s}{\frac{d^3}{2A_d} + \frac{s^3}{12}\left(\frac{1}{A_{tfL}} + \frac{1}{A_{tfR}}\right)}$ (D.1) If both flanges have similar cross-section area ($A_{tfL}=A_{tfR}=A_{tf}$): $t_{eq} = \frac{E}{G} \times \frac{a.s}{\frac{d^3}{2A_d} + \frac{s^3}{6A_{tf}}}$ (D.2)
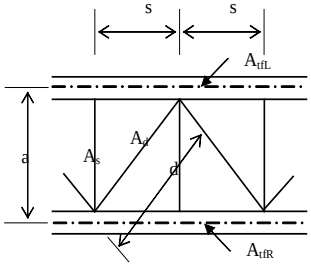 **Alternating-Diagonal system**	$t_{eq} = \frac{E}{G} \times \frac{a.s}{\frac{d^3}{A_d} + \frac{s^3}{3}\left(\frac{1}{A_{tfL}} + \frac{1}{A_{tfR}}\right)}$ (D.3) If both flanges have similar cross-section area ($A_{tfL}=A_{tfR}=A_{tf}$): $t_{eq} = \frac{E}{G} \times \frac{a.s}{\frac{d^3}{A_d} + \frac{2s^3}{3A_{tf}}}$ (D.4)
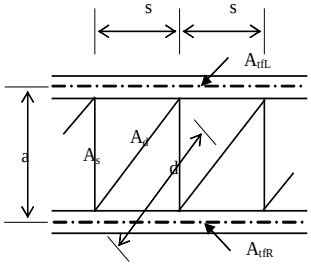 **Single-Diagonal system**	$t_{eq} = \frac{E}{G} \times \frac{a.s}{\frac{d^3}{A_d} + \frac{a^3}{A_s} + \frac{s^3}{12}\left(\frac{1}{A_{tfL}} + \frac{1}{A_{tfR}}\right)}$ (D.5) If both flanges have similar cross-section area ($A_{tfL}=A_{tfR}=A_{tf}$): $t_{eq} = \frac{E}{G} \times \frac{a.s}{\frac{d^3}{A_d} + \frac{a^3}{A_s} + \frac{s^3}{6A_{tf}}}$ (D.6)

where:

a : Top width of girder (measured between centerline of top flange)

s : Panel length (spacing of strut)

d : Diagonal length : $d \cong \sqrt{a^2 + s^2}$

A_{tfL}, A_{tfR} : Cross-sectional area of left and right top flange, respectively

A_d : Cross-sectional area of diagonal bracing member

A_s : Cross-sectional area of strut bracing member

E : Bracing member Young's modulus

G : Bracing member shear modulus

APPENDIX E

Determining Shear Center Location of an Open-section Trapezoidal Box Girder

Appendix E presents more detailed explanations on how to use the force method and the numerical method to locate the shear center of an open-section trapezoidal box girder.

E.1 FORCE METHOD

Figure E. 1 shows the simplified general representation of an open-section trapezoidal box girder whose dimensions will be used in the derivation of the closed-form solution. In general, the shear center of an open-section trapezoidal box girder is located some distance e_y below the bottom flange. The shear center of a singly symmetric section like a trapezoidal box girder is located on the y-axis (axis of symmetry). In order to locate the shear center along the y-axis (i.e. determine e_y), the shear force in the direction of the x-axis V_x is applied through the shear center and the shear stress distribution is determined as shown in Figure E. 2.

The magnitude of shear stress τ at any point in the cross-section is

$$\tau = \frac{V_x Q_Y}{I_Y t} \tag{E.1}$$

The shear stresses at points 1 through 3 are

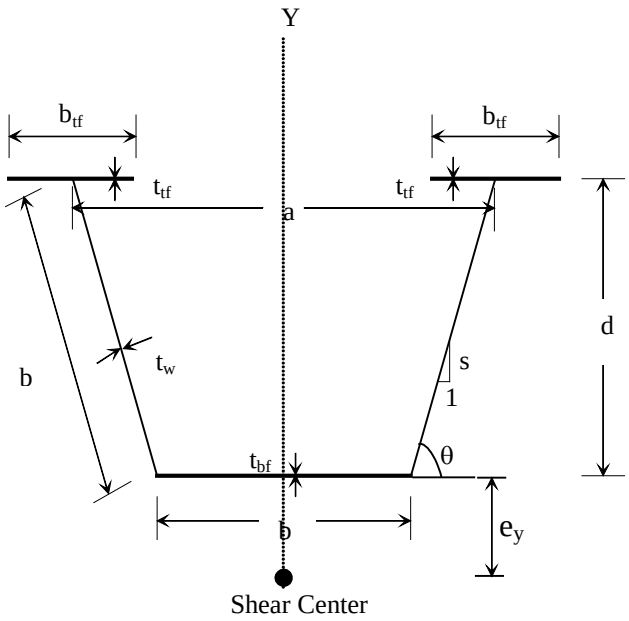

Notations:

a : Girder top width
b_{tf} : Top flange width
t_{tf} : Top flange thickness
s : Slope of sloping web
b_w : Sloping web width, measured from centroid of top flange to centroid of bottom flange
t_w : Sloping web thickness
b_{bf} : Bottom flange width
t_{bf} : Bottom flange thickness
d : Girder depth, measured from centroid of top flange to centroid of bottom flange
A_{tf} : Cross-section area of top flange
A_w : Cross-section area of web
A_{bf} : Cross-section area of bottom flange
e_y : Distance between shear center and the centroidal axis of bottom flange

Figure E. 1 Notations for an open-section trapezoidal box girder

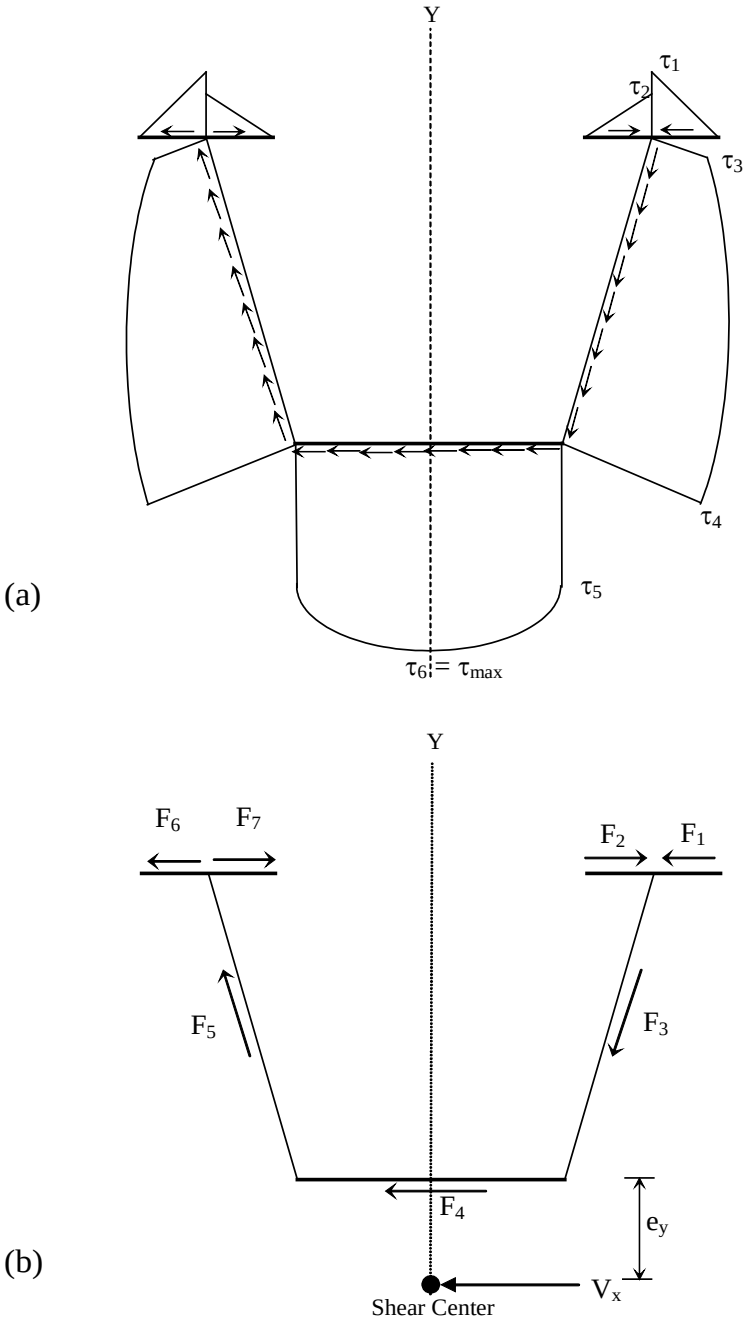

Figure E. 2 Shear stress distribution and shear flow in an open trapezoidal cross-section

$$\tau_1 = \frac{V_X\left(\frac{A_{tf}}{2}\right)\left(\frac{a}{2}+\frac{b_{tf}}{4}\right)}{I_Y t_{tf}} \quad \text{(E.2)}$$

$$\tau_2 = \frac{V_X\left(\frac{A_{tf}}{2}\right)\left(\frac{a}{2}-\frac{b_{tf}}{4}\right)}{I_Y t_{tf}} \quad \text{(E.3)}$$

$$\tau_3 = \frac{V_X\left(A_{tf}\right)\left(\frac{a}{2}\right)}{I_Y t_w} \quad \text{(E.4)}$$

where I_Y is the moment of inertia about the Y-axis.

The general equation for the shear stress along the sloping web τ_w shown in Figure E. 3 is

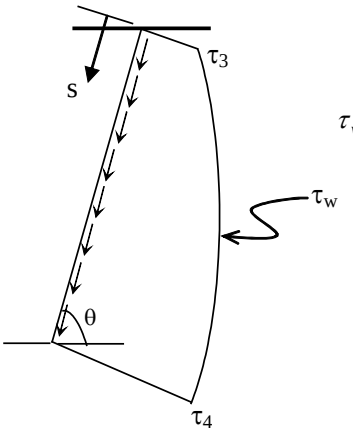

$$\tau_w = \frac{V_X\left(A_{tf}\right)\left(\frac{a}{2}\right)}{I_Y t_w} + \frac{V_X\left(\frac{b_{bf}}{2}+\frac{a-b_{bf}}{2}-\frac{s.\cos\theta}{2}\right)\left(t_w s\right)}{I_Y t_w} \quad \text{(E.5)}$$

Figure E. 3 Shear stress diagram along the sloping web

It should be noted that s in Eq.E.5 is the coordinate system along the sloping web (i.e. $s = 0$ is at the junction between web and top flange and $s = b_w$ is at the junction between web and bottom flange). Shear stress at point 3, τ_3, can be

calculated by plugging in $s = 0$ into Eq.E.5 and τ_4, can be calculated by plugging in $s = b_w$ into Eq.E.5.

The shear flow q on a cross-section is constant even though the thickness of the section wall varies. Therefore, shear flow at point 5, q_5, must equal to the shear flow at point 4, q_4. And τ_5 is

$$
\begin{aligned}
q_5 &= q_4 \\
\tau_5 t_{bf} &= \tau_4 t_w \\
\tau_5 &= \left(\frac{t_w}{t_{bf}}\right)\tau_4 \\
\tau_5 &= \left(\frac{t_w}{t_{bf}}\right)\left(\frac{V_X\left(A_{tf}\right)\left(\frac{a}{2}\right)}{I_Y t_w} + \frac{V_X\left(\frac{b_{bf}}{2} + \frac{a-b_{bf}}{2} - \frac{b_w.\cos\theta}{2}\right)\left(t_w b_w\right)}{I_Y t_w}\right)
\end{aligned}
\qquad \text{(E.6)}
$$

Having calculated τ_5, the shear stress at point 6, τ_6, can be calculated and expressed in Eqs. E.7. It should be noted that τ_6 is the shear stress at the neutral axis (Y-axis) and it is the maximum shear stress.

$$\tau_6 = \tau_5 + \frac{V_X\left(\frac{A_{bf}}{2}\right)\left(\frac{b_{bf}}{4}\right)}{I_Y t_{bf}} \qquad \text{(E.7)}$$

For a thin-walled cross-section, the shear stress due to bending τ is assumed to be constant across the thickness of the wall. Therefore, the equivalent force F of the shear stress τ acting on the wall thickness t is

$$F = (\text{Area under } \tau\text{-diagram})\,(t) \qquad \text{(E.8)}$$

Knowing the shear stress distribution diagram (shown in Figure E. 2(a)) and the values of τ_1 through τ_6, the equivalent shear force F on each element can be calculated and expressed in Eqs.E.9 through E.15.

$$F_1 = \left(\frac{1}{2}\tau_1 \frac{b_{tf}}{2}\right) t_{tf}$$

$$= \frac{V_X A_{tf}\left(\frac{a}{2} + \frac{b_{tf}}{4}\right) b_{tf}}{8 I_Y} \qquad \text{(E.9)}$$

$$F_2 = \left(\frac{1}{2}\tau_2 \frac{b_{tf}}{2}\right) t_{tf}$$

$$= \frac{V_X A_{tf}\left(\frac{a}{2} - \frac{b_{tf}}{4}\right) b_{tf}}{8 I_Y} \qquad \text{(E.10)}$$

$$F_3 = \left(\int_0^{bw} \tau_w ds\right) t_w$$

$$F_3 = \frac{V_X}{I_Y}\left(\frac{1}{2} a A_{tf} b_w + t_w\left(\frac{1}{4} a {b_w}^2 - \frac{1}{6}(\cos\theta){b_w}^3\right)\right) \qquad \text{(E.11)}$$

$$F_4 = \left(\tau_5 b_{bf} + \frac{2}{3}(\tau_6 - \tau_5) b_{bf}\right) t_{bf}$$

$$F_4 = \frac{V_X b_{bf}}{I_Y}\left(\frac{A_{tf} a}{2} + \frac{A_w (a + b_{bf})}{4} + \frac{2}{3} b_{bf} \frac{A_{bf}}{8}\right) \qquad \text{(E.12)}$$

Knowing F_1 through F_4 and using the advantage of symmetrical shear stress distribution, F_5 through F_7 are

$$F_5 = F_3 \qquad \text{(E.13)}$$

$$F_6 = F_1 \qquad \text{(E.14)}$$

$$F_7 = F_2 \tag{E.15}$$

All seven equivalent shear forces (F_1 through F_7) must be statically equivalent to the resultant force V_X acting through the shear center. In other words, the following relationships must be satisfied:

$$\Sigma F_x = 0 \;\Rightarrow\; F_1 - F_2 + F_3 \cos\theta + F_4 + F_5 \cos\theta + F_6 - F_7 = V_X \tag{E.16}$$

$$\Sigma F_y = 0 \;\Rightarrow\; F_3 \sin\theta = F_5 \sin\theta \;\Rightarrow\; F_3 = F_5 \tag{E.17}$$

In addition, the moment of the shear force V_X about any point in the cross-section is equal to the moment of all seven equivalent shear forces (F_1 through F_7) about the same point. This moment relationship provides an equation from which the distance e_y to the shear center can be found. It is usually convenient to take the moment about the shear center, where the moment produced by V_X is zero. For an open-section trapezoidal box girder, the sum of moment about shear center is

$$\begin{gathered}(F_1 - F_2 + F_6 - F_7)(d + e_y) + F_4 e_y - 2 F_3 w = 0 \\ 2 (F_1 - F_2)(d + e_y) + F_4 e_y - 2 F_3 w = 0\end{gathered} \tag{E.18}$$

where w is the perpendicular distance from the sloping web to the shear center as shown in Figure E. 4 and is expressed in Eq.E.19 as follows:

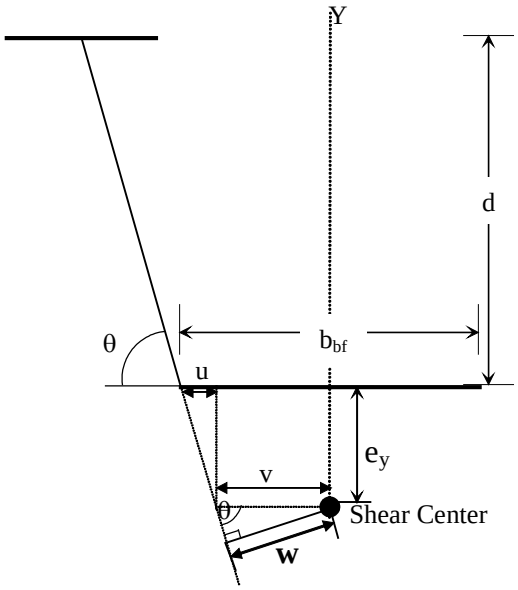

$$\tan\theta = \frac{e_y}{u} \quad \Rightarrow \quad u = \frac{e_y}{\tan\theta}$$

$$v = \frac{b_{bf}}{2} - u$$

$$\sin\theta = \frac{w}{v} \Rightarrow w = v\sin\theta$$

$$w = \left(\frac{b_{bf}}{2} - u\right)\sin\theta$$

$$w = \left(\frac{b_{bf}}{2} - \frac{e_y}{\tan\theta}\right)\sin\theta \qquad \text{(E.19)}$$

Figure E. 4 Perpendicular distance from sloping web to the shear center

Distance e_y can be found by plugging in F_1, F_2, F_3, F_4, and w into equation E.18. The final closed-form solution of e_y is

$$e_y = \frac{2s\left\{db_{bf}\left[aA_{tf} + \frac{1}{2}\left(a - \frac{2}{3}\frac{d}{s}\right)A_w\right] - \frac{1}{4}db_{tf}{}^2A_{tf}\right\}}{sb_{tf}{}^2\left(A_w + \frac{A_{bf}}{3}\right) + 2asb_{bf}\left(A_{tf} + \frac{A_w}{2}\right) + 4\left[\left(ad + \frac{b_{tf}{}^2s}{8}\right)A_{tf} + \frac{1}{2}\left(a - \frac{2}{3}\frac{d}{s}\right)dA_w\right]} \quad \text{(E.20)}$$

E.2 NUMERICAL METHOD

This section presents a more detailed procedure and numerical example for determining the shear center location for an open-section trapezoidal box girder by using a numerical method proposed by Heins (1975). In order to apply the numerical method, the reference point (i.e. starting point of element's flow vector for the entire cross-section) and the element's flow vector needs to be determined first. Figure E. 5(a) shows the simplified representation of an open-section trapezoidal box girder and Figure E. 5(b) shows the chosen reference point and element's flow vector. The choice of flow direction is arbitrary.

Table E- 1 shows the required input that needs to be determined to use the numerical method. The dimensions used in Table E- 1 are shown in Figure E. 1. For simplification, it is sufficient to use the dimensions of the centroidal axis of each element. The procedure to determine the shear center location using the numerical method can be summarized as follows:

1. Find the centroid of the cross-section (i.e. determine y_c using Eq.4.1)
2. Find the moment of inertia about the y-axis I_y.
3. List the x and y-coordinates of all points on the cross-section (columns (2) and (3) in Table E- 1). The origin of the x-y coordinate system is chosen at the centroid.

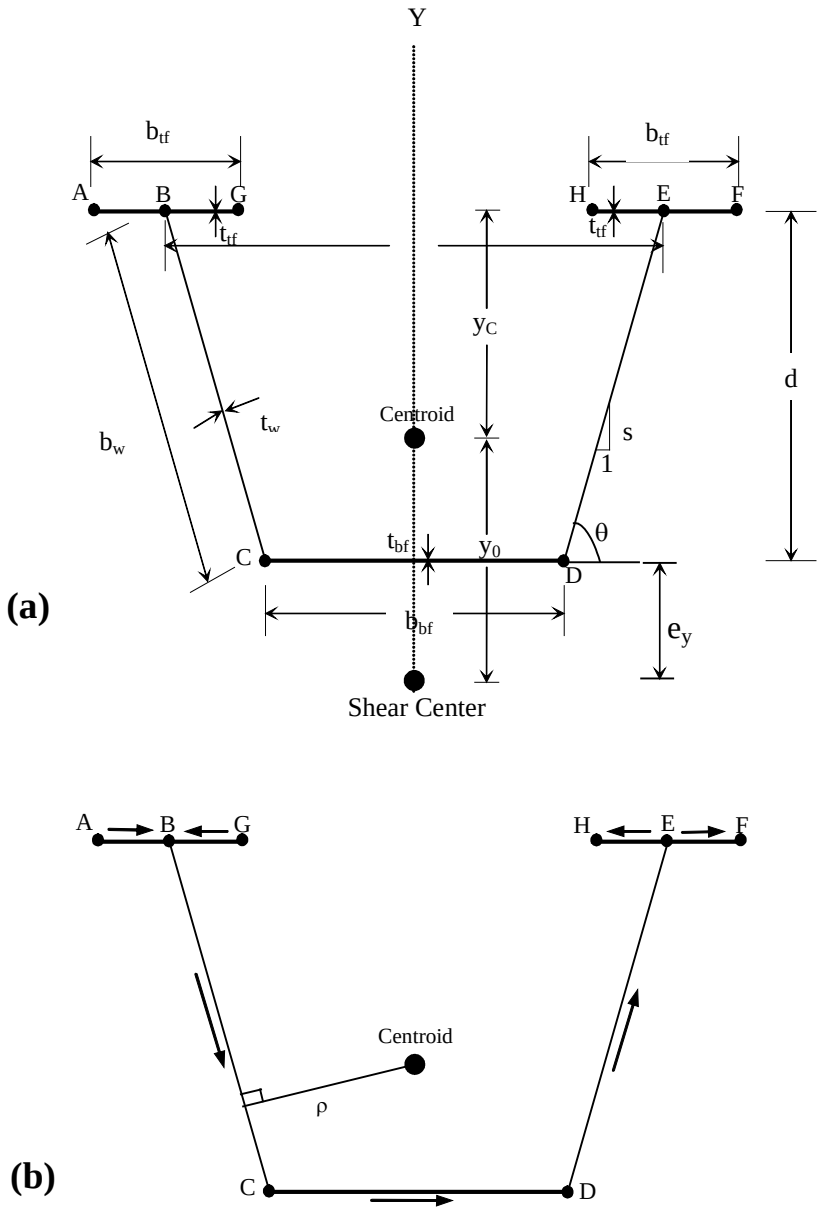

Figure E. 5 Selected element's flow vector on open-section trapezoidal box girder

4. List the thickness and length of each element (columns (4) and (5) in Table E- 1)
5. Calculate the perpendicular distance ρ from the centroid of the cross-section to the tangent line between the end points of each element (column (6) in Table E- 1). The sign of ρ_{ij} is defined as positive if the centroid of cross-section resides on the left-hand side of the element *ij*, whose flow vector goes from point *i* to point *j*.
6. Calculate $w_{ij} = \rho_{ij} * L_{ij}$ for each element.
7. Determine the absolute value of w at each point by summing the w_{ij} values and assuming $w_A = 0$, where A is the reference point.
8. Determine I_{wx} using Eq.4.9.
9. Determine the location of shear center with respect to centroid of cross-section using Eq.4.8.

Table E- 2 shows the numerical example of finding the shear center of Model 1, which is shown in Figure E. 6.

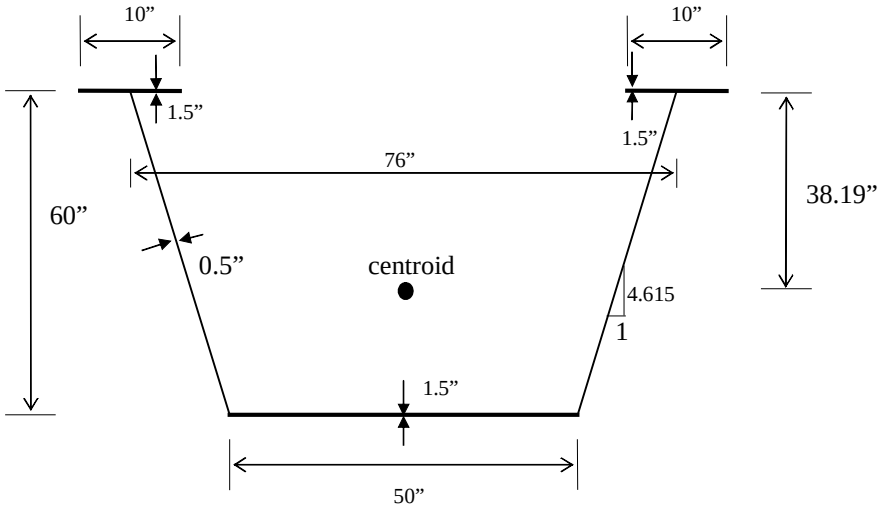

Figure E. 6 Cross-section dimension of the open-section of Model 1

Table E- 1 Required input to determine shear center using numerical method

(1)	(2)	(3)	(4)	(5)	(6)
Point	x	Y	t_{ij}	L_{ij}	ρ_{ij}
A	$-\frac{(a+b_{tf})}{2}$	y_C			
			t_{tf}	$\frac{b_{tf}}{2}$	$-y_C$
B	$-\frac{a}{2}$	y_C			
			t_w	b_w	$\left(\frac{a}{2}-\frac{y_C}{s}\right)\frac{d}{b_w}$
C	$-\frac{b_{bf}}{2}$	d - y_C			
			t_{bf}	b_{bf}	d - y_C
D	$\frac{b_{bf}}{2}$	d - y_C			
			t_w	b_w	$\left(\frac{a}{2}-\frac{y_C}{s}\right)\frac{d}{b_w}$
E	$\frac{a}{2}$	y_C			
			t_{tf}	$\frac{b_{tf}}{2}$	$-y_C$
F	$\frac{(a+b_{tf})}{2}$	y_C			
B	$-\frac{a}{2}$	y_C			
			t_{tf}	$\frac{b_{tf}}{2}$	$-y_C$
G	$-\frac{(a-b_{tf})}{2}$	y_C			
E	$\frac{a}{2}$	y_C			
			t_{tf}	$\frac{b_{tf}}{2}$	y_C
H	$\frac{(a-b_{tf})}{2}$	y_C			

From Chapter 4, the distance between the centroidal axis and the centroidal axis of its top flange is 38.19 inches.

The location of the shear center with respect to the centroid y_0 is

$$y_0 = -\frac{I_{wx}}{I_y} \tag{E.21}$$

where I_y = 120976 in^4. I_y value corresponds to the dimensions of the centroidal axis of each element. It is slightly different than I_y obtained using Eq.4.3. Having calculated both I_{wx} and I_y, y_0 can be calculated as follows:

$$y_0 = -\frac{I_{wx}}{I_y} = -\frac{5883770}{120976} = -48.6 \text{ inch}$$

Therefore, the shear center of Model 1 is located 48.6 inches below the centroid of the cross-section or 26.8 inches below the centroidal axis of the bottom flange.

Table E- 2 Numerical example to find shear center for Model 1

Point	X	Y	t_{ij}	L_{ij}	$t_{ij} L_{ij}$	ρ_{ij}	w_{ij}	w	$w_i \cdot X_i$	$w_j \cdot X_j$	$w_i \cdot X_j$	$w_j \cdot X_i$	$(w_iX_i+w_jX_j)tL$	$(w_iX_j+w_jX_i)tL$
A	-43.00	38.19						0						
			1.50	5.0	7.5	-38.2	-191		0	7256	0	8211	54419	61580
B	-38.00	38.19						-191						
			0.500	61.4	30.7	29.1	1784		7256	-39815	4774	-60519	-999434	-1711154
C	-25.00	-21.81						1593						
			1.50	50.0	75.0	21.8	1091		-39815	67079	39815	-67079	2044781	-2044781
D	25.00	-21.81						2683						
			0.500	61.4	30.7	29.1	1784		67079	169734	101960	111667	7269226	6557506
E	38.00	38.19						4467						
			1.50	5.0	7.5	-38.2	-191		169734	183857	192068	162478	2651933	2659093
F	43.00	38.19						4276						
B	-38.00	38.19						*-191*						
			1.50	5.0	7.5	-38.2	-191		7256	12604	6301	14514	148951	156113
G	-33.00	38.19						-382						
E	38.00	38.19						*4467*						
			1.50	5.0	7.5	38.2	191		169734	153704	147401	176992	2425783	2432946
H	33.00	38.19						4658						
Sum					166								**13595660**	**8111302**

I_{wx} can be found by using Eq.4.9 as follows:

$$I_{wx} = \frac{1}{3}\Sigma\left(w_i x_i + w_j x_j\right)t_{ij} L_{ij} + \frac{1}{6}\Sigma\left(w_i x_j + w_j x_i\right)t_{ij} L_{ij} = \frac{1}{3}(13595660) + \frac{1}{6}(8111302) = 5883770 \text{ in}^5$$

APPENDIX F

Table for Area Integration of Two Linear Functions

Table F- 1 Table of area integration of two functions F1 and F2: $\int_A F_1 F_2 \, dA$

F_1 \ F_2	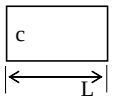	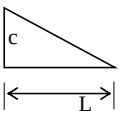	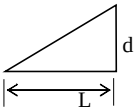	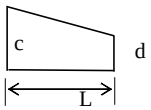
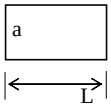	a c (A)	$\frac{1}{2}ac(A)$	$\frac{1}{2}ad(A)$	$\frac{1}{2}a(c+d)(A)$
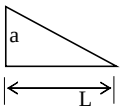	$\frac{1}{2}ac(A)$	$\frac{1}{3}ac(A)$	$\frac{1}{6}ad(A)$	$\frac{1}{6}a(2c+d)(A)$
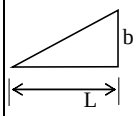	$\frac{1}{2}bc(A)$	$\frac{1}{6}bc(A)$	$\frac{1}{3}bd(A)$	$\frac{1}{6}b(2d+c)(A)$
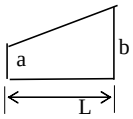	$\frac{1}{2}c(a+b)(A)$	$\frac{1}{6}c(2a+b)(A)$	$\frac{1}{6}d(2b+a)(A)$	$\frac{1}{6}\left\{\begin{matrix} a(2c+d) \\ +b(2d+c) \end{matrix}\right\}(A)$

Note: A : Area = L * thickness of the element

References

AASHTO (2003). "Guide specifications for horizontally curved steel girder highway bridges." American Association of State Highway and Transportation Officials, Washington, D.C.

AISC. (2003). *Manual of steel construction. Load & resistance factor design.* American Institute of Steel Construction, Chicago, Illinois.

Barber, J. (2001). *Intermediate mechanics of materials*. McGraw-Hill, Boston.

Basler, K., and Kollbrunner, C. F. (1969). *Torsion in structures – An engineering approach*, Springer-Verlag, Berlin, Germany.

Bickford, W. (1998). *Advanced mechanics of materials*, Addison-Wesley, Menlo Park, California.

Boresi, A.P., Sidebottom, O.M., Seely, F.B., and Smith, J.O. (1978). *Advanced Mechanics of Materials*, John Wiley and Sons, New York.

Branco, F.A. (1981). "Composite box girder bridge behavior," thesis presented to the University of Waterloo, in partial fulfillment of the requirements for the degree of Master of Applied Science.

Branco, F.A. and Green, R. (1985). "Composite Box Girder Behavior During Construction." *Journal of the Structural Engineering Division*, ASCE, Vol. 111, No.3, March, pp.577-593.

Chen, B. S. (1999). "Top flange lateral bracing of steel U-shaped girders." thesis presented to The University of Texas at Austin, in partial fulfillment of the requirements for the degree of Master of Science in Engineering.

Chen, B. S. (2002). "Top-lateral bracing systems for trapezoidal steel box-girder bridges." dissertation presented to The University of Texas at Austin, in partial fulfillment of the requirements for the degree of Doctor of Philosophy.

Dabrowski, R. (1968). *Curved Thin-Walled Girders-Theory and Analysis*. Translation, Cement and Concrete Association, London.

Flint, A.R. (2001). Steel Box Girder Bridges. The Institution of Structural Engineers. (*http://www.istructe.org.uk/technical/index.asp?page=47*) (March 20 2002)

Gere, J.M. and Timoshenko, S.P. (1997). *Mechanics of materials*. 4th Edition. PWS Pub Co., Boston.

Green, R. (1978). *Composite box girder bridges – The construction phase.* Canadian Structural Engineering Conference.

Hall, Dann H. (1997). "Why Steel Box Girders?" *Modern Steel Construction*, AISC, Vol. 37, No.4, April, pp.13-16.

Heins, C.P. (1975). *Bending and Torsional Design in Structural Members*. Lexington Books, Lexington, Massachusetts.

Heins, C.P. (1978). "Box Girder Bridge Design—State of the Art." *Engineering Journal*, AISC, Vol. 15, No. 4, Fourth Quarter, pp. 126-142.

Helwig, T. and Fan, Z. (2000). “Field and computational studies of steel trapezoidal box girder bridges,” *Research Report No. 1395-3*, The University of Houston, August.

Megson, T.H.G. (1999). *Aircraft Structures for engineering students*. Third Edition. Arnold, London.

Memberg, M.A. (2002). “A design procedure for intermediate external diaphragms on curved steel trapezoidal box girder bridges” thesis presented to The University of Texas at Austin, in partial fulfillment of the requirements for the degree of Master of Science in Engineering.

Nakai, H. and Yoo, C.H. (1988). *Analysis and Design of Curved Steel Bridges*. McGraw-Hill Book Company, New York.

Tung, D.H. and Fountain, R.S. (1970). “Approximate torsional analysis of curved box girders by the M/R method” *Engineering Journal*, AISC, Vol 7, No. 3, pp. 65-74.

Oleinik, J.C. and Heins, C.P. (1974). “Diaphragm spacing requirements for curved steel box beam bridges.” *C.E. Report No. 58*, Civil Engineering Research, Civil Engineering Department, University of Maryland at College Park, Maryland, August.

Oleinik, J.C. and Heins, C.P. (1975). “Diaphragms for curved box beam bridges.” *Journal of the Structural Engineering Division*, ASCE, Vol. 101, No.ST10, Oct, 1975, pp.2161-2179.

Seaburg, P.A. and Carter, C.J. (1997). *Steel Design Guide for Torsional Analysis of Structural Steel Members*. Steel design guide series 9. American Institute of Steel Construction, Chicago.

Sennah, K.M and Kennedy, J.B. (2001). “State of the Art in Design of Curved Box-Girder Bridges.” *Journal of Bridge Engineering*, Vol. 6, No. 3, May/June, pp. 159-167.

Sennah, K.M. and Kennedy, J.B. (2002). “Literature Review in Analysis of Box-Girder Bridges.” *Journal of Bridge Engineering*, American Society of Civil Engineers, Vol. 7, No. 2, March/April, pp. 134-143.

Siddiqui, A.H. (1985). “Effects of diaphragms on warping and distortional stresses in box girder bridges.” thesis presented to the University of Ottawa, Ontario, Canada in partial fulfillment of the requirements for the degree of Master of Applied Science in Civil Engineering.

Siddiqui, A.H. and Ng, S. F. (1988). “Effect of Diaphragms on Stress Reduction in Box Girder Bridge Sections.” *Canadian Journal of Civil Engineering*, National Research Council Canada, Vol. 15(1), February, pp.127-135.

Topkaya, C., Yura, J.A., Williamson, E.B., and Frank, K.H. (2002). UTRAP: Finite-element-based software for the analysis of curved trapezoidal girders under construction loads. *Report No. FHWA/TX-03/1898-3*. Texas Department of Transportation, Research and Technology Implementation Office, Austin, Texas.

US Steel. (1978). *Steel / Concrete Composite Box-Girder Bridges: A Construction Manual*. United States Steel

Vlasov, V. Z. (1961). *Thin-walled elastic beams*. 2nd edition, National Science Foundation, Washington D.C.

Wolchuk, R. and Mayrbaurl. (1980). “Proposed design specifications for steel box girder bridges.” *Final Report No. FHWA-TS-80-205*. U.S. Department of

Transportation, Federal Highway Administration, Office of Development, Washington D.C.

Wright, R.N., Abdel-Samad, S.R., Robinson, A.R. (1968). "BEF Analogy for Analysis of Box Girders." *Journal of the Structural Engineering Division*, ASCE, Vol. 94, No.ST7, July, pp.1719-1743.

Yabuki, T. and Arizumi, Y. (1989). "A Provision on intermediate diaphragm spacing in curved steel-plated box-bridge-girders." *Structural Engineering / Earthquake Engineering*, Japan Society of Civil Engineers, Vol. 6, No.2, October, pp. 207-216.

Young, W.C. and Budynas, R.G. (2002). *Roark's formulas for stress and strain.* 7th edition. Mc.Graw-Hill, New York.

Zbirohowski-Koscia, K. (1967). *Thin walled beams: From theory to practice.* Crosby Lockwood & Son Ltd, London.

Vita

Widianto was born in Jakarta, Indonesia, to Hadi Wibowo and Widyastuti Grahita on July 13, 1980. After completing his work at Regina Pacis High School in Bogor, Indonesia, he attended Iowa State University from August 1998 to August 2000. In 1999 and 2000, he received the Annual Scholars and Leaders Recognition for the Top 2 % in Academic Ranking in the College of Engineering. In August 2000, he transferred to The University of Texas at Austin. In the spring of 2001, he was awarded the Undergraduate Research Fellowship from The University Cooperative Society and The University of Texas at Austin. He received the degree of Bachelor of Science in Civil Engineering with Highest Honors from The University of Texas at Austin in December 2001.

In January 2002, he enrolled in the structural engineering graduate program at The University of Texas at Austin. He has been employed as a Graduate Research Assistant while in pursuit of his graduate degree. After graduating, he plans to pursue a PhD in structural engineering at The University of Texas at Austin.

Permanent Address: 1801 S. Lakeshore Blvd. # 209
Austin, TX 78741

This thesis was typed by the author